Gas Turbines

edited by
Injeti Gurrappa

Gas Turbines
Edited by Injeti Gurrappa

Contents

Preface

During my experience of research for the last 25 years, I have felt the need for a text book written specifically for Design Engineers and Materials Scientists. Although there have been a number of excellent books written on the subject, they are now either out of date or fundamental in nature. There is a growing need to adopt advanced techniques / technologies to meet the ever increasing demand for high efficiency in existing engines and to develop modern gas turbines for strategic and special applications. The aim, therefore, has been to fill this gap and provide recent developments not only in designing modern engines for a variety of applications, maintaining them with maximum efficiency for more than a designed period but also the associated topics of life time modeling and failure investigations.

This book is intended to provide valuable information for the analysis and design of various gas turbine engines for different applications. The target audience for this book is design, maintenance, materials, aerospace and mechanical engineers. The design and maintenance engineers in the gas turbine and aircraft industry will benefit immensely from the integration and system discussions in the book. The chapters are of high relevance and interest to manufacturers, researchers and academicians as well.

This book covers a broad spectrum of chapters spanning the entire gas turbine and aerospace industry- from advances in engine design and characterization for engineering design, high temperature corrosion, design and development of smart protective coatings to provide total protection, turbine monitoring, diagnostics, various types of gas turbines, life prediction modeling and finally failure analysis of coatings and components. The contents provide useful feedback for further developments aimed at effective utilization of various types of gas turbines. The book comprises articles that bring out contemporary developments in gas turbines and thematically classified into the following categories:

1. ADVANCES IN DESIGNING GAS TURBINE COMPONENTS
2. GAS TURBINE TECHNOLOGIES
3. APPLICATIONS OF GAS TURBINES
4. ENVIRONMENTAL EFFECTS
5. COATINGS DEVELOPMENT AND THEIR APPLICATIONS
6. MONITORING AND DISGNOSTICS
7. LIFE PREDICTION

The book commences with articles on advances in designing gas turbine engines and related technologies, thus opening up the areas of challenge for designers, researchers and academia. Several issues which are of interest to industry, researchers, maintenance engineers and academicians such as the effect of environmental effects, the role of coatings for life time enhancement which in turn for increased efficiency, production of electricity cogeneration, monitoring and assessment of turbines and coatings as well as related topics have been addressed in the book.

Life prediction of components and coatings is a very important aspect in gas turbines. Hence, the emphasis on life prediction modeling of materials and coatings has been described. Several articles focus on integrity of gas turbine components as well as damage and performance assessment. In addition, failure investigations with advanced techniques and numerical analysis issues have also been addressed.

The editor thanks all the contributors for the rich technical content of the chapters based on their vast experience and expertise. The editor also thanks the Sciyo Publishers for their timely efforts in the publication of this book.

September 2010

Editor

Prof. Dr. Injeti Gurrappa
Defence Metallurgical Research Laboratory
Kanchanbagh PO, Hyderabad,
India

Advances in Aerodynamic Design of Gas Turbines Compressors

Ernesto Benini
University of Padova
Italy

1. Introduction

Aerodynamic design techniques of gas turbine compressors have dramatically changed in the last years. While traditional 1D and 2D design procedures are consolidated for preliminary calculations, emerging techniques have been developed and are being used almost routinely within industries and academia.

The compressor design still remains a very complex and multidisciplinary task, where aerothermodynamic issues, traditionally considered prevalent, now become part of a more general design approach, where aeromechanical, technological, structural, noise-related concerns and many other matters have to be taken into account simultaneously, thus leading to a very challenging problem for designers.

To this respect, designer experience still plays a decisive role; however, the complexity evidenced above claims for a more structured and organized way of handling the problem, where mathematical and statistical tools are implemented and used as a decisive support in the decision making process.

Nowadays, interesting and alternative options are in fact available for compressor 3D design, such as new blade shapes for improved on-off design efficiency, endwall contouring and casing treatments for enhanced stall margin and many others.

For this reason, while experimental activity remains decisive for ultimate assessment of design choices, numerical design optimization techniques, along with Computational Fluid Dynamics (CFD) are assuming more and more importance for the detailed design and concrete evaluation of options.

In this chapter, a contribution to illustrating the roadmap for modern compressor design technique development, as well as an updated picture of available procedures, is given. Starting from the precise formulation of the design problem and the choice of the so-called "design" or "nominal" condition, both conventional and advanced techniques will be presented and discussed.

2. Choice of the design point

In both stationary and aircraft medium-to-high size gas turbines, axial-flow compressor design is always part of a more general framework involving the engine as a complex system. In this perspective, compressors are seen mainly as one of the engine components, specifically those carrying out the compression phase; however, due to the peculiar way in

which energy transfer occurs and the flow pattern which consequently establishes within them, compressors are perhaps the most crucial component to be designed, at least from the aerodynamic point of view.

In many gas turbine designers' opinion in fact, compressors are often regarded as "delicate" turbomachines, whose design heavily affects the overall engine performance, both in design and, above all, in off-design operations.

In stationary gas turbines, most of the interest is concentrated on the compressor design around the nominal condition, i.e. when the compressor delivers almost a constant mass flow rate for a fixed shaft speed at the maximum possible efficiency; this occurs almost invariably for both single and multi-shaft engine configurations, since the gas turbine load is always kept as much constant as possible in order to preserve engine's peak efficiency. In such cases, load variations, when necessary, are implemented so as not to modify the thermodynamic cycle of the gas turbine, bur rather to change the air flow, a goal which is pursued by changing the compressor stator vanes' attitude, e.g. using inlet guide vanes (IGV) and/or variable stator vanes (VSV). Usually, in stationary gas turbines, the nominal condition at which the compressor will operate most of the time is well defined and characterized by a unique combination of mass flow rate, rotational speed and pressure ratio derived from the cycle analysis at sea level ISA inlet conditions. Corrections for non-standard ISA operations can be accounted for at the early design phase when the engine is supposed to work far away from the sea level or under extreme temperature conditions.

In principle, compressors adopted in aircraft gas turbine engines, often referred to as aeroengines, require completely different design criteria (even though some stationary gas turbines are often derived and adapted from aeroengines to fulfil heavy-duty operation). In fact, aeroengines are designed mainly to fulfil many, often conflicting, technical objectives, such as specific thrust, range and fuel consumption within a wide range of flight conditions which typically require the engine to operate far away from its nominal conditions. Moreover, some limiting constraints reduces the engine design space, for instance direct operating costs and mean time between overhauls, which have to be traded-off and have a significant impact on the engine design. As a result, the compressor design gives rise to a multi-point and multidisciplinary approach which should be able to incorporate off-design requirements into the design phase.

Among aeroengine compressor designers it is of common practice to define the nominal operating condition, or at least the one chosen for the preliminary compressor sizing, as the one where the engine runs at fixed point, i.e. when it develops a static thrust, a condition representative for a real aircraft at departure. This because the fixed point operation can be easily characterized by experiments on a static test bench when a prototype of the designed engine will be available; another reason rely on the fact that engine performance at fixed point are independent of the type of aircraft to which the engine is destined. Following this criteria, the cycle analysis gives a unique combination for mass-flow rate, rotational speed and compression ratio that make the basis for the preliminary design.

Nowadays, aeroengine manufactures rarely develop a new engine neglecting the type of aircraft it will joined with, particularly in civil applications. Indeed, today the engine is born closer and closer with the aircraft and its design is mainly driven by issues regarding thrust class and specific fuel consumption along some typical flight envelopes. This in turn allows to clearly identify a cruise point, in particular standard ambient conditions and flight Mach number, from which compressor quantities can be derived. In such case, compressor behaviour over the entire operating range, especially at relevant points such as take-off and

landing, can be accounted for only afterwards, mainly as a check. If not satisfactory, the designer iterates until well defined compressor characteristics are found at cruise conditions which satisfy all the constraints in the off-design one. IN fact, more sophisticated design procedures attempt to identify the nominal condition by weighting some relevant compressor operating points along its operating line on the desirable map, including both fixed point and cruise conditions.

In the following, we shall make the assumption that, whatever the case in which the compressor will operate, either within ground or onboard power plants, a nominal condition has already been defined using some criteria such that the compressor characteristics are known.

3. Aerodynamic design problem formulation

Qualitatively speaking, compressor aerodynamic design is the procedure by which the compressor geometry is calculated which fulfils the design cycle requirements in the best possible way. Using a more definite statement, we can formulate the design problem by identifying objectives, boundary conditions, constraints, and design (or decision) variables as follows:

- Objectives: maximize adiabatic efficiency (η), maximize stall margin (*SM*), both at nominal condition.
- Boundary conditions: inlet conditions (pressure p_a, temperature T_a), flight Mach number (in the case of an aeroengine).
- Decision variables: number of stages, compressor and stage geometry parameters.
- Functional constraints: mass flow rate, *m*, (based on engine Power or Thrust requirements), Pressure Ratio, *PR*, (from Cycle analysis), correct compressor-component matching (i.e. intake-compressor, compressor-combustor, and above all compressor-turbine) as determined by a Matching Index (*MI*).
- Side Constraints: each decision variables must be chosen within feasible lower and upper bounds (sides).
- Multi-disciplinary constraints: structural and vibrational, weight, costs, manufacturability, accessibility, reliability.

It is worth considering that, although not explicitly involved in the aerodynamic design, other criteria must be accounted from the very beginning: these can derive either from other engineering requirements (structural, technological, constructive) or from non-technical aspects (mainly economical).

To this respect, the aerodynamic design of an axial-flow compressor is inherently a multiobjective constrained optimization problem, which can be written in mathematical terms as follows:

For given p_a, T_a (and flight Mach number, *M*, in aeroengines)

$$\text{Maximize} \qquad (\eta, SM) = f(\mathbf{X})$$

Subject to:
$$m = m(\mathbf{X})$$
$$PR = PR(\mathbf{X})$$
$$\text{Matching Index } (MI) = MI(\mathbf{X})$$
$$\text{Cost function} = \text{Cost function}(\mathbf{X})$$
$$\text{Weight, Structural, technological and other constraints} = g(\mathbf{X}),$$

being $\mathbf{X} = (x_1, x_2, \ldots, x_n)^T$ and $x_{i,min} < x_i < x_{i,max}$ for $i = 1, \ldots, n$ and *n* the number of decision variables.

It is worth underlying that this might not be the general formulation, as some constraints could be turned into objectives, mainly depending on compressor's final destination and/or manufacturer's strategies.

For example, in a stationary gas turbine used for electric power generation, the compressor aerodynamic design problem can be stated as follows:

For given p_a, T_a

Maximize	$(\eta$, load-response$) = f(\mathbf{X})$
Subject to:	$m = m(\mathbf{X})$
	$PR = PR(\mathbf{X})$
	Matching Index $(MI) = MI(\mathbf{X})$
	Cost function = Cost function$(\mathbf{X})$
	Weight, Structural, technological and other constraints = $g(\mathbf{X})$,

where a great importance is given both to the compressor peak efficiency and to the function called "load_response" which quantifies the rapidity of the compressor in adjusting the airflow delivered by means of IGVs and/or VSVs. In this case, of course, an intervention aimed at regulating the delivered power of the gas turbine has an effect also on the mass flow conveyed by the compressor.

In another example, i.e. an aeroengine for military use, the problem can be set up in the following way:

For given p_a, T_a, M

Maximize	$(\eta$, $SM) = f(\mathbf{X})$
Minimize	weight = weight$(\mathbf{X})$
Subject to:	$m = m(\mathbf{X})$
	$PR = PR(\mathbf{X})$
	Static thrust at sea level index = $q(\mathbf{X})$
	Matching Index $(MI) = MI(\mathbf{X})$
	Cost function = Cost function$(\mathbf{X})$
	Structural, technological and other constraints = $g(\mathbf{X})$,

where a significant merit is attributed to reaching the best trade-off between performance and weight, objectives which are intuitively conflicting each other, while cost function is inevitably different to the one assigned to the civil application. Finally, a constraint based on the static thrust to be delivered by the overall engine at seal level is set which inevitably influences compressor design.

From the problem formulations given above, remarkable importance is attributed to maximize or minimize some compressor performance indexes or figures of merit. Therefore, before examining how to deal with such problems, it is worth analyzing how performance can be significantly affected by the choice in the design variables. For instance, maximizing adiabatic efficiency requires a deep understanding of the physics governing stage losses, which have to be minimized either in design and off-design conditions. This, in turn, will have an important impact on the choice of stage geometrical and functional variables. On the other hand, maximizing stall margin involves acquiring a proper insight of stall physics and minimizing stall losses. Again, such problem can be tackled if proper stage geometry is foreseen. Finally, minimizing compressor weight (at least from the aerodynamic point of view) implicates reducing the number of compressor stages and increasing individual stage loading, a fact which ultimately affects the choice of the blade shape, particularly cascade parameters.

Based on the arguments above, in the following a brief summary of basic and advanced compressor aerodynamics is given.

4. Summary of compressor losses at design and off-design conditions

Despite the remarkable advances regarding the physical origin of compressor losses, driven by both experimental and numerical analyses, a general theory for their estimation is not yet available. Today, perhaps the most reliable way to estimate losses accurately and generally is to use in fact Computational Fluid Dynamics (CFD), with the help of which significant results have been documented in the open literature.

The fundamentals of CFD and its application to compressor design are beyond the scope of this chapter. The reader is referred to Denton & Dawes, 1999 for an exhaustive treatment of the subject.

For the purpose here, a much simpler approach can still be adopted which is based on pseudo-empirical relationships to explain and describe fluid dynamic losses and exit flow deviation. Such an approach gives rise to the so-called "loss and deviation" correlation method, among which the one proposed by Koch & Smith, 1976, together with those available in Lieblein, 1960, seem to be among the most comprehensive and reliable for subsonic compressors. A work by Schobeiri, 1996 confirms this. A step further is required when inlet supersonic flows have to be dealt with (as in the case of transonic stages), for which the predictive models given by Miller et al., 1961, is by far the most used.

As it is well known, with reference to a generic compression stage (Fig. 1), a flow deviation occurs at each cascade exit as a consequence of the non-infinite number of guiding blades, as well as because of the actual operating profile incidence, camber and thickness, Mach number and three-dimensional effects taking place close to blade hub and tip. When NACA-65 or Double Circular Arc (DCA) profiles are considered, flow deviation δ can be estimated using the following equation:

$$\delta = \frac{1}{K}\left[\left(K_\delta\right)_t\left(\delta_0\right)_{10} + \frac{\left(m\right)_{\sigma=1}}{\sigma^b}\vartheta\right] + \Delta\delta_{ref} + \left(\frac{d\delta}{di}\right)_{i_{ref}}\left(i - i_{ref}\right) \qquad (1)$$
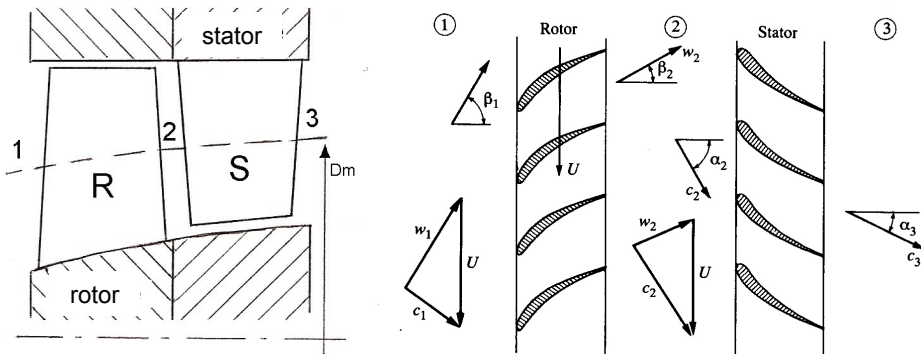

Fig. 1. Sketch of a compressor stage (left) and cascade geometries at midspan (right).

where K is a compressibility coefficient, σ the cascade solidity, $(K_\delta)_t = f(s_{max}/l)$, $(\delta_0)_{10}$ is a basic deviation for symmetrical 10% thickness-to-chord profiles, $(m)_{\sigma=1}$ is a parameter referred to a sample cascade having solidity equal to 1 and ϑ is the profile camber. Moreover $\Delta\delta_{ref} = f(Ma_i, x/b)$ depends on the actual cascade Mach number and $(d\delta/di)_{i_{ref}}(i-i_{ref})$ takes into account the effect of off-design performance on deviation by estimating the actual incidence angle i with respect to the reference, o minimum loss, one i_{ref}. Terms in equation (1) are usually given in graphical form (Koch & Smith, 1976) but can be easily implemented numerically.

Usually stage losses are divided into profile, secondary and tip-clearance ones. Corrections are foreseen in order to modify the basic profile losses to account for Reynolds and Mach number effects. Addictive terms are finally introduced to estimate the shock wave losses when supersonic incoming flow occurs.

A well established approach is to account for the various loss sources, in both on and off-design operation, according to the following equation

$$\zeta = \zeta_{(M=0)}\chi_R\chi_M + \zeta_{sh} + \zeta_s + \zeta_\delta + K_M\left(i - i_{ref}\right)^2 \tag{2}$$

where:

- $\zeta_{(M=0)}$ is the basic loss coefficient for incompressible flow;
- χ_R is the Reynolds-based correction;
- χ_M is the Mach-based correction;
- ζ_{sh} is the shock correction;
- ζ_s is the secondary loss coefficient;
- ζ_δ is the tip clearance loss coefficient;
- K_M is the off-design coefficient, function of the Mach number.

Losses are computed for both rotors and stators using the following relation:

$$\zeta_R = \frac{h_2 - h_{2,is}}{w_1^2/2} \qquad \zeta_S = \frac{h_3 - h_{3t}}{c_2^2/2} \tag{3}$$

$$\zeta \approx 1/\left[0.5(k-1)M_i^2\right]\left\{1 + 0.5(k-1)M_i^2 - \left[(1-\varpi)\left(1 + 0.5(k-1)M_i^2\right)^{\frac{k}{k-1}} + \varpi\right]^{\frac{k-1}{k}}\right\} \tag{4}$$

Being ϖ the conventional total pressure loss coefficient:

$$\varpi_R = \Delta p_R^o(0.5\rho_1 w_1^2) \qquad \varpi_S = \Delta p_S^o(0.5\rho_2 w_2^2) \tag{5}$$

In estimating the profile losses, the basic loss coefficient is a function of a series of parameters according to the following:

$$\varpi_p = 2\left(\frac{\vartheta}{l}\right)\frac{\sigma}{\cos\alpha_{ex}}\left(\frac{\cos\alpha_i}{\cos\alpha_{ex}}\right)^2\left(\frac{2H}{3H-1}\right)\left(1 - H\left(\frac{\vartheta}{l}\right)\frac{\sigma}{\cos\alpha_{ex}}\right)^{-3} \tag{6}$$

where ϑ/l is the non-dimensional momentum thickness of the blade boundary layer (i.e. referred to the profile chord) which in turns depends on the Lieblein local diffusion factor:

$$DR_R = \frac{w_1}{w_2}\left\{1.12 + .61\frac{\cos^2\beta_1}{\sigma_R}\left[\tan\beta_1 - \frac{c_{m2}}{c_{m1}}\tan\beta_2 - \frac{u_1}{c_{m1}}\left(1 - \frac{r_2^2}{r_1^2}\right)\right]\right\}$$

$$DR_S = \frac{c_2}{c_1}\left\{1.12 + 0.61\frac{\cos^2\alpha_2}{\sigma_S}\left[\tan\alpha_2 - \frac{c_{m3}}{c_{m2}}\tan\alpha_3\right]\right\}$$

(7)

while α_i and α_{ex} are the inlet and outlet flow angles of the generic cascade (i.e. $\alpha_i = \beta_1$ and $\alpha_{ex} = \beta_2$ for a rotor cascade), and H is a shape factor, whose values are found between 1.05 and 1.2.

Reynolds correction is due to the fact that the shear stress boundary layer on the blade, to which losses are linked, depends on the chord-based Reynolds blade number according to the following:

$$\chi_R = \frac{\varpi_p}{\varpi_{p,ref}} = \frac{\zeta_p}{\zeta_{p,ref}} = \frac{c_f}{c_{f\,ref}}$$

(8)

where $c_f = f(\text{Re})$ is the shear stress coefficient of a smooth flat plate.

Mach correction offers an explanation for compressibility effects, which become non-negligible when Mach number exceeds, say, 0.3 and remarkable for $M > 0.75$. A special case occurs for supersonic cascades (incidence $M > 1$), for which $\chi_M > 1.5$.

Shock correction applies only to supersonic blades and can be calculated reasonably well using the two-dimensional shock loss model provided by Miller et al., 1961, to which the reader is referred for details.

Secondary losses are caused both by friction on the endwalls and secondary vorticity located on planes perpendicular to the shaft axis. According to Suter, 1960 secondary losses are linked to an energy dissipation coefficient c_d which, in turn, depends on the blade geometry and a work parameter referred to the blade midspan ($\overline{\Psi}$), being the latter empirically determined:

$$c_d = \chi_R\left(F\overline{\Psi} + 0.004\right)$$

(9)

where $F = f(l_a / b)$ being l_a and b the blade axial chord and blade height, respectively, while χ_R is the Reynolds-based correction. A more rigorous modelling for secondary losses will break down the contribution due to the endwall friction and secondary vorticity according to the following (valid for a rotor blade):

$$\zeta_{S\_annulus} = 0.004\chi_R\frac{l_a / b}{(1+Y)sen\overline{\beta_1}}\left[\left(\frac{w_{\infty R}}{w_1}\right)^3 + Y\left(\frac{c_{\infty S}}{w_1}\right)^3\right]$$

$$\zeta_{S\_vorticity} = 0.032\chi_R\overline{\Psi}\frac{(l_a / b)^{0.15}}{(1+Y)sen\overline{\beta_1}}\left[\left(\frac{w_{\infty R}}{w_1}\right)^3 + Y\left(\frac{c_{\infty S}}{w_1}\right)^3\right]$$

(10)

where $\vec{w}_{\infty R} = 0.5\left(\vec{w}_{1R} + \vec{w}_{2R}\right)$ and $\vec{c}_{\infty S} = 0.5\left(\vec{c}_{2S} + \vec{c}_{3S}\right)$.

Tip clearance losses are a complex function of blade geometry, tip gap and functional parameters. Traupel suggests the following expression for a rotor blade:

$$\zeta_\delta = K_\delta \left(\frac{\Delta w_t}{u_2}\right)_S \frac{1}{sen\gamma_{tS}} \left(\frac{w_{1s}}{\overline{\overline{w_1}}}\right)^2 \frac{D_s \delta}{D_m b} \tag{11}$$

where:
- γ_{tS} is the blade stagger angle, measured with respect to the tangential direction;
- K_δ is an empirically derived coefficient, function of the ratio between actual and design flow coefficients; its values are found in the range [0.8-2] when ϕ/ϕ^* belongs to [0.8-1.3].
- δ is the tip clearance gap;
- $\left(\Delta w_t / u_2\right)_S$ is the work coefficient of the rotor.

A blockage factor can also be accounted for in order to estimate the correct mass flow delivered by a generic stage using the following expression, proposed by Smith, 1970, whose calculation is based on the actual boundary layer displacement thicknesses at the root δ^*_R and at the tip δ^*_S of the blade:

$$\delta^*_R = \delta^*_{R0} + \frac{\psi}{\psi_{max}}\delta'' \quad \delta^*_S = \delta^*_{S0} + \frac{\psi}{\psi_{max}}\delta' \tag{12}$$

being δ'' and δ' the clearance gaps of the rotor and stator blades, respectively, and δ^*_{R0} and δ^*_{S0} the displacement thicknesses corresponding to null values of the gaps in the rotor and stator blades. Consequently, the following blockage factor can be calculated:

$$\xi = 1 - \left[\int_{r_R}^{r_R+\delta_R}\left(\overline{\rho w_m} - \rho w_m\right)2\pi r\,dr - \int_{r_S-\delta_S}^{r_S}\left(\overline{\rho w_m} - \rho w_m\right)2\pi r\,dr\right] / \overline{\rho w_m}\pi\left(r_S^2 - r_R^2\right) \tag{13}$$

where the actual mass flow rate is $\dot{m} = \xi\overline{\rho w_m}\pi\left(r_S^2 - r_R^2\right)$, i.e.:

$$\xi = 1 - \frac{2\left(\delta^*_R r_R + \delta^*_S r_S\right)}{r_S^2 - r_R^2} = 1 - \frac{4\left(D_R \delta^*_R + D_S \delta^*_S\right)}{D_S^2 - D_R^2} \tag{14}$$

Correlations presented above are able to give a reasonable insight into the loss mechanisms and to capture the correct entities for the various sources involved in both design and off-design conditions. An example of prediction obtained by the author using such an approach is given in Fig. 2, where the map of the Rolls-Royce HP9 compressor stage (Ginder & Harris, 1989) has been predicted by the author and compared to available experimental data. Another example is given by Wisler et al., 1977, where a preliminary design study was conducted using correlations to identify an advanced core compressor for use in new high-bypass-ratio turbofan engines to be introduced into commercial service in the 1980's.

5. Advanced design techniques

Independently from the particular case under study, modern compressor design philosophy can be summarized as in Fig. 3.
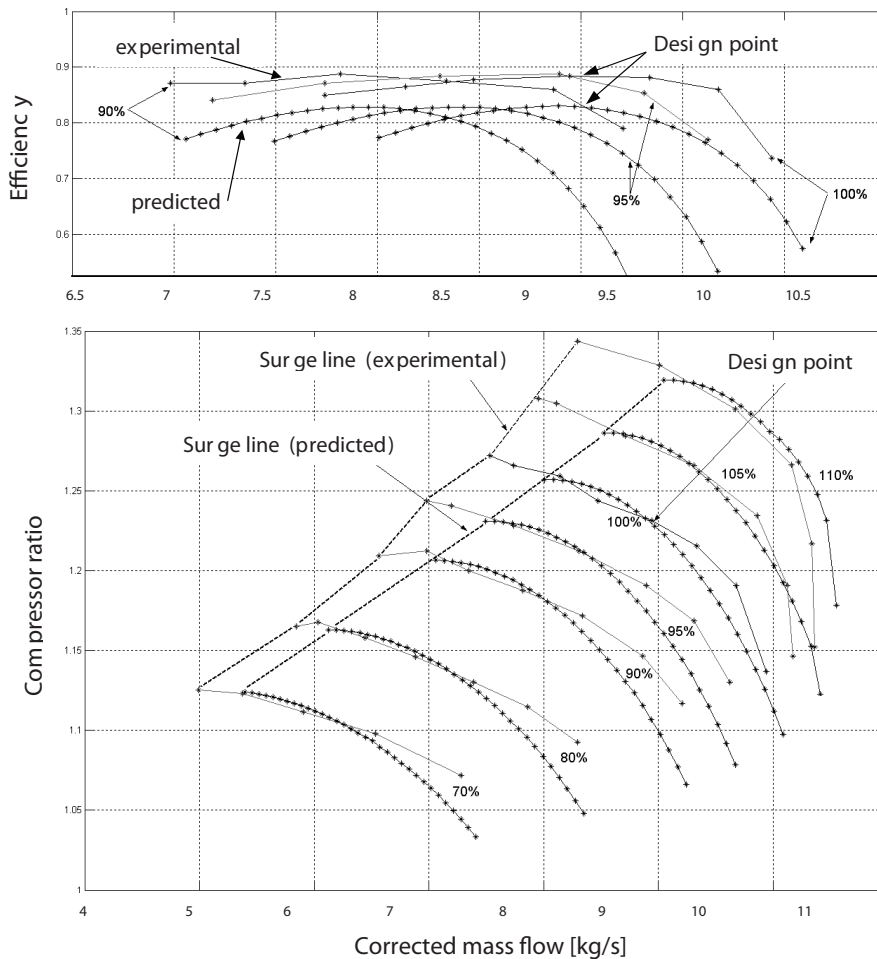
Fig. 2. Experimental and predicted map of the Rolls-Royce HP-9 compressor.

A preliminary design is usually carried out at first, aiming at defining some basic features such as number of stages, inlet and outlet radii and length. Stage loading and reaction is established as well on the basis of preliminary criteria driven by basic theory and experiments. Such procedure is based on one-dimensional (1D) methods, where each stage characteristics are condensed into a single "design block", to which basic thermo- and fluid-dynamics equations are applied. Therefore, no effort is spent to account for flow variations other than those which characterize the main axial flow direction within each stage at a time. Then, stages are stacked together to determine the overall compressor design, regardless any mutual stage interaction. Within this process, which will be described later on, technological and process constraints, as well as restrictions on weight and cost, play an important role that must be properly accounted for. In this framework, some early choices could be revisited and subject to aerodynamic criteria checking, so that an iterative process occurs until a satisfactory preliminary design is obtained.
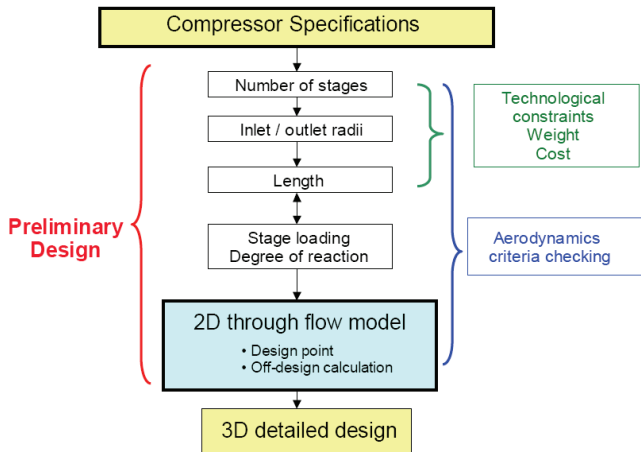
Fig. 3. Compressor design flow chart.

A second preliminary step, distinct from the 1D procedure, is the two-dimensional design (2D), which include both cascade and throughflow models, from which a characterization of both design and off-design multi-stage compressor performance can be carried out after some iterations, if necessary. In this case, both direct and inverse design methodologies have been successfully applied. Numerical optimization strategies may be of great help in this case as the models involved are relatively simple to run on a computer. Often an optimization involves coupling a prediction tool, e.g. a blade to blade solver and/or a throughflow code, and an optimization algorithm which assists the designer to explore the search space with the aim of obtaining the desired objectives.

Finally, a fully three-dimensional (3D) design is carried out including all the details necessary to build the aerodynamic parts of the compressor. In this phase, some design intervention is needed to account for the real three-dimensional, viscous flows in the stages, especially tip clearance, secondary flows and casing treatment for stall delay. This is usually carried out using CFD models, where the running blade is modelled in its actual deformed shape, analyzed and, if necessary optimized. While traditional 3D analyses are aimed at evaluating and improving compressor performance of a single stage, the recent availability of powerful computers makes the analyses of multistage compressors an affordable task for most industries. Most advanced CFD computations include evaluation of complex unsteady effects due to successive full-span rotor-stator interaction.

5.1 Preliminary design techniques

A simple meanline one-dimensional method usually forms the basis of a preliminary design. Examples of such methods are almost uncountable in the literature (see, among others, the one developed by Casey, 1987). In the following, a synthesis of such methods is provided.

For a given design condition, the compressor total pressure ratio is known from which the total number of compressor stages can be estimated. To this respect, the designer can use statistical indications based on typical values of admissible peripheral speeds and stage loading (see Fig. 4). More in details, it is worth considering that the elementary compressor ratio, π_c, that can be developed by a single stage obeys to the following equation, which can be easily derived from the Euler equation for an axial stage at the root-mean-square radius:
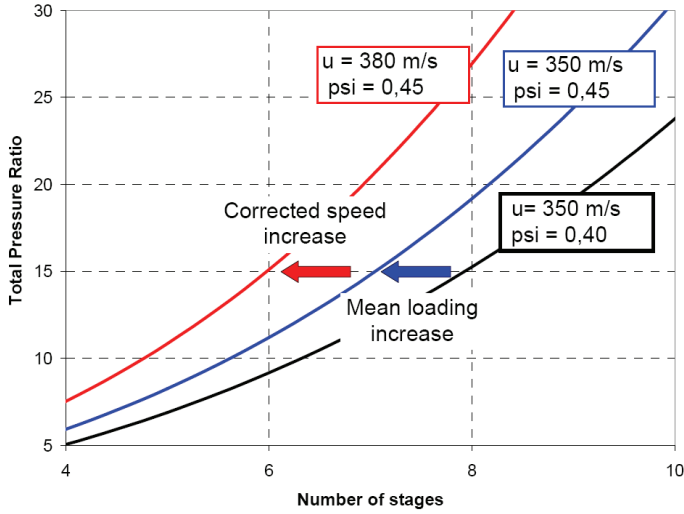
Fig. 4. Preliminary estimation of the compressor number of stages based on typical peripheral mean velocities and stage loading.

$$\pi_c = \frac{p_2^0}{p_1^0} = \left(1 + (k-1)\frac{u^2}{kRT_1^0}\psi\right)^{\frac{k\eta_{pol}}{k-1}} = \left(1 + (k-1)M_{w01}^2\cos^2\beta_1\frac{\psi}{\phi^2}\right)^{\frac{k\eta_{pol}}{k-1}} \qquad (1)$$

where k is the ratio of specific heats for an ideal gas, R=287 J/(kgK), u is the peripheral velocity at the mean radius, T_1^0 the total temperature at stage inlet, ψ and ψ the work and flow coefficients, M_{w01} the Mach number of inlet relative velocity with respect the stagnation speed of sound, β_1 the mean inlet flow angle measured and, finally, η_{pol} the estimated stage polytropic efficiency.

From the above equation, a preliminary design chart can be obtained as reported in Fig. 5. This is very useful for estimating the preliminary stage pressure ratio once the range for the other functional parameters has been settled. For instance, it is well known that the work coefficient is today always less that 0.45 for an ordinary subsonic stage in order not to overload it and to limit stall susceptibility. At the same time, the flow coefficient does not exceed 0.6 and very rarely goes below 0.2 (at least for subsonic stages). Actually, the work and flow coefficients are linked together via the blade degree of reaction ε_R, and cannot be chosen separately:

$$\phi^2 = \left(\frac{c_z}{u}\right)^2 = \left\{M_{w1}^2\left[\left(\frac{a_1^0}{u}\right)^2 - \frac{k-1}{2}(1-\varepsilon_R - \psi/2)^2\right] - \left[\varepsilon_R + \psi/2\right]^2\right\} / \left(1 + \frac{k-1}{2}M_{w1}^2\right) \quad (2)$$

Fig. 6 displays this relation in graphical form for both industrial and aeronautical compressors.

Moreover, due to theoretical arguments going back to Howell, 1942 inlet flow angles never stay far away from 55 degrees, being the maximum theoretical stage efficiency in the
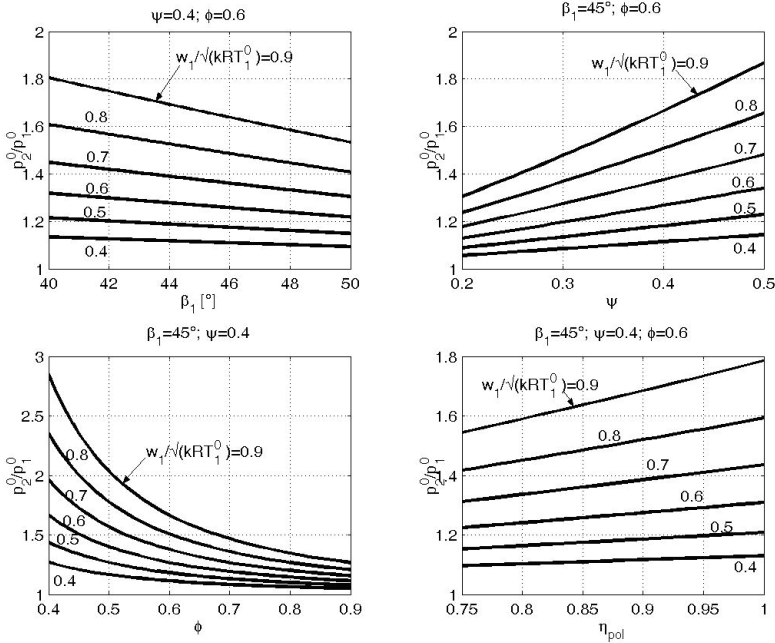
Fig. 5. Preliminary compressor design chart.
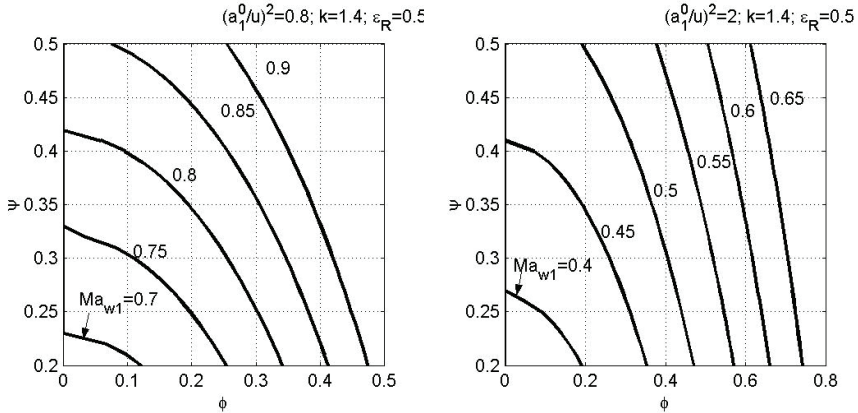
Fig. 6. Load and flow coefficients as functions of the relative Mach number for a given degree of reaction for aeronautical (left) and industrial (right) stages.

neighbourhood of $\tan\beta_m = 0.5\left(\tan\beta_1 + \tan\beta_2\right)$ =45° and the maximum flow turning in the order of 20° for a decelerating cascade. Finally, the operating Mach number is less than 0.75 for a subsonic cascade, but can go up to 2 and more at the tip of a transonic blade. This is the reason why modern subsonic stages can develop pressure ratios in the order of 1.5-1.8 (see Fig. 7), while transonic stages operate with 2 and more while maintaining an acceptable

value for the polytropic efficiency. In a well designed subsonic stage, the latter reaches values not very much higher than 0.9, while 0.89 is by far one of the highest documented values for transonic bladings.

Based on these indications, the total number stages can therefore be estimated from admissible stage compression (Figure 8).

Without going very much into details, the 1-D methods rely in the sequential calculation or assumption of the following quantities:

- peripheral mean stage rotor velocity (300-350 m/s for subsonic rotors, up to 600 m/s for transonic ones);
- Annulus radius ratio, i.e. R_{hub}/R_{tip}, usually chosen between 0.45 (front stages) and 0.6 (rear stages);
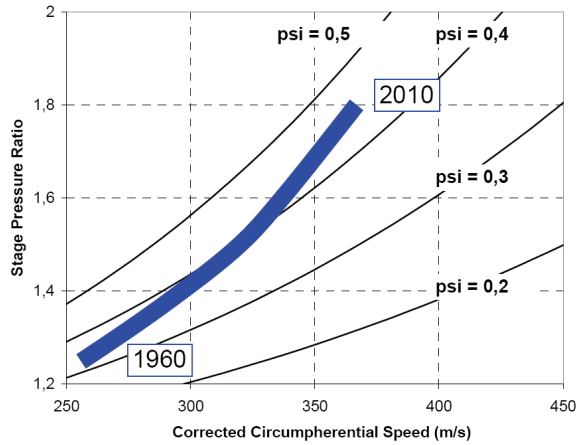
Fig. 7. Time evolution for compressor circumferential speed and stage loading.
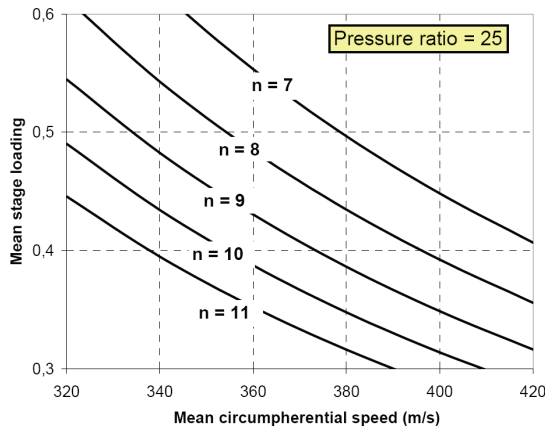
Fig. 8. Estimation of the number of compressor stages based on stage loading and mean circumpherential speed.
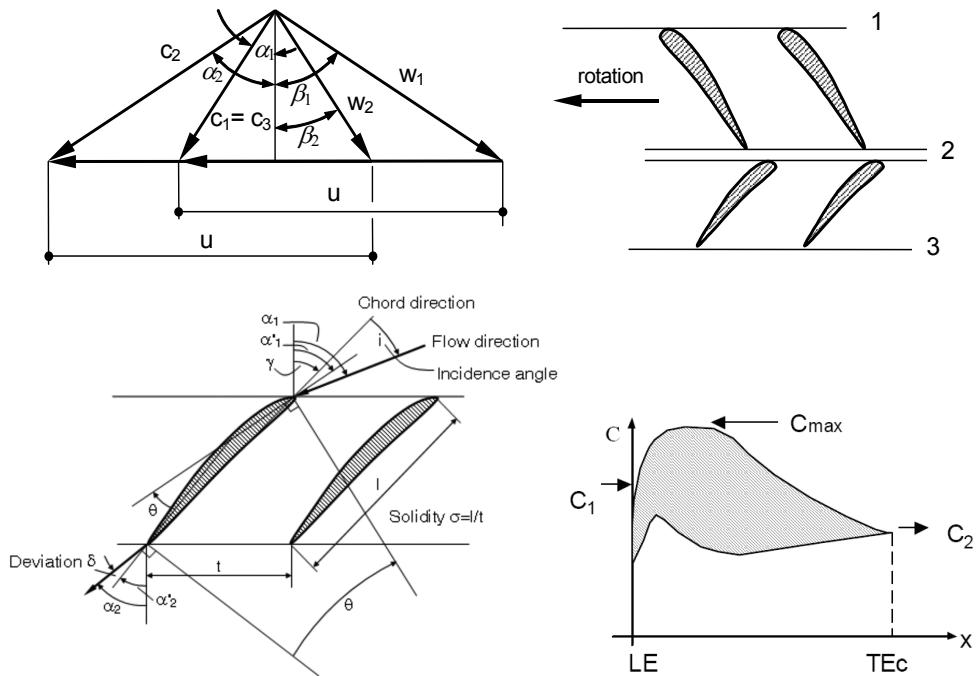
Fig. 9. Estimation of the number of compressor stages based on stage loading and mean circumpherential speed.

- Choice of the stage degree of reaction (possibly around 0.5, work and flow coefficients and subsequent determination of the velocity triangles (Fig. 9);
- Mean radius basic cascade characteristics (based in the Howell's method or Mellor charts, see Emery et al., 1957; Horlock, 1958; Mellor, 1956);
- Estimation of the diffusion performance (based on acceptable Lieblein diffusion factors or De Haller numbers, Fig. 10, see Lieblein, 1960):
- Calculation of the blade height at the stage exit based on acceptable blade aspect ratios;
- Stage stacking;
- Iteration;
- 2D approach.

Result of stage stacking consists in the flowpath definition, from which the distribution of stage parameters along the mean radii can be obtained. Because the stacking procedure is intrinsically iterative, a loop is required to satisfy all the design objectives and constraints.

As a first check, the axial Mach distribution along the stages must be calculated and a value not exceeding 0.5 is tolerated for both subsonic and transonic stages. By imposing such a constraint, the values of stage area passage can be derived from the continuity equation (Fig. 11).

Next, the values of the hub-to-tip ratios must be defined. To this purpose, it is worth recalling that such value comes from a trade-off between aerodynamic, technological and economic constraints. For inlet stages, values between 0.45 and 0.66 can be assigned, while outlet stages often are given a higher value, say from 0.8 to 0.92, in order not to increase the exit Mach number (a condition which is detrimental for pneumatic combustor losses).
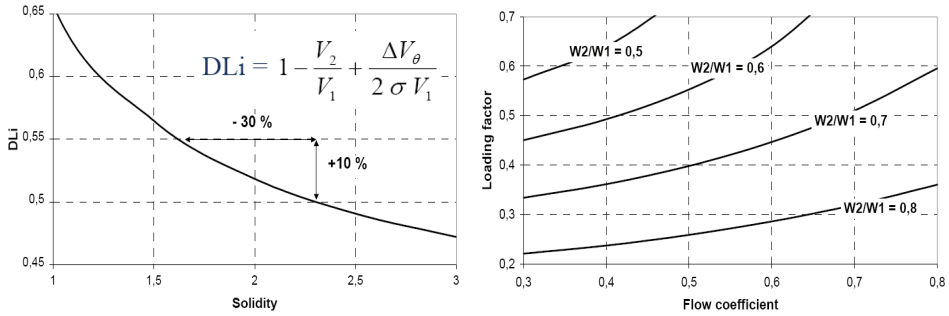
Fig. 10. Lieblein's Diffusion Factor (DLi) level versus solidity for given flow and work coefficient (left). Iso De Haller number in the φ, ψ diagram (right).
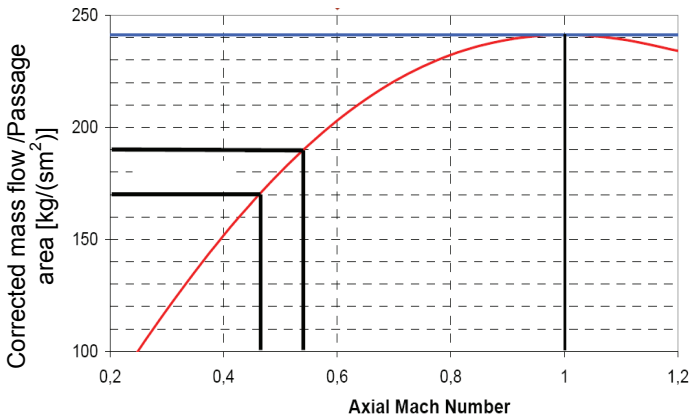
Fig. 11. Corrected mass flow over stage area passage as function of the axial Mach number.

Despite its relative simplicity, meanline 1D methods based on stage-stacking techniques still play an important role in the design of compressor stages as also demonstrated by Sun & Elder, 1998. In their work, a numerical methodology is used for optimizing a stator stagger setting in a multistage axial-flow compressor environment (seven-stage aircraft compressor) based on a stage-by-stage model to 'stack' the stages together with a dynamic surge prediction model. A direct search method incorporating a sequential weight increasing factor technique (SWIFT) was then used to optimize stagger setting, while the objective function was penalized externally with an updated factor which helped to accelerate convergence.

A recent example of how 1D models can still be used in the preliminary design of axial compressors is given by Chen et al., 2005. In their work, a model for the optimum design of a compressor stage, assuming a fixed distribution of axial velocities, is presented. The absolute inlet and exit angles of the rotor are taken as design variables. Analytical relations between the isentropic efficiency and the flow coefficient, the work coefficient, the flow angles and the degree of reaction of the compressor stage were obtained. Numerical examples were provided to illustrate the effects of various parameters on the optimal performance of the compressor stage.

5.2 Advanced throughflow design techniques (2D)

Throughflow design allows configuring the meridional contours of the compressor, as well as all other stage properties in a more accurate way compared to 1D methods. They make use of cascade correlations for total pressure loss/flow deviation and are based on throughflow codes, which are two-dimensional inviscid methods that solve for axisymmetric flow (radial equilibrium equations) in the axial-radial meridional plane (Fig. 12). A distributed blade force is imposed to produce the desired flow turning, while blockage factor that accounts for the reduced area due to blade thickness and distributed frictional force representing the entropy increase due to viscous stresses and heat conduction can be incorporated.

Three methods are basically used for this purpose: streamline curvature methods SCM (Novak, 1967), matrix throughflow methods MTFM (Marsh, 1968) and streamline throughflow methods STFM (Von Backström & Rows, 1993).

SCM has the advantage of simulating individual streamlines, making it easier to be implemented because properties are conserved along each streamline but is typically slower compared to the other methods. On the other hand, MTFM uses a fixed geometrical grid, so that streamline conservation properties cannot be applied. However, despite stream function values must be interpolated throughout the grid, the MTFM is numerically more stable than SCM. Finally STFM is a hybrid approach which combines advantages of accuracy of SCM with stability of MTFM.

These methods have recently been made more realistic by taking account of end-wall effects and spanwise mixing by four aerodynamic mechanisms: turbulent diffusion, turbulent convection by secondary flows, spanwise migration of airfoil boundary layer fluid and spanwise convection of fluid in blade wakes (Dunham, 1997). Other remarkable results consist in incorporating a throughflow code into a Navier-Stokes solver for shortening the calculation phase (Sturmayr & Hirsch, 1999).

As a result of the application of throughflow codes, the compressor map in both design and off design operation can be obtained exhibiting high accuracy.

Remarkable developments in the design techniques have been obtained using such codes. Among others, Massardo et al., 1990 described a technique for the design optimization of an axial-flow compressor stage. The procedure allowed for optimization of the complete radial
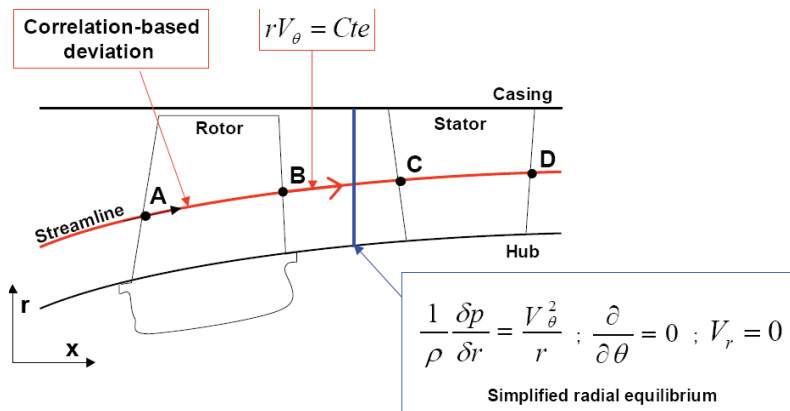
Fig. 12. Domain sketch for throughflow calculations.
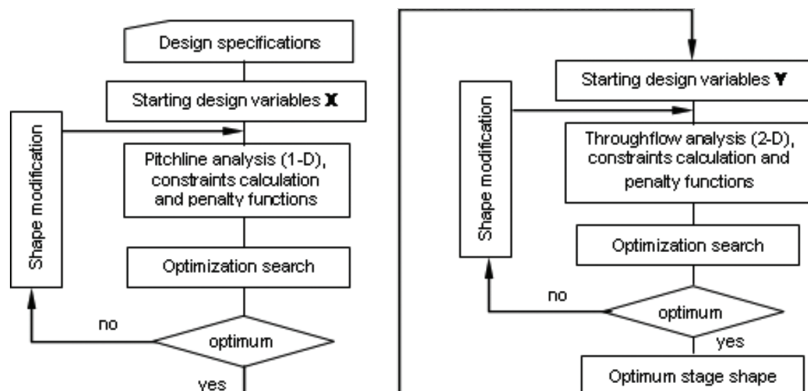
Fig. 13. Optimization procedure proposed in Massardo et al., 1990

distribution of the geometry, being the objective function obtained using a throughflow calculation (Fig. 13). Some examples were given of the possibility to use the procedure both for redesign and the complete design of axial-flow compressor stages.

Howard & Gallimore, 1993, incorporated a viscous throughflow method into an axial compressor design system such that the meridional velocity defects in the endwall region and consequently blading could be designed that allowed for the increased incidence, and low dynamic head, near the annulus walls.

A very interesting application of a throughflow multiobjective design optimization has been recently given by Oyama & Liou, 2002. In this paper, a throughflow code based on the streamline curvature method is used along with a multiobjective evolutionary algorithm to design a four-stage compressor (Fig. 14, left) for maximization of the overall isentropic efficiency and the total pressure ratio. The diffusion factor was constrained to avoid designs involving flow separation. Total pressure and solidities at the rotor trailing edges, and flow angles and solidities at the stator trailing edges were considered as design parameters. In Fig. 14 (right), the final Pareto optimal solutions are plotted which reveal a significant superiority with respect to the baseline compressor from which the optimization started. The procedure made it also possible to obtain the full span distribution of design variables. e.g. the solidity of a blade which maximized one objective (see, for example, Fig. 14).

5.3 Advanced cascade design techniques (2D)

A great benefit in compressor design for maximum performance can derive from advanced 2D cascade aerodynamic design using both direct and indirect methods.

Direct methods

These are design methods where a blade-to-blade geometry is first assessed and subsequently analyzed using available CFD flow solvers. Then, shape modifications take place and resulting geometries evaluated until an acceptable or even optimal configuration is found. Iterative methods perfectly suit for this purpose, so that optimization loops are often used in the framework of this approach. Among optimization techniques available today, evolutionary algorithms (Goldberg, 1989; Schwefel, 1995) are preferable to other "local" methods since they have revealed to be powerful tools in handling multimodal, non convex and multi-objective problems. Gradient-based optimization methods are still in use only for special "quadratic" cases.
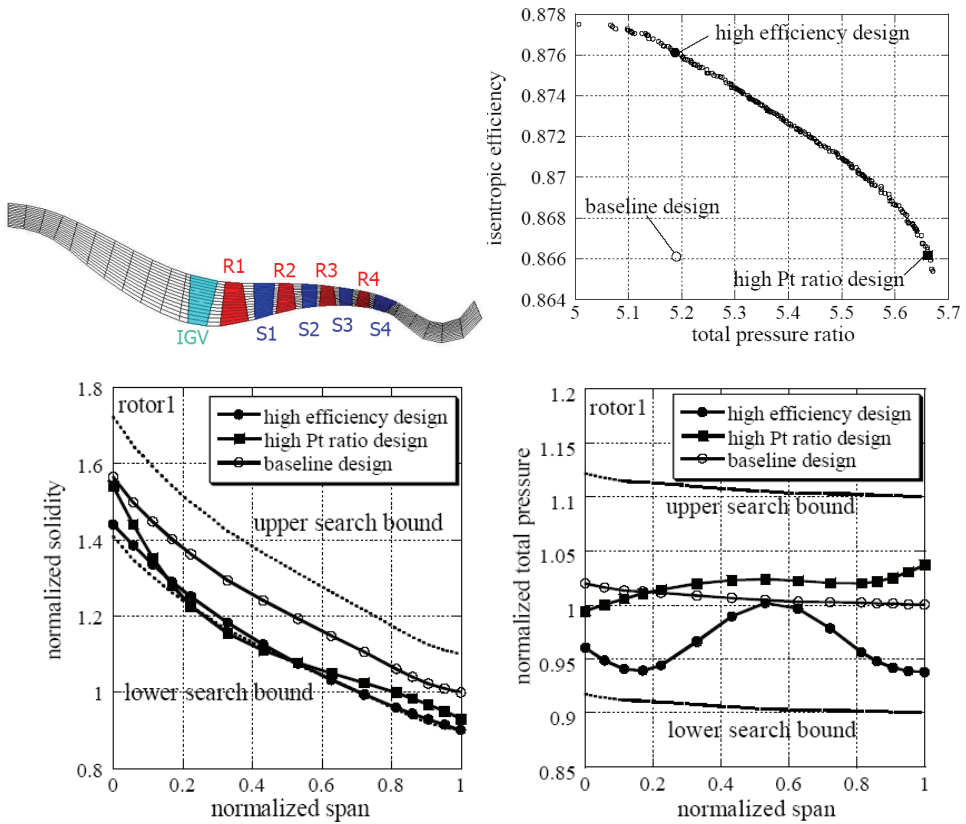
Fig. 14. Throughflow optimization of a multistage compressor (from Oyama & Liou, 2002).

Obayashi, 1997 faced the multi-objective optimization problem of maximizing the pressure rise and efficiency of compressor cascades with a Pareto-Genetic Algorithm and a Navier-Stokes solver. Pierret, 1999 used an artificial neural network coupled with a Navier-Stokes solver to maximize the efficiency and/or operating range of two-dimensional compressor cascades and then staggered them in radial direction to obtain the three dimensional blade. Köller et al., 2000 and Küsters et al., 2000 developed a new family of compressor airfoils, characterized by low total pressure losses and larger operating range with respect to standard Controlled Diffusion Airfoils (CDA), using a gradient optimization method and an inviscid/viscous code.

Until today, the use of evolutionary techniques in combination with CFD codes for solving multi-objective optimization problems in compressor aerodynamics has been limited by the tremendous computational effort required. Since the large majority of the computational time is spent in the evaluation process of the objective function, a faster solution approach to calculate the flow field would be more appropriate. From this point of view, the use of Euler solvers with integral boundary layer approach are more desirable than Navier-Stokes codes, at least to predict flow quantities in the vicinity of the design point of the machine. On the other hand, the available evolutionary optimization techniques are not enough effective in exploiting information from a population of candidate solutions to the optimization

problem, so that the number of generations required to get the optimum is usually great, thus penalizing the convergence process.

A powerful evolutionary optimization code was developed by Toffolo & Benini, 2003 to support the development of a new design methodology of optimal airfoils for axial compressors (Benini & Toffolo, 2004).

In fact, the ultimate goal of compressor cascade design is to create a blade with maximum pressure rise and minimum total pressure loss along with an acceptable tolerance to incidence angles variations. A number of different design choices can be carried out to reach this scope. Considering a cascade of airfoils, the flow may be turned by a high cambered profile at low incidence angles or, equivalently, by a low cambered profile having marked positive incidence. In this respect, the shape of the profile plays an important role because it affects the nature of the boundary layer on the suction side and therefore the amount of profile losses. On the other hand, the designer may use a high solidity cascade in order to decrease the aerodynamic loading on a single profile, thus reaching the maximum pressure rise with the whole blade row, or may adopt a low solidity cascade to minimize the friction losses for a prescribed pressure rise. All these choices involve a decision-making process that makes the design a challenging task.

An option to handle this problem is to parameterize the shape of the airfoil first, e.g. by using Bézier parametric curves (see Fig. 15). Next, a proper problem formulation is needed, e.g. to maximize pressure ratio and minimize total pressure losses across the cascade for a given inlet Mach number, inlet and outlet flow inclinations (fixed flow deflexion). Moreover, in order to assure efficient off-design operation and acceptable profile thickness, one can impose a constraint regarding maximum allowable total pressure losses over the operating range of the cascade; for a generic cascade, for instance the total pressure loss can be measured in five operating conditions defined by β_i-$\beta_1{}^*$=0, ±2.5 deg, ±5 deg and compared to the one of the design: to satisfy the constraint, the following condition had to be verified at each operating point i, i.e. $\omega_i / \omega^* \leq 2 \quad \forall i = 1,...,5$, being ω the total pressure loss coefficient of the cascade.
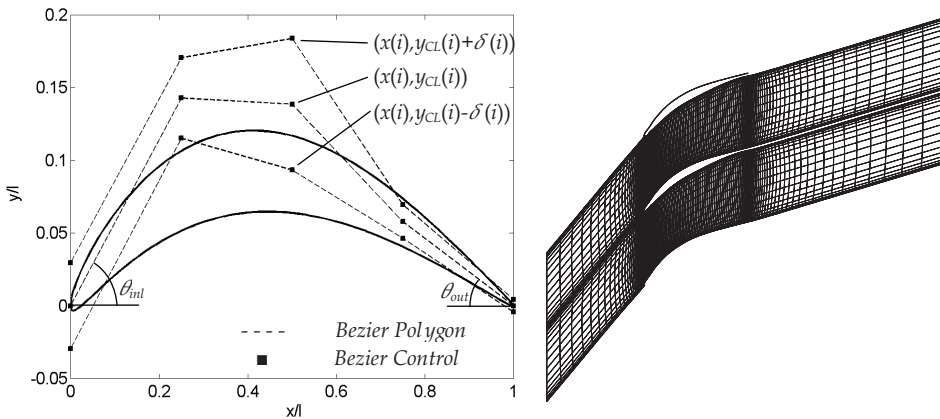
Fig. 15. Geometry parameterization of an airfoil using Bezier curves; squares represent control points of Bezier curves (left). I-type grid used in the simulations of a compressor cascades (right). From Benini & Toffolo, 2002.

An efficient algorithm can be used to handle the problem. A typical multiobjective evolutionary strategy (Schwefel, 1995) with genetic diversity preserving mechanism (GeDEM) can be used (Fig. 16, left) to obtain Pareto-optimal solutions (Fig. 16 right). The shape of the Pareto front confirms that at low pressure ratios it is possible to increase profile loading without penalizing efficiency in a very significant way; on the other hand, as the flow turning moves toward its maximum, a sudden drop in the profile efficiency is unavoidable.

It is worth noting that the individuals belonging to the Pareto front "dominate" the cascades of NACA 65 profiles. In particular, the cascade of NACA 65-8-10, NACA 65-12-10 and NACA 65-15-10 are dominated by individuals A, B, C with respect to profile efficiency (PR being fixed), and by individuals A1, B1, C1 with respect to pressure ratio (profile efficiency being fixed).
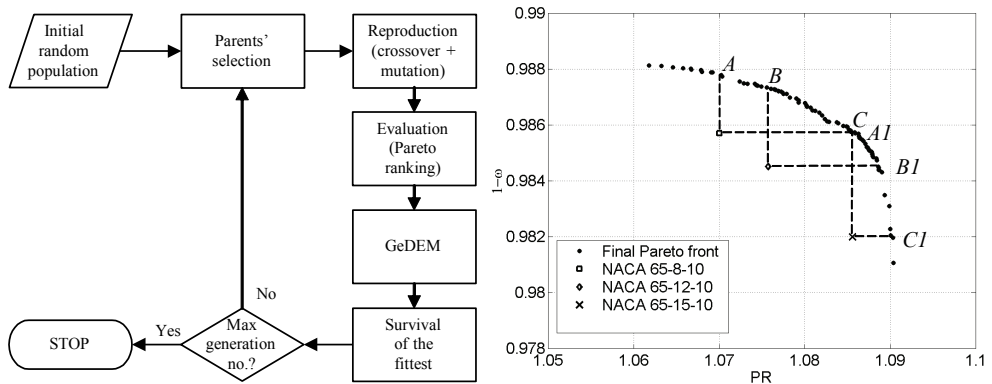
Fig. 16. Scheme of the optimization used for cascade optimization (left). Pareto front of the optimization compared with performance figures of NACA 65 cascades (right). PR=Pressure ratio, w=total pressure loss coefficient. From Benini & Toffolo, 2002.
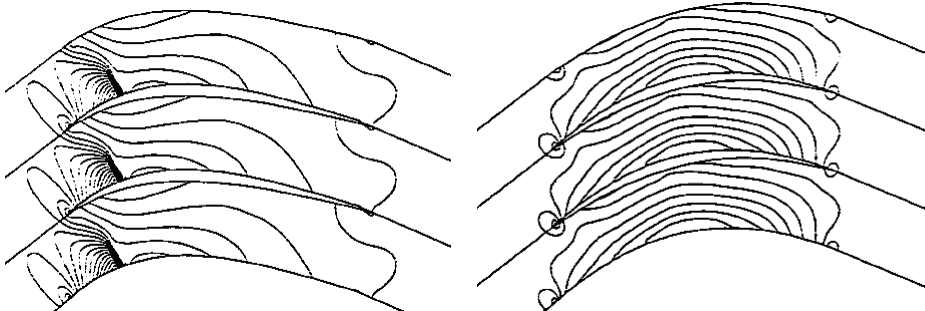
Fig. 17. Comparison between non optimal (left) and optimal (right) Mach number contour plot in a transonic compressor cascade (from Ahmadi, 1998).

Inverse methods

In inverse design, the required cascade performance is specified and the blade shape is sought accordingly. Although widely used in both academia and industry, they are far from

being as accurate as direct methods. The reason for this relies in the simplifications which characterize them, particularly that inviscid flow equations (Euler equations) are solved.

In 2D cascades, performance is defined by the design specification of either the flow properties on one or both sides of the blade, typically pressure, velocity or Mach number distribution (Lighthill, 1945; Giles & Drela, 1987; Leonard & Van Den Braembussche, 1992).

A noticeable application of inverse methods for the design of transonic compressor cascade is given by Ahmadi, 1998, who implemented a cell-vertex finite volume method on unstructured triangular meshes. In this design method, the mass-averaged swirl schedule and the blade thickness distribution were prescribed. The design method then provided the blade shape that would accomplish this loading by imposing the appropriate pressure jump across the blades and satisfying the blade boundary condition. The method was first validated for a compressor cascade and then used to redesign a transonic ONERA cascade with the aim of removing the passage shock (Fig. 17).

5.4 Advanced 3D design techniques

Direct methods

Advanced optimization techniques can be of great help in the design of 3D compressor blades when direct methods are used. These are usually very expensive procedures in terms of computational cost such that they can be profitably used in the final stages of the design, when a good starting solution, obtained using a combination of 1D and/or 2D methods, is already available. Moreover, large computational resources are necessary to obtain results within reasonable industrial times.

Examples of 3D designs of both subsonic and transonic compressor bladings are today numerous in the open literature.

Direct methods involving optimization techniques and direct objective evaluation

Among others, Lee & Kim, 2000 developed a numerical optimization technique combined with a three-dimensional Navier-Stokes solver to find an optimum shape of a stator blade in an axial compressor through calculations of single stage rotor-stator flow. For numerical optimization, searching direction was found by the steepest decent and conjugate direction methods, and the golden section method was used to determine optimum moving distance along the searching direction. The object of present optimization was to maximize efficiency. An optimum stacking line was also found to design a custom-tailored 3-D blade for maximum efficiency with the other parameters fixed.

Sieverding et al., 2004 showed an example of advanced 3D design of industrial compressors blades, which typically require a wider range from surge to choke than typical gas turbine compressors in order to meet the high volume flow range requirements of the plant in which they operate. The method combined a parametric geometry definition method, a powerful blade-to-blade flow solver and an optimization technique (breeder genetic algorithm) with an appropriate fitness function. Particular effort has been devoted to the design of the fitness function for this application which includes non-dimensional terms related to the required performance at design and off-design operating points. It has been found that essential aspects of the design (such as the required flow turning, or mechanical constraints) should not be part of the fitness function, but need to be treated as so-called "killer" criteria in the genetic algorithm. Finally, it has been found worthwhile to examine the effect of the weighting factors of the fitness function to identify how these affect the performance of the sections. It is worth

noting that the system has been tested on the design of a repeating stage for the middle stages of an industrial axial compressor and the resulting profiles showed an increased operating range compared to an earlier design using NACA65 profiles.

A multiobjective design optimization method for 3D compressor rotor blades was developed by Benini, 2004, where the optimization problem was to maximize the isentropic efficiency of the rotor and to maximize its pressure ratio at the design point, using a constraint on the mass flow rate. Direct objective function calculation was performed iteratively using the three-dimensional Navier-Stokes equations and a multi-objective evolutionary algorithm featuring a special genetic diversity preserving method was used for handling the optimization problem. In this work, blade geometry was parameterized using three profiles along the span (hub, midspan and tip profiles), each of which was described by camber and thickness distributions, both defined using Bézier polynomials. The blade surface was then obtained by interpolating profile coordinates in the span direction using spline curves. By specifying a proper value of the tangential coordinate of the first midspan and the tip pro- files' control point with respect to the hub profile, the effect of blade lean was achieved. Results confirmed the superiority of optimized leaned profiles with respect to the baseline configuration as far as efficiency and pressure ratio were concerned. Performance enhancement derived from a drastic modification in the shock structure within the blade channel which led to less severe shock losses (Fig. 18). Computational time was huge, involving about 2000 CPU hours on a 4-processor machine.
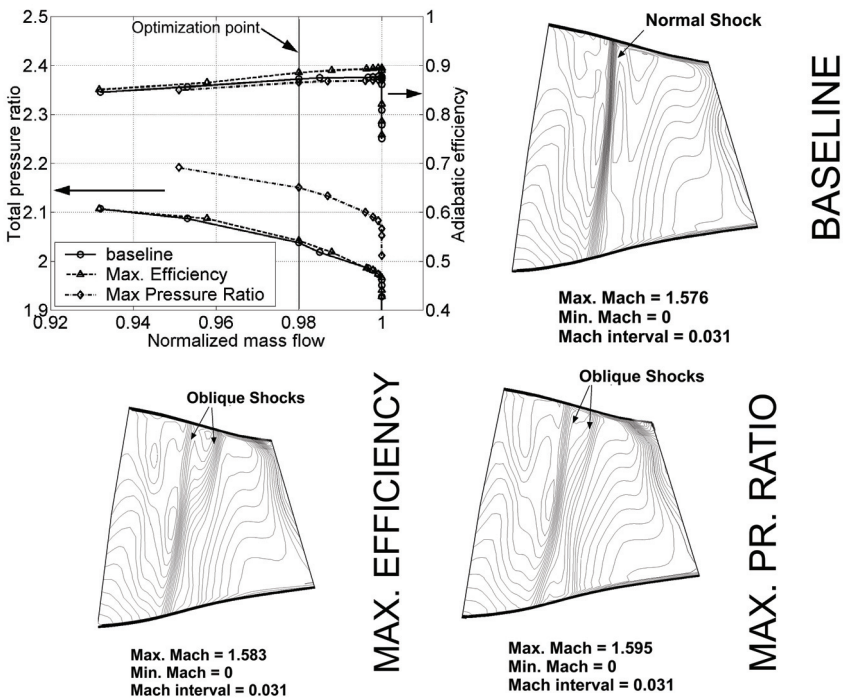

Fig. 18. Performance map and Mach number contours of baseline and optimized compressor configurations (from Benini, 2004).

Direct methods involving optimization techniques and surrogate methods

In order to accelerate convergence toward the design optima without using intensive calls of a CFD solver, the use of approximations of the objective functions is becoming a popular technique. This is often referred to as a "response surface methodology" (RSM) and the practice of building an approximation of the true objective function is named "metamodelling" or "surrogate model construction". Considering the competing requirements of computational economy, that is, employing as few data points as possible for constructing a surrogate model, and fidelity, that is, offering high accuracy in representing the characteristics of the design space, the assessment of the performance of surrogate models is of critical importance. In a recent work, Samad et al., 2008 multiple surrogate models for compressor optimization were considered including polynomial response surface approximation, Kriging, and radial basis neural networks. Once that the response surface was constructed, a sequential quadratic programming was used to search the optimal point based on these alternative surrogates. Three design variables characterizing the blade regarding sweep, lean, and skew were selected along with the three-level full factorial approach for design of experiment. The optimization was guided by three objectives aimed at maximizing the adiabatic efficiency, as well as the total pressure and total temperature ratios. The optimized compressor blades yielded lower losses by moving the separation line toward the downstream direction. The optima for total pressure and total temperature ratios were similar, but the optimum for adiabatic efficiency is located far from them. It was found that using multiple surrogates can improve the robustness of the optimization at a minimal computational cost.

Direct methods involving optimization techniques and adjoint equations

Another, remarkable, direct design optimization procedure makes use of adjoint methods (Chung, 2004). The formulation tries to encompass the drawbacks related to the long time required by traditional optimization techniques to converge. Adjoint methods are characterized by the definition of a classical Lagrangian functional, where the goal is to minimize a nonlinear objective function subject to the governing flow equations as constraints. The Lagrangian multipliers, called adjoint variables, are chosen such that they satisfy the functional, or adjoint equation, which eliminates the dependency of the optimality condition on flow variables. For the computation of adjoint variables, an adjoint sensitivity code needs to be built corresponding to the flow solver. However, the adjoint formulation enables the gradients of an objective function with respect to all design variables to be obtained simultaneously, at a negligible computational cost. This implies that a shape optimization based on the adjoint formulation becomes economical when the design involves a large number of design variables, as in 3D designs of complex geometry. However, obtaining accurate adjoint sensitivities is inherently difficult in internal flow problems due to the close proximities of the boundaries.

Inverse methods

In the last two decades, three-dimensional inverse design methods have emerged and been applied successfully for a wide range of designs, involving both radial/mixed flow turbomachinery blades and wings (Zangeneh, 1991; Demeulenaere & Van Den Braembussche, 1996; Dulikravich & Baker, 1999).
Quite a new approach to the 3D design of axial compressor bladings has been recently proposed by Tiow, 2002. In this work, an inverse method was presented which is based on

the flow governed by the Euler equations of motion and improved with viscous effects modelled using a body force model as given by Denton, 1987. However, contrary to the methods cited above, the methodology is capable of providing designs directly for a specific work rotor blading using the mass-averaged swirl velocity distribution.
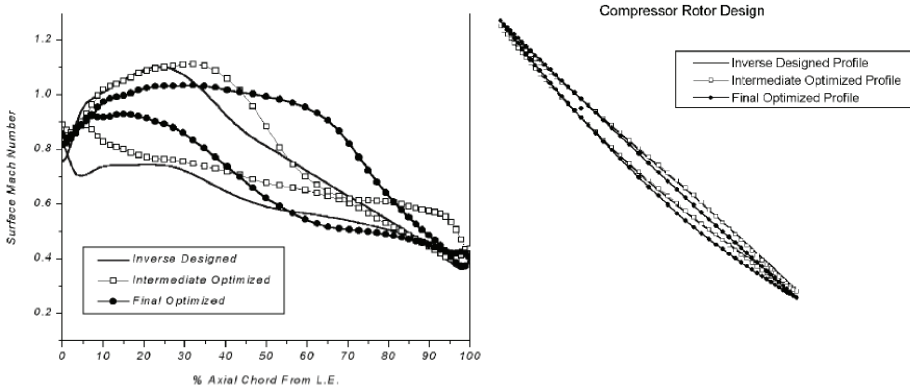
Fig. 19. Surface Mach number and geometry of inverse designed and final blades (from Tiow, 2002).
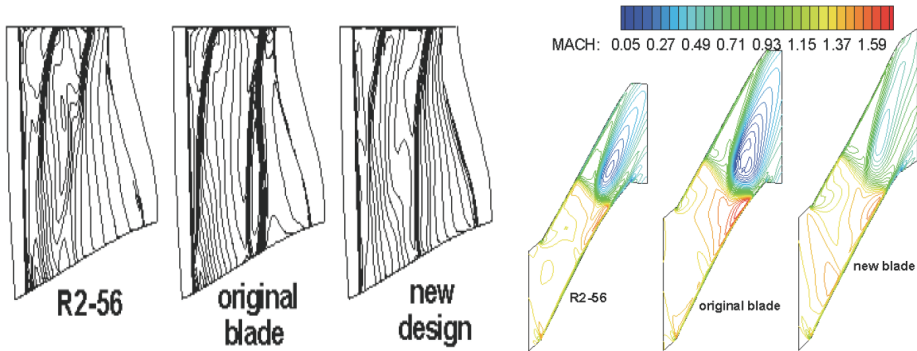
Fig. 20. Comparison of blade loading distributions of an original supersonic blade, a new design (prescribed by inverse mode), and a reference blade (R2-56 blade) for a given pressure ratio (left); comparison of passage Mach number distributions at 95% span (from Dang et al., 2003).

Moreover, the methodology proposed by Tiow, 2002 joins the capabilities of an inverse design with the search potential of an optimization tool, in this case the simulated annealing algorithm (Kirkpatrick et al, 1983). The entire computation required minimal human intervention except during initial set-up where constraints based on existing knowledge may be imposed to restrict the search for the optimal performance to a specified domain of interest. Two generic transonic designs have been presented, one of which referred to compressor rotor, where loss reductions in the region of 20 per cent have been achieved by imposing a proper target surface Mach number which resulted in a modified blade shape (Fig. 19).

An interesting application of a three-dimensional viscous inverse method was developed by Dang et al., 2003 ad applied to the design and analysis of a supersonic rotor, where aspiration was applied to enhance the operating range of a compressor. Results in Fig. 20 showed that an optimum combination of pressure-loading tailoring with surface aspiration can lead to a minimization of the amount of sucked flow required for a net performance improvement at design and off-design operations. By prescribing a desired loading distribution over the blade the placement of the passage shock in the new design was about the same as the original blade. However, the passage shock was weakened in the tip region where the relative Mach number is high.

6. Conclusion

Gas turbine compressors, either stationary or aeronautical, have reached a relatively mature level of development and performance. Nevertheless, the availability of advanced materials for blade construction makes it possible to rich levels of aerodynamic loading never experienced in the past while preserving high levels of on-off design efficiency. This holds especially for highly-subsonic and transonic blades, where tangential velocities are now becoming higher that 600 m/s, thus leading to stage pressure ratios of 2 and more. In fact, transonic bladings make it possible to reduce the number of stages for a prescribed total compression ratio, thus leading to huge savings in compressor costs, weight and complexity. To properly design such machines, multiobjective and multicriteria problems are to be dealt with which claim for rigorous and robust procedures, more often assisted by solid mathematical tools that help the designer to complete his/her skills and experience.

In view of the above, continuous effort is currently being spent in building advanced design techniques able to tackle the problem efficiently, cost-effectively and accurately. Plenty of design optimization techniques has been and are being developed including standard trial-and-error 1D procedures up to the most sophisticated methods, such as direct or indirect methods driven by advanced optimization algorithms and CFD.

Advanced techniques can be used in all stages of the design. In the field of 1D, or meanline methods, correlation-based prediction tools for loss and deviation estimation can be calibrated and profitably used for the preliminary design of multistage compressors.

2D methods supported by either throughflow or blade-to-blade codes in both a direct and an indirect approach, can be used afterwards, thus leading to a more accurate definition of the flow path of both meridional and cascade geometry. To enhance the potentialities of such methods, optimization algorithms can be quite easily used to drive the search toward optimal compressor configurations with a reasonable computational effort.

Detailed 3D aerodynamic design remains peculiar of single stage analyses, although several works have described computations of multistage configurations, either in steady and unsteady operations. However, the latter is an approach suitable for verification and analysis purposes, thus with a limited design applicability. 3D design optimization techniques can realistically be used if local refinements of a relatively good starting geometry is searched for. On the other hand, if more general results are expected, simplified design methods are mandatory, such as those based on supervised learning procedures, where surrogate models of the objective functions are constructed. Other very promising techniques include adjoint methods, where the number of design iteration can be potentially reduced by an order of magnitude if local derivatives of physical quantities with respect to the decision variables are carefully computed.

7. References

Ahmadi, M. (1998). Aerodynamic inverse design of turbomachinery cascades using a finite volume method on unstructured meshes. *Inverse Problems in Science and Engineering*, Vol. 6, Issue 4, pp. 281-298, ISSN: 1741-5977.

Benini, E. (2004). Three-Dimensional Multi-Objective Design Optimization of a Transonic Compressor Rotor. *Journal of Propulsion and Power*, Vol. 20, No. 3 (May/June), pp. 559-565, ISSN: 0748-4658.

Benini, E. & Toffolo, A. (2002). Development of High-Performance Airfoils for Axial Flow Compressors Using Evolutionary Computation. *Journal of Propulsion and Power*, Vol. 18, No. 3, pp. 544-554, ISSN: 0748-4658.

Casey, M.V. (1987). A mean-line prediction method for estimation the performance characteristics of an axial compressor stage. *Proceedings of the IMechE 1987, Turbomachinary Efficiency Prediction and Improvement*, pp. 145–55, ISBN: 0852986300.

Chen, L.; Luo, J.; Sun, F. ; Wu, C. (2005). Optimized efficiency axial-flow compressor. *Applied Energy*, Vol. 81, No. 4, pp. 409-419, ISSN: 0306-2619.

Chung, J.; Martin G. & Lee, K. D. (2004). Aerodynamic Design of 3D Compressor Blade Using an Adjoint Method. *AIAA Paper 2004-0027.*

Dang, T. Q.; Van Rooij, M. & Larosiliere, L. M. (2003). Design of Aspirated Compressor Blades Using Three-Dimensional Inverse Method. *NASA/TM − 2003-212212.*

Demeulenaere, A. & Van Den Braembussche, R. A. (1996). Threedimensional inverse method for turbomachinery blading design. *ASME paper 96-GT-39.*

Denton J. D. & Dawes W. N. (1999). Computational fluid dynamics for turbomachinery design. *Journal of Mechanical Engineering Science, IMechE Proc. Part C*, Vol. 213, No. C2, pp. 107-124, ISSN: 0022-2542.

Denton, J. D. (1986). The use of a distributed body force to simulate viscous effects in 3D flow calculations. *ASME paper 86-GT-144.*

Dulikravich, G. S. & Baker, D. P. (1999). Aerodynamic shape inverse design using a Fourier series method. *AIAA paper 99-0185.*

Dunham, J. (1997). Modelling of spanwise mixing in compressor through-flow computations. *Proceedings of the Institution of Mechanical Engineers, Part A: Journal of Power and Energy,* Vol. 211, No. 3, pp. 243-251, ISSN: 0957-6509.

Emery J. C.; Herrig L. J.; Erwin J. R. & Felix A. R. (1957). Systematic Two-Dimensional Cascade Test of NACA 65-Series Compressor Blades at Low Speeds. *NACA Rept. 1368.*

Giles, M. & Drela, M. (1987). Two-dimensional transonic aerodynamic design method. *AIAA Journal*, Vol. 25, No. 9, 1199-1205, ISSN: 0001-1452.

Ginder, R.B. & Harris D. (1989). *AGARD Pep Working Group 18: Compressor Test Case E/CO-3*, Royal Aerospace Establishment.

Goldberg, D. E. (1989). *Genetic Algorithms for Search, Optimization and Machine Learning, Reading*, MA, Addison Wesley, ISBN: 0201157675.

Horlock J. H. (1958). *Axial-flow Compressors*, Butterworths, London, UK.

Howard, M. A. & Gallimore, S. J. (1993). Viscous Throughflow Modeling for Multistage Compressor Design. *Journal of Turbomachinery*. Vol. 115, Issue 2, pp. 296-305.

Howell, A. R. (1942). The present Basis of Axial Flow Compressor Design: Part 1 Cascade Theory and performance. 2095. *Aeronautical Research Council Reports and Memoranda.*

Kirkpatrick, S.; Gelatt, C. D. & Vecchi, M. P. (1983). Optimization by simulated annealing. Science, Vol. 220, pp. 671–680.

Koch, C. C. & Smith, L. H. (1976). Loss sources and magnitudes in axial-flow compressors. *ASME Transactions, Journal for Engineering and Power*, Vol. 98, No. 3, pp. 411-424.

Köller, U.; Mönig, R.; Küsters, B. & Schreiber, H.-A. (2000). Development of Advanced Compressor Airfoils for Heavy-Duty Gas Turbines – Part I: Design and Optimization. *Journal of Turbomachinery*, Vol. 122, pp. 397-405, ISSN: 0889-504X.

Küsters, B.; Schreiber, H.-A.; Köller, U. & Mönig, R., (2000). Development of Advanced Compressor Airfoils for Heavy-Duty Gas Turbines – Part II: Experimental and Theoretical Analysis. *Journal of Turbomachinery*, Vol. 122, pp. 406-415, ISSN: 0889-504X.

Lee S.-Y. & Kim, K.-Y. (2000) Design optimization of axial flow compressor blades with three-dimensional Navier-Stokes solver. *KSME International Journal*. Vol. 14, No. 9, pp. 1005-1012, ISSN: 1226-4865.

Leonard O. & Van Den Braembussche, R. (1992). Two-dimensional Transonic aerodynamic design method. *Journal of Turbomachinery*, Vol. 114, No.3, pp. 553-560, ISSN: 0889-504X.

Lieblein, S. (1960). Incidence and deviation angle correlations for compressor cascades. *Trans. ASME Journal of Basic Engineering,* Vol. 82, pp. 575–587.

Lighthill, M. (1945). A new method of two-dimensional aerodynamic design. *Aeronautical research Council RxM 2104.*

Marsh, H. (1968). A digital computer program for the throughflow fluid mechanics in an arbitrary turbomachine using a Matrix Method. *Aeronautical Research Council. 3509.*

Massardo, A.; Satta, A. & Marini M. (1990). Axial Flow Compressor Design Optimization: Part II—Throughflow Analysis. *Journal of Turbomachinery*. Vol. 112, No. 3, pp. 405-411, ISSN: 0889-504X.

Mellor G. (1956). The NACA 65-Series Cascade Data. *Gas Turbine Laboratory Charts, MIT, Cambridge, MA.*

Miller, G.R.; Lewis, G.W. & Hartmann M.J. Jr (1961). Shock Losses in Transonic Compressor Blade Rows, *Trans. ASME Journal of Engineering for Power*, Vol. 83, July, pp., 235–242.

Novak, R. E. (1967). Streamline curvature computing procedures for fluid-How problems. *J. Eng. Power (Trans. ASME)*, Vol. 89, No. 4, pp. 478-490.

Obayashi, S. (1997). Pareto Genetic Algorithm for Aerodynamic Design Using the Navier-Stokes Equations, In: *Genetic Algorithms in Engineering and Computer Science*, Quagliarella et al. Eds., Wiley, New York.

Oyama, A. & Liou, M.-S. (2002). Multiobjective Optimization of a Multi-stage Compressor Using Evolutionary Algorithm. *AIAA paper 2002-3535*.

Pierret, S. (1999). Three-Dimensional Blade Design by Means of an Artificial Neural Network and Navier-Stokes Solver. *VKI Lecture Series 1999-02 on Turbomachinery Blade Design Systems*.

Samad, A.; Kim, K.-Y.; Goel, T.; Haftka, R.T. & Shyy, W. Multiple (2008). Surrogate Modeling for Axial Compressor Blade Shape Optimization, *Journal of Propulsion and Power*. Vol. 24, No. 2, pp. 302-310, ISSN: 0748-4658.

Schobeiri, M. T. (1996). Advanced Compressor Loss Correlations, Part I: Theoretical Aspects. *International Journal of Rotating Machinery.* Vol. 3, No. 3, pp. 163-177, ISSN (printed): 1023-621X.

Schwefel, H.-P. (1995). *Evolution and optimum seeking*, Wiley, New York, ISBN: 0471571482.

Sieverding, F.; Ribi, B. & Casey, M. (2004). Design of Industrial Axial Compressor Blade Sections for Optimal Range and Performance. *Journal of Turbomachinery* , Volume 126, No. 2, pp. 323-332, ISSN: 0889-504X.

Smith, L. H. (1970). Casing Boundary Layers in Multistage Axial Flow Compressors, in L. W. Dzung, *Flow Research in Blading*, Elsevier.

Smith, L.H. (1970). Casing Boundary Layers in Multistage Axial Flow Compressors, in *Flow Research in Blading* (L. W. Dzung Ed.), Elsevier.

Sturmayr, A. & Hirsch, Ch. (1999). Throughflow model for design and analysis integrated in a three-dimensional Navier-Stokes solver. *Proceedings of the Institution of Mechanical Engineers, Part A: Journal of Power and Energy.* Vol. 213, No. 4, pp. 263-273, ISSN: 0957-6509.

Sun, J. & Elder, R. L. (1998). Numerical optimization of a stator vane setting in multistage axial-flow compressors. *Proceedings of the Institution of Mechanical Engineers, Part A: Journal of Power and Energy.* Vol. 212, No 4, pp. 247-259, ISSN: 0957-6509.

Suter, P. (1960). Theoretische Untersuchung uber die Seitenwandgrenzschikter in Axialverdichtern. *Mitt. Inst. Therm. Turbomasch*. ETH Zürich, n. 5.

Tiow, W. T.; Yiu, K. F. C. & Zangeneh M. (2002). Application of simulated annealing to inverse design of transonic turbomachinery cascades. *Proceedings of the Institution of Mechanical Engineers, Part A: Journal of Power and Energy,* Vol. 216, No. 1, pp. 59-73, ISSN: 0957-6509.

Toffolo, A. & Benini, E. (2003). Genetic Diversity as an Objective in Evolutionary Algorithms. *Evolutionary Computation*, Volume 11, No. 2, pp. 151-167, ISSN 1063-6560.

Von Backström & T.W. & Roos, T.H. (1993). The streamline through-flow method for axial turbomachinery flow analysis. *Papers from the Eleventh International Symposium on Air Breathing Engines*, Tokyo, Japan, pp. 347 - 354.

Wisler, D. C.; Koch, C. C. & Smith, L. H. Jr. (1977). Preliminary design study of advanced multistage axial flow core compressors. *NASA Report -CR-135133.*

Zangeneh, M. (1991). A compressible three-dimensional design method for radial and mixed flow turbomachinery blades. *International Journal of Numerical Methods in Fluids*. Vol. 13, pp. 599–624, ISSN: 0271-2091.

Exergy and Environmental Considerations in Gas Turbine Technology and Applications

Richard 'Layi Fagbenle

BSME, PhD (Illinois), MSME(Iowa State),
USA

1. Introduction

Global CO_2 emissions by sector in 1990 for transportation, electric power, buildings, synfuels & hydrogen production, and industry were 20%, 27%, 15%, 0% and 38% respectively *[IPIECA Workshop, Baltimore, USA, 12-13 October 2004]*. In a 2095 scenario limiting the GHG to 550 ppm CO_2, the sectoral CO_2 emissions for transportation, electric power, buildings, synfuels & hydrogen production, and industry are 40%, 23%, 19%, 1% and 17% respectively *[IPIECA Workshop, Baltimore, USA, 12-13 October 2004]*. It is argued that the high cost of alternatives, and the strong demand for mobility, limits the effects of climate policies on the transportation sector, while more cost-effective emission reductions are found in the electric power and the industry sectors *[IPIECA Workshop, Baltimore, USA, 12-13 October 2004]*. While it is noted that climate change scenarios are replete with assumptions, the global growth of the transportation sector is undeniable, in both developing and developed countries, as the worldwide passenger travel vs. GDP by region in the figure below for the period 1950-1997 shows *[IPIECA Workshop, Baltimore, USA, 12-13 October 2004]*.

Figure 3: Passenger travel and GDP by region, 1950–97
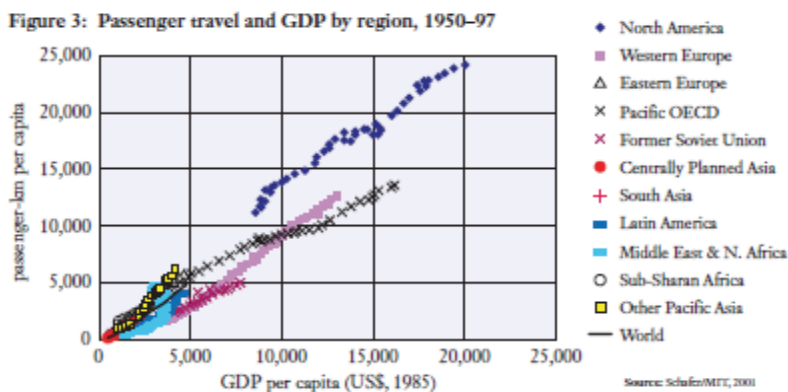
IPIECA Workshop, Baltimore, USA, 12-13 October 2004

In the EU, sectoral CO_2 emissions in 2005 for Energy, Transport, Industry, and Households were 34%, 27%, 21%, and 11%. The Transportation sector breakdown was Road (71.2%), Sea

Industry
328 (28%)

Transport
362 (31%)

Railways
9 (2.5%)

Aviation
50 (14%)

Inland Waterways
5 (1.4%)

Road Transport
297 (82%)

Households,
services, etc.
481 (41%)

*Final energy consumption 2005 in EU27
by sector and transport mode
(million tonnes oil equivalent)
Source: DG TREN 2007*

From: Rail Transport and Environment, page 5 – Facts & Figures, Nov. 2008.

Local air pollution
(1 person, Berlin - Frankfurt, 545 km)

gram

NOx
PM10

Car   369
Train   25
Plane   283
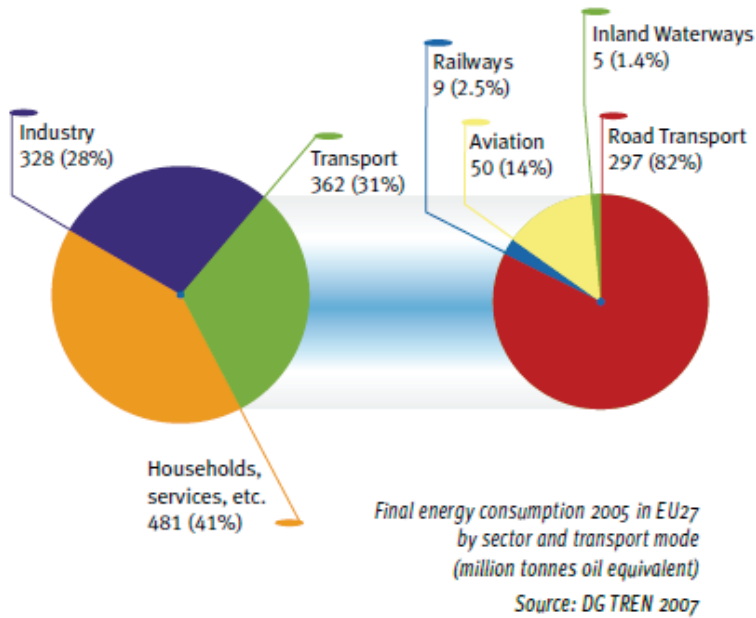
Source: www.ecopassenger.org 2008

From: Rail Transport and Environment, page 20 – Facts & Figures, Nov. 2008

and Inland Waterways (14.5%), Aviation (11.9%). From: Rail Transport and Environment, page 5 – Facts & Figures, Nov. 2008 *[Rail Transport and Environment, page 5 – Facts & Figures, Nov. 2008]*. The sectoral energy consumption for 2005 appears in the figure shown below, from which the Transportation sector had the second largest share of 31% after the Households & Services sector. Aviation's share of the Transportation sector energy consumption was 14%, second to Road Transport. A similar trend would be found in other regions of the developed world which accounts for the bulk of the global energy consumption and carbon emission.

Similarly, local air pollution data for NO_x and PM_{10} appears below for a journey of 545 km by three modes of transportation.

Transportation of 100 tons of cargo for a distance of 700 km between the Netherlands and Switzerland generates the local pollution information as shown in the figure below:

From: Rail Transport and Environment, page 19 – Facts & Figures, Nov. 2008.

Energy efficiency is of utmost importance in addressing the climate problem. Some significant strides have been made by some sub-sectors as the figure below indicates.

In Germany, the consumption of specific energy for Deutsche Bahn, both for regional passenger trains and freight has decreased constantly since 1990, due to the energy efficiency action plan of the company.

Specific primary energy consumption (per pkm or tkm) 1990 - 2007, Deutsche Bahn
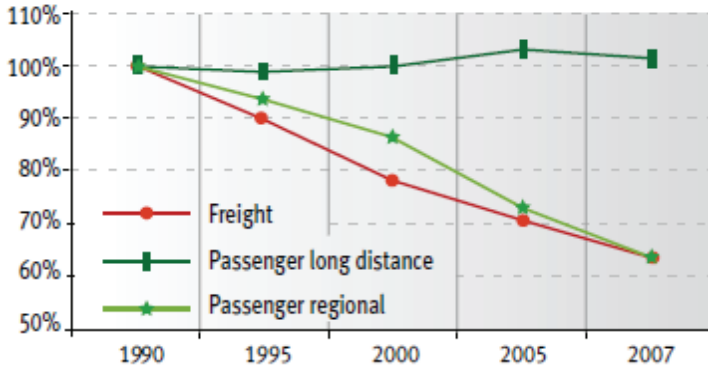
Source: Deutsche Bahn

From: Rail Transport and Environment, page 11 – Facts & Figures, Nov. 2008.

Finally, a look at the noise profile of some modes of transportation is instructive.

Percentages of citizens who are "highly disturbed" when exposed to rail, air and road traffic noise

L_{NIGHT} (outside, façade)
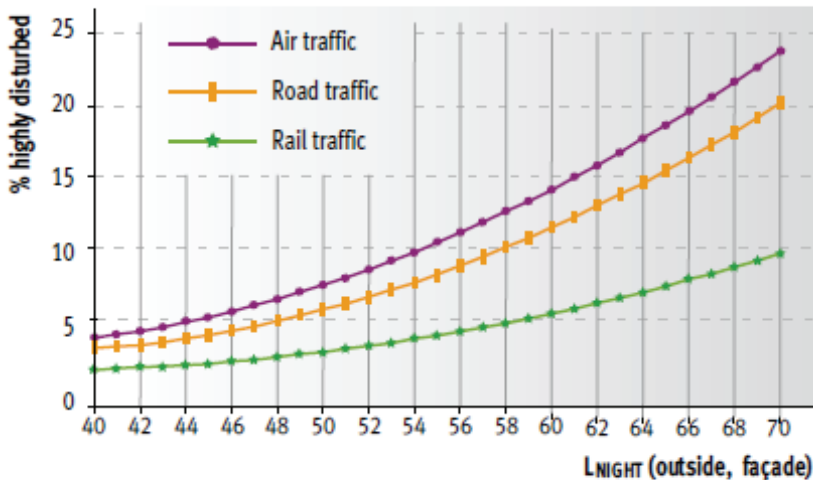
Source: EC 2004

From: Rail Transport and Environment, page 22 – Facts & Figures, Nov. 2008.

From the above, it is clear that just as the other sectors are called upon to reduce their GHG emission, the same should hold for the transportation sector. Gas turbines are employed in the air transportation sub-sector as well as in industry generally. It is claimed that air transport accounts for some 2-3 per cent of all anthropogenic CO2 emissions *[IPIECA Workshop, Baltimore, USA, 12-13 October 2004]*. As of 2004 IPIECA Workshop, there was no substitute envisioned for jet fuel neither was there any niche alternative fuel on the horizon. However, between 2008 and 2010, several test flights have been undertaken with synthetic jet fuel derived from natural gas *[Airline Industry Information, May 3, 2010]* as well as second generation biofuels from 50:50 blend of jathropha oil and standard A1 jet fuel *[The Seattle Times, Dec. 31, 2008]*. Similarly, the Airline Industry Information publication of 16 January 2009 reported that the US Federal Aviation Administration (FAA) has announced the results of a commercial airline test flight using a mixture of jet fuel and biofuel derived from algae and jatropha plants early in January 2009. In June 2009, the aviation fuels subcommittee of the ASTM International was reported to have approved specifications for synthetic aviation fuel, derived from a 50/50 blend of synthetic Fischer-Tropsch fuels and petroleum-derived fuels.

Gas turbines are employed in the Energy, Industrial, and the Transportation Sectors; sectors which have been shown to be responsible for most of the carbon emissions globally. Hence it is imperative to sustain the current drive for improvement in the energy, exergy and environmental performance of gas turbines in general (land, aviation, and marine gas turbine technology). We shall consider some of these issues in this chapter.

2. The Brayton open-cycle components – simple cycle and combined cycle gas turbines

Combustion Chamber/Combustor

Compressed air from the compressor (either centrifugal or axial-flow type) flows directly into the combustion chamber (such as that shown in Fig. 2.1 below) in a Brayton open simple cycle gas turbine where part of it (< 1/3) is used in a direct-fired air heater to burn the fuel after which the remaining air is mixed with the combustion products, all of which is to be carried out with minimum pressure loss. Minimization of pressure is critical at all stages from inlet to the compressor to entry into the turbine to ensure optimal power production from the gas turbine.

The Turbine Chamber of a 3-stage gas turbine plant is shown in Fig. 2.2 and Fig. 2.3 shows a typical turbine stage blades. Substantial volumes of air and combustion gases are moved smoothly and vibration-free through the gas turbine at very high velocities in an axial flow machine, being taken through a series of processes. These processes follow the Brayton cycle processes, viz.: non-isentropic compression from the atmospheric inlet conditions of the compressor to the isobaric (constant-pressure) combustion of the fuel in the combustion chamber, and then followed by adiabatic (non-isentropic) expansion of the hot gases and finally discharging the gases into the atmosphere, all of which is done in a continuous flow process. The energy transfer between the fluid and the rotor in the compression and expansion processes is achieved by means of kinetic action rather than by positive displacement as occurs as in reciprocating machines.

Fig. 2.1. A Combustion Chamber Can. [From Shepherd, D.G., Introduction to the Gas Turbine, D. Van Nostrand Co., Inc.
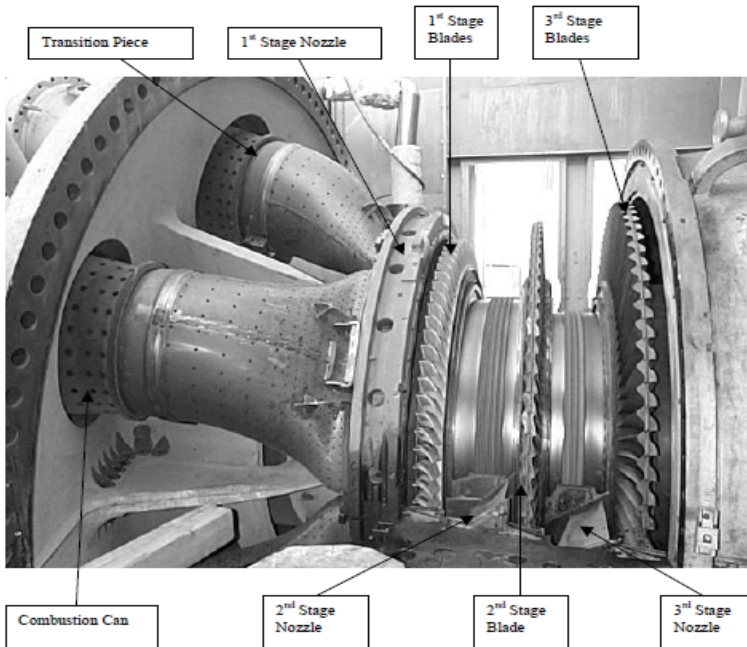
Fig. 2.2. The Turbine Chamber of a 3-stage turbine plant. [From Shepherd, D.G., Introduction to the Gas Turbine, D. Van Nostrand Co., Inc.
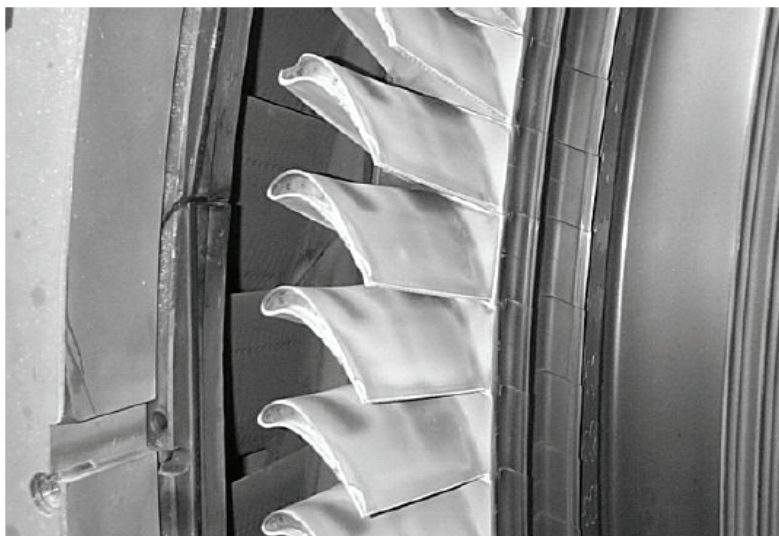
Fig. 3.3. Typical turbine stage. [From Shepherd, D.G., Introduction to the Gas Turbine, D. Van Nostrand Co., Inc.

4. Gas turbine fuels – conventional and new fuels

Conventional gas turbine fuels currently in use are exclusively liquid and gaseous and usually hydrocarbons. Solid gas turbine fuel technology is still in the research and developmental stages. New gas turbine fuels, as mentioned earlier in the Introduction, include the synthetic Fischer-Tropsch aviation jet fuels and the second generation biofuels.

Conventional gas turbine fuels – Liquid and gaseous fuels

Conventional gas turbine liquid fuels include the range of refined petroleum oils from highly refined gasoline through kerosene and light diesel oil to a heavy residual oil (Bunker C or No. 6 fuel oil). Table 4-1 gives the ultimate analysis of some liquid fuels.

Fuel	Carbon	Hydrogen	Sulfur	Ash, etc.
100 Octane petrol	85.1	14.9	0.01	-
Motor petrol	85.5	14.4	0.1	-
Benzole	91.7	8.0	0.3	-
Kerosene (paraffin)	86.3	13.6	0.1	-
Diesel oil	86.3	12.8	0.9	-
Light fuel oil	86.2	12.4	1.4	-
Heavy fuel oil	86.1	11.8	2.1	-
Residual fuel oil	88.3	9.5	1.2	1.0

Table 4.1. Ultimate analysis of some liquid fuels. (From Applied Thermodynamics for Engineering Technologists, S.I. Units by Eastop & McConkey, 2nd ed., 1970).

Table 4-2 below also indicates some of the key properties of some of the many known hydrocarbons.

Team, Air, and Gas Power Family / Name		Formu-la	Melting Temp, °C	Boiling Temp, °C	SIT++ °C	Specific Gravity	API Gravity	HHV kJ/kg	LHV kJ/kg	Mixture kJ/m³	Latent Heat, kJ/kg	Octane Rating	Performance No. (4 ml TEL/gal.) Lean[a]	Rich	Mol. Wt.
1. Gas C_nH_{2n+2}	Methane	CH_4	-182.2	-161.1	730	0.424	202.5	55,475	50,235	3241.5	576.85	110[a]	......	......	16.0
2. Gas C_nH_{2n+2}	Ethane	C_2H_6	-172.2	-88.3	566	0.546	194.0	52,102	47,909	3439.0	407.05	104[a]	......	......	30.0
3. LPG C_nH_{2n}	Propane	C_3H_8	-186.7	-42.2	535	0.582	142.0	50,358	46,555	3491.2	388.44	100	......	......	44.0
4. LPG C_nH_{2n}	Butane	C_4H_{10}	-135	-0.56	516	0.570	116.5	49,544	46,043	3532.1	383.79	92	......	......	58.1
5. LPG C_nH_{2n}	Pentane	C_5H_{12}	-129.4	36.1	501	0.626	94.5	49,079	45,583	3550.8	374.49	61	63	63	72.1
6. Gasoline C_nH_{2n+2}	n-Heptane	C_7H_{16}	-90.6	98.9	478	0.684	75.5	48,497	45,143	3591.8	307.03	0	0[b]	0[b]	100.2
7. Gasoline C_nH_{2n+2}	Triptane	C_7H_{16}	-25	81.1	......	0.690	......	......	44,427	......	290.75	......	200	360	100.2
8. Gasoline C_nH_{2n}	Iso-Octane	C_8H_{18}	-107.8	99.4	732	0.692	73.5	47,869	44,564	3558.2	297.73	100	153	153	114.2
9. Fuel Oil C_nH_{2n+2}	Decane	$C_{10}H_{22}$	-30	173.9	463	0.730	62.5	47,916	44,671	3599.2	251.21	......	......	......	142.3
10. Fuel Oil C_nH_{2n+2}	Dodecane	$C_{12}H_{26}$	-10	216.1	......	0.749	57.5	47,799	44,596	3610.4	248.88	......	......	......	170.3
11. Fuel Oil C_nH_{2n+2}	Hexadecane	$C_{16}H_{34}$	18.3	280	......	0.774	51.5	47,497	44,348	3610.4	....	100	......	......	226.4
12. Fuel Oil C_nH_{2n+2}	Octadecane	$C_{18}H_{38}$	27.8	307.8	......	0.782	49.5	47,450	44,303	3625.3	....	......	......	......	245.5
13. Olefins C_nH_{2n}	Propene	C_3H_6	-185	-47.8	......	0.61	103.0	48,846	45,241	3595.5	....	85	......	......	42.1
14. Olefins C_nH_{2n}	Butene-1	C_4H_8	-195	-6.7	......	0.625	......	48,613	45,008	3614.1	....	82	84	......	56.1
15. Olefins C_nH_{2n}	Hexene-1	C_6H_{12}	-137.8	63.3	......	0.675	76.0	44,310	41,317	3576.9	388.44	84.1	......	......	84.1
16. Napthenes C_nH_{2n} Cyclopentane		C_5H_{10}	-94.4	49.4	......	0.746	56.7	43,682	40,691	3506.1	....	82	100	>160	70.1
17. Naphthenes C_nH_{2n} Cyclohexane		C_6H_{12}	6.7	80.6	......	0.778	51.6	43,519	40,547	3506.1	362.86	77	84	130	84.1
18. Aromatics C_nH_{2n-6} Benzene		C_6H_6	5.6	80.6	739	0.88	29.0	42,240	39,984	3606.7	393.09	110[a]	68	>160	78.1
19. Aromatics C_nH_{2n-6} Toluene		C_7H_8	-95	110.6	811	0.87	31.0	42,566	40,612	3688.6	362.86	104[a]	95	>160	92.1
20. Aromatics C_nH_{2n-6} Xylene		C_8H_{10}	-26.1	140.6	......	0.86	31.0	43,031	40,705	3632.7	337.27	105[a]	......	......	106.2
21. Alcohols	Methanol	CH_3OH	-97.8	65	......	0.792	46.4	22,725	20,106	3353.3	1167.65	98	<75	>180	32.0
22. Alcohols	Ethanol	C_2H_6O	-117.2	77.8	......	0.785	47.1	29,726	26,991	3494.9	921.10	99	<75	>180	46.0
23. Tetraethyl lead		$C_8H_{20}Pb$	-136.1	182.2	......	1.653	......	....	....	....	169.80	......	......	......	......
24. Hydrogen (gas)		H_2	....	......	......	......	......	....	10,002	....	....	......	......	......	2.0
25. Water		H_2O	0	100	......	0.998	......	....	0	....	2256.22	......	......	......	18.0
26. Carbon (solid)		C	....	......	......	......	......	....	32,564	....	....	......	......	......	12.0
27. Gasoline (straight run)		......	-60	43-149	......	......	......	....	44,194	....	....	140[a]	78	93	....
28. Carbon monoxide		CO	....	-191.7	609	......	......	10,111	10,111	....	....	......	......	......	28.0

Table 4.2. Abstracted from Table V Properties of Hydrocarbons of Steam, Air & Gas Power by Severns, Degler & Miles, John Wiley, 5th ed. 1964. S.I. Units conversion done by Prof. Richard Fagbenle. SIT – Self-ignition temperature;

Fig. 4-1 below shows typical distillation characteristics for military and commercial aircraft fuels. Relative to the "pure substance" single evaporation temperatures of water and ethyl alcohol, gasoline is a mixture of liquid several hydrocarbons and its various components boil off at different temperatures as can be seen in the graphs.
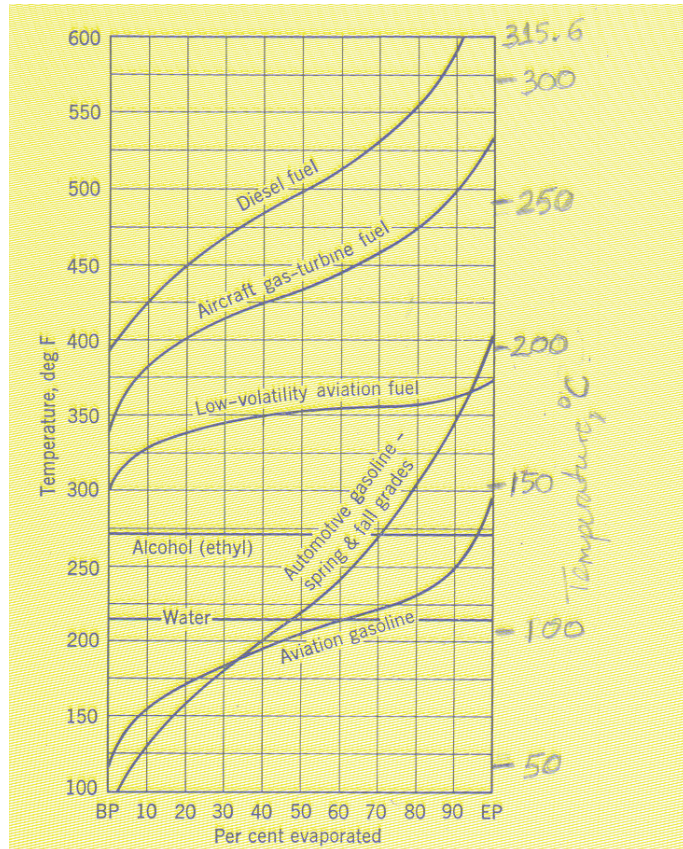
Fig. 4.1. Typical ASTM distillation characteristics for various types of fuels. Degree Centigrade scale supplied by Prof. R. 'Layi Fagbenle. Abstracted from Steam, Air, and Gas Power by Severns, Degler & Miles, John Wiley & Sons Inc. 1964.

The aviation gasoline graph at the bottom of the graph is for piston-engine powered aircraft and it has a low flash point to improve its ignition characteristics. It is usually a high-octane gasoline known as "avgas". Turbine engines on the other hand can operate with a wide range of fuels, but typically use fuels with much higher flash points, less flammable and generally safer to store and transport. Most jet fuels are basically kerosene-based. Both the Jet A specification fuel used in the USA and the Jet A-1 standard specification of most of the rest of the world have a relatively high flash point of 38°C and a self-ignition temperature (SIT) (or auto-ignition temperature) of 210°C, making them safer to handle than the traditional avgas. The open air burning temperature in Table 4-2 can be compared with the typical distillation characteristics for aircraft gas turbine fuel in Fig. 4-1.

Physical Properties	Jet A-1	Jet A
Flash Point	> 38°C (100.4 °F)	
Self- (auto-) ignition temperature	210 °C (410 °F)	
Freezing point	< -47 °C (-52.6 °F)	< -40 °C (-40 °F)
Open air burning temperature	287.5 °C (549.5 °F)	
Density (per litre)	0.775 kg/l – 0.840 kg/l	
Specific energy (calorific value)	> 42.80 MJ/kg	

Table 4.2. Typical Specifications for Jet A and Jet A-1 Aircraft Fuels (from Wikipedia)

Specifications for Heavy-Duty Gas Turbine Fuels

Heavy-duty gas turbines are able to burn a wide range of gaseous fuels and hence are less restricted in their fuel classifications. A typical heavy-duty gas turbine fuel specification (range only indicated) appears in Table 4-3 below.

Fuel	LHV [MJ/m^3]	Major Components
Natural Gas and Liquefied Natural Gas (LNG)	29.81 – 7.45	Methane
Liquefied Petroleum Gas [LPG]	85.70 – 119.23	Propane; Butane
Gasification Gases (Air Blown)	3.73 – 5.50	CO; H_2; N; H_2O_v
Gasification Gases (Oxygen Blown)	7.45 – 14.90	CO; H_2; H_2O_v
Process Gases	11.20 – 37.30	CH_4; H_2; CO; CO_2

Table 4.3. Range of typical heavy-duty gas turbine fuel classification (adapted from GEI 41040G – GE Gas Power Systems, Revised January 2002).

The feedstock for gasification fuels can be coal, petroleum coke or heavy liquids. Gasification fuels generally have lower much lower heating values than other fuel gases, and they are produced by one of two processes: oxygen blown or air blown gasification process.

Process gases are generated by many petrochemical and chemical processes and are suitable for fuelling gas turbines, for example refinery gases). Constituents of process gases include CH_4, H_2, CO, and CO_2. Other process gases used as gas turbine fuels are byproducts of steel production such as blast furnace gases and coke oven gases. Blast Furnace Gases (BFG) have heating values below minimal allowable limits for gas turbine fuels, necessitating blending with other fuels such as coke oven gas, natural gas or hydrocarbons such as propane or butane.

Typical gas turbine fuel specification ranges appear in Table 4-4 below. In addition to such specifications which may be particular to each turbine manufacturer, allowable gas fuel contaminant levels are also specified for such trace metals as (Pb, V, Ca, and Mg), Alkali metals (Na and K) and particulates. Sodium (Na) is the only trace metal contaminant normally found in natural gas, and it source is salt water in the ground gas wells.

Sources of contaminants in heavy-duty gas turbine applications include particulates arising largely from corrosion chemical reactions in gas pipelines, liquid (water and/or hydrocarbon) condensates and lubricating oils from compressor stations; sulfur (as H_2S or COS); trace metals; steam and water for injection; alkali metals contained in compressor discharge; and the fuel.

Fuel Properties	Max	Min	Notes
Lower Heating Value, MJ/m^3	None	3.73 –11.20	
Modified Wobbe Index (MWI) - Absolute limits - Range within limits	54 +5%	40 -5%	
Flammability Ratio		2.2:1	Rich:Lean Fuel/Air Ratio, volume basis
Constituent Limits, mole % Methane, CH$_4$ Ethane, C$_2$H$_6$ Propane, C$_3$H$_8$ Butane C$_4$H$_{10}$ + higher paraffins (C$_4$+) Hydrogen, H$_2$ Carbon monoxide, CO Oxygen, O$_2$ Total Inerts (N$_2$+CO$_2$+Ar) Aromatics (Benzene C$_6$H$_6$, Toluene C$_7$H$_8$, etc.) Sulfur	 100 15 15 5 Trace Trace Trace Trace 15 Report Report	 85 0 0 0 0 0 0 0 0 0 0	 % of reactant species % of reactant species % of reactant species % of reactant species % of reactant species % of reactant species % of reactant species % of reactant species % of total (reactants + inerts)

Table 4.4. Range of typical heavy-duty gas turbine fuel specification (adapted from GER 41040G – GE Gas Power Systems, Revised January 2002).

Conventional and New Environmental-conscious Aero and Industrial Gas Turbine Fuels

Conventional aero gas turbine fuels are commonly:
i.   Kerosene from crude petroleum sources using established refining processes, and
ii.   synthetic kerosene from Fischer-Tropsch (FT) synthesis using coal, natural gas, or any other hydrocarbon feedstock (e.g. shale, tar sands, etc.). These are produced by first gasifying the hydrocarbon resource followed by liquefaction to form hydrocarbon liquids (e.g. as earlier noted, the Airline Industry Information update dateline 26 June 2009)

New Environmentally-conscious aero gas turbine fuels are:
i.   Bio-fuels from bio-derived Fatty Acid Methyl Esters (FAME) mixed with conventional aero fuel (kerosene) in regulated proportions,
ii.   Bio-ethanol and bio-methanol neat or mixed in regulated proportions with gasoline,
iii. Biofuels produced from Fischer-Tropsch Synthesis (FTS) process using biomass feedstock such as oil seeds – jathropha, palm oil, soybeans, rapeseed (canola), sunflower, camelina, etc., as well as animal fats,
iv.   Bio-syngas produced by gasification of biomass, lignocellulosic biomass and other agricultural wastes used as feed into the FTS (2nd generation biofuels) to produce liquid fuels (FTL), and
v.   Liquefied petroleum gas (LPG) which is really not a cryogen; Liquefied gases such as LNG, Methane and Hydrogen. Both methane and hydrogen will have to be liquefied for use as aircraft fuel.

Table 4.5 below gives relative properties of conventional aviation kerosene and typical biodiesel aircraft fuel (will vary with Fatty Acid Methyl Esters [FAME] type):

Property	Aviation Kerosene	Bio-diesel	20% Blend	Impact
Heat of combustion [MJ/kg] typical	43.2	32 – 39	41.0 – 42.4 (spec. min: 42.8)	Airframe range/loading
Density [kg/m³] range	775 – 840	860 – 900	792 – 852	
Viscosity [mm2/sec @ -20°C max.				Wing tank temp. limits, Cold Starts & Relight.
Approx. Carbon length	C14 – C15 max (trace levels)	C16 – C22	C16 – C22	Combustion emissions
Flash point, °C min.	38	>101	Unchanged	
Freeze Point,°C max	-47	-3? 0	-5 to -10 with additives	Wing tank temp. limits, Cold Start and Relight.
Sulfur [ppm] max	3000	10		
Acidity [mg KOH/g] max	0.015	0.5	0.11	Material compatibility
Phosphorous [ppm] max	Excluded	10	2	Hot-end life
Metals [ppm] max	Excluded	5	1	Hot-end life
Thermal Stability	Controlled to well defined level	Not controlled	Not known	Fuel system & injector life
Composition	Hydrocarbon	FAME	20% FAME	Elastomer compatibility

From: Ppt. Presentation by Chris Lewis, Company Specialist – Fluids, Rolls Royce plc, titled "A Gas Turbine Manufacturer's View of Biofuels". 2006.

In the steam-reforming reaction, steam reacts with feedstock (hydrocarbons, biomass, municipal organic waste, waste oil, sewage sludge, paper mill sludge, black liquor, refuse-derived fuel, agricultural biomass wastes and lignocellulosic plants) to produce bio-syngas. It is a gas rich in carbon monoxide and hydrogen with typical composition shown in Table 4.6 below.

Constituents	% by vol. (dry & N$_2$-free)
Carbon monoxide (CO)	28 – 36
Hydrogen (H$_2$)	22 – 32
Carbon dioxide (CO$_2$)	21 – 30
Methane (CH$_4$)	8 – 11
Ethene (C$_2$H$_4$)	2 – 4
Benzene-Toluene-Xylene (BTX)	0.84 – 0.96
Ethane (C$_2$H$_5$)	0.16 – 0.22
Tar	0.15 – 0.24
Others (NH3, H2S, HCl, dust, ash, etc.)	< 0.021

Source: M. Balat et al. Energy Conversion and Management 50 (2009) 3158 – 3168).

Table 4.6. Typical composition of bio-syngas from biomass gasification.

A useful reference for the thermo-conversion of biomass into fuels and chemicals can be found in the above referenced paper by M. Balat et al.

Ethanol-powered gas turbines for electricity generation

In a 2008 report by Xavier Navarro (RSS feed), a company called LPP Combustion (Lean, Premixed, Prevaporized) was claimed to have demonstrated that during gas turbine testing, emissions of NOx, CO, SO_2 and PM (soot) from biofuel ethanol (ASTM D-4806) were the same as natural gas-level emissions achieved using dry low emission (DLE) gas turbine technology. It was also claimed that the combustion of the bio-derived ethanol produced virtually no net CO_2 emissions.

Gas Turbines and Biodiesels

A recent study by Bolszo and McDonnell (2009)[1] on emissions optimization of a biodiesel-fired 30-kW gas turbine indicates that biodiesel fluid properties result in inferior atomization and longer evaporation times compared to hydrocarbon diesel. It was found that the minimum NOx emission levels achieved for biodiesel exceeded the minimum attained for diesel, and that optimizing the fuel injection process will improve the biodiesel NOx emissions.

A theoretical study was recently carried out by Glaude et al. (2009)[2] to clarify the NOx index of biodiesels in gas turbines taking conventional petroleum gasoils and natural gas as reference fuels. The adiabatic flame temperature T_f was considered as the major determinant of NOx emissions in gas turbines and used as a criterion for NOx emission. The study was necessitated by the conflicting results from a lab test on a microturbine and two recent gas turbine field tests, one carried out in Europe on rapeseed methyl ester (RME) and the other in USA on soybean methyl ester (SME), the lab test showing a higher NOx emission while the two field tests showed slightly lower NOx emission relative to petroleum diesel. It is however clear that biodiesels have reduced carbon-containing emissions and there is agreement also on experimental data from diesel engines which indicate a slight increase in NOx relative to petroleum diesel. The five FAME's studied by Glaude et al. were RME, SME, and methyl esters from sunflower, palm and tallow.

The results showed that petroleum diesel fuels tend to generate the highest temperatures while natural gas has the lowest, with biodiesel lying in-between. This ranking thus agrees with the two field tests mentioned earlier. It was also found out that the variability of the composition of petroleum diesel fuels can substantially affect the adiabatic flame temperature, while biofuels are less sensitive to composition variations.

5. Factors limiting gas turbine performance

The Joule cycle (also popularly known as the Brayton cycle) is the ideal gas turbine cycle against which the performance (i.e. the thermal efficiency of the cycle η_{CY}) of an actual gas turbine cycle is judged under comparable conditions. We prefer to restrict the use of Joule

---

[1] C. D. Bolszo and V. G. McDonell, Emissions optimization of a biodiesel fired gas turbine, Proceedings of the Combustion Institute, Vol 32, Issue 2, 2009, Pages 2949-2956.

[2] Pierre A. Glaude, Rene Fournet, Roda Bounaceur and Michel Moliere, (2009). Gas Turbines and Biodiesel: A clarification of the relative NOx indices of FAME, Gasoil and Natural Gas.

cycle to the ideal gas turbine cycle while the Brayton cycle is exclusively used for the actual gas turbine cycle. The ideal gas turbine "closed"cycle (or Joule cycle) consists of four ideal processes – two isentropic and two isobaric processes – which appear as shown in Fig. 5.1. The thermal efficiency of the Joule cycle in terms of the pressure ratio r_p given by $r_p = \frac{p_B}{p_A}$ and the pressure ratio parameter ρ_p given by $\rho_p = r_p^{(\gamma-1)/\gamma}$ is:

$$\eta_{\text{Joule}} = \left(1 - \frac{1}{r_p^{(\gamma-1)/\gamma}}\right) = \left(1 - \frac{1}{\rho_p}\right) \tag{5.1}$$

Hence, the thermal efficiency of the ideal gas Joule cycle is a function only of the pressure ratio. Since for isentropic processes 1-2 and 3-4, $\frac{T_2}{T_1} = \frac{T_3}{T_4} = \rho_p$, the Joule efficiency is also dependent of the isentropic temperature ratios only, but independent of the compressor and the turbine inlet temperatures separately without a knowledge of the pressure ratio. Thus, ρ_p is essentially the isentropic temperature ratio, the abscissa in Fig. 5.1. If air is the working fluid employed in the ideal Joule cycle, the cycle is referred to as the air-standard Joule cycle.
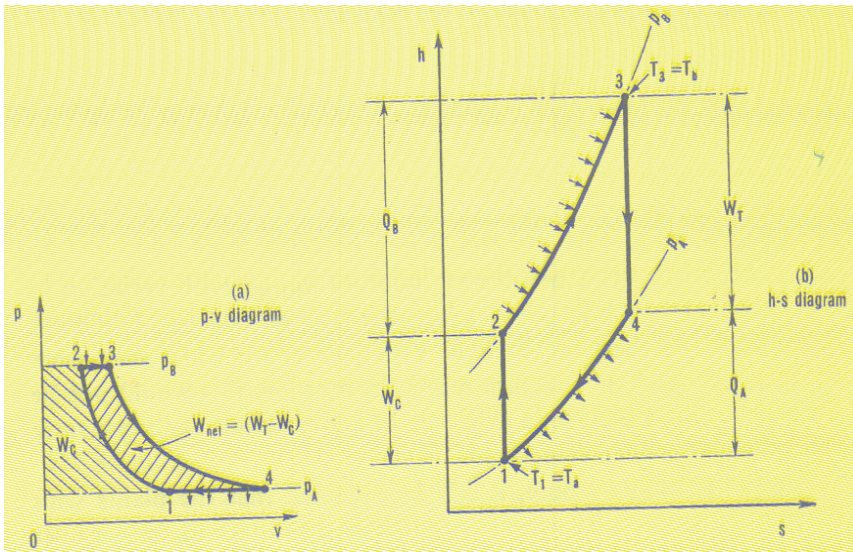

Fig. 5.1. Ideal Joule cycle (a) p-V and (b) T-s state diagrams. From Haywood [ ].

Fixing the inlet temperature to the compressor T_a and the inlet temperature to the turbine T_b automatically sets a limit to the pressure ratio r_p, which occurs when the temperature after isentropic compression from T_a is equal to the TIT T_b. However, when this occurs, the net work done is seen to be equal to zero, as the area of the cycle on the T-s and p-V diagrams indicate.

Haywood considers an interesting graphical representation of eq. 5.1 above for $T_a = 15°C$ and $T_b = 100°C$ as shown in Fig. 5.2

For T_a = 15°C and T_b = 100°C, η_{Joule} increases continuously with rp right up to the limiting value as the curve labeled "reversible" shows. The limiting pressure ratio r_p = 99.82 approximated to 100 in the figure is attained when $\rho_p = \theta$ = T_b/T_a = 1073/288 = 3.7257. Under this condition, a sketch of the Joule cycle on the T-s diagram shows that as r_p approaches this value, the area enclosed by the cycle approaches zero. However, In practical terms, a pressure ratio this large is never used when issues of process irreversiblities are considered, to which the remaining two curves in the graph pertain.
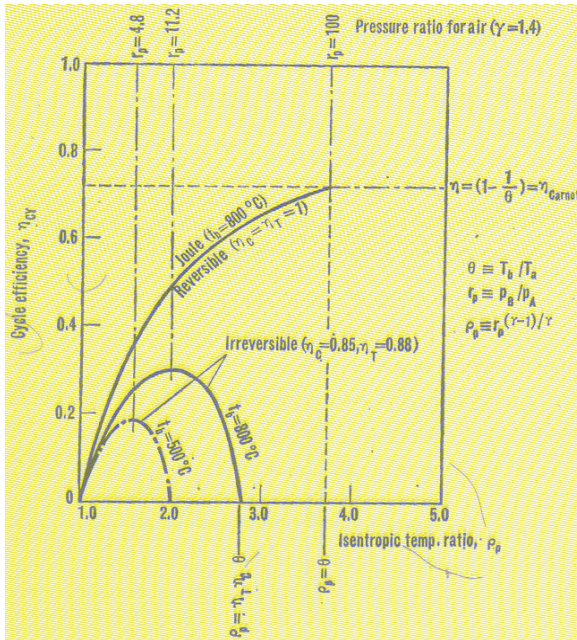
Fig. 5.2. Variation of cycle efficiency with Isentropic temperature ratio ρ_p (t_a = 15°C). From Haywood [ ].

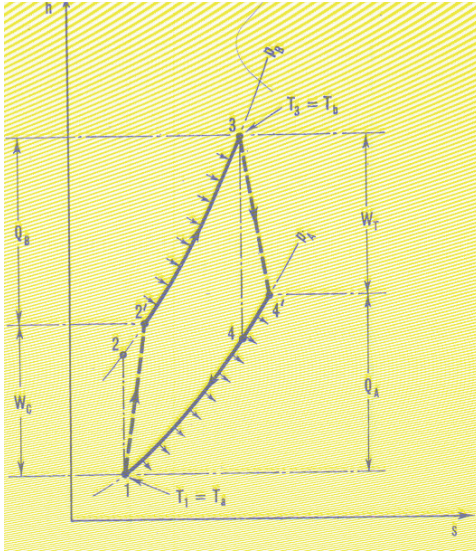## 5.1 Effect of irreversibilities in the actual gas turbine cycle

In an actual plant, frictional effects in turbines and compressors and pressure drops in heat exchangers and ductings and combustion chamber are basically lost opportunities for production of useful work. The h-s curve diagram for such a gas turbine Brayton cycle appears in Fig. 5.3, wherein the heat and work terms in each of the processes are identified, ignoring the frictional effects in the heat exchangers, ductings and combustion chamber. We note that the compressor work input required W_C, is now much larger than its previous value for the ideal Joule cycle while the turbine work output W_T is considerably smaller than for the ideal Joule cycle, revealing the considerable effect of turbine and compressor inefficiencies on the cycle thermal efficiency. An analytic expression for the Brayton cycle thermal efficiency can be shown to be:

$$\eta_{Brayton} = \frac{(1 - 1/\rho_p)(\alpha - \rho_p)}{(\beta - \rho_p)} \tag{5.2}$$

where $\alpha = \eta_C \eta_T \theta$, $\beta = [1 + \eta_C(\theta - 1)]$, and $\theta = T_b/T_a$.

In Fig. 5.2, the actual Brayton cycle performance is depicted for turbine and compressor isentropic efficiencies of 88% and 85% respectively, t_a = 15°C for two values of t_b = 800°C and 500°C respectively. The optimum pressure ratio is now reduced from approximately 100 to 11.2 for t_b = 800°C, and to only 4.8 at t_b = 500°C. This optimum pressure ratio is more realistically achievable in a single compressor. Here also, we find that $\eta_{Brayton}$ is highly dependent on $\theta = T_b/T_a$, showing a drastic reduction from TIT = 800°C to TIT = 500°C.

The compressor work input per unit mass of working fluid is

$$W_c = c_p(T_{2'} - T_a) = \frac{c_p T_a}{\eta_c}(\rho_p - 1) \qquad (5.3)$$

while

$$W_T = c_p(T_b - T_4') = c_p \eta_T T_b \left(1 - \frac{1}{\rho_p}\right) \quad (5.4)$$

and

$$W_{net} = (W_T - W_C) = \frac{c_p T_a}{\eta_c}\left(1 - \frac{1}{\rho_p}\right)(\alpha - \rho_p) \quad (5.5)$$

with $\alpha = \eta_C \eta_T \theta$ and $\theta = T_b/T_a$ as before.

From 5.5, W_{net} vanishes when $\rho_p = 1$ and when $\rho_p = \alpha$. Also from differentiating 5.5 w.r.t. ρ_p, we obtain that W_{net} is maximum when $\rho_p = \sqrt{\alpha}$. The variation of W_{net} with the adiabatic temperature ratio ρ_p appears in Fig. 5.4.

Fig. 5.3. Enthalpy-entropy diagram for Actual Brayton cycle, with turbine and Compressor inefficiencies. From Haywood [ ].
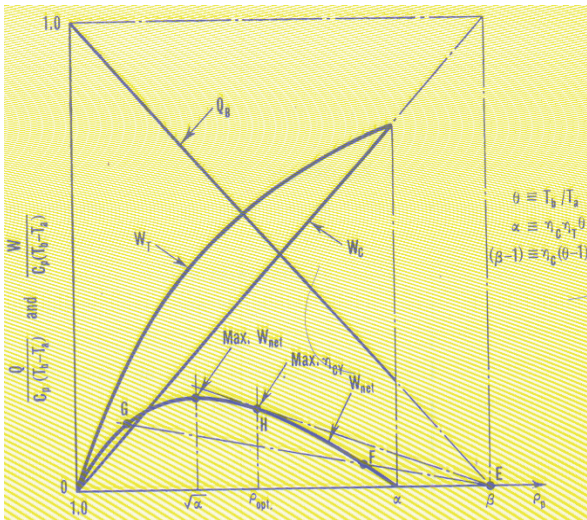
Haywood [] discusses the graphical construction in Fig. 5.4 due to Hawthorne and Davis [ ] for the variation of Q_B, W_T, W_C, and W_{net} with variation in ρ_p for fixed values of T_a and T_b. The maximum efficiency is obtained at the value of ρ_p corresponding to the point H at which a straight line from point E is tangent to the curve for W_{net}, i.e at $\rho_p = \rho_{opt}$. The method indicates that the points of maximum thermal efficiency of the Brayton cycle η_{CY} and the maximum W_{net} are not coincident; rather the value of ρ_p is greater for the former than for the latter. It may also be shown that, if ρ_W and ρ_{opt} are the values of ρ_p for maximum W_{net} and maximum η_{CY} respectively, then $\dfrac{\rho_w}{\rho_{opt}} = \sqrt{(1 - \eta_m)}$ where η_m is the maximum value of the thermal efficiency of the Brayton cycle.

Fig. 5.4. Variation of heat supplied to the combustor Q_B, turbine work output W_T, compressor work input W_C, and W_{net} with isentropic temperature ratio ρ_p. From Haywood [ ].

Figs. 5.5 and 5.6 show the schematic of the simple-cycle, open-flow gas turbine with a single shaft and double shaft respectively. The single shaft units are typically used in applications requiring relatively uniform speed such as generator drives while in the dual shaft applications, the power turbine rotor is mechanically separate from the high-pressure turbine and compressor rotor. It is thus aerodynamically coupled, making it suitable for variable speeds applications.
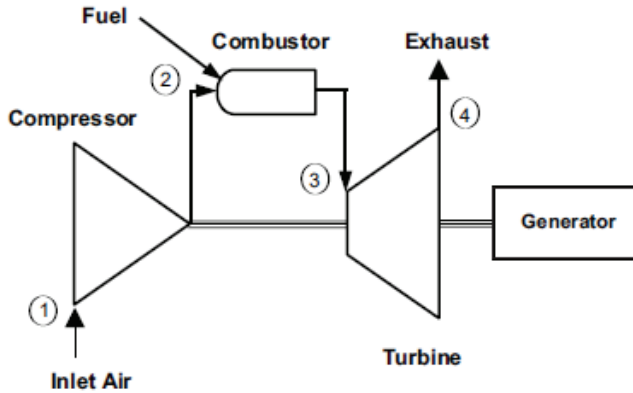
Fig. 5.5. Simple-cycle, open-flow, single-shaft gas turbine
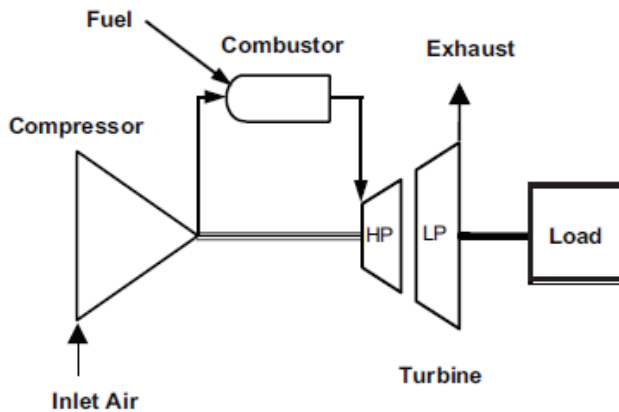
Fig. 5.6. Simple cycle, open-flow, dual-shaft gas turbine for mechanical drives.

5.2 Simple-cycle vs. Combined-cycle gas turbine power plant characteristics

Fig. 5.7 shows the variation of output per unit mass and efficiency for different firing temperatures and pressure ratios for both simple-cycle and combined-cycle applications. In the simple-cycle top figure, at a given firing temperature, an increase in pressure ratio results in significant gains in thermal efficiency. The pressure ratio resulting in maximum efficiency and maximum output are a function of the firing temperature; the higher the pressure ratio, the greater the benefits from increased firing temperature. At a given

pressure ratio, increasing the firing temperature results in increased power output, although this is achieved with a loss in efficiency mainly due to increase in cooling air losses for air-cooled nozzle blades.

On the other hand, pressure ratio increases do not affect efficiency markedly as in simple-cycle plants; indeed, pressure ratio increases are accompanied by decreases in specific power output. Increases in firing temperature result in marked increases in thermal efficiency. While simple-cycle efficiency is readily achieved with high pressure ratios, combined-cycle efficiency is obtained with a combination of modest pressure ratios and higher firing temperatures. A typical combined-cycle gas turbine as shown in Fig. 5.7 (lower cycle) will convert 30% to 40% of the fuel input into shaft output and up to 98% of the remainder goes into exhaust heat which is recovered in the Heat Recovery Steam Generator (HRSG). The HRSG is basically a heat exchanger which provides steam for the steam turbine part of the combined-cycle. It is not unusual to utilize more than 80% of the fuel input in a combined-cycle power plant which also produces process steam for on- or off-site purposes.
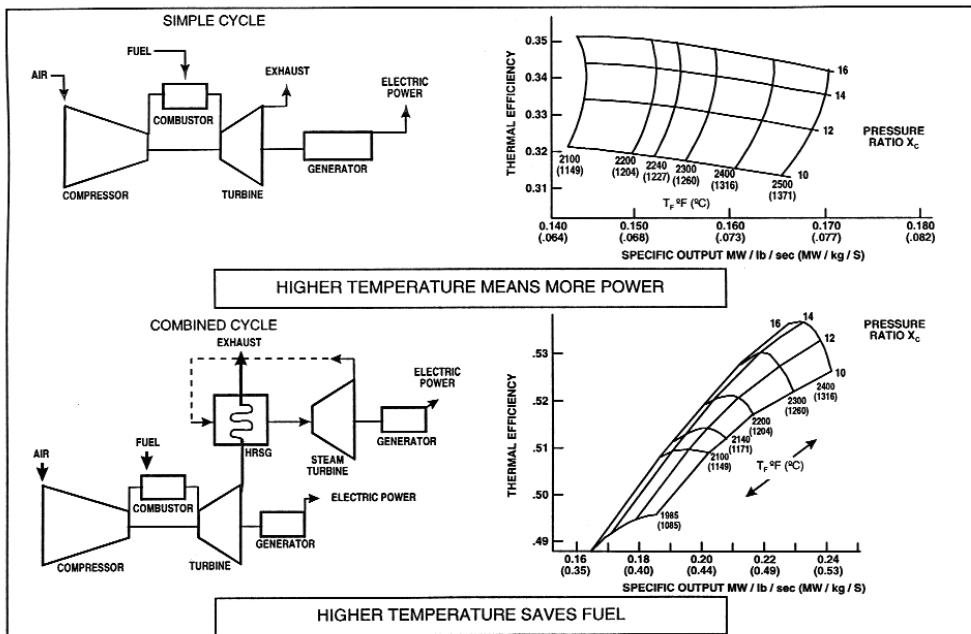
Fig. 5.7. Gas turbine characteristics for simple-cycle (above) and for combined-cycle (below). Abstracted from GE Power Systems.GER-3567H 10/00.

5.3 Other factors affecting gas turbine performance

Other factors affecting the performance of a gas turbine (heat rate, power output) include the following: Air temperature (compressor inlet temperature) and pressure; Site elevation or altitude; humidity; inlet and exhaust losses resulting from equipment add-ons such as air filters, evaporative coolers, silencers, etc. The usual reference conditions stated by manufacturers are 59F/15C and 14.7 psia/1.013 bar. In general, output decreases with increasing air temperature while the heat rate increases less steeply. Similarly, altitude

corrections are provided by manufacturers with factors less than 1.0 at higher latitudes. The density of humid air is less than that of dry air and it affects both the heat rate and the specific output of a gas turbine. The higher the humidity, the lower the power output and conversely the higher the heat rate. Inlet and exhaust pressure losses result in power output loss, heat rate increase and exhaust temperature increase.

5.4 Gas turbine emissions and control

Over the past three to four decades, many developed countries have put in place applicable state and federal environmental regulations to control emissions from aero, industrial and marine gas turbines. This was the case even before the current global awareness to the Climate Change problem. Only NOx gas turbine emission was initially regulated in the early 1970s and it was found that injection of water or steam into the combustion zone of the combustor liner did produce the then required low levels of NOx reduction without serious detrimental effects on the gas turbine parts lives or the overall gas turbine cycle performance.

However, as more stringent requirements emerged with time, further increase in water/steam approach began to have significant detrimental effects on the gas turbine parts lives and cycle performance, as well increased levels of other emissions besides NOx. Alternative or complimentary methods of emission controls have therefore been sought, some internal to, and others external to, the gas turbine, namely:

i.   Dry Low NOx Emission (DLN) or DLE burner technology
ii. Exhaust catalytic combustion technology
iii. Overspray fogging

While NOx emissions normally include Nitrous oxide (NO) and Nitrogen dioxide (NO_2), NOx from gas turbines is predominantly NO, although NO_2 is generally used as the mass reference for reporting NOx. This can be seen from the typical exhaust emissions from a stationary industrial gas turbine appearing in Table 5.1.

Major Species	Typical Concentration (% Volume)	Source
Nitrogen (N_2)	66 - 72	Inlet Air
Oxygen (O_2)	12 - 18	Inlet Air
Carbon Dioxide (CO_2)	1 - 5	Oxidation of Fuel Carbon
Water Vapor (H_2O)	1 - 5	Oxidation of Fuel Hydrogen
Minor Species Pollutants	**Typical Concentration (PPMV)**	**Source**
Nitric Oxide (NO)	20 - 220	Oxidation of Atmosphere Nitrogen
Nitrogen Dioxide (NO_2)	2 - 20	Oxidation of Fuel-Bound Organic Nitrogen
Carbon Monoxide (CO)	5 - 330	Incomplete Oxidation of Fuel Carbon
Sulfur Dioxide (SO_2)	Trace - 100	Oxidation of Fuel-Bound Organic Sulfur
Sulfur Trioxide (SO_3)	Trace - 4	Oxidation of Fuel-Bound Organic Sulfur
Unburned Hydrocarbons (UHC)	5 - 300	Incomplete Oxidation of Fuel or Intermediates
Particulate Matter Smoke	Trace - 25	Inlet Ingestion, Fuel Ash, Hot-Gas-Path Attrition, Incomplete Oxidation of Fuel or Intermediates

Table 5.1. Typical exhaust emissions from a stationary industrial gas turbine. Abstracted from GE Power Systems – GER-4211-03/01.

NOx are divided into two main classes depending on their mechanism of formation. NOx formed from the oxidation of free nitrogen in either the combustion air of the fuel are known as "thermal NOx", and they are basically a function of the stoichiometric adiabatic flame temperature of the fuel. Emissions arising from oxidation of organically bound nitrogen in the fuel (the fuel-bound-nitrogen, FBN) are known as "organic NOx". Of the two, efficiency of conversion of FBN to NOx proceeds much more efficiently than that of thermal NOx.
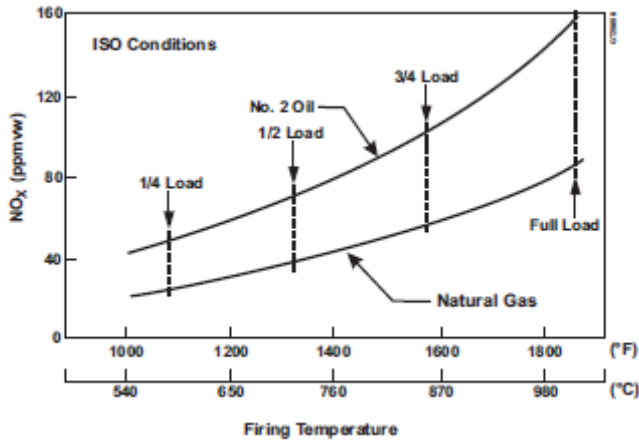
Fig. 5.8. Typical NOx emissions for a class of Industrial gas turbines. Abstracted from GE Power Systems – GER-4311-03/01.
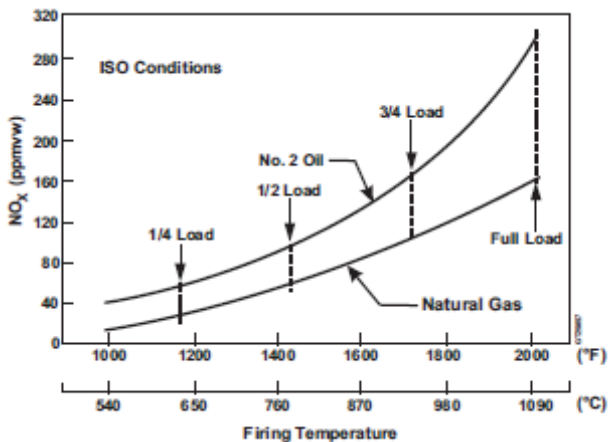
Fig. 5.9. Typical NOx emissions for a class of Industrial gas turbines. Abstracted from GE Power Systems – GER-4311-03/01.

Thermal NOx is relatively well studied and understood, but much less so for organic NOx formation. For thermal NOx production, NOx increases exponentially with combustor inlet air temperature, increases quite strongly with F/A ratio or with firing temperature, and increases with increasing residence time in the flame zone. It however decreases exponentially with increasing water or steam injection or increasing specific humidity. Figs.

5.1 and 5.2 show typical NOx emissions for industrial gas turbines operating on natural gas fuel and No.2 distillate as a function of firing temperature.

As regards organic NOx, reduction of flame temperature (as through water or steam injection) does scant little to abate it. Water and steam injection are known to actually increase organic NOx in liquid fuels. As noted earlier, organic NOx is important only for fuels containing significant amount of FBN such as crude or residual oils.

Carbon Monoxide (CO) emissions as seen from Table 5.1 can be of comparable magnitude with NO emission, depending on the fuel and the loading condition of the gas turbine. Fig. 5.10 is a typical industrial gas turbine CO emission as a function of firing temperature. We note that, contrary to the NOx trend, CO emission increases significantly as the firing temperature is reduced below about 816°C (1500°F). It is noted that carbon monoxide is normally expected from incomplete combustion and hence inefficiency in the combustion process.

Fig. 5.10. CO emissions from an industrial gas turbine. Abstracted from GE Power Systems – GER-4311-03/01.

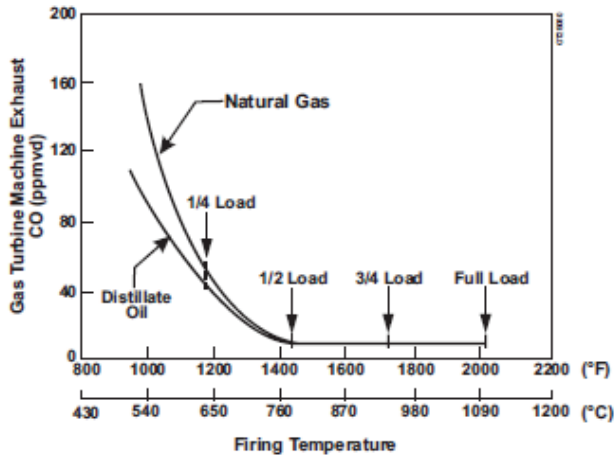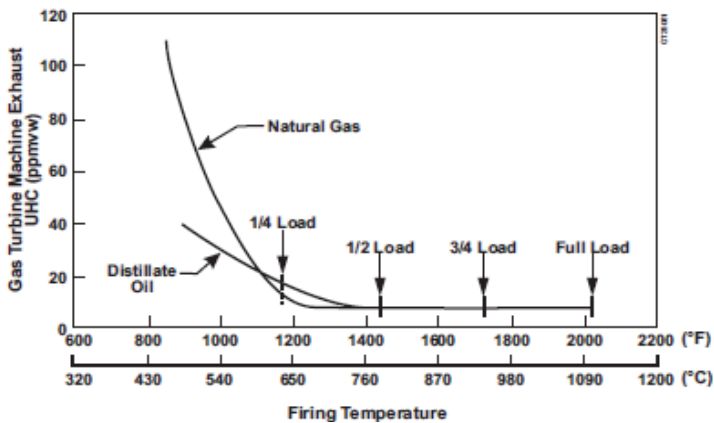Fig. 5.11. UHC emissions from an industrial gas turbine. Abstracted from GE Power Systems – GER-4311-03/01.

Unburned hydrocarbons (UHC) are also products of the inefficiency in the combustion process. Fig. 5.11 shows a typical industrial gas turbine UHC emission as a function of firing temperature.

Particulates.

Fuel properties, combustor operating conditions and the design of the combustor all affect the gas turbine exhaust particulate emission, whose main components are smoke, ash, erosion and corrosion products in the metallic ducting and piping of the system.

Gas Turbine Emission Control Techniques

Emission	Control technique
NOx	Lean Head End Liner; Water or Steam Injection; Dry Low NOx Emission (DLE); Overspray fogging
CO	Combustor Design; Catalytic reduction
UHC & VOC	Combustor Design
SOx	Control of sulfur in fuel
Particulates & PM-10	Fuel composition influencing Sulfur & Ash;
Smoke	Combustor design; Fuel composition; Air atomization

6. Exergy considerations

Publication of research articles on exergy consideration in power cycles dates back about four decades now, possibly with the initial work of Kalina (1984) on the combined cycle system with novel bottoming cycle and that of El-Sayed and Tribus (1985) on a theoretical comparison of the Rankine and Kalina cycles. This was followed with the work of Zheng et al. (1986a) on Energy Utilization Diagram (EUD) for two types of LNG power-generation systems; Zheng (1986b) on graphic exergy analysis for coal gasification-combined power cycle based on EUD; Ishida et al. (1987) on evaluation of a chemical-looping-combustion power-generation system by graphic exergy analysis; and Wall et al. (1989) ending the first decade with an exergy study of the Kalina cycle that began the decade.

In the second decade belong the works of Najjar (1990) on hydrogen fuelled and cooled gas turbines; Ishida et al. (1992a) on graphic exergy analysis of fuel-cell systems based on EUDs; Jin & Ishida (1993) on graphical analysis of complex cycles; Joshi et al. (1996) on a review of IGCC technology; and Jaber et al. (1998) on gaseous fuels (derived from oil shale) for heavy-duty gas turbines and Combined Cycle Gas Turbines.

The third decade began with the analysis of Bilgen (2000) on exergetic and engineering analysis of gas turbine-based cogeneration systems; Thongchai et al. (2001) on simplification of power cycles with EUDs; Marrero et al. (2002) on 2nd law analysis and optimization of a combined triple power cycle; Jin & Ishida (2004) on graphic presentation of exergy loss in mixing on an EUD; Khaliq (2004) on second-law analysis of the Brayton/Rankine combined power cycle with reheat; Khaliq (2004b) on thermodynamic performance evaluation of combustion gas turbine cogeneration systems with reheat; Ertesvag et al. (2005) on exergy analysis of a gas turbine combined cycle power plant with pre-combustion CO_2 capture; Tae won Song et al. (2006) on performance characteristics of a MW-class SOFC/GT hybrid system based on a commercially available gas turbine; Guillermo Ordorica-Garcia et al. (2006) on technoeconomic evaluation of IGCC power plants for CO_2 avoidance; Fagbenle et

al (2007) on thermodynamic analysis of biogas-fired integrated gasification steam-injected gas turbine (BIG/STIG) plant; Karellas et al. (2008) on thermodynamic evaluation of combined cycle plants; Fadok et al. (2008) on an update on advanced hydrogen turbine development; Bartieri et al. (2008) on biomass as an energy resource – the thermodynamic constraints on the performance of the conversion process in producing synthetic gas (syngas) for high efficiency internal combustion engines such as CCGT as well as in fuel cells (MCFC and SOFC) after adequate cleaning up and reforming; Khaliq (2009a) on exergy analysis of a gas turbine trigeneration system for combined production of power, heat and refrigeration; Khaliq (2009b) on energy and exergy analyses of compression inlet air-cooled gas turbines using the Joule-Brayton refrigeration cycle; Khaliq (2009c) on exergy analysis of the regenerative gas turbine cycle using absorption inlet cooling and evaporative aftercooling; Farzaneh-Gord et al. (2009) on a new approach for enhancing performance of a gas turbine using as a case study the Khangiran refinery in Iran; Fachina (2009) on Exergy accounting – the energy that matters; and finally closing the highly productive decade with Baratieri et al. (2009) on the use of syngas in IC engines and CCGT.

The fourth decade has begun with Woudstra et al. (2010) on thermodynamic evaluation of combined cycle plants. This does in no way claim to be a complete account of all the contributions to exergy analyses of power cycles from inception to the present time, rather we have tried to give some highlights on the journey so far.

Exergetic Analyses of Power Cycles – Gas Turbines, CCGTs, IGCC & BIG/STIG

Dincer and Rosen (2007) have listed the following benefits of using exergy analysis in industrial plant equipment and processes:

- Efficiencies based on exergy, unlike those based on energy, are always measures of the approach to true ideality, and therefore provide more meaningful information when assessing the performance of energy systems. Also, exergy losses clearly identify the locations, causes and sources of deviations from ideality in a system.
- In complex systems with multiple products (e.g., cogeneration and trigeneration plants), exergy methods can help evaluate the thermodynamic values of the product energy forms, even though they normally exhibit radically different characteristics.
- Exergy-based methods have evolved that can help in design-related activities. For example, some methods (e.g., exergoeconomics and thermoeconomics) can be used to improve economic evaluations. Other methods (e.g., environomics) can assist in environmental assessments.
- Exergy can improve understanding of terms like energy conservation and energy crisis, facilitating better responses to problems.

The following table comparing energy and exergy from Dincer & Cengel [ ] is also useful in appreciating exergy.

According to Szargut et al. [1988], "exergy is the amount of work obtainable when some matter is brought to a state of thermodynamic equilibrium with the common components of the natural surroundings by means of reversible processes, involving interaction only with the above mentioned components of nature". Four different types of exergy are identifiable in principle, denoted as kinetic, potential, physical and chemical exergy, Masim and Ayres [ ], viz.:

$$\varepsilon = \varepsilon_k + \varepsilon_p + \varepsilon_{ph} + \varepsilon_{ch}$$

ENERGY	EXERGY
Is dependent on the parameters of matter or energy flow only, and independent of the environment parameters.	Is dependent on both the parameters of matter or energy flow and on the environment parameters.
Has the values different from zero (equal to mc^2 upon Einstein's equation)	Is equal to zero (in dead state by equilibrium with the environment).
Is governed by the 1st Law of Thermodynamics (FLT) for all the processes.	Is governed by the 1st Law of Thermodynamics (FLT) for reversible processes only (while it is destroyed partly or completely in irreversible processes).
Is limited by the 2nd Law of Thermodynamics (SLT) for all processes (including reversible ones).	Is not limited for reversible processes due to the 2nd Law of Thermodynamics (SLT).
Is motion or ability to produce motion.	Is work or ability to produce work.
Is always conserved in a process, so can neither be destroyed or produced.	Is always conserved in a *reversible* process, but is always consumed in an irreversible process.
Is a measure of quantity only.	Is a measure of quantity and quality due to entropy.

Table 6.1.

Kinetic and potential exergy (ε_k & ε_p) have the same meaning as their corresponding energy or work terms, W_k and W_p, both of which are usually negligible in the analysis of most common industrial processes. Physical exergy is the work obtainable by taking a substance through reversible physical processes from its initial state at temperature T and pressure p to the final state determined by the temperature T_o and pressure p_o of the environment, Szargut et al. [1988]. Consideration of physical exergy is important for optimization of thermal and mechanical processes including heat engines and power plants. However, it is of secondary importance and often negligible when attention is focused on very large systems, such as chemical and metallurgical processes, where chemical exergy dominates in resource accounting and environmental analyses Masim and Ayres [ ]. Chemical exergy is the work that can be obtained by bringing a substance having the temperature and pressure (T,p) to a state of thermodynamic equilibrium with the datum level components of the environment. It has two components – one associated with chemical reactions occurring in isolation, and the other associated with the diffusion of reaction products into the surroundings, Masim and Ayres [ ]. Hence the importance of defining a reference state when calculating both physical and chemical exergy. The exergy function is thus a measure of the difference between two states, namely the state of the "target" system and that of its surroundings (or, more appropriately, the ultimate state of the combined system plus its surroundings, after they have reached mutual equilibrium of pressure p_o, temperature T_o, and chemical composition μ_o). As Masim and Ayres [ ] put it, the analytical expression for exergy shows that exergy is a measure of the "thermodynamic distance" of the target system from equilibrium, or alternatively, a measure of the "distinguishability" of the target system from its environment.

For a closed system with (T,p), the exergy (loss) $\Delta\varepsilon$ is given by:

$$\Delta\varepsilon = B = S(T-T_o) - V(p-p_o) + \sum \mu_i(N_i - N_{io})$$

where Ni is the number of moles of the ith system and μ_i is its chemical potential. As noted earlier, $\Delta\varepsilon \leq 0$, the equality holding only when the process is reversible. Here p_o and T_o are, appropriately, the ambient atmospheric pressure and temperature respectively.

For a flow or open system, where mass crosses the system boundaries,

$$\Delta\varepsilon = B = (H - H_o) - T_o(S - S_o) - \sum\mu_i(N_i - N_{io})$$

where H is enthalpy. In this case, it is important to have a knowledge of the detailed average chemical composition of the reaction products and the environmental sink with which the system reacts Masim and Ayres [ ].

Exergetic Analyses of Gas Turbine Cogeneration/Combined Cycle Plants

The generic name "*Cogeneration or Combined Cycle*" plants is used for gas turbine top cycle plant whose hot exhaust is used for generating steam in a heat recovery steam generator (HRSG) for a steam turbine bottom cycle. In these plants, the gas turbine combustion chamber (combustor) is fuelled normally with liquid or gaseous fuels piped to the plant from nearby storage tanks; the fuel is thus not produced on-site. Cogeneration/Combined Cycle plants therefore generate additional power from the steam turbine. However, they may also generate both power and steam from the steam turbine if process steam is required on-site or elsewhere, as in district heating systems. In such a case, the Cogeneration/CC plant would properly qualify to be called a Combined Heat and Power (CHP) Plant, although this appellation is technically reserved for any power plant whose hot combustion product gases are used to generate steam for on-site or other uses. Thus a CHP need not have a gas turbine in its power production train, it could be any power plant that generates "waste" heat from which we are able to extract "useful" thermal energy. In this regard, many CHP plants are powered by large diesel Internal Combustion (I.C.) engines.

We first consider the work of Bilgen (2000) on exergetic analyses of gas turbine cogeneration systems in which gas turbine cogeneration systems involving three different combinations of power and steam generation from a gas turbine and a steam turbine fed with steam from a HRSG were studied (see Figures 6.1, 6.2 and 6.3). The gas turbine exhaust gases produce the steam in the HRSG.
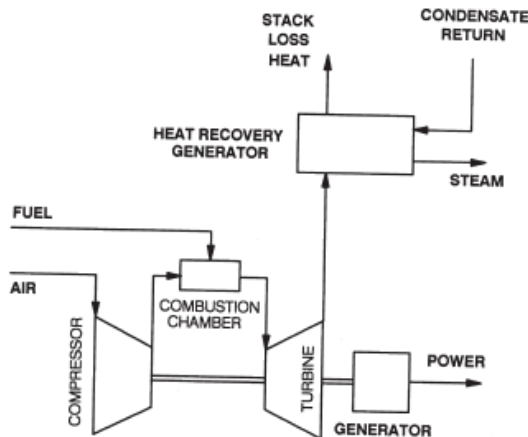
Schematic of the cycle for gas turbine electric power production–process heat production.

Fig. 6.1. From Bilgen (2000).
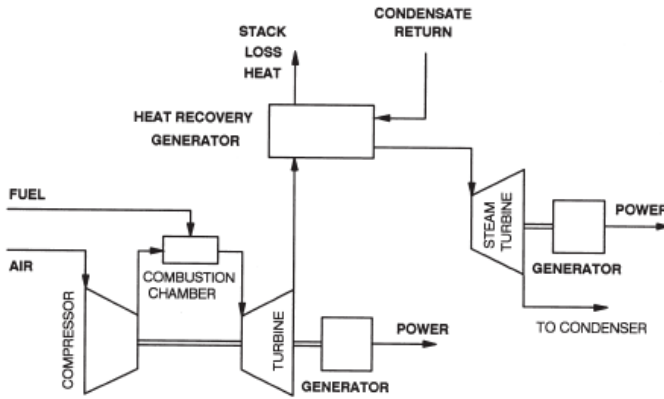
Schematic of the cycle for gas turbine electric power production–electric power production by steam turbine.

Fig. 6.2. From Bilgen (2000)
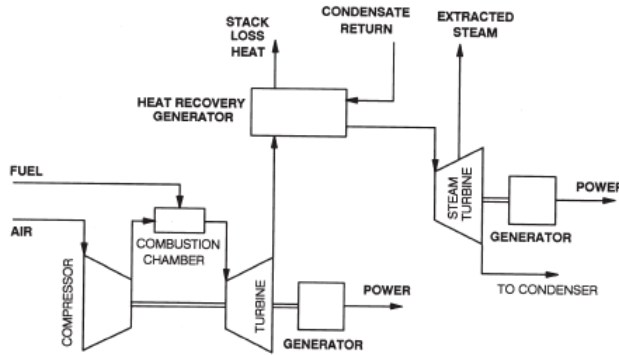
Fig. 3.   Schematic of the cycle for gas turbine electric power production–electric power production by steam turbine–process heat production.

Fig. 6.3. From Bilgen (2000).

Bilgen undertook a combustion analysis by calculating the composition of the fuel gas mixture using direct minimization of the Gibbs function of formation of each compound I from its constituent elements, using Lagrangian multipliers. The fuel utilization efficiency or the 1st Law efficiency is given by

$$\eta = C\frac{(W_e + Q_p)}{E_f} \tag{6.1}$$

Where E_f is the energy of the fuel, W_e and Q_p are the electrical energy and the thermal energy of the process respectively while C is 0.98 as the parasitic system loss is assumed to be 2%. The second law or exergy efficiency is defined as

$$\varepsilon = \frac{(W_e + B_p)}{B_f} \tag{6.2}$$

Where We is work, hence considered all exergy as earlier discussed, Bp is the exergy content of process heat produced and Bf is the exergy content of fuel input. Expressions for the energy and exergy terms above were given by Bilgen as follows:

$$E_f = \sum_p n_e h_e - \sum_r n_i h_i \qquad (6.3)$$

$$B_f = (\sum_r n_i g_i - \sum_p n_e g_e) + RT_o \ln\left(\frac{y_{O_2}^{y_1}}{y_{CO_2}^{x_1} y_{H_2O}^{x_2}}\right) \qquad (6.4)$$

where h_i, h_e are enthalpies and g_i, g_e are the Gibbs functions of reactants (shown with r) and products (shown with p) for stoichiometric reaction of fuel evaluated at 1 bar and 298 K; y_i^α is the mole fraction of component I in the environment.
A fuel exergy factor is defined as

$$\varepsilon_f = \frac{B_f}{E_f} \qquad (6.5)$$

The exergy of the process heat produced is given by

$$B_p = m_s[(h - h_c) - T_o(s - s_c)] \qquad (6.6)$$

where m_s and s are the mass and entropy of the steam produced, sc is the entropy of the condensate return, both at the process heat pressure, and T_o is temperature of the environment. Further,

$$Q_p = m_s(h - h_c) \qquad (6.7)$$

Process heat exergy factor and power-to-heat ratio are defined as

$$\varepsilon_p = \frac{B_p}{Q_p} \qquad \text{and} \qquad r_{ph} = \frac{W_e}{Q_p} \qquad (6.8a,b)$$

A relationship can be established between exergy, ε, and fuel utilization, η, efficiencies using the above equations as follows, Bilgen (2000):

$$\varepsilon = \frac{\eta}{\varepsilon_f}\left[\frac{r_{ph} + \varepsilon_p}{1 + r_{ph}}\right] \qquad (6.9)$$

Two Case Studies corresponding to Figures 6.1 and 6.3 were considered in detail, and in both cases, natural gas was used as fuel. Plant capacity factor was assumed to be 80%. The data for Case Study I appear in Table 6.2 for base-load gas turbine at ISO conditions of 288 K and 101.325 kPa, and 60% relative humidity and they are from a case study earlier reported for an industrial gas turbine (the GE LM2500PE reported by Rice (1987) and Huang (1990). Other parameters employed in the Case Study are isentropic efficiencies of compressor and turbine of 70.4% and 92.6% respectively; intake air temperature same as ISO condition of 288K; process steam is saturated at 2026 kPa; temperature of condensate return is 373 K; and the pinch point temperature difference is 50 K. Bilgen calculated the composition of the products of combustion of natural gas with 226% air (in moles) as follows:

1 CO_2; 0 CO; 2 HO_2; 0.001 OH; 0 NO_2; 0 NO; 24.515 N_2; 4.52 O_2. He also presented the following parameters from his study which agreed quite well with those of Rice (1987) and Huang (1990): cycle efficiency, air flow, specific work output, and exhaust temperature compared quite well with Rice (1987) and fuel utilization efficiency, exergy efficiency, and power-to-heat ratio compared quite well with Huang (1990).

Turbine shaft work (kW)	22007.0
Cycle efficiency (%)	37.0
Cycle pressure ratio	18.7
Air mass flow rate (kg/s)	66.9
Specific work output (kJ/kg air)	328.9
Turbine rotor inlet temperature (K)	1485.0
Exhaust temperature (K)	786.0
Exhaust excess air (%)	226.0
Compressor isentropic efficiency (%)	70.4
Turbine isentropic efficiency (%)	92.6

Table 6.2. Base-load gas turbine data for Case Study I of Bilgen (2000).

The cycle efficiency of 37.62% in Table 6.3 below is for the gas turbine without cogeneration while the fuel efficiency of 77.02% in the same Table 6.3 is for the cogeneration system. This implies a 105% efficiency improvement. The exergy efficiency of the cogeneration system is 50.06% while Bilgen reports an exergy efficiency of only 35.78% for the system without cogeneration, yielding a 40% improvement.

Comparison with the reported data for GE, LM2500PE turbine cited in [4,5] and this study

	Ref. [4]	Ref. [5]	This study
Cycle efficiency (%)	37.00		37.62
Air mass flow rate (kg/s)	66.90		66.33
Specific work output (kJ/kg air)	328.90		331.66
Exhaust temperature (K)	786.15		786.15
Fuel-utilization efficiency (%)		77.00	77.02
Exergy efficiency (%)		52.00	50.06
Power-to-heat ratio		0.92	0.93

Table 6.3. Comparison of the results of Bilgen (2000) with those of Rice (1987) and Huang (1990).

Process heat results of Bilgen (2000) appear in Table 6.4 below.
Fig. 6.4 below shows the 1st law and exergy (2nd law) efficiency and % steam extraction as a function of power-to-heat ratio. The trends of the 1st and 2nd law efficiencies in the figure are quite consistent with equations 6.1, 6.2, and 6.8b. The slow variation of the second law efficiency with power-to-heat ratio indicates that the exergy content of the steam plus power generated from the steam turbine is little degraded.

Process heat results

	Case (i)	Case (ii)
Process steam temperature (K)	486.19	686.15
Saturation temperature of steam (K)	486.19	486.15
Pinch point temperature (K)	536.19	536.19
Process heat produced (kJ/kg air)	358.28	179.16
Specific steam flow rate (kg/kg air)	0.151	0.120
Steam mass flow rate (kg/s)	10.02	3.98
Exergy of process heat (kJ/kg air)	132.37	57.71
Exergy factor of process heat	0.37	0.32
Temperature of extracted steam (K)		599.59
Pressure at steam turbine outlet (kPa)		4.00
Specific work of steam turbine (kJ/kg air)		66.92
Steam turbine shaft work		4440.00

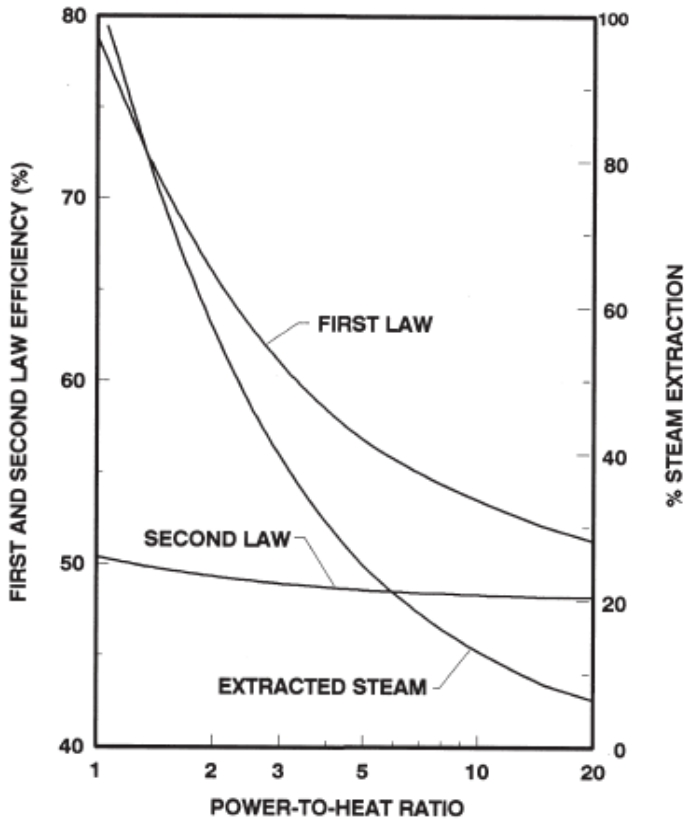Table 6.4. Process heat results of Bilgen (2000).

Fig. 6.4. shows the 1st law and exergy (2nd law) efficiency and % steam extraction as a function of power-to-heat ratio.

Similarly, Fig. 6.5 shows power from the steam turbine, total power, process heat production and payback period as a function of the power-to-heat ratio. The process steam production (in t/h) follows the same relationship as that of the % steam extraction in Fig. 6.4.
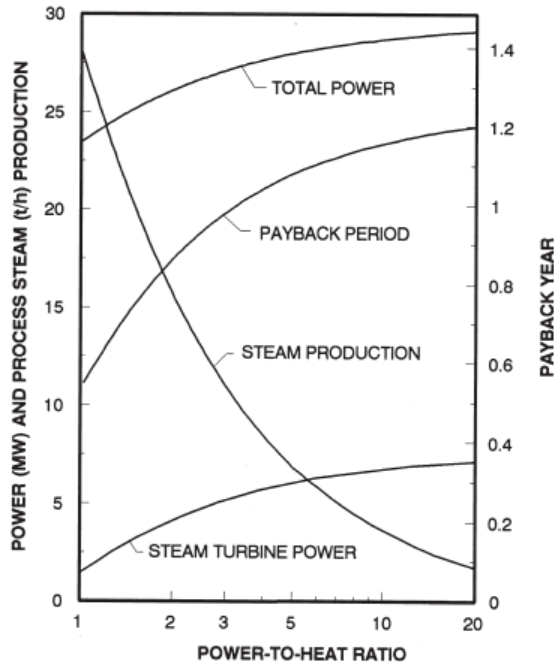

Fig. 6.5. Total power, steam turbine power, process heat production and payback period as a function of the power-to-heat ratio.

Exergy analysis of integrated gasification combined cycle gas turbine (IGCC) plants

Integrated Gasification Combined Cycle (IGCC) plants, as distinct from the general Combined Cycle/Cogeneration plants, have an integrated fuel production unit (gasifier) which provides the fuel (normally gaseous) required by the gas turbine combustors. The feed into the gasifier could be a solid hydrocarbon (usually coal) or biomass (e.g. agricultural wastes, lignocellulosic plants, etc.) as earlier noted in the section on Conventional and New Environmental-conscious Aero and Industrial Gas Turbine Fuels. A schematic of a coal-fired gasifier in an integrated coal gasification combined cycle gas turbine plant (ICGCC) plant appears in Fig. 6.XXX below.

We shall consider a biogas-fired integrated gasification steam-injected gas turbine (BIG/STIG) plant studied by Fagbenle et al. (2007) and shown schematically in Fig. 6.6 below. The Energy Utilization Diagram (EUD) popularized by the Ishida group and discussed in section 6 of this chapter was used to highlight the exergy losses in the various sub-systems of the plant. The EUD is a useful tool for exergy analysis of chemical processes and plants in which the energy level or availability factor (A) is plotted against the energy-transformation quantity (AH), enabling easy identification of subsystems with potentials for performance improvement.
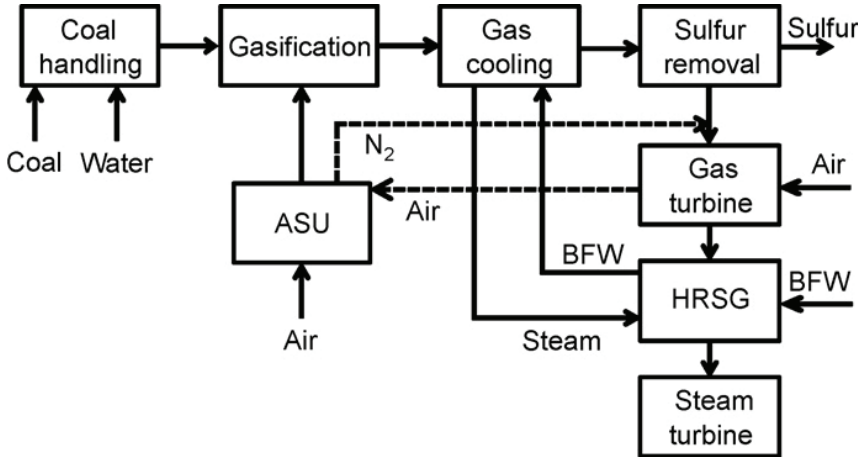
Fig. 6.XXX. Simplified diagram of an integrated coal gasification combined cycle (ICGCC) gas turbine plant. From Emun et al. (2010).

The BIG/STIG plant of Fig. 6.6 consists of a 53 MW gas turbine plant fuelled by fuel gas (syngas assumed to be largely CH_4) from a biogas gasifier and gas clean-up system. The adiabatic combustion temperature was found from the 1st Law to be 1895K but a more realistic (from metallurgical standpoint) turbine inlet temperature (TIT) of 1450 K was used in the analysis. The turbine exhausts at 410 °C (TET) into a Heat Recovery Steam Generator (HRSG) which produces steam for three purposes: injection steam into the turbine for blade cooling, injection steam into the combustor for NOx emission reduction, and blast steam required by the gasifier chemical process. The stack gases exhaust into the atmosphere at 151°C. Air flow of 141 kg/s and at 32.2 bar leaves the compressor, out of which 131.9 kg/s is fed into the combustor while the remaining 9.1 kg/s is fed into the gasifier.

Basis of the Energy Utilization Diagram

The exergy change $\Delta\varepsilon_i$ over all the energy donors and acceptors "i" in the energy-transformation system is:

$$\sum_i \Delta\varepsilon_i = \sum_i (\Delta H_i - T_0 \Delta S_i) \tag{6.10}$$

By the 1st law of thermodynamics, the first term on the RHS of the above equation is zero, since the energy released by the energy donor must equal that gained by the energy acceptor. Also, by the 2nd law of thermodynamics, to total entropy change in the system must be greater than or equal to zero, the equality being for isentropic (lossless) processes, i.e.

$$\sum_i \Delta S_i \geq 0 \tag{6.11}$$

Hence,

$$\sum_i \Delta\varepsilon_i = -T_o \sum_i \Delta S_i \tag{6.12}$$

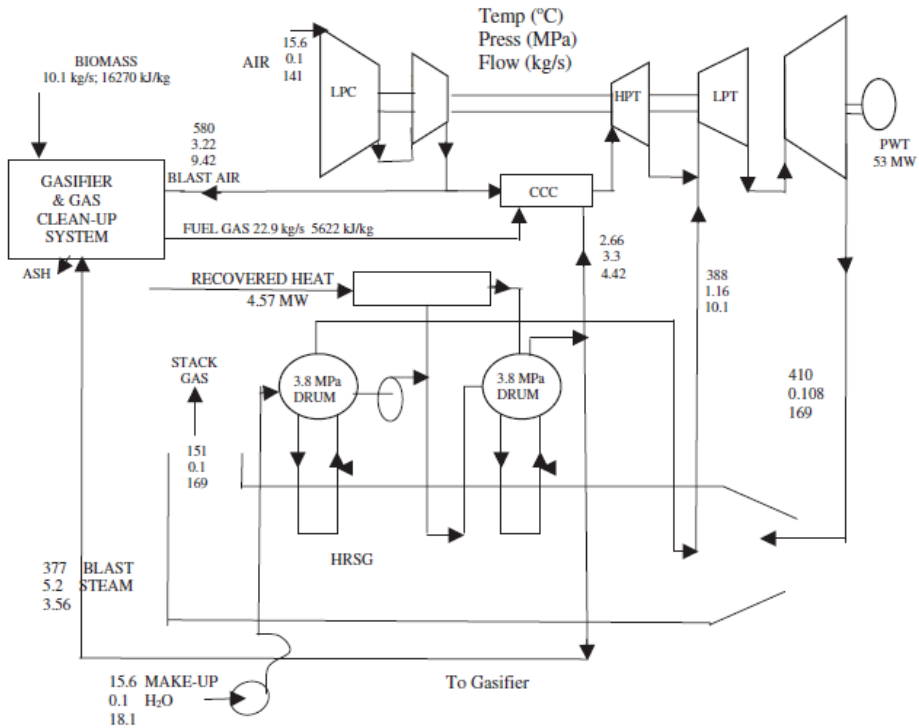The availability-factor or the energy level (an intensive parameter) is defined by

Fig. 6.6. BIG/STIG based on GE LM 5000 aero-derivative gas turbine [Williams (1988)].

$$A = \frac{\Delta\varepsilon}{\Delta H} = 1 - T_0 \frac{\Delta S}{\Delta H} \qquad (6.13)$$

It is seen that the relationship between the availability-factor of energy donors and energy acceptors is $A_{ed} \geq A_{ea}$ since in the energy change of the acceptor process, $\Delta H_{ea} > 0$. The exergy loss in the system is thus given by

$$-\sum \Delta\varepsilon_i = \sum_i \Delta H_{ea}(A_{ed} - A_{ea}) \geq 0 \qquad (6.14)$$

which, in the limit, gives the system exergy loss as:

$$-\sum \Delta\varepsilon_i = \int_0^{H_{ea}} (A_{ed} - A_{ea}) dH_{ea} \qquad (6.15)$$

A plot of the energy level of the energy donating process (A_{ed}) and the energy accepting process (A_{ea}) against the transformed energy (ΔH_{ea}) gives the energy loss in the system as the area between the curves of A_{ed} and A_{ea}. This is the EUD diagram and the energy level difference ($A_{ed} - A_{ea}$) is indicative of the driving force for the energy transformation process. A summary of the operating conditions together with the results of the 1st law efficiencies appears in Table 6.5 below, assuming compressor and turbine isentropic efficiencies of 98% each. The first law efficiency based on power production alone is 41.5% while it is 45% based on both heat and power.

Summary of operating conditions and first law efficiencies of the BIG/STIG plant

Flow rates, kg/s	
Air to combustion chamber	131.9
Air to gasifier	9.1
Fuel gas	22.9
Air/fuel ratio kg_{air}/kg_{fuel}	5.76
Steam injected to combustion chamber	4.42 @ 256 °C
Steam injected to turbine	10.1 @ 388 °C
Fuel subsystem	
Fuel type: fuel gas from biomass gasifier NCV, kJ/kg	5622
Power subsystems	
$\eta_{isen,compressor}$	0.98
$\eta_{isen,turbine,}$	0.98
LP & HP compressor, MW	85.0
HP turbine, MW	50.0
LP & Power turbine	93.0
Net generated power (NGP)	53.4
Efficiency (power-based) η_{th}, %	41.5
Efficiency, (power and heat based) η_{th}, %	45.0
Gasifier	
kg fuel-gas/kg biomass	2.27
Blast steam, kg/s	3.56

Table 6.5.

2nd Law or Exergy Analysis and synthesis

Irreversibilities in the turbines and the compressors processes.
The processes through the 2 stages each of the turbines (LP & HP) and the compressors (LP & HP) as well as that through the power turbine (PT) are done irreversibly, and their irreversibilities are
For the turbines:

$$I_t = (1 - \eta_t)W_{HPT,LPT \& PT} = (1 - 0.98)(143) = 2.9 \text{ MW}$$

For the compressors:

$$I_c = I_c = (\frac{1}{\eta_c} - 1)W_{LPC \& HPC} = 1.7 MW$$

The gross power input to the compressors is therefore $W_{gross,c}$ = 85 + 1.73 = 86.7 MW, while the net generated power is $W_{net, generated}$ = 140.14 - 86.73 = 53.4 MW.
Irreversibility due to the discharge of hot combustion products at 151°C and 1 bar into the environment is given by $I_{exh} = \varepsilon_{stack \ gases}$ = 3.6 MW as detailed below:

Gas	Exergy loss, MW
N_2	2.28
CO_2	0.148
CO	0.278
H_2O	0.860

The Heat Recovery Steam Generator, HRSG

The pinch point on the heat donor side is 546 K and on 512 K on the acceptor side, giving AT_{pinch} = 34°C, while the irreversibility was found to be I_{HRSG} = 7.7 MW.

Combustion chamber subsystem reaction

The total exergy loss in the combustion chamber, I_{cc}, assuming the steam is not dissociated, is given by

$$I_{cc} = \varepsilon_{fuel} - \Delta\varepsilon_{air} - \Delta\varepsilon_{steam}$$

Assuming that the ratio φ of the specific chemical exergy of the fuel to its net calorific value is 0.98, then

$$Icc = (0.98)(5622kJ/kg)(22.9 \text{ kg/s}) - \Delta\varepsilon_{air} - \Delta\varepsilon_{steam}$$

$$= 126.17 - 58.4 - 7$$

$$= 60.8 \text{ MW}$$

It is seen that the exergy loss in the combustion chamber (60.8 MW) is about 49% of the fuel exergy (126.17 MW). Table 6.6 summarizes the results.

Net generated power	53.4 MW		
Exhaust temperature	151 °C		
Pinch point	273 °C		
Minimum ΔT	34 °C		
Location	Exergy Loss (MW)	Fuel exergy, %	Total exergy loss, %
Total exergy loss	76.7	60.8	1000
HRSG	7.7	6.1	10.1
Combustion chamber	60.8	48.2	79.3
Stacks exhaust gases	3.6	2.9	4.7
Turbines	2.9	2.3	3.8
Compressors	1.7	1.3	2.2

Table 6.6. Summary of the net generated power and the exegy loss (Irreversibilities) in the BIG/STIG plant.

The Energy Utilization Diagrams (EUDs) for the combustion chamber and the HRSG

The EUD for the combustion chamber and the HRSG appear in Figs. 6.7 and 6.8 respectively. The largest single subsystem exergy loss occurs in the combustion chamber, being about 79% of the total system exergy loss. The EUD for the HRSG indicates a pinch point of 273°C on the heat donor side and a ΔT = 34°C. The cross-hatched area approximately equals the calculated values shown in Table 6.6.

The irreversibility of the combustion process can be reduced by reducing the effective temperature difference across which the heat transfer is taking place, i.e. between the acceptor and the donor. In this case, preheating the reactants with the exhaust stack gases would reduce the irreversibility of the combustion process. Both the energy and the exergy in the stack gases in this case are both lost. Exergy loss associated with the steam injection mixing process in the combustion chamber has not been taken into consideration, primarily because the amount of steam injected is relatively small.
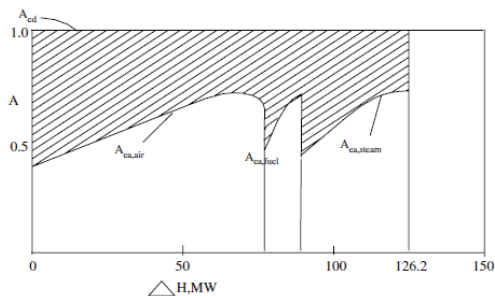
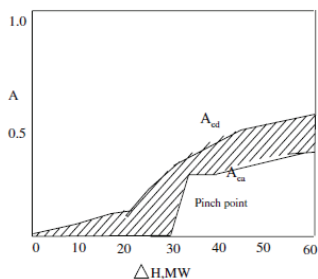Fig. 6.5. Energy-utilization for the combustion chamber.

Fig. 6.6. Energy-utilization diagram for the heat recovery steam generator (HRSG).

7. References

Emun, F., Gadalla, M., Majozi, T. and Boer, D. (2010). Integrated gasification combined cycle simulation and optimization. Computers and Chemical Engineering, 34 (2000) 331-338.

Fagbenle, R. Layi, Oguaka, A.B.C., Olakoyejo, O.T. (2007). A thermodynamic analysis of a biogas-fired integrated gasification steam injected gas turbine (BIG/STIG) plant. Applied Thermal Engineering 27 (2007) 2220-2225.

Woudstra, N., Woudstra, T., Pirone, A. and van der Stelt, T. (2010). Thermodynamic evaluation of combined cycle plants. Energy Conversion and Management 51 (2010) 1099-1110.

IPIECA Workshop (2004), Baltimore, USA, 12-13 October 2004.

Rail Transport and Environment – Facts and Figures, Nov. 2008.

Airline Industry Information, May 3, 2010.

The Seattle Times, Dec. 31, 2008.

Shepherd, D. G. Introduction to the Gas Turbine, D. van Nostrand Co. Inc. 1949.

Eastop, T. D. and McConkey, A. Applied Thermodynamics for Engineering Technologists. 2nd. Ed. Longmans, London. 1970.

Wikipedia, Typical specifications for Jet A-1 Aircraft Fuels. 2010.

Specifications for Fuel Gases for Combustion in Heavy-Duty Gas Turbines. GE Power Systems, GEI 41040G, Revised Jan. 2002.

Chris Lewis, (2006). A gas turbine manufacturer's view of Biofuels. Ppt presentation, Rolls Royce plc.

Balat., M., Balat, M., Kirtay, E. and Balat, H. (2009). Main routes for the thermo-conversion of biomass into fuels and chemicals. Part I: Pyrolysis systems. Energy Conversion and Management 50 (2009) 3147-3157.

Balat., M., Balat, M., Kirtay, E. and Balat, H. (2009). Main routes for the thermo-conversion of biomass into fuels and chemicals. Part 2: Gasification systems. Energy Conversion and Management 50 (2009) 3158-3168.

Balat., M. and Balat, H. (2009). Recent trends in global production and utilization of bio-ethanol fuel. Applied Energy 86 (2009) 2273-2282.

Balat., M. and Balat, H. (2010). Progress in biodiesel processing. Applied Energy 87 (2010) 1815-1835.

Baratieri, M., Baggio, P., Fiori, L. and Grigiante, M. (2008). Biomass as an energy source: Thermodynamic constraints on the performance of the conversion process. Bioresource Technology 99 (2008) 7063-7073).

Navarro, X. (2008). Ethanol-powered gas turbine to generate electricity. RSS Feed. Feb. 17th 2008.

C. D. Bolszo and V. G. McDonell, Emissions optimization of a biodiesel fired gas turbine, Proceedings of the Combustion Institute, Vol 32, Issue 2, 2009, Pages 2949-2956.

Pierre A. Glaude, Rene Fournet, Roda Bounaceur and Michel Moliere, (2009). Gas Turbines and Biodiesel: A clarification of the relative NOx indices of FAME, Gasoil and Natural Gas.

Haywood, R. W. Analysis of Engineering Cycles. 2nd edition (SI Units). Pergamon Press. 1975.

Severns, W. H., Degler, H. E. and Miles, J. C. (1964). Steam, Air and Gas Power by Severns, John Wiley, 5th ed. 1964.

Frank J. Brooks, (2000) GE Gas Turbine Performance Characteristics, GER-3567H. GE Energy Services, Atlanta, GA, USA. March 2001.

Pavri, R. and Moore, G. D., Gas Turbine Emissions and Control. GER4211. GE Energy Services, Atlanta, GA. USA. March 2001.

Dincer, I. and Rosen, M. A. Exergy, Energy, Environment and Development, Elsevier. 2007.

Bilgen, E. (2000). Exergetic and engineering analyses of gas turbine based cogeneration systems. Energy 25 (2000) 1215-1229.

Williams, R. H. (1992). Renewable energy on a large scale. In P. E. Trudeau, ed. Energy for a Habitable World, A Call for Action. Crane Russak, New York.

Srinophakun, T., Laowithayangkul, S. and Ishida, M. (2001). Simulation of power cycle with energy utilization diagram. Energy Conversion and Management 42 (2001) 1437-1456.

Khaliq, A. and Kaushik, S. C. (2004). Thermodynamic performance evaluation of combustion gas turbine cogeneration system with reheat. Applied Thermal Engineering 24 (2004) 1785-1795.

Khaliq, A. and Kaushik, S. C. (2004). Second-law based thermodynamic analysis of Brayton/Rankine combined power cycle. Applied Energy 78 (2004) 179-197.

Khaliq, A. (2009). Exergy analysis of gas turbine trigeneration system for combined production of power, heat and refrigetation. International Journal of Refrigeration 32 (2009) 534-545.

Karellas, S., Karl, J. and Kakara, E. (2008). An innovative biomass gasification process and its coupling with microturbine and fuel cell systems. Energy 33 (2008) 284-291.

Ertesvag, I, Kvamsdal, H. M. and Bolland, O. (2005). Exergy analysis of a gas-turbine combined-cycle power plant with precombustion CO_2 capture. Energy 30 (2005) 5-39.

Song, T. W., Sohn, J. L., Kim, T. S. and Ro, S. T. (2006). Performance characteristics of a MW-class SOFC/GT hybrid system based on a commercially available gas turbine. Journal of Power Sources 158 (2006) 361-367.

Ordorica-Garcia, G., Douglas, P., Croiset, E. and Zheng, L. (2006). Technoeconomic evaluation of IGCC power plants for CO_2 avoidance. Energy Conversion and Management 47 (2006) 2250-2259.

Design and Development of Smartcoatings for Gas Turbines

I.Gurrappa[1] and I.V.S. Yashwanth[2]
[1]Defence Metallurgical Research Laboratory
Kanchanbagh PO, Hyderabad-500 058,
[2]M.V.S.R. Engineering College, Nadargul, Hyderabad-501 510,
India

1. Introduction

Development of newer materials / coatings that are multifunctional, smart and possess physical and engineering properties superior to the existing materials / coatings are constantly necessitated for continued technical advances in a variety of fields. In modern times, the design, development, processing and characterization of newer materials / coatings have been greatly aided by novel approaches to materials / coatings design and synthesis that are based on intelligent and unified understanding of the processing - structure properties - performance relationships for a wide range of materials / coatings. The ever increasing demands in gas turbines for cost savings as well as restrictions concerning emission of pollutants and noise require steady improvement in engine efficiency, performance, and reliability. The availability of materials / coatings with requisite combination of properties largely dictates performance improvements of the gas turbines. The blades in modern aero, marine and industrial gas turbines are manufactured exclusively from Ni - based superalloys. A section of a typical gas turbine engine is shown in Fig.1. It is to be noted that hot sections of engine are dominated by Ni- based superalloys. The advanced gas turbine engines need to operate at higher temperatures for obtaining maximum efficiency. The efficiency is directly proportional to operating temperature. Increased temperatures lead to increased high temperature corrosion i.e. oxidation and hot corrosion. High temperature corrosion and in particular hot corrosion (type I and II) is highly detrimental as it causes catastrophic failures if proper materials in association with high performance coatings are not chosen [1-3]. Advances in processing of Ni-based superalloys have allowed evolution of microstructures from equiaxed structures about three decades ago to directionally solidified (DS) multi-grain and single crystal (SC) components today, which enhance temperature capability up to 1250°C. The majority of Ni - based superalloy developmental efforts has been directed towards improving the alloy high temperature strength with relatively minor concern being shown to its high temperature corrosion resistance. Further, it is not always possible to achieve both high temperature strength and high temperature corrosion resistance simultaneously because some alloying elements help to improve high temperature corrosion resistance while some may help to improve high temperature strength. It is rare that an alloying element leads to enhancement both in high temperature strength and the high temperature corrosion resistance. This is
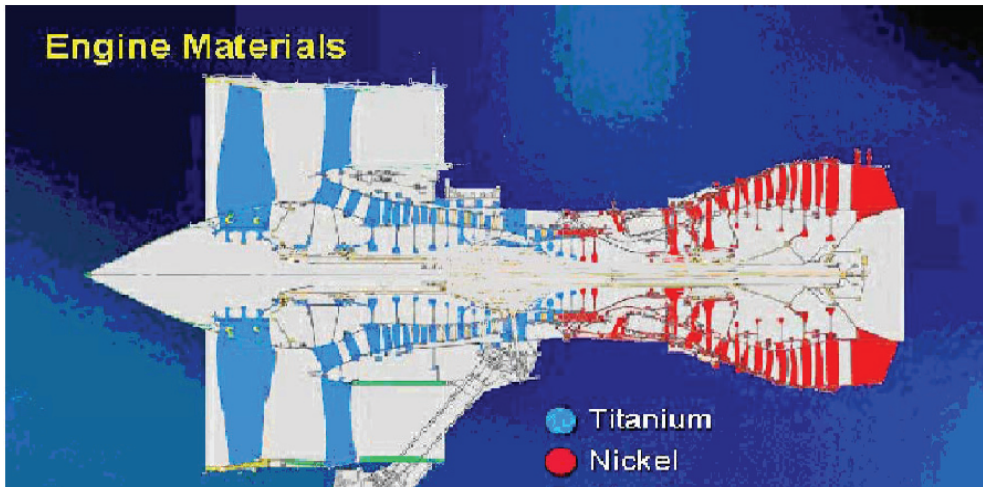
Fig. 1. Significance of nickel based superalloys and titanium based alloys in gas turbine engines

further complicated for marine applications by the aggressivity of the environment, which includes sulphur and sodium from the fuel and various halides contained in seawater. These features are known to drastically reduce the superalloy component life and reliability by consuming the material at an unpredictably rapid rate, thereby reducing the load-carrying capacity and potentially leading to catastrophic failure of components [1,3]. Thus, the high temperature corrosion resistance of superalloys is as important as their high temperature strength in gas turbine engines [4-7].

2. Hot corrosion of superalloys

Fig.2 shows the hot corrosion behavior of few superalloys like Nimonic-75, Nimonic-105, Inconel 718 and CM 247 LC corroded in pure Na_2SO_4 and NaCl containing environments at 900° C. In the presence of pure sodium sulphate, the weight loss was less for all the superalloys [7]. Appreciable corrosion was reported for all the superalloys in the presence of NaCl. It indicates that NaCl plays a significant role in causing severe corrosion, thereby reducing the superalloy life considerably. Among the superalloys, CM 247 LC was corroded severely indicating that the superalloy is highly susceptible to hot corrosion. In fact many cracks were developed on the scale and subsequently spallation took place for CM 247 LC superalloy. However, there were no cracks and no spallation of oxide scales was reported for other superalloys. In case of CM 247LC alloy, no material was left after exposure of 70 hours to the NaCl containing environment and only corrosion products with high volume of oxide scales was reported [7]. The appreciable corrosion attack of CM 247 LC superalloy was clearly evidenced by observing large corrosion affected zone (due to appreciable diffusion of corrosive elements present in the environment). Formation of precipitates was further confirmed by EPMA measurements [7]. Sulphur diffusion and formation of metal sulphides preferentially chromium and nickel sulphides was reported to be the influential factor. When sulphide phases are formed in superalloys, Ni- based alloys are inferior to cobalt and iron base alloys, which are especially effective in destroying the corrosion resistance of
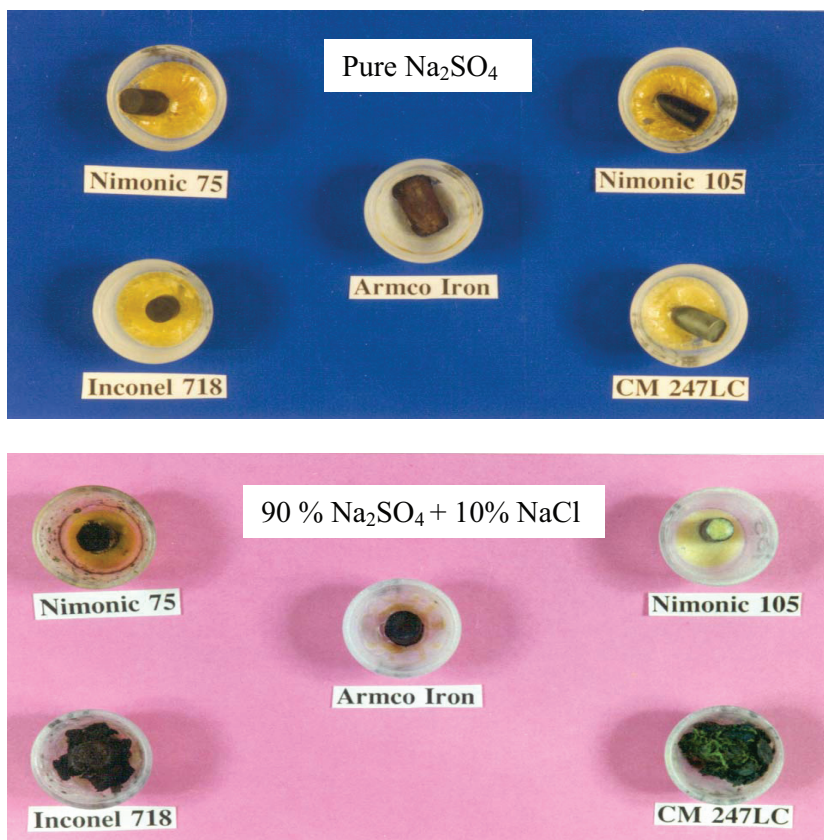
Fig. 2. As hot corroded superalloys at 900°C in different environments

alloys [7-8]. It was also reported that the simple Nimonic-75 alloy is more corrosion resistant over complicated CM 247LC because of the presence of small amount of titanium, which helps in forming a protective, adherent and dense chromia layer. Titanium oxide forms beneath the chromia layer and thereby improves the adherence capability of chromia scale [8]. Thus, the alloying elements play a significant role and decide the life of superalloys under hot corrosion conditions [9]. This type of attack greatly reduces the high temperature strength properties and thereby affects the efficiency of the system due to failure of components during service conditions [10].

It is generally accepted that the high temperature capability increases with decreasing Cr content. Therefore, the chemistry of new superalloys were greatly influenced by reducing Cr content and increasing rhenium (Re) content with a view to enhance the temperature capability. As a result, the third and 4th generation superalloys contain only 2 to 4% Cr but instead contain about 6% Re, which is a great contrast to the first generation superalloys containing about 10% Cr and no Re. Similarly, 5th generation superalloys contain osmium and ruthenium in addition to high amount of Re and very low content of Cr. Rhenium is a unique element which can increase high temperature creep strength considerably. However, it makes the superalloys susceptible to high temperature corrosion [10]. It is due to the fact that the

superalloys cannot form corrosion resistant alumina or chromia scale because of high Re content. Its effect is similar to Mo on oxidation i.e. as the high vapour pressure of its oxide. Therefore, rhenium is a harmful element for high temperature corrosion resistance of Ni-based superalloys. Hence, the need to apply high performance coatings for their protection under high temperature conditions as the gas turbine blades experience high temperature corrosion.

3. Surface coating technologies

As mentioned above, there are a number of cases reported in the literature where the gas turbine blades suffered severe corrosion due to which failures took place [1-3]. Failure investigations confirmed that it was due to hot corrosion, in which extensive penetration of sulphur took place into the superalloys leading to the formation of metal sulphides that in turn led to reduction in their mechanical properties resulting catastrophic failures. A typical failed blade is presented in fig.3. It is known that it is not possible to develop an alloy having both high temperature strength and high temperature corrosion resistance simultaneously since alloying elements often have opposing effects on the two properties. Particularly, tungsten, molybdenum and vanadium additions to superalloys are helpful in improving the high temperature strength, but their presence makes the superalloys highly susceptible to hot corrosion [7]. Therefore, it is mandatory to prevent oxidation as well as both types of hot corrosion by using appropriate coating technology [11-13] so as to increase the life of gas turbine engine components to the designed service life.
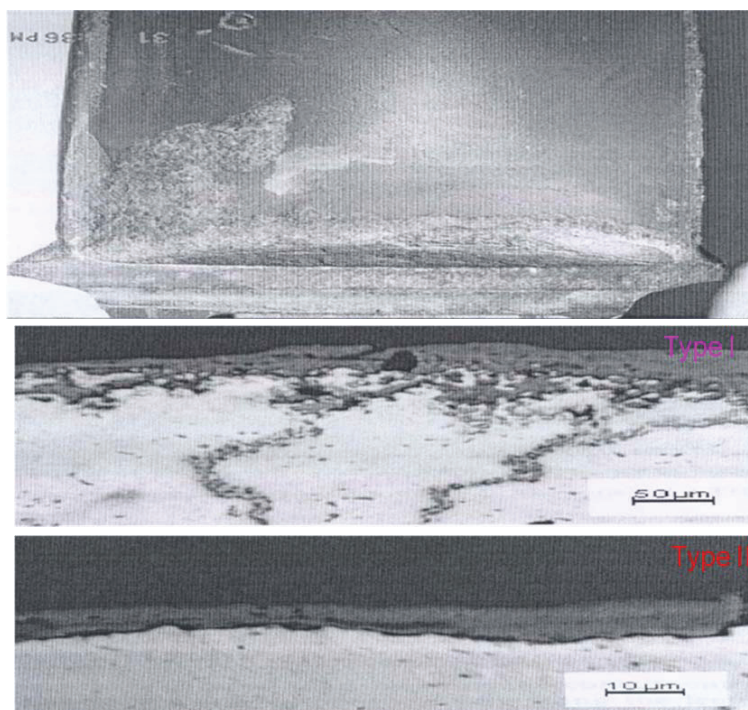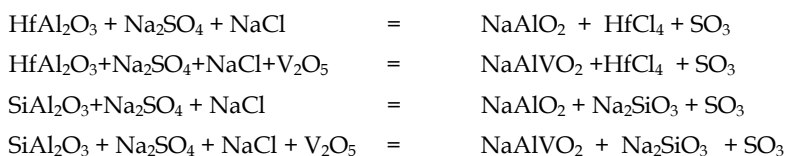

Fig. 3. Typical failed gas turbine blade due to type I and II hot corrosion

4. Types of coatings

The present coatings are broadly divided into two types, diffusion and overlay. In diffusion coating application process, aluminium is made to react at the surface of substrate, forming a layer of mono-aluminide. For coatings applied over Ni-based superalloys, nickel aluminide is the resulting species. This type of coatings and surface modification is one of the most widely used for tailoring the surface properties of components. Though diffusion coatings are well bonded to the substrate they have limited compositional flexibility and their usefulness is strongly dependent on substrate chemistry. The most important improvement in the diffusion coatings has been the incorporation of platinum in aluminide coatings [14-18]. This process involves the deposition of platinum by electrochemical method followed by aluminizing at the suitable temperature for the required period. While overlay coatings are generally MCrAlY coatings where M is Ni or NiCo and essentially comprises a mono-aluminide component contained in a more ductile matrix of a solid solution. The supply of aluminium for formation of protective alumina scale comes largely from the dispersed mono-aluminide phase during the useful life of such coatings. Overlay coatings are typically well bonded and have a wide compositional flexibility. Research and development on this type of coatings has led to a variety of compositions with improved scale adherence [13].

It was also reported that traces of silicon as well as hafnium in MCrAlY coatings reduce the coating life drastically [13]. The underlying mechanism is that hafnium and silicon that are present in the grain boundaries of alumina scale leach out selectively by readily reacting with chlorine, vanadium, sodium and sulphur present in the corrosive environment to form corresponding compounds. This results in dislodging the grains of alumina scale and creates instability of the oxide scale and thereby reducing the life of coatings significantly. Further, the oxides of silicon and hafnium are soluble in molten basic sulphate and the basic fluxing dominates in the high temperature hot corrosion region (850-950º C) [13]. The reaction mechanisms leading to reducing the life of coatings containing silicon or hafnium are given below:

$$HfAl_2O_3 + Na_2SO_4 + NaCl \qquad = \qquad NaAlO_2 + HfCl_4 + SO_3$$

$$HfAl_2O_3 + Na_2SO_4 + NaCl + V_2O_5 \qquad = \qquad NaAlVO_2 + HfCl_4 + SO_3$$

$$SiAl_2O_3 + Na_2SO_4 + NaCl \qquad = \qquad NaAlO_2 + Na_2SiO_3 + SO_3$$

$$SiAl_2O_3 + Na_2SO_4 + NaCl + V_2O_5 \qquad = \qquad NaAlVO_2 + Na_2SiO_3 + SO_3$$

Diffusion and overlay coatings can provide protection against oxidation and hot corrosion and act as bond coats for zirconia based thermal barrier coating (TBC) systems. In both the cases, slow growth rates and optimum adherence of the alumina scales formed on the coatings during high temperature exposure are of significant for component life. These requirements can be fulfilled only by using coatings with sufficiently high aluminium contents to ensure protective alumina scale formation and re-healing after oxide spallation / reaction with the environment. The life of a coating is mainly limited by aluminium depletion occurring upon aluminium consumption as a result of alumina scale growth and repeated spallation and re-healing of the alumina scale during oxidation process. If a point is reached where the aluminium level in a bond coating falls below the level at which protective alumina scale cannot be formed preferentially, faster interaction between the corrosive species present in the environment and the non-protective oxides of other
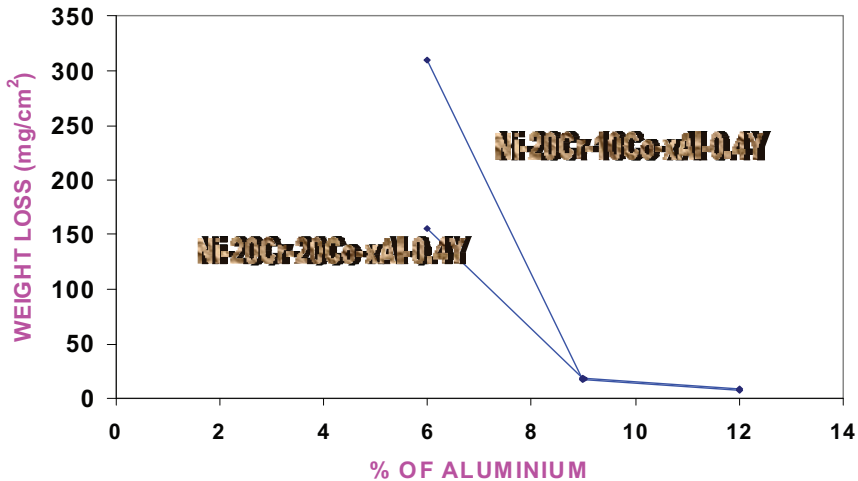
Fig. 4. Determination of optimum content of aluminium required in MCrAlY coatings for their hot corrosion resistance

constituents of the bond coating occurs and thereby affects the coating life considerably under hot corrosion conditions. Further, the constituents of ceramic thermal barrier coatings react easily with the corrosive species and shorten the coating life significantly. Therefore, optimum content of aluminium in the coatings is extremely necessary to enhance their lifetime. Fig.4 illustrates the influence of aluminium on weight loss in the MCrAlY based coating model alloys. It is very clear that aluminium plays a major role in affecting the hot corrosion resistance of MCrAlY alloys though the concentration of other alloying elements remains constant [13].

Another important aspect is the selection of suitable surface engineering technique by which the coatings are applied since the life of a coating depends not only on coating composition but also on the surface engineering technique employed for its application. Therefore, selection of appropriate surface engineering technique as well as suitable coating composition becomes a challenging task.

5. Surface engineering techniques

Surface engineering technique, which modifies properties of the component's surface to enhance their performance, should not only be effective but also economical. The following are the most common surface engineering techniques available at present:

a. Electro-deposition
b. Diffusion coating processes
c. Thermal spray techniques
d. Ion implantation
e. Hardening & cladding
f. Selective surface hardening by transformation of phase and
g. vapour deposition.

Electro-deposition, diffusion and thermal spraying techniques are widely in use to improve the surface of components for hot corrosion resistance. Particularly, thermal spray and

vapour deposition techniques are the most efficient techniques for prolonging the life of components significantly.

Researchers in the field were attempted to innovate new coating compositions by using different application techniques and concepts [19-25]. However, systematic research in simulating gas turbine engine conditions has been lacking.

6. Smart coatings

6.1 Concepts

Gas turbines used in aero engines suffer from high temperature oxidation and hot corrosion when they move across the sea. In marine and industrial gas turbines, hot corrosion is a major problem and in fact decides the life of components. Hot corrosion takes place under two temperature ranges and named type I (800-950ºC) and type II (600-750ºC). High performance coatings should combat high temperature oxidation and both forms of hot corrosion as gas turbines encounter all the problems during service. If a single coating can operate successfully over a range of temperatures with different forms of corrosion attack like type I and II hot corrosion and high temperature oxidation, the coating essentially respond to local temperature in such a way that it will form either alumina or chromia protective scale as appropriate. High purity alumina scales offer best protection against high temperature oxidation and type I hot corrosion and chromia scales against type II hot corrosion. Ideally a single coating should satisfy both the requirements. It is possible for a coating only if it contains chromium and aluminium rich graded coatings. The base coating should be a standard MCrAlY coating enriched with aluminum at its outer surface and a chromium rich layer at its inner surface. Under high temperature oxidation and type I hot corrosion conditions, the outer layer of the coating forms alumina scale, which provides protection and it, offers less protection under low temperature conditions. Under type II hot corrosion conditions, chromium rich layer forms chromia scale at a faster rate and provides protection. Thus, the smart coating can provide optimum protection by responding suitably to the temperatures that are encountered under actual service conditions of gas turbine engines. This optimum protection is possible because of the formation of most suitable protective oxide scale in each temperature range of operation envisaged. In this sense, the coating responds to its environment in a pseudo-intelligent manner and hence the name **SMART COATING.** With this type of coatings only, it is possible to obtain total protection for the gas turbine engines under all operating conditions which in turn possible to achieve ever greater efficiency of advanced gas turbine engines.

It is pertinent to note that the smart coating should have optimum composition with sufficient reservoir of critical elements like aluminium and chromium to form protective oxide scales depending on the surrounding temperatures. Additionally, the smart bond coating should promote slow growth rates of protective scales for enhanced service life. It helps to improve the durability of TBCs as well since TBC performance is essentially depends on the life of bond coatings [26-29] and hence necessitates compositionally optimised bond coatings. Such characteristics are possible with only MCrAlY (where M is Ni or NiCo) type bond coatings.

Therefore, the development of smart coatings design involves the preparation of multilayered coating consisting of an appropriate MCrAlY base, enriched first in chromium, then aluminium to provide a chemically graded structure. The intermediate chromium rich phase provides protection under low temperature hot corrosion conditions; while

aluminium rich surface layer provides resistance to high temperature oxidation and type I hot corrosion. Diffusion barrier coatings at the bottom help in preventing inter-diffusion of coating and substrate elements. Thus, the smart coating permits operation of gas turbine engines over a wide range of temperatures successfully for more than the designed life and helps in enhancing the efficiency significantly by effectively preventing oxidation, type I and type II hot corrosion [10].

6.2 Preparation
6.2.1 Selection of suitable surface engineering technique
Preparation of smart coatings is really a challenging task because the performance of coatings basically depends on it. Therefore, selection of suitable surface engineering techniques to produce a quality coating is extremely essential. Here, selection of a single technique may not be of any help, but a combination of techniques is quite useful. Further, the order of usage of selected techniques is also important. Therefore, one has to be extremely careful in selection and utilizing the techniques for production of high performance coatings in order to achieve maximum efficiency. Among the surface engineering techniques, thermal spraying, diffusion, electro-plating and laser treatments appear to be more effective in producing smart coatings. Application of suitable diffusion barrier on the superalloy followed by an optimized MCrAlY coating and chromized treatment to get Cr rich coating and then electroplating followed by pack cementation makes it possible to obtain graded structure as desired. Alternatively, multiple layers of optimized MCrAlY coatings rich with Cr and Al on diffusion barrier coating followed by pack cementation by using combination of surface engineering techniques makes it possible to obtain smart coatings. However, extensive research essentially helps to establish the process parameters of each surface engineering technique, coating thickness, suitable annealing treatments etc. to obtain a smart coating of desired characteristics.

The microstructures of coatings also play a significant role in enhancing the life of components. Therefore, obtaining an appropriate microstructure by identifying suitable surface engineering technique is of paramount importance. The selection of technique for coating preparation should be based on the parameters that are controllable to get required microstructure. As mentioned earlier, the smart coating is a graded coating consisting of different zones (Fig.5). Each zone has its specific microstructure with definite composition. The microstructure of each zone varies depending on the coating composition and surface engineering technique used. The composition of each zone requires detailed analysis to understand the effect of smart coating. The first layer should contain high amount of aluminium, the second layer should be rich with chromium, the third layer as that of MCrAlY coating composition and the bottom diffusion layer should contain heavy elements. Extensive research both at the laboratory and field augment to establish the appropriate coating compositions, thickness, microstructures, coating techniques and superior performance of smart coatings over conventional coatings.

6.3 Performance of a developed smart coating
Recently, a smart bond coating has been developed which is optimised compositionally and promotes appropriate protective scale formation depending on the surrounding environmental conditions that enhances the durability of TBC, which in turn the life of CM 247 LC superalloy components. The performances of various compositions of MCrAlY bond
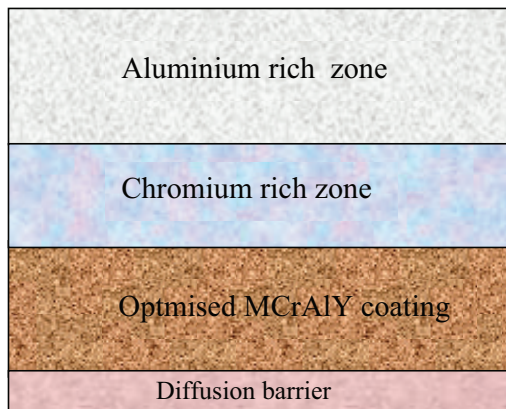
Fig. 5. A schematic representation of microstructure of a smart coating

coatings applied on CM 247 LC superalloy (without TBC) were evaluated systematically at 900ºC in simulating gas turbine engine environments. Among the coatings, NiCoCrAlY coating exhibited a maximum life of more than 300 hours. The high performance of this coating is due to its ability to form continuous, adherent and protective alumina scale on the surface of the bond coating during high temperature corrosion at 900ºC (Fig.6).

Table I presents the life of uncoated superalloy, smart coating as well as different thicknesses of zirconia based TBCs at 900ºC in simulating gas turbine engine environments. The results indicate that 100 μm thick TBC improved the superalloy life by four hundred fifty times to that of bare superalloy. It was also evident that 300 μm thick TBC in association with compositionally optimised 125 μm thick NiCoCrAlY bond coating (smart bond coating) enhanced the superalloy life by about 600 times, which was found to be optimum. Thick ceramic coatings could not help in improving the hot corrosion resistance of superalloys further due to adherence problem associated with spallation at higher temperatures. The maximum life of NiCoCrAlY (smart coating) + 300 μm thick TBC was attributed to the formation of protective alumina and chromia scales not only on the surface of bond coating but also on the TBC surface (Fig.7 & 8). It was observed that yttria and zirconia are still intact even after continuous exposure of 1175 hours and not reacted with the corrosive elements (Figs.7 & 9). Further, neither sulphur nor oxygen was diffused into the coating indicating an excellent protection provided by 300 μm thick TBC in association with a smart bond coating to the superalloy. It is known that TBC reduces the temperature of bond coating / substrate by about 200ºC. It indicates that the substrate or bond coating temperature is about 700ºC only. Under such environmental conditions i.e. at 700ºC, the bond coating promoted chromia and alumina scale formation that is clearly observed in Fig.9. It was also observed that the bond coating promoted protective alumina scale formation at 900ºC in the same environments (Fig.6). It indicates that the NiCoCrAlY bond coating forms alumina scale at 900ºC i.e. without TBC and chromia and alumina scale in the presence of TBC at the same environmental conditions and provides maximum life to the TBC which in turn the superalloy components.

As already mentioned, the MCrAlY type bond coatings can provide protection against oxidation and hot corrosion and act as bond coatings for zirconia based thermal barrier coating systems. Slow growth rates and optimum adherence of protective scales forming on

Type of coating	Life (hours)
Uncoated superalloy	< 2
Smart coating	300
Smart coating +100 µm TBC	910
Smart coating +200 µm TBC	975
Smart coating +300 µm TBC	1175
Smart coating +400 µm TBC	1170

Table I. Life times of CM 247 LC alloy with smart coating + different thicknesses of thermal barrier coatings in 90%Na_2SO_4 + 5% NaCl + 5% V_2O_5 environments at 900°C
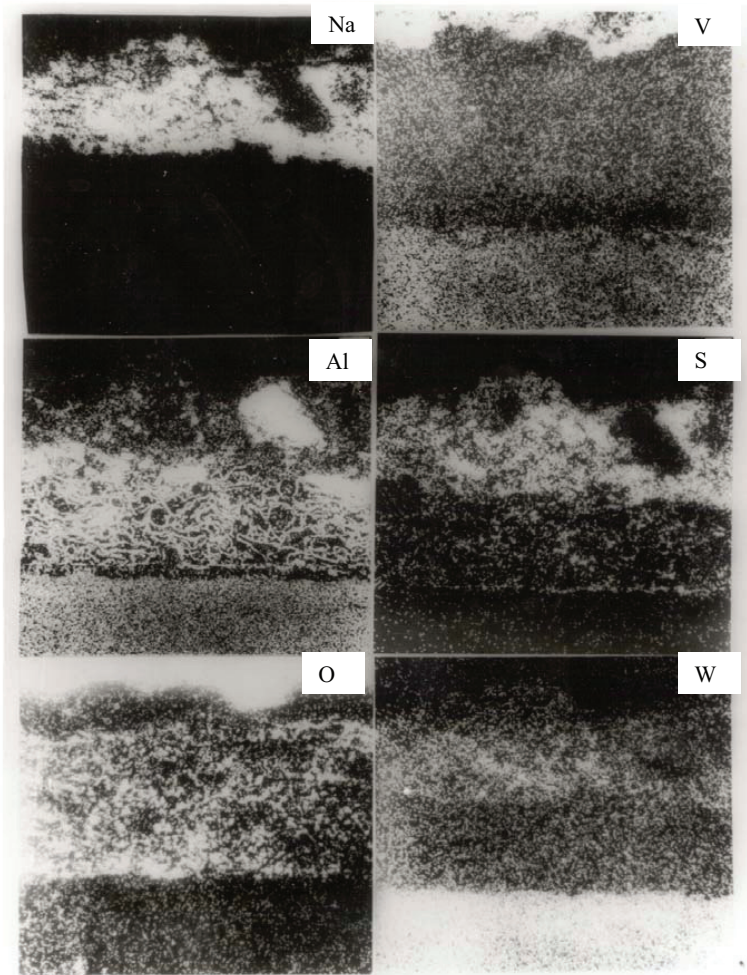

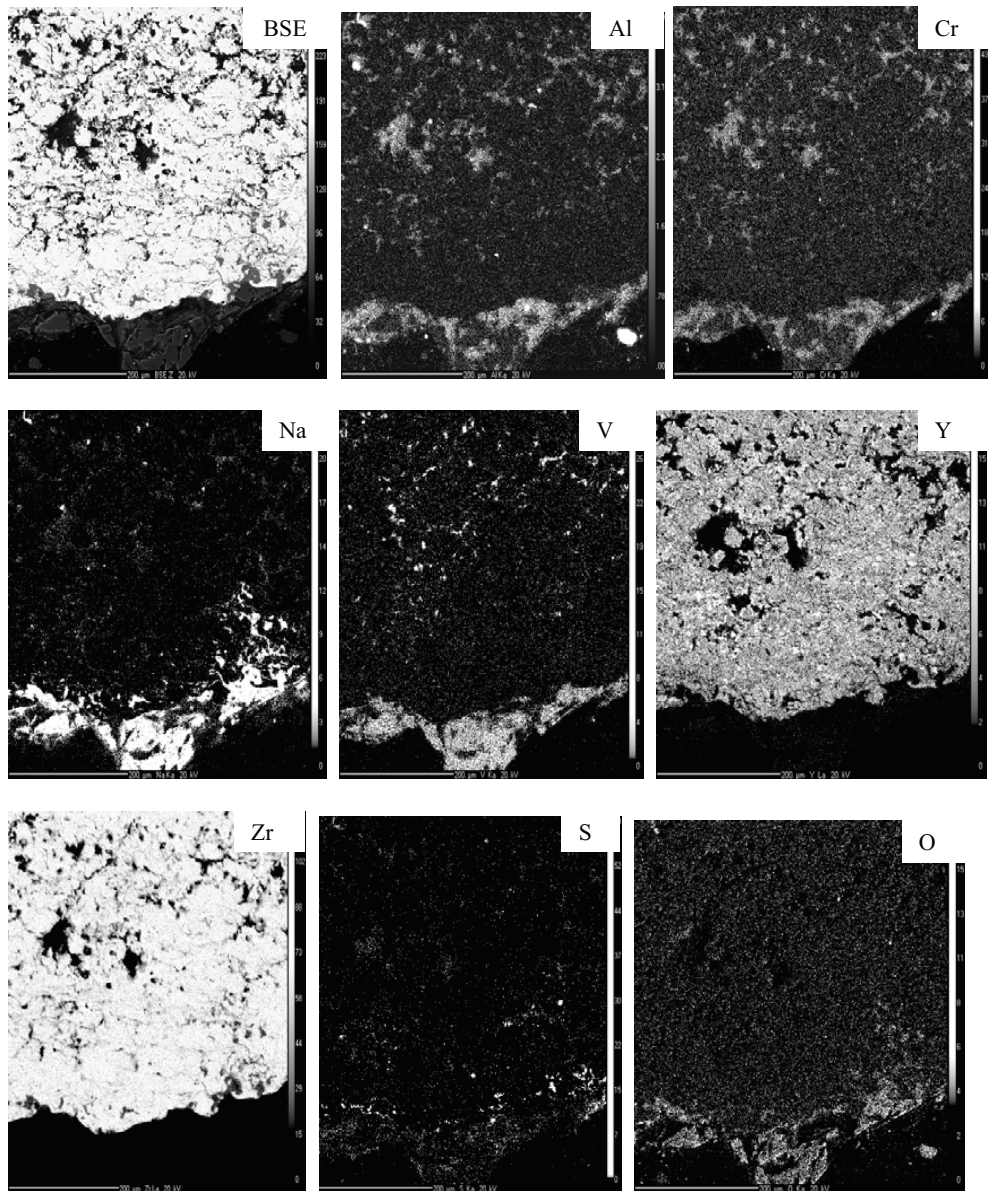Fig. 6. Elemental distribution of 125 µm thick smart coating after hot corrosion studies

Fig. 7. Elemental distribution of 300 μm thick TBC + smart coating (external layer) after hot corrosion studies
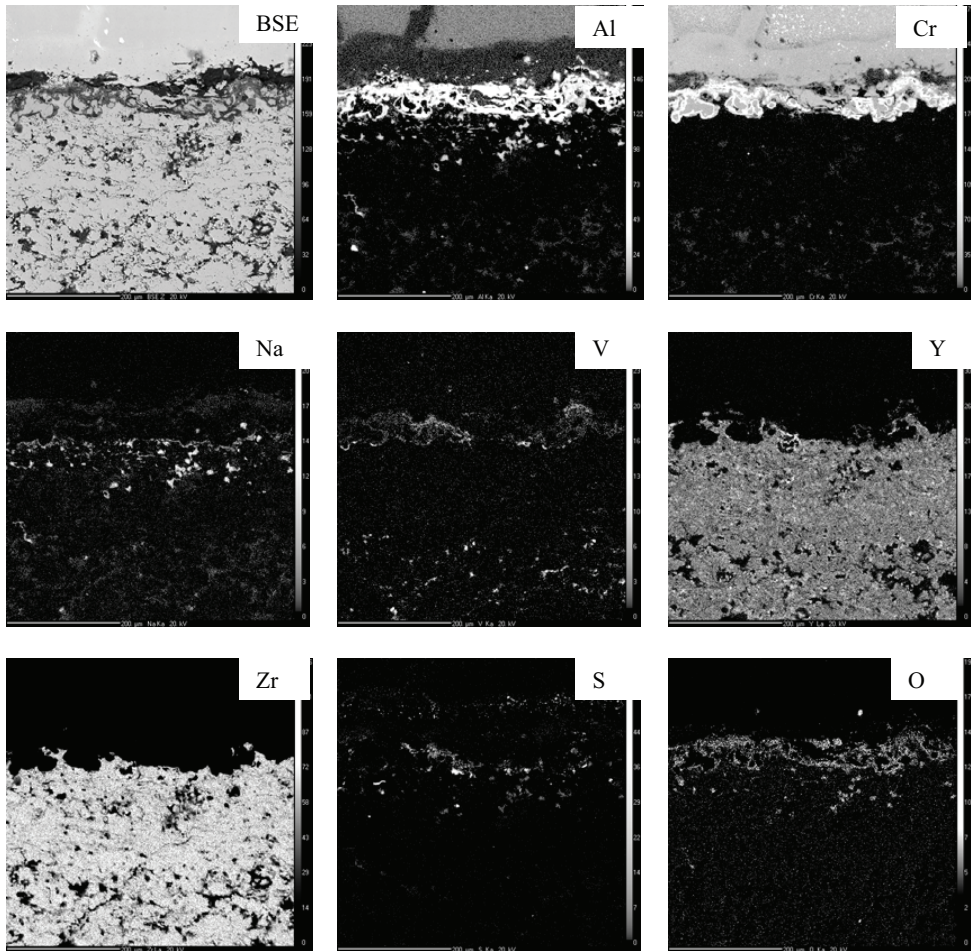
Fig. 8. Elemental distribution of 300 µm thick TBC + smart coating (internal layer) after hot corrosion studies

the bond coatings during high temperature exposure are of significant for component life. These requirements can be fulfilled only by using compositionally optimised coatings with sufficiently high aluminium and chromium contents to ensure protective scale formation and re-healing after reaction with the environment. The lives of coatings are mainly limited by aluminium and chromium depletion occurring upon their consumption as a result of alumina and chromia scale growth and repeated reaction with the corrosive species. If a point is reached where the aluminium and chromium level in the bond coatings falls below the level at which protective scales cannot be formed preferentially, faster interaction between the corrosive species present in the environment by penetrating through the pores of TBC and the non-protective oxides of other constituents of the bond coating occurs and thereby affects the coatings life considerably. The performance of the smart bond coating was confirmed by employing advanced characterisation techniques.

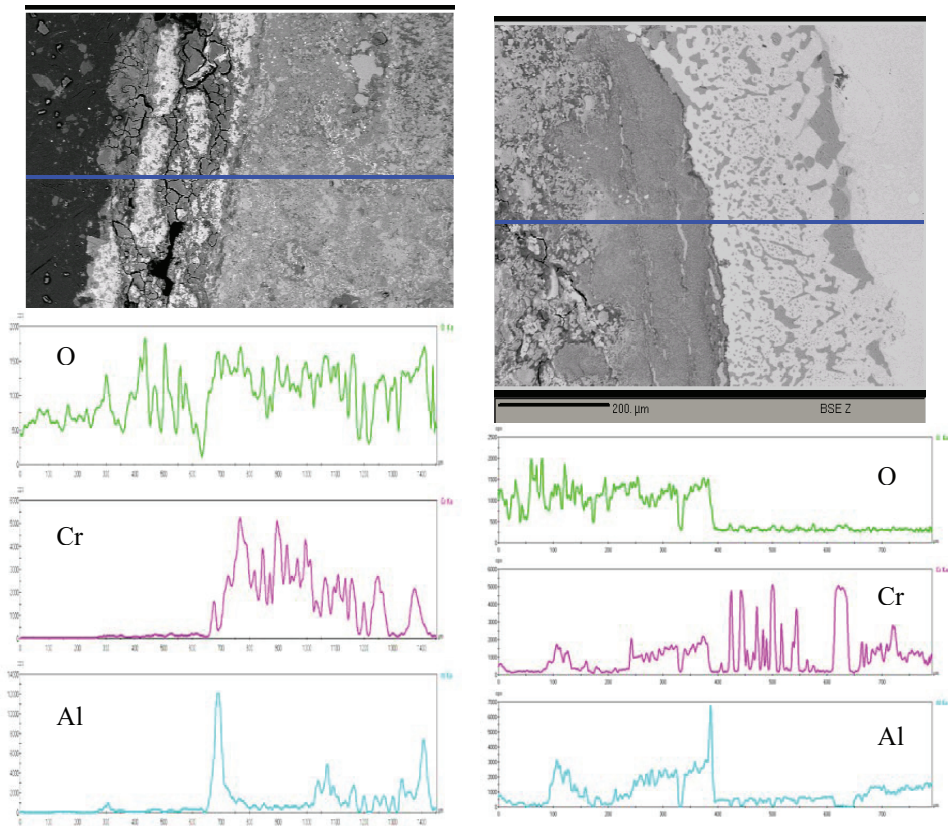Fig. 9. Line scan data of hot corroded two layered smart coating showing alumina and chromia scale formation both on top coating surface as well as at the interface

Hence, the developed bond coating exhibited intelligence behaviour both in the presence and absence of TBC and formed suitable protective scales and hence named as smart bond coating. Another important observation is the formation of protective alumina and chromia scales on the surface of TBC as well and prevented the diffusion of corrosive elements like chlorine, vanadium, sulphur and oxygen. Thus, a smart bond coating was successfully developed for TBCs that promotes appropriate protective scales preferentially depending on the environmental conditions and enhances the life of superalloy components significantly, which is essential for advanced gas turbines for their increased efficiency. Therefore, it is a potential bond coating for advanced gas turbines of different types i.e. aero, marine and industrial for their protection against high temperature oxidation, type I and type II hot corrosion.

7. Summary

The design and development of smart coatings to combat type I & type II hot corrosion and high temperature oxidation in gas turbines is a challenging problem to the Corrosion Engineer. The developmental work in this area has successfully resulted a smart coating, which provided an excellent protection to the superalloys against all the concerns that are

being experienced by all types of gas turbines. Further research is highly essential for their understanding and to develop alternative smart coatings. Extensive research is needed both at the laboratory level and field to optimize coating composition, thickness, microstructure, identification of appropriate surface engineering techniques, and their priority of use in order to prove their performance.

8. Acknowledgements

9. References

[1] M.R. Khajavi and M.H. Shariat, Engineering Failure Analysis, 11 (2004) 589

[2] J.M. Gallardo, J.A.Rodriguez and E.J. Herrera, Wear, 252 (2002) 264

[3] N. Eliaz, G. Shemesh and R.M. Latanision, Engineering Failure Analysis, 9 (2002) 31

[4] J. Stringer, Mater.Sci.Technol., 3 (1987) 482

[5] A.S.Radcliff, Mater. Sci. & Tech., 3 (1987) 554

[6] R.F.Singer, Mater. Sci. & Tech., 3 (1987) 726

[7] I.Gurrappa, Oxid. Met., 50 (1999) 353

[8] I.Gurrappa, J.High Temp.Mater.Sci., 38 (1997) 137

[9] I.Gurrappa, Mater.Sci.Technol., 19 (2003) 178

[10] I.Gurrappa, 'Design and Development of smart Coatings for Aerospace applications', Final Project Report, European Commission, July 2008

[11] H.W. Grunling, H. Rechtanbacher and L. Singheiser, Mater. Sci. Forum, 251-254 (1997) 483

[12] S.Kuroda, J.Kawakita, M. Watanabe and H. Katamoda, Sci. Tech. Adv. Mater., 9 (2008) 33002

[13] I.Gurrappa, I.V.S.Yashwanth, A.K.Gogia, H.Murakami and S.Kuroda, Intl. Mater. Rev., (Submitted)

[14] I.Gurrappa, Platinum Met.Rev., 45 (2001) 124

[15] I.Gurrappa and A.K.Gogia, Mater. Sci. Technol., 17 (2001) 581

[16] I.Gurrappa, Surf.Coat.Technol., 139 (2001) 216

[17] K.T.Chiang, F.S.Pettit and G.H.Meier, High Temperature Corrosion (ed.) R.A.Rapp, NACE, Houston, Texas, (1981) p 519

[18] G.Lehnert and H.Meinhardt; Electrodep. Surf. Treat., 1 (1972) 171

[19] M.P.Bacos, P. Josso, N.Vialas, D. Poquillon, B.Pieraggi, D.Monceau, J.R.Nicholls, N. Simms, A.Encinas-Oropesa, T.Ericsson and S.Stekovic, Appl.Thermal.Eng., 24 (2004) 1745

[20] F.Wu, H. Murakami, A. Suzuki and H. Harada, Surf. Coat. Tech., 168 (2003) 62-69

[21] P. Kuppusami, H. Murakami and T. Ohnuma, J. Vac. Sci. Tech., A22 (2004) 1208

[22] C.E.Campbell, W.J.Boettinger, U.R.Kattner, Acta Mater., 50 (2002) 775

[23] L.Lee, D.Windover, M.Audino, D.W.Matson, E.D.MacClanahan, Surf. Coat.Techonol., 149 (2002) 62

[24] Y.N. Wu, A. Yamaguchi, H.Murakami and S. Kuroda, J. Mater. Res., 22 (2007) 206

[25] K. Kawagishi, A. Sato and H. Harada, JOM (2008) 31 (www.tms.org/jom.html)

[26] I.Gurrappa, Proceedings of International convention on Surface Engineering (INCOSURF 2004), August 2004, Bangalore, India, p 115

[27] M.Y.Ali, S.Q-Nusier and G.M.Newaz, Intl. J. Solid Struct., 38 (2001) 3329

[28] D.R. Mumm and A.G.Evans, Durable Surf., 197 (2001) 199

[29] R.Vassen, G.Kerkhof and D.Stover, Mater. Sci. Eng., A 303 (2001) 100

Development of Granular Catalysts and Natural Gas Combustion Technology for Small Gas Turbine Power Plants

Zinfer R. Ismagilov[1], Mikhail A. Kerzhentsev[1], Svetlana A. Yashnik[1],
Nadezhda V. Shikina[1], Andrei N. Zagoruiko[1], Valentin N. Parmon[1],
Vladimir M. Zakharov[2], Boris I. Braynin[2] and Oleg N. Favorski[2]
[1]Boreskov Institute of Catalysis, 630090, Novosibirsk
[2]Central Institute of Aviation Motors, Moscow
Russia

1. Introduction

Gas turbine power plants (GTPPs) of low power (tens of kW to 1.5-2 MW) are promising autonomous sources of energy and heat. The application of gas turbine technologies saves fuel, solves heat supply and water shortage problems. The nominal efficiency of GTTPs belonging to different generations varies from 24% to 38% (average weighted efficiency – 29%). This is 1.5 times higher than that of combined heat power plants.

The main GTPP drawback is significant emission of toxic nitrogen oxides due to high temperature combustion of the gas fuel. The main approach used today to decrease the emission of nitrogen oxides from GTPPs is based on the use of the so-called homogeneous combustion chambers working with premixed lean fuel-air mixtures with two-fold excess of air. The decrease of NO_x formation is principally the result of the low flame temperatures that are encountered under lean conditions (Correa 1992). This technology makes it possible to decrease significantly the temperature in the combustion zone relative to traditional GTPP combustion chambers with separate supply of fuel and air to the combustion zone. As a result, the concentration of nitrogen oxides in the flue gases decreases from 100 ppm to 10-20 ppm. The downside of this approach is, however, that it results in low heat release rates, which, in turn, may negatively affect combustion stability.

The most efficient way to decrease emissions of nitrogen oxides in GTPPs is to use catalytic combustion of fuel (Trimm, 1983; Pfefferle & Pfeferle., 1987; Ismagilov & Kerzhentsev 1990; Parmon et al., 1992; Ismagilov et al., 1995; Ismagilov & Kerzhentsev, 1999; Ismagilov et al., 2010). In the catalytic chamber, efficient combustion of homogeneous fuel-air mixture is achieved at larger excess of air and much lower temperatures in the zone of chemical reactions compared to modern homogeneous combustion chambers.

In the last decade, the obvious advantages of the catalytic combustion chambers in GTPPs initiated intense scientific and applied studies in the USA (Catalytica) and Japan (Kawasaki Heavy Industries) which are aimed at development of such chambers for GTPPs for various applications (Dalla Betta et al., 1995; Dalla Betta & Tsurumi, 1995; Dalla Betta & Rostrup-Nielsen, 1999; Dalla Betta & Velasco, 2002).

The catalyst in a gas-turbine combustor has to withstand continuous operation for at least 10,000 h under severe operation conditions: high gas hourly space velocity (GHSV) and temperatures over 1200 K (McCarty et al., 1999). Material development is therefore one of the key issues in the development of catalytic combustion for gas turbines. Such catalyst has to possess high mechanical strength and the ability to initiate methane oxidation in lean mixtures at low temperatures 620-720 K and maintain stable oxidation during long time at temperatures above 1200 K (Dalla Betta et al., 1995; Dalla Betta & Rostrup-Nielsen, 1999).

Today catalysts for gas turbines are prepared in the form of monoliths from foil made of special corrosion-resistant alloys with deposited porous support and the active component based on platinum and/or palladium (Dalla Betta et al., 1995a; McCarty et al. 2000; Carroni et al. 2003). However, application of such catalysts requires many problems to be solved. The main problems are related to the high temperature of gas typical for modern gas turbines that requires the catalyst to operate at temperatures exceeding 1200 K for prolonged periods of time (total operation time of modern GTPPs reaches 100000 hours) (McCarty et al., 1999). The use of metal supports at temperatures above 900°C is limited due to possible thermal corrosion, especially in the presence of water vapor. It results in the catalyst destruction, peeling of the support and loss of noble metals decreasing the catalytic activity and shortening the catalyst lifetime. So, the improvement of the catalyst stability is an urgent problem.

One of the approaches to solve this problem is based on development of catalysts on granulated supports and design of a catalytic package for GTPP combustion chamber, which would provide minimum emissions of NO_x, CO and HC at moderate temperatures (930-950°C). In this chapter we present our results on development and study of alternative granular catalysts with reduced Pd content for methane catalytic combustion in mini gas turbines of 400-500 kW power with regenerative cycle, intended for decentralized power supply. The small power of these turbines results in reduced catalyst loading and makes possible the use of granular catalysts which are less expensive and can be easily manufactured using existing industrial facilities.

2. Selection of catalysts for application in gas turbine combustors

The most available fuel for GTPPs is natural gas, which consists largely of methane, which is the least readily oxidizable hydrocarbon. Therefore, it is necessary to produce catalysts capable of initiating methane oxidation at minimum possible temperatures and withstanding long-term exposure to temperatures above 930°C.

It is very difficult to find catalysts meeting requirements of both high activity at low temperature and good thermal stability at high temperatures. Therefore, in catalytic gas combustors generally staged combustion is employed: a highly reactive catalyst for the low-temperature (350 °C < T_{in} < 450 °C) conversion of CH_4 must be combined with a second catalyst which converts fuel at higher temperatures (T_{in} approx. 700 °C, T_{out} > 900 °C) (Carroni et al. 2002).

It is well known that catalysts based on noble metals are most active in oxidation reactions. They can initiate combustion at low temperatures, but it is inappropriate to use them above 750°C because of a high volatility of the noble metals (Arai et al. 1986). Use of palladium as the active component in the high-temperature oxidation of methane is most promising. This is because palladium has a high specific activity in this reaction (Burch & Hayes, 1995; Lee & Trimm, 1995) and a relatively low volatility in comparison with other noble metals, as was

determined by studying the interaction of the metals with oxygen at 730–1730°C (McCarty et al., 1999). It is these properties of palladium that attract researchers' interest to its behavior in the methane oxidation reaction. It is well known that, up to 800° C, palladium exists as PdO_x which undergoes reduction to palladium metal as the temperature is further raised. This reaction is reversible up to ca. 900°C, so a decrease in temperature leads to the reoxidation of Pd to PdO_x in air. As a consequence, the temperature dependence of the methane conversion always shows a hysteresis (Farrauto et al., 1992). There is still no consensus as to what form of oxidized palladium — bulk PdO, Pd with oxygen chemisorbed on its surface, or Pd particles covered by PdO —is the most active species in combustion ((McCarty, 1995; Burch, 1996; Su et al., 1998a; Su et al., 1998 b; Lyubovsky & Pfefferle, 1998; Lyubovsky & Pfefferle, 1999).

Supporting of palladium on a substrate, primarily γ- or α-Al_2O_3 or Al_2O_3 modified with rare-earth metal oxides, raises the activity and thermal stability of the catalyst through an increase in the degree of dispersion of the active component and in its aggregation stability (Baldwin & Burch, 1990; Groppi et al., 1999, Ismagilov et al., 2003, Ozawa et al., 2003, Liotta & Deganello, 2003; Yue et al., 2005).

Alternative catalytic systems for methane combustion are catalysts based on hexaaluminates and transition metal oxides. Hexaaluminates are the class of compounds with a general formula $AB_xAl_{12-x}O_{19}$, where A is a rare-earth or alkaline-earth metal, such as La and Ba, and B is a transition metal with an atomic radius comparable to the radius of aluminum (B = Mn, Co, Fe, Cr, Ni) (Machida et al., 1987; Machida et al., 1989). Hexaaluminates form from oxides at temperatures above 1200°C, and this is why they are very stable up to high temperatures. The specific surface area of hexaaluminates and, accordingly, their activity in methane oxidation depend on the preparation method (Chouldhary et al., 2002). However, irrespective of their specific surface area, the hexaaluminates are much less active than the palladium catalysts. In view of this, there have been attempts to enhance the catalytic activity of hexaaluminates by introducing Pd (Jang et al., 1999). In our earlier work (Yashnik et al. 2006), it was shown that introducing 0.5 wt % Pd into the hexaaluminate $(Mn,Mg)LaAl_{11}O_{19}$ resulted in a significant increase in the catalyst activity expressed as a 110°C decrease in the temperature of 50% methane conversion ($T_{50\%}$). In addition, a synergistic effect in the Pd–$(Mn,Mg)LaA_{11}O_{19}$ system was detected.

It was demonstrated earlier that thermally stable catalysts could be prepared from manganese oxides (Tsikoza et al., 2002; Tsikoza et al., 2003). The activity of these catalysts in hydrocarbon oxidation can be enhanced by their calcination at 900–1100°C. In our works (Tsikoza et al., 2002; Tsikoza et al., 2003), it was found that Mn–Al–O catalysts supported on γ-Al_2O_3 containing χ-Al_2O_3 and modified with Mg, La, or Ce were more active and thermally more stable (up to 1300°C) than the same catalysts supported on pure γ-Al_2O_3. We believe that the high degree of disorder of the χ-Al_2O_3 structure in comparison with γ-Al_2O_3 favors deeper interaction of manganese and modifiers with the support at the impregnation and low-temperature calcination stages. This yields Mn–Al–O compounds of complex composition (solid solutions and/or hexaaluminates) at 1300°C, due to which the catalysts are stable and highly active in methane oxidation.

Thus, based on literature data and our research results, two types of catalysts were selected for further development and study: (1) active Pd catalysts with low ignition temperature for initiation of methane combustion and (2) thermally stable hexaaluminate catalysts for methane combustion at temperatures over 900°C.

3. Synthesis of granular catalysts for methane combustion

3.1 Preparation of catalysts

In catalyst preparation, we used γ-alumina supports developed at the Boreskov Institute of Catalysis (Shepeleva et al., 1991; Ismagilov et al., 1991, Koryabkina et al., 1991; Koryabkina et al., 1996) prepared in the form of spheres and rings. Their characteristics are presented in Table 1.

Property	Spherical Al_2O_3	Ring-shaped Al_2O_3
Diameter, mm	2.2–2.5	7.5
Length, mm	-	7.5
Inner diameter, mm	-	2.5
Bulk density, g/cm³	0.8	0.7
Pore volume (H_2O), cm³/g	0.45	0.45
Specific surface area, m²/g	180	200
Crushing strength under static conditions, kg/cm²	270	23
Phase composition	γ-Al_2O_3	60% γ-Al_2O_3 40% χ-Al_2O_3

Table 1. Physicochemical properties of the spherical and ring-shaped aluminas

Pd–Ce–Al$_2$O$_3$. The catalyst was prepared on the ring-shaped support and contained 12 wt %CeO$_2$ and 2 wt % Pd. It was prepared by the incipient-wetness impregnation of the support with a cerium nitrate (Ce(NO$_3$)$_3$ · 6H$_2$O) solution and then with an aqueous Pd(NO$_3$)$_2$ solution. Before being loaded with palladium, the alumina support modified with cerium was calcined at 600°C. After supporting of palladium, it was additionally calcined at 1000°C. The pilot catalyst batch was designated IK-12-60-2.

*Mn–Al$_2$O$_3$.*The catalyst was prepared on the ring-shaped support by the incipient wetness impregnation of the support with an aqueous manganese nitrate (Mn(NO$_3$)$_{2*}$ 6H$_2$O) solution. It contained 11 wt % manganese oxides in terms of MnO$_2$. The catalyst calcination temperature was 900°C. It was similar in composition to the commercial catalyst IKT-12-40; for this reason, its pilot batch is hereafter designated IKT-12-40A.

Mn-La–Al$_2$O$_3$. This catalyst was prepared on the ring-shaped support by successive incipient-wetness impregnation of alumina with lanthanum and manganese nitrate solutions using the procedure described in (Yashnik et al., 2006). It contained 8–11 wt % manganese in terms of MnO$_2$ and 10–12 wt % lanthanum in terms of La$_2$O$_3$. These concentrations of manganese and lanthanum are sufficient to ensure a high catalytic activity and stability of the catalyst (Yashnik et al., 2006). The calcination temperature was 1000°C, lower than the temperature used in our previous study (Yashnik et al., 2006) and was equal to the onset temperature of hexaaluminate phase formation. This allowed us to increase the specific surface area of the sample. The pilot catalyst batch was designated IK-12-61.

Pd–Mn–La–Al$_2$O$_3$. This catalyst was prepared on the ring-shaped support by successive incipient-wetness impregnation with lanthanum and manganese nitrate solutions. Next, the samples were dried and calcined at 400°C. Thereafter, the samples were loaded with a palladium nitrate solution by impregnation. Final calcination was carried out at 1000°C. The resulting catalyst contained 8–11 wt % Mn in terms of MnO$_2$, 10–12 wt % La in terms of La$_2$O$_3$, and was 0.65 wt % Pd. The pilot batch of the catalyst was designated IK-12-62-2.

3.2 Characterization of catalysts

When developing and optimizing the catalysts based on manganese oxides, including those additionally containing lanthanum and palladium, we investigated how their physicochemical and catalytic properties depend on their chemical composition, the active component and modifier (manganese, lanthanum, palladium, and hexaaluminate phase) contents, the chemical nature of Mn and Pd precursors, the calcination temperature, and the active component introduction method (Yashnik et al., 2006; Tsikoza et al., 2002; Tsikoza et al., 2003). Measuring the catalytic activity of catalyst samples in methane oxidation allowed us to find the optimal catalytic systems, whose properties are listed in Table 2.

The catalysts on the ring-shaped alumina support (IK-12-60-2, IKT-12-40A, IK-12-61, IK-12-62-2) were tested in natural gas combustion at 930°C in the pilot plant at the Boreskov Institute of Catalysis.

The results of these tests are presented in Table 3. The catalyst IK-12-60-2 retained its high activity over 100 h: the ignition temperature (T_{ign}) was 240°C, and the reaction products were almost free of CO and NO_x. The manganese-containing catalysts were less active: with these catalysts, T_{ign} and the residual CO and NO_x contents were higher than with IK-12-60-2. However, the initial activity of the catalyst IK-12-61 did not decrease, but even gradually increased during testing: in 200 h, T_{ign} falls from 365 to 350°C, the NO_x concentration in the reaction products remained at the 0–1 ppm level, and the CO concentration decreased from 55 to 34 ppm. The catalyst IK-12-61 modified with 0.65 wt % palladium (IK-12-62-2) allowed us to reduce the ignition temperature of the methane–air mixture almost by 100°C and the CO concentration in the reaction products by more than one order of magnitude. Service life tests suggested that all catalysts are tolerant to high temperatures (up to 930°C) and to the action of the reaction medium. The ignition temperature and the methane–air combustion efficiency remained unchanged at least over 100 h of testing.

The investigation of the physicochemical properties of the initial samples (Table 2) showed that, in IK-12-60-2, the active component PdO is finely dispersed and this allows one to initiate combustion of the methane–air mixture at low temperatures.

The initial catalysts based on Mn and La oxides (IK-12-61 and IK-12-62-2) contain the hexaaluminate phase, which is known to be resistant to high temperatures. The durability tests altered the structural and textural characteristics of the catalysts (Table 4). Over the first 50 h of testing, the specific surface area and pore volume of the IK-12-60-2 catalyst decreased because of the coarsening of alumina particles and the onset of α-Al_2O_3 formation via the δ-Al_2O_3 – α-Al_2O_3 phase transition under prolonged heating. The active component PdO underwent partial decomposition to Pd^0. In the next 50 h, the textural parameters stabilized and the degree of dispersion of the remaining PdO phase increased. The degree of dispersion of metallic Pd^0 decreased with testing time. The Mn catalysts are more tolerant to high temperatures and are less prone to aggregation than the Pd–Ce catalyst. Some changes in the phase composition of the catalysts occur because of the formation of high-temperature phases, namely, α-Al_2O_3 and a (Mn, Al)Al_2O_4 solid solution in IKT-12-40A and manganese hexaaluminate in IK-12-61 and IK-12-62-2.

The catalytic activity of the hexaaluminate-based samples in the CH_4 oxidation reaction after 100-h-long testing was similar to the activity of the fresh catalysts: T_{50} is 470–480°C for the catalyst IK-12-61 and 363–380°C for IK-12-62-2 at GHSV = 1000 h^{-1} (Fig. 1). The activity of the catalysts Pd–Ce–Al_2O_3 and MnO_x–Al_2O_3 decreased slightly, and T_{50} increased by 50°C.

Catalyst	Calci-nation tempe-rature, °C	Chemical compo-sition, wt %	Phase composition*	S_{sp},** m²/g	V_Σ (N$_{ads}$)***, cm³/g	Strength, kg/cm²	T, 50% CH4,**** °C
IK-12-60-2	1000	Pd – 2.1 Ce – 10.1	δ-Al$_2$O$_3$, CeO$_2$ (~200 Å, S_{33}=1100), PdO (~180 and 250 Å, S_{39} = 480)	74	0.26	24	330
IKT-12-40A	900	Mn – 6.9	Mixture of (δ + γ)-Al$_2$O$_3$, α-Al$_2$O$_3$, Mn$_2$O$_3$	80	0.23	23	400
IK-12-61	1000	Mn – 6.9 La – 10.1	MnLaAl$_{11}$O$_{19}$ (S_{37} = 60), LaAlO$_3$, γ-Al$_2$O$_3$#	43	0.18	34	420
IK-12-62-2	1000	Pd – 0.65 Mn – 7.1 La – 9.4	MnLaAl$_{11}$O$_{19}$ (S_{37} – traces),γ-Al$_2$O$_3$ (a = 7.937 A),PdO (~400 A, S_{39} = 70)	48	-	25	385

*The particle size was derived from the size of coherent-scattering domain region. Relative phase contents were estimated from peak areas (S_i, arb.units) in diffraction patterns. γ-Al$_2$O$_3$# is a solid solution based on γ-Al$_2$O$_3$. ** S_{sp} is specific surface area, ***V_Σ (N$_{ads}$) is pore volume found form N$_2$ adsorption, ****T, 50% CH4 is temperature of 50% methane conversion on catalyst fraction 0.5-1.0 mm at GHSV = 1000 h^{-1} and methane concentration in air equal to 1%.

Table 2. Physicochemical and catalytic properties of the initial catalysts on spherical and ring-shaped supports

Catalyst	Test duration, h	T$_{ign}$, °C	Residual content, ppm	
			CO	NO$_x$
IK-12-60-2	100	240	0-1	0-1
IKT-12-40A	100	350	84-55	0-1
IK-12-61	200	365-350	55-34	0-1
IK-12-62-2	200	290	2-3	0-1

Table 3. Results of catalyst durability tests in natural gas combustion at 930°C in a bench testing unit at the Boreskov Institute of Catalysis

The catalytic activity of the hexaaluminate-based samples in the CH$_4$ oxidation reaction after 100-h-long testing was similar to the activity of the fresh catalysts: T$_{50}$ is 470–480°C for the catalyst IK-12-61 and 363–380°C for IK-12-62-2 at GHSV = 1000 h^{-1} (Fig. 1). The activity of the catalysts Pd–Ce–Al$_2$O$_3$ and MnO$_x$–Al$_2$O$_3$ decreased slightly, and T$_{50}$ increased by 50°C.

Catalyst	Test duration, h	Phase composition	S_{sp}, m²/g	V_Σ (N_{ads}), cm³/g	Strength, kg/cm²
IK-12-60-2	50	δ-Al_2O_3, α-Al_2O_3 (traces), CeO_2 (~200 Å, S_{33} = 1100), PdO (~ 300 Å, S_{39} = 180), Pd° (~ 300 Å, S_{47} = 120)	42	0.18	21
	100	δ-Al_2O_3, α-Al_2O_3 (traces), CeO_2 (~200 Å, S_{33} = 1100), PdO (~ 160 Å, S_{39} = 180), Pd° (~500 Å, S_{47} = 80)	38	0.17	19
IKT-12-40A	100	α-Al_2O_3, γ-Al_2O_3-based solid solution (Mn, Al)Al_2O_4 (a = 8.151 Å)	66	0.22	19
IK-12-61	30	$MnLaAl_{11}O_{19}$ (S_{37} = 240), $LaAlO_3$, α-Al_2O_3	41	0.18	30
	50	$MnLaAl_{11}O_{19}$ (S_{37} = 250), $LaAlO_3$, α-Al_2O_3	33	0.15	28
	100	$MnLaAl_{11}O_{19}$ (S_{37} = 240), $LaAlO_3$, α-Al_2O_3	31	0.13	28
IK-12-62-2	50	$MnLaAl_{11}O_{19}$ (S_{37} = 230), γ-Al_2O_3# (a = 7.937 Å), Pd° (S_{41} = 90), PdO (400 Å, S_{39} = 160)	31	-	29
	100	$MnLaAl_{11}O_{19}$ (S_{37} = 230), γ-Al_2O_3# (a = 7.937 Å), Pd° (>400 Å, S_{47} = 40), PdO (>400 Å, S_{39} = 160)	30	-	32
	200	$MnLaAl_{11}O_{19}$ (S_{37} = 340), γ-Al_2O_3# (a = 7.937 Å), α-Al_2O_3 (S_{29} = 30), PdO (>400 Å, S_{39} = 180), Pd° (>400 Å, S_{47} = 40)	30	-	35

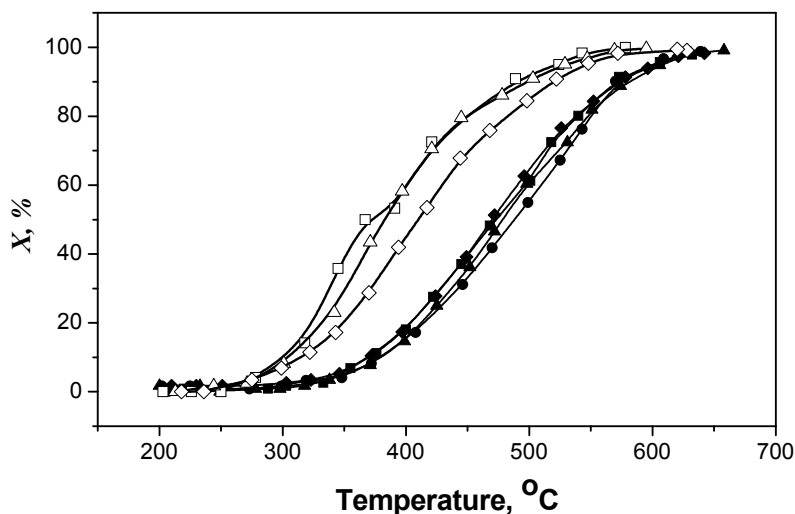Table 4. Physicochemical properties of the catalysts after durability tests in natural gas combustion

Fig. 1. Temperature dependences of methane conversion (1 vol % CH_4 in air, GHSV=1000 h^{-1}) on the catalysts: IK-12-61: ▲ – initial; ●-after 30 h; ■ - after 50 h; ◆ - after 100 h testing in CH_4 combustion at 930°C; IK-12-62-2: △- initial; □- after 50 h; ◊- after 100 h testing.

4. Kinetic studies of methane catalytic oxidation

Kinetic studies of methane catalytic oxidation were performed in a flow reactor. The reaction order with respect to methane was found to be equal to 1. In kinetic calculations, we used activity data for the 0.5–1.0 mm size fractions of the catalysts in methane oxidation at GHSV = 1000, 24000, and 48000 h^{-1}. The results obtained by data processing in the plug flow approximation are presented in Table 5. The obtained kinetic parameters were used further for modeling of methane combustion.

Catalyst	k_0, s^{-1}	E, kJ/mol
IK-12-60-2	4.36×10^7	81.4
IKT-12-40A	1.09×10^5	71.2
IK-12-61	1.09×10^5	71.2
IK-12-62-2	3.29×10^5	63.8

Table 5. Kinetic parameters of the total methane oxidation reaction

5. Experimental studies of natural gas combustion in a catalytic combustion chamber

5.1 Experimental procedures

Experimental studies of natural gas combustion were carried out in a stainless-steel tubular vertical catalytic combustion chamber (CCC) with an internal diameter of 80 mm. The CCC is schematically shown in Fig. 2. The volume of the catalytic package was 1.3 L.
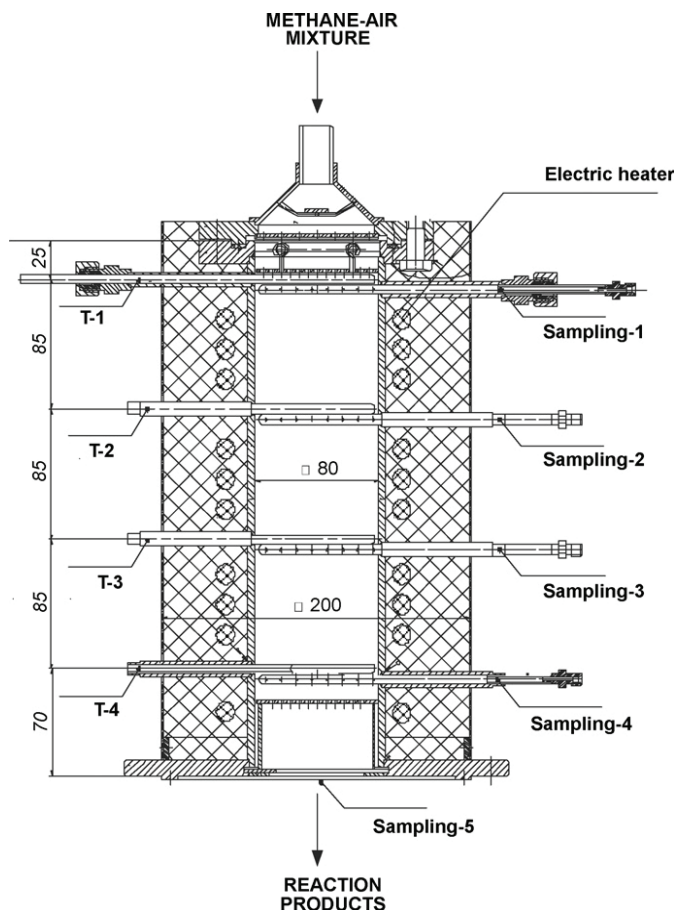
Fig. 2. Schematic view of the catalytic combustion chamber: T-1 to T-4: thermocouples,
sampling 1–5: gas samplers.

The air/fuel equivalence ratio (α) was selected to be close to the minimum value of this
parameter in the operating regime of full-power GTPP (α= 6.4–6.8). The inlet temperature of
the fuel–air mixture (T_{in}) was varied between 470 and 600°C, the temperature at the chamber
exit (T_{ex}) was 900–985°C, the GHSV of the fuel–air mixture was 8500–15,000 h^{-1}.

Natural gas was introduced into the combustion chamber after reaching the light-off
temperature. Due to the natural gas combustion, the temperature in the catalyst bed
increased and reached the values close to the desired ones in 30–40 min. The temperature
mode was corrected by smooth variation of the air and natural gas flows.

When the desired temperature regime was reached, temperatures along the length of the
catalytic chamber were measured. The radial temperature profile was measured before and
after the pilot-plant tests. A reference manometer was used to measure the pressures in the
catalyst bed. The gas phase composition at the CCC outlet was analyzed using a "Kristall-
2000 M" gas chromatograph. The gas probes were also analyzed in parallel using ECOM-AC
gas analyzer.

The catalytic packages studied are schematically presented in Fig. 3.

1. uniform loading with ring shaped high temperature resistant oxide catalyst
2. two high temperature catalysts with different granule shape. According to the results of modeling, the methane conversion should increase with change of granule shape as: ring < cylinder < sphere. However, the use of spherical catalyst for entire reactor is impossible due to a high pressure drop. Therefore, the reactor consists of two sections: the first with ring shaped oxide catalyst (or Pd-Mn-Al-O) and the second downstream section with spherical catalyst having lower fractional void volume. This combination with a short bed of spherical catalyst provides rather high methane combustion efficiency at a minor increase of pressure drop.
3. two ring shaped catalysts with different catalytic activity. In this case, a short bed (ca.10%) of the highly active Pd-Ce-catalyst is located in the upstream section at low temperature, and it initiates methane combustion. The larger bed of high temperature resistant oxide catalyst in the downstream section provides high efficiency of methane combustion. This design of catalytic reactor allows a reduction of total Pd loading and an increase of methane combustion efficiency at a low inlet temperature.
4. three catalysts with different catalytic activity and fractional void volume. The highly active Pd-catalyst in the upstream section initiates methane oxidation, the high temperature resistant catalyst in the larger middle section provides stable methane combustion. The bicomponent spherical Pd-Mn-Al-O catalyst with a low Pd-content and low fractional void volume in the downstream section improves the efficiency regarding the residual traces.
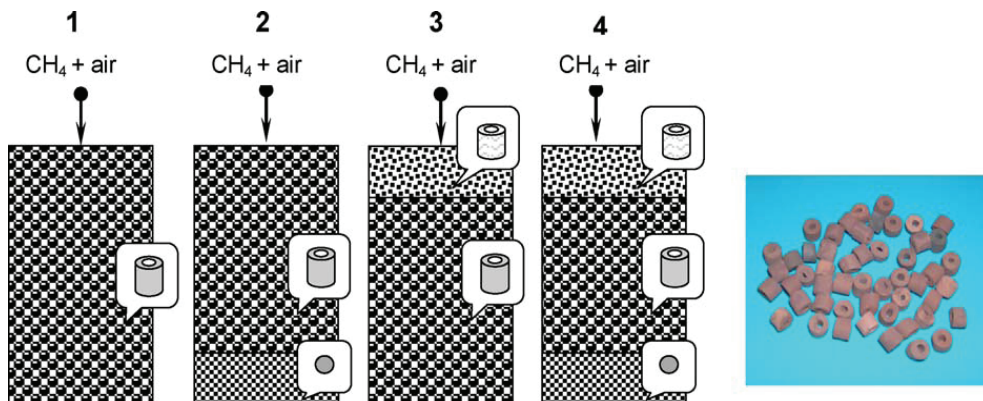

Fig. 3. Schemes of uniform (1) and structured (2–4) loading of the reactor and photo of granulated catalyst (Yashnik et al., 2009, Ismagilov et al., 2010)

5.2 Tests of the catalytic combustion chamber with uniform catalyst package

First, we tested CCC loaded with one catalyst. Such loading will be hereafter denoted as "uniform" and provides for one-stage combustion of the natural gas–air mixture. Such experiments allowed us to analyze the perspectives of using manganese–alumina catalysts and evaluate their catalytic properties in natural gas combustion by such parameters as outlet temperature and emission of hydrocarbons. $Mn–Al_2O_3$, $Mn–La–Al_2O_3$ and $Pd–Mn–La–Al_2O_3$ catalysts shaped as rings were tested for 72–120 h in a temperature cycle mode.

The temperature cycle mode consisted of four cycles of gas combustion, catalyst cooling and repeated start of the combustion process. The combustion process was carried out at GHSV= 15,000 h^{-1} and inlet temperature 580–600 $^{\circ}$C. The value of α was maintained at 6.8–6.9. The height of the catalytic package was 300 mm. The dynamics of changes in the activity of different catalysts are presented in Fig. 4.
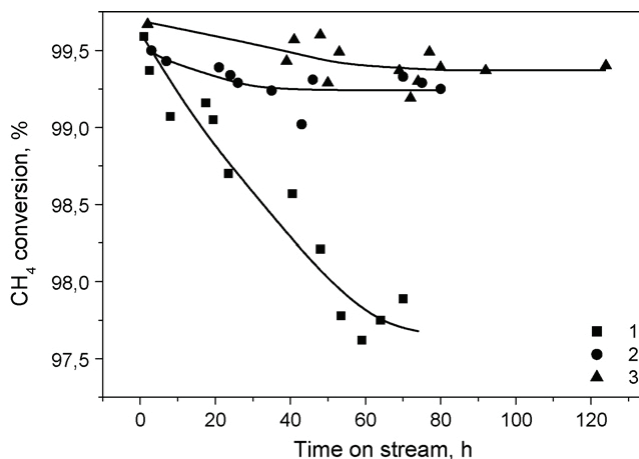

Fig. 4. Methane conversion vs. operation time in CCC at GHSV: 14,900–15,100 h^{-1} and α = 6.7–6.8. Uniform catalyst package loaded with: (1) Mn–Al$_2$O$_3$ (T$_{in}$ – 600 °C); (2) Mn–La–Al$_2$O$_3$ (T$_{in}$ – 600 °C); (3) Pd–Mn–La–Al$_2$O$_3$ (T$_{in}$ – 575–580 °C).

The data presented in Fig. 4 indicate that the catalysts Mn–Al$_2$O$_3$, Mn–La–Al$_2$O$_3$ and Pd–Mn–La–Al$_2$O$_3$ differ both by their activity and stability. For example, the activity of the Mn–Al$_2$O$_3$ catalyst gradually decreased as evidenced by gradual increase of the methane and CO concentration at the CCC outlet. The methane conversion decreased from 99.6% to 97.9% during the first 50–54 h on stream. Then the catalyst activity stabilized and did not change in the following 80 h on stream (Fig. 4, curve 1). At the end of the experiment the methane and CO concentrations stabilized at 330 and 110 ppm, respectively (Table 6).

Table 6 compares the outlet temperatures and emissions of CH$_4$ and CO during natural gas combustion over Mn–Al$_2$O$_3$ catalysts with different fractional compositions at GHSV= 8500–15,000 h^{-1}.It was shown that the methane combustion efficiency over large catalyst granules with the external ring diameter 15mm was low.

Even at a low load on the catalyst (GHSV = 8500 h^{-1}) the methane conversion was 97% whereas the methane and CO emissions at the outlet were 500 and 300 ppm, respectively. Note that under similar CCC operation conditions the application of catalyst granules with the external diameter 7.5 mm allowed for a 10-fold decrease of the methane emission and 30-fold decrease of the CO emission. In both cases the CCC efficiency also depended on contact time. The contact time increase from 0.24 s (GHSV = 15,000 h^{-1}) to 0.42 s (GHSV = 8500 h^{-1}) affected more significantly the efficiency of CCC loaded with the catalyst with smaller internal and external diameters of the granules (7.5 mm), i.e. lower fractional void volume of the catalyst bed. These data indicate that the mass transfer of the reagents and reaction products to/from the catalyst surface substantially affects the total CCC efficiency in methane combustion at the inlet temperature 600 $^{\circ}$C. At this temperature methane

oxidation proceeds mainly on the catalyst surface and the contribution of homogeneous reactions is negligible, which is confirmed by substantial improvement of methane conversion with the increase of the catalysts geometrical surface.

These data agree with the work (Hayashi et al., 1995) where the authors showed the dependences of relative contributions of heterogeneous and homogeneous methane oxidation reactions on the monolithic Pt–Pd catalyst on the inlet temperature, pressure and the catalyst channel density. Placing the catalysts with small cells (200 cpsi) in the front part of the reactor allowed the increase of heat release there at 600 °C (Hayashi et al., 1995), at the same time in the monolith with larger channels (100 cpsi), especially at temperature 700 °C the homogeneous oxidation reaction was prevailing.

Frac-tion, mm	G_{air}, m³/h	G_{NG}, l/h	GHSV, h⁻¹	α	T_{in} °C	T_1* °C	T_2* °C	T_3* °C	T_4* °C	C_{CH4}, ppm	C_{CO}, ppm	C_{NOx} ppm	X_{CH4} %
7.5	19.4	309	14900	6.78	577	659	867	920	917	328	102	1	97.89
7.5	15.0	243	11500	6.70	567	677	903	926	905	164	41	2	98.68
7.5	11.1	180	8500	6.67	571	728	923	925	896	48	9	1	99.69
15	19.2	324	14800	6.41	590	623	763	898	918	987	943	1	93.87
15	15.0	267	11500	6.10	570	604	783	909	919	630	616	2	96.28
15	11.1	204	8500	5.90	562	591	790	903	897	504	344	2	97.13

G_{air} is volume flow rate of air, G_{GN} is volume flow rate of natural gas, C_{CH4}, C_{CO}, C_{NOx} are outlet concentrations of CH_4, CO and NO$_x$; X_{CH4} is methane conversion, *temperatures measured by thermocouples placed along the catalyst bed at different distances from the CCC inlet: T_1 – 25 mm; T_2 – 110 mm; T_3 – 195 mm; T_4 – 280 mm.

Table 6. Parameters of methane combustion over Mn-Al$_2$O$_3$ catalysts with different fractional composition

The activity of Mn–La–Al$_2$O$_3$ and Pd–Mn–La–Al$_2$O$_3$ catalysts also decreased in the first 30–40 h on stream. However, the activity decrease was less dramatic compared to the Mn–Al$_2$O$_3$ catalyst (Fig. 4). The methane conversion over Mn–La–Al$_2$O$_3$ and Pd–Mn–La–Al$_2$O$_3$ catalysts decreased from 99.5% to 99.3% (Fig. 4, curve 2) and from 99.7% to 99.4% (Fig. 4, curve 3), respectively. The concentrations of methane and CO stabilized at 100 and 85 ppm, correspondingly. Note that the Pd–Mn–La–Al$_2$O$_3$ catalyst showed these values of the residual CH_4 and CO concentrations at a lower inlet temperature 575 °C than the Mn–La–Al$_2$O$_3$ catalyst that showed similar values at 600 °C inlet temperature. The NO$_x$ concentration at the outlet of the catalyst package did not exceed 0–2 ppm on all the catalysts. Thus, the obtained results demonstrate that the activity of the Pd–Mn–La–Al$_2$O$_3$ catalyst was higher than that of the catalysts without Pd. Meanwhile, the stability of this catalyst was comparable to that of Mn–La–Al$_2$O$_3$ being determined by the Mn–hexaaluminate phase. The stability of these catalysts was much higher than that of the catalyst based on Mn oxide. These results of the catalysts testing under the above conditions are in good agreement with our results on the study of the catalysts activity in methane oxidation in a laboratory reactor (Yashnik et al., 2006; Tsikoza et al., 2002; Tsikoza et al., 2003). It was shown that modification of Mn-alumina catalysts with oxides of rare earth metals allowed a considerable increase of thermal stability of the catalysts due to the

formation of manganese–hexaaluminate phase (Yashnik et al., 2006; Tsikoza et al., 2002). Introduction of 0.5 wt.% Pd into Mn–La–Al$_2$O$_3$ resulted in a substantial decrease of the light-off temperature of the air–natural gas mixture (Yashnik et al., 2006).

The pressure drop on the full height of the catalyst bed for uniform loading of the catalysts in the form of 7.5 mm × 7.5 mm × 2.5 mm rings for the catalysts Mn–Al$_2$O$_3$, Mn–La–Al$_2$O$_3$ and Pd–Mn–La–Al$_2$O$_3$ was 35, 23 and 14 mbar at GHSV= 14,900, 11,500 and 8500 h^{-1}, respectively. These values are less 4% of the total pressure which was 1 bar.

Figure 5 shows the effect of the air/fuel equivalence ratio on the outlet temperature and methane conversion over the catalyst package loaded with the Mn–La–Al$_2$O$_3$ catalyst. The variation of α between 6.2 and 7.2 showed that its decrease (enrichment of the fuel–air mixture with methane) resulted in a growth of the temperature at the outlet of the catalyst bed and, consequently, increase of the methane conversion. For instance, when α was decreased from 7 to 6.2, the methane conversion increased from 99.3% to 99.93% and the temperature grew from 937 to 992 °C at GHSV= 15,000 h^{-1}. However, Fig. 5 shows that methane conversion above 99.9% was observed when the temperature in the catalyst bed exceeded 980°C. So high temperature is undesirable because the catalyst overheating during prolonged operation will inevitably lead to its deactivation. Therefore, alternative methods of increasing the methane conversion are required.

As it is known from the literature, one of the ways to increase the CCC efficiency is to use multistage (multizone) combustion. This method allows one to control the temperature profile by varying the catalyst activity in different zones of the catalytic combustion chamber. Several methods for stepwise combustion of hydrocarbon fuels in the GTPP CCC have been implemented. American companies Catalytica (Dalla Betta & Tsurumi, 1993) and Westinghouse Electric Corp. (Young & Carl, 1989) suggested feeding the fuel–air mixture to a monolith catalyst consisting of alternating channels with an active component and without it. If the surface reaction in the channel with a catalyst takes place in the diffusion-controlled regime, adiabatic heating to the flame temperature does not occur because the heat is transferred to the inert channel of the monolith. The fuel–air mixture exiting the inert channels is burnt at the exit of the monolith catalyst.
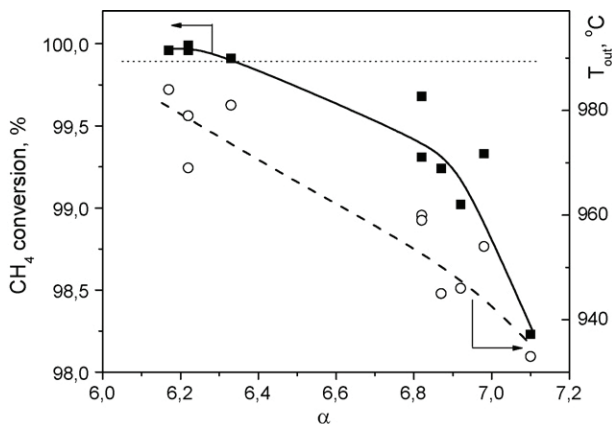

Fig. 5. Dependence of methane conversion (filled symbols) and catalyst temperature at the CCC outlet (open symbols) during methane combustion in CCC loaded with Mn–La–Al$_2$O$_3$ catalyst on α. GHSV= 15,000 h^{-1}, T$_{in}$ = 600 °C.

In patents (Dalla Betta & Tsurumi, 1993; Pfefferle, 1997) it was suggested to use multi-section catalysts with different levels of activity to carry out combustion in the kinetically controlled regime. The catalytic activity is regulated by varying the concentration of the noble metal (most often Pd) in the range of 5–20 wt.% or the nature of the active component (noble metal, transition metal oxides). It was also suggested (Dalla Betta & Velasco, 2002) to use a two-stage monolithic catalyst combined from catalytic systems with different thermal stabilities. A catalyst with low ignition temperature requiring minimal heating is placed at the entrance zone whereas a catalyst resistant to the action of high temperatures is placed at the exit.

5.3 Tests of CCC with combined two-stage catalyst package

We suggested a design of a two-stage catalyst package consisting of catalysts with the same chemical composition but different fractional compositions. Using the Pd–Mn–La–Al_2O_3 catalyst as an example we studied the effect of the catalyst bed fractional void volume on the methane conversion in CCC. The main part of the catalyst package was loaded with the catalyst formed as 7.5 mm × 7.5 mm × 2.5 mm rings having the fractional void volume (ε) 0.52. A catalyst layer with 60 mm height consisting of 4–5 mm spherical granules with fractional void volume 0.42 was placed near the outlet of the package. The total Pd concentration in the catalyst package was 0.6 wt.%.

The application of the spherical catalyst at the CCC outlet made it possible to achieve over 99.9% combustion efficiency (Fig. 6) and decrease the methane concentration from 85 ppm to 0–5mm and the CO concentration to 4–8 ppm at inlet temperature 580°C and α in the range of 6.7–7.1. Fig. 7 presents the methane and CO profiles along the reactor length. One can see that more than 90% of methane is oxidized at the distance ca. 200 mm from the inlet. The maximum CO concentration is observed in this region. Further combustion of methane and CO to concentrations below 10 ppm is observed mostly at 280–340 mm from the inlet of
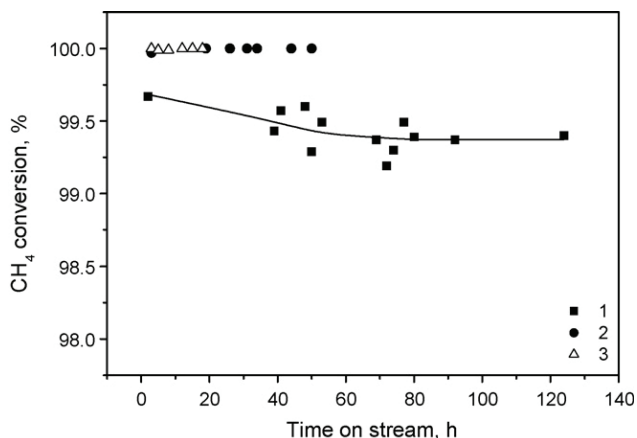

Fig. 6. Methane conversion vs. operation time in CCC for different catalyst packages: (1) uniform catalyst package Pd–Mn–La–Al_2O_3, rings (T_{in} = 575–580 °C, GHSV= 15, 100 h^{-1}, α= 6.8-6.9); (2) combined catalyst package: Pd–Mn–La–Al_2O_3, rings and spheres (Tin = 575–580 °C, GHSV= 12,500 h^{-1}, α = 6.7–6.8); (3) combined catalyst package: Mn–La–Al_2O_3, rings, and Pd–Mn–La–Al_2O_3, spheres (T_{in} – 575–580°C, GHSV= 12,500 h^{-1}, α = 6.7-6.8).

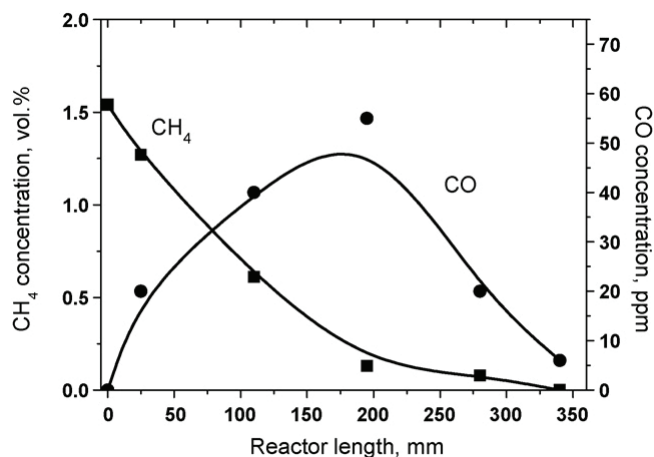Fig. 7. Profiles of methane and CO concentrations along the reactor length during combustion of natural gas on a combined catalyst package Pd–Mn–La–Al_2O_3: 280 mm of rings and 60 mm of spherical granules (T_{in} = 580 ∘C, GHSV= 12,500 h^{-1}).

the catalyst package, i.e. in the area where the spherical catalyst is loaded. The layer of this catalyst has a higher density and higher geometrical area, which provides more efficient use of the catalyst, and thus increases the CCC efficiency.

Then, we determined the role of catalyst activity in the total CCC efficiency. We carried out tests on a combined catalyst package consisting on Mn–La–Al_2O_3 (rings) and Pd–Mn–La–Al_2O_3 (spheres) and compared the methane conversion with the results of the previous test. The ratio of the layer heights was similar to that used in the previous test – 280/60mm. The total Pd content in CCC was much lower - about 0.1 wt.% because most of the catalyst package consisted of the Mn–La–Al_2O_3 catalyst. The activity of this catalyst ($T_{50\% CH4}$) is lower than that of Pd–Mn–La–Al_2O_3 (Table 3). However, the substitution of the more active catalyst with a less active and a 6-fold decrease of the total Pd content (Fig. 6, curve 3) did not decrease the methane combustion efficiency compared to the previous test (Fig. 6, curve 2) where the total Pd content was 0.6 wt.%. Thus, increase of the efficiency of the use of the catalyst granules even at a relatively short length of the CCC results in a noticeable improvement of the overall CCC efficiency at a low total Pd loading.

However, such CCC design produced a larger pressure drop than the uniform catalyst package with ring-shaped catalysts. The pressure drop in the two-stage catalyst package was 48 mbar at GHSV= 12,500 h^{-1} and 30 mbar at GHSV= 10,000 h^{-1}. The pressure drop in the layer of the spherical Pd–Mn–La–Al_2O_3 catalyst was 20 and 13 mbar, respectively.

The tests of CCC with a combined two-stage catalyst package at lower inlet temperature showed that the inlet temperature decrease from 580 to 470 ∘C decreased the methane combustion efficiency. The methane conversion over the catalyst package Pd–Mn–La–Al_2O_3 (rings)/Pd–Mn–La–Al_2O_3 (spheres) decreased from 99.93% to 99.7% with methane and CO concentrations increasing to 37 and 150 ppm, respectively. The methane conversion over the catalyst package Mn–La–Al_2O_3 (rings)/Pd–Mn–La–Al_2O_3 (spheres) at the inlet temperature

470 $\circ$C was only 99.4% with methane and CO concentrations 90 and 220 ppm, respectively. The increase of the methane combustion efficiency at low inlet temperature was made possible by organizing a three-stage catalyst package.

5.4 Tests of CCC with combined three-stage catalyst package

In the three-stage catalyst package we placed a highly active Pd–Ce–Al_2O_3 catalyst with 2 wt.% Pd at the entrance zone. Most of the package consisted of Mn–La–Al_2O_3 catalyst. Both catalysts were shaped as 7.5 mm × 7.5 mm × 2.5 mm rings. Pd–Mn–La–Al_2O_3 catalyst in the form of 4–5 mm spherical granules was placed in the downstream part of the catalyst package. The ratio of the catalyst layer heights was 40/240/60mm. Similarly to the tests of two-stage packages, the ratio of the heights of ring and spherical granules was 280/60mm. The tests were carried out at the inlet temperature 470 $\circ$C, GHSV= 10,000 h^{-1} and α = 5.2. Under such conditions the temperature at the outlet zone of the catalyst package remained at about 950 $\circ$C.

Figure 8a shows the temperature profile along the CCC length. In the inlet zone filled with the Pd–Ce–Al_2O_3 catalyst at 25 mm from the inlet the feed is heated from 470 to 580 $\circ$C due to catalytic combustion of methane. The latter temperature is sufficiently high for effective functioning of the main Mn–La–Al_2O_3 catalyst bed. Further temperature growth from 580 to 950$\circ$C takes place on this catalyst.

The profiles of the methane and CO concentrations along the CCC length are shown in Fig. 8b. The methane concentration profile shows a sharp concentration fall in the inlet zone where the Pd–Ce–Al_2O_3 catalyst is located. The main decrease of the concentration from 1.4% to 170 ppm takes place in the zone of the main catalyst Mn–La–Al_2O_3 (40–280 mm). Then at the CCC exit in the layer of the spherical Pd–Mn–La–Al_2O_3 catalyst the residual amounts of methane burn from 170 to 0–10 ppm concentrations. The concentration of the CO intermediate initially grows. Then, when most methane is oxidized, the CO concentration also decreases from 300 to 40 ppm in the Mn–La–Al_2O_3 bed. Finally, residual CO is burned in the spherical Pd–Mn–La–Al_2O_3 catalyst to 10 ppm concentrations. The pressure drop in the catalyst package was 29–30 mbar.

Thus, the use of the three-stage combined catalyst package including a thin layer of the active palladium–ceria catalyst located at the CCC entrance before the main oxide catalyst bed allows us to increase the CCC efficiency for methane combustion and obtain required low methane emission value of 10 ppm at low inlet temperature 470$\circ$C. This additional catalyst layer provides the initial methane conversion and temperature increase before the main catalyst bed.

6. Modeling of methane combustion processes in a catalytic combustor

6.1 Model description

The catalytic packages used in modeling are schematically presented in Fig. 3. For calculation of the catalyst package performance, we used a model of a steady-state adiabatic plug-flow reactor. The calculation of the temperature profiles and methane conversion was performed at variation of catalyst methane oxidation activity and geometry of catalyst granules, ratio of bed lengths of different catalysts in the package, temperature, pressure and gas space velocity in the combustor.
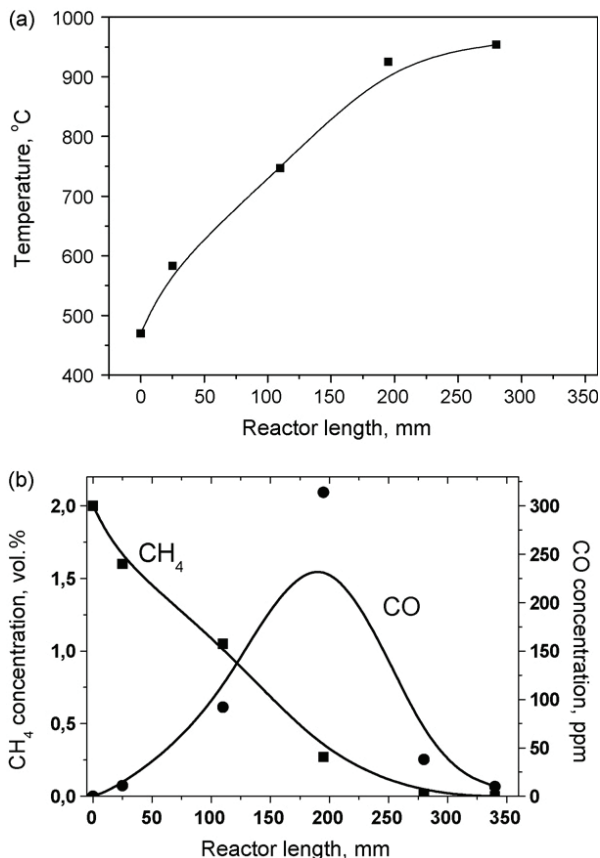
Fig. 8. Profiles of temperature (a) and methane and CO concentrations (b) along the reactor length during combustion of natural gas on a combined catalyst package Pd–Mn–La–Al$_2$O$_3$/Mn–La–Al$_2$O$_3$/Pd–Ce–Al$_2$O$_3$ (T_{in} = 470 ∘C, GHSV= 10,000 h^{-1}, α = 5.2).

The reaction rate was calculated using Eqs. (1) and (2):

$$W = k\, C_{CH_4} \left(\frac{P}{P_0} \right) \tag{1}$$

$$k = \eta\, k_0 (1 - \varepsilon) \exp\left(-\frac{E/R}{T} \right) \tag{2}$$

where k is the kinetic constant (s^{-1}), C_{CH4} is the methane concentration (molar fraction), P is the operating pressure (bar), P$_0$ is the pressure (bar) at which the reaction kinetics is studied experimentally (in this case it is equal to 1 bar), η is efficiency factor (dimensionless), k$_0$ is the pre-exponential factor of the kinetic constant (s^{-1}), E is the activation energy (J mol^{-1}), R is the univeral gas constant (J mol^{-1}K^{-1}), ε is the fractional void volume in the catalyst bed (dimensionless).

The values of kinetic parameters (k_0 and E) determined earlier in kinetic experiments over these catalysts (Ismagilov et al, 2008) (see Table 5) were used in the calculations.

The efficiency factor η, accounting for the internal mass transfer limitations, was determined using the standard Thiele equation for the first-order reaction (Malinovskaya et al. 1975).

A heat and mass steady-state model of an ideal displacement adiabatic reactor was used in the simulations of the catalyst bed:

$$u \frac{\partial C_{CH_4}}{\partial \ell} = -W = \beta(C_{CH_4}^* - C_{CH_4}) \tag{3}$$

$$u \frac{\partial T_G}{\partial \ell} = x C_{CH_4}^{in} \Delta T_{AD} = \frac{\alpha}{c_p}(T_C - T_G) \tag{4}$$

$$\ell = 0 \Rightarrow C_i = C_i^{in}; T = T_{in} \tag{5}$$

Here u is the superficial linear gas flow velocity in the reactor reduced to standard conditions and full reactor cross-section area (m/s), ℓ is the coordinate along the reactor height (m), x is the methane conversion, C^* and C are methane concentrations at the surface of the catalyst grain and in the gas flow, respectively, β is the mass exchange coefficient for methane (s^{-1}), T_G and T_C are gas and catalyst temperatures (K), correspondingly, ΔT_{AD} is the adiabatic heating of the reaction (K), α is the heat exchange coefficient ($Wm^{-3} K^{-1}$), c_p is the gas thermal capacity ($Jm^{-3} K^{-1}$), index *in* corresponds to the conditions at the reactor inlet.

The mass and heat transfer coefficients were calculated according to the equations presented in (Aerov et al. 1979) with representation of different catalyst pellets shapes by the spheres of equivalent diameter. Equations used for calculations are presented in detail elsewhere (Ismagilov et al., 2008; Ismagilov et al., 2010).

6.2 Selection of shape and size of catalyst granules

The ultra-low emission characteristics of catalytic combustion chamber are determined not only by the catalyst activity but also by geometric parameters of the catalyst package, such as the bed height and the shape and size of catalyst granules, which are responsible for the efficiency of mass and heat transfer in the fixed catalyst bed. Therefore, the effects of the catalyst granule shape and size on characteristics of the process of catalytic methane combustion: methane conversion, temperature in the bed and pressure drop were studied. Modeling of the process was performed taking into account the influence of the internal and external diffusion on the kinetic parameters (k_0 and E) for the reaction $CH_4 + 2O_2 \rightarrow CO_2 + 2H_2O$ proceeding on each individual catalyst. The calculations were performed for typical operation conditions of the CCC (Parmon et al., 2007): methane concentration in methane–air mixture 1.5 vol.%, GHSV = 5000–40,000 h^{-1} and inlet temperature 723–873 K. The model CCC was represented by a tubular reactor with 80 mm inner diameter and 300 mm catalyst bed height.

The methane combustion modeling shows that the shape of the catalyst granules has a substantial effect on methane conversion, and hence on the residual methane content and the temperature in the catalyst bed. This effect increases with a decrease of the inlet temperature and an increase of the space velocity, being most marked for catalysts with

lower activity. Fig. 9 shows simulated profiles of the residual methane content upon methane oxidation in uniform beds of the IK-12-61 catalysts with different shape: ring
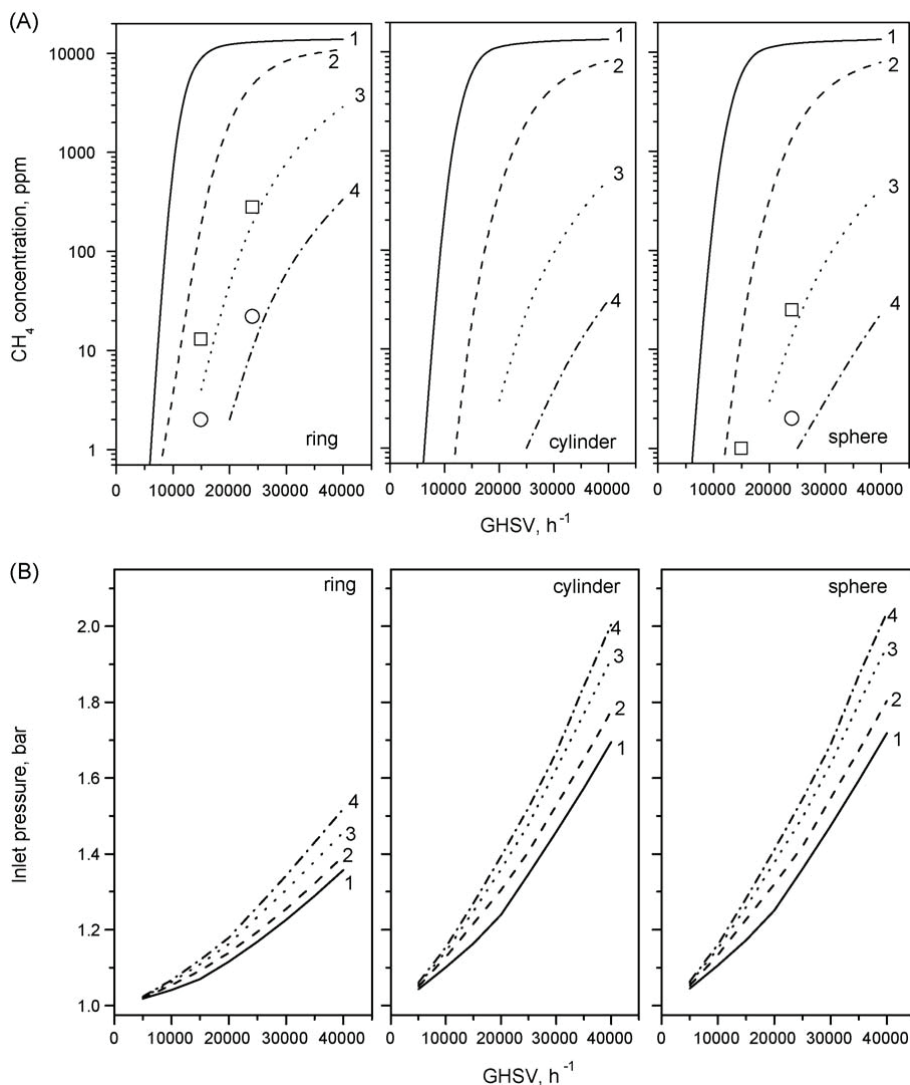

Fig. 9. Simulated profiles of residual methane concentration (A) and inlet pressures (B) vs. GHSV at temperatures: 723 K (Curve 1), 773 K (Curve 2), 823 K (Curve 3) and 873 K (Curve 4) for uniform catalyst package loaded with Mn-La-Al$_2$O$_3$ catalyst (IK-12-61) as ring, spherical, and cylindrical granules with size 7.5 mm x 7.5 mm x 2.5 mm, 5.0 mm, and 4.5 mm x 5 mm, respectively. The CCC diameter is 80 mm and the height is 300 mm. Methane concentration is 1.5 vol.%, α = 6.9. Experimental data are presented for comparison: 773 K (□) and 873 K (O).

(7.5 mm × 7.5 mm × 2.5 mm), cylinder (4.5 mm × 5.0 mm) and sphere (5.0 mm). At 723 K and 10,000 h^{-1}, the residual methane contents attained in the beds of spherical and ring-shaped granules of IK-12-61 catalyst are different by a factor of 4.5, but neither of the catalyst shapes provides the required methane emission level (not exceeding 10 ppm) at GHSV higher than 5000 h^{-1}. At higher GHSV, the required methane residual concentration is attained only at the increase of the inlet temperature with a similar effect of the granule shape. For instance, at GHSV below 20,000 h^{-1} the residual methane content less than 10 ppm is observed at the inlet temperature of 823 K for the beds of both ring-shaped and spherical granules, while at 35,000 h^{-1} this methane concentration is attained only on the spherical granules and at a higher temperature of 873 K.

According to modeling, the methane conversion increases with the change of granule shape in the sequence: ring < cylinder < sphere. However, the use of cylindrical and spherical catalyst for the entire reactor is impossible due to a high pressure drop (Fig. 9B). As shown in Fig. 9B, catalytic packages with a height of 300 mm containing ring-shaped and spherical granules give the pressure loss of up to 0.5 and 1.2 bar, respectively.

Thus, in the loading of the CCC with granulated catalysts, the attention should be paid not only to the ultra-low emission characteristics, but also to the minimization of the pressure drop in the catalyst bed. The structured combined catalytic package containing two or three catalysts with optimal catalytic properties and geometrical parameters seems to be promising to meet these two requirements. In design of a combined catalytic package with a high efficiency and a long lifetime, first of all, the light-off temperature and the operation temperature limit of the catalysts should be taken into account, because the CCC having a low light-off temperature of lean methane–air mixtures and high thermal stability provides stable combustion of methane–air mixtures and low emission characteristics. It should be noted that at high inlet temperatures and high methane concentrations the maximum temperature in the catalyst bed can be as high as 1373–1473 K, which can result in the reduction of the catalyst lifetime. Further, three types of catalyst packages complying with the above requirements are examined.

6.3 Variation of the structure of combined catalyst loading in the CCC
6.3.1 Two high temperature catalysts with different granule shapes

The reactor consists of two sections: the first one with the ring shaped oxide catalyst Mn-La-Al$_2$O$_3$ or this catalyst modified by Pd (0.5–0.8 wt.%), and the second downstream section with the spherical catalyst having lower fractional void volume. This combination with a shorter bed of spherical catalyst (about 20%) provides rather high methane combustion efficiency at a minor increase of pressure drop (not exceeding 20%) in comparison with the uniform catalytic package. For example, at 40,000 h^{-1} and 873 K, the residual CH$_4$ content decreased twice and the pressure drop increased only by 18%, when 20% of the ring-shaped Mn-La-Al$_2$O$_3$ catalyst was replaced by the spherical granules (Figs. 9A and 10A).

The simulation of methane combustion process shows that the catalytic package with Pd-Mn-La-Al$_2$O$_3$ (Fig. 10B) is more effective than the one with Mn-La-Al$_2$O$_3$ (Fig. 10A). At similar conditions, the former provides the residual methane concentration 10 times lower than the latter, methane content being below 10 ppm at 25,000 h^{-1} and a temperature as low as 773 K. This catalytic package has also high efficiency at 40,000 h^{-1}, although at a higher inlet temperature (873 K). The catalytic packages with both Pd-Mn-La-Al$_2$O$_3$ and Mn-La-Al$_2$O$_3$ have a similar thermal stability at temperatures up to 1373 K.
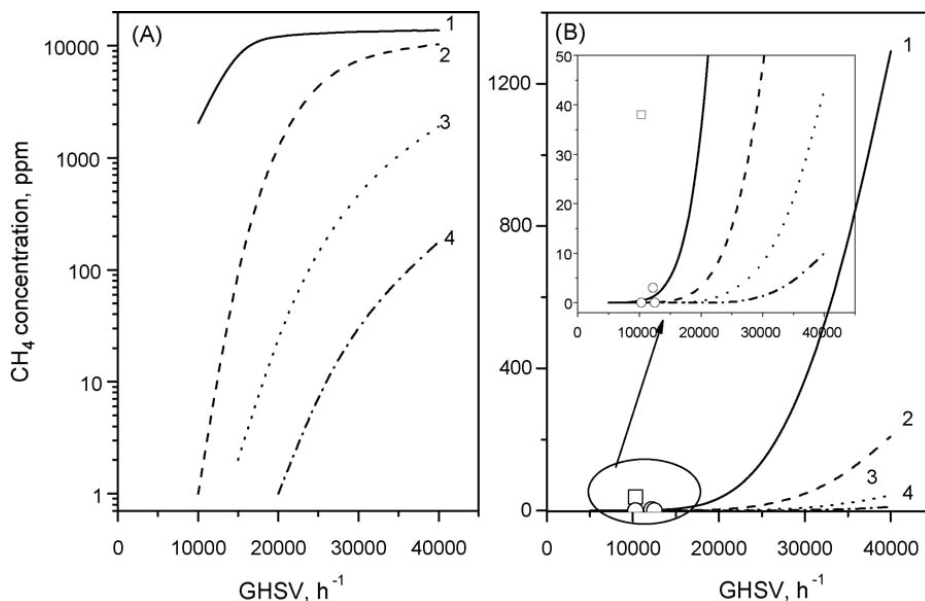
Fig. 10. Simulated profiles of residual methane concentration vs. GHSV at temperatures: 723 K (Curve 1), 773 K (Curve 2), 823 K (Curve 3) and 873 K (Curve 4) for combined catalyst package loaded with Mn-La-Al$_2$O$_3$ (A) and Pd-Mn-La-Al$_2$O$_3$ (B) catalysts in accordance with Scheme 2 {ring (7.5 mm x 7.5 mm x 2.5 mm), L = 280 mm} + {sphere (5.0 mm), L = 60 mm}. Methane concentration is 1.5 vol.%, α = 6.9. Experimental data are presented for comparison: 743 K (□) and 853 K (O).

6.3.2 Two ring shaped catalysts with different catalytic activity

In this case, a short ignition bed (ca. 10%) of the highly active Pd catalyst is located in the upstream section with a lower temperature. The larger bed of high temperature tolerant Mn-La-Al$_2$O$_3$ or Pd-Mn-La-Al$_2$O$_3$ catalyst in the downstream section provides practically total methane combustion. This design of the catalyst package allows a reduction of the total Pd loading and an increase of methane combustion efficiency at low inlet temperatures.

Modeling of methane combustion process shows that the use of Pd-CeO$_2$-Al$_2$O$_3$ catalyst is more preferable; however the catalyst package formed from Pd-Mn-La-Al$_2$O$_3$ is also rather efficient. The location of a more active catalyst in the upstream section is more advantageous in comparison with a variant of its downstream location (Fig. 11). For example, at the same conditions of 40,000 h^{-1} and 873 K, the simulated residual methane content achieved over the former package does not exceed 10 ppm, while with the latter it is as high as 125 ppm. The effect of the variation of the length of the two sections and space velocity on the process parameters was also studied and showed that the optimal loading of highly active Pd catalyst is close to 10% of the total catalyst loading of the CCC.

6.3.3 Three catalysts with different catalytic activity and fractional void volume

The highly active Pd catalyst in the upstream section initiates methane oxidation, the high temperature tolerant catalyst in the larger middle section provides stable methane
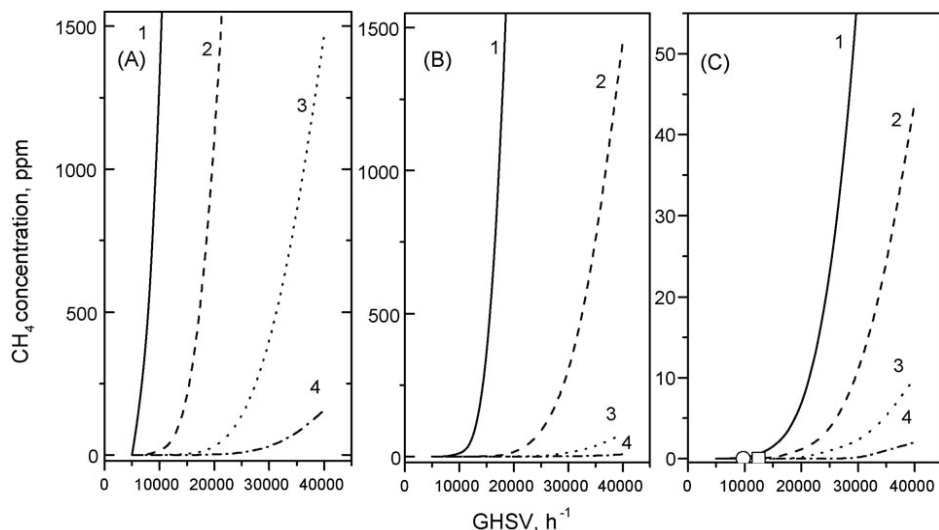
Fig. 11. Simulated profiles of residual methane concentration vs. GHSV at temperatures: 723 K (Curve 1), 773 K (Curve 2), 823 K (Curve 3) and 873 K (Curve 4) for combined catalyst packages in accordance with Scheme 3 (A and B) and Scheme 4 (C). Methane concentration is 1.5 vol.%, α = 6.9. Experimental data are presented for comparison: 743 K ($\square$) and 853 K (O). (A) Mn-La-Al_2O_3 {ring 7.5 mm x 7.5 mm x 2.5 mm, L = 260 mm} + Pd-Mn-La-Al_2O_3 {ring 7.5 mm x 7.5 mm x 2.5 mm, L = 40 mm}, (B) Pd-Mn-La-Al_2O_3 {ring 7.5 mm x 7.5 mm x 2.5 mm, L = 260 mm} + Mn-La-Al_2O_3 {ring 7.5 mm x 7.5 mm x 2.5 mm, L = 40 mm}, (C) Pd-CeO_2-Al_2O_3 {ring 7.5 mm x 7.5 mm x 2.5 mm, L = 40 mm} + Mn-La-Al_2O_3 {ring 7.5 mm x 7.5 mm x 2.5 mm, L = 240 mm} + Pd-Mn-La-Al_2O_3 {sphere 5.0 mm, L = 60 mm}.

combustion. The bicomponent Pd-Mn-La-Al_2O_3 catalyst with a low Pd content and low fractional void volume in the downstream section improves the efficiency by removal of methane residual traces.

The modeling showed that the substitution of 10% of Mn-La-Al_2O_3 catalyst (Fig. 10A) for Pd-CeO_2-Al_2O_3 in the upstream section and the introduction of spherical Pd-Mn-La-Al_2O_3 catalyst in the downstream section of the catalytic package (Fig. 11C) allow a decrease of the inlet temperature and an increase of GHSV. For example, at 20,000 h^{-1} the inlet temperature can be reduced from 873 to 723 K. For the package operation at a higher GHSV (30,000 h^{-1}), an increase of the inlet temperature to 773 K is required. It should be noted that the cost of the combined catalyst package is not significantly higher than that of the uniform Mn-La-Al_2O_3 catalyst bed.

6.4 Comparison of simulated and experimental data

Experimental runs with a model reactor (1.3 l catalyst) demonstrated very good correlation with the results of the modeling (Figs. 9A, 10B and 11C). The catalytic package with the spherical or ring-shaped granules of the IC-12-61 catalyst provided methane combustion to 1 ppm and 15 ppm residual methane concentration, respectively, in the pilot test installation at 15,000 h^{-1} and 773 K and to 2 ppm at 24,000 h^{-1} and 873 K (Fig. 9).
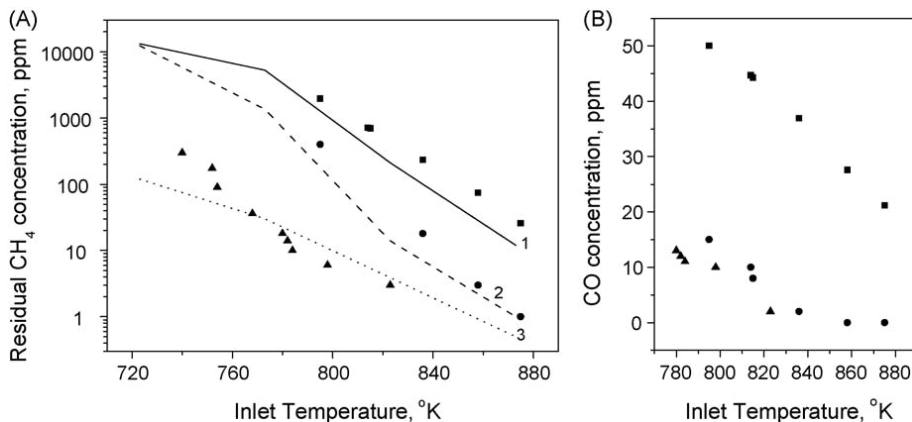
Fig. 12. Residual methane concentration (A) and CO concentration (B) vs. inlet temperature of CCC at GHSV = 24,000 h-1 and α = 6.8. Uniform catalyst package loaded with Mn-La-Al₂O₃ catalyst (IK-12-61) as rings (■, Curve 1) and spheres (●, Curve 2), having size 7.5 mm x 7.5 mm x 2.5 mm and 5 mm, respectively, and Pd-Mn-La-Al₂O₃ catalyst (IK-12-62-2) as rings (▲, Curve 3) with size 7.5 mm x 7.5 mm x 2.5 mm. The symbols are experimental data, the lines are calculated data.

Figure 12 shows the correlation between the simulated and experimental data for the residual methane concentrations in a uniform catalytic package with the ring-shaped Mn-La-Al₂O₃ and Pd-Mn-La-Al₂O₃ catalysts at 24,000 h⁻¹ as a function of the inlet temperature. The observed deviation of the experimental data on residual methane content from the simulated curves can be explained by two causes. The excess of the experimental values over the simulated ones can be caused by the heat loss. Lower experimental values of the residual methane content in comparison with the calculated ones for the catalyst Pd-Mn-La-Al₂O₃ in the range of the inlet temperatures 773–823 K are probably due to the contribution of other heterogeneous reactions (different from deep oxidation) and gas-phase homogeneous methane oxidation. The carbon dioxide reforming and the partial methane oxidation as well as gas phase reactions have not been incorporated into our simulation yet, because we have not observed CO and H₂ formation in the kinetic experiments (Ismagilov et al., 2008). Noticeable amount of CO (10–14 ppm, Fig. 12B) was observed in the pilot test installation when the CCC was loaded by ring-shaped and/or spherical catalyst granules with a size 7.5 mm x 7.5 mm x 2.5 mm and 5 mm, respectively.

Carbon monoxide can be formed as an intermediate product of homogeneous methane oxidation, which has been shown in the study of methane oxidation in lean mixtures at 900–1400 K (Reinke et al., 2005). Our assumption about the contribution of gas phase methane oxidation agrees with a decrease of the CO concentration when the ring-shaped granules are totally (Fig. 12B) or partially substituted (Fig. 13B) for spherical granules. The ring-shaped and spherical granules are different by the specific external surface (593 and 693 m⁻¹, respectively) and the void fraction in the catalyst bed (ε = 0.5 and 0.42, respectively). It is well known that the increase of the surface and the reduction of the void fraction lead to an increase of free radical decay.

On the other hand, there is strong evidence that the catalyst surface affects the gas-phase chemistry (Sidwell et al., 2003; Deutschmann et al., 2000; Chou et al., 2000; Aghalayam et al.,

2003; Quiceno et al., 2000). The hexaaluminate catalyst surface is assumed to act as a sink for methyl radicals, suppressing gas-phase reactions (Sidwell et al., 2003). The authors made this assumption from comparison of the experimental data with numerical models that include both surface and gas phase chemistry. We also observed that the CO concentration changes along the catalyst bed increasing with the temperature increase up to 1173 K but decreasing at the further rise of the temperature (Fig. 13). The arched profile of the formed CO can be evidence that CO is the intermediate in the multi-step surface reactions mechanism proposed by Deutschmann and coworkers (Deutschmann et al., 2000; Quiceno et al., 2000), Chou et al. (Chou et al., 2000) and Aghalayam (Aghalayam et al., 2003) for the oxidation of lean methane–air mixtures.
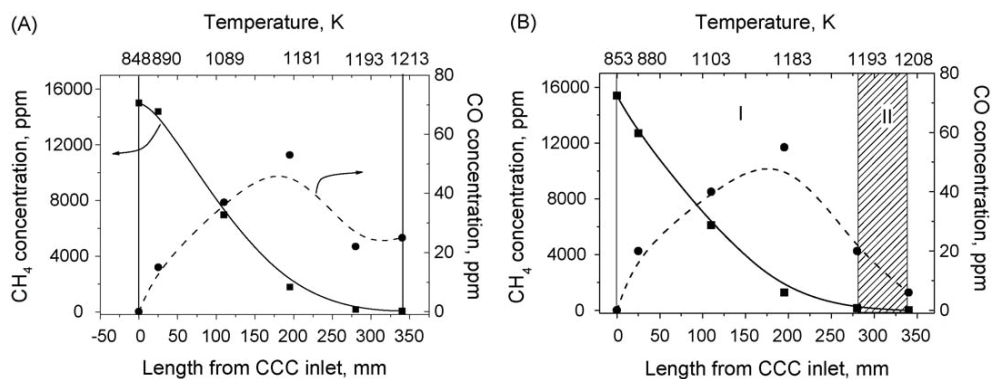

Fig. 13. Profiles of methane (■) and CO (●) concentrations and temperatures along the CCC length during combustion of natural gas in a combined catalyst package: (A) Scheme 1: Pd-Mn-La-Al_2O_3 (ring, 340 mm) at T_{in} = 575°C, GHSV = 15,000 h^{-1}, α = 6.8; (B) Scheme 2: Pd-Mn-La-Al_2O_3 (ring, 280 mm)/Pd-Mn-La-Al_2O_3 (sphere, 60 mm) at Tin = 580°C, GHSV = 15,000 h^{-1}, α = 6.9.

7. Development and testing of a prototype catalytic combustor

Based on the research results a prototype catalytic combustor for a gas turbine with a power 400 kW was designed and fabricated at CIAM (Perets et al., 2009) (Fig. 14). The combustor has a preheating chamber to heat the catalyst to ignition temperature by hot combustion gases and an annular catalyst module with a catalyst loading of 70 kg.

Testing of the prototype combustor demonstrated high efficiency of methane combustion (>99.97%) and low emission of toxic compounds: NOx 0-5 ppm, CO 4-6 ppm, HC 6-20 ppm at inlet temperature 835-880 K, outlet temperature 1145-1160 K, GHSV = 27000-31200 h^{-1}, α = 6.78-7.13, pressure 5 atm (Table 7). It should be noted that nitrogen oxides appeared at all and at low concentrations only if a part of fuel was burned in the preheater.

8. Conclusion

Granular catalysts for natural gas combustion in gas turbine power plants were developed: Pd-Ce-Al_2O_3 catalyst for initiation of methane combustion at low temperatures and the catalysts based on oxides of Mn, hexaaluminates of Mn and La for high temperature
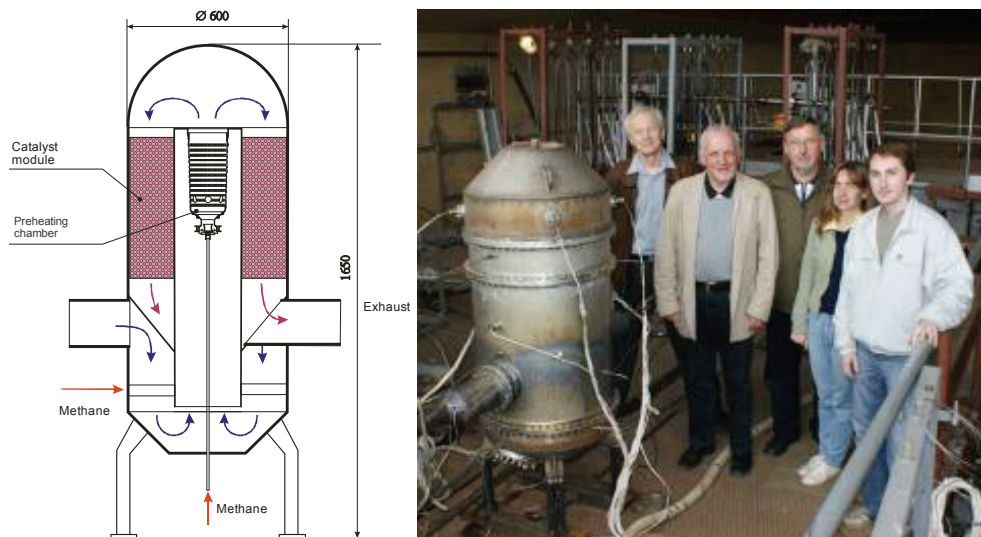
Fig. 14. Scheme and photo of the prototype gas turbine catalytic combustor

Characteristic		Regime 1 Initial test	Regime 2 Modified combustor
Temperature at the combustor inlet		880 K	840 K
Pressure at the combustor inlet		5.0 atm	5.0 atm
Air flow velocity at the combustor inlet		830 g/s (2310 nm^3/h)	960 g/s (2670 nm^3/h)
Methane flow velocity in the preheating chamber		0 g/s (0 nm^3/h)	0.89 g/s (4.5 nm^3/h)
Methane flow velocity in the combustor		6.9 g/s (37.5 nm^3/h)	7.45 g/s (37.5 nm^3/h)
GHSV		27000 h^{-1}	31200 h^{-1}
Air/fuel equivalence ratio		7.13	6.78
Temperature at the catalyst bed inlet		835-860 K	880 K
Temperature at the catalyst bed outlet		1145-1160 K	1145 K
Concentrations at the combustor outlet	HC	18-20 ppm	6 ppm
	CO	4.2-6.0 ppm	4.2 ppm
	NO$_x$	0 ppm	4.6 ppm

Table 7. Results of tests of the prototype catalytic combustor

methane combustion. The catalytic combustion of natural gas over uniform and combined loadings of granulated manganese-oxide and palladium-containing catalysts was studied for optimization of the design of a catalytic package for use in CCC. The catalysts based on manganese–hexaaluminate showed high efficiency and thermal stability during combustion of natural gas for more than 200 h at the temperature in the catalyst bed as high as 1223-1258 K.

Different schemes of catalytic packages were designed. Modeling of methane combustion in several types of catalyst packages composed of 1, 2 or 3 beds of granulated catalysts with different chemical compositions, shapes and sizes of pellets has been performed.

Granules in the form of rings with dimensions 7.5mm×7.5mm×2.5mm were shown to be the optimal form of the catalysts. At the catalyst package height 300 mm and GHSV= 8,500–15,000 h^{-1} the pressure drop in the catalyst package was lower than 40 mbar. This is less than 4% of the total pressure in CCC (1 bar). The use of 4-5 mm spherical granules in the combined loading increased the pressure drop to 48 mbar at GHSV= 12,500 h^{-1} and 30 mbar at GHSV= 10,000 h^{-1}. However, the use of a thin layer of such granules (less than 17.5%) is acceptable for afterburning residual unburned fuel and CO at the CCC exit.

The highly active Pd-Ce-Al$_2$O$_3$ and Pd-Mn-La-Al$_2$O$_3$ catalysts should be used in the CCC upstream section for the initiation of methane oxidation. The Mn-La-Al$_2$O$_3$ and Pd-Mn-La-Al$_2$O$_3$ catalysts with hexaaluminate structure exhibiting good high-temperature activity and high thermal stability can be recommended for the stable methane combustion at a high combustion efficiency in the CCC downstream section. The replacement of 20% of the ring-shaped Mn-La-Al$_2$O$_3$ catalyst by the spherical low-percentage Pd-hexaaluminate catalyst in the exit part of the CCC downstream section results in improvement of methane combustion efficiency at a minor increase of the pressure drop (not exceeding 20%). The addition of 10% of the highly active Pd-CeO$_2$-Al$_2$O$_3$ and Pd-Mn-La-Al$_2$O$_3$ catalysts with ring shape in the CCC upstream section of such catalytic package provides the required emission characteristics (CH < 10 ppm) at the low inlet temperature (about 723 K) and the high GHSV of lean methane–air mixtures (>20,000 h^{-1}). Experimental runs in the pilot reactor (1.3 kg catalyst) demonstrated very good correlation with the results of the modeling.

Based on the research results a prototype catalytic combustor for a gas turbine with a power 400 kW was designed and fabricated. Experimental runs with a prototype combustor demonstrated high efficiency of methane combustion (>99.97%) and low emission of toxic compounds: NOx < 1 ppm, CO < 10 ppm, HC < 10 ppm.

9. Acknowledgments

10. References

Aerov, M.E.; Todes, O.M. & Narinskii, M.A. (1979). *Apparaty so statsionarnym zernistym sloem: Gidravlicheskie i teplovye osnovy raboty (Fixed-Bed Apparatuses: Hydraulic and Thermal Principles of Their Operation)*, Khimiya, Moscow

Aghalayam, P.; Park, Y. K.; Fernandes, N.; Papavassiliou, V.; Mhadeshwar, A. B. & Vlachos, D.G. (2003). A C1 mechanism for methane oxidation on platinum. *J. Catal.*, 213, pp. 23-38, 0021-9517

Arai, H.; Yamada, T.; Equchi, K. & Seiyama, T. (1986). Catalytic Combustion of Methane over Various Perovskyte-Type Catalysts. *Appl. Catal.*, A26, pp. 265-279, 0166-9834

Baldwin, T.R. & Burch, R. (1990). Catalytic combustion of methane over supported palladium catalysts *Appl. Catal.*, 1990, vol. 66, 337-358, 0166-9834

Burch, R & Hayes M.J. (1995). C–H bond activation in hydrocarbon oxidation on solid catalysts. *J. Mol. Catal. A*, 100, pp. 13–33, 1381-1169

Burch, R. (1996). Low NOx options in catalytic combustion and emission control. *Pure Appl. Chem.*, 68, p. 377-385, 0033-4545

Carroni, R.; Schimdt V. & Griffin T. (2002). Catalytic combustion for power generation. *Catal. Today,* 75, pp. 287-295, 0920-5861

Carroni, R.; Griffin, T.; Mantzaras, J. & Reinke, M. (2003). High-pressure experiments and modeling of methane/air catalytic combustion for power generation applications. *Catal. Today*, 83, pp. 157–170, 0920-5861

Chou, C.P.; Chen, J.Y.; Evans, G.H. & Winters, W.S. (2000). Numerical studies of methane catalytic combustion inside a monolith honeycomb reactor using multi-step surface reactions. *Combust. Sci. Technol*, 150, pp. 27-57, 0010-2202

Chouldhary, T.V.; Banerjee, S. & Choudhary, V.R. (2002). Catalysts for combustion of methane and lower alkanes. *Appl. Catal., A*, 234, pp. 1-23, 0926-860X

Correa, S. (1992). A Review of NOx Formation Under Gas-Turbine Combustion Conditions. *Combust. Sci. Tech.*, 87, pp. 327-362, 0010-2202

Dalla Betta, R.A.; Schlatter, J.C.; Yee, D.K. ; Loffler, D.G. & Shoji, T. (1995). Catalytic Combustion Technology to Achieve Ultra Low NOx Emissions: Catalyst Design and Performance Characteristics. *Catal. Today*, 26, pp. 329-335, 0920-5861

Dalla Betta, R.A. & Tsurumi K. (1993). Graded palladium-containing partial combustion catalyst and a process for using it. *US patent,* 5,248,251

Dalla Betta, R.A. & Tsurumi, K. (1995) Partial combustion catalyst of palladium on a zirconia support and a process for using it, *US patent* 5,405,260

Dalla Betta R.A. & Rostrup-Nielsen T. (1999). Application of catalytic combustion to a 1.5 MW gas turbine. *Catal. Today.* 47, pp. 369-375, 0920-5861

Dalla Betta, R.A. & Velasco M.A. (2002). Method of thermal NOx reduction in catalytic combustion systems, *US patent,* 6,718,772

Deutschmann, O.; Maier, L.I.; Riedel, U.; Stroemman A.H. & Dibble, R.W. (2000). Hydrogen assisted catalytic combustion of methane on platinum. *Catal. Today*, 59, 141-150, 0920-5861

Farrauto, R. J., Hobson, M.C., Kennelly, T. and Waterman, E. M. (1992). Catalytic hemistry of Supported Palladium for Combustion of Methane. *Appl. Catal. A*, 81, 227-237, 0926-860X

Groppi, G.; Cristiani, C.; Lietti, L., Ramella, C.; Valentini, M. & Forzatti, P. (1999). Effect of ceria on palladium supported catalysts for high temperature combustion of CH_4 under lean conditions. *Catal. Today*, 50, pp. 399-412, 0920-5861

Hayashi, S.; Yamada, H. & Shimodaira K. (1995). High-pressure reaction and emissions characteristics of catalytic reactors for gas turbine combustors. *Catal. Today*, 26, pp. 319-327, 0920-5861

Ismagilov, Z.R. & Kerzhentsev, M.A. (1990). Catalytic Fuel Combustion - A way of Reducing Emission of Nitrogen Oxides. *Catal. Rev. Sci. Eng.,* 32(1-2), pp. 51-103, 0161-4940

Ismagilov, Z.R.; Shepeleva, M.N.; Shkrabina, R.A. & Fenelonov, V.B. (1991). Interrelation between structural and mechanical characteristics of spherical alumina granules and initial hydroxide properties. *Appl. Catal.* 69, pp. 65 – 73, 0166-9834

Ismagilov, Z.R.; Shkrabina, R.A.; Barannik, G.B. & Kerzhenzev, M.A. (1995). New catalysts and processes for environmental protection. R*eact. Kinet. Catal. Lett.,* 55, 2, pp. 489 – 499, 0133-1736

Ismagilov, Z.R. & Kerzhentsev, M.A. (1999). Fluidized Bed Caytalytic Combustion. *Catal. Today,* 47, pp. 339-346, 0920-5861

Ismagilov, Z.R.; Kerzhentsev, M.A.; Sazonov, V.A.; Tsikoza, L.T.; Shikina, N.V.; Kuznetsov, V.V.; Ushakov, V.A.; Mishanin, S.V.; Kozhukhar, N.G.; Russo, G. & Deutschmann, O. (2003). Study of Catalyts for Catalytic Burners for Fuel Cell Power Plant Reformers. *Korean J. Chem. Eng.,* 20, pp. 461-467, 0256-1115

Ismagilov, Z.R; Shikina, N.V.; Yashnik, S.A.; Zagoruiko, A.N.; Khairulin, S.R.; Kerzhentsev, M.A.; Korotkikh, V.N.; Parmon, V.N.; Braynin, B.I.; Zakharov, V.M. & Favorski, O.N. (2008). *Kinet. Catal.* 49, 6, pp. 873-885, 0023-1584

Ismagilov, Z.R.; Shikina, N.V.; Yashnik, S.V.; Parmon, V.N.; Braynin, B.I.; Zakharov, V.M.; Khritov, K.M. & Favorski, O.N. (2009). Method of Burning Hydrocarbon Fuels (Versions) and Catalysts to This End. *Patent of RF*, RU2372556

Ismagilov, Z.R.; Shikina, N.V.; Yashnik, S.A.; Zagoruiko, A.N.; Kerzhentsev, M.A.; Ushakov, V.A.; Sazonov, V.A.; Parmon, V.N.; Zakharov, V.M.; Braynin, B.I & Favorski, O.N. (2010). *Catal. Today,* http://dx.doi.org/10.1016/j.cattod.2010.04.008   online publication, 0920-5861

Koryabkina, N.A.; Ismagilov, Z.R.; Shkrabina, R.A.; Moroz, E.M. & Ushakov, V.A. (1991). Influence of the method of alumina modification on formation of low-temperature solid solution in magnesia-alumina systems. *Appl. Catal.,* 72, pp. 63 – 69, 0166-9834

Koryabrina, N.A.; Shkrabina, R.A.; Ushakov, V.A. & Ismagilov, Z.R. (1996). Synthesis of a mechanically strong and thermally stable alumina support for catalysts used in combustion processes. *Catal. Today*, 29. pp. 427 – 431, 0920-5861

Jang, B.W.-L.; Nelson, R.M.; Spivey, J.J.; Ocal, M.; Oukaci, R. & Marcelin, G. (1999). Catalytic oxidation of methane over hexaaluminates and hexaaluminate-supported Pd catalysts. *Catal. Today,* 47, pp. 103-113, 0920-5861

Lee, J. H. & Trimm, D. L. (1995). Catalytic Combustion of Methane. *Fuel Process. Technol.,* 42, pp. 339–359, 0378-3820

Liotta, L. F. & Deganello, G. (2003) Thermal stability, structural properties and catalytic activity of Pd catalyst support on Al_2O_3-CeO_2-BaO mixed oxides prepared by sol-gel method. *J. Molec. Catal. A,* 204-205 , pp. 763-770, 1381-1169

Lyubovsky, M. & Pfefferle, L.(1998). Methane combustion over the -alumina supported Pd catalyst: Activity of the mixed Pd/PdO state. *Appl. Catal.,*173, pp. 107-119, 0166-9834

Lyubovsky, M. & Pfefferle, L. (1999). Complete methane oxidation over Pd catalyst supported on alpha.-alumina. Influence of temperature and oxygen pressure on the catalyst activity. *Catal. Today,* 47, pp. 29-44, 0920-5861

Machida, M.; Eguchi, K. & Arai, H. (1987). Effect of additives on the surface area of oxides supports for catalytic combustion. *J. Catal.*, 103, pp. 385-393, 0021-9517

Machida M, Eguchi K, and Arai H. (1989). Catalytic properties of $BaMnAl_{11}O_{19-\delta}$ (M = Cr, Mn, Fe, Co and Ni) for high-temperature catalytic combustion. *J, Catal.,* 1989, 120, pp. 377-386, 0021-9517

Malinovskaya, O.A.; Beskov, V.S. & Slin'ko, M.G. (1975). *Modelirovanie kataliticheskikh protsessov na poristykh zernakh (Modeling of Catalytic Processes on Porous Pellets),* Nauka, Novosibirsk

McCarty, J. G. (1995). Kinetics of PdO combustion catalysis. *Catal. Today*, 26, 283-293, 0920-5861

McCarty, J.G.; Gusman, M.D.; Lowe, M.; Hildenbrand, D.L. & Lau, K.N. (1999). Stability of supported metal and supported metal oxide combustion catalysts, *Catal. Today*, 47, pp. 5–17, 0920-5861

McCarty, J.G. & Wong, V. (2000). Catalytic combustion process, *US patent* 6,015,285

Ozawa, Y.; Tochihara, Y.; Nagai, M. & Omi, S. (2003). PdO/Al_2O_3 in catalytic combustion of methane: stabilization and deactivation, *Chem. Eng. Sci.*, 58, 671-677, 0009-2509

Parmon, V.N.; Ismagilov, Z.R. & Kerzhentsev, M.A. (1992). Catalysis in Energy Production. *Perspectives in Catalysis, Chemistry for 21st Century, Monograph*, J.T. Thomas, K.I. Zamaraev (Eds.), Blackwell Scientific Publication, Oxford, pp. 337-357

Parmon, V.N.; Ismagilov, Z.R.; Favorski, O.N.; Belokon, A.A. & Zakharov, V.M. (2007) Application of Catalytic Combustion Chambers in Gas Turbine Units of Decentralized Energy Supply. *Herald Russ. Acad. Sci.*, 77, 819-830

Perets, V.N.; Zakharov V.M.; Favorski, O.N. & Braynin, B.I. (2008). Gas Turbine Plant With Regenerative Cycle And Catalyst Combustion Chamber. *Patent of RF*, RU2342601

Pfefferle, L.D. & Pfefferle, W.C. (1987). Catalysis in Combustion. *Catal. Rev. Sci. Eng.,* 29, pp. 219-267, 0161-4940

Pfefferle, W.C. (1997). Catalytic method. *US patent,* 5,601,426

Quiceno, R.R.; Perez Ramirez, J.; Warnatz, J. & Deutschmann, O. (2000). Modeling the high-temperature catalytic partial oxidation of methane over platinum gauze: detailed gas phase and surface chemistries coupled with 3D flow field simulation. *Applied Catalysis A*: *General,* 303, pp. 166–176, 0926-860X

Reinke, M.; Mantzaras,J.; Bombach R.,; Schenker, S. & Inauen A. (2005). Gas phase chemistry in catalytic combustion of methane/air mixtures over platinum at pressures of 1 bar to 16 bar. *Combustion and Flame,* 141, 448-468, 0010-2180

Sidwell, R.W.; Zhu, H.; Kee, R.J. & Wickham D.T. (2003). Catalytic Combustion of Premixed Methane-in-air on a High Temperature Stagnation Surface," Combustion and Flame, 134, pp. 55-66, 0010-2180

Shepeleva, M.N.; Shkrabina, R.A.; Fenelonov, V.B. & Ismagilov, Z.R. (1991). Production of spherical granules of alumina with controlled porous structure. *Appl. Catal.* 78, 175 – 184, 0166-9834

Su, S.C.; Carstens, J.N.; & Bell, A.T. (1998a). A study of the dynamics of Pd oxidation and PdO reduction by H_2 and CH_4 *J. Catal.,* 176, 125-135, 0021-9517

Su, S.C.; Carstens, J.N.; & Bell, A.T. (1998b). Factors affecting the catalytic activity of Pd/ZrO2 for the combustion of methane *J. Catal.,* 176, 136-142, 0021-9517

Trimm, D. L. (1983). Catalytic combustion (Review). *Appl. Catal.*, 7. No 3, pp. 249-282, 0166-9834

Tsikoza, L.T.; Yashnik, S.A.; Ismagilov, Z.R.; Shkrabina, R.A.; Korjabkina, N.A. & Kuznetsov, V.V. (2002). Catalyst For High-Temperature Combustion Of Hydrocarbon Fuel (Versions). *Patent,* RU 2185238

Tsikoza, L.T.; Ismagilov, Z.R.; Ushakov, V.A.; Kuznetsov, V.V. & Ovsyannikova, I.A. (2003). Fuel Combustion Reactions and Catalysts: XXI. Synthesis and Characterization of Modified Mn–Al–O Catalysts for High-Temperature Oxidation. *Kinet. Catal. (Engl. Transl.),* 44, pp. 806-812, 0023-1584

Yashnik, S.A.; Ismagilov, Z.R.; Kuznetsov, V.V.; Ushakov, V.V.; Rogov, V.A. & Ovsyannikova, I.A. (2006). *Catal. Today,* 117, pp. 525-535, 0920-5861

Yashnik, S.A.; Shikina, N.V.; Ismagilov, Z.R.; Zagoruiko, A.N.; Kerzhentsev, M.A.; Parmon, V.N.; Zakharov, V.M.; Braynin, B.I.; Favorski, O.N. & Gumerov, A.M. (2009). *Catal. Today,* 147S, pp. S237–S243, 0920-5861

Young, W.E. & Carl, D.E. (1989). Passively cooled catalytic combustor for a stationary combustion turbine. *US patent,* 4,870,824

Yue, B.; Zhou, R.; Wang, Y. & Zheng, X. (2005). Effect of rare earths (La, Pr, Nd, Sm and Y) on the methane combustion over $Pd/Ce–Zr/Al_2O_3$ catalysts. *Appl. Catal., A*, 295, pp. 31-39

Electricity Cogeneration using an Open Gas Turbine

Anita Kovac Kralj
University of Maribor (Faculty of Chemistry and Chemical engineering)
Slovenia

1. Introduction

A gas turbine is a rotary engine that extracts energy from a flow of combustion gas. Gas turbines operate on the principle that fuel and air will burn in a combustion chamber. The outlet gas serves as a working fluid (Fig.1).
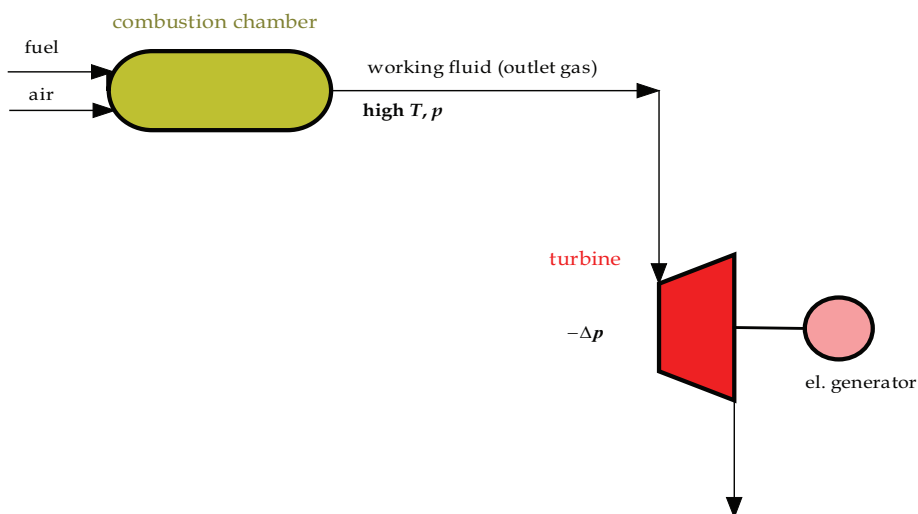

Fig. 1. Gas turbine

2. Important

Our main purpose is to use existing gases during chemical processes, in order to drive a turbine. Processes, which operate under high pressures, followed the cleaning at low pressures, can be exploited for electricity cogeneration. The high operating pressure at a reactor's outlet can be exploited to produce electricity using the open gas turbine system (Fig. 2).
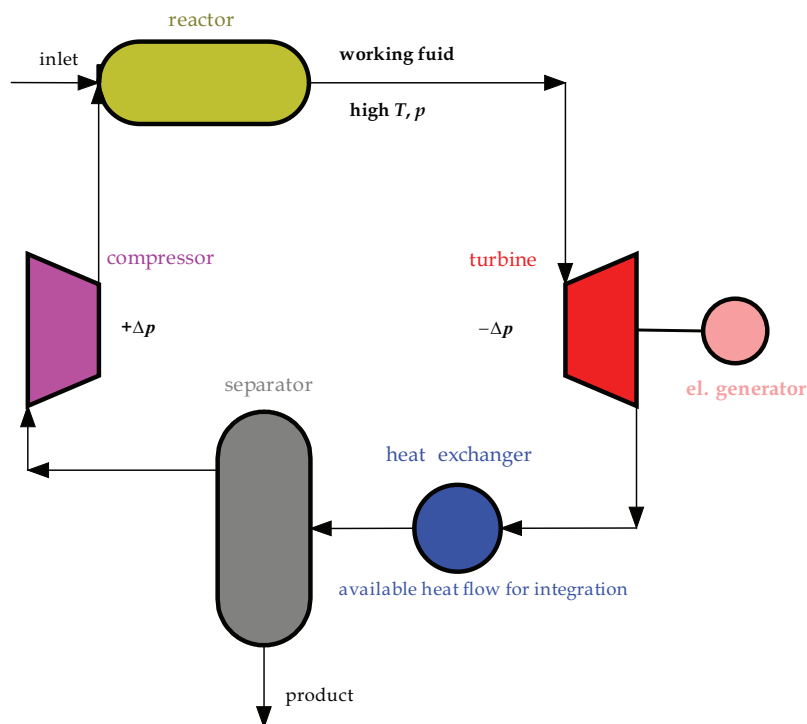
Fig. 2. Open gas turbine system

3. Open gas turbine system

The gas turbine has rendered increasing service within the petrochemical industry. Open-cycle gas turbine power plants are widely applied throughout industry. A conventional power plant uses fuel energy to produce work.

Usually, a gas turbine operates by internal combustion. Air and fuel pass through a compressor into a combustion chamber. The combustion products are then expanded in a turbine, which drives an electric generator.

Many chemicals are produced under high pressure and at high temperatures. The reactor acts as the combustion chamber of the gas turbine plant. Then, separation at lower pressure and temperature follows and this pressure change can be used to drive a turbine, coupled to an electricity generator.

Our main purpose is to use existing gases from within the chemical processes to drive the turbine by using an open gas turbine system. An open gas turbine system includes the following process units, in order (Fig. 3):

- reactor (R)
- gas turbine (T) with electric generator
- heat exchanger (H)
- separator (S), where the liquid product separates off and
- compressor (C).

The high operating pressure at the reactor's outlet can be exploited to produce electricity using an open gas turbine. The open gas turbine is a basic gas turbine unit. This turbine uses processed gas as a working fluid. The working fluid comes from the reactor and circulates through the following units (Fig. 3):

- gas turbine (T)
- heat exchanger (H)
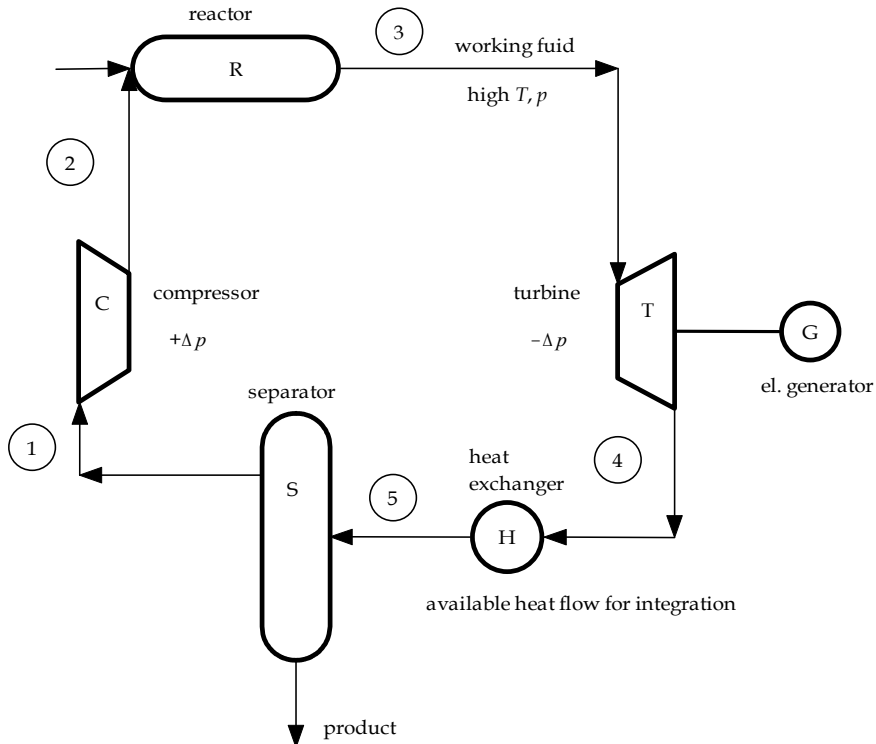- separator (S), where the liquid product separates off and
- compressor (C).

Fig. 3. Open circuit gas turbine system

The power cycle of the open gas turbine system is described as the "Brayton cycle". The working fluid undergoes the following process steps, as shown in a simplified T/s (temperature/mass entropy) diagram (Fig. 4):

- 1–2 adiabatic compression
- 2–3 reaction
- 3–4 adiabatic expansion of reaction outlet stream in a turbine
- 4–5 cooling or/and available heat flow for heat integration
- 5   separation.

The individual processes' units in the open gas turbine system have their own importance, and will be presented individually.
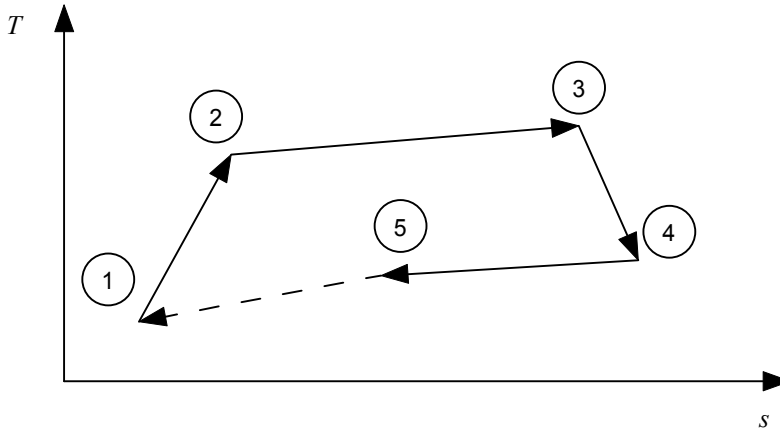
Fig. 4. The simplified temperature/mass entropy (T/s) diagram

3.1 Reactor (R)

The reactor processing unit for the production of various products, in our case concentrating in particular, on those that operate and produce under high pressures. The high pressure reactor model is presented with all components s (s = 1,...S), which react at different reactions r (r = 1,...R). The amount flow rate from the reactor affects the power of the turbine. The thermodynamic and kinetic properties of the chemical reactions (r = 1, …, R) provide a good prediction about flow rate and the compositions of the raw material, its conversion to a product, and parameter conditions. The amount flow rate (F) for any component (s = 1, …, S) depends on the equilibrium constant (K_e). For the hypothetical reversible chemical reaction:

$$\nu_A A + \nu_B B \leftrightarrows \nu_C C + \nu_D D$$
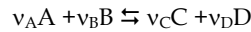
the equilibrium constant is defined as:

$$K_e = \frac{c_C^{\nu_C} \cdot c_D^{\nu_D}}{c_A^{\nu_A} \cdot c_B^{\nu_B}},$$

where ν_s are stoichiometric coefficients, and c_s concentrations of components s.

The equilibrium constant determines the extent of a chemical reaction at equilibrium. It can be calculated if the equilibrium concentration of each reactant and product in a reaction at equilibrium is known.

The conversion rate of reaction r (ω_r) can be calculated from the differential change of the reaction extent ($d\xi_r$), after time t:

$$\omega_r = d\xi_r / dt \qquad r = 1, …, R \tag{1}$$

Any differential change in the reaction extent ($d\xi_r$) can be calculated from the differential change in its amount (dn_s), and its stoichiometric coefficient (ν):

$$d\xi_r = dn_s / \nu_{s,r} \qquad s = 1, …, S \quad r = 1, …, R \tag{2}$$

The extent of a reaction characterizes how far the advancement of the reaction has taken place. Equation 2 has to integrate from an initial $\xi_r = 0$ and $n_s = n_{s,in}$ to outlet ξ_r and $n_{s,out}$:

$$\int_{n_{s,in}}^{n_{s,out}} dn_s = v_{s,r} \int_0^{\xi_r} d\xi_r \quad s = 1,...,S \quad r = 1,...,R \tag{3}$$

and the outlet amount for component s for reaction r is:

$$F_{s,out} = n_{s,in} + \sum_r v_{s,r} \, \xi_r \quad s = 1, \dots, S \quad r = 1, \dots, R \tag{4}$$

The amount flow rate F is defined as:

$$F_s = dn_s / dt \quad s = 1, \dots, S \tag{5}$$

and outlet amount flow rate for component s is:

$$F_{s,out} = F_{s,in} + \sum_r v_{s,r} \, \omega_r \quad s = 1, \dots, S \quad r = 1, \dots, R \tag{6}$$

The total outlet amount flow rate (F) is:

$$F = \sum_s F_{s,out} \quad s = 1, \dots, S \tag{7}$$

The equilibrium constant (K_r) of reaction r (Smith & Ness, 1987) can be calculated by the minimization of Gibbs (free) energy (ΔG):

$$K_r = e^{(-\Delta Gr / RT)} \quad r = 1, \dots, R \tag{8}$$

High reactant flow rate favours reactions with higher conversion and optimization of raw material composition and can increase production.

The changing amount flow rate for reactant (ΔF) affects the heat flow rate of the outlet reaction stream (Φ), which can enlarge electricity cogeneration and heat integration during a process (Fig. 5). This simultaneous approach can optimize the trade-off between heat and electricity cogenerations. Cogeneration is constrained by the lowest possible outlet temperature of the gas turbine. Cogeneration chooses the lowest temperature limit, thus cogeneration is usually more profitable than heat integration.

3.2 Turbine (T)

The power of the gas turbine depends on the primary variables: inlet temperature, compressed pressure ratio and mass flow. The inlet temperature is restricted by the metallurgical limit of the turbine's blades to about 800 ºC.

The medium pressure of the designed turbine can be varied. Its power (P_{tur}) is a function of the outlet temperature ($T_{tur, out}$), molar heat capacity (C_m) and the amount flow rate (F; see Equation 9):

$$P_{tur} = C_m \cdot (T_{tur, in} - T_{tur, out}) \cdot F \tag{9}$$

Gas turbine power (P_{tur}) is a function of:
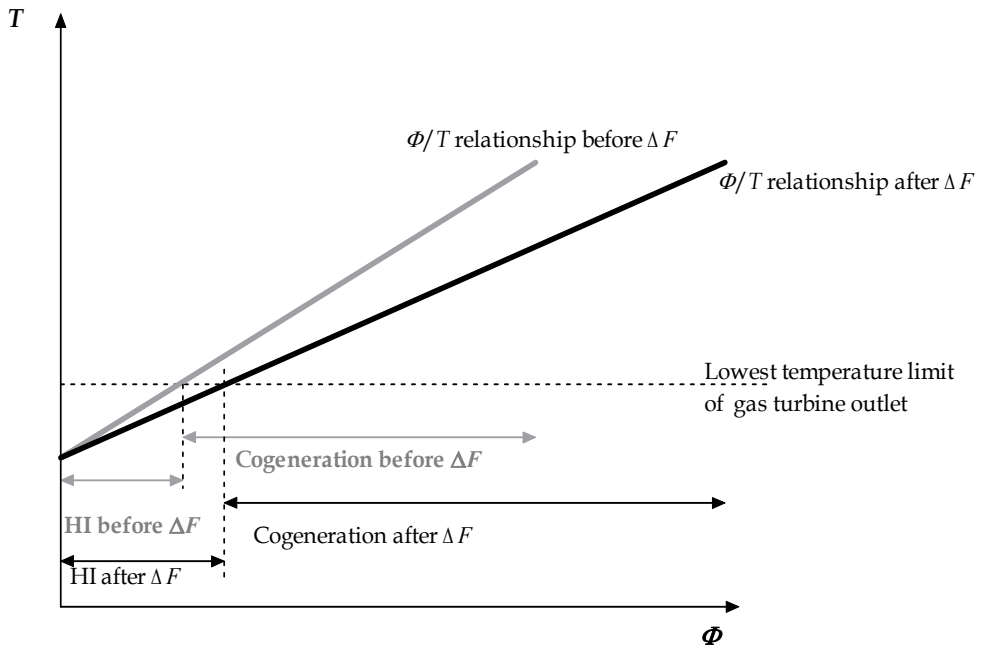- outlet temperature ($T_{tur,out}$)

Fig. 5. The simplified temperature/heat flow rate (T/Φ) diagram before and after changing the flow rate (ΔF) of the raw material: performing heat integration (HI), and cogeneration before and after ΔF.

- molar heat capacity (C_m)
- amount flow rate (F)

The inlet temperature ($T_{tur,in}$) is kept constant. The thermodynamic efficiency of the medium pressure turbine (η_{tur}) and the mechanical efficiency of the generator (η_{gen}) is supposed to be 85 % for each.

The annual depreciation of the medium pressure turbine ($C_{d,tur}$ in EUR/a) is a function of the power (P_{tur}; Biegler et al., 1997):

$$C_{d,\,tur} = (22\,946 \;+\; 13.5 \cdot P_{tur}) \cdot 4 \tag{10}$$

The published cost equations for the equipment are not usually adjusted to the real, higher industrial costs, therefore, the costs are multiplied by a factor (4), determined by experience.

3.3 Heat exchanger (H)

The residual heat in the heat exchanger (H) can usefully be applied to the heat integration. The heat flow (Φ) can be calculated with known inlet (T^{in}_H) and outlet temperatures (T^{out}_H), by using equation 11:

$$(T^{in}_H - T^{out}_H) \cdot CF_H = \Phi_H \tag{11}$$

where CF_H is the heat capacity flow rate of the stream in heat exchanger.

3.4 Separator (S)

The separator has the task of separating liquid from the vapour phase. The product is in liquid phase. Vapour flow is compressed in the compressor (C). The balanced amounts of the separation for all the components (s = 1...S) are:

$$F^{in} = F^{out,v} + F^{out,l} \tag{12}$$

$$F^{in} \cdot x^{in}_s = F^{out,v} \cdot x^{out,v}_s + F^{out,l} \cdot x^{out,l}_s \quad s = 1, ..., S \tag{13}$$

$$\sum_s^S x^{out,v}_s = 1 \tag{14}$$

$$\sum_s^S x^{out,l}_s = 1 \tag{15}$$

$$K_s = d_s + c_s \cdot T^{out} + b_s \cdot (T^{out})^2 \quad s = 1, ..., S \tag{16}$$

where d_s, c_s and b_s are equilibrium constants during separation

$$x^{out,v}_s = K_s \cdot x^{out,l}_s \quad s = 1, ..., S \tag{17}$$

The inlet amount flow rate for separation (F^{in}) is the sum of the outlet amounts flow rates of the vapour ($F^{out,v}$) and liquid phases ($F^{out,l}$; see Equation 12). Equation 13 includes the amount flow fractions. x is the amount fraction in vapour (v) or liquid phase (l). The equilibrium constant (K) of the sth component during separation is a function of temperature (see Equation 16).

3.5 Compressor (C)

Vapour flow from the separator is compressed within the compressor (C). The temperatures at the outlets of the compressor (T^{out}_c; depend on the inlet temperatures (T^{in}_c), and can be calculated by the equation:

$$T^{out}_c = a_c + b_c \cdot T^{in}_c \tag{18}$$

where a_c and b_c are the temperature constants for polytropic compression.
Once we know, the whole model of the open gas turbine system can be optimized, using different methods.

4. Case study

The suggested open gas turbine system was tested in an existing complex, low-pressure Lurgi methanol plant producing crude methanol by using nonlinear programming (NLP; Biegler et al., 1997). The parameters in the model of an open gas turbine were simultaneously optimized using the GAMS/MINOS (Brooke at al.; 1992). This NLP can be solved using a large-scale reduced gradient method (e. g. MINOS). The model is non-convex, it does not guarantee a global optimization solution but it quickly gives good results for non-trivial, complex processes. The NLP model contains variables of all those process'

parameters: molar heat capacities, material flow rates, heat flow rates, and temperatures, which are limited by real constraints.

4.1 Results

The simultaneous NLP of heat and power integration, and the optimization selected for electricity generation using a gas turbine pressure drop from 49.7 bar to 35 bar with an outlet temperature of $T_{tur, out}$ = 110 °C (Fig. 6). This structure enables the generation of 12.7 MW of electricity. The steam exchanger (HEST) needs 16.5 MW of heat flow rate. The integrated process streams in HEPR, exchange 3.6 MW of heat flow rate. The power of the first and the second compressors are 2.0 MW and 2.8 MW, respectively. The HEW1 exchanges 2.0 MW. Within the heat exchangers, HEW and HEA 7.1 MW and 4.7 MW of heat flow rate are exchanged with the existing areas, respectively, when cooling. The additional annual of methanol production is 0.75 mol/s, purge gas outlet flow rate is decreased from 210 mol/s to 190 mol/s.
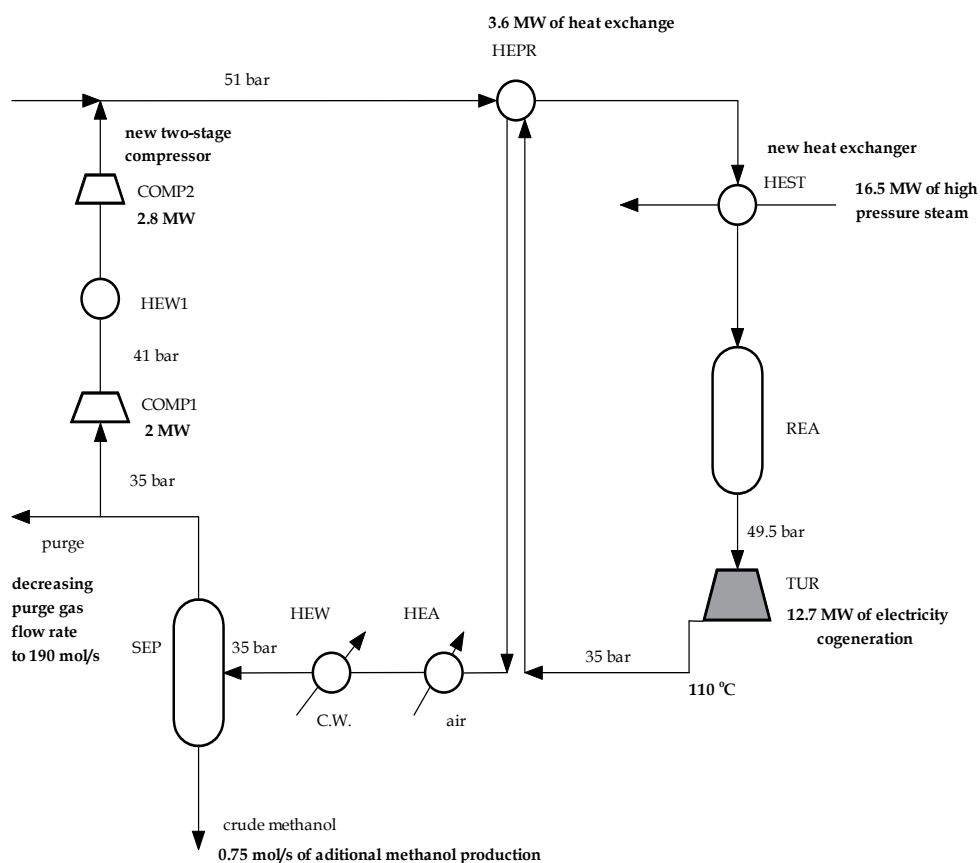

Fig. 6. Optimised flow sheet for crude methanol production, using a open gas turbine system

The additional annual depreciation of the gas turbine, new heat exchangers (HEST, HEW1, having areas of 527 m^2 and 324 m^2), and the new two-stage compressor, is 2 040 kEUR/a (Table 1). The cost of the high pressure steam used in HEST is 1 750 kEUR/a. In the depreciation account for retrofit, we included additional costs to the new units only: 30 kEUR/a for the instrumentation cost (which is estimated to be 15 % of the additional direct plant cost), 10 kEUR/a for the contingency (estimated at 5 % of the additional direct plant cost), 4 kEUR/a for the maintenance cost (estimated as 2 % of the additional direct plant cost), and 15 kEUR/a for the turbine down time (estimated as 5 % of the additional plant direct cost). The additional annual income of the electricity produced is 5 530 kEUR/a. The additional annual income of the methanol produced is 79 kEUR/a. The additional profit from process and power integration is estimated to be 1 760 kEUR/a for the modified process.

Installed cost of heat exchanger[*]/EUR: $(8\,600 + 670\,A^{0,83}) \cdot 3.5 \cdot 2$ [#]
Installed cost of compressor, C_{com}[&]/EUR: $2\,605 \cdot P^{0,82}$
Installed cost of gas turbine, C_{tur}[&]/(EUR/a): $(22\,946 + 13.5\,P_{tur}) \cdot 4$ [#]
Price of methanol (C_M) [+]/(EUR/t): 115.0
Price of electricity (C_{el})[**]/(EUR/(kW · a)): 435.4
Cost of 37 bar steam (C_{37})[**]/(EUR/(kW · a)): 106.3
Cost of cooling water (C_{CW})[**]/(EUR/(kW · a)): 6.2

     *   Tjoe and Linnhoff, 1986; A = area in m^2
   **   Swaney, 1989
    &   Biegler et al., 1997; P = power in kW
    +   ten years average
    #   published cost equations for the equipment are adjusted to the real,
         higher industrial costs using multipliers (2 or 4).

Table 1. Cost items for example process

7. Conclusion

The inclusion of open gas turbine can increase the operating efficiency of the process. The gas turbine with its pressure and temperature drop can be included in the process cycle. The working fluid comes from the reactor and circulates through the process units: gas turbine, heat exchanger, separator (where the liquid product separates), and the compressor.

8. References

Biegler, L. T.; Grossmann, I. E. & Westerberg, A. W. (1997). *Systematic methods of chemical process design*, Prentice Hall, Upper Saddle River, New Jersey, 1–408.
Brooke, A.; Kendrick D. & Meeraus, A. (1992). *GAMS: A User's Guide*, Palo Alto, Scientific Press.

Smith, J.M. & Van Ness, H.C. (1987). *Introduction to chemical engineering thermodynamics,* McGraw-Hill, New York, 496–518.

Swaney, R. (1989). Thermal integration of processes with heat engines and heat pumps, *AIChE Journal* 35/6, pp. 1010.

Tjoe, T. N. & Linnhoff, B. (1986). Using pinch tehnology for process retrofit. *Chem. Engng* 28 47–60.

Gas Turbine Condition Monitoring and Diagnostics

Igor Loboda
National Polytechnic Institute
Mexico

1. Introduction

Gas turbine monitoring and diagnostics belong to a common area of condition monitoring (health monitoring) of machinery and mechanical equipment such as spacecrafts, aircrafts, shipboard systems, various power plants and industrial and manufacturing processes. They can be considered as complex engineering systems and become more sophisticated during their further development that results in potential degradation of system reliability. In order to keep reliability high, various diagnostic tools are applied. Being capable to detect and identify incipient faults, they reduce the rate of gross failures.

Considerable increase of industrial accidents and disasters has been observed in the last decades (Rao, 1996). Mechanical failures cause a considerable percentage of such accidents. Various deterioration factors can be responsible for these failures. Among them, the most common factors that degrade a healthy condition of machines are vibration, shock, noise, heat, cold, dust, corrosion, humidity, rain, oil debris, flow, pressure, and speed (Rao, 1996).

In these conditions, health monitoring has become an important and rapidly developing discipline which allows effective machines maintenance. In two last decades the development of monitoring tools has been accelerated by advances in information technology, particularly, in instrumentation, communication techniques, and computer technology.

Modern sensors trend to preliminary signal processing (filtering, compressing, etc.) in order to realize self-diagnostics, reduce measurement errors, and decrease volume of data for subsequent processing. So, sensors become more and more "intelligent" or "smart". Development of communication techniques, in particular, wireless technologies drastically simplifies data acquisition in the sites of machine operation. Data transmission to centralized diagnostic centres is also accelerated. In these centres great volume of data can effectively be analyzed by qualified personnel. The personal computer has radically changed as well. Large numbers of powerful PCs united in networks allow easy sharing the measured data through the company, fast data processing, and suitable access to the diagnostic results. Development of the PC technology also allows many independent disciplines to be integrated in condition monitoring.

Success of monitoring not only depends on perfection of monitoring hardware and software themselves, but also is determined by tight monitoring integration with maintenance when the both disciplines can be considered as one multidiscipline. Behind this trend lies a well

known concept of Condition Based Maintenance (CBM) as well as ideas of Condition Monitoring and Diagnostic Engineering Management (COMADEM) (Rao, 1996) and Prognostics and Health Management (PHM) (Vachtsevanos et al., 2006). As illustrated by many examples in (Rao, 1996), the proper organization of the total monitoring and maintenance process can bring substantial economical benefits. Numerous engineering systems, which considerably differ in nature and principles of operation, need individual techniques in order to realize effective monitoring. The variety of known monitoring techniques can be divided into five common groups: vibration monitoring, wear debris analysis, visual inspection, noise monitoring, and environment pollution monitoring (Rao, 1996). The two first approaches are typical for monitoring rotating machinery, including gas turbines.

A gas turbine engine can be considered as a very complex and expensive machine. For example, total number of pieces in principal engine components and subsystems can reach 20,000 and more; heavy duty turbines cost many millions of dollars. This price can be considered only as potential direct losses due to a possible gas turbine failure. Indirect losses will be much greater. That is why, it is of vital importance that the gas turbine be provided by an effective monitoring system.

Gas turbine monitoring systems are based on measured and recorded variables and signals. Such systems do not need engine shutdown and disassembly. They operate in real time and provide diagnostic on-line analysis and recording data in special diagnostic databases. With these databases more profound off-line analysis is performed later.

The system should use all information available for a diagnosed gas turbine and cover a maximal number of its subsystems. Although theoretical bases for diagnosis of different engine systems can be common, each of them requires its own diagnostic algorithms taking into account system peculiarities. Nowadays parametric diagnostics encompasses all main gas turbine subsystems such as gas path, transmission, hot part constructional elements, measurement system, fuel system, oil system, control system, starting system, and compressor variable geometry system. In order to perform complete and effective diagnosis, different approaches are used for these systems. In particular, the application of such common approaches of rotating machinery monitoring as vibration analysis and oil debris monitoring has become a standard practice for gas turbines.

However, the monitoring system always includes another technique, which is specific for gas turbines, namely gas path analysis (GPA). Its algorithms are based on a well-developed gas turbine theory and gas path measurements (pressures, temperatures, rotation speeds, and fuel consumption, among others). The GPA can be considered as a principal part of a gas turbine monitoring system. The gas path analysis has been chosen as a representative approach to the gas turbine diagnosis and will be addressed further in this chapter. However, the observations made in the chapter may be useful for other diagnostic approaches.

The gas path analysis provides a deep insight into gas turbine components' performances, revealing gradual degradation mechanisms and abrupt faults. Besides these gas path defects, malfunctions of measurement and control systems can also be detected and identified. Additionally, the GPA allows estimating main engine performances that are not measured like shaft power, thrust, overall engine efficiency, specific fuel consumption, and compressor surge margin. Important engine health indicators, the deviations in measured variables induced by engine deterioration and faults, can be computed as well.

The gas path analysis is an area of extensive studies and thousands of technical papers can be found in this area. Some common observations that follow from these works and help to explain the structure of this chapter are given below.

First, it can be stated that gas turbine simulation is an integral part of the diagnostic process. The models fulfil here two general functions. One of them is to give a gas turbine performance baseline in order to calculate differences between current measurements and such a baseline. These differences (or deviations) serve as reliable degradation indices. The second function is related to fault simulation. Recorded data rarely suffice to form a representative classification because of the rare and occasional appearance of real faults and very high costs of real fault simulation on a test bed. That is why mathematical models are involved. The models connect degradation mechanisms with gas path variables, assisting in this way with a fault classification that is necessary for fault diagnosis.

Second, a total diagnostic process can be divided into three general and interrelated stages: common engine health monitoring (fault detection), detailed diagnostics (fault identification), and prognostics (prediction of remaining engine life). Since input data should be as exact as possible, an important preliminary stage of data validation precedes these principal diagnostic stages. In addition to data filtration and averaging, it also includes a procedure of computing the deviations, which are used practically in all methods of monitoring, diagnostics, and prognostics.

Third, gas turbine diagnostic methods can be divided into two general approaches. The first approach employs system identification techniques and, in general, so called thermodynamic model. The used models relate monitored gas path variables with special fault parameters that allow simulating engine components degradation. The goal of gas turbine identification is to find such fault parameters that minimize difference between the model-generated and measured monitored variables. The simplification of the diagnostic process is achieved because the determined parameters contain information on the current technical state of each component. The main limitation of this approach is that model inaccuracy causes elevated errors in estimated fault parameters. The second approach is based on the pattern recognition theory and mostly uses data-driven models. The necessary fault classification can be composed in the form of patterns obtained for every fault class from real data. Since patterns of each fault class are available, a data-driven recognition technique, for example, neural network, can be easily trained without detailed knowledge of the system. That is why, this approach has a theoretical possibility to exclude the model (and the related inaccuracy) from the diagnostic process.

Fourth, the models used in condition monitoring and, in particular, in the GPA can be divided into two categories – physics-based and data-driven. The physics-based model (for instance, thermodynamic model) requires detailed knowledge of the system under analysis (gas turbine) and generally presents more or less complex software. The data-driven model gives a relationship between input and output variables that can be obtained on the basis of available real data without the need of system knowledge. Diagnostic techniques can be classified in the same manner as physics-based or model-based and data-driven or empirical.

Illustrating the above observations, Fig. 1 presents a classification of gas path analysis methods. Taking into the account the observations and the classification, the following topics will be considered below: real input data for diagnosis, mathematical models involved, preliminary data treatment, fault recognition methods and accuracy, diagnosis and monitoring interaction, and application of system identification methods for fault diagnosis.
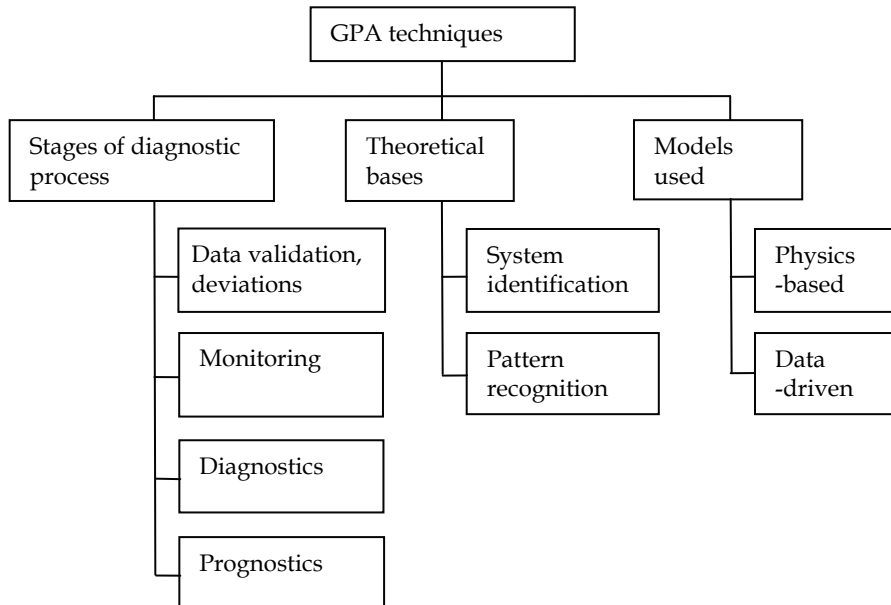
Fig. 1. Classification of gas path analysis techniques

2. Diagnostic models

2.1 Nonlinear static model

In the GPA the physics-based models are presented by thermodynamic models for simulating gas turbine steady states (nonlinear static model) and transients (nonlinear dynamic model). Since the studies of Saravanamuttoo et al., in particular, (Saravanamuttoo & MacIsaac, 1983), application of the thermodynamic model for steady states has become common practice and now this model holds a central position in the GPA. Such a model includes full successive description of all gas path components such as input device, compressor, combustion chamber, turbine, and output device. Such models can also be classified as non-linear, one-dimensional, and component-based.

The thermodynamic model computes a ($m{\times}1$)-vector $\vec{Y}$ of gas path monitored variables as a function of a vector $\vec{U}$ of steady operational conditions (control variables and ambient conditions) as well as a ($r{\times}1$)-vector $\vec{\Theta}$ of fault parameters, which can also be named health parameters or correction factors depending on the addressing problems. Given the above explanation, the thermodynamic model has the following structure:

$$\vec{Y} = F(\vec{U}, \vec{\Theta}) . \tag{1}$$

There are various types of real gas turbine deterioration and faults such as fouling, tip rubs, seal wear, erosion, and foreign object damage whose detailed description can be found, for example, in the study (Meher-Homji et al., 2001). Since such real defects occur rarely during maintenance, the thermodynamic model is a unique technique to create necessary class descriptions. To take into account the component performance changes induced by real

gradual deterioration mechanisms and abrupt faults, the model includes special fault parameters that are capable to shift a little the components' maps.

Mathematically, the model is a system of nonlinear algebraic equations reflecting mass, heat, and energy balance for all components operating under stationary conditions.

The thermodynamic model represents complex software. The number of algebraic equations can reach 15 and more and the software includes dozens of subprograms. The most of the subprograms can be designed as universal modules independent of a simulated gas turbine, thus simplifying model creation for a new engine.

System identification techniques can significantly enhance model accuracy. The dependency $\vec{Y} = f_1(\vec{U})$ realized by the model can be well fitted and simulation errors can be lowered up to a half per cent. Unfortunately, it is much more difficult to make more accurate the other dependency $\vec{Y} = f_2(\vec{\Theta})$ because faults rarely occur. The study presented in (Loboda & Yepifanov, 2010) shows that differences between real and simulated faults can be visible.

As mentioned before, the thermodynamic model for steady states has wide application in gas turbine diagnostics. First, this model is used to describe particular faults or complete fault classification (Loboda et al., 2007). Second, the thermodynamic model is an integral part of numerous diagnostic algorithms based on system identification such as described in (Pinelli & Spina, 2002). Third, this nonlinear model allows computing simpler models (Sampath & Singh, 2006), like a linear model (Kamboukos & Mathioudakis 2005) described below.

2.2 Linear static model

The linear static model present linearization of nonlinear dependency $\vec{Y} = f_2(\vec{\Theta})$ between gas path variables and fault parameters determined for a fixed operating condition $\vec{U}$. The model is given by a vectorial expression

$$\delta\vec{Y} = H\delta\vec{\Theta}. \tag{2}$$

It connects a vector $\delta\vec{\Theta}$ of small relative changes of the fault parameters with a vector $\delta\vec{Y}$ of the corresponding relative deviations of the monitored variables by a matrix H of influence coefficients (influence matrix).

Since linearization errors are not too great, about some percent, the linear model can be successfully applied for fault simulation at any fixed operating point. However, when it is used for estimating fault parameters by system identification methods like in study (Kamboukos & Mathioudakis, 2005), estimation errors can be significant. Given the simplicity of the linear model and its utility for analytical analysis of complex diagnostic issues, we can conclude that this model will remain important in gas turbine diagnostics.

The matrix H can be easily computed by means of the thermodynamic model. The gas path variables $\vec{Y}$ are firstly calculated by the model for nominal fault parameters $\vec{\Theta}_0$. Then, small variations are introduced by turns in fault parameters and the calculation of the variables $\vec{Y}$ is repeated for each corrected parameter. Finally, for each pair Y_i and Θ_j the corresponding influence coefficient is obtained by the following expression

$$H_{ij} = \frac{\delta Y_i}{\delta \Theta_j} = \frac{Y_i(\vec{\Theta}_j) - Y_i(\vec{\Theta}_0)}{Y_i(\vec{\Theta}_0)} \Bigg/ \frac{\Theta_j - \Theta_{0j}}{\Theta_{0j}}. \tag{3}$$

2.3 Nonlinear dynamic model

Although methods to diagnose at steady states are more developed and numerous than the methods for transients, current studies demonstrate growing interest in the gas turbine diagnosis during dynamic operation (Loboda et al., 2007; Ogaji et al., 2003). A thermodynamic gas path model (dynamic model) is therefore in increasing demand. As distinct from the static model (1), in the dynamic model a time variable t is added to the argument set of the function $\vec{Y}$ and the vector $\vec{U}$ is given as a time function, i.e. a dynamic model has a structure

$$\vec{Y} = F(\vec{U}(t), \vec{\Theta}, t). \tag{4}$$

A separate influence of time variable t is explained by inertia nature of gas turbine dynamic processes, in particular, by inertia moments of gas turbine rotors. The gas path parameters $\vec{Y}$ of the model (4) are computed numerically as a solution of the system of differential equations in which the right parts are calculated from a system of algebraic equations reflecting the conditions of the components combined work at transients. These algebraic equations differ a little from the static model equations, that is why the numeric procedure of the algebraic equation system solution is conserved in the dynamic model. Therefore, the nonlinear dynamic model includes the most of static model subprograms. Thus, the nonlinear static and dynamic models tend to be united in a common program complex.

2.4 Neural networks

Artificial Neural Networks (ANNs) present a fast growing computing technique in many fields of applications, such as pattern recognition, identification, control systems, and condition monitoring (Rao, 1996; Duda et al., 2001). The ANN can be classified as a typical data-driven model or black-box model because it is viewed solely in terms of its input and output without any knowledge of internal operation. During network supervised learning on the known pairs of input and output (target) vectors, weights between the neurons change in a manner that ensures decreasing a mean difference (error) e between the target and the network output. In addition to the input and output layers of neurons, a network may incorporate one or more hidden layers of nodes when high network flexibility is necessary.

The multilayer perceptron (MLP) has emerged as the most widely used network in gas turbine diagnostics (Volponi et al., 2003). Its foundations can be found in any book devoted to ANNs and we give below only a brief perceptron description. The MLP is a feed-forward network in which signals propagate through the network from its input to the output with no feedback. The diagram shown in Fig.2 helps to understand better perceptron operation. The presented network includes input, hidden, and output layers of neurons. For each hidden layer neuron, the sum of inputs of a vector $\vec{p}$ multiplied by waiting coefficients of a matrix W_1 is firstly computed. The corresponding bias from a vector $\vec{b}_1$ is added then, forming a neuron input. Finally, inputs of all neurons are transformed by a hidden layer transfer function f_2 into an output vector $\vec{a}_1$. The described procedure can be written by the following expression
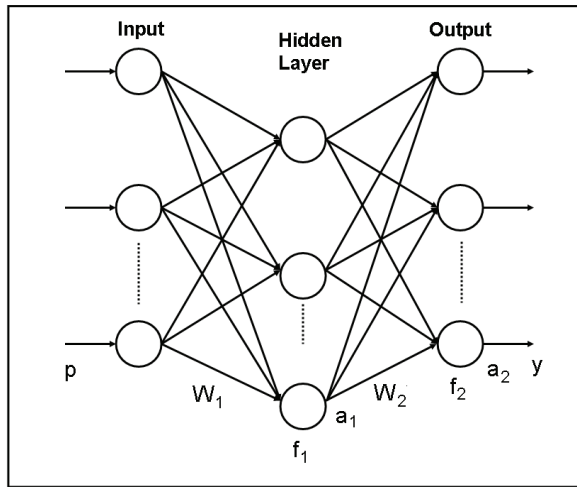
$$\vec{a}_1 = f_1(W_1 \vec{p} + \vec{b}_1). \tag{5}$$

Fig. 2. Perceptron diagram

The same procedure is then repeated for the output layer considering $\vec{a}_1$ as an input vector. Similarly to formula (5), the output layer is given by

$$\vec{y} = \vec{a}_2 = f_2(W_2 \vec{a}_1 + \vec{b}_2).$$ (6)

Before the use the network should be trained on known pairs of the input vector and the output vector (target) in order to determine unknown waiting coefficients and biases. The MLP has been successfully applied to solve difficult pattern recognition problems since a back-propagation algorithm had been proposed for the training. It is a variation of so called incremental or adaptive training mode that changes unknown coefficients after presentation of every individual input vector. In the back-propagation algorithm the error between the target and actual output vectors is propagated backwards to correct the weights and biases. The correction is repeated successively for all available inputs and targets united in a training set. Usually it is not sufficient to reach a global minimum between all targets and network outputs and a cycle of calculations with learning set data is repeated many times. That is why this algorithm is relatively slow. To apply the back-propagation algorithm, a layer transfer function should be differentiable. Generally, it is the tan-sigmoid, log-sigmoid, or linear type.

There is another training mode called a batch mode because a mean error e between all network targets and outputs is computed and used to correct the coefficients. In this mode the training comes to a common nonlinear minimization problem in which the error $e(W_1, b_1, W_2, b_2)$ should be minimized in a multidimensional space of all unknown coefficients, waits and biases. This error can be reduced but should not be vanished because the network must follow general systematic dependencies between simulated variables and should not reflect individual random errors of every input and output.

Though the trained network is ready for practical use in a gas turbine diagnosis, an additional stage of network verification is mandatory. There is a common statistical rule that

a function determined on one portion of the random data should be tested on another. Consequently, to verify the MLP determined on a training set, we need one more data portion called a validation set. If the neural network describes well training data but loses its accuracy on validation data it is a clear indication of an overlearning effect. The network begins to take into account training set random peculiarities and therefore loses its capability to generalize data.

In addition to the MLP described above, some other network types are also used in the gas path analysis, in particular, Radial Basis Networks, Probabilistic Neural Networks (Romessis & Mathioudakis, 2003; Romessis et al., 2007), and Bayesian Belief Networks (Romessis & Mathioudakis, 2006; Romessis et al., 2007). Foundations of these particular recognition and approximation tools can be found in any book in the area of ANNs, for instance, in (Haykin, 1994). The language of technical computing MATLAB developed by the MathWorks, Inc. offers convenient tools to experiment with different neural networks. It contains a neural networks toolbox that simplifies network creation, training, and use. MATLAB also allows choosing between various training functions and calculation options.

With respect to diagnostic problems where the ANNs are used, it can be concluded that in most cases networks are employed for gas turbine fault identification, in particular, to form fault classification (Ogaji et al., 2003) and to estimate fault parameters (Romessis & Mathioudakis, 2006). However, the ANNs not only are applied for recognition problems, but they also are famous as good function approximators in many fields including gas turbine monitoring (Fast et al., 2009). In addition to ANNs, other and simpler data-driven models like polynomials can be successfully applied to simulate gas turbine performances.

2.5 Polynomials

It is proven in (Loboda et al., 2004) that complete second order polynomials give sufficient approximation of healthy engine performance (baseline). For one monitored gas path variable Y as a function of three arguments u_i, such polynomial is written as

$$Y_0(\vec{U}) = a_0 + a_1 u_1 + a_2 u_2 + a_3 u_3 + a_4 u_1 u_2 + a_5 u_1 u_3 + a_6 u_2 u_3 + a_7 u_1^2 + a_8 u_2^2 + a_9 u_3^2 . \tag{7}$$

The polynomials for all monitored variables can be given in the following generalized form:

$$\vec{Y_0^T} = \vec{V^T} \mathbf{A} , \tag{8}$$

where $\vec{Y_0^T}$ is a (1×m)-vector of monitored variables, $\vec{V^T}$ is a (1×k)-vector of components $1, u_1, u_2, ... u_2^2, u_3^2$, and $\mathbf{A}$ presents a (k×m)-matrix of unknown coefficients a_i for all m monitored variables. Since measurements at one steady-state operating point are not sufficient to compute the coefficients, data collected at n different points are included into the training set and involved into calculations. With new matrixes $\mathbf{Y}$ (n×m) and $\mathbf{V}$ (n×k) formed from these data, equation (8) is transformed in a linear system

$$\mathbf{Y} = \mathbf{VA} . \tag{9}$$

To enhance estimations $\hat{a}_i$, large volume n>>k of input data is involved and the least-squares method is applied to solve system (9), resulting in the well known solution:

$$\overset{\wedge}{\mathbf{A}} = (\mathbf{V}^T\mathbf{V})^{-1}\mathbf{V}^T\mathbf{Y} \ . \tag{10}$$

As can be seen, polynomials present a typical data-driven model because only input and output data are used to compute polynomials' coefficients. In the below sections that describe the stages of a total diagnostic process, we will return to polynomials and other described above models considering their particular applications in the GPA methods.

3. Data validation and preliminary processing

3.1 Deviations

Modern instrumentation and data recording tools allow collecting a great volume of test bed and field data of different types. Typically, historical engine sensor data are used in diagnostics that were previously filtered, averaged, and periodically recorded (once per flight, day, or hour) at steady states. Every measurement section (snapshot) includes engine operational conditions $\vec{U}$, which set an engine operating point, and monitored variables $\vec{Y}$. When recorded over a long period of time, these snapshots can provide valuable information about the deterioration and faults. The most common cause of stationary gas turbines' deterioration is compressor fouling and the data with fouling and washing cycles are widely used in order to verify diagnostic techniques.

By direct analysis of the variables themselves it is difficult to discriminate performance degradation effects from great changes due to different operating modes. To draw useful diagnostic information from raw recorded data, a total gas turbine diagnostic process usually includes a preliminary procedure of computing deviations. The deviations, also known as residuals and deltas, are defined as differences between measured and engine baseline values. As the baseline depends on an engine operating condition, it can be written as function $\vec{Y}_0(\vec{U})$ usually called a baseline function or model. With this model the deviations for each monitored variables $Y_{i,i=1,m}$ is computed in a relative form

$$\delta Y_i^* = \frac{Y_i^* - Y_{0i}(\vec{U})}{Y_{0i}(\vec{U})}, \tag{11}$$

where Y_i^* denotes a measured value.

The deviation consists of the systematic influence (signal) induced by engine degradation or faults and a noise component, which is explained by sensor errors and a baseline model inadequacy. When properly computed, the deviations can have relatively high quality (signal-to-noise ratio) and can potentially be good indicators of engine health. Since success of all principal diagnostic stages directly depends on the deviations' quality, best efforts should be applied to keep deviation errors to a minimum.

Figure 3 exemplifies the exhaust gas temperature (EGT) deviations of a gas turbine for natural gas pumping stations. Let us call this engine GT1. The deviations are plotted here against an operation time t (here and below a variable t is given in hours). As can be seen, the presented data cover approximately 4.5 thousand hours. The deviations δY^* computed on real measurements with noise are marked by a grey colour while a black line denotes ideal deviations δY without noise. A compressor washing at the time point $t = 7970$ as well as fouling periods before and after the washing are well-distinguishable in the figure.
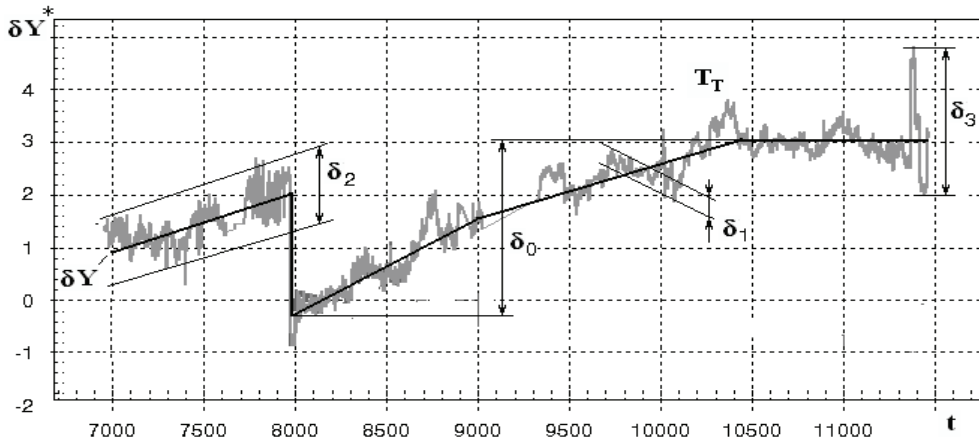
Fig. 3. Deviations' characteristics

A difference $\varepsilon_\Sigma = \delta Y^* - \delta Y$ can be considered as an error. If we designate the maximum deviation δY as δ_0, the signal-to-noise ratio

$$\bar{\delta}_0 = \delta_0 / \sigma(\varepsilon_\Sigma), \tag{12}$$

where $\sigma(\varepsilon_\Sigma)$ is a standard deviation of the errors, will be an index of diagnostic quality of the deviations δY^*. To enhance the quality we should reduce the errors ε_Σ. According to Fig.3, there are three elemental errors given here by error intervals δ_1, δ_2, and δ_3. Total error ε_Σ consists correspondingly of three components and can be given by the formula:

$$\varepsilon_\Sigma = \varepsilon_1 + \varepsilon_2 + \varepsilon_3, \tag{13}$$

where ε_1 is a normal noise smaller than 0.2% that is observed at every time point,

    ε_2 presents slower fluctuations of the amplitude limited by 0.8%, and

    ε_3 means single outliers with the amplitude greater than 0.8%.

The errors can be induces by both sensor malfunctions and baseline model inadequacy. Let us analyse separately these error sources.

3.2 Sensor malfunction detection

Developed graphical tools of monitoring systems can promote a successful exploration of abnormal sensor behaviour. In particular, different deviation plots can be applied because the deviations are very sensitive to sensor errors. However, these plots can not sometimes explain a true cause of detected abnormal fluctuations in the deviations. Additional plots like the time plot of some parallel measurements of the same variable assist to identify the problem. For special cases theoretical analysis can also be applied to make clear the origin of the fluctuations. Some examples of sensor malfunctions revealed by the described graphical tools are given below.

It was found in (Loboda & Santiago, 2001) that great outliers δ_3 at the end of the analysed time interval of Fig.3 are related with wrong measurement of a gas turbine inlet temperature t_{in}. As a result of numerical analysis it was found that the inlet temperature error influences

the deviations according to the following mechanism: [increasing of temperature t_{in} due to the errors] → [drop of the calculated value of a corrected rotation speed] → [reducing an inlet guide vane angle by the control system] → [gas flow decreasing and the corresponding power drop below the setting level] → [feeding the additional fuel by the control system to reach the power setting] → [the increase of gas path variables due to the compressor condition change and the regime raising] → [deviation increase]. Thus, the input temperature errors resulted in wrong control system operation and undesirable EGT increase.

Another example of input temperature sensor errors is described in (Loboda et al., 2009). It was found in the data recorded in a gas turbine driver for an electric generator. Let us call this engine GT2. Figure 4 illustrating this case presents the plots of the variables T_{in} and T_H and EGT deviations dTt. As can be seen, the T_H curve changes a little but the T_{in} curve shows frequent spikes and shifts that are synchronous with anomalies in the dTt curve. The explanation is that an abnormal increase in the variable T_{in}, which is a baseline function argument, results in a function increment for all monitored temperatures and the corresponding fall in the deviations dTt, which is about -5%. Such errors are capable to hide degradation and fault effects completely and to render useless gas turbine monitoring.
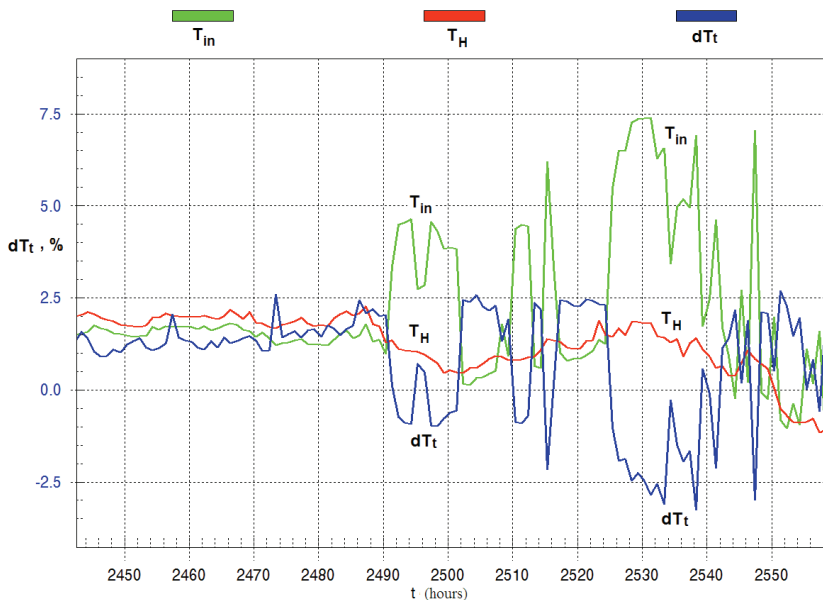
Fig. 4. GT2 inlet temperature sensor faulty operation

The next example of sensor data anomalies is related with a fuel consumption, which can be regarded as one of the most important variables for control and monitoring systems. In fuel consumption deviations dGf computed for one of the units of the GT2, an unusual decrease of approximately 7% over a prolonged period of time was found and described in (Loboda et al., 2009). Analyzing data from two other units, similar prolonged shifts in the consumption deviations were also revealed. The idea arose about a possible common cause of the consumption deviation shifts in different gas turbine units. Figure 5 helps to verify

this idea. The deviations dGf are plotted here vs. a calendar time for all three units. The deviation shifts are well visible from the end of January to the beginning of April and they begin and end at the same time for different units. What reasonable explanation can there be to the puzzling fact that independent fuel consumption sensors have a common source of errors? The answer was related with a variable chemical structure of fuel gas supplied from a common source that produces synchronous fluctuations of a gas calorific value in the units.
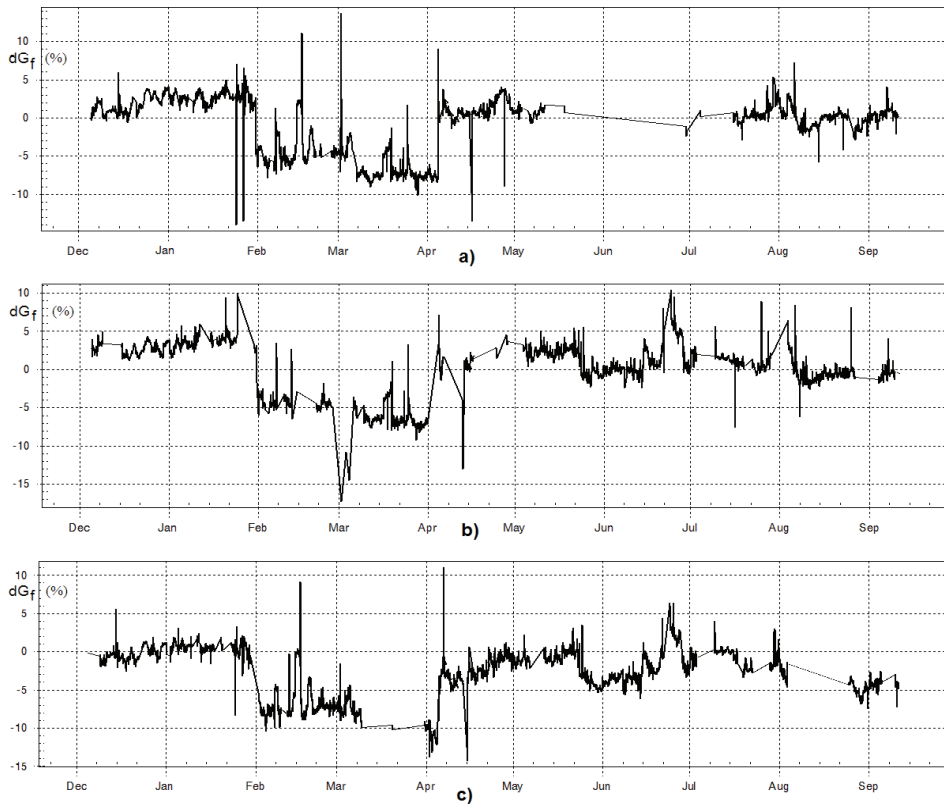
Fig. 5. Fuel consumption deviations vs. calendar time (a – unit 1, a – unit 2, a – unit 3)

The described above cases of sensor abnormal behaviour were found with the use of deviation plots. Nevertheless, parallel measurements of the same variable, for example, a suite of thermocouple probes installed in a high pressure turbine discharge station of the GT2, can also be useful to detect sensor problems. Although the thermocouple data were filtered and averaged before recording, some cases of single thermocouple probe faults have been found. Graphs (a) and (b) in Fig. 6 illustrate them. Observing two 25% spikes in graph (a) and a 50% spike in graph (b), we can conclude with no doubt that they are results of probe faults. Opposite spike directions in the graphs probably indicate different thermocouple fault origins. The outliers are well visible in the figure and the used filtering algorithm should be modified to exclude them.
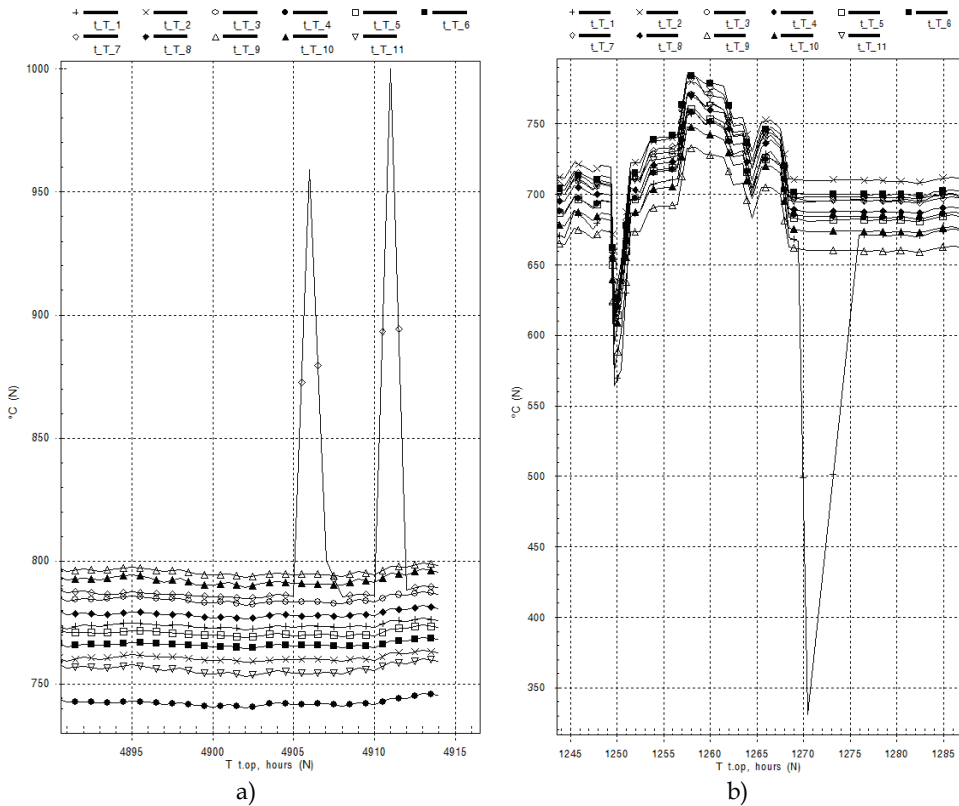
Fig. 6. EGT probes' errors: a – single gross errors, unit 1; b – a single gross error, unit 3

In this way, the deviation quality can be enhanced by the sensor malfunction detection and data cleaning from wrong data. The next mode to improve deviations is to make the baseline model as adequate as possible.

3.3 Baseline model improvement

The baseline model adequacy considerably depends on the learning set but the problem to compose a proper set for model determination seems to be challenging. On the one hand, to satisfy approximation requirements, the learning set must incorporate extensive data collected at all possible operating conditions. On the other hand, a technological process requires certain gas turbine power and does not allow arbitrary changes of an operating point. Moreover, data collection period is limited by a short time when a gas turbine condition can be considered as healthy and invariable. As a result, the baseline model is not adequate at the operating conditions not presented in the learning set. Two described below methods overcome mentioned difficulties. In the first method, the thermodynamic model is applied.

To demonstrate the possibility and advantages of the baseline model created on the basis of the thermodynamic model (see Loboda et al., 2004), two learning set variations are formed. *Variation 1.* The learning set is created from 694 consecutive recorded operating points of the

GT1. As can be seen in the Fig.7a, the learning set points occupy only two limited zones of the operating space "G_f - n_{PT} - T_H" (n_{PT} denotes power turbine rotation speed). To overcome this obstacle, it is suggested to apply the thermodynamic model for learning set generation. *Variation 2.* The learning sample includes 270 operating points generated by the thermodynamic model. With the help of Fig.7b one can see the advantages of such a model based learning set: the points are uniformly distributed in a much greater zone than in the case of real data.

On the basis of the described data sets two corresponding polynomial baseline models have been calculated as explained in section 2.2. The deviations were computed then for each model and with the same real data that are shown in Fig.3. Figure 8 illustrates these two series of the EGT deviations and helps to compare two concerned modes to calculate the baseline model. As can be seen, the model based learning set allow computing the deviations with notably lower errors. Thus, the use of the thermodynamic model can be recommended.
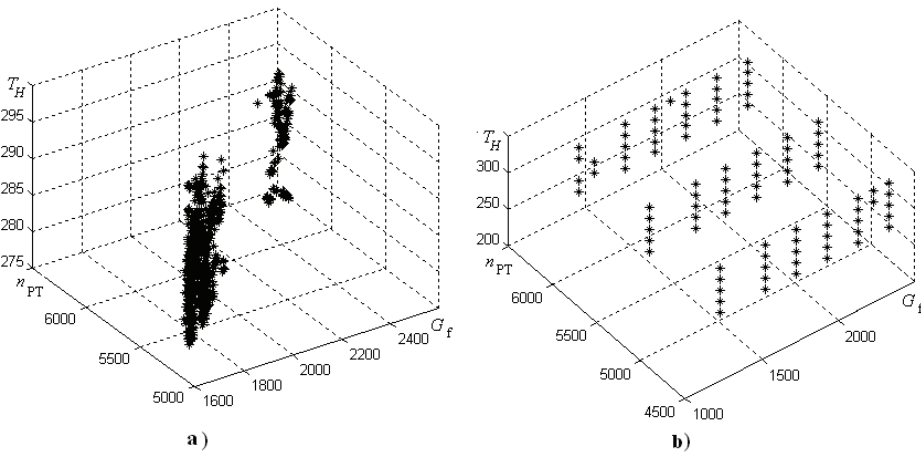
Fig. 7. Learning set points (a – real data; b – thermodynamic model data)
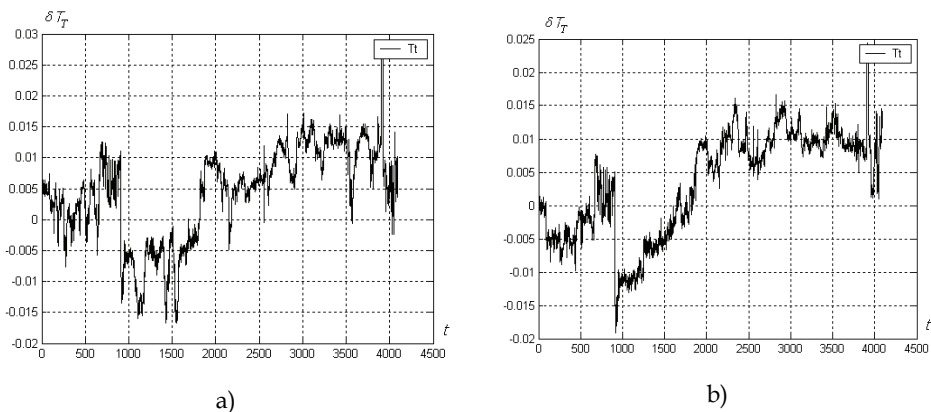

Fig. 8. EGT deviations (a – data based learning set; b – model based learning set)

The second method overcoming the learning set difficulties is related with a degraded engine model (Loboda et al., 2009), from which the necessary baseline model can be derived. Since a compressor fouling severity depends on the engine operation time $\bar{t}$ after the last washing, it is natural to add this variable to the arguments of the baseline function (7) in order to describe a degraded engine. Consequently, the degraded engine model can be given by

$$Y(\vec{U}_m, t) = Y_0(\vec{U}_m) + c_{15}\bar{t} + c_{16}\bar{t}^2 . \tag{14}$$

Once computed, such model can be easily transformed into the necessary baseline model by putting $\bar{t}$ equal to zero. Since model (14) takes into consideration a varying deterioration level, all recorded data could be used to compute unknown coefficients.

To examine the idea, the data recorded in unit 1 of the GT2 during the second and third periods of fouling (1800 points in total) have been included in the learning set. With the baseline model found in this way, the deviations were computed then for all available unit 1 data and considerable deviation enhancement was achieved.

The method can be further improved. To that end, for each analyzed fouling period a particular model of a degraded engine is computed using all data recorded during the period. The resulting baseline model is then determined by averaging the particular baseline functions. Traditional and new methods for baseline model formation are illustrated in Fig.9. One can see significant deviation improvement provided by the new method. Consequently, the idea of a degraded engine model seems to be promising for computing the deviations in practice.
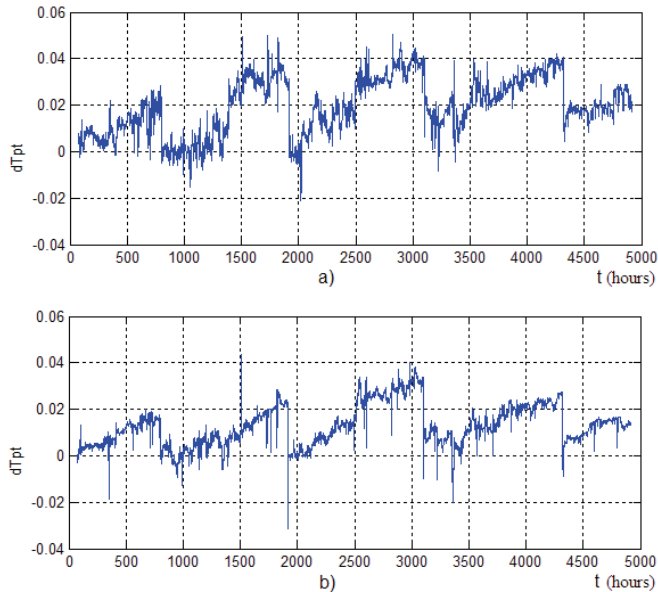

Fig. 9. Unit 1 power turbine temperature deviations for two methods of baseline model computation (a - model determined with 200 successive operating points, b - averaged model with the use of a time variable)

Choosing the best baseline function arguments (Loboda et al., 2004) can also improve the deviations. Unlike a real engine, the baseline model allows to change parameters setting an operating point (function arguments). This gives the possibility to examine all measured variables as such parameters. The numeric experiment has been conducted with the GT1 real data included 2608 operating points. The results are given in Table 1, which contains averaged errors of each deviation and their mean number presented for all possible arguments and ranged according to this mean number. At the first glance, the variable n_{hp} of high pressure rotor speed measured with high accuracy could be the best argument. However, it can be seen from the table that the parameters n_{hp} and G_f are situated in the lower part of the table while the parameter T_T occupies the first place. The explanation is that argument quality not only depends on its measurement accuracy, but also is defined by its influence on the gas turbine behaviour which is great for the parameter n_{hp}.

Argu-ment	Deviations								
	T_T	T_{PT}	P_C	P_T	G_f	T_C	n_{hp}	N_e	mean
T_T	-	0.12	0.07	0.08	0.13	0.12	0.39	0.17	0.108
T_{PT}	0.18	-	0.11	0.11	0.17	0.11	0.13	0.15	0.127
P_C	0.08	0.08	-	0.66	0.18	0.45	0.17	1.20	0.141
P_T	0.09	0.08	0.74	-	0.16	0.92	0.19	6.11	0.143
G_f	0.12	0.10	0.15	0.16	-	0.67	0.31	0.51	0.157
T_C	0.12	0.08	0.36	0.33	0.86	-	0.27	1.10	0.167
n_{hp}	0.35	0.14	0.19	0.21	0.36	0.26	-	0.29	0.216
N_e	0.17	0.11	1.42	1.69	1.01	1.41	0.25	-	0.224

Table 1. Deviation errors for different arguments

In all described above methods improving the baseline model, polynomials and the least square method have successfully been applied. The resulting model adequacy was sufficient for reliable monitoring gas turbine deterioration effects. Nevertheless, artificial neural networks are also famous as good function approximators in many fields including gas turbine monitoring. Investigations report wide use of artificial neural networks as a tool to describe an engine baseline, for example, for a stationary gas turbine (Fast et al., 2009) and an aircraft engine (Volponi et al., 2007).

The growing network application in gas turbine monitoring on the one hand and, on the other hand, our own positive experience with the use of polynomials have encouraged us to conduct a thorough comparative study of these two techniques. The paper (Loboda & Feldshteyn, 2010) verifies whether the application of such a powerful modelling tool as artificial neural networks (ANN) instead of polynomials yields higher adequacy of the baseline model and better quality of the corresponding deviations. The variety of analyzed neural network structures were considered and extensive field data of two different gas turbines were involved to compute and validate both techniques in order to draw sound conclusions on the network applicability to approximate healthy engine performance. In a part of the considered cases, polynomials were better in accuracy and, in the other cases the compared techniques were practically equal. However, no manifestations of network superiority were detected. Thus, this study shows that a polynomial baseline model can be successfully used in real monitoring systems instead of neural networks. At least, it seems to be true for simple cycle gas turbines with gradually changed performance, like the turbines considered in the study.

Concluding section 3, we would like to note that the considered here stage of data validation and computing deviations has received increased attention because this preliminary stage has utmost importance for subsequent general stages of a total diagnostic analysis. Among these stages, detailed diagnosis or fault identifications can be considered as a principal stage and it is addressed in the most of studies in the area of gas turbine diagnostics. A considerable part of these studies are based on the pattern recognition theory.

4. Diagnosis by pattern recognition methods

4.1 Technical approach to diagnosis at steady states

As mentioned in sections 2 and 3, models are used in gas turbine diagnostics to describe engine performance degradation and faults and the deviations are employed to reveal the degradation influence. That is why, a fault classification necessary to apply pattern recognition methods is usually constructed in a deviation space using nonlinear or linear static models.

Employing the nonlinear model, the normalized deviations induced by a change $\Delta\vec{\Theta}$ in fault parameters can be written as

$$Z_i = \frac{Y_i(\vec{U},\vec{\Theta}_0 + \Delta\vec{\Theta}) - Y_i(\vec{U},\vec{\Theta}_0)}{Y_i(\vec{U},\vec{\Theta}_0)a_{Yi}} + \varepsilon_i, i = 1, m , \tag{15}$$

where coefficients a_{Yi} are employed to normalize deviations. In expression (15) amplitudes of random errors ε_i are equal to one for all monitored variables Y_i. Such normalization simplifies fault class description and enhances diagnosis reliability. The deviation vector $\vec{Z}^*$ is considered as a pattern to be recognized and a fault classification is presented as a set of such patterns.

Engine faults vary considerably. Hence, for the purposes of engine diagnostics this variety has to be broken down into a limited number of classes. In the pattern recognition theory, it is often supposed that an object state D can belong only to one of q preset classes

$$D_1, D_2, ..., D_q . \tag{16}$$

We accept this hypothesis for a gas turbine fault classification. It is also assumed that each class corresponds to one engine component and is described by the correction factors of this component. Two types of classes are simulated: a single fault class and a multiple one. The single fault class is formed by changing one fault parameter. The multiple fault class has two independently changed parameters for the same component, namely, a flow parameter ΔA and an efficiency parameter $\Delta\eta$.

Each class is given by a representative sample of the deviation vectors $\vec{Z}^*$ computed according to expression (15). During the calculations a variable fault severity is determined by a uniform distribution and errors are generated according to a normal distribution. The whole classification is a composition of these samples **Z1** called a learning set.

A nomenclature of possible diagnoses $d_1, d_2, ..., d_q$ corresponds to the accepted classification (16). To make a diagnosis d, a method-dependent criterion $R_j = R(\vec{Z}^*, D_j)$ is introduced as a measure of membership of a current pattern $\vec{Z}^*$ to class D_j. To determine the functions $R_j = R(\vec{Z}^*, D_j)$, the learning set is used. After calculating all values $R_j, j = 1, q$, a decision rule

$$d = d_l \quad \text{if} \quad R_l = \max(R_1, R_2, ..., R_q) \tag{17}$$

is applied.

To verify a diagnostic algorithm determined with the help of the learning set, one more set is required. The necessary set **Zv**, called a validation set, is created in the same way as the set **Zl**. The only difference is that other series of random numbers is generated to simulate fault severity and errors in the deviations. Every pattern in the validation set pertains to a known class. That is why, comparing this class D_j with the diagnosis d_l, we can compute probabilities $Pd_{lj} = P(d_l / D_j)$ and compose a known confusion matrix **Pd**. Its diagonal elements Pd_{ll} form a vector $\vec{P}$ of true diagnosis probabilities that are indices of classes' distinguishability. Mean number of these elements – scalar $\bar{P}$ – characterizes total engine diagnosability. No diagonal elements help to identify the causes of bad class distinguishability. These elements make up probabilities of false diagnosis $Pe_j = 1 - P_j$ and $\bar{Pe} = 1 - \bar{P}$.

Thus, the described approach to gas turbine diagnosis under stationary conditions includes the fault classification stages, formation of a diagnostic algorithm, and estimation of diagnosis reliability indices. With several small corrections this approach is also applicable for diagnosis at transients (Loboda et al., 2007). A transient interval is divided into T time points and, with measurements at these points, a generalized deviation vector is computed. It is a pattern to be recognized in diagnosis under transient conditions.

Following the presented approach, some studies have been conducted for the GT1 chosen as a test case. In these studies steady state operation is determined in the thermodynamic model by a fixed gas generator speed and standard ambient condition. Eleven full and part-load steady states are set by the following speeds: 10700, 10600, …, 9800, 9700 rpm. Six simulated gas path variables correspond to a standard measurement system of the GT1. The single type fault classification consists of nine classes, which are simulated by nine fault parameters. The multiple type classification comprises four items corresponding to four main components: an axial air compressor, a combustion chamber, a gas generator turbine, and a power turbine. The learning and validation sets include 1000 patterns for each class that are sufficient to ensure the necessary computational precision. The first conducted study (Loboda & Yepifanov, 2006) compares different recognition tools.

4.2 Comparison of recognition techniques

Three recognition techniques that present different approaches in a recognition theory have been chosen for diagnosing. The first technique is based on the Bayesian approach (Duda et al., 2001), in which each fault class D_j should be described by its probability density function $f(\vec{Z}^* / D_j)$ and a posteriori probability $P(D_j / \vec{Z}^*)$ is employed as a decision criterion. Difficulty of this method is related with the function $f(\vec{Z}^* / D_j)$ as far as density function assessment is a principal problem of mathematical statistics, that is why this function can be determined only for a simplified class description. The second technique operates with the Euclidian distance to recognize gas turbine fault classes. The criterion R_j for this technique is an inverse averaged distance between an actual pattern and all patterns of a fault class D_j. The third technique applies the neural networks, in particular, a multilayer perception. The resulting diagnosis reliability indices – the probabilities of false diagnosis Pe_j and $\bar{Pe}$ for the multiple faults – are placed in Table 2. The given indices demonstrate that

probabilities of erroneous diagnosis by methods 1 and 3 are approximately equal and significantly lower than the corresponding probabilities of method 2. The calculations for single faults have confirmed this conclusion. It is important that neural networks are not inferior in diagnosis accuracy to the Bayesian approach, because the latter in its turn is known as the best recognition technique if we use the criterion of a correct decision probability. Additionally, neural networks do not need the simplifications of the fault class description required for Bayesian approach. In this way, neural networks can be recommended for the use in real condition monitoring systems.

Neural networks will also be used in the next study. It proposes and verifies the idea of the generalized fault classification (Loboda, Yepifanov et al., 2007; Loboda & Feldshteyn, 2007) that drastically simplifies practical realization of diagnostic algorithms.

Indices		Methods		
		1	2	3
$\vec{P}e$	d_1	0.109	0.237	0.104
	d_2	0.216	0.373	0.214
	d_3	0.060	0.051	0.072
	d_4	0.117	0.051	0.127
$\bar{P}e$		0.1256	0.1790	0.1293

Table 2. False diagnosis probabilities (multiple type classification)

4.3 Generalized fault classification

The approach presented in subsection 4.1 implies that a laborious procedure of fault classification formation is repeated for every new operating condition. It will be difficult to realise this approach in practice because an engine frequently changes its operating mode. The same problem arises for diagnosis at transients but existing works do not answer how to overcome it.

Diagnosing the considered gas turbine (GT1) at different operating modes, it has been found out that the class presentation in the diagnostic space $\vec{Z}$ is not strongly dependent on a mode change. Therefore we intended to draw up the classification that would be independent from operational conditions. This classification has been created by incorporating patterns from all 11 steady states into each class of the reference and testing sets. Such generalized classification was successively applied to diagnose at each steady state. In the classification, a region occupied by any class is more diffused that induces greater class intersection, which in its turn leads to losses in the diagnosis reliability. But how significant are these losses?

Numeric experiments with traditional and new classifications helped to quantify such losses. To ensure firm conclusions, the classification comparison was drawn for both single and multiple class types. Table 3 contains the results for the single class type. In this table, the row "Conv." means the probabilities for the conventional classification averaged over all steady states. The row "Gen." contains the probabilities for the generalized classification created for, and applied at, the same steady states. It can be noted that differences of the probabilities $\vec{P}_e$ between the considered classifications are small for the both class types. The

mean probability $\overline{P}_e$ also rises just a little, by about 0.5%, in the row "Gen.". So the diagnosis reliability losses resulting from the classification generalization are insignificant.

Classifi-cation	$\vec{P}_e$									$\overline{P}_e$
	ΔA_c	$\Delta\eta_c$	ΔA_{hpt}	$\Delta\eta_{hpt}$	ΔA_{pt}	$\Delta\eta_{pt}$	$\Delta\sigma_{cc}$	$\Delta\eta_{cc}$	$\Delta\sigma_{in}$	
Conv.	0.166	0.266	0.132	0.265	0.146	0.172	0.154	0.174	0.168	0.1827
Gen.	0.156	0.275	0.131	0.269	0.148	0.190	0.161	0.184	0.180	0.1883

Table 3. Diagnosis errors for single faults (indices of fault parameters ΔA and $\Delta\eta$ mean compressor, high pressure turbine, power turbine, combustion chamber, and input device)

For additional verification of the generalized classification, the previous analysis was also carried out for real operational conditions. Two sets of 25 operating points were made up from a six-month database of gas turbine performance registration at different operational field conditions. The points of each set correspond to the maximally different conditions. The results show (Loboda, Yepifanov et al., 2007) that differences between two classifications are small and can be considered as random calculation errors. Consequently, the proposed classification does not cause additional accuracy losses. This still holds true when the classification is used at the operating points different from the points of classification formation. So, the generalized classification can be applied not only to the steady state points used for its creation but also to any other points.

The principle of a generalized classification was also examined for transient operations. In (Loboda, Yepifanov et al., 2007) the examination is conducted at 16 transients with different transient profiles and ambient temperatures. The resulting accuracy losses due to the classification use did not exceed 3.5%. More cases of transient operation are considered in (Loboda & Feldshteyn, 2007). The losses are estimated at the level of 2% and it is shown that they could be lower in practice.

In this way, the proposed classification principle was verified separately for steady states and transients. In both cases, the results have shown that the generalized classification practically does not reduce the diagnosis accuracy level. On the other hand, the suggested classification drastically simplifies the gas turbine diagnosis because it is formed once and used later without changes. Therefore, the diagnostic technique based on the generalized fault classification can be successfully implemented in gas turbine health monitoring systems.

The next study briefly described below also deals with networks-based diagnosis under variable operating conditions. In contrast to the previous study, the data from different operating points (modes) are grouped to set only a single diagnosis. Such multipoint diagnosis promises considerable accuracy enhancement.

4.4 Multipoint diagnosis

Although some works deal with the influence of operating conditions on the diagnostic process (Kamboukos & Mathioudakis, 2006), no full-length analyses are yet available. It is known that multipoint methods, which group the data registered at different operating points in order to make a single diagnosis, ensure higher accuracy when compared with conventional one-point (one-mode) methods. However, questions arise as to how significant this effect is and what its causes are. The diagnosis at transient operation (Ogaji et al., 2003)

poses the similar questions. To make one diagnosis, this technique joins data from successive measurement sections of one transient and in this regard looks like multipoint diagnosis. From a theoretical and practical standpoint, it would be interesting to find out how much these two approaches differ in accuracy.

The investigation to answer the questions has been conducted in (Loboda, Feldshteyn et al., 2007) for the GT1 and an aircraft engine, called GT3. The following conclusions were drawn. First, a total diagnosis accuracy growth due to switching to the multipoint diagnosis and data joining from different steady states is significant. It corresponds to a decrease in the diagnosis errors by 2-5 times. Second, the main effect of the data joining consists in an averaging of the input data and smoothing of the random measurement errors. It is responsible for the main part of the total accuracy growth. If variations in fault description at different operating points are slight as for the GT1, the averaging effect is responsible for the whole growth. Under these conditions, the generalized classification has a certain advantage as compared to the conventional one-point diagnosis. Third, if the variations are considerable (GT3), they give new information for the fault description and produce an additional accuracy growth for the multipoint option. This part depends on the class type but in any case it is essentially smaller than the principal part. The diagnosis at transients may cause further accuracy growth of this type. However, it will be limited and the averaging effect will be a principal part of the total accuracy growth relative to the one-point diagnosis.

We complete here the descriptions of the studies in the area of diagnosis (fault identification) based on pattern recognition. In the next section it will be shown how to extend the described approach on the problem of gas turbine monitoring (fault detection).

5. Integrated monitoring and diagnosis

Detection algorithms deal with two classes, a class of healthy engines and a class of faulty engines. In multidimensional space of the deviations they are divided by a healthy class boundary (internal boundary). The healthy class implies that small deviations due to usual engine performance degradation can certainly take place, although they are not well distinguishable against a background of random measurement and registration errors. The faulty class requires one more boundary, namely, faulty class boundary (external boundary) that means an engine failure or unacceptable maintenance costs.

Classification (16), created for the purpose of diagnosis and presented by the learning set, corresponds to a hypothetical fleet of engines with different faults of variable severity. To form a new classification necessary for monitoring, we suppose that the engine fleet, the distributions of faults, and their severities are the same. Hence, patterns of the existing learning set can be used for a new classification but the classes should be reconstructed. The paper (Loboda et al., 2008) thoroughly investigates such approach considering monitoring and diagnosis as one integrated process. Below we only give a brief approach description and the most important observations made.

Each former class D_j is divided into two subclasses $DM1_j$ and $DM2_j$ by the healthy class boundary. There is an intersection between the patterns $\vec{Z}^*$ of these subclasses because of the errors ε in patterns. A totality of subclasses

$$DM1_1, DM1_2, \ldots, DM1_q \qquad (17)$$

constitutes the classification of incipient faults for the diagnosis of healthy engines, while subclasses

$$DM2_1, DM2_2, \ldots, DM2_q \tag{18}$$

form the classification of developed faults for the diagnosis of faulty engines.

To perform the monitoring, the subclasses $DM1_1, DM1_2, \ldots, DM1_q$ compose a healthy engine class M_1, while the subclasses $DM2_1, DM2_2, \ldots, DM2_q$ make up a faulty engine class M_2. Thus, the classification for monitoring takes the form of

$$M_1, M_2. \tag{19}$$

It is clear that the patterns of these two classes are intersected, resulting in α- and β-errors.

Figure 10 provides a geometrical interpretation of the preceding explanations. The former and the new classifications are presented here in the space of deviations Z_1 and Z_2. A point "O" means a baseline engine; lines OD_1, OD_2, …, and OD_q are trajectories of fault severity growth for the corresponding single classes; closed lines B1 and B2 present boundaries of a healthy class M_1 (indicated in green) and faulty class M_2 (indicated in yellow).
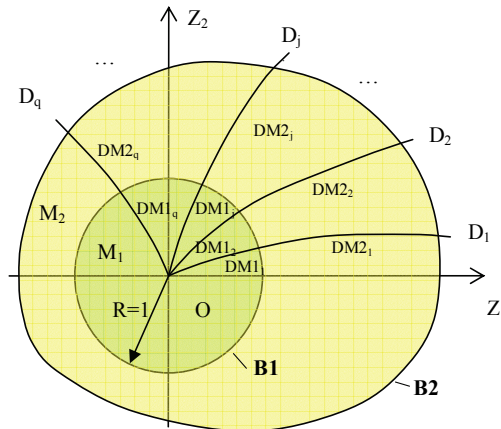
Fig. 10. Schematic class representation for integrated monitoring and diagnosis

With these three classifications, monitoring accuracy and diagnosis accuracy were estimated separately for healthy and faulty classes and some useful results were obtained. First, the recognition of incipient faults was found to be possible and advisable before a gas turbine is recognized as faulty by fault detection algorithms. Second, the influence of the boundary on the monitoring and diagnosis accuracy was also investigated. Third, it has been shown that the introduction of an additional threshold, which is different from the boundary, can reduce monitoring errors. Fourth, it was demonstrated that a geometrical criterion, which is much simpler in application than neural networks, can provide the same results and thus can also be used in real monitoring systems.

The pattern recognition-based approach considered in this section is not however without its limitations. The diagnoses made are limited by a rigid classification and fault severity is not estimated. The second approach maintained in gas turbine diagnostics and based on system identification techniques can overcome these difficulties.

6. Diagnosis by system identification methods

This approach is based on the identification techniques of the models (1), (2) or (4). These techniques compute estimates $\hat{\vec{\Theta}}$ as a result of distance minimization between simulated and measured gas path variables. In the case of model (1) this minimization problem can be written as

$$\hat{\vec{\Theta}} = \arg\min \left\| \vec{Y}^* - \vec{Y}(\vec{U},\vec{\Theta}) \right\| . \tag{20}$$

It is an inverse problem while a direct problem is to compute $\vec{Y}$ with use of known $\vec{\Theta}$. The estimates contain information on the current technical state of each engine component therefore further diagnostic actions will be simple. Furthermore, the diagnosis will not be constrained by a limited number of determined beforehand classes.

Among system identification methods applied to gas turbine diagnostics, the Kalman filter, basic, extended, or hybrid, is mostly used, see, for example (Volponi et al., 2003). However, this method uses a linear model that, as shown in (Kamboukos & Mathioudakis, 2005), can result in considerable estimation errors. Moreover, every Kalman filter estimation depends on previous ones. That is why abrupt faults are detected with a delay.

Other computational scheme is maintained in (Loboda, 2007). Independent estimations are obtained by a special inverse procedure. Then, with data recorded over a prolonged period, successive independent estimation are computed and analyzed in time to get more accurate results.

Following this scheme, a regularizing identification procedure is proposed and verified on simulated and real data in (Loboda et al., 2005). The testing on simulated data has shown that the regularization of the estimated state parameters makes the identification procedure more stable and reduces an estimation scatter. On the other hand, the regularization shifts mean values of the estimations and should be applied carefully. In the conditions of fulfilled calculations, the values 0.02-0.03 of the regularization parameter were recommended. The application of the proposed procedure on real data has justified that the regularization of the estimations can enhance their diagnostic value.

Next diagnostic development of the gas turbine identification is presented in (Loboda, 2007). The idea is proposed to develop on the basis of the thermodynamic model a new model that takes gradual engine performance degradation in consideration. Like the polynomial model of a degraded engine described in section 3.3, such a model has an additional argument, time variable, and can be identified on registered data of great volume. If we put the time variable equal to zero, the model will be transformed into a good baseline function for diagnostic algorithms. Two purposes are achieved by such model identification. The first purpose consists in creating the model of a gradually degraded engine while the second is to have a baseline function of high accuracy. The idea is verified on maintenance data of the GT1. Comparison of the modified identification procedure with the original one has shown that the proposed identification mode has better properties. The obtained model taking into account variable gas path deterioration can be successfully used in gas turbine diagnostics and prognostics. Moreover, this model can be easily converted into a baseline model of a high quality. Such a model can be widely used in monitoring systems as well.

Another novel way to get more diagnostic information from the estimations is to identify a gas turbine at transients as shown in (Loboda & Hernandez Gonzalez, 2002). However, this paper is only the first study, which needs to be continued.

7. Conclusions

In this chapter, we tried to introduce the reader into the area of engine health monitoring. The chapter contains the basis of gas turbine monitoring and a brief overview of the applied mathematical techniques as well as provides new solutions for diagnostic problems. In order to draw sound conclusions, the presented studies were conducted with the use of extended field data and different models of three different gas turbines.

The chapter pays special attention to a preliminary stage of data validation and computing deviations because the success of all subsequent diagnostic stages of fault detection, fault identification, and prognostics strongly depends on deviation quality. To enhance the quality, the cases of abnormal sensor data are examined and error sources are identified. Different modes to improve a baseline model for computing the deviations are also proposed and justified.

On the basis of pattern recognition, the chapter considers monitoring and diagnostic stages as one united process. It is shown that the introduction of an additional threshold, which is different from the boundary between healthy and faulty classes, reduces monitoring errors.

Many improvements are proposed, investigated, and confirmed for fault diagnosis by pattern recognition and system identification methods, in particular, generalized fault classification, regularized nonlinear model identification procedure, and model of a degraded engine.

We hope that the observations made in this chapter and the recommendations drawn will help to design and rapidly tailor new gas turbine health monitoring systems.

8. References

Benvenuti, E. (2001). Innovative gas turbine performance diagnostics and hot parts life assessment techniques, *Proceedings of the Thirtieth Turbomachinery Symposium,* pp.23-31, Texas, USA, September 17-20, 2001,Texas A&M University, Houston

Duda, R.O.; Hart, P.E. and Stork, D.G. (2001), *Pattern Classification*, Wiley-Interscience, New York

Fast, M.; Assadi, M.; Pike, A. and Breuhaus, P. (2009). Different condition monitoring models for gas turbines by means of artificial neural networks, *Proceedings of IGTI/ASME Turbo Expo 2009*, 11p., Florida, USA, June 8-12, Orlando, ASME Paper GT2009-59364

Haykin, S. (1994). *Neural Networks*, Macmillan College Publishing Company, New York

Kamboukos, Ph. and Mathioudakis K. (2005). Comparison of linear and non-linear gas turbine performance diagnostics, *Journal of Engineering for Gas Turbines and Power*, Vol.127, No. 1, pp.49-56

Kamboukos, Ph. and Mathioudakis, K. (2006). Multipoint non-linear method for enhanced component and sensor malfunction diagnosis, *Proceedings of IGTI/ASME Turbo Expo 2006*, 9p, Barcelona, Spain, May 8-11

Loboda, I. and Santiago, E.L. (2001). Problems of gas turbine diagnostic model identification on maintenance data, *Memorias del 6 Congreso Nacional de Ingenieria Electromecanica*, pp.332-334, IPN ESIME-Zacatenco, Mexico

Loboda, I. and Hernandez Gonzalez, J. C. (2002). Nonlinear Dynamic Model Identification of Gas Turbine Engine, *Aerospace Technics and Technology. Journal: National Aerospace University*, *Kharkov, Ukraine,* No. 31, pp. 209 - 211, ISBN 966-7427-08-0, 966-7458-58-X

Loboda, I.; Yepifanov, S. and Feldshteyn, Ya. (2004). Deviation problem in gas turbine health monitoring, *Proceedings of IASTED International Conference on Power and Energy Systems*, 6p., Clearwater Beach, Florida, USA

Loboda, I.; Zelenskiy, R.; Nerubasskiy, V. and Lopez y Rodriguez, A.R. (2005). Verification of a gas turbine model regularizing identification procedure on simulated and real data, *Memorias del 4to Congreso Internacional de Ingenieria Electromecanica y de Sistemas, ESIME, IPN*, 6p., Mexico, November 14-18, ISBN: 970-36-0292-4

Loboda, I. and Yepifanov, S. (2006). Gas Turbine Fault Recognition Trustworthiness, *Cientifica, ESIME-IPN*, Mexico, Vol. 10, No. 2, pp. 65-74, ISSN 1665-0654

Loboda, I. (2007). Gas turbine diagnostic model identification on maintenance data of great volume, *Aerospace Technics and Technology. Journal: National Aerospace University*, Kharkov, Ukraine, No. 10(46), pp. 198 – 204, ISSN 1727-7337

Loboda, I. and Feldshteyn, Ya. (2007). A universal fault classification for gas turbine diagnosis under variable operating conditions, *International Journal of Turbo & Jet Engines*, Vol. 24, No. 1, pp. 11-27, ISSN 0334-0082

Loboda, I.; Yepifanov, S. and Feldshteyn, Ya. (2007). A generalized fault classification for gas turbine diagnostics on steady states and transients, *Journal of Engineering for Gas Turbines and Power*, Vol. 129, No. 4, pp. 977-985

Loboda, I.; Feldshteyn, Ya. and Yepifanov, S. (2007). Gas turbine diagnostics under variable operating conditions, *International Journal of Turbo & Jet Engines*, Vol.24, No. 3-4, pp. 231-244, 2007, ISSN 0334-0082

Loboda, I.; Yepifanov, S. and Feldshteyn, Ya. (2008). An integrated approach to gas turbine monitoring and diagnostics, *Proceedings of IGTI/ASME Turbo Expo 2009*, 9p., Germany, June 9-13, Berlin, ASME Paper No. GT2008-51449

Loboda, I.; Yepifanov, S. and Feldshteyn, Ya. (2009). Diagnostic analysis of maintenance data of a gas turbine for driving an electric generator, *Proceedings of IGTI/ASME Turbo Expo 2009*, 12p., Florida, USA, June 8-12, Orlando, ASME Paper No. GT2009-60176

Loboda, I. and Yepifanov, S. (2010). A Mixed Data-Driven and Model Based Fault Classification for Gas Turbine Diagnosis, *Proceedings of ASME Turbo Expo 2010: International Technical Congress*, 8p., Scotland, UK, June 14-18, Glasgow, ASME Paper No. GT2010-23075.

Loboda, I. and Feldshteyn, Ya. (2010). Polynomials and Neural Networks for Gas Turbine Monitoring: a Comparative Study, *Proceedings of ASME Turbo Expo 2010: International Technical Congress*, 11p., Scotland, UK, June 14-18, Glasgow, ASME Paper No. GT2010-23749.

Meher-Homji, C.B.; Chaker, M.A. and Motivwala, H.M. (2001). Gas turbine performance deterioration, *Proceedings of Thirtieth Turbomachinery Symposium*, pp.139-175, Texas, USA, September 17-20, 2001,Texas A&M University, Houston

Ogaji, S.O.T.; Li, Y. G.; Sampath, S. et al. (2003). Gas path fault diagnosis of a turbofan engine from transient data using artificial neural networks, *Proceedings of IGTI/ASME Turbo Expo 2003,* 10p., Atlanta, Georgia, USA

Pinelli, M. and Spina, P.R. (2002). Gas turbine field performance determination: sources of uncertainties, *Journal of Engineering for Gas Turbines and Power*, Vol. 124, No. 1, pp. 155-160

Rao, B.K.N. (1996). *Handbook of Condition Monitoring*, Elsevier Advanced Technology, Oxford

Romessis, C. and Mathioudakis, K. (2003). Setting up of a probabilistic neural network for sensor fault detection including operation with component fault, *Journal of Engineering for Gas Turbines and Power*, Vol. 125, No. 3, pp. 634-641

Romessis, C. and Mathioudakis, K. (2006). Bayesian network approach for gas path fault diagnosis, *Journal of Engineering for Gas Turbines and Power*, Vol. 128, No. 1, pp. 64-72.

Romessis, C.; Kyriazis, A. and Mathioudakis, K. (2007). Fusion of gas turbine diagnostic inference – the Dempster-Schafer approach, *Proceedings of IGTI/ASME Turbo Expo 2007,* 9p., Canada, May 14-17, 2007, Montreal, ASME Paper GT2007-27043.

Sampath, S. and Singh, R. (2006). An integrated fault diagnostics model using genetic algorithm and neural networks, *Journal of Engineering for Gas Turbines and Power,* Vol. 128, No. 1, pp. 49-56

Saravanamuttoo, H. I. H. and MacIsaac, B. D. (1983). Thermodynamic models for pipeline gas turbine diagnostics, *ASME Journal of Engineering for Power*, Vol.105, No. 10, pp. 875-884

Vachtsevanos, G.; Lewis, F.; Roemer, M. et al. (2006). *Intelligent Fault Diagnosis and Prognosis for Engineering Systems*, John Wiley & Sons, Inc., New Jersey

Volponi, A.J.; DePold, H. and Ganguli, R. (2003). The use of Kalman filter and neural network methodologies in gas turbine performance diagnostics: a comparative study, *Journal of Engineering for Gas Turbines and Power*, Vol. 125, No. 4, pp. 917-924

Volponi, Al.; Brotherton, T. and Luppold, R. (2007). Empirical tuning of on-board gas turbine engine model for real-time module performance estimation, *Proceedings of IGTI/ASME Turbo Expo 2007*, 10p., Montreal, Canada, May 14-17, 2007, ASME Paper GT2007-27535.

Micro Gas Turbines

Flavio Caresana[1], Gabriele Comodi[1],
Leonardo Pelagalli[1] and Sandro Vagni[2]
[1]Dipartimento di Energetica – Università Politecnica delle Marche
[2]Università degli Studi e-Campus
Italy

1. Introduction

Conventional gas turbines (GTs) range from a size of one or a few MWe to more than 350 MWe (GTW, 2009). Those at the small end of the range are commonly used in industrial applications, for mechanical or onsite electrical power production, while the larger ones are usually installed in large-scale electrical power plants, often in combined cycle plants, and are typically located far away from the consuming region.

In the future distributed energy systems based on small local power plants are likely to spread; since they lie close to the final users, they reduce electrical transport losses, and make thermal energy recovery profitable both in energy-related and in economic terms (Papermans et al., 2005; IEA, 2002). These benefits explain the increasing interest in small-size generation systems.

Recently, gas turbines < 1 MWe, defined as micro gas turbines (MGTs), have appeared on the market. MGTs are different from large GTs and cannot therefore be considered merely as their smaller versions. Their advantages as distributed energy systems lie in their low environmental impact in terms of pollutants and in their competitive operation and maintenance (O&M) costs. MGTs appear to be particularly well suited for service sector, household and small industrial applications (Macchi et al., 2005; Zogg et al., 2007).

2. The technology of Micro Gas Turbines

The small power size of MGTs entails implications that affect the whole structure. In particular the low gas mass flow rate is reflected in machine size and rotational speed: the smaller the former, the greater the latter. MGTs therefore differ significantly from GTs, mainly in (i) the type of turbomachines used; (ii) the presence of a regenerator; and (iii) the high rotational speed, which is independent of grid frequency. In fact unlike GTs, MGTs commonly use high-revving, single-stage radial turbomachines rather than multi-stage axial ones, to achieve greater compactness and low manufacturing costs. As a consequence of the high rotational speed, the electrical current is generated at high frequency and is then converted to the grid frequency value (50 or 60 Hz) by power electronics. The turbocompressor and turbine are usually fitted on the same shaft as the electrical generator, which also serves as the starting motor. Single-stage radial machines afford limited compression ratios and need a regenerative cycle to attain satisfactory electrical efficiency.

Therefore a regenerator is usually installed between the compressor and the combustion chamber. Figures 1 and 2 show, respectively, the layout and corresponding thermodynamic cycle of a typical cogeneration MGT.

PE	Power Electronics	CC	Combustion Chamber
EG	Electrical Generator	R	Regenerator
GC	Gas Compressor	BPV	ByPass Valve
GT	Gas Turbine	HRB	Heat Recovery Boiler
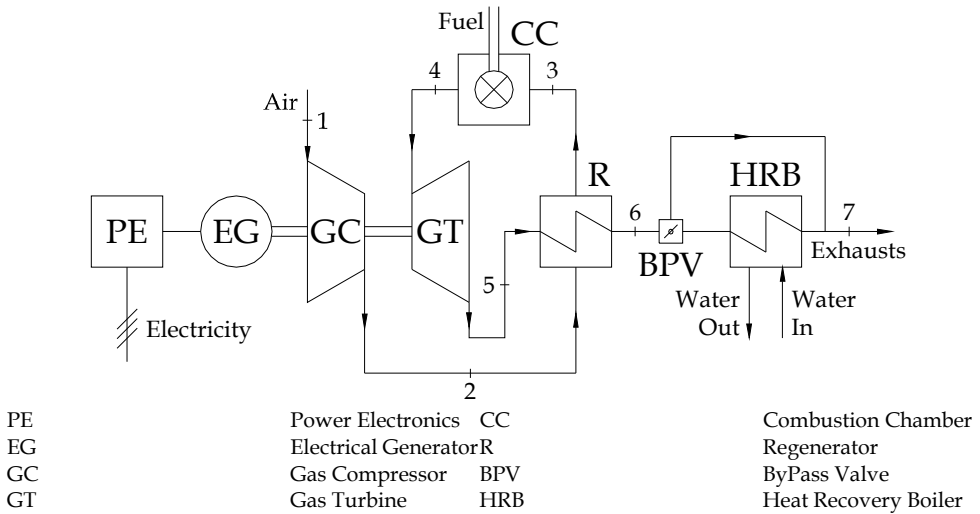
Fig. 1. Layout of a typical cogeneration MGT
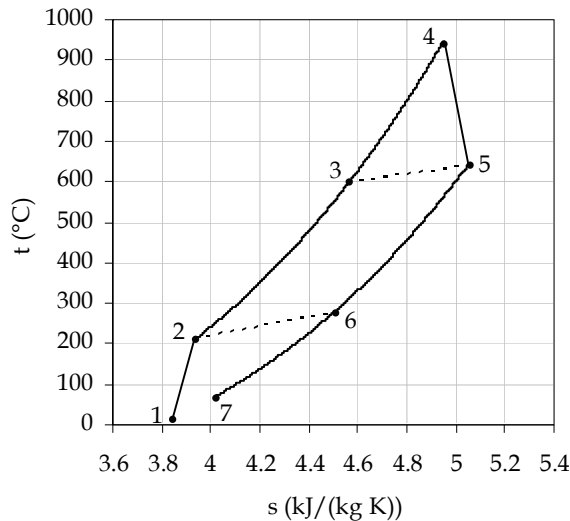
Fig. 2. MGT regenerative Brayton-Joule cycle

The ambient air (1, in both figures) is compressed by the centrifugal compressor; it then enters the regenerator (2), where it is preheated by the exhausts coming from the turbine, and is conveyed from the regenerator (3) to the combustion chamber, where it is used in the

combustion process to achieve the design turbine inlet temperature (4). The hot gases then expand through the turbine (5) and enter the regenerator. Given their fairly high temperature at the power unit exit (6), the exhausts can be sent to a heat recovery boiler (HRB), where they are used to heat water, before being discharged to the flue (7). In this configuration combined heat and power (CHP) production increases fuel energy conversion efficiency. When the thermal power demand is lower than the power that can be recovered from the exhausts, part of the fumes is conveyed directly to the chimney (7) via a bypass valve (BPV). The core power unit is fitted with auxiliary systems that include (i) fuel, (ii) lubrication, (iii) cooling, and (iv) control systems. The fuel feeding system compresses the fuel to the required injection pressure and regulates its flow to the combustion chamber according to the current operating condition. The lubrication system delivers oil to the rolling components, with the dual effect of reducing friction and removing heat. The cooling system keeps the operational temperatures of the different components, lubrication oil included, in the design ranges. The cooling fluid can be air, water, or both. The function of the electronic control system is to monitor MGT operation through continuous, real time checking of its main operational parameters.

3. Operation modes

MGTs can usually operate in two modes:
1. **Non-cogeneration** (electricity production only): the MGT provides the electrical power required by the user and all the available thermal power is discharged to the flue.
2. **Cogeneration** (combined production of electrical and thermal energy): the MGT produces the electrical and thermal power required by the user. MGTs operating in cogeneration mode can usually be set to work with electrical or with thermal power priority.
   a. *Electrical priority operating mode*
      In this operating mode the MGT produces the electrical power set by the user, while heat production is regulated by the BPV installed before the HRB. This is not an energy efficiency-optimized operating mode, because in conditions of high electrical and low thermal power demand a considerable amount of the recoverable heat is discharged to the flue.
   b. *Thermal priority operating mode*
      Thermal priority operation involves complete closure of the MGT bypass valve, so that all the exhaust gases from the regenerator pass through the HRB for thermal power recovery. Thermal power production is regulated by setting the electrical power. This mode maximizes MGT efficiency in all operating conditions.

4. Performance and emissions

The considerations made so far apply to most MGTs. The data presented below have been obtained from theoretical studies and experimental testing of a specific machine, a Turbec T100 PH (Turbec, 2002), which the authors have been using for their research work for several years (Caresana et al., 2006). With due caution, these findings can be extended to most MGTs. In this section, the performance and emissions of a real MGT-based plant are reported and some criticalities connected to MGT behaviour highlighted.
The main performance parameters of an MGT are:

- electrical power P_{el};
- thermal power P_{th};
- electrical efficiency η_{el}, defined as:

$$\eta_{el} = \frac{P_{el}}{\dot{m}_f LHV} \tag{1}$$

- thermal efficiency η_{th}, defined as:

$$\eta_{th} = \frac{P_{th}}{\dot{m}_f LHV} \tag{2}$$

- total efficiency η_{tot}, defined as:

$$\eta_{tot} = \frac{P_{el} + P_{th}}{\dot{m}_f LHV} = \eta_{el} + \eta_{th} \tag{3}$$

where $\dot{m}_f$ and LHV are the mass flow rate and the Lower Heating Value of the fuel, respectively.

Since electrical power is the main final output, we have represented the dependence of the other performance parameters on P_{el} (Figures 3-7). Unless specified otherwise, the experimental data refer to ISO ambient conditions, i.e. temperature and relative humidity (R.H.) equal to 15 °C and 60 % respectively (ISO, 1989).
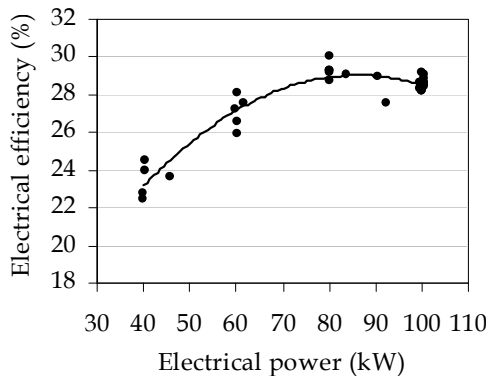
Fig. 3. Electrical efficiency

Figure 3 plots the trend of the electrical efficiency, which is consistently high from the nominal power down to a partial load of about 70 %, with a maximum slightly > 29 % around 80 kWe. Figures 4 and 5 report the thermal power and total efficiency data, respectively, for different degrees of BPV opening, calculated as the ratio between the thermal power recovered and that which can be recovered at the nominal power. The tests were conducted at a constant water flow rate of 2 l/s entering the HRB at a temperature of 50 °C.
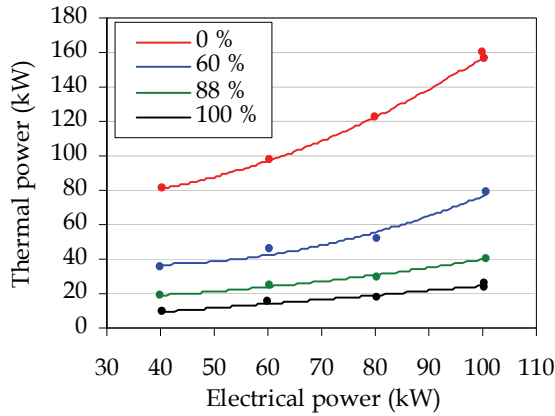
Fig. 4. Thermal power for different degrees of BPV opening
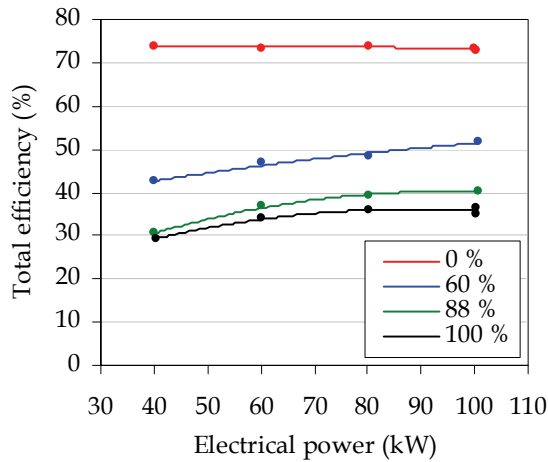
Fig. 5. Efficiencies for different degrees of BPV opening

As expected, greater BPV opening entailed a progressive reduction in the thermal power recovered, and consequently reduced total efficiency. This confirms that the thermal priority cogeneration mode maximizes fuel energy conversion efficiency. Figure 4 shows that a small part of the discharged thermal power is however transferred from the exhausts to the water, even with a completely open BPV. If this thermal power (about 25 kW at full load) is usefully recovered, total efficiency remains greater than electrical efficiency, as shown in Figure 5, otherwise total and electrical efficiencies necessarily coincide.

Figures 6 and 7 show the level of pollutants CO and NO_X, respectively. CO concentrations in the exhausts are low from 70 % to 100 % of the load, but they rise steeply with lower loads. The NO_X concentration is very low in all working conditions.
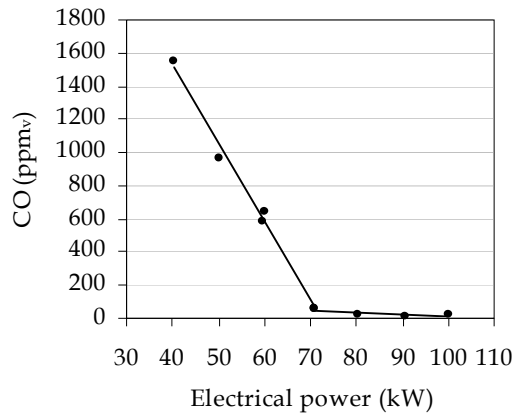
Fig. 6. CO concentration @ 15 % O_2
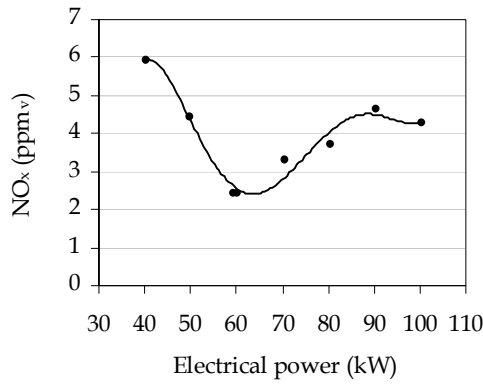
Fig. 7. NO_X concentration @ 15 % O_2
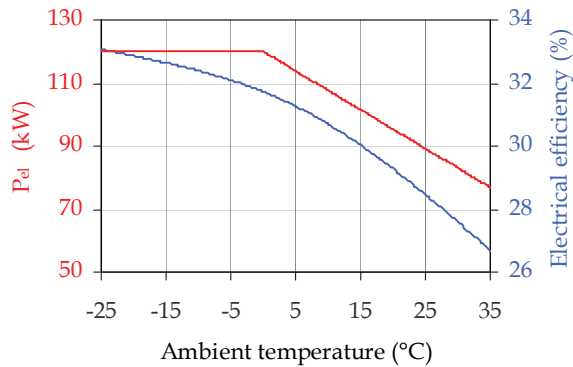
Fig. 8. Electrical performance vs ambient temperature

4.1 Influence of ambient parameters

The performance of MGTs, like those of GTs, are strongly affected by ambient conditions, particularly temperature. Figure 8 shows the values of nominal electrical power and efficiency as a function of the ambient temperature. In the T100 PH machine, electrical power generation at temperatures < 0 °C is limited electronically, to avoid overworking the machine. The decline observed at higher temperatures is explained by the lower air density and consequently lower mass flow rate through the power unit. A parallel decrease in electrical efficiency can also be noted.

4.2 Influence of heat recovery

The performance of a cogeneration system can be evaluated by comparison with the separate production of heat and electricity. The most commonly used index is the Primary Energy Saving (*PES*) index which, as the name suggests, quantifies the primary energy savings offered by a CHP plant compared with (conventional) separate production of electrical and thermal energy.

The *PES* index is calculated as (European Parliament, 2004):

$$PES = 1 - \frac{1}{\dfrac{\overline{\eta}_{el}}{\eta_{el\_ref}} + \dfrac{\overline{\eta}_{th}}{\eta_{th\_ref}}} \tag{4}$$

where:

- $\overline{\eta}_{el}$ and $\overline{\eta}_{th}$ are the electrical and thermal efficiencies of the cogeneration system averaged over a given period; and
- η_{el_ref} and η_{th_ref} are the reference values of efficiency for separate production of electrical and thermal energy.

A positive value of the index means that the primary energy consumption of the CHP system is lower compared with separate production over the time period considered. Figure 9 shows the *PES* index of a Turbec T100 PH in different operating conditions for
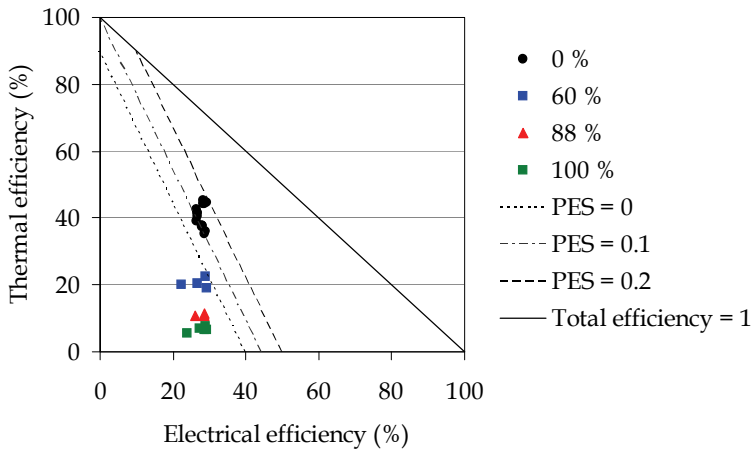
Fig. 9. PES for different degrees of BPV opening

different degrees of BPV opening, calculated considering values of 40 % and 90 % of η_{el_ref} and η_{th_ref}, respectively. It is worth noting that heat recovery is crucial to achieve a positive *PES*. In fact, even minor opening of the BPV adversely affects the index. This confirms that thermal priority operation (0 % BPV opening) is the mode maximizing fuel savings and consequently that it is preferable to the electrical priority mode.

5. Enhancing performances

As noted above, major limitations to the further spread of MGTs are their lower electrical efficiency compared with their main competitors, i.e. reciprocating engines, and lower electrical power production at rising ambient temperatures. Their main advantages, low emissions and competitive O&M costs, do not seem to offset these drawbacks.

In the following paragraphs we describe the research work being conducted by the Systems for Energy and the Environment team of Dipartimento di Energetica, Università Politecnica delle Marche, Ancona, Italy, to enhance MGT performance. We employed the same MGT model that was used to obtain the experimental performance and emissions data, focusing on:

1. Inlet Air Cooling (IAC);
2. Bottoming organic Rankine cycles;
3. Micro STIG;
4. Trigeneration.

5.1 Inlet Air Cooling (IAC)

The simplest way to limit the power reduction consequent to rising ambient temperature is to cool the air entering the compressor.

The air intake system of the MGT studied consists of a single duct carrying the working air and the cooling air, which both enter a single ambient inside the cabinet. From here part of the air is sucked in by the compressor, while the remaining air flow is conveyed to the cooling system via an external fan. Clearly, only the air processed by the compressor influences performance. Hence the need for separating the two flows, in order to cool only the working air. This can be achieved with minimum changes to the MGT cabinet and by mounting a cooling system in the working air inlet duct.

For the MGT model studied ice formation in the air flow and on the walls, a common risk in GTs, is excluded by the manufacturer, who states extreme working condition (-25 °C air temperature, 100 % R.H.) that are much more severe than those that can be achieved with any cooling system.

We used a test bed to evaluate two different IAC techniques:

- direct expansion IAC system;
- fogging IAC system.

The tests were conducted in the summer in the ambient condition of an Adriatic seaside town in central Italy.

Direct expansion IAC system

This system consists of a refrigerating engine, whose evaporator is housed directly in the working air intake duct. The refrigerating engine and the condenser fans are electrically driven by means of inverters, to improve efficiency. The system uses R507A as the refrigerating fluid and is designed to keep the inlet air temperature at the value set by the user, external ambient conditions and refrigerating engine power permitting. In fact,

although an inlet air cooled temperature of 15 °C (ISO, 1989) was set for all the tests, it was not reached consistently. As an example, Figures 10 and 11 show the electrical power and efficiency, respectively, in relation to ambient temperature, R.H., and corresponding IAC temperature over 200 time steps (about 15 min), with the machine working at maximum load. Since the R.H. was greater than the design R.H. (50 %), the minimum IAC temperature that could be achieved was slightly > 15 °C (about 17 °C).
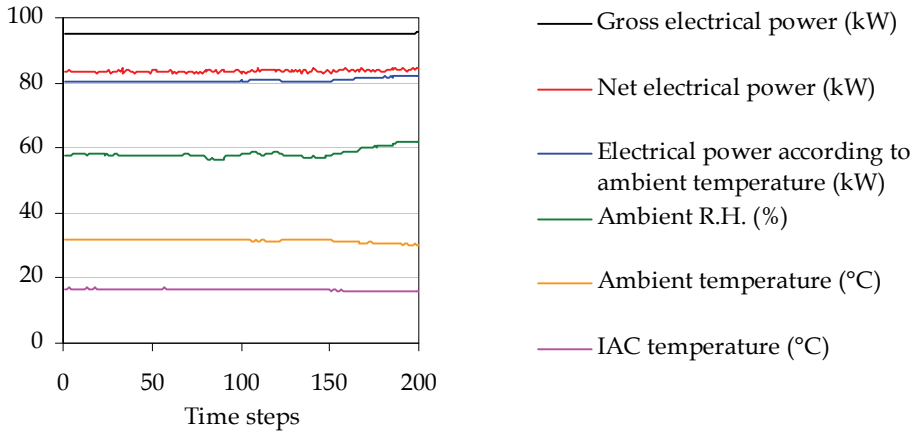

Fig. 10. Effects of the direct expansion IAC system on inlet air and MGT electrical power production
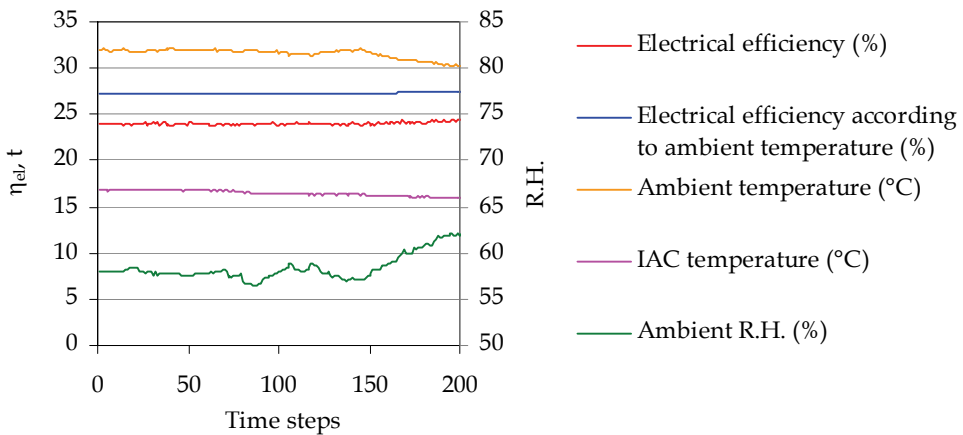
Fig. 11. Effects of the direct expansion IAC system on inlet air and MGT electrical efficiency

The IAC temperature induced a significant increase in gross electrical power production, from about 80 kW (without IAC) to around 95 kW.

However, the net electrical power, which is the crucial output, reached only 84 kW, due to the strong influence of the refrigerating engine performance: the lower its coefficient of

performance (COP), the higher its consumption and the lower the net electrical power of the MGT. The COP thus emerges as a crucial parameter, since an excessively low COP can entail a net electrical power even lower than the one without IAC. The COP measured during these tests was about 2.5. The power increase notwithstanding, the consumption of the refrigerating engine adversely affects the electrical efficiency of the MGT. To sum up, the direct expansion IAC system can be used to increase electrical power, but it does not enhance efficiency.

Fogging IAC system

This system cools the inlet working air via adiabatic saturation (Chaker et al., 2000). The main components of the apparatus are nozzles (4 in our test bed) and a high-pressure pump. Demineralized water is pumped at a pressure of 70 bar to the nozzles, housed in the intake duct, and is then nebulized as droplets whose diameter is usually < 20 μm (Chaker et al., 2002). The fogging system thus achieves nearly total adiabatic saturation by cooling the air to wet bulb temperature, which is the lowest achievable temperature, at an R.H. of about 100 %. For this reason, the final cool air temperature cannot be preset, but is strongly dependent on ambient conditions: the drier the air, the greater the temperature reduction. Figures 12 and 13 show electrical power and efficiency, respectively, over a period of 200 time steps with the machine working at its maximum load. Thanks to the IAC temperature, electrical power production increases from about 84 kW to 88 kW, but unlike in the direct expansion IAC system, here it is very close to the net electrical power, since the high-pressure pump consumes only 550 W. Furthermore, the fogging system slightly improves electrical efficiency, by about 1 %.

In conclusion, both IAC techniques were effective in limiting the electrical power reduction consequent to rising ambient temperature. Despite the comparable power gain, the fogging technique is however preferable, ambient conditions permitting, since besides enhancing efficiency it involves a much simpler and, last but not least, cheaper plant. Expansion techniques would be interesting if the refrigerating engine were also used for other purposes, such as air conditioning of large spaces (e.g. shopping malls, cinemas, office blocks). Since air conditioning plants are designed on the warmest local conditions, they work at partial load most of the time; the residual power could therefore be used for IAC.
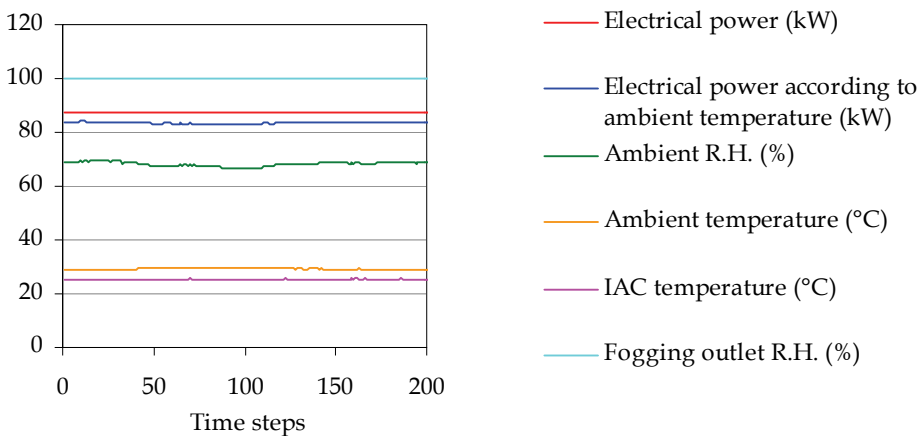

Fig. 12. Effects of the fogging IAC system on inlet air and MGT electrical power production
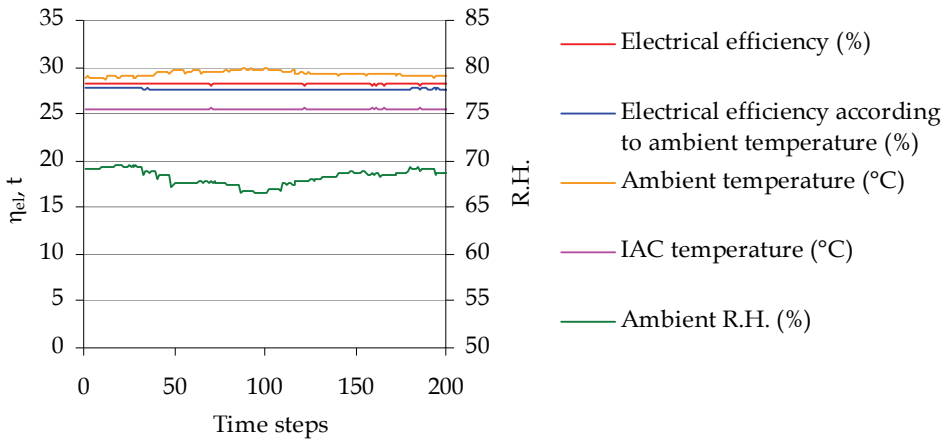
Fig. 13. Effects of the fogging IAC system on inlet air and MGT electrical efficiency

5.2 Bottoming organic Rankine cycles

The solution proposed here aims to enhance the electrical efficiency of the MGT by recovering the heat lost, producing additional electricity. This goal can be achieved with a micro combined cycle using bottoming organic Rankine cycles (Caresana et al., 2008). This micro combined configuration consists of an MGT, a Heat Recovery Vapour Generator (HRVG), and a bottoming vapour plant (Figure 14). This solution minimizes the changes to the standard CHP model, since it merely requires replacing the original HRB with an HRVG. The MGT exhausts enter the HRVG and are discharged to the environment after heating the bottoming working fluid. The vapour generated in the HRVG expands through a turbine that drives an electrical generator.

EG	Electrical Generator	GC	Gas Compressor
GT	Gas Turbine	CC	Combustion Chamber
R	Regenerator	C	Condenser
VT	Vapour Turbine	HRVG	Heat Recovery Vapour Generator
P	Pump		
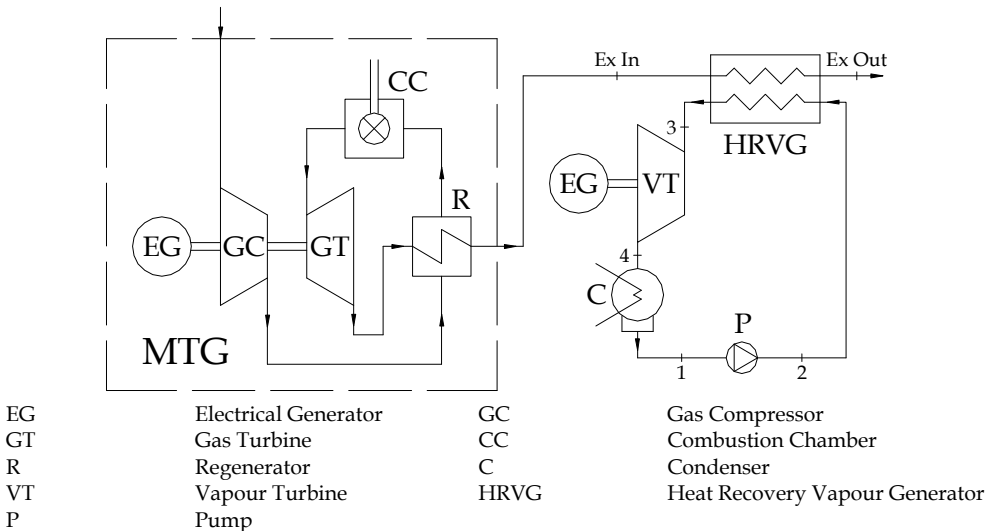
Fig. 14. Layout of the micro combined plant

Clearly, this configuration greatly affects the cogeneration plant's performance, since the thermal energy is discharged at the bottoming cycle condenser at very low temperatures.

Selection of the bottoming cycle working fluid

Whereas traditional, large-size, combined plants commonly use water as the bottoming cycle working fluid, organic fluids seem to be more appropriate in micro scale plants, because their thermodynamic properties are better suited to the low temperature of the exhausts leaving the MGT. Compared with steam, organic fluids allow both more compact solutions, by virtue of their higher density, and simpler layouts, by virtue of their significantly narrower density variation through evaporation and expansion.

This work does not examine some common, technically suitable organic fluids, i.e. chlorofluorocarbons (CFCs), because they have been banned (United Nations, 2000), and hydrochlorofluorocarbons (HCFCs), because they will be banned in the European Union, from January 1st 2015 (European Parliament, 2000). Therefore the choice necessarily falls on hydrofluorocarbons (HFCs) due to thermo-physical and technical criteria. In fact, the fluid in question needs to be:

- thermally stable in the range of pressures and temperatures involved in the cycles;
- non-toxic;
- non-corrosive;
- non-explosive;
- non-flammable;
- compatible with the plant's process component materials;
- low ozone-depleting;
- global warming-neutral.

HFCs meeting these criteria include R245ca, R245fa, R134a, R407C and R410A, the last two being mixtures. Their liquid-vapour curves are reported in a T-s diagram in Figure 15 and their critical properties in Table 1.
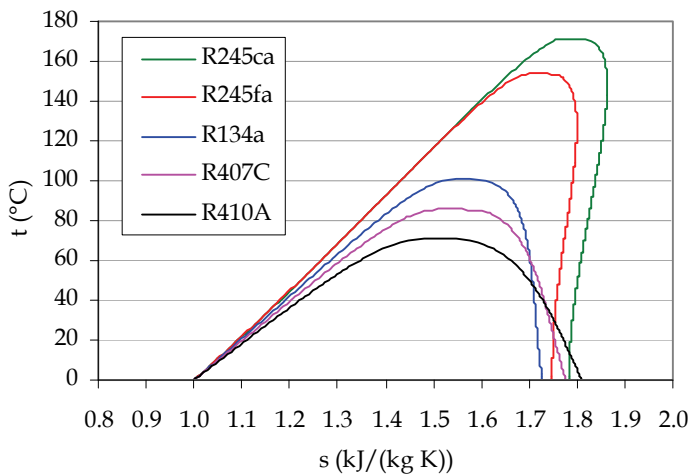
Fig. 15. T-s diagrams of five HFC organic fluids

In particular Figure 15 shows that R245fa and R245ca are "dry fluids", R407C and R410A are "wet fluids", and R134a is an almost "isoentropic fluid". A dry fluid is one whose vapour saturation curve with reference to a given temperature interval has a positive slope on a T-s diagram (dT/dS>0); a wet fluid is one having a negative slope (dT/dS<0), and an isoentropic fluid is a fluid having a vertical saturation line (dT/dS= ∞).

	R245ca	R245fa	R134a	R407C	R410A
Temperature (°C)	174.42	154.05	101.06	86.03	71.36
Pressure (MPa)	3.925	3.640	4.059	4.630	4.903

Table 1. Critical points of the five HFCs

Bottoming cycles

Vapour cycles can be: (i) non-superheated or Rankine type; (ii) superheated or Hirn type; or (iii) supercritical. Steam cycles are commonly superheated, due to thermodynamic efficiency requirements and to the need for limiting droplet condensation during vapour expansion through the turbine. With organic cycles the latter problem is partially addressed by proper selection of the working fluid. Use of a dry fluid prevents droplet condensation in the turbine even without superheating. In fact, at a suitable evaporating pressure the expanding dry fluid does not enter the liquid-vapour equilibrium zone and condensation does not take place, even starting from the saturated vapour line. However, superheating is still a valuable option, since the benefit of removing the superheater must be weighed against the consequent decrease in efficiency. In this subsection we present the results of simulations, performed with an in house-developed program, where different vapour cycle configurations were tested using the five organic fluids mentioned above.

Since the exhaust mass flow rate and outlet temperature of the MGT studied are known, the bottoming cycles can be defined completely by setting the values of the following parameters:

- vapour cycle condensing pressure, p_c ;
- HRVG pressure, p_v ;
- vapour cycle maximum temperature, t_3 .

Furthermore, setting the exhaust temperature at the HRVG outlet, $t_{Ex\ Out}$, allows calculation of the thermal power that can be recovered from the exhausts, P_{t_rec} , as:

$$P_{t\_rec} = \dot{m}_{eg} \cdot c_{p\_eg} \cdot \left(t_{Ex\ In} - t_{Ex\ Out} \right) \tag{5}$$

where $\dot{m}_{eg}$ and c_{p_eg} are the exhaust mass flow rate and its specific heat, respectively. Considering the HRVG as adiabatic, the organic fluid mass flow rate, $\dot{m}_V$, is therefore:

$$\dot{m}_V = \frac{P_{t\_rec}}{q_{in}} \tag{6}$$

where q_{in} is the heat received by the organic fluid unit of mass (see fluid states of Figure 14), which is equal to the increase in enthalpy through the HRVG:

$$q_{in} = h_3 - h_2 \tag{7}$$

The condensing pressure p_c depends closely on the temperature of the cooling fluid at the condenser, t_{cf_in}, and results in a condensing temperature, t_c, of:

$$t_c = t_{cf\_in} + \Delta t_{cf} + \tau \qquad (8)$$

where, as shown in Figure 16, Δt_{cf} is the temperature increase of the cooling fluid through the condenser and τ is the temperature difference between the condensing organic fluid and the cooling fluid at the outlet.

The values of τ and Δt_{cf} are the result of a technical and economic trade-off. The lower these values, the lower the condensing temperature and the greater the cycle's efficiency, as well as the heat exchanger's surface and cost. The study considers four condensing technologies, of which the water-cooled system is the most appropriate. However, it also addresses cooling technologies that reduce the amount of water needed, such as cooling towers, or that completely obviate the need for it, such as air condensers for use at sites where water is not consistently available. Finally, it examines condensation with water coming from a panel heating system, which makes the plant a micro combined cogeneration system. The condensing technologies considered, the assumed values of t_{cf_in}, Δt_{cf}, τ and the resulting t_c and p_c are reported in Table 2.
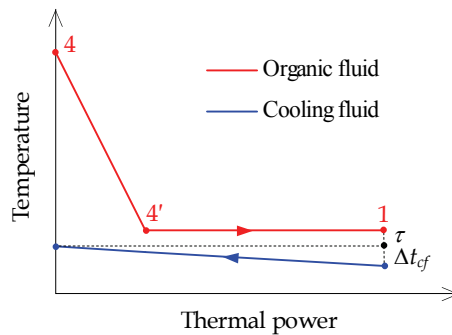
Fig. 16. Condenser heat exchange diagram

Condensing technology	t_{cf_in} (°C)	Δt_{cf} (°C)	τ (°C)	t_c (°C)
Condenser cooled by ambient air	15	8	7	30
Condenser cooled by ambient water	12	8	7	27
Condenser cooled by water from cooling tower	15	8	7	30
Condenser cooled by water from panel heating	30	5	7	42

Table 2. Main parameters of the condensing technologies

An air temperature of 15 °C and an R.H. of 60 % are assumed for condensers cooled by ambient air and by water from a cooling tower, according to the ambient ISO conditions considered for the gas cycle. In particular, the temperature of the water from the cooling

tower is assumed to be 4 °C warmer than the wet bulb temperature of the air, which is about 11 °C in ISO conditions. For the water cooled condenser, the ambient water temperature is assumed to be 12 °C. Finally, if the heat discharged by the vapour cycle is recovered in a panel heating plant, it is considered to require water at 35 °C, which then returns to the condenser at 30 °C.

Once p_c has been calculated, all relevant plant parameters can then be obtained using the set of equations listed in Table 3, where the indexes refer to the points in Figures 14-22 and the assumed efficiencies are listed in Table 4.

The efficiency of the combined plant was then optimized for Rankine, Hirn and supercritical bottoming cycles using this set of equations (eqs. 5-18).

For each condensing pressure, the optimization process involved identification of the combination of p_v and t_3 maximizing the efficiency of the combined plant and meeting the following conditions:

1. minimum vapour quality at the turbine outlet equal to 0.9;
2. minimum temperature difference, τ_{min}, of 15 °C between the exhausts and the organic fluid inside the HRVG.

The heat exchange and T-s diagrams of the different cycle configurations examined are reported in Figures 17-22.

Vapour cycle output heat per unit of mass	$q_{out} = h_4 - h_1$	(9)
Vapour cycle expansion work per unit of mass	$l_{turbine} = h_3 - h_4 = (h_3 - h_{4is}) \cdot \eta_{turbine}$	(10)
Vapour cycle pumping work per unit of mass	$l_{pump} = h_2 - h_1 = \dfrac{h_{2is} - h_1}{\eta_{pump}}$	(11)
Vapour cycle thermodynamic efficiency	$\eta = \dfrac{l_{turbine} - l_{pump}}{q_{in}}$	(12)
Vapour cycle electrical power	$P_{el\_V} = \left[\left(l_{turbine} \cdot \eta_{m\_t} \cdot \eta_{el\_g} \right) - \left(\dfrac{l_{pump}}{\eta_{m\_p} \cdot \eta_{el\_p}} \right) \right] \cdot \dot{m}_v \cdot \eta_{aux}$	(13)
Combined plant electrical power	$P_{el\_CC} = P_{el} + P_{el\_V}$	(14)
Combined plant electrical efficiency	$\eta_{el\_CC} = \dfrac{P_{el\_CC}}{\dot{m}_f \cdot LHV}$	(15)
Vapour cycle thermal power output	$P_{th\_CC} = \dot{m}_V \cdot q_{out}$	(16)
Combined plant thermal efficiency (panel heating system)	$\eta_{th\_CC} = \dfrac{P_{th\_CC}}{\dot{m}_f \cdot LHV}$	(17)
Combined plant global efficiency (panel heating system)	$\eta_{g\_CC} = \dfrac{P_{el\_CC} + P_{th\_CC}}{\dot{m}_f \cdot LHV}$	(18)

Table 3. Equations used to define the main parameters of the combined plant

Turbine efficiency	$\eta_{turbine}$	0.75
Turbine mechanical efficiency	η_{m_t}	0.98
Electrical generator efficiency	η_{el_g}	0.97
Pump efficiency	η_{pump}	0.70
Pump mechanical efficiency	η_{m_p}	0.98
Pump motor electrical efficiency	η_{el_p}	0.92
Auxiliary system efficiency (water-cooled condenser and panel heating system) *	η_{aux}	0.90
Auxiliary system efficiency (air condenser and cooling tower)*	η_{aux}	0.80
* The power used by fan coils is assumed to reduce the auxiliary system efficiency of the air-cooled condenser and of the cooling tower		

Table 4. Efficiency values assumed for the calculations
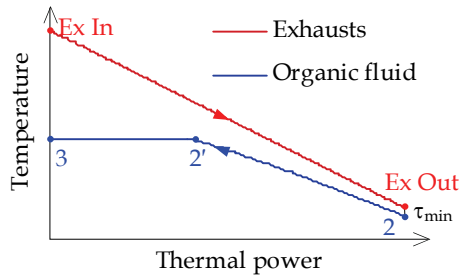
Fig. 17. Rankine cycle heat exchange diagram
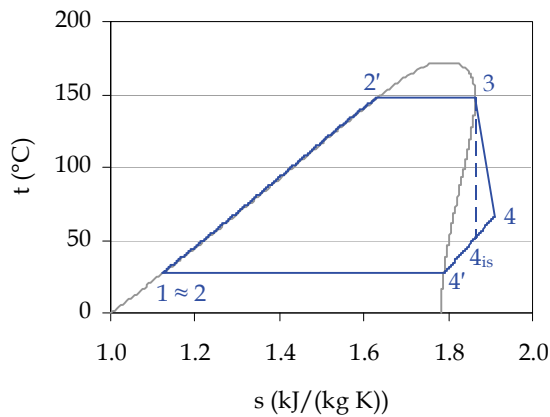
Fig. 18. Rankine cycle
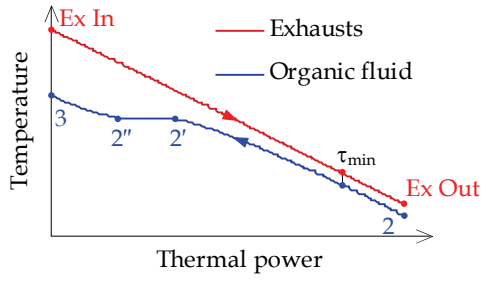
Fig. 19. Hirn cycle heat exchange diagram
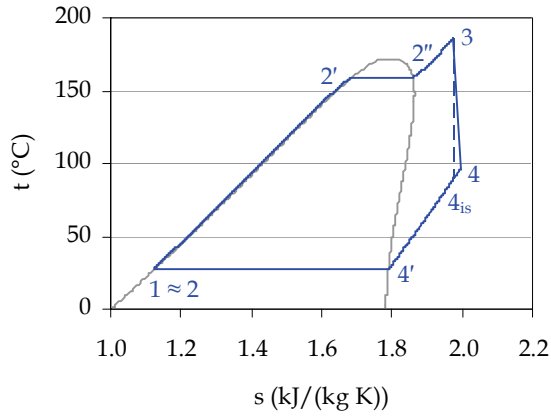
Fig. 20. Hirn cycle
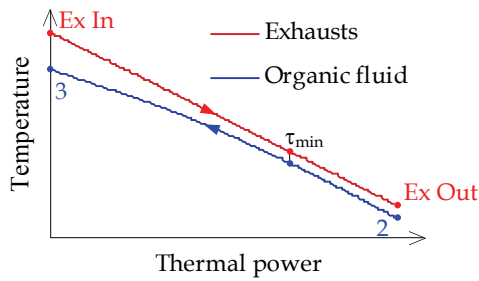
Fig. 21. Supercritical cycle heat exchange diagram
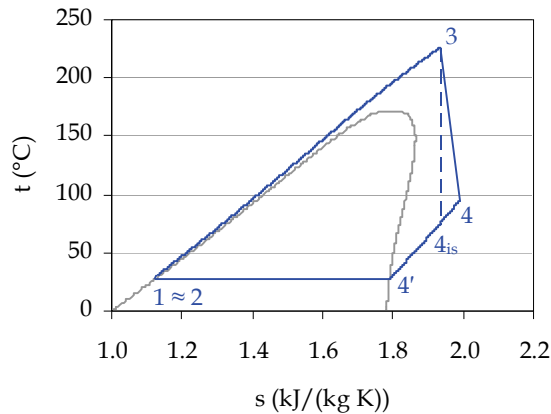
Fig. 22. Supercritical cycle

Performance and results

As expected, the optimization process highlighted that the ambient water condensing technology maximizes the power production of all bottoming cycle configurations with all the organic fluids studied, thus also maximizing both the power production and the electrical efficiency of the whole micro combined plant. The main results of the optimization processes for the ambient water condenser are reported for illustrative purposes in Table 5, where the operating data of each cycle configuration and organic fluid are compared. Only the dry fluids R245 ca and R245 fa are entered for the Rankine cycle. For the Hirn cycle the evaporating pressure is clearly lower than the critical one.

Table 5 shows the organic fluids R245ca and R245fa to be those offering the best performance, with slightly better results for the former. Even though these fluids can be employed in Rankine cycles, achieving an electrical efficiency of 36 - 37 %, compared with the original 30 % of the MGT, better results are achieved with the Hirn (37 %) and, especially, the supercritical cycle (37 - 38 %). The performances of the latter cycles are slightly better than that of the Rankine cycle, but they are based on significantly higher values of HRVG pressure and of t_3. The Rankine bottoming cycle therefore remains a good option, due to the lower pressure and temperature levels and to the simpler plant configuration.

The results of the optimization process of the ambient water condenser with R245fa supercritical cycles are shown in Figure 23, where the electrical power produced by the bottoming cycle is plotted as a function of the evaporating pressure and is parameterized with reference to the t_3.

The electrical power that can be achieved based on t_c with R245ca supercritical cycles as a function of the evaporating pressure is reported in Figure 24 with reference to the water cooling technology. These data are also representative of the other condensing technologies, the only difference being the efficiency of the auxiliary system.

Supercritical						
Working fluid	p_v (MPa)	t_v (°C)	η (%)	$\dot{m}_v$ (kg/s)	P_{el_V} (kW)	P_{el_CC} (kW)	η_{el_CC} (%)
R245ca	7.82	226	17.11	0.577	26.57	126.57	38.01
R245fa	8.92	226	16.51	0.594	25.66	125.66	37.74
R134a	8.25	181	13.71	0.702	21.13	121.13	36.38
R407C	8.33	161	11.78	0.736	17.89	117.89	35.40
R410A	9.65	160	11.74	0.716	17.66	117.66	35.33

Hirn						
Working fluid	p_v (MPa)	t_v (°C)	η (%)	$\dot{m}_v$ (kg/s)	P_{el_V} (kW)	P_{el_CC} (kW)	η_{el_CC} (%)
R245ca	3.72	186	16.24	0.586	25.37	125.37	37.65
R245fa	3.63	183	15.15	0.598	23.68	123.68	37.14
R134a	4.05	180	11.54	0.604	17.94	117.94	35.42
R407C	4.33	162	9.34	0.630	14.47	114.47	34.38
R410A	4.60	162	8.36	0.601	12.93	112.93	33.91

Rankine						
Working fluid	p_v (MPa)	t_v (°C)	η (%)	$\dot{m}_v$ (kg/s)	P_{el_V} (kW)	P_{el_CC} (kW)	η_{el_CC} (%)
R245ca	2.45	148	15.10	0.658	23.62	123.62	37.12
R245fa	2.31	129	13.66	0.728	21.32	121.32	36.43

Table 5. Condenser cooled by ambient water (t_c = 27 °C)
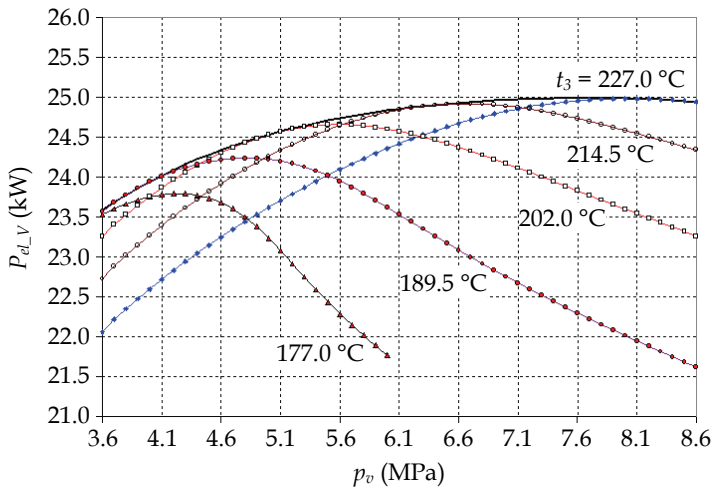
Fig. 23. P_{el_V} as a function of p_v and t_3 for an R245fa supercritical cycle at t_c = 27 °C
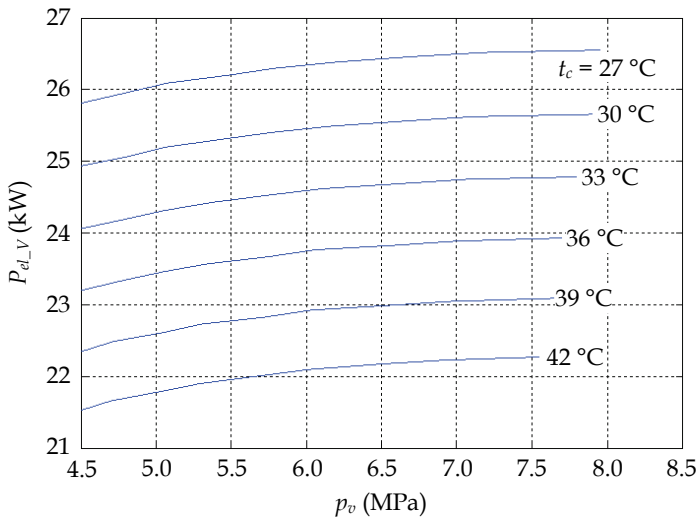
Fig. 24. P_{el_V} as a function of p_v and t_c for an R245ca supercritical cycle

Figure 24 confirms that the lower the condensing pressure, the more the electrical power generated; this applies to all the organic fluids studied. Nevertheless, despite the influence of the high condensing temperature on electrical performances, the cogeneration solution with the panel heating system results in increased global efficiency due to heat recovery.

5.3 Micro STIG

The acronym STIG stands for "Steam-Injected Gas" turbines, a technique used to improve the electrical and environmental performance of large-size GTs. The enhanced electrical power production and system efficiency are related to the different composition and quantity of the working fluid mass flowing through the turbine, due to the steam injected into the combustion chamber zone. The steam also involves a reduction in the combustion temperature and therefore of the NO_x formed in the exhausts.

Our group has recently addressed the advantages of applying the well-known STIG technique to MGTs, from a theoretical standpoint.

In the micro STIG plant layout reported in Figure 25 the original HRB is replaced with a heat recovery steam generator (HRSG), which produces the steam to be injected into the combustion chamber.

The aim was to devise a mathematical model of the micro STIG plant. Each component was defined by a set of equations describing its mass and energy balances and its operating characteristics, the most significant of which are the performance curves of the turbomachines.

The model was used to assess the influence of steam mass flow rate on electrical power and efficiency. Figures 26 to 28 report examples of the preliminary results obtained with the model. In particular, Figures 26 and 27 show electrical power and efficiency, respectively, as a function of the injected steam mass flow rate in fixed thermodynamic conditions (10 bar and 280 °C). Figure 28 shows, for a given flow rate (50 g/s), the trend of the electrical efficiency as a function of steam pressure and temperature.

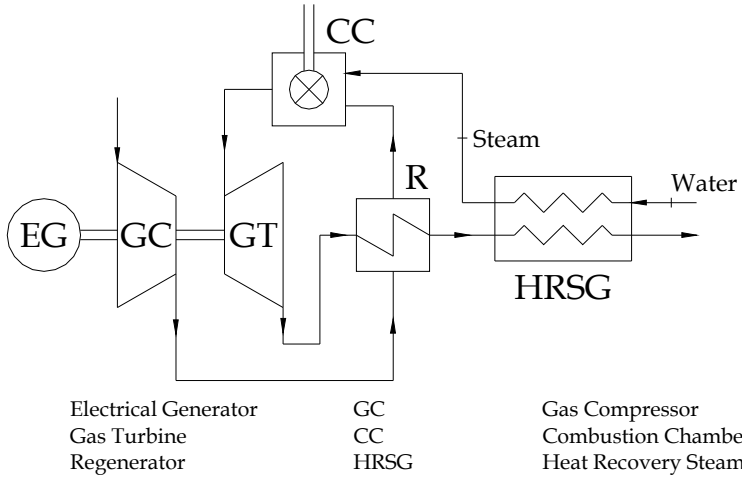| EG | Electrical Generator | GC | Gas Compressor |
| GT | Gas Turbine | CC | Combustion Chamber |
| R | Regenerator | HRSG | Heat Recovery Steam Generator |

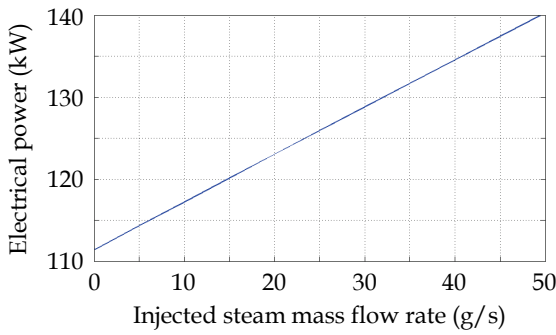Fig. 25. Layout of the STIG cycle-based micro gas turbine

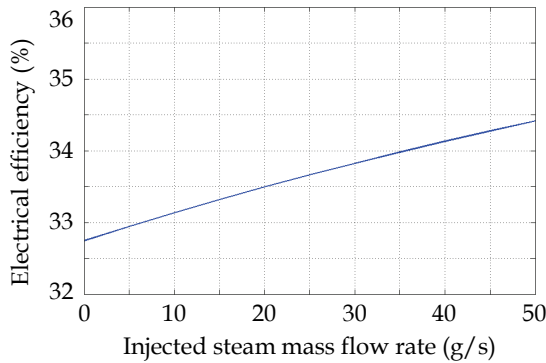Fig. 26. Electrical power vs. injected steam mass flow rate

Fig. 27. Electrical efficiency vs. injected steam mass flow rate

Preliminary simulations showed that the more steam is injected the greater are electrical power and efficiency. Nevertheless, the amount of steam that can be injected is affected on the one hand by the thermal exchange conditions at the HRSG—which limit its production—and on the other by the turbine choke line, which limits the working mass flow rate.

Once the amount of steam to be injected has been set, the higher its temperature and pressure, the greater the electrical efficiency.
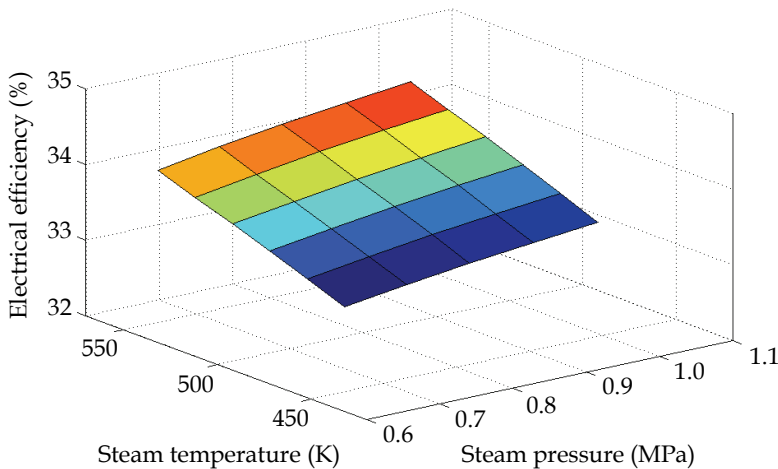
Fig. 28. Electrical efficiency vs. injected steam thermodynamic state

We are currently conducting a sensitivity analysis to assess the thermodynamic state and the amount of injected steam that will optimize the performance of the STIG cycle.

5.4 Trigeneration

The issue of heat recovery has been addressed in paragraph 4.2. Cogeneration systems are characterized by the fact that whereas in the cold season the heat discharged by the MGT can be recovered for heating, there are fewer applications enabling useful heat recovery in the warm season. In fact, apart from industrial processes requiring thermal energy throughout the year, cogeneration applications that include heating do not work continuously, especially in areas with a short winter. The recent development of absorption chillers allows production of cooling power for air conditioning or other applications. This configuration, where the same plant can simultaneously produce electrical, thermal and cooling power, is called trigeneration. The main components of an actual trigeneration plant, designed by our research group for an office block, is shown in Figure 29. The plant, whose data acquisition apparatus is still being developed, consists of a 100 kWe MGT (right) coupled to a heat recovery boiler (centre) and to a 110 kWf absorption chiller (left). The exhausts can be conveyed to the boiler or to the chiller, the latter being a direct exhausts model.

Fig. 29. Trigeneration plant

6. Conclusions

This overview of the state of the art of MGTs has highlighted the critical function of heat recovery in enhancing the energy competitiveness of the technology. Cogeneration or trigeneration must therefore be viewed as native applications of MGTs. The main limitations of the MGT technology are the high sensitivity of electrical power production to ambient temperature and electrical efficiency. The dependence on ambient temperature can be mitigated by using IAC techniques; in particular, the fogging system was seen to be preferable under all respects to an ad hoc-designed direct expansion plant.

Two options have been analysed to increase electrical efficiency: organic Rankine cycles and a STIG configuration. The former technology is easier to apply, since it does not require design changes to the MGT, but merely replacement of the recovery boiler with an organic vapour generator. Furthermore, the technology is already available on the market, since it has already been developed for other low-temperature heat recovery applications.

In contrast, the STIG configuration requires complete redesign of the combustion chamber, as well as revision of both the control system and the housing. Both technologies enhance electrical efficiency to the detriment of global efficiency, since both discharge heat at lower temperature, so that cogeneration applications are often not feasible.

7. Acknowledgements

8. References

Caresana, F.; Pelagalli, L., Comodi, G. & Vagni, S. (2006); Banco prova per la verifica delle prestazioni di una microturbina a gas ad uso cogenerativo, *Atti della Giornata Nazionale di Studio MIS-MAC IX, Metodi di Sperimentazione nelle Macchine,* pp. 207-218, ISBN: 88-89884-02-9, Trieste, March 2006

Caresana, F.; Pelagalli, L., Comodi, G. & Vagni, S. (2008); Micro combined plant with gas turbine and organic cycle, *Proceedings of the ASME Turbo Expo 2008,* Volume 1, pp. 787-795, ISBN: 978-0-7918-4311-6, Berlin, May 2008

Chaker, M.; Meher-Homji, C. B. & Mee III, T. R. (2000) Inlet fogging of gas turbine engines - Part A: Theory, psychrometrics and fog generation, *Proceedings of ASME Turbo Expo 2000*; pp. 413-428, Volume 4 A, Munich, May 2000

Chaker, M.; Meher-Homji, C. B., Mee III, T. (2002) Inlet fogging of gas turbine engines - Part B: Fog droplet sizing analysis, nozzle types, measurement and testing, *Proceedings of the ASME Turbo Expo 2002*; Volume 4 A, 2002, pages 429-441, Amsterdam, June 2002

European Parliament (2000). Regulation (EC) No 2037/2000 of the European Parliament and of the Council of 29 June 2000 on substances that deplete the ozone layer

European Parliament (2004). Directive 2004/8/EC of the European Parliament and of the Council of 11 February 2004 on the promotion of cogeneration based on a useful heat demand in the internal energy market and amending Directive 92/42/EEC

GTW (2009) - *Gas Turbine World Handbook 2009* – Volume 27

IEA (2002), International Energy Agency. *Distributed generation in liberalised electricity markets*. http://www.iea.org/textbase/nppdf/free/2000/distributed2002.pdf, OECD/IEA 2002

ISO (1989). ISO 2314: 1989, "Gas turbines - Acceptance tests"

Macchi E.; Campanari, S. & Silva, P. (2005). *La Microcogenerazione a gas naturale*. Polipress ISBN 8873980163 Milano.

Pepermans G.; Driesen J., Haeseldonckx, D., Belmans R. & D'haeseleer, W. (2005). Distributed generation: definition, benefits and issues, *Energy Policy*, 33 (2005), pp. 787–798, ISSN 0301-4215

Turbec (2002)."Technical description", D12451, Turbec AB, 17 June 2002

United Nations (2000). United Nations Environment Programme, Secretariat for The Vienna Convention for the Protection of the Ozone Layer & The Montreal Protocol on Substances that Deplete the Ozone Layer, "Montréal Protocol on Substances that Deplete the Ozone Layer as either adjusted and/or amended in London 1990 Copenhagen 1992 Vienna 1995 Montreal 1997 Beijing 1999", March 2000

Zogg, R.; Bowman, J., Roth, K. & Brodrick, J. (2007). Using MGTs for distributed generation. *ASHRAE Journal,* 49 (4), pp. 48-51 (2007), ISSN 0001-2491.

8

Gas Turbine Power Plant Modelling for Operation Training

Edgardo J. Roldán-Villasana[1], Yadira Mendoza-Alegría[1], Ma. Jesús Cardoso G.[1],
Victor M. Jiménez Sánchez[1] and Rafael Cruz-Cruz[2]
[1]Instituto de Investigaciones Eléctricas, Gerencia de Simulación
[2]Centro Nacional de Capacitación Ixtapantongo
México

1. Introduction

Of the \$11.4 billion worth of non-aviation gas turbines produced in 2008, \$9.6 billion—more than 80 percent—were for electrical generation (Langston, 2008). Particularly, in Mexico, about 15% of the installed electrical energy (no counting the electricity generated for internal consuming by big enterprises) is based on gas turbine plants (CFE web page), either working alone or in combined cycle power plants (and 8% produced directly by gas turbines) that offers an important roll in improving power plant efficiency with its corresponding gains in environmental performance (Rice, 2004).

The economical and performance results of a power plant, including those based on gas turbines, are directly related to different strategies like modernisation, management, and, in particular, the training of their operators. Although the proportion that corresponds to the training is difficult to be assessed, there exists a feedback from the plant's directors about improvement in speed of response, analysis of diverse situations, control of operational parameters, among other operator's skills, due to the training of the operation personnel with a full scope simulator. In general, all these improvements lead to a greater reliable installation.

The Comisión Federal de Electricidad (CFE[1], the Mexican Utility Company) generates, transmits, distributes and commercialises electric energy for about 27.1 millions of clients that represent almost 80 millions of people. About one million of new costumers are annually added. Basically, the infrastructure to generate the electric energy is composed by 177 centrals with an installed capacity of 50,248 MW (the CFE produces 38,791 MW and the independent producers 11,457 MW).

The use of real time full scope simulators had proven trough the years, to be one of the most effective and confident ways for training power plant operators. According to Hoffman (1995), using simulators the operators can learn how to operate the power plant more efficiently during a lowering of the heat rate and the reducing of the power required by the auxiliary equipment. According to Fray and Divakaruni (1995), even not full scope simulators are used successfully for operators' training.

---

[1] Some acronyms are written after their name or phrase spelling in Spanish. A full definition of the used acronyms in this chapter is listed in Section 13.

The Simulation Department (SD) belongs to the Electrical Research Institute (IIE) and is a group specialised in training simulators that design and implement tools and methodologies to support the simulators development, exploiting and maintenance.

In 2000 the CFE initiated the operation of the Simulator of a Combined Cycle unit (SCC) developed by the IIE based on ProTRAX, a commercial tool to construct simulators. However, because there is no full access to the source programs, the CFE determined to have a new combined cycle simulator using the open architecture of the IIE products. The new simulator was decided to be constructed in two stages: the gas-turbine part and the steam-heat recovery part. In this chapter the gas-turbine simulator development and characteristics are described.

2. Modelling approaches and previous works

There is not a universal method to simulate a process. The approach depends on the use the model will be intended for and the way it is formulated. A model may be used for different purposes like design, analysis, optimisation, education, training, etc. The modelling techniques may vary from very detailed physical models (governing principles) like differences or finite elements, to empirical models like curves fitting, in the extremes, with the real time modelling approach (for operators' training) somewhere in the middle. In fact there would be a huge task trying to classify the different ways a model may be designed.

Here, deterministic models of industrial processes are considered (ignoring the stochastic and discrete events models). The goal is to reproduce the behaviour of, at least, the variables reported in the control station of a gas turbine power plant operator in such a way the operator cannot distinguish between the real plant and the simulator. Thus, this reproduction may be made considering both, the value of the variables and their dynamics. The approach was a sequential solution with a lumping parameters approach (non-linear dynamic mathematical system based on discrete time). A description of the technique to formulate and solve the models is explained below in this chapter.

To accomplish with the described goal, the "ANSI/ISA S77.20-1993 Fossil-Fuel Power Plant Simulators Functional Requirements" norm was adopted as a design specification.

The models for operation training are not frequently reported in the literature because they belong to companies that provide the training or development simulators services and it is proprietary information (see, for example, Vieira *et al.*, 2008). Besides, Colonna & van Putten (2007) list various limitations on this software. Nevertheless, a comparison between the approaches of the IIE and other simulators developer was made, showing the first to having better results (Roldán-Villasana & Mendoza-Alegría, 2006).

Some gas turbine models have been reported to be used in different applications. A common approach is to consider the work fluid as an ideal gas. All the revised works report to have a gas turbine system like the presented in Figure 1.

A dynamic mathematical model of a generic cogeneration plant was made by Banetta *et al.* (2001) to evaluate the influence of small gas turbines in an interconnected electric network. They used Simulink as platform and they claim that the model may be utilised to represent plants with very different characteristics and sizes, although the ideal gas assumption was used, the combustor behaves ideally and no thermodynamic properties are employed.

Kikstra & Verkooijen (2002) present a model based on physical principles (very detailed) for a gas turbine of only one component (helium). The model was developed to design a control system. No details are given concerning the independent variables. The model validation was performed comparing the results with another code (Relap).
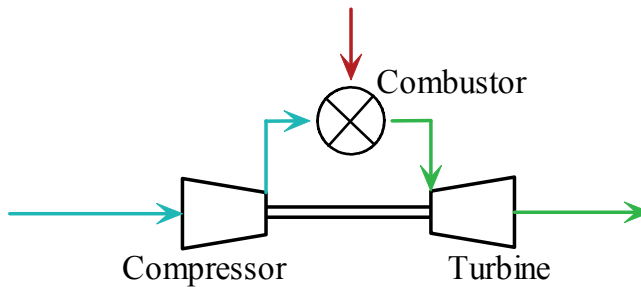
Fig. 1. Typical simplified gas turbine representation.

Ghadimi *et al*. (2005) designed a model based on ideal gas to diagnostic software capable of detecting faults like compressor fouling. The combustion was considered perfect and no heat losses were modelled. The fouling of the compressor was widely studied. No information was provided regarding the input variables.

Jaber *et al*. (2007) developed a model to study the influence of different air cooling systems. They validated the model against plant data. An ideal gas model was considered and the gas composition was not included. The input data were the ambient conditions and the air cooling system configuration. The combustion was simulated with a temperature increase of the gas as a function of the mass flow and the fuel high heating value.

A model for desktop for excel was elaborated by Zhu & Frey (2007) to represent a standard air Brayton cycle. The combustor model considers five components and the combustion reaction stoichiometrics with possibilities of excess of oxygen. Instead using well known thermodynamic properties, the output temperatures of the turbine are a second degree equation in function of the enthalpy. The inputs are variables like efficiencies, some pressure drops, temperatures, etc. This approach is not useful for a training simulator.

A model to diagnose the operation of combined cycle power plants was designed by González-Santaló *et al*. (2007). The goal was to compare the real plant data with those produced by a model that reproduces the plant variables at ideal conditions. The combustor was modelled considering a complete combustion like a difference between the enthalpy of formation of the reactants and the combustion products. Compressors and turbines take into account the efficiencies (adjusted with plant results) and the enthalpies of the gases (but no information was provided how the enthalpies are calculated as a function of measured plant data).

Kaproń & Wydra (2008) designed a model based on gas ideal expansion and compression to optimise the fuel consumption of a combined cycle power plant when the power has to be changed by adjusting the gradient of the generated power change as a function of the weather forecast. In the conclusions the authors point that the results have to be confirmed on the real plant and that main problem is to develop highly accurate plant model.

Rubechini *et al.* (2008) simulated a four stage gas turbine using a fully three-dim, multistage, Navier-Stokes analyses to predict the overall turbine performance. Coolant injections, cavity purge flows and leakage flows were included. Four different gas models were used: three based on gas ideal behaviour (the specific heat *Cp* evaluation was the difference among them) and one using real gas model with thermodynamic properties (TP) from tables as basis of the modelling. The combustion was not simulated. The conclusion was that a good model has to reproduce the correct thermodynamic behaviour of the fluid.

Even when detailed modelling of the flow through the equipment, heat transfer phenomena and basing the process on a temperature-entropy diagram, the ideal gas assumption was present (Chen *et al.*, 2009). In this case the gas composition was neglected, (considering only an increase of the temperature) and the model, designed for optimisation, runs around the full load point.

Watanabe *et al.* (2010) used Simulink to support a model to analyse the dynamical behaviour of industrial electrical power system. An ideal gas approach was used. The governor system model and a simple machine infinite bus were considered (with an automatic voltage regulator model). The model was validated against real data. No details of the combustor model are mentioned.

None of the works revised here, mentioned anything about real time execution. In the present work, the total plant was simulated, including the combustion products and all the auxiliary systems to consider all the variables that the operator may see in his 20 control screens and all the combinations he desires to configure tendency graphs. For example, the set compressor- combustor –turbine was simulated considering the schematic presented in Figure 2.

The real time execution that is required for a training simulator is accomplished by the IIE simulator.
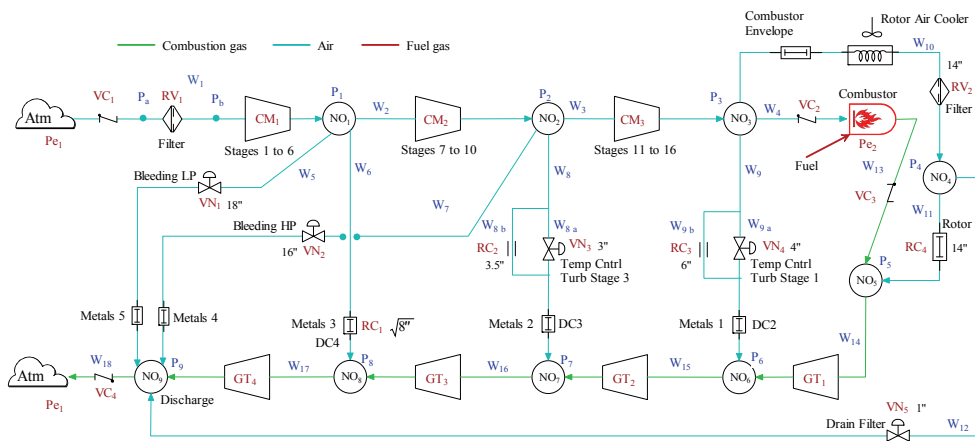
Fig. 2. Schematic gas turbine-compressor-combustor diagram.

3. The importance of training based on simulators

Some of the significant advantages of using training simulators are: the ability to train on malfunctions, transients and accidents; the reduction of risks of plant equipment and personnel; the ability to train personnel on actual plant events; a broader range of personnel can receive effective training, and   eventually, high standard individualised instruction or self-training (with simulation devices designed with these capabilities in mind).

A cost benefit analysis of simulators is very difficult to be estimated; especially because "what would have happened if…" situations should be addressed. However, in a classical study made at fossil fuel power plants simulators (Epri, 1993) there are identified benefits of simulators in four categories: availability savings, thermal performance savings, component

life savings, and environmental compliance savings. It is estimated a payback of about three months. Most often, the justification for acquiring an operator training simulator is based on estimating the reduction in losses (Hosseinpour & Hajihosseini, 2009).

This is easy to probe for high-capacity plants where savings approach millions of dollars for a few days of lost production. Justification also comes from the ability of the simulator to check out the automation system and provide operators with a better understanding of a new process. With greater exposure to the simulator, operators gain the confidence to bring the plant up and running quicker, thus shortening startups significantly and improving the proficiency of less-experienced operators in existing plants. Specifically in Mexico, in a period of 14 years, the use of simulators for operators' training has estimated savings of 750 millions dollars for the power plants (Burgos, 1998).

In Mexico exist three training centres based on simulators: the Laguna Verde Nuclear Power Plant Training Centre, the Geothermal Training Centre, and the National Centre for Operator's Training and Qualification (CENAC), the three of them belong to CFE and have infrastructure developed by the IIE.

Roldán-Villasana *et al*. (2006) show that in the Geothermal Training Centre, according to their statistics for the Cerro Prieto generation plants, the number of trips due to human errors and also the percentage of this kind of trips regarding the total numbers of trips have been diminishing through time since 2000 when the Centre began its training program. The operational cost of the training centre is inferior to the cost of the non generated energy because of trips due to human errors (considering only Cerro Prieto power plants).

The CENAC, a class world company, is the main centre in Mexico where the training of the operation personnel based on simulators is achieved. This centre attends people that work in fuel fossil generation plants, including combined cycle and gas turbine. Also trains operational workers of the independent producers (that base their production in combined cycle plants).

The CENAC receives in periodical basis information (retrofit) from its users that allows the improvement and development of new training technologies, considering from adjustments on their training plans to the changes on the scope or development of new simulators to meet the particular needs of the production centres.

The CENAC's commitment is provide excellent services, ensuring to the producers high levels of quality training not only within the technical areas but in all their processes:
- To guarantee, within a competency framework and updated technology, the continuous electricity service, in terms of quantity, quality and price, with well-diversified sources of energy.
- To optimize the utilization of their physical, commercial, and human resources infrastructure.
- To provide an excellent service to its clients.
- To protect the environment.
- To promote the social development.
- To respect the values of the population who live in the new areas of electrification.

The SD has developed diverse work related with the training. The main covered areas by the IIE developments are: computer based training systems, test equipment simulators, and simulators for operators' training. Tables 1, 2 and 3 summarise the development indicating the year they were delivered to the costumers.

Computer Based Training Systems	Year
Computer-Based Training System Web Version	2003
Substation Operator System Training Simulator with a Static Vars Compensator	2005
Computer Based Training System by Internet.	2007
Virtual Reality System for the Transmission Lines Maintenance Personnel	2008

Table 1. Computer based training systems developed by the IIE.

Testing Equipment Stimulated Simulators	Year
Real-time Simulator for Synchronous machines SITIRAMS I.	1995
SITIRAMS II y III.	1996
Update of the Simulator System for Tests of Excitation	2005
Expanding the Applications of the Simulator System for Tests of Excitation	2008
Simulation Module to Test Hydraulic Governors Responses	2008

Table 2. Testing Equipment Stimulated Simulators developed by the IIE.

Present and near future developments include: a scope extension of the virtual reality system for the transmission lines maintenance personnel; duplication of the simulator system for tests for speed control and voltage regulator; national network simulation for the simulator system for tests for speed control and voltage regulator; simulator for training of the operators of a generator experimental rig; module for malfunction analysis of simulated equipments; training centre of hydrocarbon process (with at least eight full scope simulators); and simulators maintenance and clients support.

4. Reference plant

In order to have a comparison point, all the simulators developed by IIE have a reference plant. For this particular simulator the unit 5 of the power plant "El Sauz", located in Querétaro, in the middle of the Mexican territory, was selected as the reference plant. The choice of this plant was based on the geographical proximity of the plant with the CENAC and IIE installations (to optimise the information compilation) and the availability of the design and operational data. In the plant, the used fuel is natural gas provides by PEMEX to produce a nominal electric power of 150 MW. The plant is a pack generation unit Econopac 501F from Westinghouse. This unit is formed for the gas turbine, the generator and the auxiliary systems, and uses a system of low nitrogen oxide emissions DLN2. In Figure 3 a general view of a gas turbine power plant is presented.

The plant was designed to operate in simple cycle with natural gas only. The primary equipment consists of a combustion turbine which impulse the hydrogen-cooled generator. The gas compressor-turbine system handles the fuel into a stream of compressed air. It has an upstream air axial flow compressor mechanically coupled to a downstream turbine and a combustion chamber in between. Energy is released when compressed air is mixed with fuel and it is burned in the combustor. The resulting gases are directed over the turbine's blades, spinning the turbine, and mechanically powering the compressor and rotating the generator. Finally, the gases are passed through a nozzle, generating additional thrust by accelerating the hot exhaust gases by expansion back to atmospheric pressure.

Simulators for Operators' Training	Year
Simulator I of a 300 MW Thermal-Electric Units	1984
Simulator of the Collective Transport System (Metro) of Mexico City	1991
Laguna Verde Nuclear Power Plant Simulator	1991
Partial Scope Simulator for Turbine Rolling Operations	1993
Simulator of a 350 MW Units	1994
Simulator of a 110 MW Geo Thermal-Electric Unit	2003
Simulator of a 350 MW Dual Unit (Coal and Fuel)	2006
Simulator of the Systems of a 300 MW Thermal-Electric Unit	2006
Simulator of Thermal-Electric Units Based on Screens	2006
Simulator of a 25 MW Geo Thermal-Electric Unit	2006
Hydrocarbon Processing Simulator Prototype of a PEP Platform	2006
Gas Turbine of a 150 MW Power Plant Simulator	2007
Combined Cycle 450 MW Power Plant Simulator	2009
Simulator of a Dual Unit with Operation Tracing	2009
Simulator of a Combined Cycle Unit with Operation Tracing	2009
Simulator for Boilers Analysis	2009
Graphic System for the Developments of Simulators	2009

Table 3. Simulators for Operators' Training developed by the IIE.

Fig. 3. General view of a gas turbine power plant.

Other plant systems that support the open cycle are: heating; ventilation and air conditioning; fire system; electrical distribution; equipment for excitation; mechanical package; lubrication oil; sealing oil of the generator; generator cooling (water/glycol); fuel gas; compressor water wash; electric turbine starting; compressed air; instrument and control air; combustor; and generator cooling air.

The plant is controlled by a Siemens TelepermXP (TXP) Digital Control System.

5. Configuration of the simulator

5.1 Hardware configuration

The gas turbine simulator consist of four PC interconnected through a fast Ethernet local area network. Each PC has a mini-tower PentiumDTM processor with 3.6 GHz, 1GB of RAM memory, 40GB HD, and Windows XP as operating system. Figure 4 shows a schematic of this architecture.
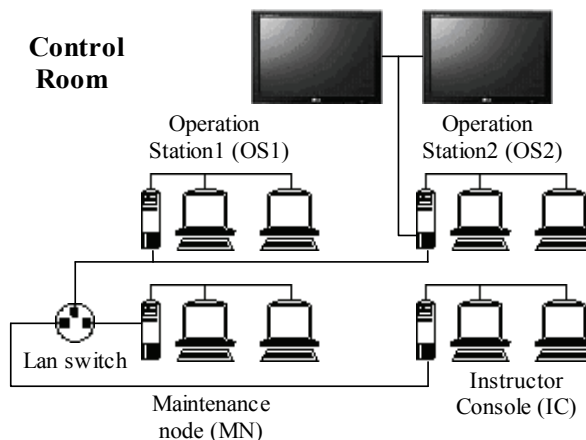
Fig. 4. Hardware architecture of the gas turbine simulator.

From the Instructor Console (IC), also named simulation node, the simulation sessions are initiated and guided. It has two 20" flat panel monitors. There exists two Operators' Stations (OS) that replicate the real control stations from the plant. The trainee uses four 20" monitors and two 54" screens to manage and control the simulated power plant. There is an additional PC, the maintenance node (MN), that is used to make modifications to the software, process or control models and where they are tested and validated by an instructor before to install it in the simulator. Also it is used as a backup of the IC. Figure 5 shows the real simulator architecture (without the MN) during a training session where the IC and the instructor appear in the first plane and the OS and two operators are at the rear.

5.2 Software configuration

The simulator was developed under Windows XP and was programmed in Visual Studio Net, Fortran Intel, Flash and VisSim. The Simulation Environment (MAS[2]), the development

---

[2] The simulation environment is proprietary software of the IIE. Also they are the generic models. The internal reports that sustain these works are not referenced here.

Fig. 5. Training session in the gas turbine simulator.

platform, has three main parts (the real time executive, the operator module, and the instructor console module). Each of these modules is hosted in a different PC, and they are communicated through a TCP/IP protocol. All the modules of the simulation environment are programmed with C# (Visual Studio), with the exception of the Flash applications.

The MAS was designed as a general tool for the SD to develop simulators. The MAS is a very useful software that acts like a development tool and like the simulator man-machine interface (MMI). The MAS basically consist of three independent but coordinated applications: the real time executive, the operator module, and the instructor console.

Real Time Executive

The real time executive coordinates all simulation functions; it is constituted for six modules according Figure 6.
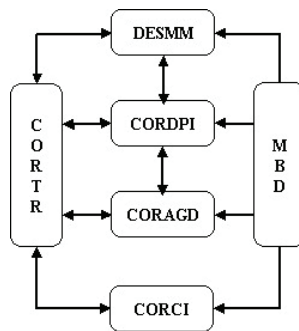
Fig. 6. Diagram of the real time executive application.

1. DESMM Mathematical model launcher. Its function is to manage the execution sequence of each mathematical model. These models may be executed in a parallel scheme, with a distributed architecture of PCs or with multi-core equipment. For the case of the gas turbine simulator, the models run sequentially.
2. CORDPI Manager module for interactive process diagrams (IPD). This module executes the IPD, provides the values of the variables, and receives/responds from/to the

control commands messages of the operator console. Other functions of the module are: to control the alarms system, to control the historical trends, to call the methods of each IPD component (valve, pump, etc), refresh each IPD periodically, and to coordinate the sequence of events in the operation consoles.

3. CORAGD Manager module for the global area of mathematical models. It is composed of a group of methods to initialise the global area of state variables belonging to the mathematical models. These values are located in a table loaded in memory for a fast access. This module is also in charge of synchronise the access of the table when parallel process attempt to connect it.

4. CORCI Manager module for the instructor console. This module receives/responds the commands from/to the instructor console (stop, freeze, malfunctions, etc.) and executes the tasks in a synchronised way during a simulation cycle. With the TCP/IP communication, this module may be hosted in a different PC of the instructor console.

5. MBD Data base driver. It is devoted to get, from each data base table, all the required information by the executive system.

6. CORTR Main module. This is the main module of the simulator and coordinates all the functions of the mentioned modules.
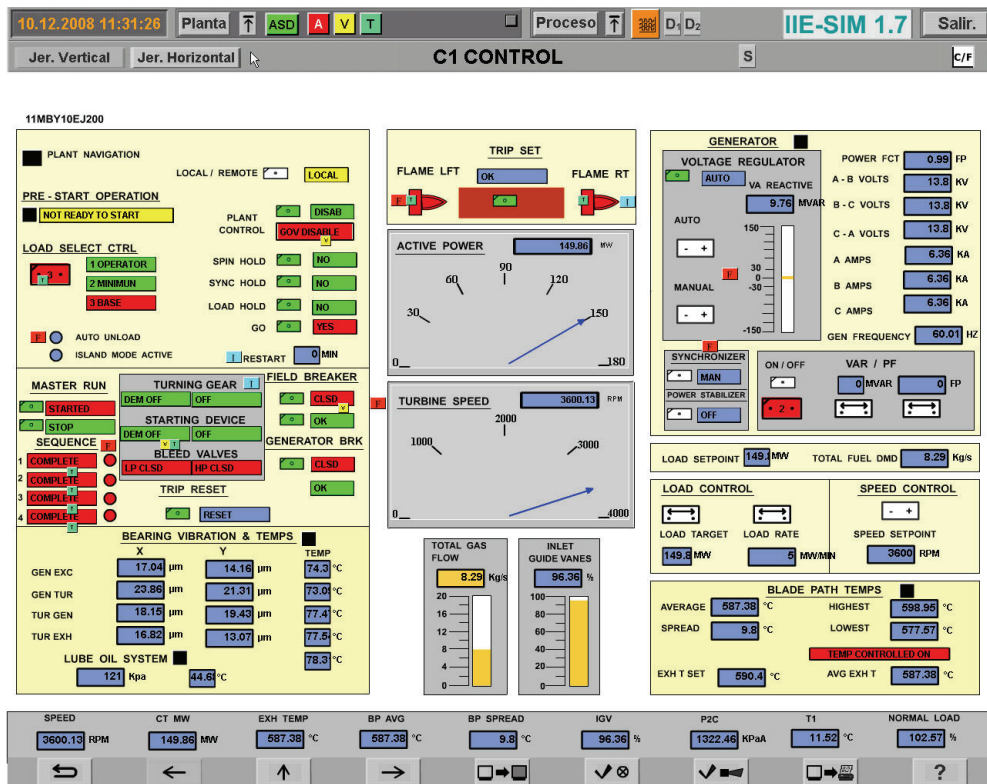
Fig. 7. Main display of the operator console.

Operator Module

The operator module is a replica of the real control screens or IPD and it manages the information flow with the executive system through the CORDPI module. A channel of bi-directional information is established through a TCP/IP socket. The IPD, than may be seen as the MMI are Flash movies inserted in a "Windows way", using the "Fscommand" interface for the communication. A total of 20 control screens, including the index, and as many tendencies displays as needed are available for the operator.

The main control screen of the operator (a replica of the Siemens control) is shown in Figure 7. The flash movies have both, static and dynamic parts. The static part is constituted by drawings of particular control screens and the dynamic part is configured with graphic components stored in a library, which are related to each one of the controlled equipments (pumps, valves, motors, etc.). These components have their own properties and they are employed during the simulation execution. An example of a tendency graph (during a plant trip) is shown in Figure 8.
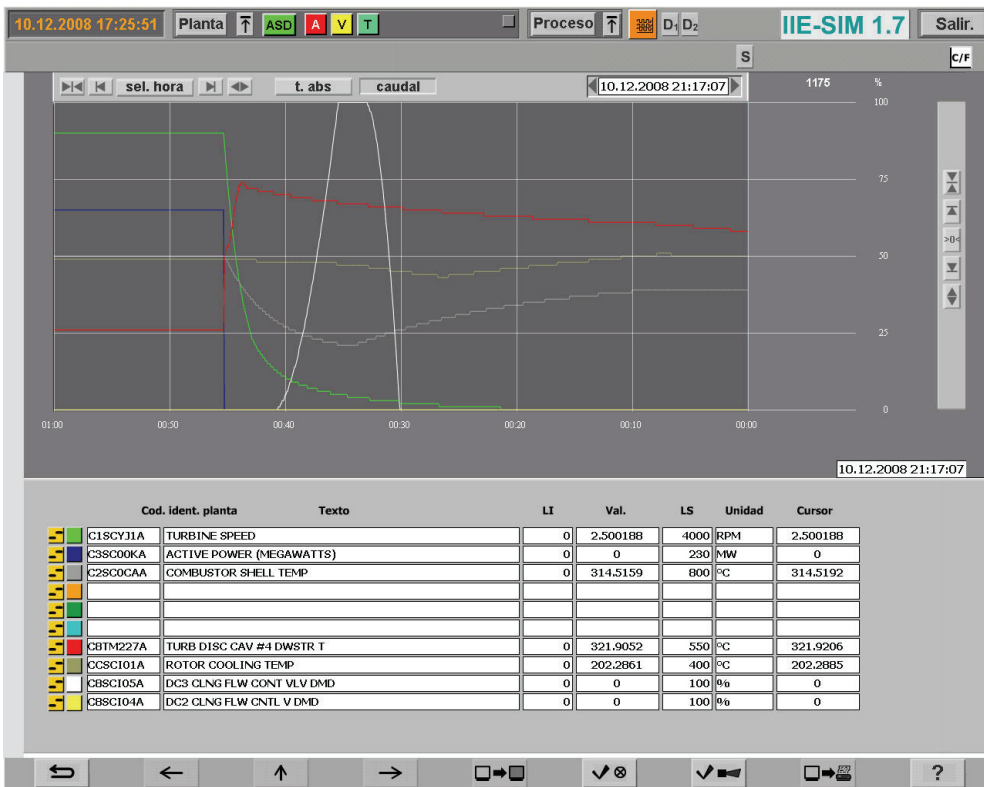
Fig. 8. Main display of a tendency graph.

The main parts of the operator module are:

1. A main module (an "Action-script" code) that loads the interactive process diagrams and gets information about the properties of the movie components.

2.   A module to exchange information with the main module and with the executive system.
3.   A module for the TCP/IP communications.

As a result of these functions, the operator (student) perceives his actions and simulator response in a very close way as it happens in the actual plant.

Instructor Console

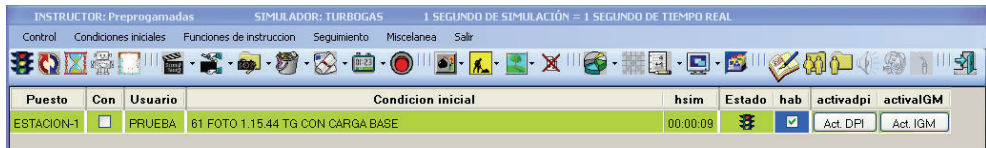This module is the MMI of the instructor and has a main menu of functions which is presented in Figure 9.

Fig. 9. Main display of the instructor console.

The IC is constituted by five modules:
1.   A main module to execute all the tasks related with the graphical interface of the instructor (DPI).
2.   A module to retrieve the static information of the simulation session, for instance, malfunctions, remote actions, etc. (CONINS)
3.   A module to store information in a data base using SQL (DBSM).
4.   The mathematical models.
5.   A module to communicate the instructor console with the real-time executive (Console Application).

In the IC the simulation session is controlled. The functions of the IC may be invoked from the list menu of the display with the mouse pointer; the functions are popped up to be selected. However, thanks that the instructor has a modified copy of the operator control screens where may follow the actions of the students some of them may be accessed from the IPD by special icons. In Section 6, the functions of the IC are fully described.

5.3 Processes and control models

To simulate the gas turbine power plant, this was divided into a set of systems (procuring these coincide with the real plant systems). A modelled system is a mathematical representation of the behaviour of the variables of the real system of the gas turbine gas power plant. The model of a simulated system (MSS), once installed in the simulator, respond to the operator's action in the same way that the real systems do (in tendency and time). Typically, the final equations are stated for each MSS system in such a way the set of equations of one MSS is mathematically independents of the set of equations of any other MSS.

Now, for each MSS the algebraic equations have to be solved simultaneously if necessary but they are mathematically independent of their differential equations. For the development of simulators, the IIE has adapted different solution methods for both, linear and non-linear equations (Newton-Raphson, Gaussian elimination and bisection partition search) and are used depending on the structure of each particular model.

The differential equations are numerically solved with one of the available methods (Euler, trapezoidal rule with one or two corrections). The integration step of the equations depends on the dynamical response of the system. The selection of the proper integration method for

a MSS is made running the model under a multistep multirate method to determine its "critical transient" (that, where the method reports more potential numerical instabilities). A numerical analysis is made on that point to determine the final method and step that the MSS should use (this analysis involves the calculation of Jacobian matrixes, the calculation of eigenvectors and eigenvalues and its relation with the state variables).

Each execution second (cycle) of the simulator was divided into ten periods of 0.1 s (frames). Thus, a particular model could be executed with an integration step of 0.1 s, 0.2 s, 0.5 s or 1 s. The sequence matrix (defined by the user) indicates the precedence of execution of the models (scheduler), the integration method and integration step of each model, and the initial period of execution of each model for each cycle.

The sequence matrix was defined using an algorithm to find an appropriated execution order. The algorithm considers the number of inlet and outlet variables between the models and the integration step to minimize the probability of mathematical instabilities.

For example, if a simulator had four MSS, let say M1, M2, M3 and M4 and three integration methods, a sequence matrix as defined in Table 4, means that model M2 is the first in being executed in the first frame (it is integrated with the method 1 and has a step of 0.1s), followed by model M1 (method 3, step 0.2s); in the second frame model M4 (method 2, step 0.2s) is executed followed by model M2; in the third frame model M3(method 1, step 0.5s) is executed, followed by models M2 and M1; the sequence continues in the same way.

Model	Frames (10 frames is a second or cycle)									
	1	2	3	4	5	6	7	8	9	10
M3			1					1		
M4		2		2		2		2		2
M2	1	1	1	1	1	1	1	1	1	1
M1	3		3		3		3		3	

Table 4. Example of a sequence matrix.

6. Instructor console

This is the main MMI for the instructor, from where the simulation sessions are initiated and guided. From there, the instructor controls and coordinates the scenarios seen by the operator under training. These scenarios could be presented to the operator as a steady state of the plant operation or under any malfunction of a particular system or equipment. To perform his tasks, the IC has a set of functions that may be invoked from the list menu of the display with the mouse pointer; the functions are popped up to be selected. The instructor has a modified copy of the operator control screens, from where can follow the actions of the students. Additionally, in these control screens some of the IC functions may be accessed from the DPI in special icons. An example of the functions displayed by pop-up in presented in Figure 10.

The main functions of the IC are explained in the following sections.

6.1 "CONTROL" menu (Control)
It has the functions that allow the instructor to define the simulator's status.

Run/Freeze. The instructor may start or freeze a dynamic simulation session.

Repetition. A simulation session can be repeated automatically including the actions of the operator and the instructor on the simulator.

Simulation speed. Normally, the simulator is executed in real time, but the instructor may execute the simulator up to ten times faster or ten times slower than real time. For example, slow thermal processes such as the cooling of the plant after a shut down process can be simulated to occur faster. Also, this option is useful when the trainee has to analyse a fast transient, therefore the simulator may run in a slow way

Automatic Exercises. The instructor may create automatic training exercises where initial conditions, malfunctions, and any action are triggered at a specified event or time. They may be stored for their subsequent use.

Simulation of a single step. This function activates the simulation for just one simulation step (0.1 *s*).
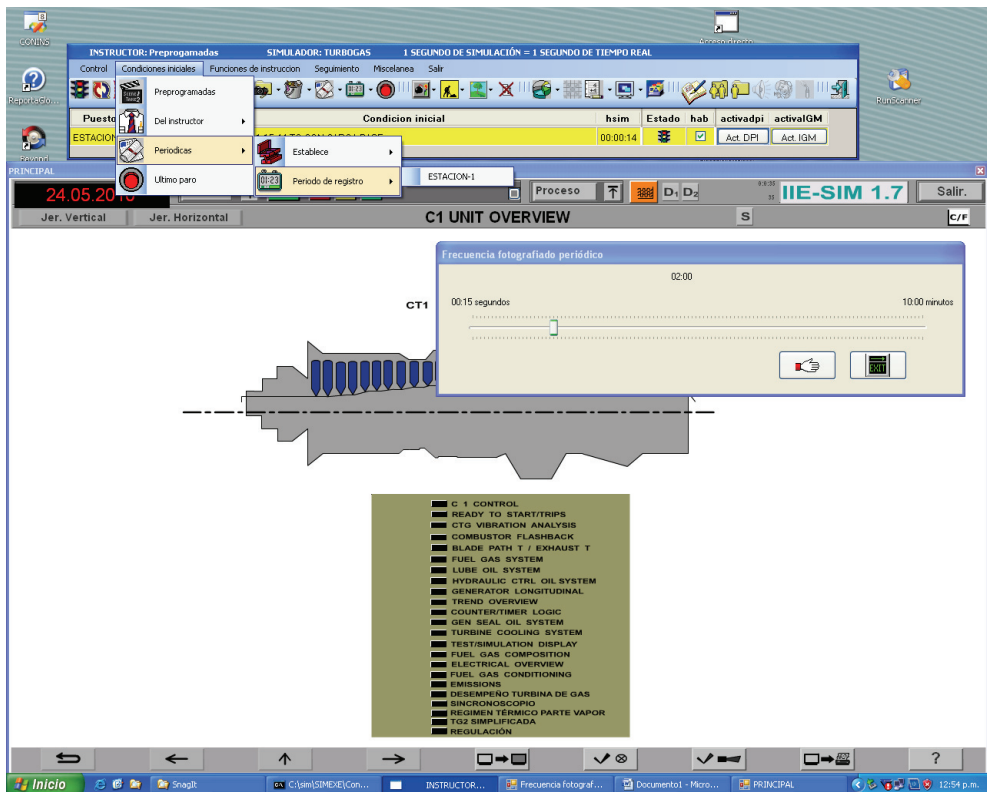
Fig. 10. Example of the functions displayed by pop-up.

6.2 "CONDICIONES INICIALES" menu (Initial conditions)

The initial conditions (ICO) allow: to establish the state of the process at the beginning of the simulation; to create a new ICO from any simulation instant; to rename an ICO; to change the description of an ICO; or to delete an existing ICO.

Initial Condition. The instructor may select an initial condition to begin the simulation session, either from the general pre-selected list or from their own catalogue (each instructor has access up to 100 initial conditions of his own). As mentioned above, it is also possible to manipulate the ICO or to record a new one.

The ICO may be one of the next:

Pre-programmed. These are the pre-defined ICO, with the main operation states of the simulator, and any instructor can establish them. The client defines how many and which ICO of this kind requires.

From an instructor. Every instructor has associated a directory in which can take or register his own ICO.

Periodicals. The simulator has an implicit function to register (snapshot) automatically and periodically an ICO. The simulator has a capacity to storage the last twenty snapshots. This function is currently running during a simulation session and the instructor may define the period of time for each snapshot between 15 seconds and 10 minutes; by default it is established in two minutes (see Figure 10).

From last stop. When the simulator is running and it is stopped, in an automatic way an ICO is registered. This ICO may be established as initial condition.

6.3 "FUNCIONES DE INSTRUCCIÓN" menu (Instruction functions)

The instruction functions allow modify the operation mode of the simulator during a training session. Such modifications may be effected in an instant or with a delay, according the instructor necessities and preferences.

Malfunctions. It is used to introduce/remove a simulated failure of equipments. There are 98 malfunctions available. Examples of them are: pumps trips, heat exchanger tubes breaking, heaters fouling, and valves obstructions. For the binary malfunctions (like trips), the instructor has the option of define its time delay and its permanence time. For analogical malfunctions (like percentage of a rupture), besides the mentioned time parameters, the instructor may define both intensity degree and evolution time.

Remote Actions. The instructor has the option to simulate the operative actions not related with actions on the plant performed from the control screens. These actions are associated with the local actions effected in the plant by an auxiliary worker. Examples of them are: to open/close valves and to turn on/off pumps or fans. There are more than 200 of them and they may have time and intensity degree parameters as instructor options.

External Parameters. They allow the instructor to modify the external conditions: atmospheric pressure and temperature (dry and wet bulb), voltage and frequency of the external system, fuel composition, etc.

6.4 "SEGUIMIENTO" menu (Tracking)

The simulator has a series of very helpful implements especially during the simulation development: simulate just one step (0.1 s), monitor and change on line the value of selected global variables, and tabulate any list of variables.

Tabulation. This function creates a file in ASCII format (in a tabular display) of a list of variables defined in other file created by the user (the first column is always the simulation time). The user may define the total period of time and the frequency of the registration. It generates a results file in ASCII code for the manipulation of the obtained data.

Values of models variables. It allows to display and to modify the value of a model on line.

Monitoring. With this function it is possible to have a continuous monitoring window for a group of variables on line. It is possible to modify the variables values.

To create a variables group. It opens an ASCII window editor to create a file with variables to be tabulated or monitored. The file can be stored for its future use.

Perturbation of a variable. It allows defining an initial value to a group of variables.

6.5 "MISCELANEOS" menu (Miscellaneous)

This menu contains several auxiliary functions that help to the administration of the instruction sessions of every one of the instructors, in order that everybody has their own accounts and the control of his own simulation sessions.

Agenda. This button enables and disables the registration of the operators' actions on the control screens. The function also registers the action of the instructor in his MMI.

Switch an instructor. This function allows changing the instructor account for another without leaving the simulation environment simulation.

Creation of an instructor account. With this function it is possible to create a new account for news instructors.

7. Modelling methodology

The models of the simulated plant were divided in two groups: the control models and the process models.

7.1 Processes

The models are a set of algebraic and differential equations obtained from the application of basic principles (energy, momentum and mass balances). The models were designed to work under a full range of performance. This is from 0% to 100% of load including all the possible transients that may be present during an operational session in the real plant.

The simulator was developed applying a methodology developed by the IIE. In fact, some of the modelling tools (concretely some generic models) were developed and/or adapted during the execution of this project. The methodology may be summarised as:

a. Information of the process is obtained and classified (system description, system operation guidelines, thermal balances, operational curves of the equipment, operational plant data, etc.).

b. The information is analyzed and a conceptual model is stated (a functional description of the system).

c. Simplifications of the system are made obtaining a simplified diagram (showing the simulated equipment with their nomenclature). In the diagram the modelled equipment and measurements points are included and it is possible to identify, for example, the valves controlled automatically from those operated by the operator or locally.

d. Main assumptions are stated and justified.

e. The configuration of the flow and pressure network is obtained and with the design operational point (normally 100% of load) the parameters of pumps, valves and fittings are automatically obtained in a excel data sheet. This sheet is a part of the final documentation and when it is modified, the updating of the simulator may be automatically performed (from excel, global variables, data and code are copied into the programs and data bases of the simulator).

f. Energy balances are programmed using the required generic models. Again, parameterisation with excel is performed. The calculations of energy balances are programmed following the flow direction and considering possible sets of equations to be solved simultaneously

g. The Equipments out the limits of the hydraulic network are parameterised (tanks, boilers, condensers, etc.) using predefined excel sheets considering the generic models available in the simulator's libraries or developing the adequate models.

h. Local tests are performed and, if necessary, adjustments in the models are made. The *MAS* and its utilities are used for this task. The local tests were performed, i.e. in the *MAS* the model is run alone and changes in some variables (inputs) are made in order to evaluate the general response of the model. At this time the *MAS* included the control screens. Eventually, some adjustments in the models were made.

i. Integration between all the different systems and their controls are performed (the coupling order is an important factor). All models are integrated into the *MAS*. For the integration, the first model incorporated was the turbine, combustor and compressor model with its associated control. Then the generator and electrical grid was added. The lubrication oil system was next and finally the models of the auxiliary systems (each with its control). The coupling was done considering the best sequence to avoid as much as possible mathematical problems. An algorithm proposed and used previously in a simulator is to consider an execution sequence trying to minimize the retarded information (variables). To prove the successful integration of each model added, an operator achieved some actions on the models.

j. Global test are made with the needed adjustments.

k. Final acceptance tests are achieved by the final user according their own procedures. The acceptance tests were performed first in the factory and finally in site in both cases with the help of the customer.

7.2 Control

The control models acquire and process the actions realized by the operator in the control room by the action on the control screens. As a response, these models generate, via the digital and analogical exits, possible changes of the process models, depending of the general condition of the simulated plan. For example, the control adjusts the demand of the valves to regulate some variables of the processes around a set point fixed by the operator (levels of tanks, pressures, temperatures, etc.).

Most of the controls are part of the distributed control system (DCS) by Siemens-Westinghouse Power Corporation and some of them are local (out of the distributed control system).

For the development of the gas turbine control models the graphics package VisSim was used. The sources of the information were diagrams provided by the CENAC. These diagrams were drawn from the control provider of the real plant that are presented in the format defined by the Scientific Apparatus Makers Association (SAMA).

The IIE determined the use of this package that had all the necessary modules to develop the modules of the control charts and analog logic simulator. The development of control models was carried out in five stages:

a.   *Identification of generic control modules*. Two hundred SAMA diagrams were reviewed and analyzed to include all the control logic for the pre-start and start permissive; speed control; temperature monitoring; load control; and temperature control. As a result of this stage 21 control models were detected to be developed which are listed in table 5.

No.	Control Model	No.	Control Model
1	Prestart and starting logic	12	System DLN control
2	Combustor	13	Rotor cooling control
3	Combustor control	14	Simulation/Test
4	Lube oil control	15	VARS/PF control
5	Auto-unload control	16	System alarms
6	Trip logic	17	Supervisory turbine
7	Generator control	18	Counter and timer logic
8	Temperature control	19	Air instrument control
9	Pilot & stage control	20	Electrical system
10	IGV control	21	Graphic trends
11	Flashback temperature monitoring		

Table 5. Control models of the gas turbine simulator.

b.   *Detection of the models not included in the DCS.* In the plant some equipments are not included in the DCS. In these cases, the diagram or description of the local controls was sought. When the information was not available, the control diagrams were developed and accorded with the client. Once the diagram was done, the model obtaining procedure was the same that for the SAMA diagrams.

c.   *Generic graphical modelling*. With generic blocks generated in VisSim, containing the functions of the SAMA diagrams, a generic graphics library was integrated to create the analog and logic diagrams into the VisSim environment. Figure 11 shows the generic modules that were developed in VisSim.

d.   *Control Modelling*. Based on the SAMA diagrams the control models of gas turbine plant simulator were developed. The diagrams were transcribed into the VisSim program using the generic modules. Each SAMA control diagram was done into a single VisSim drawing. As an example, Figures 12 and 13 show the diagram of speed control loop in the original SAMA version and in the VisSim drawing.

e.   *Translation from VisSim into C # language*. From control system diagram in VisSim an ANSI C code is automatically generated. Some adjustments to the generated code have to be done with a program developed by the IIE in order to translate the code to C#, which can run in the simulator environment. This application generates the variables definitions that are charged into the simulator database (global variables, remote functions, malfunctions, etc.). The source files of the control models kept in graphic form to facilitate the updates and corrections tests and adjustments. Table 6 presents a part of some C# code obtained from VisSim with the adjustments made by the IIE application.
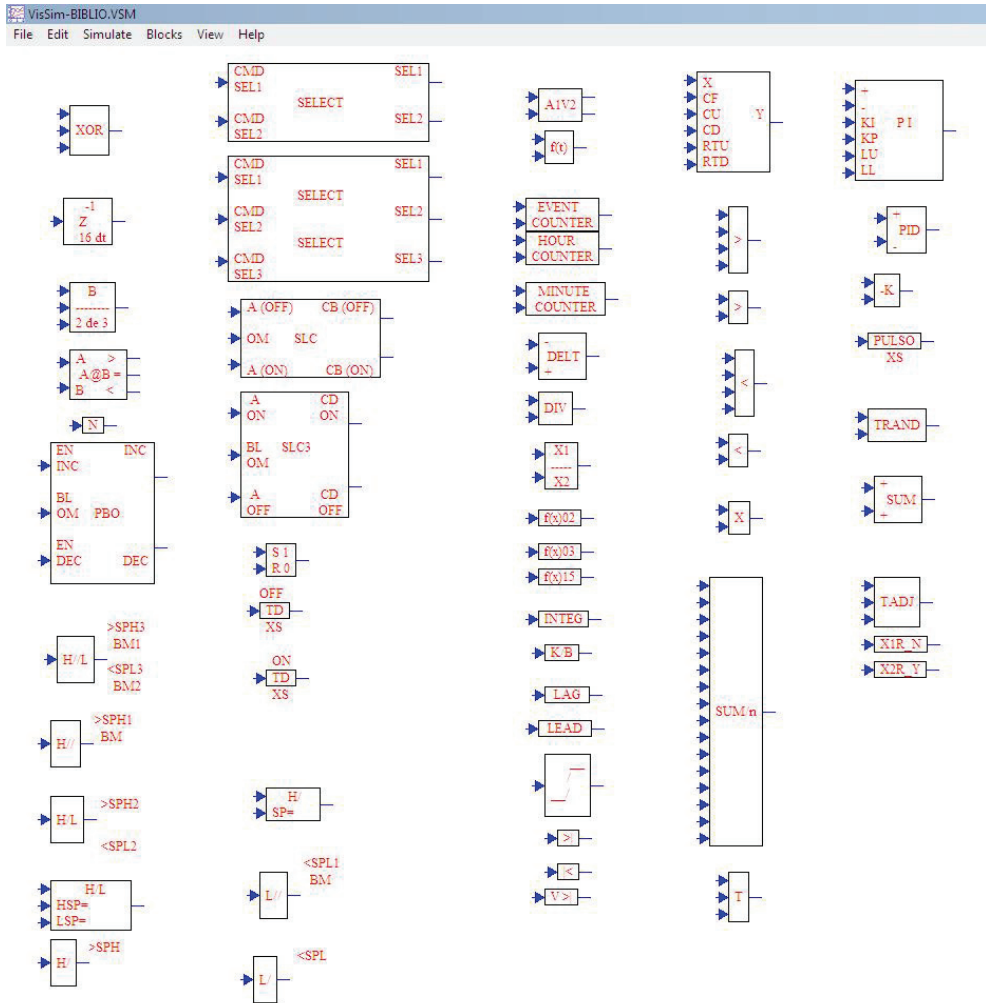
Fig. 11. Generic graphics library for the SAMA diagrams modelling in the VisSim environment.

8. Modelling development

8.1 Simulated systems

The systems that finally are simulated were selected in order to have all the information the instructor needs to train an operator. The main important characteristic of each simulated system is that it is controlled from the main control screens, from the process itself (trough remote functions in the simulator) or from the DCS, and that has an impact on the global plant status.

The systems included in the simulator are (each with its associated control systems): Fuel Gas; Gas Turbine; Compressed Air; Air for Instruments; Lubrication Oil, Control Oil, Water-
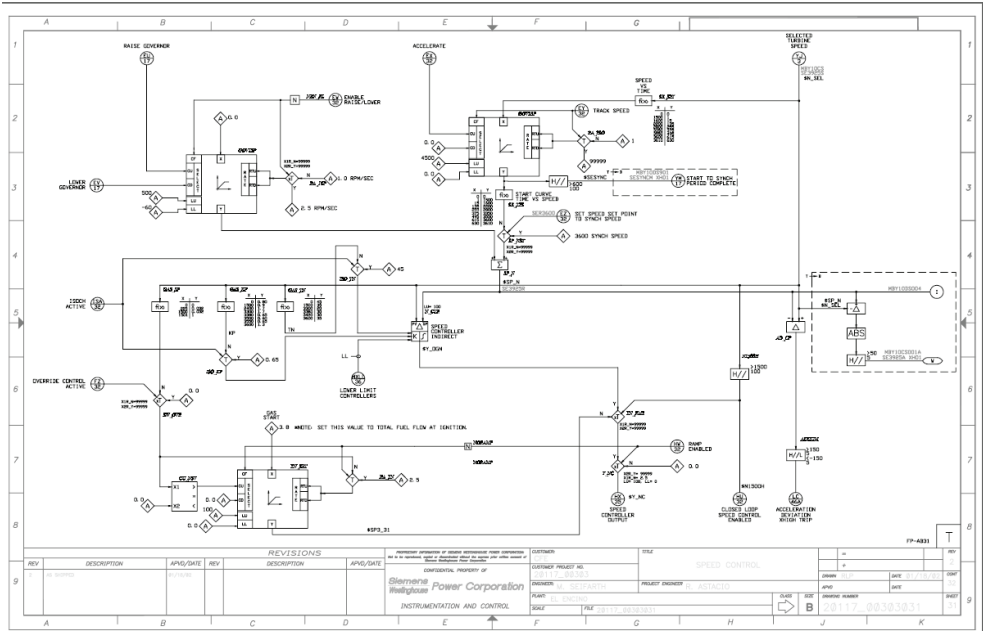
Fig. 12. Original SAMA diagram for the turbine speed control loop.
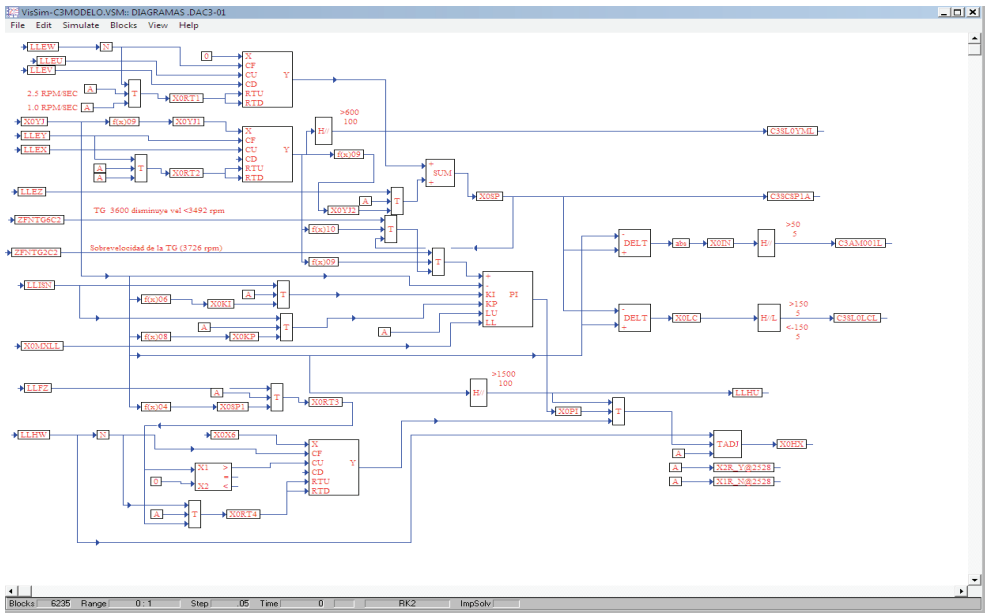
Fig. 13. VisSim diagram for the turbine speed control loop.

Ethylene Glycol, Cooling, Electrical Network; Generator; Generator Cooling with Hydrogen; Turbine (Metals Temperatures and Vibrations); Performance Calculations (Heat Rate and Efficiencies); and Combustor, including the combustor blade path temperatures (with 32 display values), the exhaust temperatures (with 16 displays), the disc cavity temperatures (with 8 displays) and emissions.

8.2 Generic models

The design of generic models (GM) allows reducing the time used to develop a simulator. For the case of a training simulation, a GM constitutes a standard tool with some built-in elements (in this case, routines), which represent a "global" equipment or system and can facilitate its adaptation to a particular case. A GM may be re-used for several applications (either in the same simulator or in different simulators).

```csharp
using System;
using System.Collections.Generic;
using System.Text;
namespace ctrlmodturbogas
{
        unsafe public class Cc3 : inivarmod
        {
        const bool LTRUE= true;
        const bool LFALSE= false;
                public void c3()
                {
                float X0MXLL;
                bool t275;
                float X0YJ;
                bool LLEZ;
                •
                •
                •
                  CXLCCS_2121 =  (float)100.0;
                  CXLCGRI_1903 =  (float)0.0;
                  CXLCGRS_1713 =  (float)500.0;
                  CXLCGRS_2442 =  (float)100.0;
                  CXLCGRI_2442 =  (float)0.0;
                LIMIT(C3SPRYJE,CXLCGRS_1903,CXLCGRI_1903);
                LIMIT(C3SPR01E,CXLCGRS_1713,CXLCGRI_1713);
                LIMIT(C3SC001E,CXLCES_2121,*C3SCMXLI);
                LIMIT(C3SPR02E,CXLCGRS_2442,CXLCGRI_2442);
                  X0MXLL = *C3SC002L ;
                  t275 = (( *C3SPRYJE > (float)500.0)&&(( *C3SPRYJE > *C3SL0YMP )|| *C3SL0YMY ));
                  X0YJ = *C3SC001L ;
                  LLEZ = *C3SC006L ;
                  XVL09_2003 = ( Math.Min(( Math.Max( (float)0.0, *C3SPRYJE )), (float)630.0));
                  X0YJ2 = ((( XVL09_2003 >= 0 )&&( XVL09_2003 <= (float)1.0))?(( XVL09_2003 *
(float)1500.0)+ (float)0.0):(((XVL09_2003 > 1 )&&( XVL09_2003 <= (float)15.0))?(( XVL09_2003 *
(float)7.14286)+ (float)1492.86):((( XVL09_2003 > 15 )&&( XVL09_2003 <= (float)135.0))?(( XVL09_2003 *
(float)5.0)+ (float)1525.0):((( XVL09_2003 > 135 )&&( XVL09_2003 <= (float)255.0))?(( XVL09_2003 *
(float)5.0)+ (float)1525.0):((( XVL09_2003 > 255 )&&( XVL09_2003 <= (float)375.0))?(( XVL09_2003 *
(float)4.58333)+ (float)1631.25):((( XVL09_2003 > 375 )&&( XVL09_2003 <= (float)495.0))?(( XVL09_2003 *
(float)1.66667)+ (float)2725.0):((( XVL09_2003 > 495 )&&( XVL09_2003 <= (float)615.0))?(( XVL09_2003 *
(float)0.416667)+ (float)3343.75):(( XVL09_2003 * (float)0.66667)+ (float)3190.0))))))));
                    X0SP = ( *C3SPR01E +( LLEZ ? *C3SP007P : X0YJ2 ));
                    X0IN =  Math.Abs((- X0YJ + X0SP ));
                *C3SC001E = X0API2;
                *C3SC0HXI = CXS6_2528;
                }
        }
}
```

Table 6. Example of C# code generated automatically from the design diagrams.

Fundamental conservation principles were used considering a lumped parameters approach and widely available and accepted empirical relations. The independent variables are associated with the operator's actions (open or close a valve, trip a pump manually, etc.) and with the control signal from the DCS.

Physical Properties

The physical properties are calculated as thermodynamic properties for water (liquid and steam) and hydrocarbon mixtures and transport properties for water, steam and air.

For the water the TP were adjusted as a function of pressure (*P*) and enthalpy (*h*). The data source was the steam tables by Arnold (1967). The functions were adjusted by least square method. The application range of the functions is between 0.1 *psia* and 4520 *psia* for pressure, and -10 ^0C and 720 ^0C (equivalent to 0.18 *BTU/lb* and 1635 *BTU/lb* of enthalpy).

The adjustment was performed to assure a maximum error of 1% respecting the reference data; to achieve this it was necessary to divide the region into 14 pressure zones. The functions are applied to three different cases: subcooled liquid saturated and superheated steam. For the saturation region, both the liquid and steam properties are only a function of pressure and they are calculated as follow:

$$(T,h,s) = k_{t,1} + k_{t,2}\sqrt{P} \tag{1}$$

where *T* is temperature, *s* is entropy, $k_{t,1}$ and $k_{t,2}$ are constants to determinate the particular TP and depends of the phase (liquid or vapour).

The densities ρ of saturated liquid and steam are calculated as:

$$\rho = k_{t,3} + k_{t,4}P + k_{t,5}P^2 \tag{2}$$

For subcooled liquid and superheated steam, the functions are:

$$(T,h,s,\rho) = k_{s,1} + k_{s,2}h + k_{s,3}h^2 \tag{3}$$

where:

$$k_{s,i} = k_{s,i}' + k_{s,i}''\sqrt{P} \tag{4}$$

To ensure an relative error less than 1%, the equations (3) and (4) were slightly modified in some regions of *P*.

The functions also calculate *dTP/dP* for the saturation region and *∂TP/∂P* and *∂TP/∂h* for the subcooled liquid and superheated steam.

The same functions may be used if the independent variables are *P* and *T*. The calculation is done for finding the unknown variable (or value) from equations (1) to (4).

Note: In all cases $k_{t,i}$ and $k_{s,i}$ has different values according to the calculated TP, the pressure region, and the specific point (liquid or steam) where the calculation is made.

The transport properties (viscosity, heat capacity, thermal expansion, and thermal conductivity) are calculated for liquid, steam and air with polynomial functions up to fourth degree (for different *P* and *T* regions).

For this simulator the hydrocarbon TP were applied for the gas fuel, air and combustion products. In this case, the calculation is based in seven cubic state and corresponding states equations to predict the equilibrium liquid-steam and properties for pure fluids and

mixtures containing non polar substances. The validity range is for low pressure to 80 bars. There are 20 components considered that possibly may be form a mixture: nitrogen, oxygen, methane, ethane, propane, n-butane, i-butane, n-pentane, n-hexane, n-heptane, n-octane, n-nonane, ndecane, carbon dioxide, carbon monoxide, hydrogen sulphide, sulphur dioxide, nitrogen monoxide, nitrogen dioxide, and water.

The cubical equations have the following general form (Reid *et al.*, 1987):

$$P = \frac{R\,T}{\hat{v} - b} - \frac{a}{\hat{v}^2 + u\,\hat{v}\,b + w\,b^2} \tag{5}$$

where R is the ideal gas constant, $\hat{v}$ is molar volume, and a, b, u, w, are constants that in fact determine the precise cubic equation that may be used: Van der Waals, Redlich-Kwong, Soave, Peng-Robinson, Lee-Kesler, Racket (for saturated liquid only), Hankinson-Brobst-Thompson (for liquid only), and Ideal Gas. Also may be used the corresponding states equation Lee Kesler:

$$Z^{(o)} = 1 + \frac{B}{V_r^{(0)}} + \frac{C}{(V_r^{(0)})^2} + \frac{D}{(V_r^{(0)})^5} + \frac{C4}{T_r^3 (V_r^{(0)})^2}\left[\beta + \frac{\gamma}{(V_r^{(0)})^2}\right]\exp\left[\frac{-\gamma}{(V_r^{(0)})^2}\right] \tag{6}$$

$$Z^{(0)} = \frac{P_r V_r^{(0)}}{T_r}; \qquad Z^{(R)} = \frac{P_r V_r^{(R)}}{T_r}; \qquad Z = Z^{(0)} + \frac{\Omega}{\Omega_R}(Z^{(R)} - Z^{(0)}) \tag{7}$$

where B, C, D, $C4$, β, and γ are characteristics (constants), and Ω is Pitzer's acentric factor.

For the solution of any of the equations for a gas mixture, the Newton-Raphson method is used.

Flows and Pressures Networks

This model simulates any hydraulic network in order to know the values of the flows and the pressures along the system. A convenient approach to represent the network (easy to solve and sufficiently exact for training purposes) is considering that a hydraulic network is formed by accessories (fittings), nodes (junctions and splitters) and lines (or pipes). The accessories are those devices in lines that drop or arise the pressure and/or enthalpy of the fluid (valves, pumps, filters, piping, turbines, heat exchangers and other fittings). A line links two nodes. A node may be internal or external. An external node is a point in the network where the pressure is known at any time, these nodes are sources or sinks of flow (inertial nodes). An internal node is a junction or split of two or more lines.

The model is derived from the continuity equation on each of the nodes, considering all the inlet (i) and output (o) flowrates (w):

$$\Sigma w_i - \Sigma w_o = 0 \tag{8}$$

Also, the momentum equation may be applied on each accessory on the flow direction x:

$$\rho \frac{\partial v}{\partial t} = -\frac{\partial P}{\partial x} - \frac{\partial \tau_{xx}}{\partial x} - \rho v_x \frac{\partial v_x}{\partial x} + \rho\,g_x \tag{9}$$

Considering that the temporal and space acceleration terms are not significant, that the forces acting on the fluid are instantly balanced, a model may be stated integrating the equation along a stream:

$$\Delta P = -L\,\Delta\tau + \rho\,g\,h \tag{10}$$

where the viscous stress tensor term may be evaluated using empirical expressions for any kind of accessories. For example, for a valve, the flowrate pressure drop (ΔP) relationship is:

$$w^2 = k'\,\rho\,Ap^\zeta\left(\Delta P + \rho g\Delta z\right) \tag{11}$$

where the flow resistance is a function of the valve aperture Ap and a constant k' that depends on the valve itself (size, type, etc.). The exponent ζ represents the characteristic behaviour of a valve in order to simulate the effect of the relation between the aperture and the flow area. The aperture applies only for valves or may represent a variable resistance factor to the flow (for example when a filter is getting dirty). For a fitting with constant resistance the term Ap^ζ does not exist. For a pump (or a compressor), this relationship may be expressed as:

$$\Delta P = k_1'\,w^2 + k_2'\,w\,\omega + k_3'\,\omega^2 - \rho\,g\,h \tag{12}$$

where ω is the pump speed and where k'_i (for i=1,2,3) are constants that fit the pump behaviour. Note that the density ρ has a much more influence on a compressor than a pump. Similar equations may be obtained for any other fitting (turbines, filters, piping, etc.).

If it is considered that in a given moment the aperture, density, and speed are constant, both equations (4) and (5) may be written as:

$$w^2 = k_a\,\Delta P + k_b \tag{13}$$

Applying equation (8) on each node and equation (13) on each accessory a set of equations is obtained to be solved simultaneously. However, a more efficient way to get a solution is achieved if equation (13) is linearised. To exemplify the linearization approach, equation (13) is selected for the case of a pump with arbitrary numerical values (but the same result may be obtained for any other accessory and any numerical scale). Figure 14 presents the quadratic curve of flowrate w on the x axis and ΔP on the y axis (dotted line). In the curve two straight lines may be defined as AB and BC and represent an approximation of the curve. The error dismisses if more straight lines were "fitted" to the curve. In this case two straight lines are used to simplify the explanation, but the model allows for any number of them.

For a given flow w, the pressure drop may be approximated by the correspondent straight line (between two limit flows of this line). This line is represented as:

$$\Delta P = m'\,w + b' \tag{14}$$

If there are two or more accessories connected in series and/or two or more lines in parallel are present, an equivalent equation may be stated:

$$\Delta P = m\,w + b \tag{15}$$
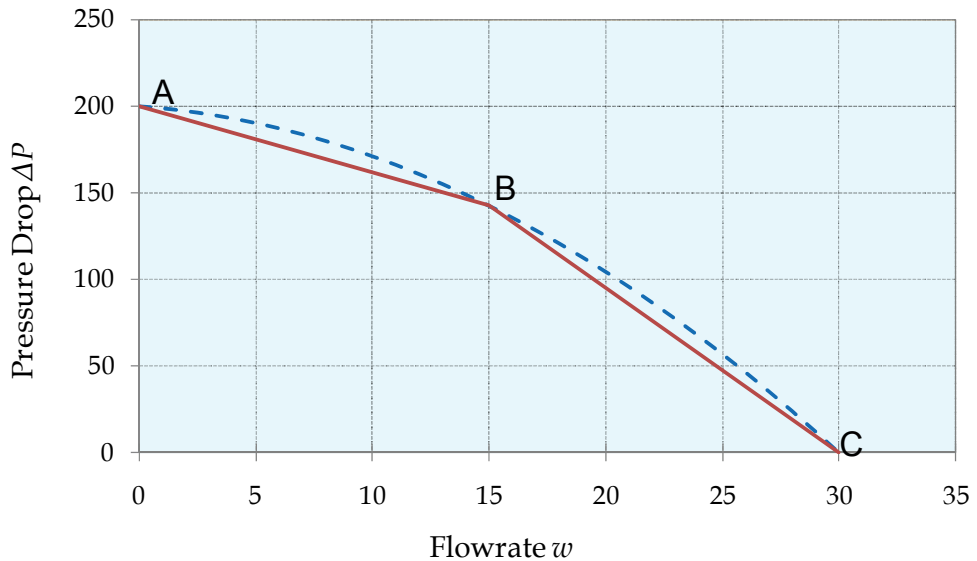
Fig. 14. Linearization of the curve that represent a fitting.

This equation may be arranged as:

$$w = C\,\Delta P + Z \tag{16}$$

Substituting equation (16) on (8), for each flow stream, a linear equations system is obtained where pressures are the unknowns. The order of the matrix that represents the equations system is equal to the number of internal nodes of the network. Flows are calculated by equation (16) once the pressures were solved.

An active topology of a network is a particular arrangement of the grid that allows flow through their elements. The active topology may change, for instance, if a stream is "created" or "eliminated" of the network because a valve is opened and/or closed or pumps are turned on or off. The full topology is that theoretical presented if all streams allow flow through them. During a session of dynamic simulation a system may change its active topology depending on the operator's actions. This means that the order of matrix associated to the equations that represent the system changes.

To obtain a numerical solution of the model is convenient to count with a procedure that guarantees a solution in any case, i.e. avoiding the singularity problem and that helps the understanding and development of models of simulators for training purposes. In the flows and pressures GM an algorithm to detect the active topology is detected in order to construct and solve only the equations related to the particular topology each integration time. The solution method is reported by Mendoza-Alegría et al. (2004) in detail. The procedure seeks the system of equations to identify the sub-systems that can be solved independently.

The valves are considered with an isenthalpic behaviour and the compressor and turbine are calculated as an isoentropic expansion and corrected with an efficiency. For example, the

properties at the compressor's exhaust are calculated as an isentropic stage by a numerical Newton-Raphson method (i.e. the isoenthalpic exhaust temperature T_e* is calculated at the exhaust pressure P_e with the entropy inlet s_i):

$$f(T_e^*) = s_i(T_i, P_i, c) - s_e^*(T_e^*, P_e, c) = 0 \tag{17}$$

where c is the gas composition. Then, the leaving enthalpy is corrected with the efficiency of the compressor:

$$h_e = \frac{(h_e^* - h_i)}{\eta} + h_i \tag{18}$$

All other exhaust properties are computed with the real enthalpy and pressure. The efficiency η is a function of the flow through the turbine. The properties at the turbine exit were formulated like the compressor but considering that the work is produced instead of consumed.

To exemplify a flows and pressures network, in Figure 15 the control screen from the OS for the water cooling system of the generator and the hydrogen supply is reproduced. Figures 16 and 17 present the simplified diagrams of the flows and pressures networks of the generator's cooling water and hydrogen supply, respectively. These simplified diagrams are the basis to parameterise the flows and pressures GM according the methodology developed by the IIE.
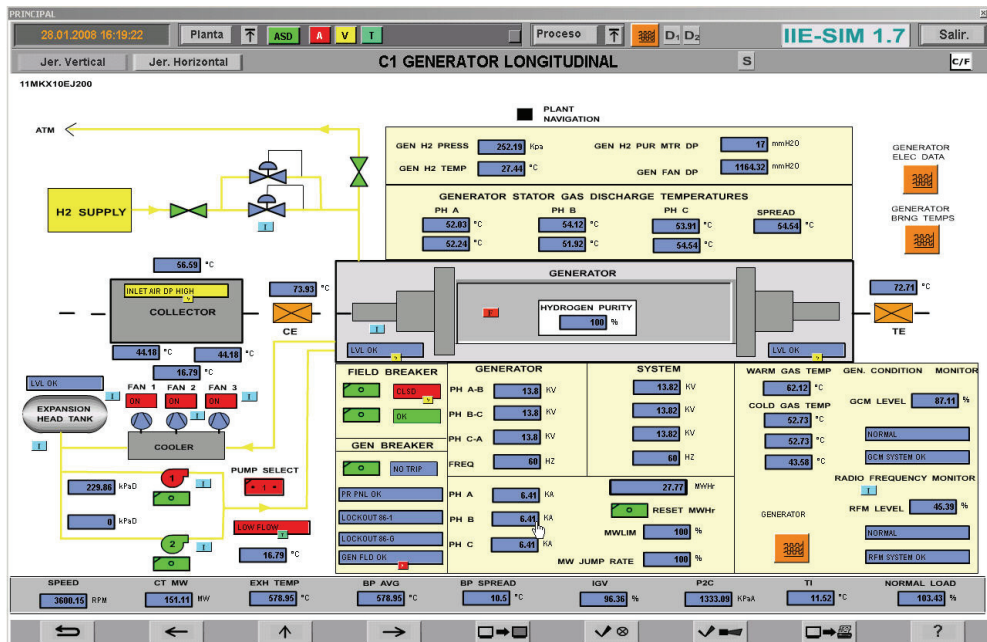
Fig. 15. Control and display screen of the generator cooling water and hydrogen supply.
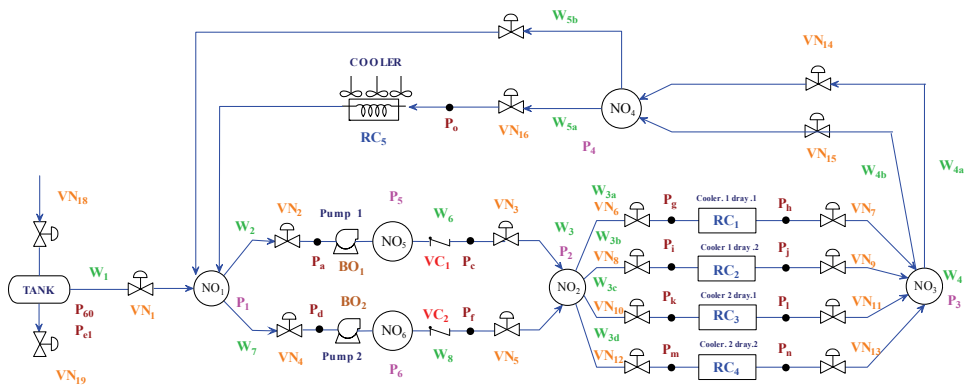
Fig. 16. Simplified diagram of the generator cooling water system.
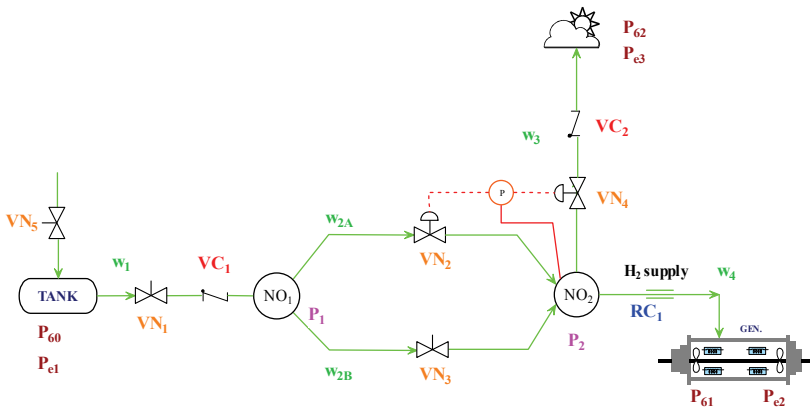
Fig. 17. Simplified diagram of the generator hydrogen supply.

Electric Phenomena Model

The generator model is not discussed here but it was simulated considering a sixth order model and equations related to the magnetic saturation of the air gap, the residual magnetism and the effect of the speed variations on the voltage. The control screen of the electric network is presented in Figure 18.

The model to simulate electrical grids was adapted from the generic model for hydraulic networks (Roldán-Villasana & Mendoza-Alegría, 2004). Basically, equations (8) and (16) may represent an electrical network in a permanent sinusoidal state by substituting flows (*w*) by currents (*I*), pressures (*P*) by voltages (*V*), conductances (*C*) by admittances (*Y*), pumping terms (*Z*) by voltage source increase (*VT*) when they exist and considering that the gravitational term does not exist in electrical phenomena, and valve apertures (*Ap*) by a parameter to represent the variation of a resistance or impedance (*Ps*). No linearization was necessary because the electric equations are linear. Although the model was designed to represent alternate current grids, it is able to represent direct current circuits. The first adaptation was made considering that it was necessary to handle complex numbers. The
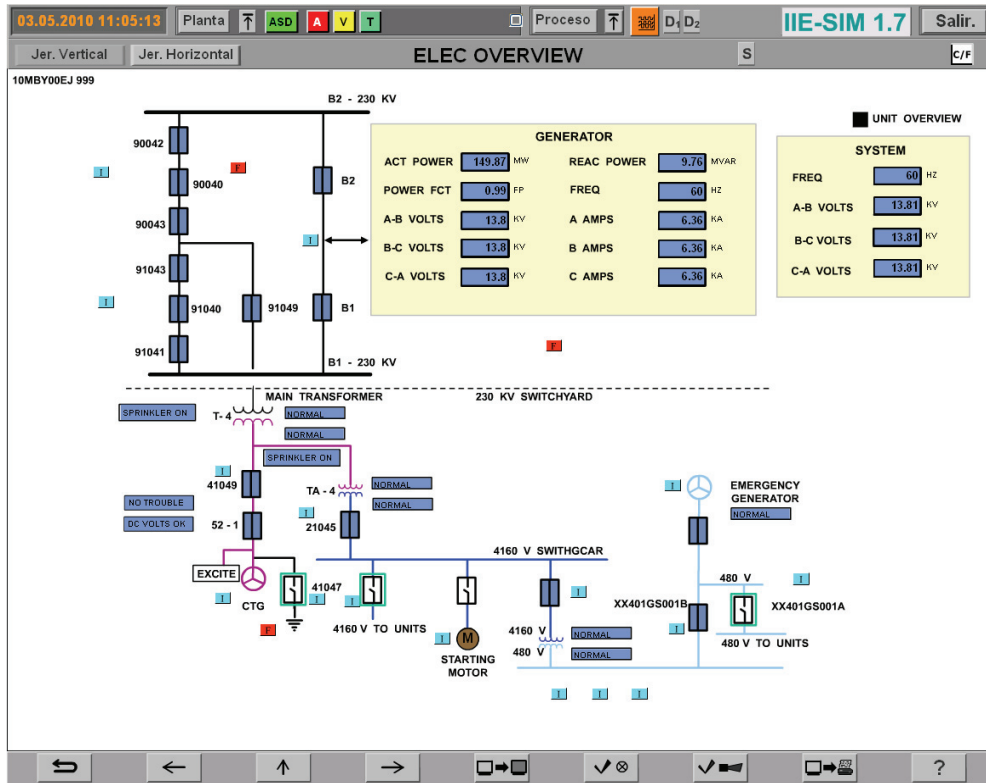
Fig. 18. Control screen of the electrical network.

algorithms proposed by Press *et al.* (1997) were adopted (an variation of the routines was effected to perform the inversion of the matrix in order to report the Thevenin equivalent impedances).

One enhancement to satisfy a special requirement of electrical networks was accomplished: to not consider the branches as having closed switches (branches with practically no resistance). In Figure 19, the schematics diagram (for parameterisation) of the electric network is shown.

Motors

From design data, the dynamics of speed and electrical current of the electrical motors are calculated, including the surge overcurrent at the startup of the motors. The current I is simulated by the adjustment of typical curves of the motor (speed ω, electrical current, slip and torques) in a simplified form to show the current's peak during the motor start up:

$$I = \frac{k_i + k_{ii}}{\omega} \tag{19}$$

The speed is calculated by the integration of its derivative which is an equation that fits the real behaviour of the motor.
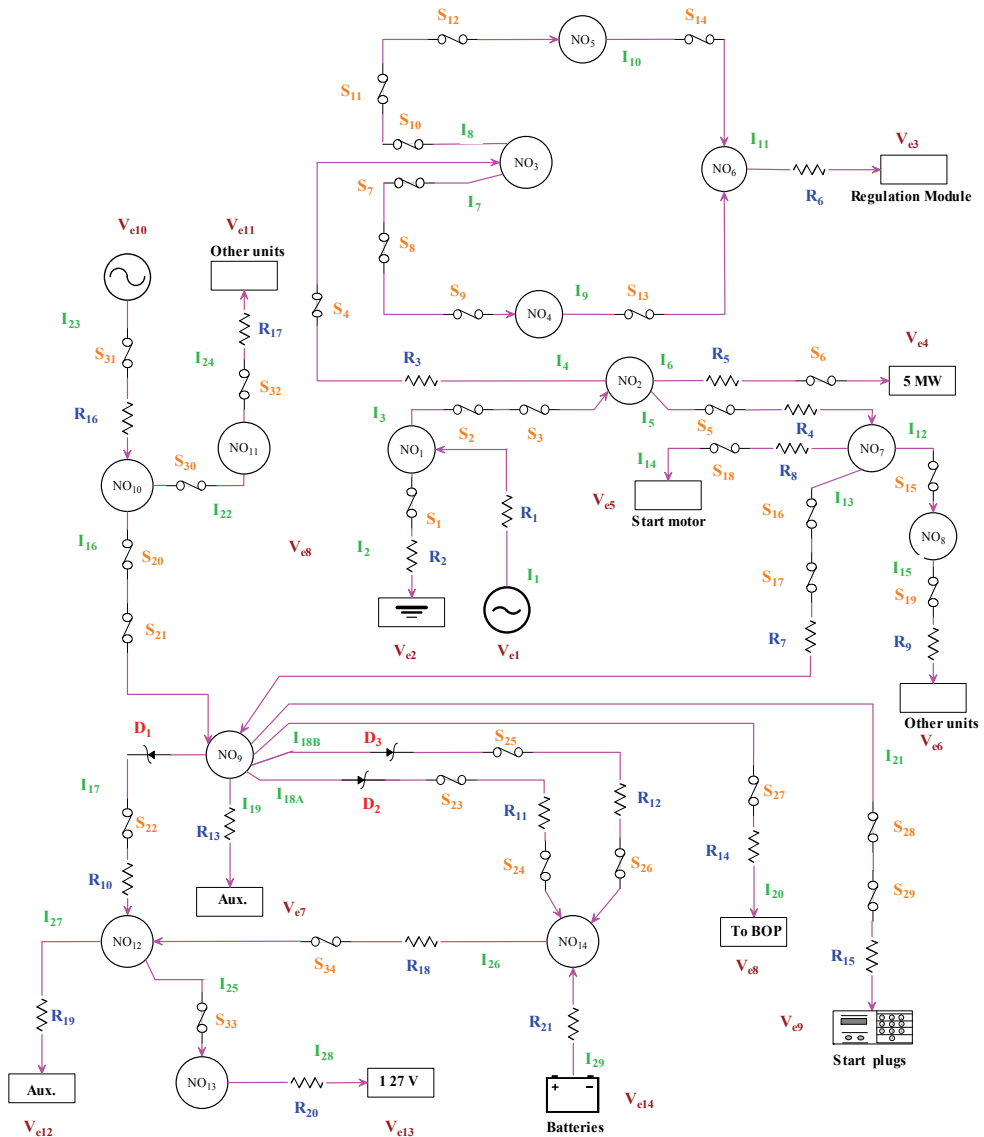
Fig. 19. Simplified diagram of the electric network as used for parameterisation.

$$\frac{d\omega}{dt} = (\omega_{nom} - \omega)\, k_{iii} \tag{20}$$

The variable ω_{nom} is nominal speed if the motor is on and is zero if the motor is off. The constant k_{iii} has two values one for the motor starting up and other value for the coast down. The heat gained by the fluid due the pumping Δh_{pump} when goes trough a pump (turned on) is:

$$\Delta h_{pump} = \left(\frac{\eta \Delta P}{\rho} \right) \tag{21}$$

where η is the efficiency. The temperature at the exit of the pump T_o is (being T_i the inlet temperature):

$$T_o = T_i + \frac{\Delta h_{pump}}{Cp} \tag{22}$$

Capacitive Nodes

There are two kinds of capacitive nodes.

The first one is a node that is part of the flows and pressures network whose pressure is calculated as explained before. An energy balance on the flows and pressures network is made where heat exchangers exist and in the nodes where a temperature or enthalpy is required to be displayed or to be used in further calculations.

In this case, the inertial variables are the enthalpy h, and the composition of all the components c_j is necessary in order to determinate all the variables of the node:

$$\frac{dh}{dt} = \frac{\sum w_i (h_i - h) - q_{atm}}{m} \tag{23}$$

In this equation, m is the mass of the node, and q_{atm} the heat lost to the atmosphere. The subindex i represent the inlet conditions of the different flowstreams converging to the node. With the enthalpy and pressure it is possible to verify if the node is a single or a two phase one (for the case of water/steam). The state variable could be the temperature if no phase change is expected and if the specific heat Cp divides the q_{atm} term.

All the steam mass balances are automatically accomplished by the flows and pressures network solution, however, the concentration of the gas components must be considered through the network. The concentration of each species j is calculated as the fraction of the mass m_j divided by the total mass m in a node. The mass of each component is calculated by integrating next equation:

$$\frac{dm_j}{dt} = \sum w_i c_{i,j} - \sum w_o c_j \tag{24}$$

The second kind of node is those that is a frontier of the flows and pressures network. Here, the state variables depend on each particular case.

In this category are the boilers, condenser, deaerators, and other equipments related with different phenomena involving water/steam operations. These equipments were not used in this simulator and their formulations are not explained here. However, regarding gas processes, two approaches are used: the simplified model used for capacitive junction nodes or gas contained in close recipients (no phase change is considered in this discussion but indeed a generic model is available), and complex gas processes like a combustion chamber.

For the simplified model, the pressure is calculated using next equation obtained with basis in an ideal gas behaviour (only the pressure change is calculated as an ideal gas, not the other properties):

$$P = \frac{n\,RT}{V} \tag{25}$$

The change in the moles n of the nodes is obtained correcting the change of the mass, being this a state variable too as indicated in equation (24) with the molecular weight. Equation (23) for the enthalpy is used too.

For complex processes where a possible change of phase occurs, the model considers to calculate the internal energy u in the node and its pressure. The derivative of the internal energy is evaluated as:

$$\frac{du}{dt} = \frac{\sum w_i h_i - \sum w_o h - u \dfrac{dm}{dt} - q_{atm}}{m} \tag{26}$$

The derivative of the total mass is the sum of the derivatives of each species as equation (24). Here, the internal energy and density are known (this later by dividing the total mass and the volume of the node). The thermodynamic properties are a function of pressure and temperature, so all the properties are calculated with a double Newton-Raphson iterative method. When two phases are present, some extra calculations are made to known the liquid and vapour volumes, but this is not treated here.

A last category of capacity nodes are tanks that are open to the atmosphere and filled with liquid. Equation (23) applies for temperature (or enthalpy) variations and a mass balance is used to calculate the derivative of the liquid mass:

$$\frac{dm}{dt} = \sum w_i - \sum w_o \tag{27}$$

Where the liquid volume is:

$$V_l = \frac{m}{\rho} \tag{28}$$

The liquid level is calculated with an adequate correlation depending on the tank's geometry.

Heat Exchangers

In the simulated plant, three varieties of heat exchangers were included: fluid (gas or water) cooled by air; metals cooled with hydrogen, air or oil; and water-water exchangers.

The fluid-air exchangers were modelled considering a heat flow q between the fluid and air:

$$q = U\,A\,\Delta T \tag{29}$$

The heat transfer coefficient U depends on the fluids properties, flowrates, and the construction parameters of the equipment. A is the heat transfer area.

The representative temperature difference between hot (h) and cold (c) streams is, generally, the logarithmic mean temperature difference calculated as (for countercurrent arrangements):

$$\Delta T = \frac{(T_{h,i} - T_{c,o}) - (T_{h,o} - T_{c,i})}{Log\left(\dfrac{T_{h,i} - T_{c,o}}{T_{h,o} - T_{c,i}}\right)} \tag{30}$$

and for each fluid, a energy balance may be stated (with a constant Cp) to calculate the exit temperature (exit enthalpy also may be used if a constant Cp is not considered

$$T_o = T_i - \left(\frac{q}{wCp} \right) \tag{31}$$

Besides, it is necessary to accomplish the thermodynamics' second law by avoiding the crossing of the temperatures in the exchanger, considering a minimal temperature differences (defined by the user) between the hot and cold streams: the outlet temperature of the cold stream does not be warmer than the inlet temperature of the hot stream and the outlet temperature of the hot stream does not be colder than the inlet temperature of the cold stream. If a crossing of temperatures is detected, clearly the heat calculated by equation (29) is too high and the limiting stream is identified, depending of which is the cold and the hot streams and the maximum heat allowed by each stream to no violate the second law. So, the heat is calculated arranging the equation (31). With the new heat, the outlet temperatures are calculated again. Clearly, an iterative procedure may be established in order to converge the last three equations with this procedure.

The model for the metals cooled with hydrogen, air or oil, was based on the fact that the metal is heated by friction (turbines, compressors, motors, etc.), electric current (generators and motors), or another fluid (radiators).

This approach is used instead equations (29) to (31). The generated temperature T_g, when the metal is heated by a fluid, is equivalent to the cooler temperature T_f. and the exchanger is a fluid-fluid one, when the dynamics is relatively slow. When the metal is heated by friction or electrical current, T_g is represented by virtual temperatures (T_I for the current and T_ω for the speed) that are calculated in order to simulate theses heating effects (a scheme of the heat transfer process is shown in Figure 20):
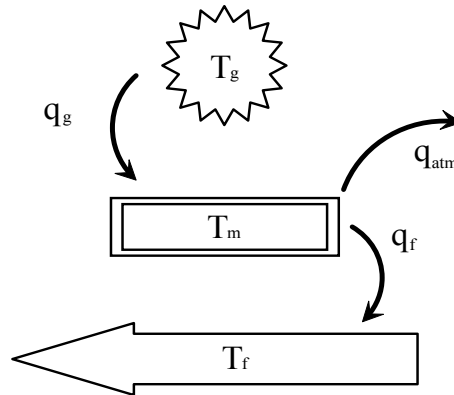
Fig. 20. Schematic representation of a generic metal-fluid heat exchange.

$$T_I = T_{amb} + k_I' I \tag{32}$$

$$T_\omega = T_{amb} + k_\omega' \omega \tag{33}$$

Thus, it is possible to calculate the total generated heat q_g by speed q_ω and current q_I to the metal using a proper correlation for the heat transfer coefficients (Pasquantonio & Macchi, 1976):

$$q_g = q_\omega + q_I = k_\omega (T_\omega - T_m) \omega^{0.4} + k_I (T_I - T_m) I^2 \tag{34}$$

So, the temperature of the metal may be calculated by integration of next equation:

$$\frac{dT_m}{dt} = \frac{q_g - q_f - q_{atm}}{Cp_m \, m_m} \tag{35}$$

q_f is calculated using equation (29) but the temperature difference ΔT is:

$$\Delta T = T_m - T_f \tag{36}$$

With this approaches any heat exchanger may be simulated, including the generator cooling with hydrogen that contains several heat exchanging stages.

Combustor

A GM for the combustor was developed by the IIE. The objective is to calculate flame temperature and the composition of the burned gases. It is possible simulate a mixture up to the same 20 components of the thermodynamic properties for the air, gas fuel and combustion products.

To calculate the flame temperature the stoichiometric coefficients are needed, thus, some of the reactions for the combustion process are:

$$
\begin{aligned}
&2n_{1,1}\, N_2 \;+\; 4n_{1,2}\, O_2 && \rightarrow && 0m_{1,1}\, N_2 + 0m_{1,2}\, O_2 + 0m_{1,18}\, NO + 4m_{1,19}\, NO_2 \\
&n_{2,1}\, O_2 && \rightarrow && m_{2,2}\;\; O_2 \\
&1n_{3,1}\, H_2S \;+\; 1.5n_{3,2}\, O_2 && \rightarrow && 0m_{3,2}\, O_2 + 0m_{3,3}\, H_2S + 1m_{3,16}\, H_2O + 1m_{3,20}\, SO_2 \\
&1n_{4,1}\, CO_2 && \rightarrow && 1m_{4,4}\, CO_2 \\
&1n_{5,1}\, CH_4 \;+\; 2n_{5,2}\, O_2 && \rightarrow && 1m_{5,4}\, CO_2 + 2m_{5,16}\, H_2O + 0m_{5,2}\, O_2 + 0m_{5,5}\, CH_4 + \\
& && && 0m_{5,17}\, CO \\
& \qquad\bullet \\
& \qquad\bullet \\
& \qquad\bullet && && && (37) \\
&10n_{15,1}\, C_{10}H_{22} \;+\; 155\, n_{15,2}\, O_2 && \rightarrow && m_{15,4}\, CO_2 + m_{15,16}\, H_2O + 0m_{15,2}\, O_2 + 0m_{15,15} \\
& && && C_{10}H_{22} + 0m_{15,17}\, CO \\
&2n_{16,1}\, H_2O && \rightarrow && 2m_{16,16}\, H_2O \\
&1n_{17,1}\, CO \;+\; 0.5n_{17,2}\, O_2 && \rightarrow && 1m_{17,4}\, CO_2 + 0m_{17,17}\, CO + 0m_{17,2}\, O_2 \\
&n_{18,1}\, NO \;+\; 0.5n_{18,2}\, O_2 && \rightarrow && 1m_{18,19}\, NO_2 + 0m_{18,18}\, NO + 0m_{18,2}\, O_2 \\
&1n_{19,1}\, NO_2 && \rightarrow && 1m_{19,19}\, NO_2 \\
&1n_{20,1}\, SO_2 && \rightarrow && 1m_{20,20}\, SO_2
\end{aligned}
$$

Water should be considered joining external flow to control the chamber temperature (to prevent emissions) and the humidity contained in the fuel. The excess of oxygen may be calculated from the flowrates of the reactive components. The total combustion efficiency $\alpha_{i,1}$ is defined as the fraction of the theoretically amount of oxygen that is consumed for a total combustion (is 1 if a complete combustion reaction is hold, for example production of

CO_2 and 0 if none of the products of a reaction is completely oxidized). The partial combustion efficiency $\alpha_{i,2}$ is defined as the fraction of the theoretically amount of oxygen that is consumed for a partial total combustion (is 1 if partial oxidised products are generated, for example production of CO and 0 if none of the products of a reaction is partially oxidised). The efficiencies are normally not constant and any function could be adjusted but considering that, to avoid imbalance problems, the restriction

$$\alpha_{i,1} + \alpha_{i,2} \leq 1 \tag{38}$$

must be satisfied at any moment.

Although no kinetics is taken into account, this approach considering these original two efficiencies, allows simulate the behaviour of the combustor. For this particular application of the combustor model, a linear function was defined for each efficiency (and for each reaction), based on the excess of oxygen (a thumb rule, but any equation could be defined). As an example the equations to obtain the stoichiometric coefficients related with the nitrogen (and the oxygen in the nitrogen reaction) are:

$$
\begin{aligned}
N \quad &: 2\, n_{1,1} = \quad 2\, m_{1,1} + m_{1,18} + m_{1,19} \\
O_2 &: n_{1,2} = \qquad 0.5\, m_{1,18} + m_{1,19} \; ; \; m_{1,2} = 0.0 \\
&\text{If excess of oxygen} \;>= 200\% \qquad \alpha_{1,1} = 0.1 \; ; \; \alpha_{1,2} = 0.0 \\
&\text{If excess of oxygen} \;= 100\% \qquad \alpha_{1,1} = 0.0 \; ; \; \alpha_{1,2} = 0.1 \\
&\text{If excess of oxygen} \;<= 50\% \qquad \alpha_{1,1} = 0.0 \; ; \; \alpha_{1,2} = 0.0
\end{aligned}
\tag{39}
$$

Here, a linear interpolation is used between the boundaries.

The reactive stoichiometric coefficients n are known variables except for the oxygen. Thus, for the nitrogen oxidation:

$$
\begin{aligned}
m_{1,19} &= 2\, \alpha_{1,1}\, n_{1,1} \\
m_{1,18} &= 2\, \alpha_{1,2}\, n_{1,1} \\
m_{1,1} &= 0.5\, (\, 2\, n_{1,1} - m_{1,18} - m_{1,19}) \\
n_{1,2} &= 0.5\, m_{1,18} + 1\, m_{1,19}
\end{aligned}
\tag{40}
$$

Similar equations may be stated for the oxidation reaction of each component and all the coefficients may be calculated. With the coefficient m, the concentration of the product is obtained. This formulation may be applied in a generic way for any quantity and any number of reactants.

An iterative process may be followed to find the flame temperature as a function of the amount of all the present species considering: the heat of combustion (automatically calculated from the component's formation heats), reactive and product sensitive heat, and heat losses by radiation and convection.

The combustor is considered to be a capacitive node and equations (24) and (26) applies for the calculation of the combustor variables considering that the product of the combustion is the inlet to the capacitive node equations and the concentration in the combustor are associated to the exit flowrate, as presented in Figure 21.

Local Controls

During the off line tests, the models run without the DCS (see Section 9), thus, independent local controls applied on valves were simulated in a simplified way to avoid the problem of
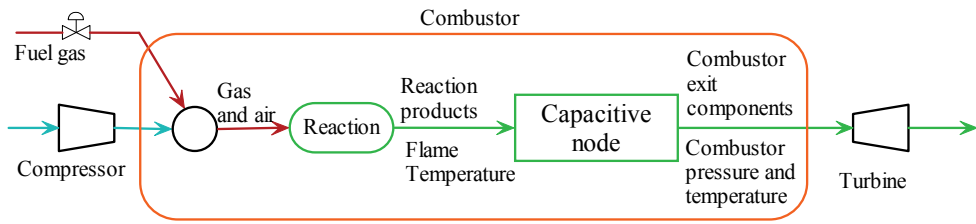
Fig. 21. Conceptual model of the combustor.

a variable increased or diminished because it is not being controlled. The model for the aperture demand *dm* is:

$$dm = Ap \pm k_p \frac{Sp - Va}{Sp} \tag{41}$$

Where *Sp* is the desired set point, *Va* the value of the variable to be controlled, and. K_p is a proportional constant whose value depends on the dynamics of the controlled variable. The aperture of the valve tends to the value of the demand with a lag (k_t) as:

$$Ap = Ap + (dm - Ap) k_t \tag{42}$$

Although the control model is not a conventional one and there does not exit an integral value, in all cases worked with enough precision for the tests purposes (in fact, the model has been applied on the final version of other full scope training simulators).

Final Remarks

There were not included in this revision the generic models developed by the IIE that were not utilised in this simulator as ejectors, air cooled condensers, deaerators, boilers, cooling tower, separators of hydrocarbon mixtures, etc.

Although first principle and well known tested and approved correlations are used as the modelling basis, some assumptions and simplifications are involved in the final models. Inevitably, differences between the model results and the plant behaviour are presented. To fit the model in order to minimize the difference to accomplish with the ANSI/ISA norm, the parameters have to be adjusted.

The simulator resulted with 1500 parameters, 8800 global variables including 33 analogical malfunctions, 65 logical malfunctions, 55 analogical remote functions and 151 binary remote functions

8.3 Malfunctions, remote functions and external parameters

Malfunctions.

The malfunctions included in the simulator were defined according the ANSI/ISA norm and the particular interest of the CENAC. They may be classified in the types generic and specials.

Generic malfunctions: problems in the pressure, temperature and flow transmitters; valves failure (open, close or stuck); filters and flow resistances fouling; heat exchanger fouling (to decrease the heat transfer coefficient); alteration of the turbine and generator vibrations;

System	Subsystem	Number of malfunctions	Number of remote functions
C1 Control System	Generator and Electric System	13	64
	Gas Turbine	7	7
Supervisory System	Ready to Start/Trips	1	5
	C1 Gen Vibrat Analysis	4	0
	C1 Combustion Flash back	3	0
	C1 Blade Path Exhaust	36	0
Auxiliary Systems	Fuel Gas System	7	4
	C1 Lube Oil System	5	35
	C1 Hydr Ctl Oil System	2	18
	C1 Generator Longitudinal	2	32
	C1 Gen Seal Oil System	2	15
	C1 Turbine Cooling System	16	26

Table 7. Number of malfunctions and remote functions for each system in the simulator.

variation of the metal temperatures in the turbine-generator metals; motors trips (for pumps, fans, compressors etc.); heat exchanger tubes breaking; and closed tanks gas leaking. *Special Malfunctions.* They are the malfunctions specifically designed to cover the CENAC's necessities: malfunctions of electric components (black out, charge of generation rejection, etc.); fault of the control components (turbine overspeed, no detection of the combustor flame, etc.); problems in the combustor (low combustion efficiency, exhaust thermocouples); low pressure of fuel gas supply; and turbine low efficiency.

Remote functions The remote functions included in the simulator were defined according the ANSI/ISA norm and the particular interest of the CENAC. The main remote functions are: opening and closing of manual valves, opening and closing of switches and relays; automatic and manual position switching; and start up and trip of equipments; selection of the equipment; and set point modification.

In Table 7 the number of malfunctions and remote functions are listed according the system-subsystem classification defined by the customer to be presented in the respective simulator pop-up menu.

External parameters.

The external parameters allow modifying the environment conditions that do not depend on the operators control as: temperature (dry and wet bulbs), atmospheric pressure, gas supply pressure, combustion factor and variation in the voltage and frequency of the external system; and both methane and nitrogen molar fraction in the gas.

9. Off line testing and coupling of the systems models

During the models development, a very important task is to define the causal relation of the models, *i.e.* to specify for each model all the variables (inputs and outputs) between the models, controls, operator console, and instructor console, and assure that all the models

have congruency. The variables (global variables) are classified and added into a data base. This data base contains the variables declaration for the C and FORTRAN programs, parameters values, malfunctions, instruments ranges, remote functions, unit conversions, etc.

Each MSS, developed independently, is tested off line without controls (open loop). In this stage it is convenient to have some simplified controls to avoid problems of process instabilities; for example in a tank model it is necessary to control the level to avoid it becomes empty or shedding. The idea of the tests is to reproduce the design data, normally data plant working at 100% of capacity. The global input variables must have an initial values registered in an ASCII format file (initial condition).

For the coupling process, the DCS models are integrated into the MAS without the process models and tested to verify its dynamics, including the control screens. The models are added one by one according the defined sequence matrix. With each model the initial condition file is actualised and some tests are performed to assure the coupling is successful. In this stage adjustments are done, to avoid mathematical instabilities.

When the last model has been added and the 100% initial condition is ready, by operating the plant there are obtained all the other initial conditions up to get the cold start initial condition.

Fabric tests are applied (the same mentioned in the following section) to the integrated simulator before it is translated to its final site in the customer's facilities.

10. Validation and results

The simulator validation was carried out proving its response against the 16 very detailed operation procedures elaborated by CFE specialised personnel, ("Acceptance Simulator Test Procedures"). The tests included all the normal operation range, from cold start conditions to full charge, including the response under malfunctions and abnormal operation procedures. In all cases the response satisfied the ANSI/ISA norm.

The customer provided the plant data for an automatic start up procedure (with a total of 302 variables). The simulator results were compared with these data. No data for other transients were considered as design data.

To selected results presented here are an automatic start-up followed by a coupling of malfunctions. During these transients no actions of the operator were allowed. The plotted variables were chosen to verify the effect of the malfunctions. In Table 8 a list of the events and the time they happen is presented.

For all the graphs, excepting Figure 22, a comparison between the real plant values and the simulator results during the first 2780 s are presented, then no plant data are available and only the simulator results are displayed up to the end of the simulation. In all the tests may be appreciated the good agreement between the real plant data and the simulation results. No further commentaries are necessary at this respect.

In Figure 22 a comparison between the expected and simulator turbine speed is presented during the turbine speed up during 830 s when the speed reaches its nominal value of 3600 rpm.

In Figure 23, the combustor pressure is presented on the left y axis and the gas delivery pressure (an external parameter where the operator has no control) is presented on the right y axis. The gas delivery pressure is measured in a pressure controlled header where the gas is stored from a duct that delivers the gas continuously.

Time (*s*)	Time (*hh:mm:ss*)	Event
0	00:00:00	Simulation is initiated.
5	00:00:05	Turbine is turned on in automatic mode.
120	00:02:00	Ignition in the combustor is triggered.
830	00:13:50	Turbine reaches its nominal speed (3600 *rpm*).
2790	00:46:30	The plant produces its nominal charge (150 *MW*).
2970	00:49:30	Initiates malfunction of low efficiency in the combustor.
3000	00:50:00	Malfunction of low efficiency in the combustor takes its final value (50% of severity).
3500	00:58:20	Initiates malfunction of pressure loss in the delivery line of gas fuel.
3680	01:01:20	Malfunction of pressure loss in the delivery line of gas fuel takes its final value (4082 *kPa*).
4200	01:10:00	End of the simulation.

Table 8. Times of the transients' events

The graph of the gas delivery pressure (Figure 23) shows how the pressure changed with a ramp between the 3500 *s* and 3680 *s*. The behaviour of the combustor pressure is explained in Table 9.

In Figure 24, the fuel gas flowrate is plotted on the left *y* axis and the apertures of two (A and C) of the gas control valve apertures are presented on the right *y* axis. There exist four gas control valves, one for the pilots and three more that distribute the flow around the combustor inlet nozzles. All they open in a prefixed sequence and their function is to control the turbine speed and the produced electrical power.
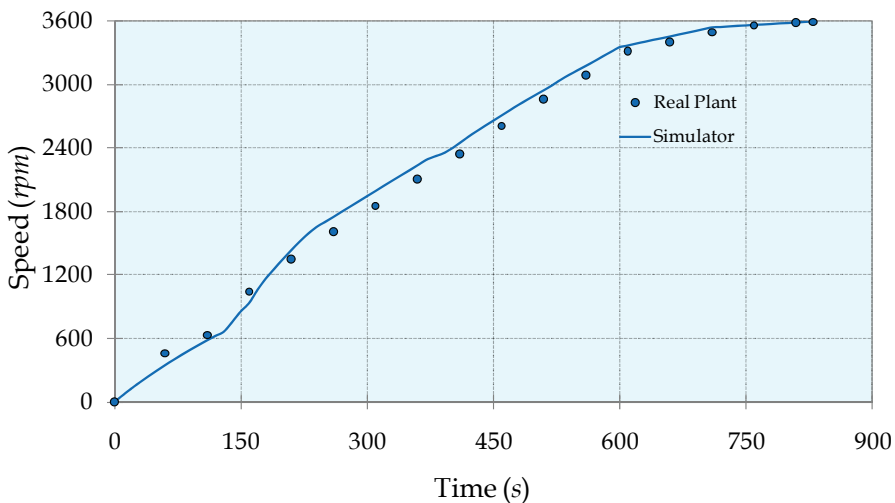
Fig. 22. Turbine speed comparison for the real plant and the simulation.
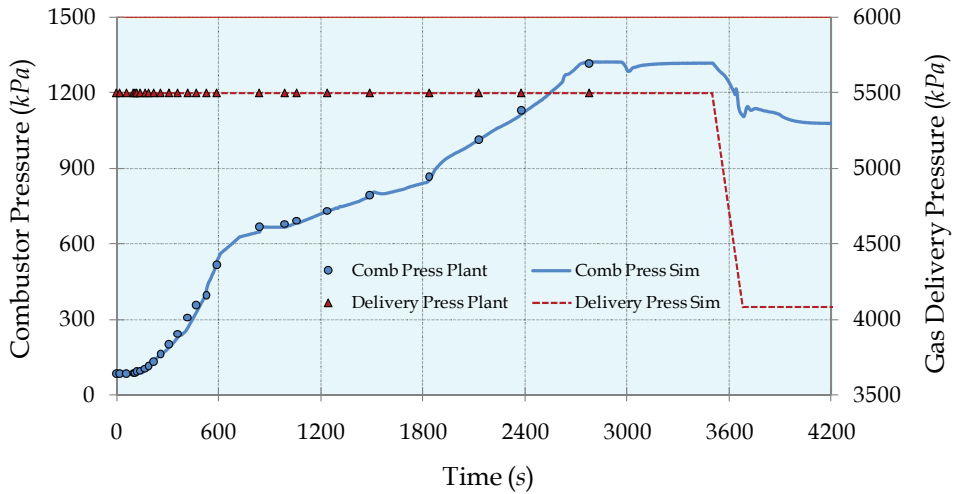
Fig. 23. Combustor pressure and gas delivery pressure

Time period (s)	Event Id	Description of the results for the combustor pressure, Fig. 23
2790 - 2970	Nominal charge - Low efficiency initiates	The pressure stabilises.
2970 - 3000	Low efficiency initiates - Low efficiency ends	The pressure drops because the combustion is affected and the temperature in the combustor descents too.
3000 - 3500	Low efficiency ends - Pressure loss initiates	Pressure arises due the effect of the gas control valves that treats to keep the charge of the plant by allowing more gas flowrate to the combustor.
3500 - 3680	Pressure loss initiates - Pressure loss ends	The pressure drops because the effect of the decreasing of the delivery pressure is greater than the effect of the gas control valves treating to keep the charge. At about 3660 s the pressure increases and then descents because the aperture of the gas oscillate due the control algorithm.
3680 - 4200	Pressure loss ends - Simulation Ends	The pressure decreases lightly trying to reach a new (and final) steady state because the gas control valves tend to stabilise their aperture.

Table 9. Description of the results for the combustor pressure, according Fig. 23

The behaviour of the gas control valves dynamics during the malfunctions transients are explained in table 10.

The changes of the fuel gas flowrate variable for the test are explained in table 11.

The exhaust temperature is measured in the gas phase on the exit of the combustor. Some comments on the behaviour of the exhaust temperature during the malfunctions transients are given in table 12.
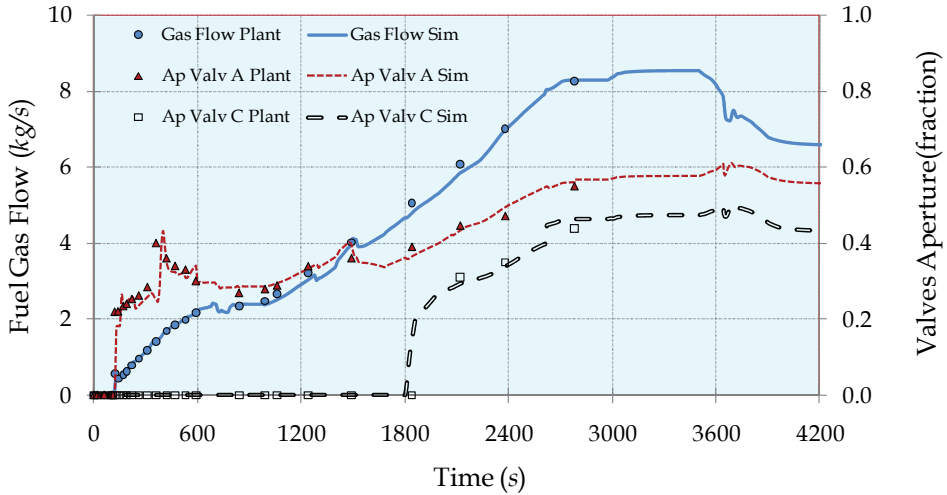
Fig. 24. Gas flowrate and apertures of gas control valves A and C.

Time period (s)	Event Id	Description of the results for the fuel gas control valves, Fig. 24
2790 - 2970	Nominal charge - Low efficiency initiates	The apertures are stable.
2970 - 3000	Low efficiency initiates - Low efficiency ends	The apertures increase their value trying to compensate the charge descending due to the loss of combustion efficiency.
3000 - 3500	Low efficiency ends - Pressure loss initiates	The gas control valves adjust their value and control the charge.
3500 - 3680	Pressure loss initiates - Pressure loss ends	The gas control valves treat to keep the charge. At about 3660 s the gas control valves have a transient because open suddenly but the control detects this abrupt change and limits the valve apertures producing a slight transient in the apertures.
3680 - 4200	Pressure loss ends - Simulation Ends	The control algorithm allows decreasing the charge and stabilise the apertures and the plant in a new steady state.

Table 10. Description of the results for the fuel gas control valves apertures, according Fig. 24.

Time period (s)	Event Id	Description of the results for the fuel gas flowrate, Fig. 24
2790 - 2970	Nominal charge - Low efficiency initiates	The fuel gas flow remains stable.
2970 - 3000	Low efficiency initiates - Low efficiency ends	The gas flowrate increases following the aperture of the gas control valves trying to compensate the losing of electrical power due the malfunction.
3000 - 3500	Low efficiency ends - Pressure loss initiates	The gas flowrate adjusts its value (grows slightly) according the gas control valves aperture to adjust the charge.
3500 - 3680	Pressure loss initiates - Pressure loss ends	The gas flowrate descents because the gas control valves are not able to keep the charge. The malfunction is too severe. At about 3660 s the gas flow has a transient because the valves open and then close (not totally) suddenly.
3680 - 4200	Pressure loss ends - Simulation Ends	The gas flow tends to stabilise reflecting the control valves apertures behaviour.

Table 11. Description of the results for the fuel gas flowrate, according Fig. 24.

In Figure 25, the generated electrical power is graphed on the left y axis and the exhaust temperature on the right y axis.

The graph of the generated electrical power in Figure 25 shows how the charge evolutes depending on the malfunctions. The behaviour of the charge is explained in table 13.
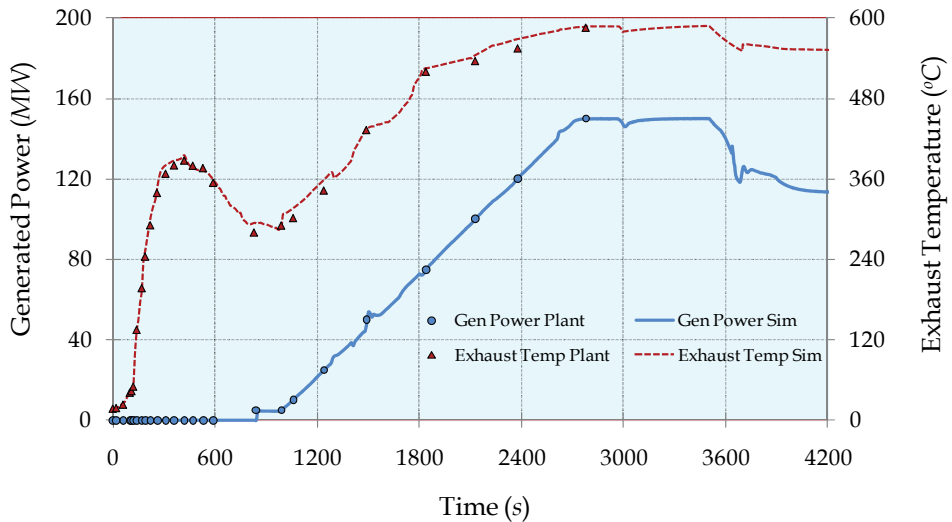
Fig. 25. Generated electrical power and exhaust temperature.

Time period (s)	Event Id	Description of the results for the exhaust temperature, Fig. 25
2790 - 2970	Nominal charge - Low efficiency initiates	The exhaust temperature stabilises.
2970 - 3000	Low efficiency initiates - Low efficiency ends	The exhaust temperature drops because the combustion is affected and the gas control valves do not respond immediately.
3000 - 3500	Low efficiency ends - Pressure loss initiates	The exhaust temperature arises due the effect of the gas control valves that treats to keep the electrical power by opening and forcing more gas flowrate to the combustor.
3500 - 3680	Pressure loss initiates - Pressure loss ends	The exhaust temperature drops. The effect of the malfunction is more important than the effect of the gas control valves. At about $3660\,s$ the exhaust temperature has a transient because the gas control valves aperture behaviour.
3680 - 4200	Pressure loss ends - Simulation Ends	The exhaust temperature decreases tending to stabilise according the gas control valves position.

Table 12. Description of the results for the fuel gas flowrate, according Fig. 25.

Time period (s)	Event Id	Description of the results for the exhaust temperature, Fig. 25
2790 - 2970	Nominal charge - Low efficiency initiates	The charge is in steady state.
2970 - 3000	Low efficiency initiates - Low efficiency ends	The charge drops because the combustion malfunction and the gas control valves do not compensate the effect that soon.
3000 - 3500	Low efficiency ends - Pressure loss initiates	The charge recovers its original nominal value due the control by the gas control valves, allowing more gas flowrate into the combustor.
3500 - 3680	Pressure loss initiates - Pressure loss ends	The charge drops because the malfunction of losing delivery pressure that cannot be nullified by the gas control valves. At about $3660\,s$ the charge oscillates due the gas control valves aperture behaviour.
3680 - 4200	Pressure loss ends - Simulation Ends	The charge tends to stabilise for the steady state defined by the control algorithm.

Table 13. Description of the results for the fuel gas flowrate, according Fig. 25.

Although they are not presented in this work, must be mentioned that all the expected alarms were presented in the precise time.

The CENAC endorsed and accepted as correct the results of the tests in accordance with the testing acceptance procedures.

11. Conclusion

A complete model of a gas turbine generation plant for operators' training has been presented. The validation of the simulator was carried out by CENAC specialised personnel under rigorous acceptance simulator testing procedures, and with reliable experience in the use of simulators. The simulator was tested in all the operation range from cold start to 100% of load and fulfils the performance specified by CENAC including a comparison of its results with plant data. The results demonstrate than the simulator is a replica, high-fidelity, plant specific simulator for operator training. Realism is provided by the use of DCS screens emulation. Now, the CENAC has one more useful tool to train the future generation of operators of the gas turbine power plants.

The robustness of the models is due, in an important part, to the generic models approach, the software tools, and the methodology that supports the development of the simulator.

From the literature review, considering that the modelling basis of the IIE has less constrains and thus a more wide scope, it may be concluded that the present models could be used for other purposes like that reported.

This simulator had several adjustments during its development to fit its dynamic behaviour to that obtained in the real plant.

An additional aspect that gives certitude and robustness to the simulator behaviour is that this has practically the same DCS that the plant which means that the process models that were obtained by the SD engineers reproduce correctly the real behaviour of the reference plant.

Presently, training scenarios were defined and used in the simulator to achieve the training program that is probing to be a successful one.

12. Acknowledgment

13. Acronyms

The list of acronyms used in this chapter is:
CFE   - The National Utility Company in Mexico
CENAC - National Centre of Training Ixtapantongo
DCS   - Distributed Control System
GM   - Generic Model
IC   - Instructor Console
ICO   - Initial Conditions

IIE   - Electrical Research Institute
IPD   - Interactive Process Diagrams
MAS   - Simulation Environment
MMI   - Man Machine Interface
MN   - Maintenance Node
MSS   - Model of a Simulated System
OS   - Operators' Station
PC   - Personal Computer
PEMEX – Mexican Oil Company
SAMA   - Scientific Apparatus Makers Association
SD   - Simulation Department
SN   - Simulation Node
TP   - Thermodynamic Properties

14. References

Arnold, E. (1967). *Steam tables: thermodynamic properties of water and steam, viscosity of water and steam, thermal conductivity of water and steam*, Electrical Research Association, London.

Banetta, S.; Ippolito, M.; Poli, D. & Possenti, A. (2001). A model of cogeneration plants based on small-size gas turbines, *16th International Conference and Exhibition on Electricity Distribution*, IEE Conf. Publ, Vol. 4, No. 482, January 18-21, 2001, Amsterdam, The Netherlands, ISSN: 0537-9989.

Burgos, E. (1998). Simuladores, dos décadas de investigación, *Boletín IIE*, Vol. 22 No.2, pp. 64-71, 1998.

CFE web page:http://www.cfe.gob.mx/QuienesSomos/queEsCFE/estadisticas/Paginas/Indicadoresdegeneracion.asp.

Chen, L.; Zhang, W. & Sun, F. (2009). Performance optimization for an open-cycle gas turbine power plant with a refrigeration cycle fro compressor inlet air cooling. Part I: thermodynamic modelling, *Journal Power and Energy. Proc. IMechE*. Vol. 223 Part A.

Colonna P.; van Putten H. (2007). Dynamic modelling of steam power cycles. Part I - Modelling paradigm and validation, *Applied Thermal Engineering*, Vol. 27, No. 2-3, pp. 467-480, ISSN 1359-4311.

Epri, (1993), Justification of simulators for fossil fuel power plants, *Technical Report TR-102690*, EPRI, USA, 1993.

Fray, R.; Divakaruni M. (1995). Compact simulators can improve fossil plant operation, *Power Engineering*, Vol. 99 No. 1, pp. 30-32, ISSN 0032-5961, 1995, United States.

Ghadimi, A.; Broomand, M, & Tousi, M. (2005). Thermodynamic model of a gas turbine for diagnostic software. *Proceedings of the IASTED International Conference on Energy and Power Systems*, pp. 32-36, , April. 18-20, 2005, , Krabi, Thailand, ISSN 088986-548-5.

González-Santaló, J.M.; González-Díaz, A. & Mariño-López, C.A. (2007). Diagnosis of the operation of power plants. *Proceedings of Power 2007*. ASME Power 2007, Jul.17-19, 2007, San Antonio, Texas.

Hoffman S. (1995), A new era for fossil power plant simulators, *Epri Journal*, Vol. 20 No. 5, pp. 20-27, 1995

Hosseinpour, F.; Hajihosseini, H. (2009), Importance of simulation in manufacturing, *World Academy of Science, Engineering and Technology*, Vol. 51, pp. 285-288, March 2009, ISSN: 2070-3724.

Jaber, Q.M.; Jaber J.O. & Kawaldah M.A. (2007). Assessment of power augmentation from gas turbine power plants using different inlet air cooling system. *Jordan journal of mechanical and industrial engineering*. Vol. 1, No.1, Sep. 2007, pp.7-17, ISSN 1995-6665.

Kaproń, H.; Wydra, M. (2008). Modelling of gas turbine based plants during power changes, *The European simulation and modelling conference modelling and simulation*, pp. 412-414, ISSN 0955301866-5.

Kikstra, J.F.; Verkooijen, A.H.M. (2002). Dynamic modelling of a cogenerating nuclear Gas turbine plant-part I: Modeling and Validation. *Journal Engenneering for Gas Turbines and Power*. Vol. 124, July 2002, pp. 725-733.

Langston, L.S. (2008). Gas turbine industry overview 2008, *Mechanical Engineering, The Magazine of ASME*, 2008.

Mendoza ,Y.; Roldán-Villasana, E.J.; Galindo, I. & Romero, J. (2004). Methodology to adapt the feedwater and condensate system, using a flow and pressure generic model, for the Laguna Verde nuclear power plant simulator, *Proceedings of Summer Computer Simulation Conference*, The Society for Modeling and Simulation International, pp. 123-128, July 25-29, 2004, San Jose California, USA, ISBN:1-56555-283-0.

Pasquantonio F. D., Macchi A. (1976). Mathematical model and boundary conditions in stress analysis relating to steam turbine rotors, under transient operating conditions. *International Journal for Numerical Methods in Engineering*, Vol. 10, Issue 2, pp. 345-360, 1976.

Press, W.H.; Teukolsky, S.A.; Vetterling, W.T. & Flannery, B.P. (1997). Numerical Recipes in Fortran 77: *The Art of Scientific Computing*, Cambridge University, New York. ISBN: 052143064X.

Reid R., Prausnitz J., Poling B. (1987), *The properties of gases and liquids*, McGraw-Hill, 3rd ed., New York, USA, pp 26-67.

Rice, J. (2004). A growing world demands a balanced portfolio of clean energy options, *World Energy*, Vol. 7 No. 1, pp. 100-103, 2004.

Roldán-Villasana E.J.; Mendoza-Alegría Y. (2004), Adaptation of a generic model to solve flows and pressures hydraulic networks for the solution of electrical networks, *Proceedings of CNS 6th International Conference on Simulation Methods in Nuclear Engineering*, Canadian Nuclear Society, pp.1-12, October 2004, Montréal Québec, Canada, ISBN: 0-919784-80-1.

Roldán-Villasana, E.J.; Mendoza-Alegría Y. (2006), Simulation of a power gas turbine system with a generic combustor model, *Proceedings of the 2006 Summer Computer Simulation Conference*, The Society for Modeling and Simulation International, pp. 285-290, July 31-August 2, 2006, Calgary, Alberta, Canada, ISBN:1-56555-307-1.

Roldán-Villasana, E.J.; Mendoza-Alegría Y. & Avalos-Valenzuela, H. (2006). Updating the computer platform of a geothermal power plant simulator, *Proceedings of the 2006 Summer Computer Simulation Conference*, The Society for Modeling and Simulation International, pp. 285-290, July 31-August 2, 2006. Calgary, Alberta, Canada, ISBN:1-56555-307-1.

Rubechini, F.; Marconcini, M.; Arnone, A.; Maritano, M.& Cecchi, S. (2008). The impact of gas modeling in the numerical analysis of a multistage gas turbine. *Journal of Turbomachinary*, Vol. 130, pp. 021022-1 – 021022-7, April 2008.

Vieira, L.; Matt, C.; Guedes, V.; Cruz, M. & Castelloes F. (2008). Optimization of the operation of a complex combined-cicle cogeneration plant using a professional process simulator. *Proceedings of IMECE2008. ASME International mechanical Engineering Congress and Exposition,* pp. 787-796, October 31-November 6, 2008, Boston, Massachusetts, USA.

Watanabe, M.; Ueno,Y.; Mitani,Y.; Iki,H.; Uriu,Y. & Urano, Y. (2008). Developer of a dynamical model for customer´s gas turbine generator in industrial power systems. 2nd. IEEE *International conference on power and energy*, (PECon 08). December 1-3, pp. 514-519, 2008, Johor Baharu, Malaysia.

Zhu, Y., Frey, H.C. (2007). Simplified performance model of gas turbine combined cycle systems. *Journal of Energy Engineering*. Vol. 133, No. 2, Jun 2007, pp. 82-90, ISSN 0733-9402.

Life Prediction of Gas Turbine Materials

Xijia Wu

Institute for Aerospace Research, National Research Council
Canada

1. Introduction

The advance of gas turbine engines and the increase in fuel efficiency over the past 50 years relies on the development of high temperature materials with the performance for the intended services. The cutaway view of an aero engine is shown in Fig. 1. During the service of an aero engine, a multitude of material damage such as foreign object damage, erosion, high cycle fatigue, low cycle fatigue, fretting, hot corrosion/oxidation, creep, and thermomechanical fatigue will be induced to the components ranging from fan/compressor sections up front to high pressure (HP) and low pressure (LP) turbine sections at the rear. The endurance of the gas turbine engine to high temperature is particularly marked by the creep resistance of HP turbine blade alloy. Figure 2 shows the trend of firing temperature and turbine blade alloy capability (Schilke, 2004). Nowadays, the state-of-the-art turbine blade alloys are single crystal Ni-base superalloys, which are composed of intermetallic γ' (Ni$_3$Al) precipitates in a solution-strengthened γ matrix, solidified in the [100] crystallographic direction. Turbine disc alloys are also mostly polycrystalline Ni-base superalloys, produced by wrought or powder metallurgy processes. Compressor materials can range from steels to titanium alloys, depending on the cost or weight-saving concerns in land and aero applications. Coatings are often applied to offer additional protection from thermal, erosive and corrosive attacks. In general, the advances in gas turbine materials are often made through thermomechanical treatments and/or compositional changes to suppress the failure modes found in previous services, since these materials inevitably incur service-induced degradation, given the hostile (hot and corrosive) operating environment. Therefore, the potential failure mechanisms and lifetimes of gas turbine materials are of great concern to the designers, and the hot-section components are mostly considered to be critical components from either safety or maintenance points of view.

Because of its importance, the methodology of life prediction has been under development for many decades (see reviews by Viswanathan, 1989; Wu et al., 2008). The early approaches were mainly empirically established through numerous material and component tests. However, as the firing temperatures are increased and the operating cycles become more complicated, the traditional approaches are too costly and time-consuming to keep up with the fast pace of product turn-around for commercial competition. The challenges in life prediction for gas turbine components indeed arise due to their severe operating conditions: high mechanical loads and temperatures in a high-speed corrosive/erosive gaseous environment. The combination of thermomechanical loads and a hostile environment may induce a multitude of material damages including low-cycle fatigue, creep, fretting and oxidation. Gas turbine designers need analytical methods to extrapolate the limited material

property data, often generated from laboratory testing, to estimate the component life for the design operating condition. Furthermore, the requirement of accurate and robust life prediction methods also comes along with the recent trend of prognosis and health management, where assessment of component health conditions with respect to the service history and prediction of the remaining useful life are needed in order to support automated mission and maintenance/logistics planning.

To establish a physics-based life prediction methodology, in this chapter, the fundamentals of high temperature deformation are first reviewed, and the respective constitutive models
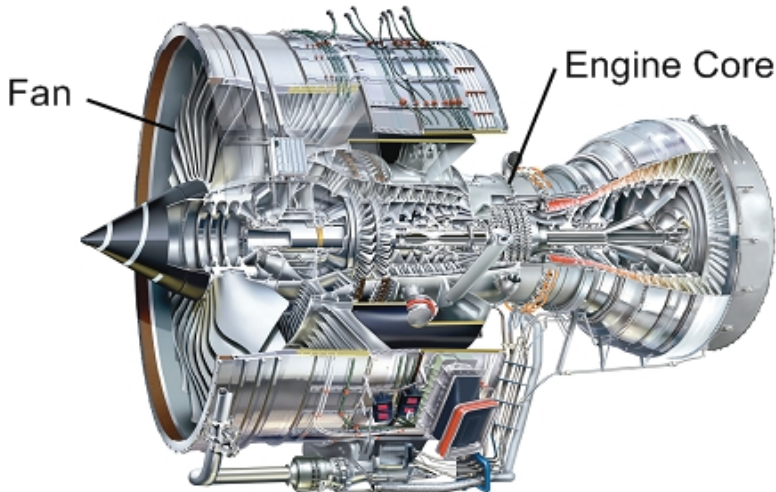
Fig. 1. Cutaway view of the Rolls-Royce Trent 900 turbofan engine used on the Airbus A380 family of aircraft (Trent 900 Optimised for the Airbus A380 Family, Rolls-Royce Plc, Derby UK, 2009).
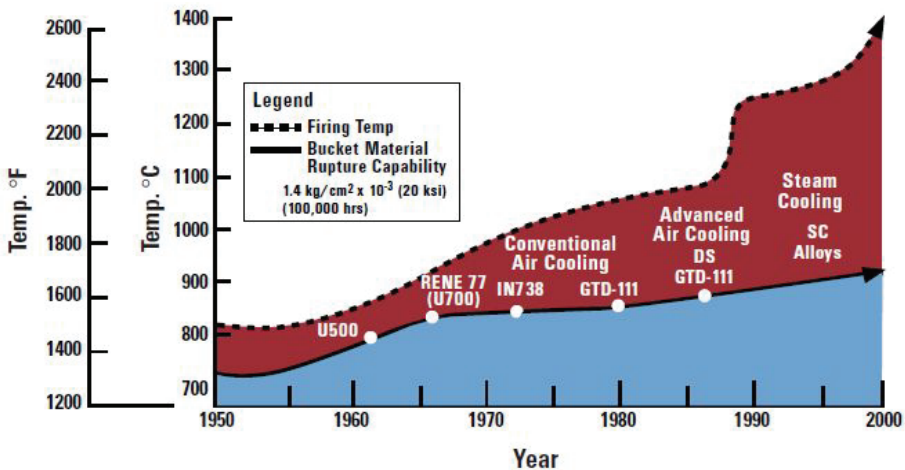
Fig. 2. Increase of firing temperature with respect to turbine blade alloys development (Schilke, 2004).

are introduced. Then, the evolution of material life by a combination of damage mechanisms is discussed with respect to general thermomechanical loading. Furthermore, crack growth problems and the damage tolerance approach are also discussed with the application of fracture mechanics principles.

2. Fundamentals of high temperature deformation

In general, for a polycrystalline material, deformation regimes can be summarized by a deformation map, following Frost and Ashby (Frost & Ashby, 1982), as shown schematically in Fig. 3. Elastic (E) and rate-independent plasticity (P) usually happens at low temperatures (i.e. $T < 0.3$ T_m, where T_m is the melting temperature). In the plasticity regime, the deformation mechanism is understood to be dislocation glide, shearing or looping around the obstacles along the path; and the material failure mechanism mainly occurs by alternating slip and slip reversal, leading to fatigue, except for ultimate tensile fracture and brittle fracture. As temperature increases, dislocations are freed by vacancy diffusion to get around the obstacles so that time-dependent deformation manifests. Time dependent deformation at elevated temperatures is basically assisted by two diffusion processes—grain boundary diffusion and lattice diffusion. The former process assists dislocation climb and glide along grain boundaries, resulting in grain boundary sliding (GBS), whereas the latter process assists dislocation climb and glide within the grain interior, resulting in intragranular deformation (ID) such as the power-law and power-law-breakdown.
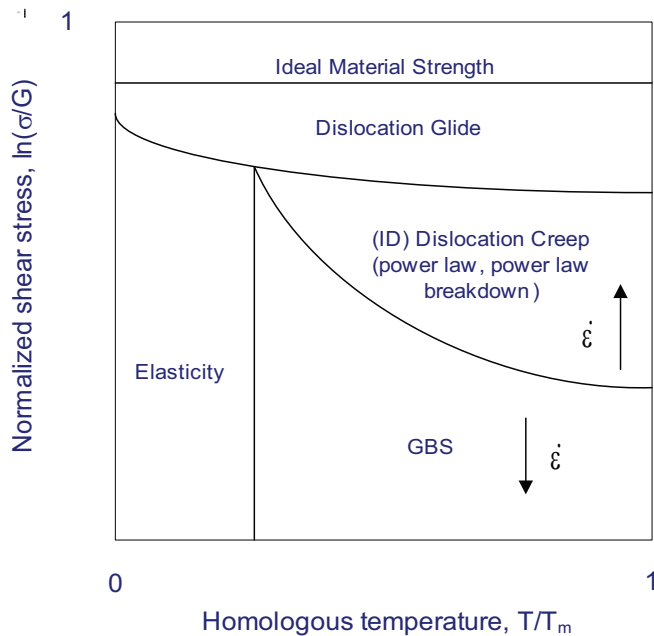
Fig. 3. A schematic deformation mechanism map.

In an attempt to describe inelastic deformation over the entire stress-temperature field, several unified constitutive laws have been proposed, e.g. Walker (1981), Chaboche & Gailetaud (1986), and most recently, Dyson & McLean (2000). These constitutive models

employ a set of evolution rules for kinematic and isotropic hardening to describe the total viscoplastic response of the material, but do not necessarily differentiate whether the contribution comes from intrgranular deformation mechanism or GBS, and hence have limitations in correlating with the transgranular, intergranular and/or mixed failure modes that commonly occur in gas turbine components. Therefore, a physics-based theoretical framework encompassing the above deformation and damage mechanisms is needed.

To that end, we proceed with the basic concept of strain decomposition that the total inelastic strain in a polycrystalline material can be considered to consist of intragranular strain ε_g and grain boundary sliding ε_{gbs}, as:

$$\varepsilon_{in} = \varepsilon_g + \varepsilon_{gbs} \tag{1}$$

The physics-based strain decomposition rule, Eq. (1), with the associated deformation mechanisms is the foundation for the development of an integrated creep-fatigue (ICF) modelling framework as outlined in the following sections (Wu et al. 2009).

2.1 Intragranular deformation

Intragranular deformation can be viewed as dislocation motion, which may occur by glide at low temperatures and climb plus glide at high temperatures, overcoming the energy barriers of the lattice. By the theory of deformation kinetics (Krausz & Eyring, 1975), the rate of the net dislocation movement can be formulated as a hyperbolic sine function of the applied stress (Wu & Krausz, 1994). In keeping consistency with the Prandtl-Reuss-Drucker theory of plasticity, the flow rule of intragranular strain, in tensor form, can be expressed as

$$\dot{\boldsymbol{\varepsilon}}_g = \dot{p}_g \boldsymbol{n}_g \tag{2}$$

where $\dot{p}_g$ is the plastic multiplier as defined by

$$\dot{p}_g = 2A(1 + Mp_g)\sinh(\psi) = \sqrt{\tfrac{2}{3}\dot{\boldsymbol{\varepsilon}}_g : \dot{\boldsymbol{\varepsilon}}_g} \tag{3}$$

where A is an Arrhenius-type rate constant, M is a dislocation multiplication factor, and $\boldsymbol{n}_g$ is the flow direction as defined by

$$\boldsymbol{n}_g = \frac{3}{2}\frac{(\boldsymbol{s} - \boldsymbol{\chi}_g)}{\sigma_g^{eq}} \tag{4}$$

where $\boldsymbol{s}$ is the deviatoric stress tensor and χ_g is the back stress tensor.

Note that the stress and temperature dependence of the plastic multiplier is described by a hyperbolic sine function, Eq. (3), with the evolution of activation energy ψ given by:

$$\dot{\psi} = \frac{V}{kT}\dot{\sigma}_g^{eq} \tag{5}$$

where V is the activation volume, k is the Boltzmann constant, and T is the absolute temperature in Kelvin. Eq. (3) covers both the power-law and the power-law-breakdown regimes in Fig. 3.

As intragranular deformation proceeds, a back stress may arise from competition between work hardening (dislocation pile-up and network formation) and recovery (dislocation climb) as:

$$\dot{\chi}_g = \frac{2}{3} H_g \dot{\varepsilon}_g - \kappa \chi_g \tag{6}$$

where H_g is the work-hardening coefficient and κ is the climb rate (see detailed formulation later). Note that more complicated expressions that consider both hardening and dynamic/static recovery terms may need to be used to formulate the back stress with large deformation and microstructural changes, but to keep the simplicity for small-scale deformation (<1%), Eq. (6) is suffice, as demonstrated in the later examples.

The effective equivalent stress for intragranular deformation is given by

$$\sigma_g^{eq} = \sqrt{\frac{3}{2}\left(s - \chi_g\right) : \left(s - \chi_g\right)} \tag{7}$$

where the column (:) signifies tensor contraction.

2.2 Grain boundary sliding

Based on the grain boundary dislocation glide-climb mechanism in the presence of grain boundary precipitates (Wu & Koul, 1995; 1997), the governing flow equation for GBS can be expressed as

$$\dot{\varepsilon}_{gbs} = \dot{p}_{gbs} n_{gbs} \tag{8}$$

with a GBS multiplier as defined by

$$\dot{p}_{gbs} = \varphi \frac{D\mu b}{kT} \left(\frac{b}{d}\right)^q \left(\frac{l+r}{b}\right)^{q-1} \frac{\left(\sigma_{gbs}^{eq}\right)\left(\sigma^{eq} - \sigma_{ic}\right)}{\mu^2} \tag{9}$$

where D is the diffusion constant, μ is the shear modulus, and b is the Burgers vector, d is the grain size, r is the grain boundary precipitate size, l is the grain boundary precipitate spacing, and q is the index of grain boundary precipitate distribution morphology (q = 1 for clean boundary, q =2 for discrete distribution, and q = 3 for a network distribution). The GBS flow direction is defined by

$$n_{gbs} = \frac{3}{2} \frac{\left(s - \chi_{gbs}\right)}{\sigma_{gbs}^{eq}} \tag{10}$$

The two equivalent stresses in Eq. (9) are given by

$$\sigma_{gbs}^{eq} = \sqrt{\frac{3}{2}\left(s - \chi_{gbs}\right) : \left(s - \chi_{gbs}\right)} \tag{11}$$

and

$$\sigma^{eq} = \sqrt{\frac{3}{2} s : s} \tag{12}$$

The evolution of the grain boundary back stress in the presence of grain boundary precipitates is given by (Wu & Koul, 1995)

$$\dot{\chi}_{gbs} = \frac{2}{3} H_{gbs} \dot{\boldsymbol{\varepsilon}}_{gbs} - \kappa \boldsymbol{\chi}_{gbs} \tag{13}$$

where H_{gbs} is the grain boundary work hardening coefficient, and κ is the dislocation climb rate as given by

$$\kappa = \frac{D\mu b}{kT} \frac{(\sigma^{eq} - \sigma_{ic})}{\mu} \tag{14}$$

The equivalent stress for GBS, σ_{gbs}^{eq}, controls the grain boundary dislocation glide with a back stress χ_{gbs}. The other equivalent stress, σ^{eq}, controls grain boundary dislocation climb, once it surpass a threshold stress, σ_{ic}, that arises from the constraint of grain boundary precipitates. As shown in Eq. (9), the GBS multiplier is controlled by the grain boundary diffusion constant D and grain boundary microstructural features such as the grain size, the grain boundary precipitate size and spacing, and their morphology. The back stress formulation, Eq. (13), states the competition between dislocation glide, which causes grain boundary dislocation pile-up, and recovery by dislocation climb. Henceforth, Eq. (9) depicts the grain boundary plastic flow as a result of dislocation climb plus glide overcoming the microstructural obstacles present at the grain boundaries. Last but not least, GBS is also affected by the grain boundary waveform, as given by the factor ϕ (Wu & Koul, 1997):

$$\phi = \begin{cases} \dfrac{2}{1 + \left(\dfrac{2h}{\lambda}\right)^2} - 1 & \textit{for trianglular boundaries} \\[6mm] \dfrac{2}{\sqrt{1 + \left(\dfrac{\pi h}{\lambda}\right)^2}} - 1 & \textit{for sinusoidal boundaries} \end{cases} \tag{15}$$

where λ is wavelength and h is the amplitude.

By solving all the components of inelasticity, the evolution of the stress tensor is governed by

$$\dot{\boldsymbol{\sigma}} = \boldsymbol{C} : (\dot{\boldsymbol{\varepsilon}} - \dot{\boldsymbol{\varepsilon}}_{in}) \tag{16}$$

3. Deformation processes and constitutive models

3.1 Cyclic deformation and fatigue

It is commonly known that a metal subjected to repetitive or flunctuating stress will fail at a stress much lower than its ultimate strength. Failures occuring under cyclic loading are generally termed *fatigue*. The underlying mechanisms of fatigue is dislocation glide, leading to formation of persistent slip bands (PBS) and a dislocation network in the material. Persistent slip bands, when intersecting at the interface of material discontinuities (surface, grain boundaries or inclusions, etc.) result in intrusions/extrusions or dislocation pile-ups, inevitably leading to crack nucleation.

To describe the process of cyclic deformation, we start with tensile deformation as follows.

For uniaxial strain-controlled loading, the deformation is constrained as:

$$\dot{\varepsilon} = \frac{\dot{\sigma}}{E} + \dot{\varepsilon}_p = \text{constant} \tag{17}$$

Substituting Eq. (3-7) into Eq. (17) (neglecting dislocation climb, i.e., $\kappa\chi_g \ll H\dot{\varepsilon}$; and multiplication, i.e., M = 0), we have the first-order differential equation of Ψ, as (Wu et al., 2001)

$$\dot{\Psi} = \frac{EV}{kT}\left[\dot{\varepsilon} - 2A\left(1 + \frac{H}{E}\right)\sinh\Psi\right] \tag{18}$$

which can be solved as

$$\left(\frac{e^{-\Psi} - a}{\chi e^{-\Psi} + b}\right) = \left(\frac{1-a}{\chi + b}\right)\exp\left\{-\frac{VE\dot{\varepsilon}(t-t_0)\sqrt{1+\chi^2}}{kT}\right\} \tag{19}$$

where

$$\chi = \frac{2A}{\dot{\varepsilon}}\left(1 + \frac{H}{E}\right), \quad a = \frac{\sqrt{1+\chi^2} - 1}{\chi}, \quad b = \sqrt{1+\chi^2} + 1 \tag{20}$$

The initial time of plastic deformation is defined by

$$\Psi_0 = \frac{(\sigma - H\varepsilon_p^0 - \sigma_0)}{kT} = 0 \tag{21}$$

where ε^0_p is the plastic strain accumulated from the prior deformation history, and σ_0, as an integration constant, represents the initial lattice resistance to dislocation glide. At the first loading, $\varepsilon^0_p = 0$. Since the deformation is purely elastic before the condition, Eq. (21), is met: $\sigma = E\dot{\varepsilon}t$, then $t_0 = \sigma_0/(E\dot{\varepsilon})$. Once the stress exceeds the initial lattice resistance in the material, i.e., $\sigma > \sigma_0$, plasticity commences. In this sense, σ_0 corresponds to the critial resolved shear stress by a Taylor factor.

From Eq. (20), we can obtain the stress-strain response as follows:

$$\sigma - H\varepsilon_p - \sigma_0 = -\frac{kT}{V}\ln\left(\frac{a + \omega(\varepsilon)b}{1 - \omega(\varepsilon)\chi}\right) \tag{22}$$

where, $\omega(\varepsilon)$ is a response function as defined by

$$\omega(\varepsilon) = \left(\frac{1-a}{\chi + b}\right)\exp\left\{-\frac{V(E\varepsilon - \sigma_0)\sqrt{1+\chi^2}}{kT}\right\} \tag{23}$$

Eq. (22) basically describes the accumulation of plastic strain via the linear strain-hardening rule with dislocation glide as the dominant process and limited dislocation climb activities. It is applicable to high strain rate loading conditions, which are often encountered during engine start-up and shutdown or vibration conditions caused by mechanical and/or aerodynamic forces.

Based on the deformation kinetics, Eq. (22) describes the time and temperature dependence of high temperature deformation. As an example, the tensile behaviors of IN738LC at 750 ºC, 850 ºC and 950 ºC are described using Eq. (22) and shown in Fig. 4, in comparison with the

experimental data. The strain rate dependence of the tensile behavior of this alloy at 950°C is also demonstrated in Fig. 5. The parameters for this material model are given in Table 1.
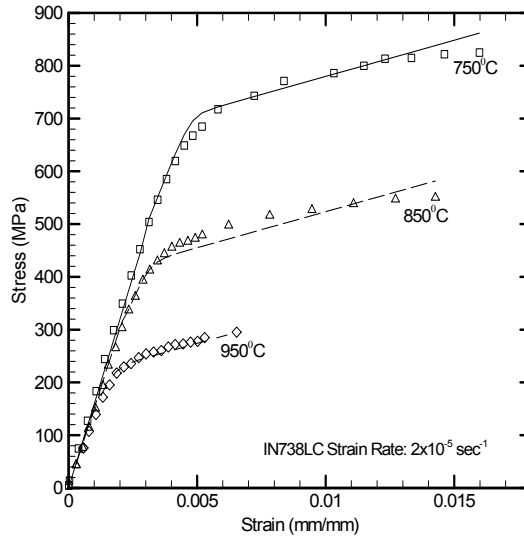
Fig. 4. Stress-strain curves for the IN738LC with the lines as described by Eq. (22).
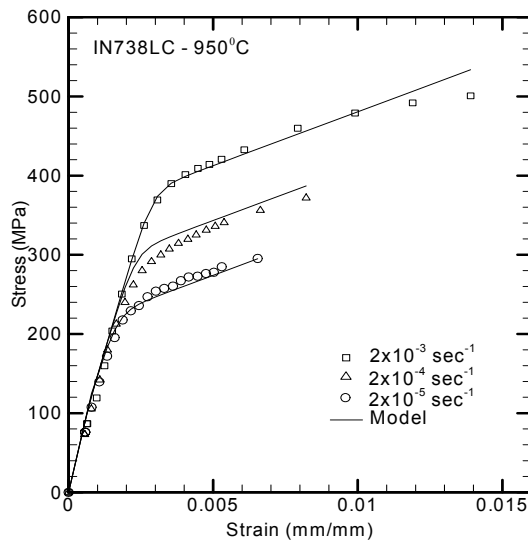
Fig. 5. Stress-strain responses of IN738LC to different loading strain rates at 950 °C.

Temperature ($^{\circ}$C)	750	850	950
Initial lattice resistance, σ_0 (MPa)	540	285	110
Work Hardening Coefficient, H (MPa/mm/mm)	15000	13736	12478
Modulus of Elasticity, E (GPa)	175.5	151.4	137.0
Strain-Rate Constant, $A = A_0\exp[-\Delta G_0^{\neq}/kT]$ (sec^{-1})	3.5x10^{-8}	1.56x10^{-7}	5.5x10^{-7}
Activation Constants			
Activation Volume, V (m^3)	3.977x10^{-22}		
Pre-exponential, A_0 (sec^{-1})	0.7		
Activation Energy, $\Delta G_0^{\neq}$ (J)	2.38×10^{-19}		

Table 1. Constitutive Model Parameters for IN738LC

This constitutive model has 6 parameters: E, H, V, σ_0, A_0 and $\Delta G_0^{\neq}$, which have defined physical meanings. The elastic modulus, E, the work-hardening coefficient, H and the initial activation stress σ_0, are temperature-dependent. The activation parameters, V, A_0 and $\Delta G_0^{\neq}$, are constants corresponding to a "constant microstructure". As far as deformation in a lifing process is concerned, which usually occurs within a small deformation range of ±1%, the description is mostly suffice. The present model, in the context of Eq. (22), also incorporates some microstructural effects via H and σ_0. The significance will be further discussed later when dealing with fatigue life prediction. But before that, let us examine the cyclic deformation process as follows.

Under isothermal fully-reversed loading conditions, first, Eq. (22) describes the monotonic loading up to a specified strain. Upon load reversal at the maximum stress point, the material has $2\sigma_0 + H\varepsilon_p$ as the total stress barrier to yield in the reverse cycle. This process repeats as the cycling proceeds. As an example, the hysteresis loop of IN738LC is shown in Fig. 6. The solid line represents the model prediction with the parameters given in Table 1 (except $\sigma_0 = 40$ MPa for this coarser grained material). The model prediction is in very good agreement with the experimental data, except in the transition region from the elastic to the steady-state plastic regimes, which may be attributed to the model being calibrated to a finer-grained material.

As Eq. (22) implies, material deforms purely elastically when the stress is below σ_0, but plasticity starts to accumulate just above that, which may still be well below the engineering yield surface defined at 0.2% offset. This means that the commencing of plastic flow may first occur at the microstructural level, even though the macroscopic behaviour still appears to be in the elastic regime. In this sense, σ_0 may correspond well to the fatigue endurance limit. Therefore, just by analyzing the tensile behaviour with Eq. (22), one may obtain an important parameter for fatigue life prediction.

Tanaka and Mura (Tanaka & Mura, 1981) have given a theoretical treatment for fatigue crack nucleation in terms of dislocation pile-ups. Fig. 7 shows a schematic of crack nucleation by a) vacancy dipole, which leads to intrusion; b) interstitial dipole which leads to extrusion, or c) tripole that corresponds to an intrusion-extrusion pair. They obtained the following crack nucleation formula:
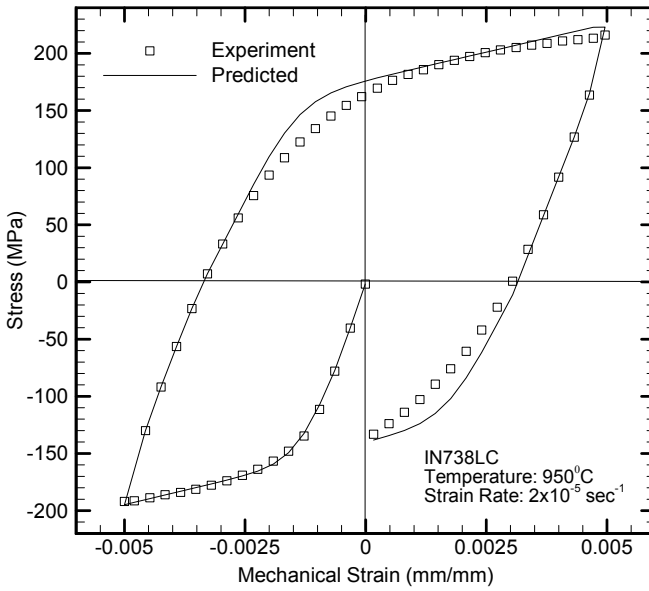
Fig. 6. Hysteresis loop of IN738LC at 950ºC.

(a) vacancy dipole

(b) interstitial dipole
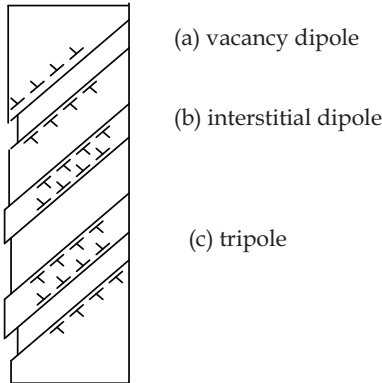
(c) tripole

Fig. 7. Dislocation pile-ups by (a) vacancy dipoles (intrusion), (b) interstitial dipoles (extrusion) and (c) tripoles (intrusion-extrusion pair).

$$N_c = \frac{4(1-\nu)w_s}{\mu b}\frac{1}{\Delta\gamma^2} \tag{24}$$

where $\Delta\gamma$ is the plastic shear strain range.

Under strain-controlled cycling conditions, $\Delta\varepsilon_p = \Delta\varepsilon - \Delta\sigma/E$, Eq. (24) can also be written in the following form:

$$\frac{1}{N} = C\varepsilon_p^2 = C\left(\Delta\varepsilon - \frac{\Delta\sigma}{E}\right)^2 \tag{25}$$

Fig. 8 shows the prediction of Eq. (25) with C = 0.009 for fully-reversed low cycle fatigue of IN738 at 400°C, in comparison with the experimental data (Fleury & Ha, 2001). The flow stress σ is obtained from Eq. (22). Since the tensile behaviour of IN738 exhibits no significant temperature dependence below 700°C, the material properties at 750°C, as listed in Table 1, are used for the evaluation. Apparently, according to Eq. (25), the material's fatigue life approaches infinity when the total strain $\varepsilon \to \sigma_0/E$. In this case, the predicted endurance limit σ_0/E is approximately 0.4, which agrees well with the experimental observation. As shown in Fig. 8, when the fatigue life is correlated with the plastic strain range, the relationship is represented by a straight line in the log-log scale, as established by Coffin (1954) and Mansion (1954), through numerous experimental observations on metals and alloys. When the fatigue life is correlated with the total strain range, the relationship becomes nonlinear.

IN738LC
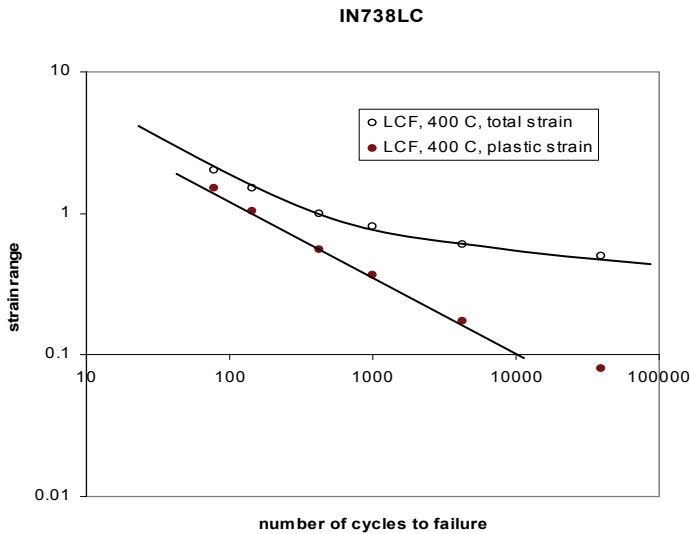
Fig. 8. LCF life of IN738 in terms of plastic and total strain (%).

The nonlinear total-strain-based fatigue life equation is often written as:

$$\Delta\varepsilon_p = \varepsilon'_f N_f^c + \frac{\sigma'_f}{E} N_f^b \tag{26}$$

where c, b, ε'_f and σ'_f are empirical constants.

Eq. (26) has been extensively used by engineers analyzing fatigue data. To establish the relationship, one needs to conduct strain-controlled cyclic tests with appreciable plastic deformation, and also stress controlled cyclic tests when plasticity is not measurable. Arbitrarily, failure cycles less than 10^4 has been termed *low cycle fatigue* (LCF), and above that *high cycle fatigue* (HCF). Laboratory LCF data are usually used to estimate the life of component with stress concentration features such as notches and holes, since it is believed that with the constraint of the surrounding elastic material, the local deformation behaviour is leaning more towards strain-controlled condition; whereas HCF data are usually used to

assess the component life under elastic stresses. For gas turbine engine components, an LCF cycle may represent major loading cycles such as engine start up -shutdown. HCF, on the other hand, occurs under low-amplitude cyclic stresses where deformation is primarily elastic. HCF failures are usually associated with vibration-induced stresses due to mistune or other geometrical damage that change the vibration characteristics of the component. It can become a life-threatening mode of failure especially when it is superimposed on LCF induced cracks. Under these conditions, components vibrate with high frequencies that can reach thousands of cycles per second, and hence exhaust its fatigue life after a short period of time.

Eq. (25) can also be extrapolated to HCF under stress controlled fatigue conditions. When the applied stress is well below the engineering yield point, the logarithm term in Eq. (22) is nearly zero such that the plastic strain can be approximated by

$$\varepsilon_p \approx \frac{\sigma - \sigma_0}{H} \tag{27}$$

and Eq. (25) can be rewritten as

$$\sigma = \sigma_0 + H(BN)^{-1/2} \tag{28}$$

Fig. 9 shows the S-N relationship of Ti-6Al-4V described with Eq. (28). In summary, it has been show that Eq. (25) can be used for both LCF and HCF regimes with the material constitutive law, Eq. (22). It can potentially simplify the fatigue analysis by calibrating with a few cyclic tests in either LCF or HCF regime.
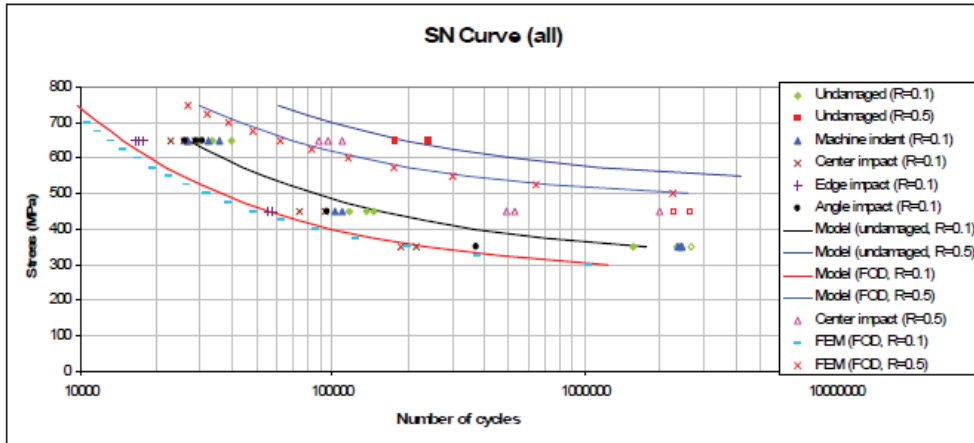
Fig. 9. S-N curves of Ti6Al4V under pristine and foreign object damaged conditions (Wu, 2009a).

3.2 Thermomechanical fatigue

Advanced turbine blades and vanes often employ a sophisticated cooling scheme, in order to survive at high firing temperatures. During engine start up and shutdown, these components experience thermal-mechanical cyclic loads, which can have a severer impact

on the life of the material than isothermal conditions. Thermomechanical fatigue (TMF) refers to the fatigue behaviour of a material under simultaneously thermal and mechanical loads. For laboratory studies, usually simple TMF cycles are employed: i) the in-phase (IP) cycle, which has a 0° phase angle between thermal and mechanical loads; ii) the out-of-phase (OP) cycle, which has a 180° phase angle; and iii) the diamond phase (DP) cycle, which has a phase angle in between; as schematically shown in Fig. 10. The OP and IP cycles represent two extreme conditions, where the maximum stress is reached at the "hot" end of IP and the "cold" end of OP temperature cycle. A more sophisticated engine cycle is shown in Fig. 11, which consists of a half diamond-phase cycle, a thermal excursion from T_{mean} to T_{max}, and a hold period at the maximum load.
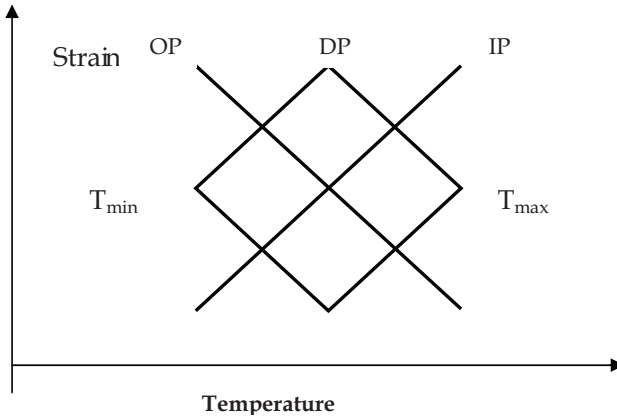
Fig. 10. Temperature-strain cycles for different TMF tests.
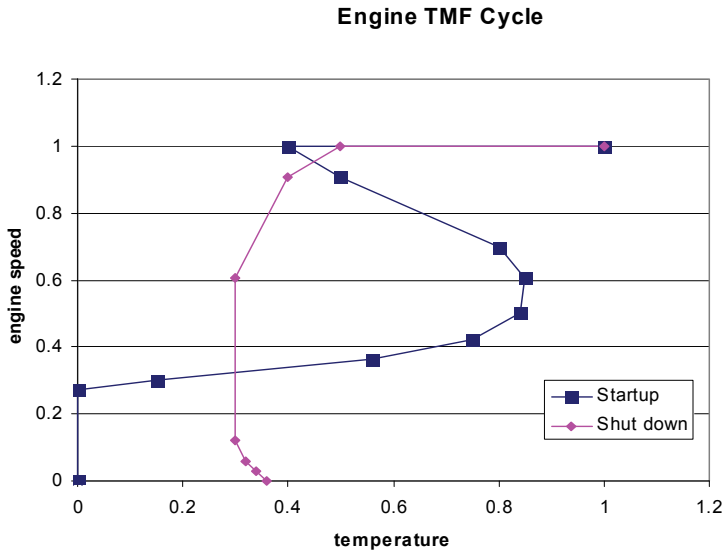
Engine TMF Cycle

Fig. 11. An engine TMF cycle.

During TMF, the total strain (ε_{tot}) is the sum of thermal and mechanical strain components:

$$\varepsilon_{tot} = \varepsilon_{th} + \varepsilon_{mech} = \alpha(T - T_0) + \varepsilon_{mech} \tag{29}$$

where ε_{th} is the thermal strain, T_0 is the reference temperature, T is the current temperature, and α is the thermal expansion coefficient. The mechanical strain (ε_{mech}) in general can be considered as the sum of the elastic and inelastic strain components.

The damage accumulation and interactions during TMF can be very complex, because it usually involves fatigue, oxidation and creep in some combination. In extreme cases, the combined effects of temperature and stress could just induce one dominant damage mode, for example, it is generally believed that the IP cycle produces predominantly creep damage, while the OP cycle induces oxide-scale cracking (Sehitoglu, 1992). However, under general TMF conditions, the combined damage mechanisms and their interactions can be complicated. Many factors such as the maximum and minimum temperature, thermal and mechanical strain ranges, the phasing between temperature and strain, the strain rate, dwell time, and environment can all influence TMF life. It is almost a formidable task to characterize these effects completely by experimental approaches such as those adopted for LCF and HCF assessments. Therefore, physics based models are needed to describe the complex damage processes under TMF loading. In this section, the cyclic thermomechanical deformation behaviour is described. Interactions with oxidation and creep under general TMF conditions will be discussed later.

For TMF, we assume that the evolution of the energy, Ψ, undergoes a series of infinitesimal isothermal steps, for each i-th step, the energy state evolves from Ψ_{i-1} to Ψ_i over the time interval $\Delta t_i = t_i - t_{i-1}$ at a constant temperature T_i. Then, Eq. (18) can be integrated into the form:

$$\ln\left(\frac{e^{-\Psi} - a}{\chi e^{-\Psi} + b}\right)\bigg|_{\Psi_{i-1}}^{\Psi_i} = -\frac{VE\dot{\varepsilon}\sqrt{1 + \chi^2}}{kT_i}\Delta t_i \qquad (i=1,2,\ldots) \tag{30}$$

Summing up all these infinitesimal steps, we have:

$$\sum_{i=1}^{N}\ln\left(\frac{e^{-\Psi} - a}{\chi e^{-\Psi} + b}\right)\bigg|_{\Psi_{i-1}}^{\Psi_i} = -\sum_{i=1}^{N}\frac{VE\dot{\varepsilon}\sqrt{1 + \chi^2}}{kT_i}\Delta t_i \tag{31}$$

Let $N\to\infty$, the left-hand side of Eq. (31) will be equal to the logarithmic difference between the final state and the initial state, and the right-hand side is an integration of the temperature-dependent terms over the loading period. After mathematical rearrangement, we have:

$$\left(\frac{e^{-\Psi} - a}{\chi e^{-\Psi} + b}\right) = \left(\frac{1 - a}{\chi + b}\right)\exp\left\{-\int_{t_0}^{t}\frac{V\mu\dot{\gamma}\sqrt{1 + \chi^2}}{kT}dt\right\} \tag{32}$$

where t_0 is the time to reach the elastic limit, or in other words, for plastic flow to commence, as defined by Eq. (21).

Let

$$\omega(t) = \left(\frac{1-a}{\chi+b}\right)\exp\left\{-\int_{t_0}^{t}\frac{VE\dot{\varepsilon}\sqrt{1+\chi^2}}{kT}dt\right\} \tag{33}$$

and assume that within the temperature range of TMF, the variation of E is moderate such that it can be represented by its average E_m, and $\sqrt{1+\chi^2}\approx 1$ since χ is usually small, the ω function can be evaluated as,

$$\omega = \left(\frac{1-a}{\chi+b}\right)\exp\left\{\mp\frac{VE_m\Delta\varepsilon\sqrt{1+\chi^2}}{k\Delta T}\ln\frac{T}{T_0}\right\} \tag{34}$$

where $\Delta T = T_{max} - T_{min}$ is the temperature range, $\Delta\varepsilon$ is the total strain range, the $-/+$ sign is used for the temperature rising or declining halves of the cycle, respectively, and T_0 denotes the temperature point at which the stress reaches the elastic limit, which can be determined based on the thermomechanical cycle profile, i.e., the T - ε relationship.

Then, Eq. (32) can be rewritten into the stress vs. strain function, similar to Eq. (22), as

$$\sigma - H\varepsilon_p - \sigma_0 = -\frac{kT}{V}\ln\left(\frac{a+\omega b}{1-\omega\chi}\right) \tag{35}$$

The stress-strain response of the coarse-grained IN738LC under an out-of-phase thermomechanical fatigue condition is predicted using Eq. (35), as shown in Figure 2.10, with the parameter values given in Table 2.1 but with a reduced $\sigma_0 = 40$MPa for the coarse-grained (d~5mm) material. The predicted hysteresis loop is in good agreement with the experimentally measured response.
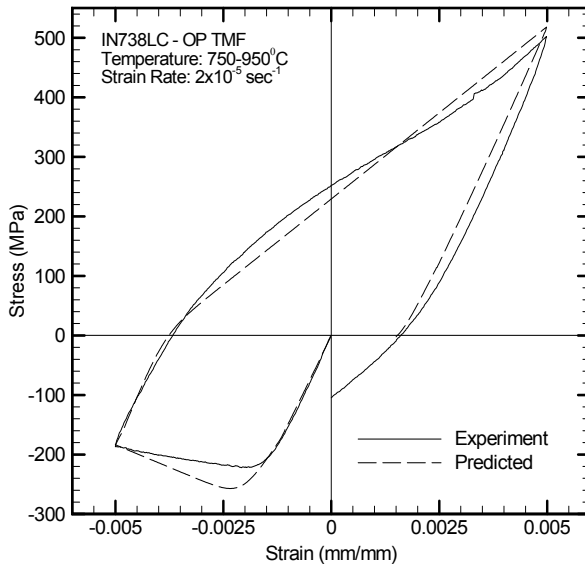
Fig. 12. Stress-strain response of IN738LC (coarse-grain) during an OP-TMF cycle.

3.3 Creep

Creep is a mode of inelastic material deformation occurring under sustained loading at high temperatures, usually above 0.3 T_m (T_m is the material's melting point). Creep can be one of the critical factors determining the integrity of components at elevated temperatures. In gas turbine engines, especially in hot sections, components such as turbine blades are subjected to sustained loads (centrifugal force and pressure) at high temperatures during the operation. Creep of a turbine blade can also cause dimensional changes that either reduce its aerodynamic efficiency or lead to elongation that rubs the engine casing, which may induce additional vibration and noise. Furthermore, creep damage may interact with fatigue that leads to significant reduction in the service life of the component.

Creep mechanisms have been extensively reviewed (Frost & Ashby, 1982; Ashby & Dyson, 1985; Wu & Koul, 1996). It is generally understood that the creep rate has different stress dependence by different mechanisms. Nevertheless, the steady-state creep rate (or the minimum creep rate) is often expressed in a Norton-Bailey form, as

$$\dot{\varepsilon} = A_0 \exp\left(\frac{Q}{RT}\right)\sigma^n \tag{36}$$

where Q is the activation energy, T is the absolute temperature, R is the universal gas constant, and A_0 and n are empirical constants.

Traditionally, creep damage assessment has been mainly based on the minimum creep rate and the Larson-Miller plot, taking into consideration the temperature compensated rate property as exhibited in Eq. (36). Fig. 13 shows the Larson-Miller plot for Astroloy. In general, the stress vs. Larson-Miller parameter relationship is nonlinear due to the multiple creep mechanisms involved, and therefore, it is merely an experimental correlation rather than a physics-based model. Extrapolation to predict the long term creep life using Larson-Miller parameter has to be based on extensive testing. For component life prediction, it needs a constitutive law of creep to describe the stress relaxation and redistribution with time as creep deformation proceeds.

It has been known that creep deformation is a continuous physical process, where a decreasing creep rate regime (transient creep: primary plus secondary) is followed by an accelerating creep rate regime (tertiary creep) beyond a minimum creep rate. Wu & Koul (1996) have proposed a creep-curve model, based on the decomposition of the total inelastic strain into grain boundary sliding and intragranular deformation, as expressed in Eq. (1), and concluded that grain boundary sliding is primarily responsible for the transient creep behaviour, while the tertiary creep evolves mostly intragranular deformation with dislocation multiplication.

Under uniaxial loading condition, the solution of Eq. (8)-(14) has the form (Wu & Koul, 1995)

$$\varepsilon_{gbs} = \varepsilon_0 + \phi\dot{\varepsilon}_{ss}t + \frac{\sigma}{\beta^2 H_{gbs}}\left[1 - \exp\left(-\frac{\beta^2\phi H_{gbs}\dot{\varepsilon}_{ss}t}{\sigma(\beta-1)}\right)\right] \tag{37}$$

where β is a microstructure parameter, and

$$\dot{\varepsilon}_{ss} = \varphi(1-\beta^{-1})\frac{D\mu b}{kT}\left(\frac{b}{d}\right)^q\left(\frac{l+r}{b}\right)^{q-1}\frac{\sigma(\sigma-\sigma_{ic})}{\mu^2} \tag{38}$$
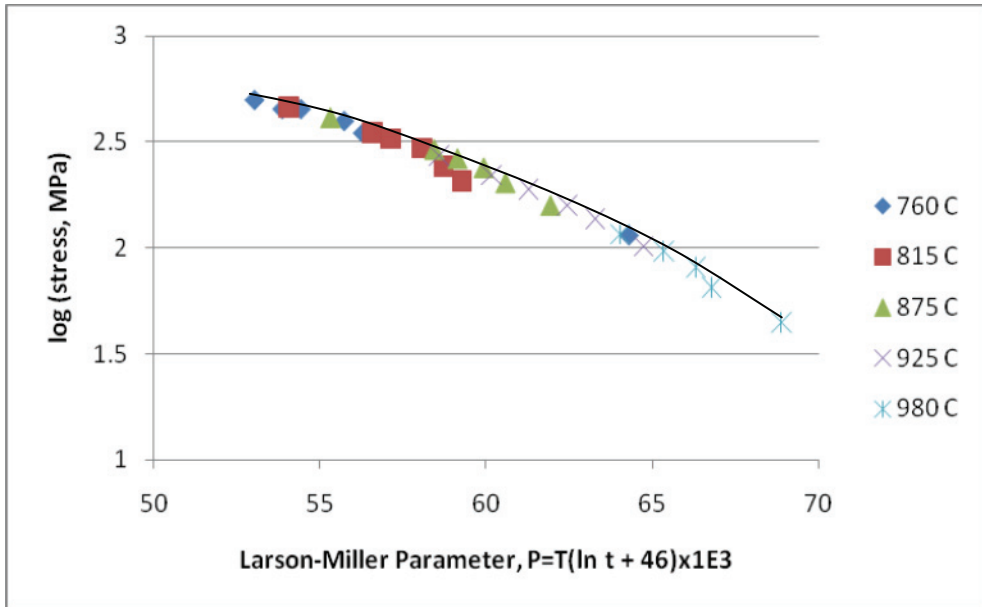
Fig. 13. The Larson –Miller plot for Astroloy.

Equation (37-38) is derived from the grain boundary dislocation glide plus climb mechanism. It states that the transient creep is a grain boundary sliding phenomenon that consists of a primary stage and a steady-state stage. It is influenced mostly by grain boundary microstructure and morphology, thus emphasizing the importance of grain boundary engineering in alloy design. According to Eq. (37), the true steady-state creep occurs at a rate as described by Eq. (38) only after an infinitely long time. Practically, a quasi-steady-state may be observed relatively soon after creep deformation starts, since the primary strain is reached as an exponential function of time. However, how long the quasi-steady-state will last depends on the time to the onset of tertiary creep, which is controlled by damage accumulation in both grain interior and along grain boundaries, such as dislocation multiplication, precipitate coarsening and cavity nucleation and growth. These processes may eventually take over and lead to an acceleration in the creep rate. Tertiary creep phenomena will be discussed later. Presently, we will discuss the important characteristics of transient creep before the commencing of tertiary creep.

First of all, the present model predicts a primary strain, as defined by

$$\varepsilon_{tr}^p = \frac{\sigma}{\beta^2 H_{gbs}} \tag{39}$$

It states that the primary strain is proportional to the applied stress σ divided by the work hardening coefficient H_{gbs}. This relationship may provide guidance for grain boundary engineering to lower the primary strain in alloy applications. Practically, the primary strain can be attained ~99 percent when the exponential term reaches 4.6, which defines the primary time as follows.

$$t_{tr}^{p} = 4.6 \frac{(\beta - 1)\sigma}{\beta^{2} H \dot{\varepsilon}_{m}}$$ (40)

Second of all, the present model predicts that ideally the GBS strain rate has a stress-dependence to the 2nd power. However, the apparent stress dependence may change since the presence of grain boundary precipitates can induce a back stress, σ_{ic}. For example, creep data on Nimonic 115 (Furrillo et al., 1979) can be correlated with Eq. (38), as shown in Fig. 14.
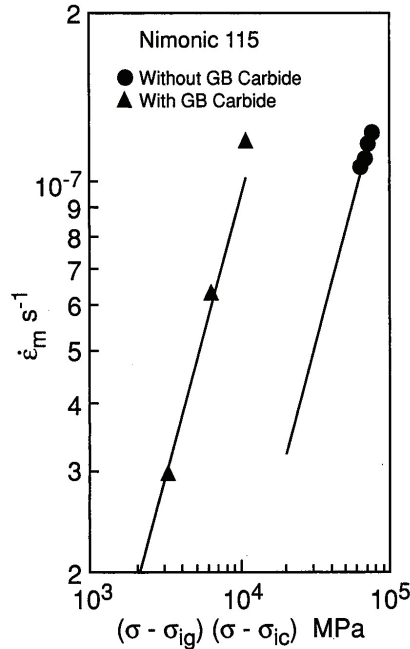
Fig. 14. The minimum creep rate correlation for Nimonic 115 (Wu and Koul, 1995).

The creep data generated by Castillo et al. (1988) on new and service exposed IN738LC turbine blade materials have also been analyzed with Eq. (37-38). Fig. 15 shows the creep curves obtained using Eq. (37) with the parameters as given in Table 2. In addition, creep curves of Alloy 718 and IN738 with planar and wavy grain boundaries are shown in Fig. 16 and Fig. 17, respectively. The descriptions have been made using Eq. (37) with the microstructure parameter and the wave factor ϕ, Eq. (15), given in Table 3. It should be noted that Eq. (37) in its present form does not include a damage parameter, and therefore only applicable to the point before tertiary creep commences. The coupling of GBS with grain boundary cavitation and/or oxidation will be discussed later.

Material Condition	Test Temperature	ε_0 (%)	β	H (GPa)	$\dot{\varepsilon}_m$ (10^{-9} s^{-1})
New	954 ºC	0.1	1.313	18.0	2.0
14159 hrs.	954 ºC	0.45	1.13	30.0	3.05

Table 2. Creep Curve Parameters for IN738LC under Stress of 90MPa
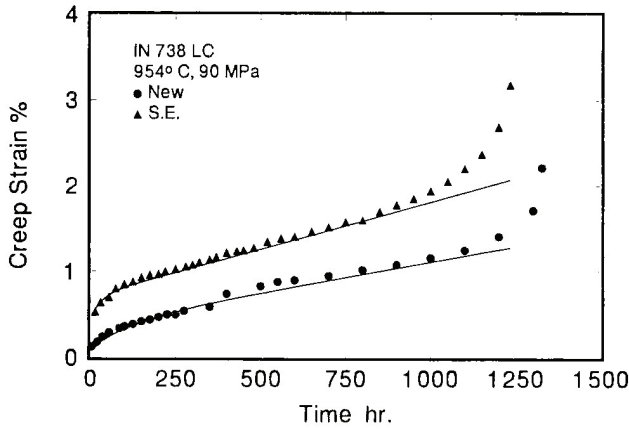
Fig. 15. Creep curves of new and service-exposed IN738LC as predicted by Eq. (37) (Wu & Koul, 1995).

Materials & Test Conditions	Grain Boundary	H (GPa)	β	φ	$\dot{\varepsilon}_m$ (hr⁻¹)
Alloy 718	(planar) h = 0	204.6	1.78	1.0	0.00233
σ = 590 MPa	λ = d				
T = 650 ºC	(triangular) h = 2 μm λ = 10 μm	204.6	1.78	0.72	0.00168
IN738LC	(planar) h = 0	106.5	1.13	1.0	0.0397
σ = 586 MPa	λ = d				
T = 760 ºC	(sinusoidal) h = 5 μm λ = 15 μm	106.5	1.13	0.38	0.0152

Table 3. Microstructure and Creep Curve Parameters of Alloy 718

Intragranular deformation has been discussed in the previous section. It can be inferred from Eq. (2)-(7) that at constant stress, deformation would stop by work-hardening due to pile-up of gliding dislocations unless dislocation climb helps the dislocations to bypass the obstacle. Thus, it is reasonable to assume that during constant-stress creep, a steady-state of back stress is attained soon upon loading such that the intragranular strain rate $\dot{\varepsilon}_i$ =const. This means that the primary creep mechanism of intragranular deformation is negligible, which is often the case as observed in single crystal materials (Carry & Strudel, 1977, 1978). The tertiary creep strain then may accumulate with dislocation climb and multiplication as (Wu & Koul, 1996):

$$\dot{\varepsilon}_g = (1 + M\varepsilon_g)\dot{\varepsilon}_i \tag{41}$$
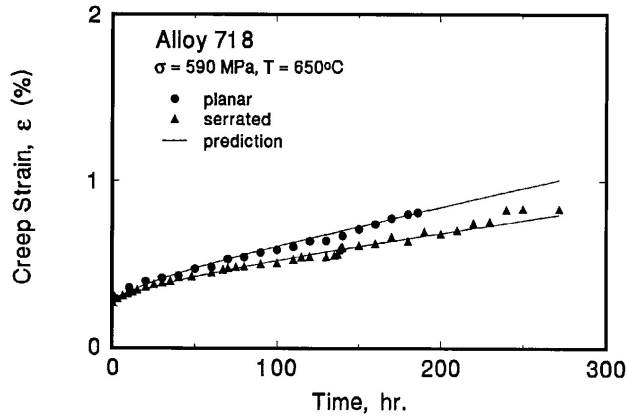
Fig. 16. Creep curves of Alloy 718 with planar and triangular wave grain boundaries, as predicted by Eq. (37) (Wu & Koul, 1997).
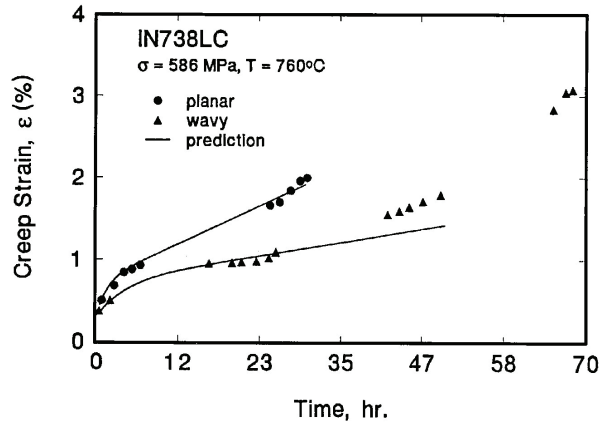
Fig. 17. Creep curves of IN738LC with planar and sinusoidal wave grain boundaries, as predicted by Eq. (37) (Wu & Koul, 1997).

where M is the normalized dislocation multiplication factor. The integration of Eq (41) leads to the following strain-time relation:

$$\varepsilon_g = \frac{1}{M}[\exp(M\dot{\varepsilon}_i t) - 1] \tag{42}$$

Then, adding the strain contributions from Eq. (37) and (42) together, according to Eq. (1), we obtain the total creep strain as

$$\varepsilon = \varepsilon_0 + \phi\dot{\varepsilon}_{ss}t + \frac{\sigma}{\beta^2 H}\left[1 - \exp\left(-\frac{\beta^2\phi H\dot{\varepsilon}_{ss}t}{\sigma(\beta-1)}\right)\right]\frac{1}{M}[\exp(M\dot{\varepsilon}_i t) - 1] \tag{43}$$

Using Eq. (43), the creep behaviour of IN738LC with and without grain boundary serration are re-analyzed with additional parameters M = 14.3 and $\dot{\varepsilon}_i$ = 0.0035 h^{-1}, the results are shown in Fig. 18. The agreement with experimental observation is corroborated with the physical rationale that the two IN738LC materials have nearly the same intragranular microstructure in terms of γ′ precipitate size and volume fraction but different grain boundary morphology.

During tertiary creep, intragranular deformation may overshadow GBS by the mere amount of strain accumulation, but grain boundary damage may still occur under stress, which limits the creep rupture life, as indeed most creep rupture occurs intergranularly in polycrystalline materials. Wu & Koul (1996) have summarized the grain boundary damage accumulation processes via cavitation and oxidation.

Continuous cavity nucleation and growth has been described by (Raj & Ashby, 1975):

$$A(t) = \rho_c(t)\pi r_c^2 + 2\pi \int_0^t \int_\tau^t r(t-\zeta)\dot{r}(t-\zeta)\dot{\rho}_c(\tau)d\zeta\,d\tau \tag{44}$$

where r_c is the critical nucleation radius, $\rho_c(t)$ is the void density and r(t) is the cavity radius at time t.
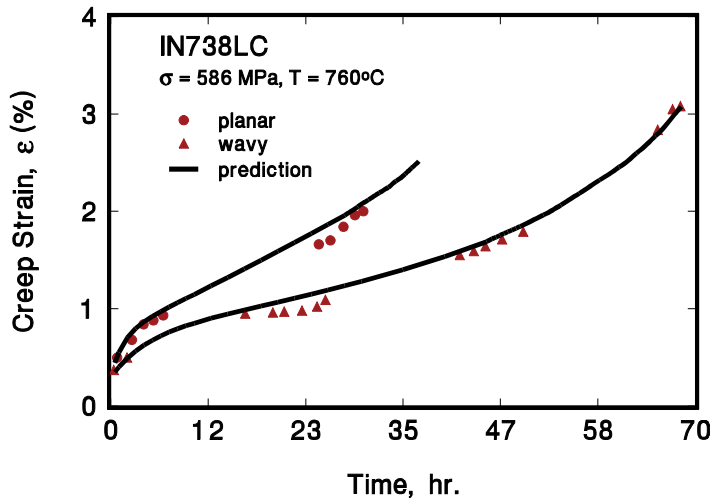
Fig. 18. Creep curves for IN738LC with planar and serrated grain boundaries, as predicted by Eq. (43) (Wu & Koul, 1996).

As a first approximation, we assume a constant cavity density and only consider the growth of these cavities, the cavity growth rate is approximately equal to $\dot{r} = \dot{\varepsilon}_{ss}d$ (note that it is the GBS deformation component that dominates the steady-state creep rate in this case). If we define the creep damage parameter as ω = A/πd², and the rupture time is reached at ω = ω$_{cr}$, then t$_r$ ∝ 1/$\dot{\varepsilon}_{ss}$. The creep behaviour of wrought Alloy 718 with planar (the SHT material) and triangular-wave (the MHT material) grain boundaries at 650 °C under stress of 593 MPa were reported (Chang et al., 1992), as shown in Fig. 19. The average rupture time of the SHT material was 450 hours. The grain boundary wave factor ϕ for the MHT material is 0.7 with h = 2 μm and λ = 10 μm (Table 3). Based on the above consideration, the creep life of the

MHT material is estimated to be $t_{rMHT} = t_{rSHT}/\phi = 642$ hours under the given test condition, which is very close to the experimental observation. This proves that indeed the transient creep and creep life is limited by GBS.

Another mechanism for grain boundary damage is gaseous environmental attack—normally at high temperatures—oxidation. Suppose that oxygen penetrate the material inward through a parabolic law until the oxide scale is broken by deformation, the rate of oxide cracking can be expressed as

$$\frac{dx}{dt}\bigg|_{ox} = \left(\frac{2D\dot{\varepsilon}_{gbs}}{\varepsilon^*} \right)^{\frac{1}{2}} \tag{45}$$

where x is the oxide crack length, D is a diffusion constant, and ε^* is the fracture strain of the oxide.
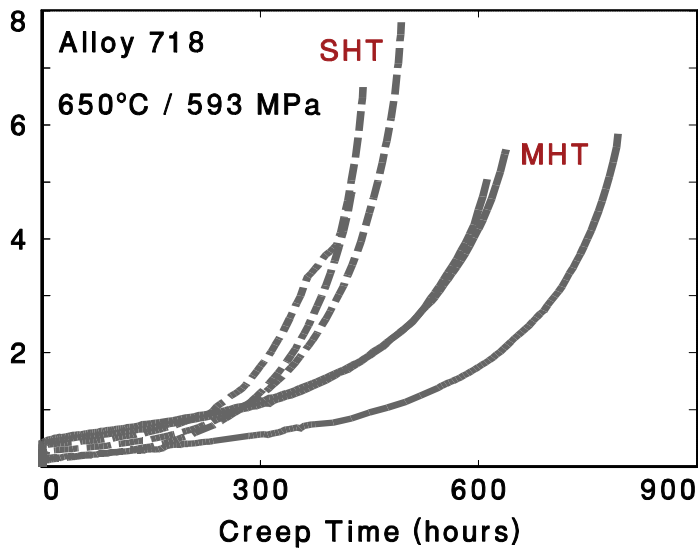
Fig. 19. Creep curves for standard and damage tolerant microstructures of Alloy 718 (Chang et al. 1992).

Sessions et al. (1977) studied the creep-oxidation interaction in Udimet 700. By re-plotting their data on the log-log scale as shown in Fig. 20, we can see that the creep rate in air increases and the rupture time decreases with the number of grains per cross-section. The air-tested creep rate increases linearly with the number of grains per cross section, and hence it follows the relationship of $\dot{\varepsilon}_{min} \propto 1/d$, but the life is inversely proportional to $\sqrt{d}$, which implies a GBS phenomenon, as predicted by Eq. (45). Suppose that GBS occur at nearly a constant rate for most of the material's creep life, when the oxide crack reaches a critical length, then Eq. (45) would lead to $t_r \propto 1/\sqrt{\dot{\varepsilon}_{min}}$. Therefore, we would expect that $t_r \propto \sqrt{d}$. In Fig. 20, the rupture time decreases with the number of grains per cross-section with a power of -1/2. This observation can be directly translated to the above statement, considering that the number of grains per cross-section is inversely proportional to the grain

size d for fixed specimen geometry. Therefore, Eq. (45) is suitable for describing the oxidation damage during creep.
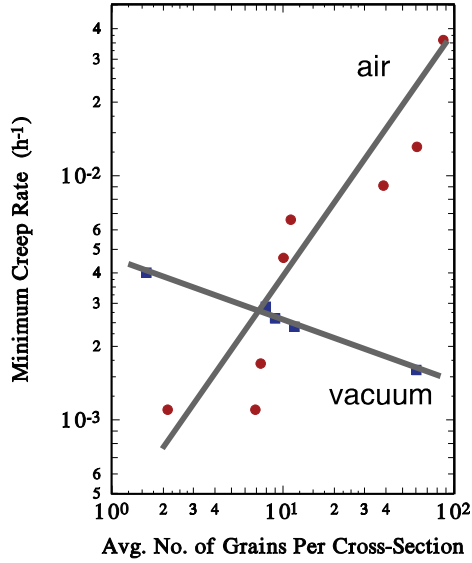
(a)
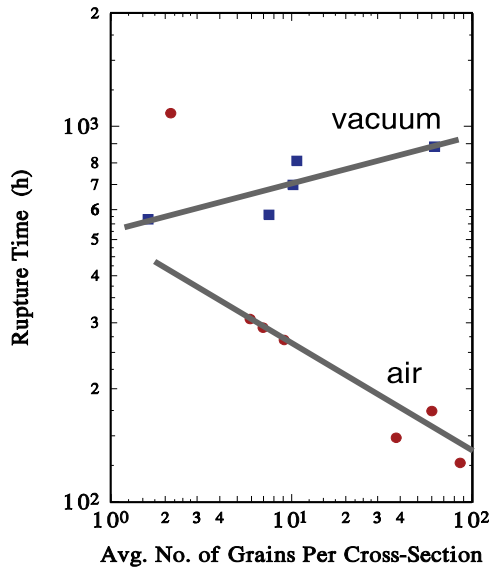
(b)

Fig. 20. (a) Minimum creep rate data and (b) rupture life data for Udimet 700 at 927°C and 172 MPa, in air and vacuum.

To overcome the weakness of grain boundaries which are susceptible to cavitation and oxidation, advanced turbine blade and vane alloys are made from directionally-solidified (DS) and single crystal (SX) N-base superalloys, which are generally casted in the $\langle 001 \rangle$ crystal direction with the lowest modulus and hence the best tolerance to thermal fatigue. With the removal of grain boundaries, the creep behaviour of DS and SX alloys is therefore mainly a result of intragranular deformation. The majority of the creep life of DS and SX Ni-base superalloys is spent in the tertiary stage with a creep ductility in the order of 20~30%. Therefore, Eq. (42) is appropriate to describe the creep behaviour of such alloys, or in other words, ignore grain boundary sliding (GBS) from Eq. (43).

Now, let

$$\dot{\varepsilon}_i = A_0 \exp\left(-\frac{\Delta G}{kT}\right) \sinh\left(\frac{V(\sigma - \sigma_0)}{kT}\right) \tag{46}$$

where A_0 is the pre-exponential constant, ΔG is the activation energy, V is the activation volume, σ_0 is the back stress, k (=$1.38 \times 10\text{-}23$ J·K^{-1}) is the Boltzmann constant, and T is the absolute temperature.

The creep behaviors of CM247LC, a DS alloy, at various stresses and temperatures are described with Eq. (42) and (46), with the parameters given in Table 4, as shown in Fig. 21. The model agrees well with the experimental creep behavior of CM247LC. The creep data at 225MPa/950°C (Satyanarayana et al., 2008), 560MPa/840°C (DeMestral et al., 1996), and 180MPa/1030°C (Kolbe et al., 1999) were used for calibration of the model to determine the parameter values of the model. One creep curve was calculated to predict the creep rupture response at 186MPa/982°C with an observed life of 120 hr. The model prediction is very close to the experimental observation. Using the same approach, the model can also be applied to SX alloys.

In summary, by the deformation decomposition rule, Eq. (1), the total creep strain is equal to the sum of intragranular strain and GBS strain. A schematic creep curve is shown in Fig. 22 by adding the two components. It should be recognized that the total (observed) secondary or minimum creep rate consists of both GBS and intragranular contributions with varying degrees, depending on the material's microstructure, the applied stress and temperature. Therefore, creep life assessment based on the measured minimum creep rates may be erroneous by extrapolating short-term test data for long-term lifetime prediction, since most short-term creep tests conducted at high stresses would induce a large amount of intragranular deformation that over shadows the true failure mechanism at grain boundaries.

There are other creep-curve equations, the most similar one to Eq. (43) is the θ-projection method proposed by Evans & Wilshire (1985) as

$$\varepsilon = \theta_1(1 - e^{-\theta_2 t}) + \theta_3(e^{\theta_4} - 1) \tag{47}$$

The θ-projection is purely empirical and mostly suitable for short-term creep tests where the secondary creep period is very short. Eq. (43), on the other hand, represents the total contribution from physical deformation mechanisms—GBS plus intragranular dislocation multiplication and climb, which can be linked to intergranular and transgranular crack propagation, leading to rupture. For DS and SX alloys, GBS diminishes and the intragranular deformation component dominates. Thus, Eq. (43) provides a holistic description of creep for complex engineering alloys.

A_0 (hr^{-1})	ΔG (J)	V (m^3)	σ_0 (MPa)	M
4.22×10^{12}	6.896×10^{-19}	2.063×10^{-28}	0	400

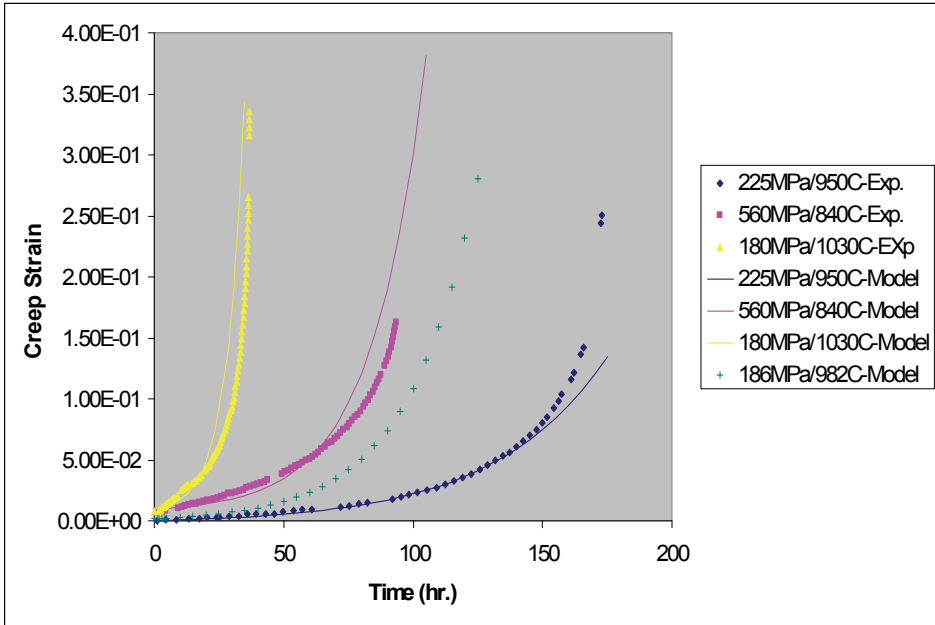Table 4. Activation Parameters for the CM247LC Creep Model

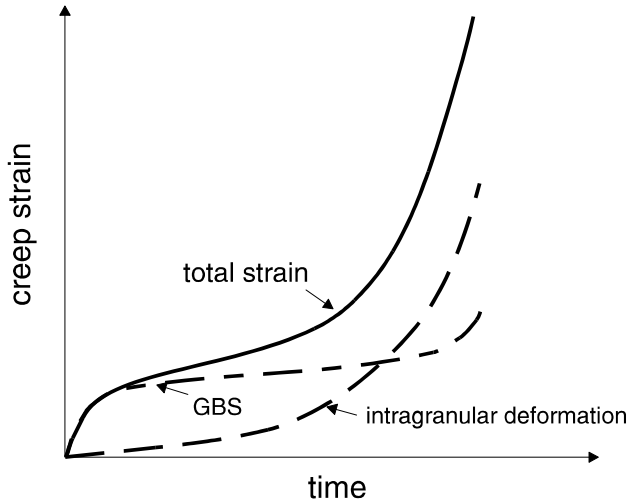Fig. 21. Experimental and model creep curves of CM247LC.

Fig. 22. Schematics of creep curves representing GBS strain, intragranular strain and the total creep strain

4. Evolution of material life under thermomechanical loading

A gas turbine engine component generally experiences thermomechanical loading during start-up/shutdown (cyclic) and cruise (steady holds) which cause thermomechanical creep-fatigue damage to the material. Researchers have been trying to develop more descriptive, more accurate, and more efficient analytical models for the dwell/creep-fatigue phenomena, in order to understand the creep-fatigue interaction for component life prediction. Existing TMF models can be largely categorized into the following three groups: 1) the linear damage accumulation model (Neu & Sehitoglu, 1989; Sehitogulu, 1992), 2) the damage-rate model (Miller, 1993), and 3) the strain-range partitioning (SRP) method (Halford et al., 1977). Recently, a holistic model of dwell/creep-fatigue has been presented (Wu, 2009b), which describes the processes of surface /subsurface crack nucleation, propagation of the dominant crack and its coalescence with internal creep cavitation damage, leading to the final fracture.

4.1 The generic TMF model

For generality, let us consider a polycrystalline material. Under thermomechanical fatigue (TMF) loading, multiple forms of damage may develop: an oxide scale forms at the material surface; cavitation develops inside the material, and fatigue damage may proceed in the form of persistent slip bands (PSB), as shown schematically in Fig. 23. Cracks may first initiate at surface flaws via intrusion/extrusion of PSB. Oxidation also occurs first at the material surface or at existing crack surfaces or a crack tip. Oxidation damage penetrates the material inwardly through diffusion processes. Subsurface cracks may also initiate at manufacturing flaws such as pores or inclusions, but they will quickly break through the surface and become surface cracks. In the mean time, creep cavities or wedge cracks may develop in the material interior, particularly along grain or interface boundaries. The life evolution process in a metallic material at high temperatures can be envisaged as nucleation of surface cracks by fatigue and/or oxidation, and inward propagation of the dominant crack, coalescing with internal cavities or cracks along its path, leading to final rupture.
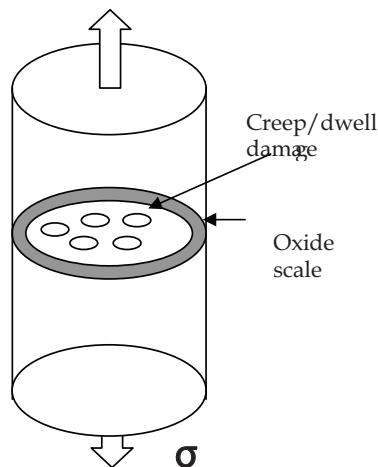
Fig. 23. A schematic of damage development in a material cross-section.

Fatigue damage can be regarded as accumulation of irreversible slip offsets on preferred slip systems. These slip offsets may occur at the surface of grains or grain boundaries or interface boundaries, which act as nuclei for cracks. Restricted slip reversal ahead of the crack tip is also recognized as the basic mechanism of transgranular fatigue crack propagation (Wu et al., 1993). Therefore, in a holistic sense, we can use the term da/dN to represent both the rate of accumulation of irreversible slip offsets leading to crack nucleation as well as the fatigue crack growth rate, bearing in mind that the functional dependencies of da/dN on the loading parameters are different for crack nucleation and crack growth.

On the other hand, creep damage may develop in the forms of cavities and/or wedge cracks (Baik & Raj, 1982). Cavity growth has been recognized as a diffusion phenomenon, whereas wedge cracking is a result of dislocation pile-up, also called Zener-Stroh-Koehler (ZSK) crack.

The coalescence of creep/dwell damage with a propagating fatigue crack will result in a total damage accumulation rate as expressed by

$$\frac{da}{dN} = \left(\frac{da}{dN}\right)_f + \frac{l_c + l_z}{\Delta N} \tag{48}$$

where l_c is the collective cavity size per grain boundary facet, l_z is the ZSK crack size, ΔN is the number of cycles during which the fatigue crack propagates between two cavities or between two ZSK cracks separated by an average distance of λ (λ~grain size or grain boundary precipitate spacing). Note that usually creep cavitation occurs at a high temperature and ZSK cracks occur at a relatively low temperature. These two types of damage usually do not occur at the same time. Here they are added together as competitive mechanisms over the entire temperature range from ambient temperature to near melting temperature.

Assume that during the period of ΔN, the dominant crack only propagates by pure fatigue, i.e., da/dN~$\lambda/\Delta N$, then we can rewrite Eq. (48), as

$$\frac{da}{dN} = \left(1 + \frac{l_c + l_z}{\lambda}\right)\left(\frac{da}{dN}\right)_f \tag{49}$$

With environmental effects such as oxidation contributing to propagation of the dominant crack in a cycle-by-cycle manner, the total crack growth rate is

$$\frac{da}{dN} = \left(1 + \frac{l_c + l_z}{\lambda}\right)\left\{\left(\frac{da}{dN}\right)_f + \left(\frac{da}{dN}\right)_{env}\right\} \tag{50}$$

4.2 Cold-dwell fatigue

Cold-dwell fatigue usually refers to fatigue with hold-times at ambient temperatures, and it could cause significant low cycle fatigue (LCF) life reduction, particularly pronounced in high strength titanium alloys such as IMI 685, IMI 829 and IMI 834, and Ti6242. Dwell fatigue of titanium alloys is often accompanied with faceted fracture along the basal planes of the α phase, as seen in Fig. 24.

It has been perceived that the faceted fracture of α grains is driven by dislocation pile-up (Bache et al., 1997). Wu & Au (2007) have treated the problem in terms of the kinetics of Zener-Stroh-Koehler crack formation.

First of all, it should be recognized that the rate of dislocation pile-up accumulation is the net result of dislocation arriving by glide and leaving by climb in a unit time, which can be expressed as

$$\frac{dn}{dt} = \rho vs - \kappa n \tag{51}$$

where ρ is the dislocation density, v is the dislocation glide velocity, s is the slip band width, κ is the rate of dislocation climb, and n is the number of dislocations in a pile-up at time t. According to the Orowan relationship, $\dot{\gamma}_p$ = ρbv (s ≈ b), Eq. (51) can be rewritten as

$$\frac{dn}{dt} = \dot{\gamma}_p - \kappa n \tag{52}$$

The number of dislocations in a pile-up at a steady-state can be obtained by integration of Eq. (52), as

$$n = \frac{\dot{\gamma}_p}{\kappa}[1 - \exp(-\kappa t)] \tag{53}$$
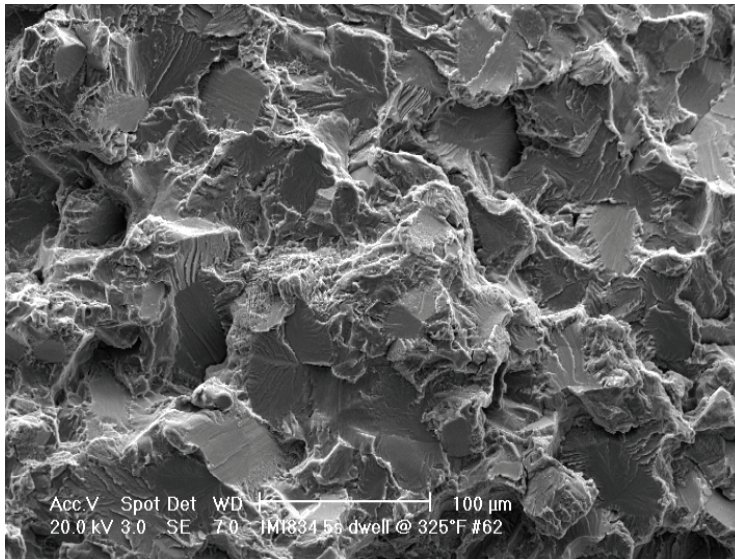
Fig. 24. A SEM micrograph of the fracture surface of IMI 834 failed by dwell faituge
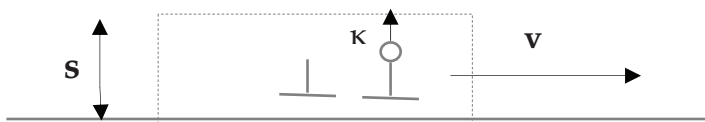
Fig. 25. Schematic of the kinetic process of dislocation pile-up.

Note that the energy release rate of a ZSK crack in an anisotropic material is given by (Wu, 2005)

$$G = \frac{1}{2} K_i F_{ij}^{-1} K_j = \frac{b_T^{(i)} F_{ij} b_T^{(j)}}{8\pi a} \tag{54}$$

where F_{ij} is an elastic matrix for anisotropic materials ($F_{11} = F_{22} = \mu/(1-\nu)$, $F_{33} = \mu$, μ—shear modulus, for isotropic materials), and $b_T = nb$ is the total Burgers vector in the pile-up group. Considering an average slip band angle of 45°, the dislocation pile-up may create a mix-mode I-II crack, by the Griffith's criteria:

$$\frac{\overline{F}_{22} b_T^2}{8\pi a} = 4w_s \tag{55}$$

where w_s is the surface energy, and $\overline{F}_{22} = (F_{11} + F_{22})/2$ is the average modulus.
From Eq. (55), we can find the crack size l (=2a) as

$$l = \frac{\overline{F}_{22} n^2 b^2}{16\pi w_s} \tag{56}$$

Substituting Eq. (53) into Eq. (56), we obtain

$$l_z = \frac{\overline{F}_{22} b^2}{16\pi w_s} \left(\frac{\dot{\gamma}}{\kappa}\right)^2 \left[1 - \exp(-\kappa\tau)\right]^2 \tag{57}$$

For constant amplitude fatigue with a constant holding period, substituting Eq. (57) into (49) and neglecting cavity formation, the integration of Eq. (49) leads to

$$N = \frac{N_f}{\left(1 + \dfrac{F_{22} b^2}{16\pi\lambda w_s} \left(\dfrac{\dot{\gamma}}{\kappa}\right)^2 \left[1 - \exp(-\kappa\tau)\right]^2\right)} \tag{58}$$

Equation (58) shows that the fatigue life is knocked down by a factor greater than one, when a dwell period is imposed on fatigue loading. This "knock down" factor depends on the material properties such as elastic constants, surface energy, and microstructure (λ), and most importantly it is controlled by the ratio of dislocation glide velocity to the climb rate in the material. This means that, if damage occurs in the form of dislocation pile-up, the dwell-effect will be more detrimental when the ratio of dislocation glide to climb is large, particularly in materials with fewer active slip systems at low temperatures. As temperature increases, climb will overwhelm glide such that dislocation pile-up can hardly form, and hence the dwell damage becomes minimal, but cavities may start to grow. Basically, this is the essence of "cold dwell" vs. "hot creep".
Bache et al. (1997) studied IMI834 and plotted the dwell fatigue life as function of dwell time and stress as shown in Figure 26 (a) and (b), respectively. The model, Eq. (58), describes the experimental behaviour very well. It shows that the dwell sensitivity, in terms of the ratio of dwell-fatigue life to the pure fatigue life, indeed follows an exponential function. Hence, given the pure fatigue life as the baseline, dwell fatigue life can be predicted, as shown in Figure 26 (b), in the form of S-N curves.
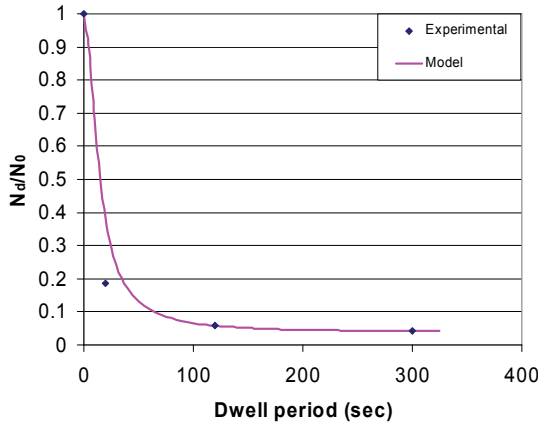
(a)
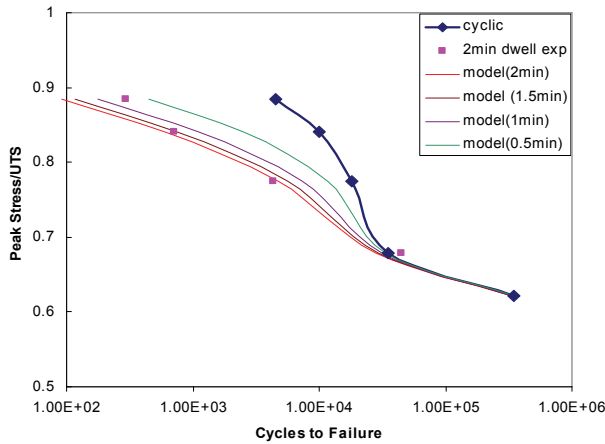
(b)

Fig. 26. Comparison of Eq. (58) with the experimental data on IMI 834 (Bache et al., 1997): a) normalized dwell fatigue life as a function of dwell time, b) S-N curves with different dwell times.

4.3 Creep-Fatigue

Creep-fatigue interaction refers to the effect of cyclic-hold interactions at high temperatures where creep damage can be significant. The simplest and hitherto the most popular way to count for the total accumulated damage is to combine Miner and Robinson's rules (Miner, 1945; Robinson, 1952), as

$$\sum \frac{N_i}{N_{fi}} + \sum \frac{t_j}{t_{rj}} = 1 \tag{59}$$

where N_{fi} is the pure fatigue life at the ith cyclic stress or strain amplitude, and t_{rj} is the creep rupture life at the jth holding stress level. The linear summation rule, as straightforward as it may be, is purely empirical and based on no physical mechanism. It does not differentiate the time spent under stress-control or strain-control conditions, or in tension or compression whatsoever, which causes different material response as stress relaxation vs. strain relaxation (creep). Many experimental investigations have shown that the fatigue life fraction vs. creep life fraction does not obey a linear relationship, as prescribed by Eq. (59), as cited by Viswanathan (1989).

Other creep-fatigue models were also proposed such as the frequency modified equation (Coffin, 1969), the hysteresis energy model (Ostergren, 1976), and the strain range partitioning (SRP) approach (Halford et al., 1977). Instead of modifying empirical equations with empirical factors accounting for the frequency effect, the SRP method tried to rationalize the complex creep-fatigue phenomena with the partition of four components in the total inelastic strain range: 1) plastic strain reversed by plasticity, $\Delta\varepsilon_{pp}$; 2) creep strain reversed by creep, $\Delta\varepsilon_{cc}$; 3) plastic strain reversed by creep, $\Delta\varepsilon_{pc}$; and 4) creep strain reversed by plasticity, $\Delta\varepsilon_{cp}$. A schematic of the occurrence of these strain components is shown in Fig. 27. Then, the total failure life is expressed as

$$\frac{1}{N} = \frac{F_{pp}}{N_{pp}} + \frac{F_{cc}}{N_{cc}} + \frac{F_{pc}}{N_{pc}} + \frac{F_{cp}}{N_{cp}} \tag{60a}$$

where

$$N_{ij} = D_{ij}\Delta\varepsilon_{ij}^{c_{ij}} \tag{60b}$$

F_{ij} is the fraction of the named strain component, and N_{ij} is the number of cycles to failure if the entire inelastic strain is comprised of the named strain only, where D_{ij} and c_{ij} are the Manson-Coffin constants. The problem of this approach with respect to life prediction is that the actual partition of these strain components is difficult to determine within the total strain range imparted to the component by a random loading cycle.

Considering physically that the total inelastic strain, ε_{in}, is comprised of intragranular deformation, ε_g, and grain boundary sliding (GBS), ε_{gbs}, as given by Eq. (1), we further assume that under cyclic-time hold conditions:

1. The intragranular deformation, when proceeds in a cyclic manner, leads to transgranular damage accumulation, such as persistent slip bands and fatigue cracking, and therefore, it is equivalent to the pp strain under cyclic conditions.
2. For short-period holds, cc, pc and cp types of inelastic strains are contributed mainly from GBS during the transient creep, since purely tertiary creep would never start upon short cycle repeats. GBS contributes to intergranular fracture.

When GBS operates, the accumulation of grain boundary damage, either in the form of cavity nucleation and growth or as grain boundary cracks, is proportional to the GBS displacement, such that

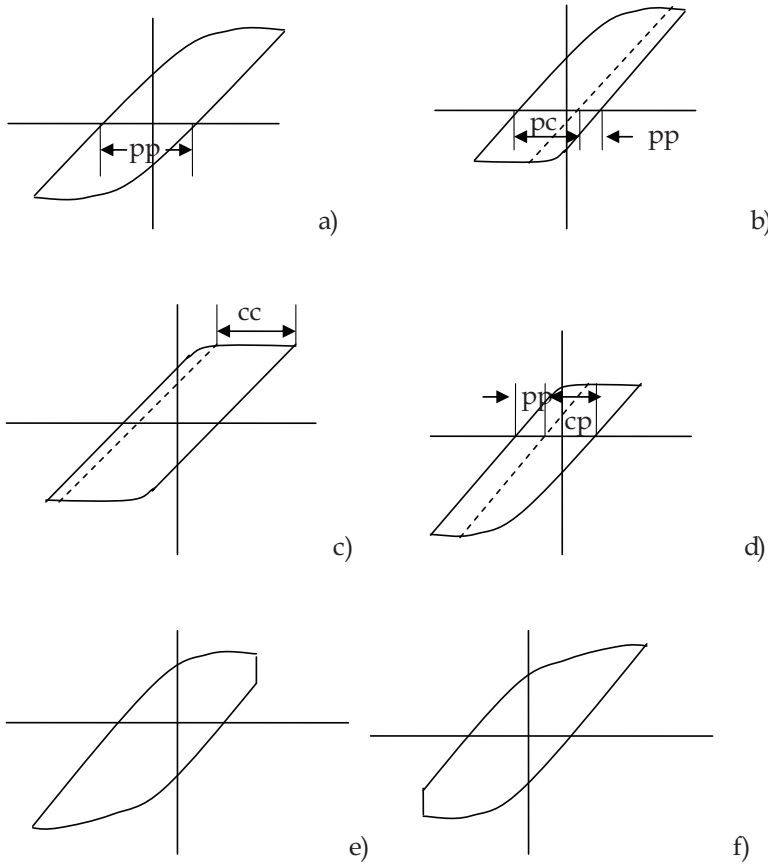$$l_c = \varepsilon_{gbs}d \tag{61}$$

where d is the grain size.

Fig. 27. The SRP cycle profiles: a) High Rate Strain Cycle (HRSC)—constant ramping in tension and compression; b) Compressive Cyclic Creep Rupture (CCCR)—ramped to a predetermined stress with compressive creep hold; reversed ramping to equal tensile strain; c) Balanced Cyclic Creep Rupture (BCCR)—creep holds in tension and compression at constant load until specific strain reached; d) Tensile Cyclic Creep Rupture (TCCR)—opposite cycle to CCCR with tensile hold; e) Tensile Hold Strain Cycle (THSC)—ramped to specific strain, stress relaxation followed by reversed ramping to equal compressive strain; f) Compressive Hold Strain Cycle (CHSC)—opposite to THSC with compressive stress relaxation.

Under cyclic creep conditions as imposed by strain controlled cycles, l_c can be stabilized once the entire hysteresis behavior is stabilized. Therefore, again under constant amplitude cycling conditions, Eq. (49) can be integrated to (in this case, neglecting dislocation pile-ups, i.e., let $l_z = 0$):

$$N = \frac{N_f}{1 + \dfrac{\varepsilon_{gbs} d}{\lambda}} \qquad (62)$$

As discussed in section 3.1, the pure LCF life, N_f, is correlated to $\Delta\varepsilon_g$ through Eq. (25), as:

$$\Delta\varepsilon_g = CN_f^{-1/2} \tag{63}$$

which can be established by HRSC tests.

For application of Eq. (62) to the asymmetrical creep-fatigue interaction tests such as CCCR, TCCR, THSC and CHSC, it should be recognized that, due to reversed plasticity, each individual grain is fatigued by the entire inelastic strain range, but GBS contributes to the effect of additional intergranular fracture. Since GBS operates in shear, it may produce grain boundary damage during either uniaxial tension or compression. Table 5 summarizes the strain partitioning of $\Delta\varepsilon_g$ and $\Delta\varepsilon_{gbs}$ for the different creep-fatigue interaction tests.

We take the data from a NASA contract report (Romannoski, 1982) and re-establish the strain partitioning rule, according to Eq. (1), as outlined in Table 5, the creep-fatigue interaction can be described by Eq. (62) for Rene 80 (in high vacuum) and IN100 (coated) as shown in Table 6 and 7, in comparison with the experimental data. For the bulk failure of these two materials under the test conditions, environmental effects can be neglected. The results are also shown in Fig. 28 and Fig. 29, respectively.

Test Type	$\Delta\varepsilon_g$	$\Delta\varepsilon_{gbs}$
HSRC	pp	0
CCCR	pp+pc	pc
TCCR	cp+cp	cp
BCCR	pp	cc
THSC	pp+cp+cc	$\Delta\sigma/E^*$
CHSC	pp+pc+cc	$\Delta\sigma/E^*$

*Note that $\Delta\sigma$ is the range of stress drop during stress relaxation in this test.

Table 5. The Strain Partitioning Concept

Spec. ID	Test	$\Delta\varepsilon_g$	$\Delta\varepsilon_{gbs}$	N_f	N	Exp.
74-U-pp-13	HRSC	0.605	0	175	175	145
21U-pp-8	HRSC	0.322	0	617	617	642
41U-pp-10	HRSC	0.179	0	1997	1997	1410
22U-pp-9	HRSC	0.026	0	94675	94675	163533
42U-pp-11	HRSC	0.051	0	24606	24606	217620
92U-pc-13	CCCR	0.554	0.46	209	45	41
28U-pc-9	CCCR	0.378	0.283	448	137	149
91U-pc-12	CCCR	0.257	0.209	969	363	356
98U-pc-16	CCCR	0.258	0.183	961	390	396
29U-pc-10	CCCR	0.204	0.164	1538	665	1415
112U-cp-11	TCCR	0.385	0.308	432	125	101
86U-cp-9	TCCR	0.289	0.306	766	222	147
30U-cp-5	TCCR	0.289	0.254	766	253	193
31U-cp-6	TCCR	0.208	0.202	1479	565	530
36U-cp-7	TCCR	0.111	0.092	5194	2992	3705

Table 6. Rene 80 at 871oC (C=0.08, d/λ=8)

Spec. ID	Test	$\Delta\varepsilon_g$	$\Delta\varepsilon_{gbs}$	N_f	N	Exp.
7	HRSC	0.129	0	796	796	635
6	HRSC	0.121	0	905	905	900
1	HRSC	0.138	0	696	696	1260
2	HRSC	0.086	0	1792	1792	2120
3	HRSC	0.059	0	3806	3806	3670
4	HRSC	0.05	0	5300	5300	9460
5	HRSC	0.031	0	13788	13788	12210
10	HRSC	0.026	0	19601	19601	17340
8	HRSC	0.028	0	16901	16901	27260
11	HRSC	0.014	0	67602	67602	48320
N12	CHSC	0.196	0.03375	345	128	250
N10	CHSC	0.105	0.02	1202	601	764
N9	CHSC	0.102	0.019375	1274	647	944
39	THSC	0.18	0.026875	409	174	239
N8	THSC	0.08	0.016875	2070	1123	1495
54	BCCR	0.09	0.168	1636	174	159
N5	BCCR	0.085	0.16	1834	204	200
56	BCCR	0.054	0.11	4544	699	383

Table. 7. IN 100(Coated) at 900°C (C=0.0364, d/λ=50)
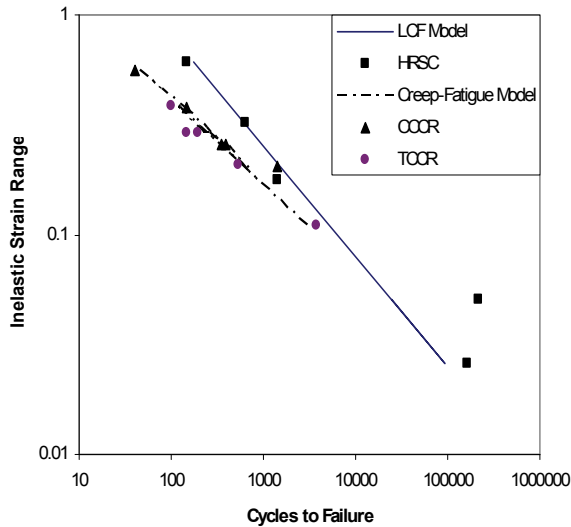
Fig. 28. Comparisons of Eq. (62-63) with experimental data for Rene 80 at 871°C

It has been shown that Eq. (62-63) can describe well the creep-fatigue interaction in complicated loading cycles. The advantage of this physics-based strain decomposition model is that, once calibrated with coupon data, it can be applied to component life prediction with ε_g and ε_{gbs} values evaluated from the constitutive model as presented in section 2. Mathematically, it unifies the SRP concept with the physical meaning that $\Delta\varepsilon_g$ represents the intragranular damage and $\Delta\varepsilon_{gbs}$ contributes to the intergranular fracture, thus it provides a complete description for the mix mode fracture.
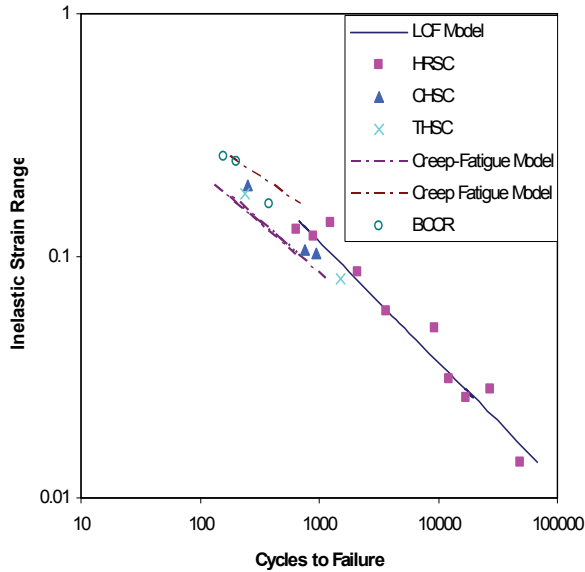
Fig. 29. Comparisons of Eq. (62-63) with experimental data for IN 100 (coated) at 1000ºC.

4.4 Fatigue-Oxidation

When gas turbine components operate in a hot gas environment, an oxide scale typically forms on the material surface. This layer of oxide will be forced to deform compatibly with the substrate until it breaks, which may lead to premature crack nucleation. The stresses in both the substrate and oxide scale can be determined, by deformation compatibility:

$$\frac{\sigma_{ox}}{E_{ox}} + \alpha_{ox}(T - T_o) = \frac{\sigma_s}{E_s} + \alpha_s(T - T_o) \tag{64}$$

and, by the force equilibrium

$$\sigma_{ox}f + (1 - f)\sigma_s = \sigma \tag{65}$$

where σ_{ox} is the stress in the oxide scale, E_{ox} is the elastic modulus and α_{ox} is the thermal expansion coefficient of the oxide scale (~8μm/mK for Al_2O_3), σ_s is the stress in the substrate, E_s is the elastic modulus and α_s is the thermal expansion coefficient of the substrate material (~14μm/mK for Ni base superalloys), and f is the volume fraction of the oxide scale, T_o is the reference temperature at which the oxide formation is stress free. From the above relations, we can deduce that

$$\sigma_{ox} = \frac{E_{ox}}{fE_{ox} + (1 - f)E_s}[\sigma + (1 - f)E_s(\alpha_s - \alpha_{ox})(T - T_0)] \tag{66}$$

In Ni-base superalloys, the oxide, e.g., Al_2O_3, may form with a negligible volume fraction, i.e., f << 1, but usually has a higher modulus than the substrate. Therefore, according to Eq.

(66), oxides act as stress raisers at the surface (multiplied by E_{ox}/E_s). During a TMF cycle, the oxidation stress may change with temperature.

Suppose the oxide growth follows a parabolic relation, as

$$h = \sqrt{2kt} \tag{67}$$

Neglecting other damage, i.e., $l_c = l_z = 0$, then, from Eq. (50), the fatigue-oxidation interaction results in the crack growth rate as:

$$\frac{da}{dN} = \left[\left(\frac{da}{dN} \right)_f + h_c \right] \tag{68}$$

where h_c is the critical penetration length.

If we normalize the crack length with the critical crack length, a_{cr}, Eq. (68) should become

$$\frac{d\phi}{dN} = \left[\left(\frac{d\phi}{dN} \right)_f + \frac{h_c}{a_{cr}} \right] \tag{69}$$

where a_{cr} is defined by

$$a_{cr} = \frac{1}{\pi} \left(\frac{K_{IC}}{Y\sigma} \right)^2 \tag{70}$$

K_{IC} is the material fracture toughness, Y is the crack configuration factor.

Consider, for example, IN738, the pure mechanical fatigue component has been described by Eq. (25) in section 3.1. With oxidation kinetics as described by Eq. (69) and the diffusion constant given by Neu & Sehitoglu (1989), the life prediction for IN738 LCF at 900ºC LCF is shown in Fig. 30. Here, for simplicity, the shape factor Y is assumed to be unity and the fracture toughness is 60 MPa√m. The prediction agrees well with the experimental data. As the comparison shows, the high temperature effect on LCF and TMF life of IN738 can largely be attributed to oxidation. Some OP and DP TMF data are also shown in Fig. 30, these data fall closer to the line representing the oxidation-fatigue interaction.

4.5 Summary

A nonlinear creep/dwell-fatigue-oxidation interaction model is derived based on nucleation and propagation of a surface fatigue crack, with the assistance of oxidation, and its coalescence with creep/dwell damages (cavities or wedge cracks) along its path inside the material.

The model has been shown to be successful in correlating both "cold" dwell-fatigue and "hot" creep-fatigue, as long as the respective damage accumulation processes are described based on the relevant deformation mechanism. In cold dwell, the damage is envisaged as dislocation pile-up, leading to formation of ZSK cracks. In hot creep, the damage accumulation is related to grain boundary sliding. Particularly, for creep-fatigue interaction, the model reconciles the SRP concept. Therefore, it provides a unified approach to deal with dwell/creep-fatigue interactions.

IN738LC (f=0.002 Hz)
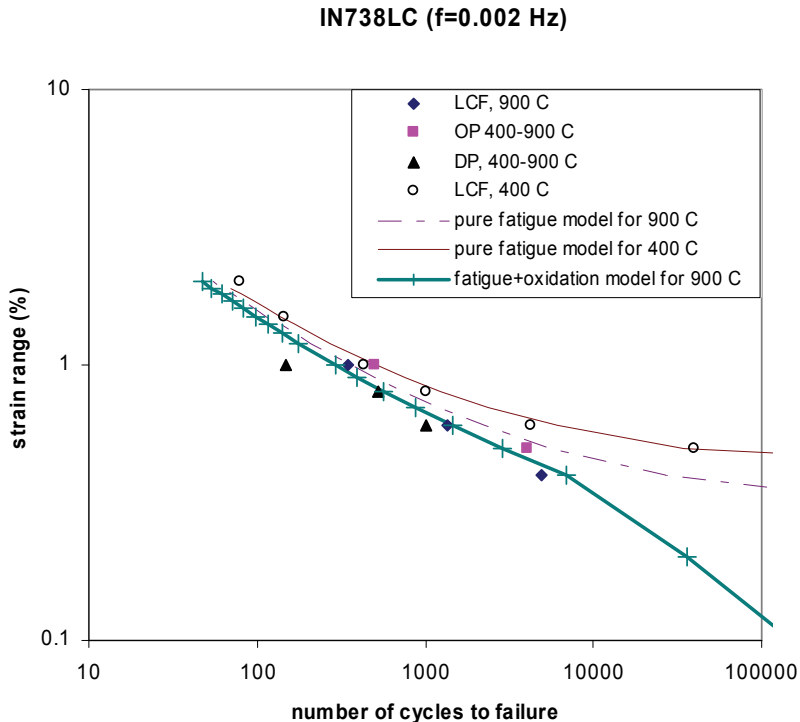
Fig. 30. Fatigue-oxidation interaction vs. pure fatigue in IN738 at high temperatures.

5. Macroscopic crack growth and damage tolerance

The previous section deals with the material life evolution under a nominal stress when the material damage state does not alter the stress distribution in a component macroscopically. This is usually called the *crack initiation life* with an engineering definition (e.g. a < 0.03') acknowledging the minimum detection limit of non-destructive inspection (NDI). When the damage state presents itself as a macroscopic crack, then fracture mechanics concepts have to be used to characterize the stress-field ahead of the crack tip and the subsequent crack growth processes. Macroscopic crack growth is usually the last stage of damage accumulation leading to catastrophic fracture of components. Understanding the crack growth process is a priori for accurate prediction of crack growth life, which is very important for ensuring structural integrity of critical gas turbine components such as discs. While focusing simplified methodologies for engineering application, this section will also treat the subject with considerations of the fundamental crack growth mechanisms and deformation kinetics, keeping consistent with that discussed in the previous sections. The microstructural damage processes that contribute to crack growth always involve certain deformation mechanisms with the influence of environmental effects. Therefore, to break through the curtain of phenomenological description, one needs to relate the observed behavior to the controlling physical mechanism, using physics based crack growth models for accurate life prediction.

5.1 Fundamentals of fracture mechanics

Fracture mechanics is the theory to describe the stress problems of cracks in continuum solids. The solution is obtained by solving the stress equilibrium and strain compatibility equations with given boundary conditions and the appropriate constitutive equations (such as Hooke's law for elasticity or some power-law for plasticity). Then, the parameter derived from the crack-tip stress field or energy is used to characterize the fracture processes in engineering materials. Depending on the material and the applied condition, fracture mechanics are categorized into i) linear elastic fracture mechanics; and ii) non-linear fracture mechanics, as briefly introduced in the following.

5.1.1 Linear-Elastic Fracture Mechanics

Linear-elastic fracture mechanics (LEFM) has been developed for crack problems in elastic continua, based on the theory of elasticity. For engineering practices, it is meant to be applied to fracture of materials under the so-called *small-scale yielding* condition, that is, the crack length is much longer than the plastic zone developed ahead of the crack tip. Details of LEFM may be seen in the book — *Fracture Mechanics: Fundamentals and Applications* (Anderson, 2005).

In general, fracture, i.e., opening of the crack, may proceed in three distinguished modes: I) the opening mode, II) the in-plane shearing mode, and III) the out-of-plane shearing mode, as schematically shown in Fig. 31. In most practical cases, however, crack growth mostly proceeds macroscopically in mode I, perpendicular to the maximum principal stress.
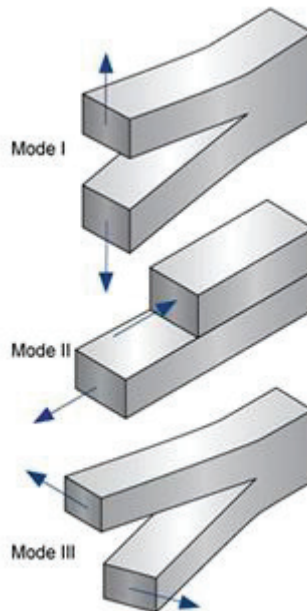
Fig. 31. A schematic of crack opening modes.

In a two dimensional (2D) crack configuration, the mode-I stress field ahead of the crack-tip (in the coordinate systems as shown in Fig. 32, where r is the distance from the crack-tip and θ is the position angle) can be expressed as

$$\sigma_{ij} = \frac{K_I}{\sqrt{2\pi r}} f_{ij}(\theta) \qquad (71)$$

where K_I is the (mode-I) stress intensity factor, and $f_{ij}(\theta)$ is an angular function.
For a 2D crack of length 2a, the stress intensity factor is given by

$$K_I = Y\sigma\sqrt{\pi a} \qquad (71)$$

where σ is the nominal applied stress and Y is the component geometry factor.
For a crack of elliptical shape with a short axis 2a and long axis 2c, the stress intensity factor is given by

$$K_I = Y\sigma\sqrt{\frac{\pi a}{Q}} \qquad (72a)$$

where

$$Q = 1 + 1.46\left(\frac{a}{c}\right)^{1.65} \qquad (72b)$$

which is an approximation of the elliptical integral of the second kind to the 2nd power.
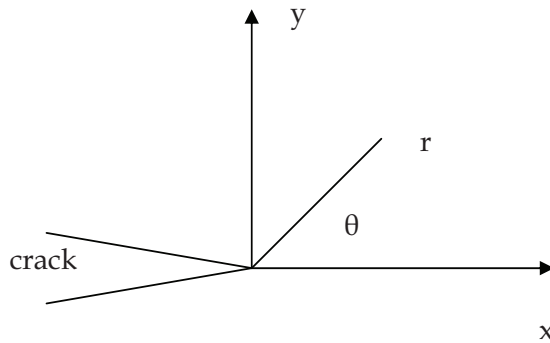
Fig. 32. The crack-tip coordinate.

K-solutions for various standard configurations have been summarized in handbooks (e.g. Tada et al. 2000). Newman & Raju (1983) have also provided numerical solutions for elliptical cracks in some standard 3D bodies. But, in most cases for cracks in engineering components, the solution is sought numerically using finite element methods, meshing for the particular component-crack geometry, which can be quite tedious and time consuming.
An alternative method to extract stress intensity factors is the weight function method (Bueckner, 1970; Rice, 1972). Based on the reciprocal theorem of elasticity, this method can be used to evaluate the stress intensity factor by integrating the stress distribution with a weight function over the crack plane for an elastic body under an arbitrary loading, as:

$$K = \int_0^a \sigma(x)m(x,a)dx \tag{73}$$

where, $\sigma(x)$ is the stress distribution as induced by the remote traction T in the uncracked body, as illustrated in Fig. 33, and m(x,a) is the weight function for the body. This method is rather attractive for engineering applications, since the stress distribution $\sigma(x)$ on the presumed crack plane can be readily determined using the finite element method for an engineering component, but the question is how to determine the weight function for the body?
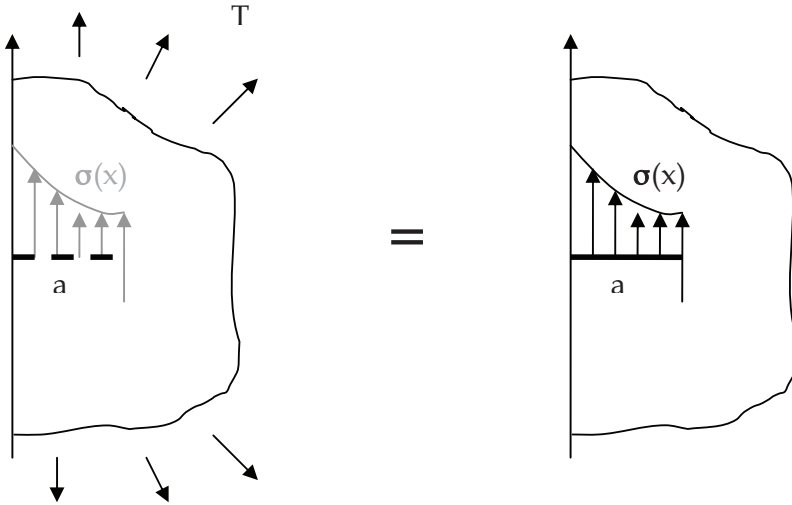
Fig. 33. Schematic illustration of the weight function method: a) stress distribution induced in the uncracked body subjected to an arbitrary remote traction T, and b) the same stress distribution loaded on the crack surface.

For two dimensional (2D) cracks, the weight function method can be generally expressed as (Bueckner, 1978; Rice, 1985)

$$K_{P'} = \iint \sigma(P(x,y))m(P,P')dA_P \tag{73}$$

where P is the integration point, P' is the crack-front point where the stress intensity factor is to be evaluated, and m(P, P') is the weight function. An example for an embedded elliptical crack in an infinite solid was given by Wang et al. (1998):

$$m(x,y;P') = \frac{\sqrt{2s}}{\pi^{3/2}l^2}\sqrt{1 - \frac{s}{8\rho_1} - \frac{s}{8\rho_2} - \frac{s}{8\rho_3} - \frac{s}{8\rho_4}} \tag{74}$$

where s is the shortest distance from P to the crack front, ρ_i (i =1, 2, 3, 4) are the distances between point C, where the extension of the shortest distance line intersects the major axis of ellipse, and the four points on the crack front that connects to point C with lines intersecting perpendicularly to crack front, as shown in Fig. 34.
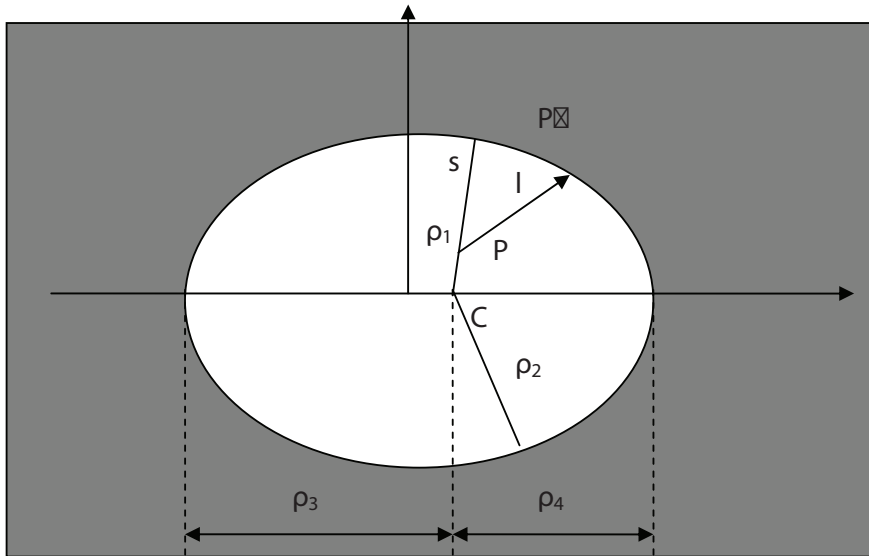
Fig. 34. Weight function for an elliptical crack.

5.1.2 Non-linear fracture mechanics

Nonlinear fracture mechanics generally deals with crack problems in materials with non-linear constitutive behaviours, e.g., monotonic plasticity. Then, the crack-tip stress field can be described by

$$\sigma_{ij} = \sigma_0 \left(\frac{J}{\sigma_0 \varepsilon_0 I_n r} \right)^{1/(n+1)} \tilde{\sigma}_{ij}(\theta, n) \tag{75}$$

which is known as the HRR field, after Hutchinson (1968) and Rice & Rosengren (1968). The singularity of the crack-tip stress field in a nonlinear material depends on the material's strain hardening exponent. Therefore, the way to extract the stress intensity as in the linear elastic material is not desirable from the mechanics point of view, since it is not universally valid for all materials. Hence, the crack-tip parameter for nonlinear materials is defined by contour-independent energy integrals, in this case, the J-integral, which is defined by

$$J = \int_\Gamma \left(W dy - \mathbf{T} \cdot \frac{\partial \mathbf{u}}{\partial \mathbf{x}} ds \right) \tag{76}$$

where $\mathbf{u}$ is the displacement vector, $\mathbf{T}$ is the surface traction vector, W is the strain energy density, and s is the arc length along the contour Γ.

For materials exhibiting time dependent deformation, similarly, the stress field can be found to be controlled by another time-dependent path-integral (Landes & Begley, 1976):

$$C(t) = \int_\Gamma \left(\dot{W} dy - \mathbf{T} \cdot \frac{\partial \dot{\mathbf{u}}}{\partial \mathbf{x}} ds \right) \tag{77}$$

In elastic materials or under small-scale yielding conditions, the J-integral and the stress intensity factor can be related as:

$$J = \frac{K^2}{E}$$

(78)

5.2 Fatigue crack growth

Fatigue crack growth phenomena have been an important subject of study, particularly because of the structural integrity airworthiness requirements. The fatigue crack growth law or model is a cornerstone of the so-called damage tolerance design, which will be elaborated later. This section concentrates on fatigue crack growth mechanism and its rate equation.

Fatigue crack growth mostly proceeds in a transgranular mode, following a power-law relationship with the cycle stress intensity factor range, ΔK, as first observed by Paris (Paris, 1963):

$$\frac{da}{dN} = C(\Delta K)^3,$$

(79)

where C and n are empirical constants.

It has been recognized that the alternating slip and slip reversal process is mostly responsible for fatigue crack nucleation and propagation (Neumann, 1974; Laird & Smith, 1982), which has been summarized as the restricted slip reversibility (RSR) concept, as schematically show in (Fong & Thomas, 1988). Based on the RSR concept and the deformation kinetics, Wu et al. (1993) have derived a transgranular fatigue crack growth rate equation as

$$\frac{da}{dN} = \frac{(\alpha_f V_r - \alpha_r V_f)}{12\pi(1-R)V_f V_r H}(\Delta K - \Delta K_{th})\left(\frac{\Delta K}{\sigma_y}\right)^2,$$

(80)

where

$$\Delta K_{th} = \frac{(1-R)HV_f V_r}{\alpha_f V_r - \alpha_r V_f}\left[\frac{1}{H}\left(\tau_{of} - \tau_{or} + \frac{\Delta G_f^{\neq}}{V_f} - \frac{\Delta G_r^{\neq}}{V_r}\right) - \ln\frac{\left(\frac{V_f H \dot{\gamma}_{of}}{2f\alpha_f \Delta K}\right)^{\frac{kT}{V_f H}}}{\left(\frac{V_r H \dot{\gamma}_{or}}{2f\alpha_r \Delta K}\right)^{\frac{kT}{V_r H}}}\right].$$

(81)

where $\dot{\gamma}_0$ is a pre-exponential strain rate constant, $\Delta G^{\neq}$ is the activation energy, V is the activation volume, τ_o is the slip resistance of the lattice, H is the work-hardening coefficient, α is the fracture work factor, k is the Boltzmann constant, T is the absolute temperature, f is the frequency, and the subscripts "f" and "r" refer slip-forward and reversal, respectively.

In mechanical fatigue, where the microstructure (grain size, precipitate size and shape) is stable and environmental effects are absent, α_f and α_r are of the same order of magnitude, and both forward and reverse slips occur by the same mechanism so that $\Delta G_f^{\neq} = \Delta G_r^{\neq}$, $V_f = V_r = V$, $\tau_{0f} = \tau_{0r}$ and $\dot{\gamma}_{0f} = \dot{\gamma}_{0r}$, and hence ΔK_{th} approaches zero, as $kT/VH \ll 1$. Therefore, for pure mechanical fatigue:
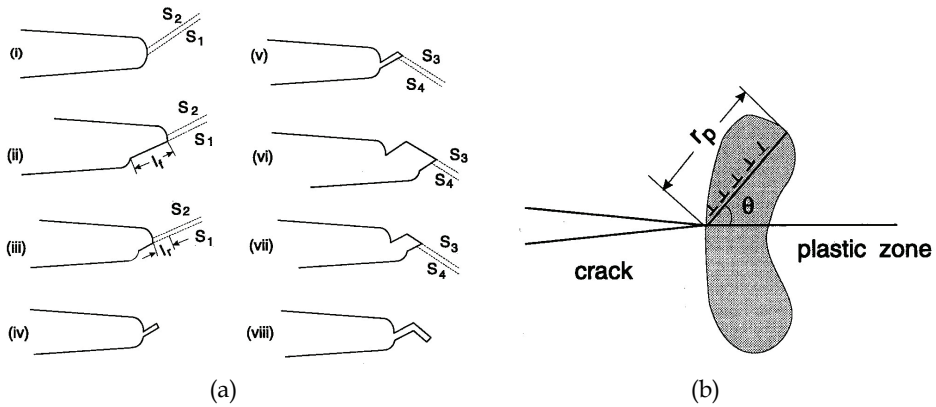
Fig. 35. (a) Schematics of fatigue crack growth by RSR: (i) Upon loading, slip systems on two favourably oriented slip planes S1 and S2 are activated. (ii) Forward slip occurs solely on S1 during the rising load cycle, producing a slip step of length l_f. (iii) During the decreasing load cycle, an increment of slip reversal l_r occurs on S1. (iv) A final slip reversal occurs on S2, producing a sharp crack tip. This process may be repeated over several load cycles (N) to produce a final crack length increment, $l_f - l_r$, after which a similar process may occur on another favourably oriented slip system variant along another pair of parallel slip planes, S3 and S4, as shown in the schematics (v) to (viii). (b) The RSR is confined within the plastic zone.

$$\frac{da}{dN} = \frac{(\alpha_f - \alpha_r)}{12\pi(1-R)VH\sigma_y^2}(\Delta K)^3. \tag{82}$$

Equation (82) takes the form of the Paris relationship with a physically defined proportional factor and a power law exponent of 3. This was indeed observed for fatigue crack growth rate data of a variety of alloys tested at room temperature in vacuum (Speidel, 1973), as shown in Fig. 36, where crack growth rate vs. ΔK relationship in a log-log plot exhibit a slope of 3 in the Paris regime. In addition, it was reported that n = 3 represents fatigue crack growth in ductile steels (Miline et al., 1988) and n = 2.92 in offshore steels (Smith & Cooper, 1989). Numerous experiments have also shown that the power law exponent of the Paris law falls within the range of 2.7~3.4 within the Paris regime. The power law exponent values found in these experiments are closer to 3 than 2 or 4, the values predicted by other models. Therefore, it may be fairly concluded that the RSR model is suitable for conventional materials where deformation is promoted by homogeneous slips.

Interestingly also, the RSR model shows that the fatigue crack growth rate depends on the materials' yield strength inversely to a power of 2, and it is also inversely proportional to the work-hardening coefficient. This implies the dependence on microstructure and temperature. For example, the yield strength depends on the grain size through the Hall-Petch relationship and it is also a function of temperature. Pure fatigue is essentially a "low temperature" phenomena occurring by the mechanism of dislocation glide, as depicted by the RSR model. The dependence of fatigue crack growth rate on yield strength was

demonstrated by Benson and Edmonds (1978) on 0.5Cr-0.5Mo-0.25V steel. A range of yield strength values, varying between 466 MPa and 834 MPa, were obtained using different heat treatment procedures. The work hardening coefficient, H, for each heat-treated material is estimated by dividing the difference between the ultimate tensile strength and the yield strength with the elongation, typically 13%. Then, the H-compensated crack growth rates at $\Delta K = 15.69$ MPa$\sqrt{m}$, which is far above the fatigue threshold of this material, are plotted against σ_y^2 as shown in Fig. 37.
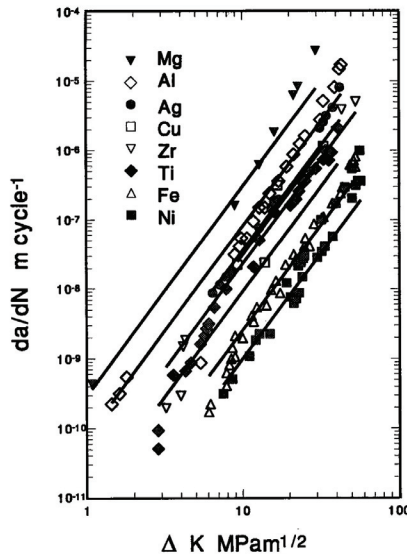
Fig. 36. Fatigue crack growth behaviours of a number of metals at room temperature in vacuum.
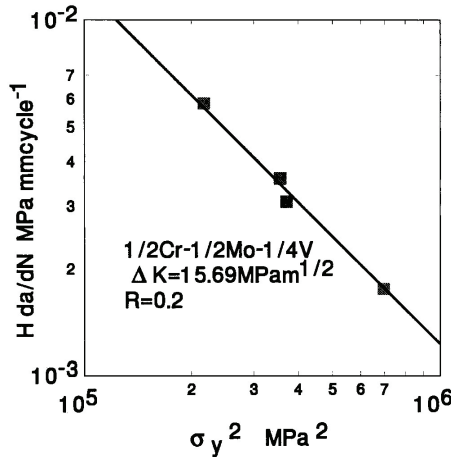
Fig. 37. H-compensated fatigue crack growth rate vs. σ_y^2 for 0.5Cr-0.5Mo-0.25V steel.

Equations (80)-(81) further predicts that the threshold in fatigue crack growth does not occur in the absence of microstructural change and environmental effects ahead of the crack tip such as in the case of pure mechanical fatigue. Some apparent thresholds ΔK_{th} does occur in coupon testing using load-decreasing procedures, due to crack closure, which will not be discussed further, since load shedding conditions are not particularly relevant to the service condition for fatigue crack growth to occur. According to Eq. (81), however, an intrinsic fatigue threshold may arise as a result of environmental interactions in a way if the environmental effects weaken the point obstacles after a new crack surface is exposed, leading to reduction of the activation barrier $\Delta G^{\neq}_r$, and τ_{0r}, and/or increase of V_r upon slip reversal. Indeed, corrosion fatigue is a complex process and the detailed kinetics of the involved chemical processes need to be considered.

Another important phenomenon of fatigue is the behaviour of short cracks (Miller, K. J. & de los Rios, 1986). While the underlying physical mechanism is the same as discussed above, the complexity of the behaviour and the scatter reflects the interaction of the crack propagation kinetics with the microstructure, which should be addressed with a probabilistic approach and it is beyond the scope of this chapter. It is noteworthy though, that small crack growth behaviour is often observed to occur below the fatigue threshold established for a long crack, which indeed supports the predication of Eq. (82).

5.3 Creep crack growth

Creep crack growth resistance is also one of the important damage-tolerance properties required for materials being used for high temperature applications (T $\geq$ 0.3 T_m, where T_m is the absolute melting temperature). Most creep crack growth tests have been conducted under constant load at high temperature in air, which is really a mixed creep-oxidation condition. Because of its apparent time-dependence, early studies on creep crack growth (CCG) mainly focused on correlating creep crack growth rates (CCGR) with some path-independent energy integrals C(t) and C* (the steady-state value of C(t)), which were good for creep-ductile materials such as Discaloy (Landes and Begley, 1976) and steels (Liu and Hsu, 1985). On the other hand, the stress intensity factor (K) has also been used to correlate CCGR, especially under small-scale creep deformation conditions and in the presence of environmental embrittlement effects, for high strength heat resistant alloys such as superalloys (Floreen, 1983; Sadananda & Shahinian, 1977).

Many mechanism based creep crack growth models have been proposed (e.g. Dimelfi & Nix, 1977; Vitek, 1978; Cocks & Ashby, 1982) and some general fracture mechanics treatments have also been given (Saxena, 1986; Riedel, 1989, Riedel, 1990), but these models did not sufficiently considered the contribution of grain boundary sliding, and therefore it is still lacking of a universal treatment to both creep-ductile and creep-brittle cases.

Considering the crack-tip stress relaxation by two deformation mechanisms—intragranular deformation and GBS, as schematically shown in Fig. 38, Xu et al. (1999) has derived a creep crack growth equation in the following form:

$$\frac{da}{dt} = \frac{d}{\lambda} \left[\frac{n+1}{n-p+1} \left(\frac{AI_n}{BI_p} \right)^{\frac{1}{n-1}} C(t) + (p+1) \left(\frac{1}{\sqrt{2\pi}} \right)^{\frac{2p}{p-1}} B^{\frac{1}{p-1}} K_l^{\frac{2}{p-1}} \left(\frac{C(t)}{I_n} \right)^{\frac{p^2-p-2}{p^2-1}} \right] \tag{83}$$

where n and p are power-law index, A and B are power-law constants, I_n and I_p are HHR field parameters associated with the HRR field of intragranular deformation and GBS, respectively; d is the grain size and λ is the critical GBS distance between cavities.
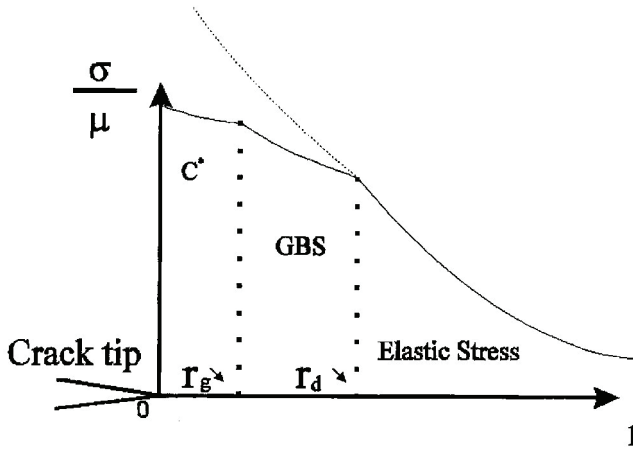

Fig. 38. A schematic of stress distribution in three zones ahead of a creep crack tip.

5.3.1 Creep-ductile cases

In creep ductile materials with small grain size, the creep zone may contain many grains, and therefore intragranular deformation plays a significant role in stress relaxation, while the contribution of GBS may be relatively small. For these cases, the first term in Eq. (83) dominates such that

$$\frac{da}{dt} = \frac{d}{\lambda} \frac{n+1}{n-p+1} \left(\frac{AI_n}{BI_p} \right)^{\frac{1}{n-1}} C(t)$$
(84)

This model basically agrees with that of Cocks & Ashby (1982).

5.3.2 Creep-brittle cases

In creep brittle materials (e.g., cast Ni-base superalloys) containing large grains, the role of intragranular deformation in crack-tip stress relaxation and creep crack growth will be limited. In that case, crack-tip deformation will mostly be concentrated in the grain boundary region, and therefore GBS plays a dominant role in the crack growth process. In such cases, the second term of Eq. (83) dominates, and particularly, considering that for pure GBS, p = 2, the rate equation reduces to:

$$\frac{da}{dt} = \frac{3}{4\pi^2} \frac{d}{\lambda} BK^2$$
(85a)

The proportional constant B depends on grain boundary diffusion and microstructure, as discussed in section 2&3, as given by

$$B = \frac{D_{gb}\mu b}{kT}\left(\frac{b}{d}\right)^{q}\left(\frac{\lambda + h}{b}\right)^{q-1} \propto d^{-q} \qquad (85b)$$

Creep crack growth behaviours on Udimet 520 at 540°C can be taken as an example to illustrate the application of Eq. (85) (Xu et al., 1999). The material was heat treated to obtain different grain sizes, all containing intragranular γ' but without any grain boundary $M_{23}C_6$ precipitates, and tested in argon and air. The test temperature was selected to ensure that no grain boundary precipitates formed during testing. Fractographic studies revealed that predominantly intergranular fracture and extensive crack tip branching occurred both in air and in argon, as shown in Fig. 39 (a) and (b) respectively. The metallurgical evidence suggests that GBS-controlled intergranular cracking and oxidation were the dominant damage mechanisms. No evidence of cavitation was found in any of the specimens. The test and material conditions satisfy the model's assumptions of the dominance of GBS.

(a)   (b)
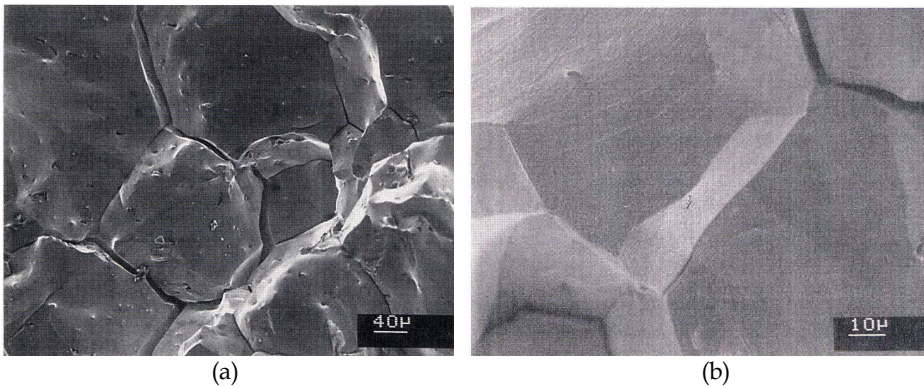
Fig. 39. SEM micrographs of the creep fracture surface of Udimet 520, (a) in air and (b) in argon, after Xu et al. (1999).

The CCGR in the argon environment, plotted in a double logarithm scale against the stress intensity factor K, exhibits a linear behaviour with the slope of 2, as shown in Fig. 40. For Udimet 520 with planar grain boundaries and no grain boundary precipitates, the stress index of GBS rate is 2 and hence, as predicted by Eq. (85), the creep crack growth rate exhibits a dependence on the stress intensity factor (K) to a power of 2. Other existing models fail to predict the K^2 dependence for creep crack growth in an inert or vacuum environment.

With regards to microstructure-dependence, the present creep crack growth model predicts that the creep crack growth rate depends inversely on the grain-size dependence to a power of q which can be related to grain boundary precipitate distribution morphology. For materials with planar and clean grain boundaries (no grain boundary precipitates, q = 1), it predicts no grain-size dependency. The data on Udimet 520 showed that the CCGR data were not sensitive to grain size variation over a grain size range of 235-464 μm, which corroborated the model prediction. For superalloys having received standard heat-treatments, where discrete grain boundary precipitates (e.g. $M_{23}C_6$ or δ phase) are present, the model predicts an inverse grain size dependence of creep crack growth rate. As reported in the literature, coarse grain size superalloys usually exhibit lower creep crack growth rates

(Floreen, 1983). For example, an inverse relation between CCGRs and grain size has been reported for Alloy 718 at 650°C (Liu et al. 1991). Stronger grain-size dependence is predicted by the model for materials with a continuous grain boundary precipitate network that may result from overaging or extended service exposure. However, no experimental work has been reported in this regard. But, it is a serious issue concerning aging gas turbine components.
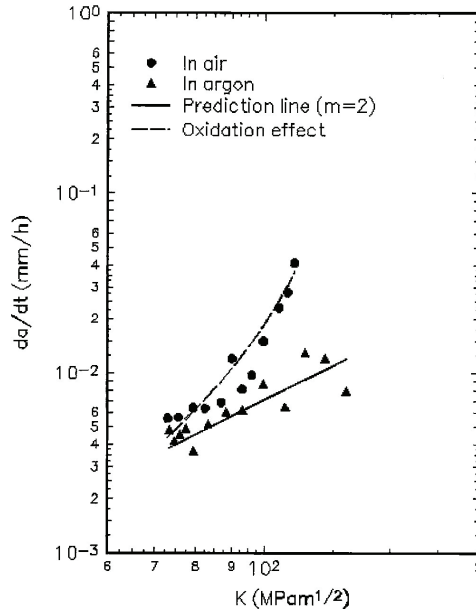
Fig. 40. Creep crack growth rate in Udimet 520 in argon and air at 540oC.

Considering environmental effect, as shown in Fig. 40, the creep crack growth rate in Udimet 520 tested in air exhibited an increasing power-dependence on K from 2 to a high value of 6.5 as K increases. This change in the K-dependence of creep crack growth rate with the environment, i.e. argon versus air, suggests that oxidation has a strong influence on the creep crack growth process.

The oxidation effects can be attributed to the reduction of the critical GBS distance λ to advance the crack in Eq. (85). An effective λ in the presence of oxide penetration may be equal to λ_0-X, where λ_0 is the critical GBS distance in the absence of oxidation effects, and X is the penetrating oxide depth measured from the external oxide surface. As time t increases, oxides will penetrate deeper into the material and λ will be significantly reduced, and therefore the creep crack growth rate will increase. Taking the effect of oxidation into consideration, Eq. (85) takes the form

$$\frac{da}{dt} = \frac{3}{4\pi^2} \frac{d}{\lambda_0 - X} BK^2 \tag{86}$$

The curve for the creep crack growth rate in air was fitted to the test data by Xu et al. (1999) using a semi-empirical approach (Xu et al. 1999).

5.4 Creep-fatigue interaction in crack growth

Crack growth under creep-fatigue conditions is another important phenomenon affecting the structural integrity of gas turbine components, since evidently most of them operate under such conditions during the takeoff-cruise-landing cycle of the aircraft. The subject has been treated by Saxena et al. (1981) who proposed a linear summation model as:

$$\frac{da}{dN} = \left(\frac{da}{dN}\right)_f + C_5 \int_0^{t_h} \left[\frac{K^2(1-v^2)}{E(n+1)t} + C^*\right]^m dt \tag{87}$$

where t_h is the hold time; n is the creep law exponent, and m ~ 1 or n/(n+1) (Cocks & Ashby, 1982), and C_5 is an empirical constant. Eq. (87) naturally reduces to a creep crack growth equation for long-term hold-times, and though it resolves into a K-dependence for short-term hold times but relates to no strong microstructural dependence, which is contrary to most experimental observations (e.g., Bain et al., 1988; Telesman et al. 2008).

Recall that, in section 4.1, we have developed a generic thermomechanical fatigue model with consideration of oxidation-creep-fatigue interactions, Eq. (50). Now, it is reasonable to consider that under creep-fatigue conditions, grain boundary sliding operates at a stress close to σ_y within the plastic zone, which is responsible for producing intergranular damage proportion to

$$l_c = d \int_0^{t_h} \varepsilon_{gbs} dt \tag{88}$$

Referring to Eq. (8) but omitting the mathematical detail of the integration, we shall propose for simplicity that

$$l_c \propto d^{1-q} \sigma_y^p t_h \tag{88}$$

Hence, substituting Eq. (88) into (50), we obtain:

$$\frac{da}{dN} = \left(1 + B\lambda^{-1}d^{1-q}\sigma_y^p t_h\right)\left\{\left(\frac{da}{dN}\right)_f + \left(\frac{da}{dN}\right)_{env}\right\} \tag{89}$$

The creep-fatigue crack growth rates in Udimet 720 observed by Bain at al (1988) are shown in Fig. 41. It shows strong grain size dependence in the crack growth behaviour. Taking the fatigue crack growth rate at 427oC as the reference for each grain-size material respectively, this grain size dependence of creep-fatigue crack growth rate in Udimet 720 can be described using Eq. (89) with q = 2.5688, as shown in Fig. 42. Note that the yield strength of these materials were almost the same and there were grain boundary phases such as TiC, $Cr_{23}C_6$, and $(Cr, Mo, W)_3B_2$ present to form a discrete/almost continuous distribution such at 2 < q < 3. The pure fatigue crack growth components (neglecting oxidation) in these materials were:

$$\frac{da}{dN} = 6.432 \times 10^{-11} \Delta K^{3.72} \qquad (ASTM0)$$
$$\frac{da}{dN} = 1.6 \times 10^{-11} \Delta K^{3.72} \qquad (ASTM3 - 8.5) \tag{90}$$
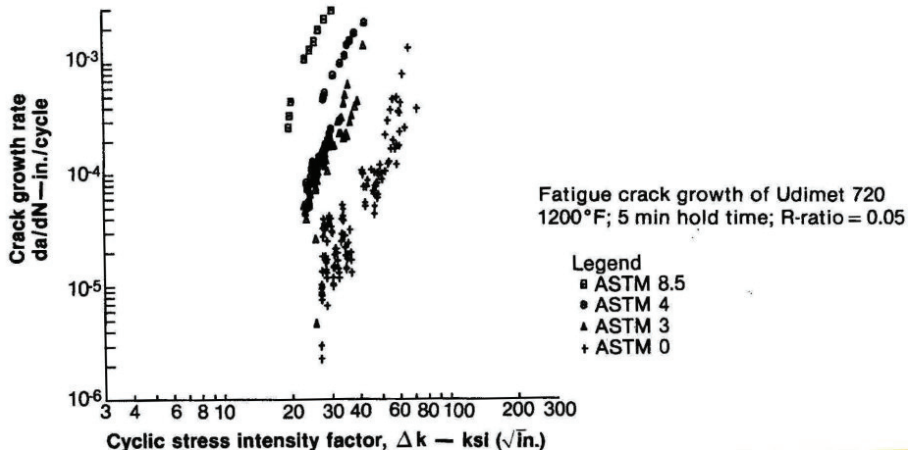
Fig. 41. Fatigue crack growth at 649oC with 5 min hold time at the maximum load (Bain et al., 1988).
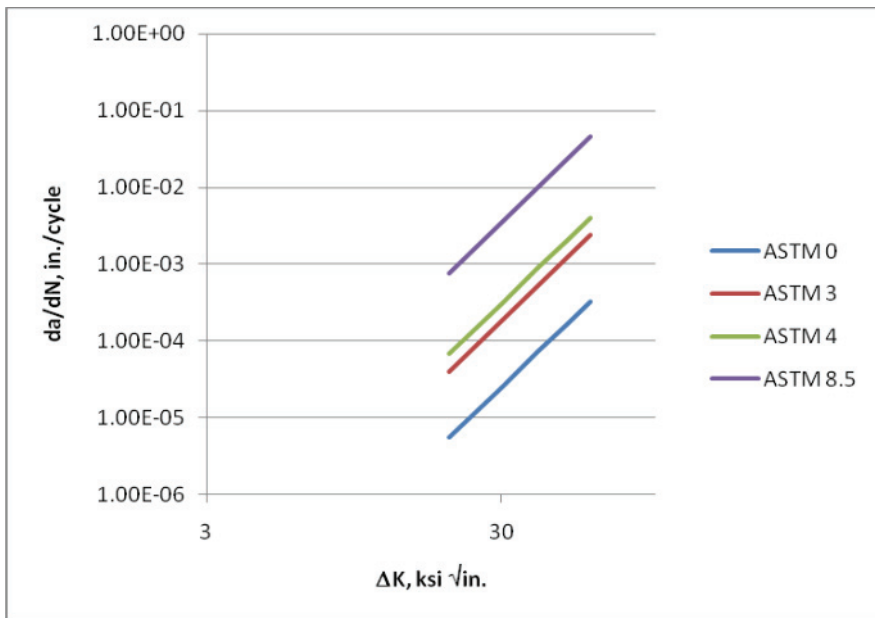
Fig. 42. The predicted Fatigue crack growth in Udmet 720 at 649oC with 5 min hold time.

Telesman et al. (2008) also observed strong microstructural dependence of the hold time fatigue crack growth rate in the LSHR P/M disk superalloy. Using heat treatments to control the grain size at constant but with different cooling rate and subsequent aging treatments to control the γ′ size, they related the increased fatigue crack growth rate with the stress relaxation potential possessed in each microstructure with different (primary, secondary and tertiary) γ′ sizes and distribution. This can also be explained qualitatively by

Eq. (89): stress relaxation would impart a lower grain boundary sliding rate, resulting in lesser grain boundary damage during the hold time and hence reducing the overall crack growth rate.

Finally, it should be pointed out that none of the above phenomena could be sufficiently addressed with Eq. (87). In general, the present model, Eq. (89), also presents the effect of creep damage in a multiplication factor, for every fatigue crack increment will induce coalescence with the creep damage accumulated ahead of the propagating fatigue crack.

5.4 Damage tolerance analysis

The damage-tolerance philosophy assumes materials or components entering into service have defects in their initial conditions. Then the component life is basically the life of crack propagation starting from an initial flaw, as:

$$N = \int_{a_0}^{a_f} \frac{da}{f(\Delta K)} \tag{91}$$

where a_0 is the initial crack size, a_f is the final crack size at fracture (or sometimes, a dysfunction crack size reduced by a safety factor), and the crack growth rate function $f(\Delta K)$ can be any of the aforementioned, particularly Eq. (79), (86) or (89), depending on the operating condition. In the simple case under pure mechanical fatigue condition, where the crack growth rate is expressed by the Paris law, Eq. (79), the damage tolerance life can be obtained by integration as

$$N = \int_{a_0}^{a_f} \frac{da}{C(\Delta K)^n} = \int_{a_0}^{a_f} \frac{da}{C(\Delta\sigma\sqrt{\pi})^n a^{\frac{n}{2}}} = \frac{1}{(\frac{n}{2}-1)C(\Delta\sigma\sqrt{\pi})^n}\left(\frac{1}{a_0^{\frac{n}{2}-1}} - \frac{1}{a_f^{\frac{n}{2}-1}}\right) \tag{92}$$

Using this philosophy, components need to be inspected before and during service. If no actual cracks are found, it is usually assumed that the initial crack size is equal to the non-destructive inspection (NDI) limit, and hence the crack propagation life marks the safe inspection interval (SII) on the maintenance schedule. Since crack propagation life is apparently sensitive to the initial crack size, an economical maintenance plan requires more advanced NDI techniques with accuracy and lower detection limits. Taking advantage of the damage tolerance properties, a component can repeatedly enter into service, as long as it passes NDI, regardless of whether the usage has exceeded the safe-life limit, and it will retire only after cracks are found. This is called retire for cause (ROC). By virtue of damage tolerance, life extension can be achieved on safe-life expired parts, as shown schematically in Figure 5.1. The damage tolerance approach is not only meant to be used as a basis for life extension, but more so to ensure the structural integrity of safety-critical structures and components to prevent catastrophic fracture, as it is required by the Aircraft Structural Integrity Program (ASIP) and Engine Structural Integrity Program (ENSIP) of the United State Air Force.

Due to the inherent properties of materials, detectable crack propagation periods are usually very short for most materials, and even more so for advanced materials such as intermetallic and ceramic materials, such that life management based on damage tolerance is totally unpractical (too many interruptions of service due to inspections, and therefore too costly). Besides, it is commonly recognized that damage accumulation spends most of its time

undetectable non-destructively, i.e., at the microstructural level and in the small (short) crack regime. Thus, new life management philosophy is required, which should put emphasis on the physics-based understanding of the continuous evolution of damage from crack nucleation, to short crack growth and long crack growth (to eventual failure), which will be called the holistic structural integrity process.
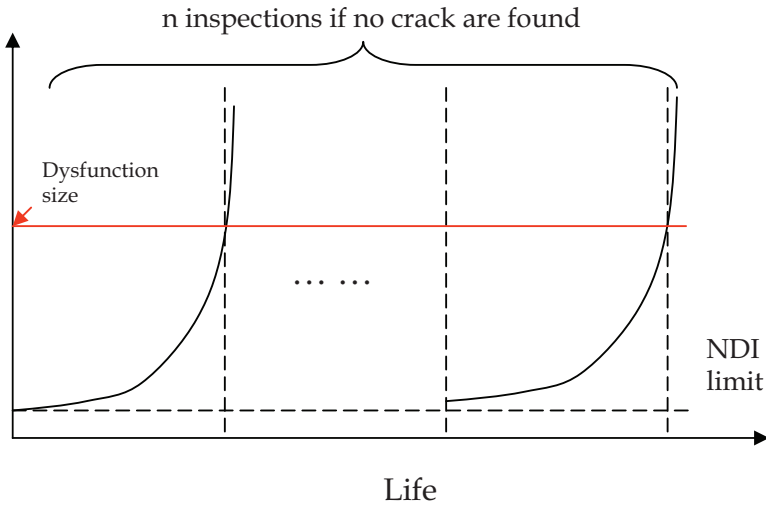

Fig. 43. Schematic of damage–tolerance life management.

6. Analyses of gas turbine components

This section demonstrates the application of the aforementioned models for two selected cases: (i) turbine blade creep and (ii) turbine blade crack growth, as follows.

6.1 Turbine blade creep

A turbine blade is modelled using the finite element method, as shown in Fig. 44. The blade was represented by a solid airfoil attached to a solid platform. Since the present analysis focused on the airfoil portion, the platform only serves as the elastic boundary condition. The temperature and pressure distribution induced by the hot gas impingement is obtained from fluid dynamics and heat transfer analyses and is applied upon the blade as the boundary conditions as shown in Fig. 45 and Fig. 46, respectively. The turbine rotates at 13800 rpm. The turbine blade material is assumed to creep by GBS only, obeying the following creep law:

$$\varepsilon_{gbs} = \varepsilon_0 + \phi \dot{\varepsilon}_{ss} t + \frac{\sigma}{\beta^2 H_{gbs}} \left[1 - \exp\left(-\frac{\beta^2 \phi H_{gbs} \dot{\varepsilon}_{ss} t}{\sigma(\beta - 1)} \right) \right] \tag{93}$$

where E = 100000 (MPa), H_{gbs}=25000 (MPa), β = 1.00925, and

$$\dot{\varepsilon}_{ss} = 10^8 \exp\left(-4 - \frac{16000}{T} \right) \left(\frac{\sigma - 150}{E} \right)^2 \tag{94}$$
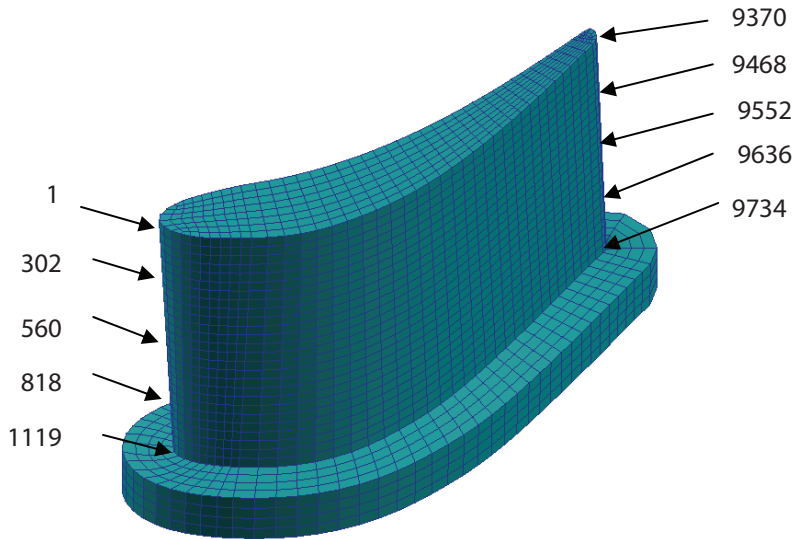
Fig. 44. FEM model of turbine blade. The numbers indicate some selected nodes. Numbers indicate the nodal points
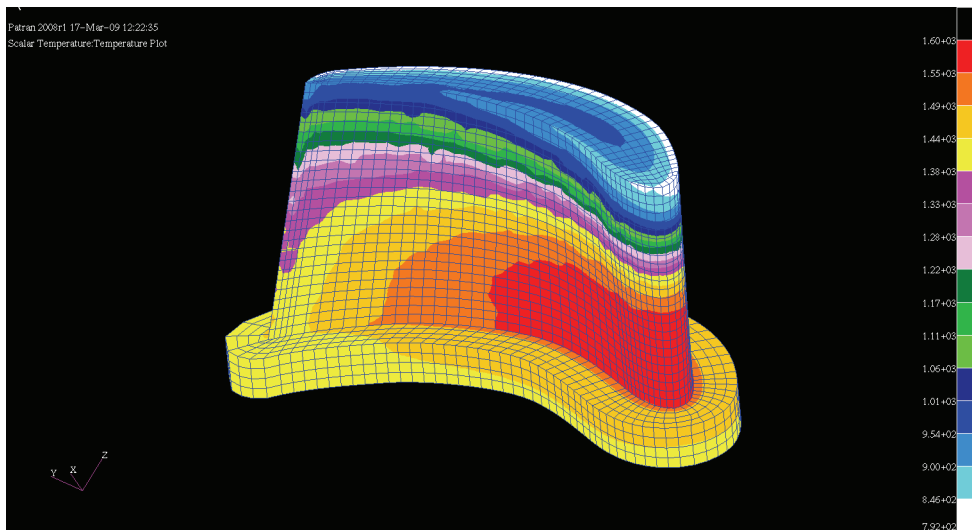
Fig. 45. Temperature profile in the blade
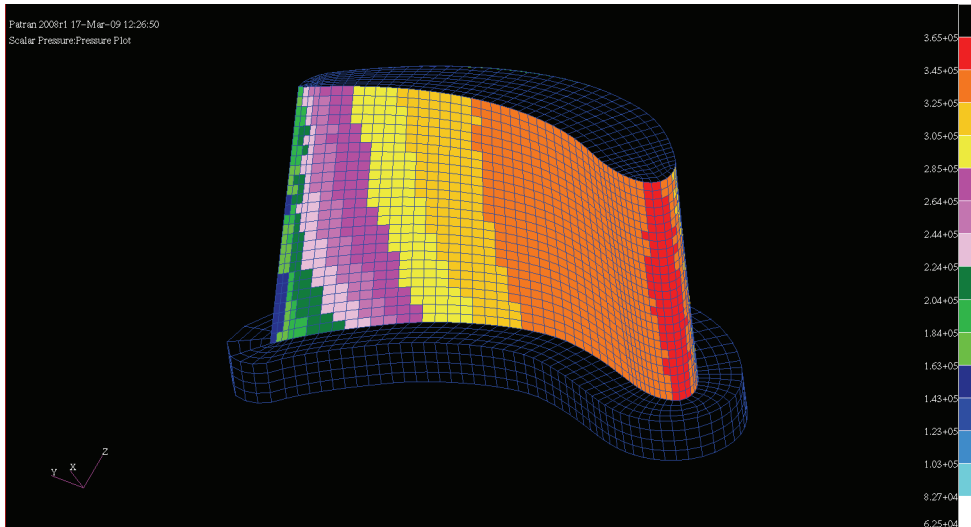
Fig. 46. Pressure profile as the boundary condition on the blade surface.

Creep simulation was conducted using MSC.Marc for 100 hours. The initial (at t = 0) and final (t=100 hours) von Mises stress distribution contours are shown in Fig. 47 and Fig. 48, respectively. The initial response of the blade is purely elastic, which results in a highly non-uniform stress distribution in the blade with particular stress concentrations at the mid-leading edge and mid-trailing edge and near the bottom attachment. After 100 hours, when creep deformation proceeds into a steady state, stress distribution became more uniform throughout the airfoil. Stress concentration remained at the bottom attachment, because, for simplicity of demonstration, the platform was assumed to deform only elastically. The final creep strain distribution contours are shown in Fig. 49. The creep strain accumulates the most where the initial elastic stress concentration appears, which then leads to stress relaxation. Creep deformation and stress relaxation curves at selected nodes along the leading/trailing edges (the nodal numbers are indicated in Fig. 44) are shown in Fig. 50 - Fig. 53, respectively. In both cases, the stress has dropped dramatically with the overall increment of the creep strain. Except those creep strain concentration regions, the majority of the airfoil, especially the upper half, practically remains in the elastic regime. The stress relaxation or "stress shakedown" in a component have a two-fold meaning on the life of the component: it may impact on the low cycle fatigue damage with a timely reduced stress, but on the other hand, it is also accompanied with an increase of creep damage in the material. From this analysis for this particular blade, it deems that the mid-leading edge and the bottom of trailing edge are critical locations. After 50 hours, creep deformation proceeds in steady state.
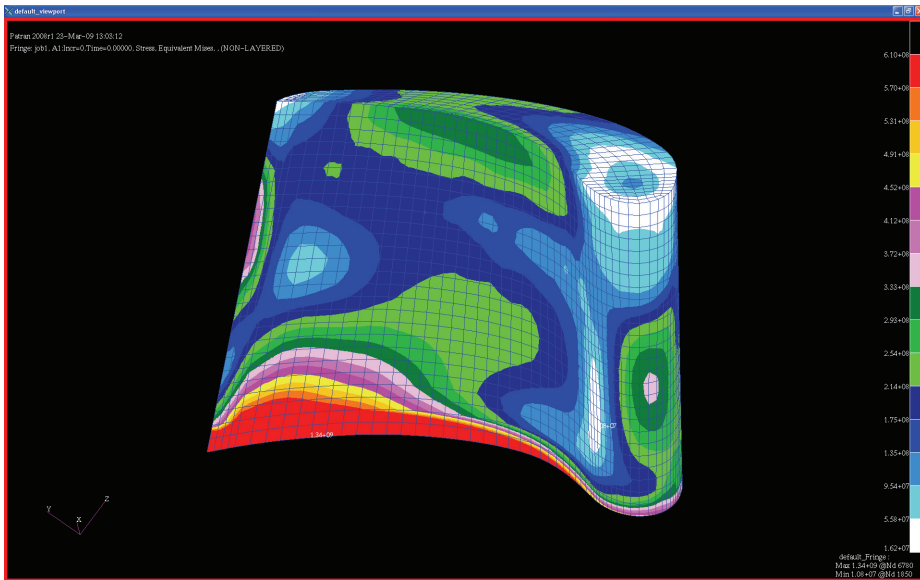
(a)
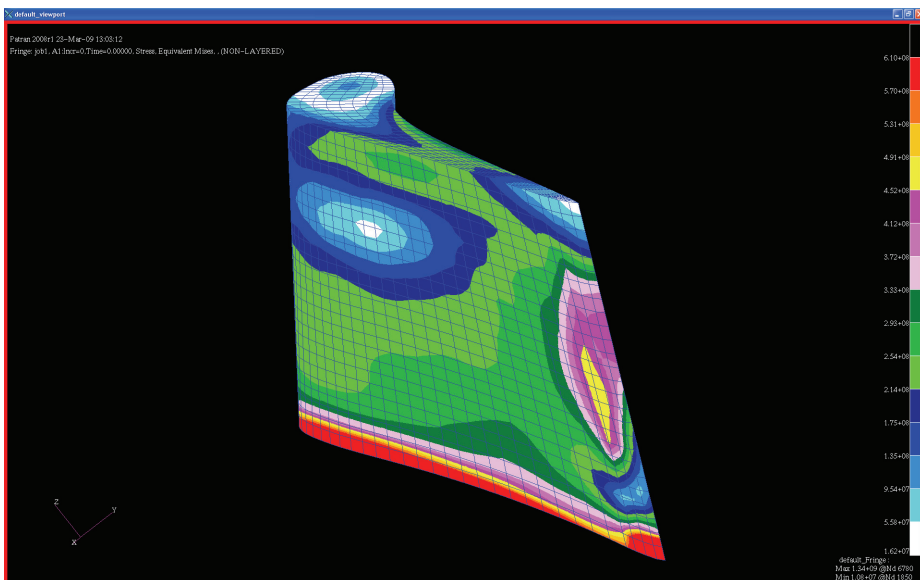
(b)

Fig. 47. Stress distribution at t=0: a) the pressure side, and b) the suction side.
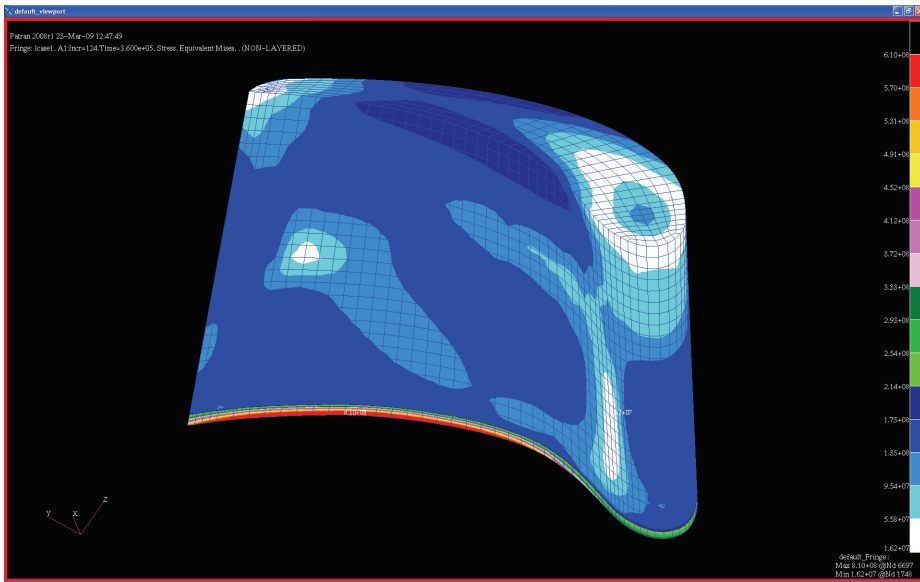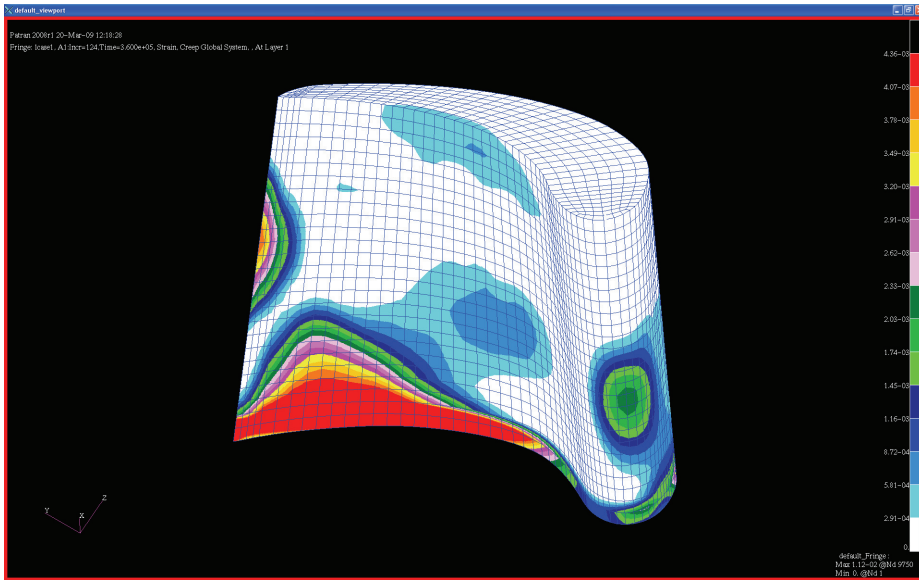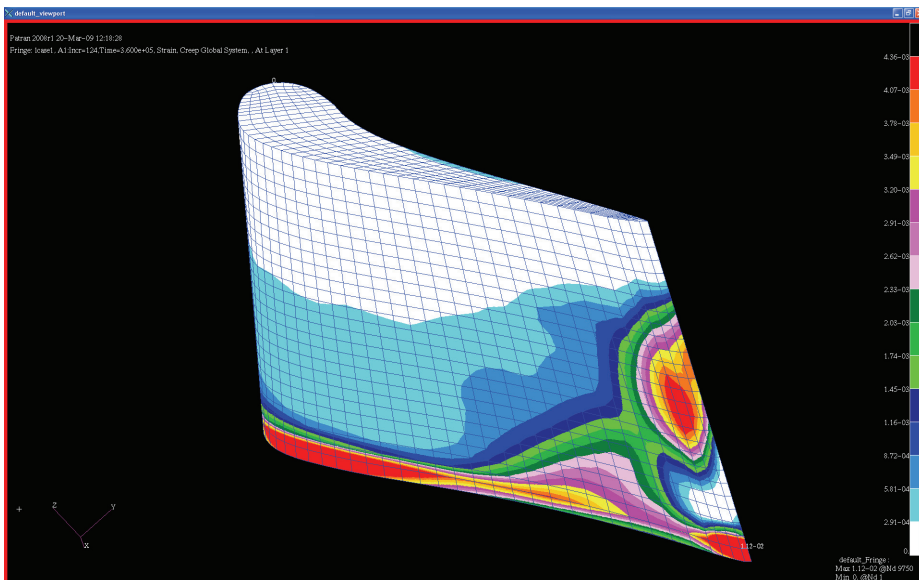
(a)
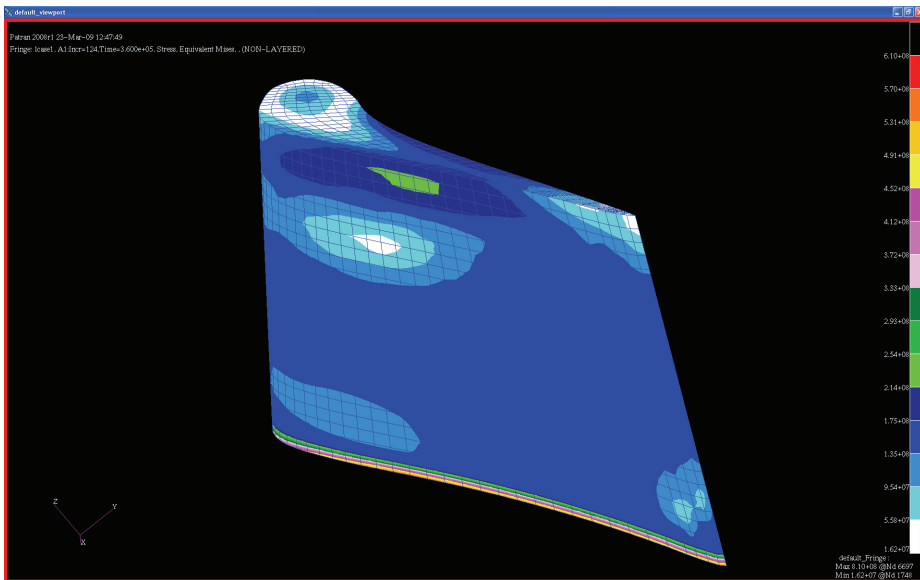
(b)

Fig. 48. Stress distribution at t =100 hrs, a) the pressure side, and b) the suction side.

(a)

(b)

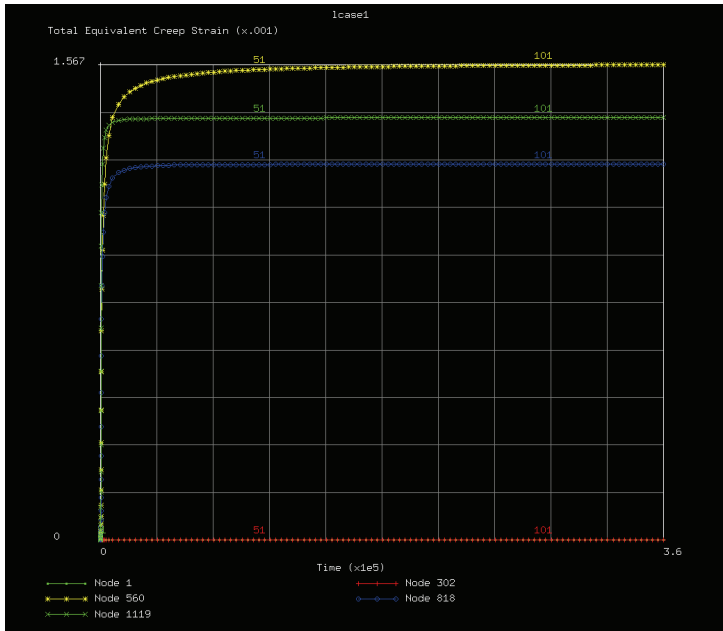Fig. 49. Creep deformation of the blade after a 100 hr., a) the pressure side, and b) the suction side.

Fig. 50. Deformation history at selected nodes along the leading edge.
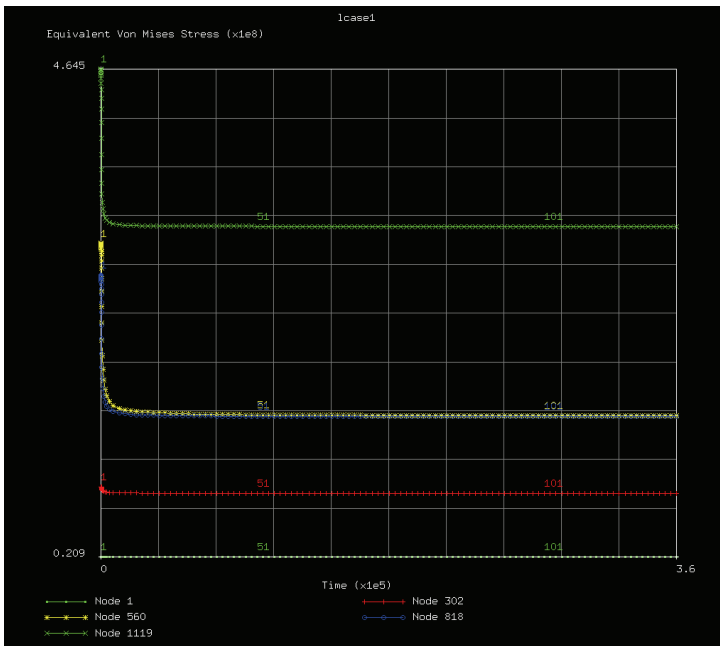

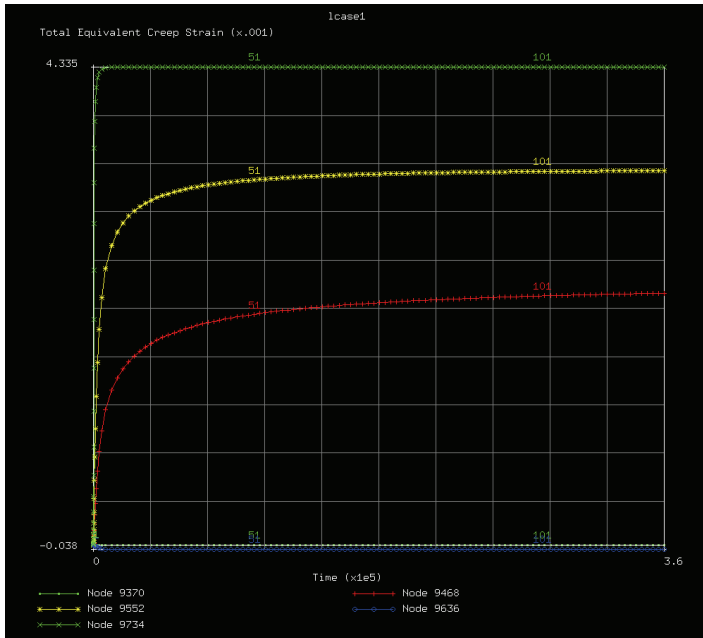Fig. 51. Stress relaxation at selected nodes along the leading edge.

Fig. 52. Deformation history at selected nodes along the trailing edge.
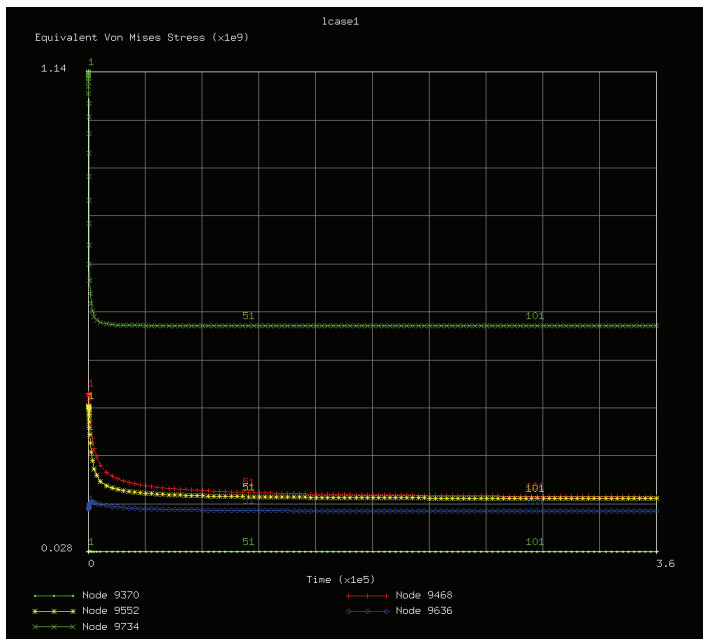
Fig. 53. Stress relaxation at selected nodes along the trailing edge.

6.2 Turbine Blade Crack Growth

Next we consider a turbine blade that experienced premature failure due to fatigue crack growth. A finite element model was created for the blade and the stress analysis was conducted with the consideration of centrifugal loading and the blade contact with the disc. The finite element mesh and the von Mises stress distribution in the blade is shown in Fig. 54.

An initial crack of semi-elliptical shape exited in the trough of the first serration on the pressure side (indicated by the arrow in Fig. 54). The principal stress over a quarter of the fir-tree root plane is shown in Fig. 55. Simulation of crack growth was conducted using the weight function method, Eq. (73-74) with appropriate boundary correction factors. The stress intensity factor results were then input into the integration for crack advancement based on the Paris-law of the material. The crack depth and aspect ratio as functions of the cycle number normalized to its failure are shown in Fig. 56. The crack depth increased monotonically. The crack aspect ratio increased initially, reached a constant value of 0.93, and then began to decline. This change reflected the fracture mechanics characteristic of the elliptical crack and the effect of stress distribution on the cracking plane in the component. When the crack was small, the stress over the crack was almost constant, the maximum stress intensity factor of the semi-elliptical crack occurred at the deepest crack front, which drove the crack toward a "circular" shape. However, when the crack became large, the stress distribution would have an effect. Since the stresses were relatively high at the notch root surface, then the stress intensity factor at the surface point began to accelerate, which then drove the crack to grow faster in the surface length direction. The variations of the stress intensity factors at both the surface and the deepest points are shown in Fig. 57.

The a) initial and b) final crack profiles as revealed by post-mortem examination of the fracture surface are shown in Fig. 58 (a) and (b), respectively. The results of the weight function method crack growth simulation are seen to agree with the observed crack growth profile on an actual component.
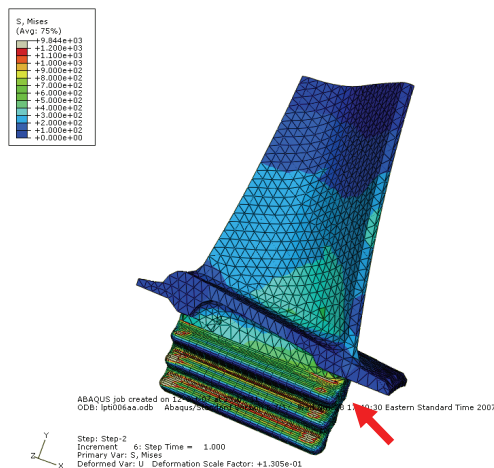

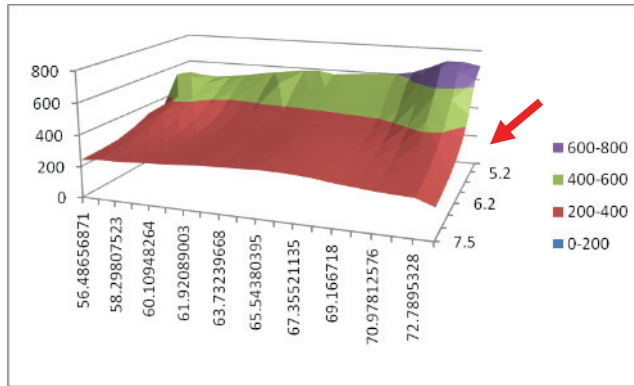Fig. 54. The von Mises stress in a turbine blade. The arrow indicates where a crack would form.

Fig. 55. Stress distribution (in unit of MPa) over a quarter of the fir-tree root plane (in unit of mm). The arrow indicates where the initial crack existed.
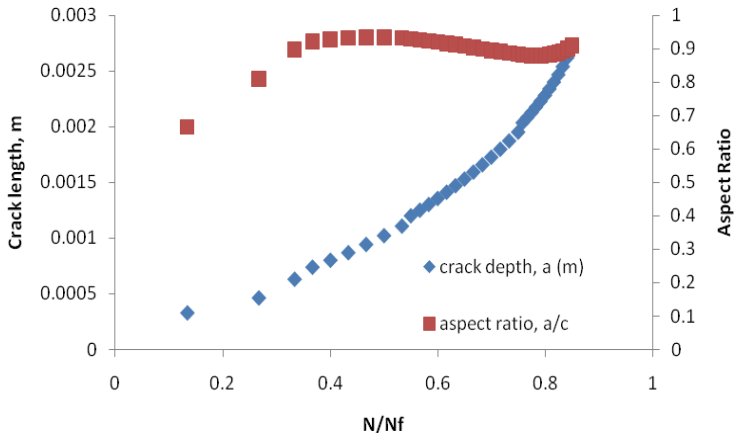

Fig. 56. Crack depth and aspect ratio as functions of the number of cycles.
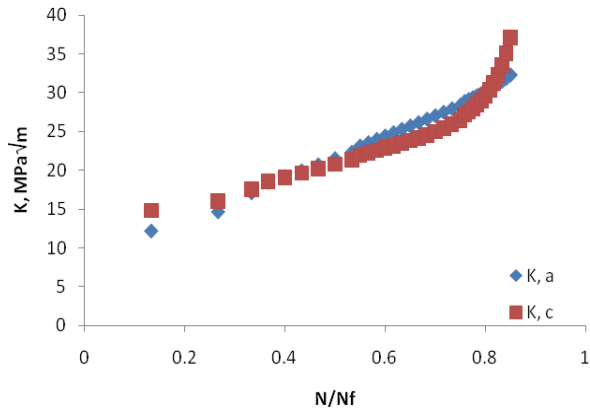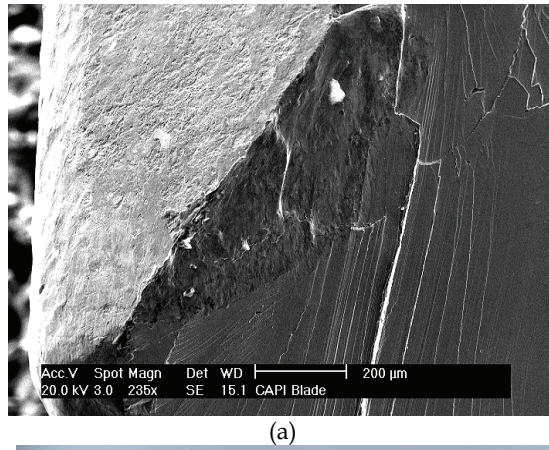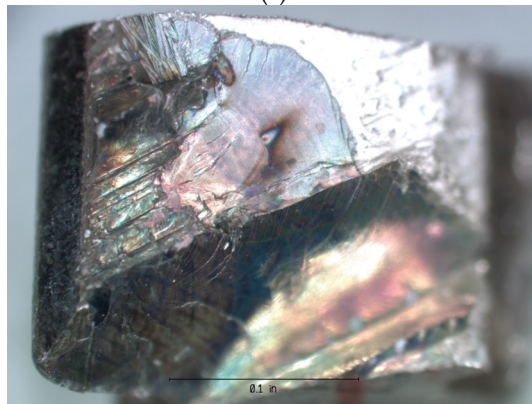
Fig. 57. Stress intensity factors at the surface and the deepest points.

(a)

(b)

Fig. 58. a) The initial crack profile, and b) the final crack profile.

7. Conclusion

In this chapter, a framework of integrated creep-fatigue (ICF) constitutive modelling is presented. The ICF model formulates deformation and damage accumulation in terms of two inelastic strain components—intragranular deformation (ID) and grain boundary sliding (GBS). This way, the model can reflect the microstructural (grain size, grain boundary morphology, grain boundary precipitates and intragranular precipitates) dependence of the deformation behaviour with respect to each deformation mechanism. As regards to damage accumulation in the form of crack nucleation and propagation, the decomposition rule founds the physical base to relate transgranular (fatigue) fracture to ID and intergranular cavitation (creep) damage to GBS for polycrystalline materials. From this premise, a general thermomechanical fatigue (TMF) model has been developed that involves creep-fatigue and oxidation-fatigue interactions.

The TMF damage accumulation model physically depicts the process of fatigue crack nucleation and propagation in coalescence with the creep/dwell damages (cavities or wedge cracks) distributed along its path inside the material. According to the present model, creep/dwell-fatigue interaction is nonlinear in nature. The model has been shown to successfully correlate both "cold" dwell-fatigue and "hot" creep-fatigue. In cold dwell, the damage is envisaged as dislocation pile-up, leading to formation of ZSK cracks. In hot creep, the damage accumulation is related to grain boundary sliding. Particularly, for creep-fatigue interaction, the model reconciles the SRP concept. Therefore, it provides a unified approach to deal with dwell/creep-fatigue interactions.

Similarly, a fatigue crack growth equation is presented based on the transgranular restricted slip reversal (RSR) mechanism, and a creep crack growth equation based on grain boundary sliding with stress relaxation ahead of the crack tip. Crack growth in creep-fatigue is also described within the same framework in association with fracture mechanics.

Overall, a physics-based holistic lifing approach has been developed; and when incorporated with the finite element method, it offers an integrated methodology for life prediction of gas turbine components, addressing a variety of failure modes under high temperature loading conditions.

8. References

Anderson, T. L. (2005). *Fracture Mechanics: Fundamentals and Applications*. 3rd Ed., Taylor & Francis Group. Boca Raton, FL.

Ashby, M.F. & Dyson, B.F. (1985). *Advances in Fracture Research*, Vol. 9 (eds. S. R. Valluri et al.), Pergamon Press, Oxford, UK.

Bache, M.R., Cope, M., Davies, H.M., Evans W.J. & Harrison, G. (1997). Dwell sensitive fatigue in a near alpha titanium alloy at ambient temperature. *Int. J. Fatigue*, 19, pp. S83-S88.

Baik, S. & Raj, R. (1982). Mechanisms of creep-fatigue interaction. *Metall. Trans. A*, 13A, pp. 1215-1221.

Bain, K.R., Gambone, M.L., Hyzak, J.H. & Thoms, M.C. (1988). Development of damage tolerant microstructure in Udimet 720. In: *Superalloys 1988*, pp. 13-22. The Metallurgical Society, Warrendale, PA.

Benson, J.P. & and Edmonds, D.V. (1978). Effects of microstructure on fatigue in threshold region in low-alloy steels. *Metal Sci.*, 12, pp. 223-232.

Bueckner, H.F. (1970). A novel principle for the computation of stress intensity factors. *Zeitschrift für Angewandte Mathematik und Mechanik*, 50, pp.529-545.

Bueckner, H.F. (1987). *Int. J. Solids & Struct.*, 23, pp. 57-93.

Carry, C. & Strudel, J.L. (1977). Apparent and effective creep parameters in single crystals of a Ni-base superalloy—I: Incubation period. *Acta Metall.*, 25, pp. 767-777.

Carry, C. & Strudel, J.L. (1978). Apparent and effective creep parameters in single crystals of a Ni-base superalloy—II: Secondary creep. *Acta Metall*, 26, pp. 859-870.

Castillo, R., Koul, A.K. & Immarigeon, J.-P. (1988). The effect of service exposure on the creep properties of cast IN-738LC subjected to low stress high temperature creep conditions. In: *Superalloys 1988*, pp. 805-813. The Metallurgical Society, Warrendale, PA.

Chaboche, J.L. & Gailetaud, G. (1986). On the calculation of structures in cyclic plasticity or viscoplasticity. *Computers & Structures,* 23, pp. 23–31

Chang, M. Au, P., Terada, T. & Koul, A.K. (1992). Damage tolerance of alloy 718 turbine disc material. In: *Superalloys 1992*, pp. 447-456. TMS, Warrendale, PA.

Cocks, A.C.F. & Ashby, M.F. (1982). The growth of a dominant crack in a creeping material. *Scripta Metall.*, 16, pp. 109-114.

Coffin, L.F. (1954). A study of the effects of cyclic thermal stresses on a ductile metal. *Transactions of the American Society of Mechanical Engineers*, 76, pp. 931-950.

Coffin, L.F. (1969). Prediction parameters and their application to high temperature low cycle fatigue. *Proceedings of Second International Conference on Fracture*, pp. 643-654, Brighton, London, Chapmans Hall, 1969.

DeMestral, B. Eggeler, G. & Klam, H.-J. (1996). On the influence of grain morphology on creep deformation and damage mechanisms in directionally solidified and oxide dispersion strengthened superalloys, *Metall. Mater. Trans. A,* 27A, pp. 879-890.

Dimelfi, R.J. and Nix, W.D. (1977). The stress dependence of crack growth rate during creep. *Int. J. Fract.*, 13, pp. 341-348.

Dyson, B.F. & McLean, M. (2000). Modelling the Effects of Damage and Microstructural Evolution on the Creep Behaviour of Engineering Alloys. *J. Eng. Mater. Technol.*, 122, pp. 273-278.

Evans, R.W. & Wilshire, B. (1985). *Creep of Metals and Alloys*, The Institute of Metals, London, UK.

Fleury, E. & Ha, J.S.(2001). Thermomechanical fatigue behaviour of nickel base superalloy IN738LC: Part 2--Lifetime prediction. *Material Science and Technology,* 17, pp. 1087-1092.

Floreen, S. (1983). Microstructural and environmental effects during creep crack growth in a superalloy. In: *Elastic-Plastic Fracture: Second Symposium, Volume I – Inealstic Crack Analysis. ASTM STP 803*, pp. I-708-720. American Society for Testing and Materials, Philadelphia, PA.

Fong C., and Thomans, D. (1988). Stage I corrosion fatigue crack crystallography in austenitic stainless steel (316L). *Metall. Trans. A*, 19A, 2765-2773.

Frost, H.J. & Ashby, M.F. (1982). *Deformation Mechanism Maps*, Pergamon, Oxford.

Furrillo, F.T., Davidson, J.M., Tien, J.K. & Jackman, L.A. (1979), The effects of grain boundary carbides on the creep and back stress of a Ni-base superalloy. *Mater. Sci. Eng.,* 39, pp. 267-273.

Halford, G.R., Saltsman, J.F. & Hirschberg, M.H. (1977). *Ductility-Normalized Strain Range Partitioning Life Relations for Creep-Fatigue Life Predictions*. NASA TM-73737.

Hutchinson, J.W. (1968). Singular behaviour at the end of a tensile crack in a hardening material. *J. Mech. Phys. Solids*, 16, pp. 13-31.

Kolbe, M. Murken, J., Pistolek, D. Eggeler, G. & Klam, H.-J. (1999). Direct assessment of the creep strength of DS cast turbine blades using miniature creep specimens. *Mat.-wiss. U. Werksofftech.*, 30, pp. 465-472.

Krausz, A.S. & Eyring, H. (1975). *Deformation Kinetics*, John Wiley& Sons, Inc., New York.

Laird, C. & Smith, G.C. (1982). Crack propagation in high stress fatigue. *Phil. Mag.*, 7, pp. 847-857.

Landes, J.D. & Begley, J.A. (1976). A fracture mechanics approach to creep crack growth. In: *Mechanics of Crack Growth, ASTM STP 590*, pp. 128-148. American Society for Testing and Materials, Philadelphia, PA.

Liu, Y.J. & Hsu, T.R. (1985). A general treatment of creep crack growth. *Eng. Fract. Mech.,* 21, pp. 437-452.

Liu, C.D., Han, Y.F., Yan, M.G., and Chaturvedi, M.C. (1991), *Proc. Superalloys 718, 625, and Various Derivatives*, E.A. Loria, ed., pp. 537-548. TMS, Warrendale, PA

Manson, S.S. (1954). Behaviour of materials under conditions of thermal stresses. *National Advisory Commision on Aeronautics Report 1170*. Lewis Flight Propulsion Laboratory, Cleveland, OH.

Miline, I., Ainsworth, R.A., Dowling, A.R. & Stewart, A.T. (1988). *Int. J. Pressure Vessels and Pipelines*, 32, pp. 3-104.

Miller, M.P. (1993). Life prediction model for thermomechanical fatigue based on microcrack propagation. In: *ASTM STP 1186*, pp. 35–49. American Society for Testing and Materials, Philadelphia, PA.

Miller, K. J. & de los Rios, E. R. (Eds.) (1986). *The Behaviour of Short Fatigue Cracks*, Mechanical Engineering Publisher, London.

Miner, M.A. (1945). Accumulative damage in fatigue. *Transactions, ASME, Journal of Applied Mechanics*, 67, pp. A159-A167.

Neu, R. & Sehitoglu, H. (1989). Thermo-mechanical fatigue, oxidation and creep: part 2-life prediction. *Met. Trans. A*, 20A, pp. 1769–1783.

Neumann, P. (1974). New experiments concerning the slip processes at propagating fatigue crack-I. *Acta Metall.*, 22, pp. 1155-1178.

Newman, J. C., Jr. & Raju, I. S. (1983). Stress-intensity factor equations for cracks in three-dimensional finite bodies. In: *Fracture Mechanics: Fourteenth Symposium – Vol. 1: Theory and Analysis*, *ASTM STP 791*, pp. 238-265. American Society for Testing and Materials, Philadelphia, PA.

Ostergren, W.J. (1976). A damage function and associated failure equations for predicting hold time and frequency effects in elevated temperature low cycle fatigue. *J. Testing & Evaluation*, 4, pp. 327-339.

Raj, R. & Ashby, M.F. (1975). Intergranular fracture at elevated temperature. Acta Metall., 23, pp. 653-659.

Romannoski, G. R., Jr. (1982). *Mechanisms of Deformation and Fracture in High Temperature Low-Cycle Fatigue of Rene 80 and IN 100*. NASA Contractor Report 165498.

Rice, J.R. (1972). Some remarks on elastic crack tip field. *Int. J. Solids & Struct.*, 8, pp. 751-758.

Rice, J.R. (1985). *J. Appl. Mech.*, 52, pp. 571-579.

Riedel, H. (1989). Creep crack growth. In: *Fracture Mechanics: Perspectives and Directions (Twentieth Symposium), ASTM STP 1020*, pp. 101-126. American Society for Testing and Materials, Philadelphia, PA.

Riedel, H. (1990). Creep crack growth under small-scale creep conditions. *Int. J. Fract*. 42, pp. 173-188.

Robinson, E.L. (1952). Effect of temperature variation on the long-time rupture strength of steels. *Transactions, ASME,* 74, pp. 777-780.

Rice, J.R. and Rosengern, G.F. (1968). Plane strain deformation near a crack tip in a power-law hardening material. *J. Mech. Phys. Solids*, 16, pp.1-12.

Sadananda, K. & Shahinian, P. (1977). Creep crack growth in Alloy 718. *Metall. Trans. A*, 8, pp. 439-449.

Satyanarayana, D.V.V. Omprakash, C.M. Jagadeesan, B. & Niranjan Das (2008). Effect of section thickness on creep and stress rupture behaviour of DS CN247 nickel base superalloy. *Materials at High Temperatures* 25, pp. 17-26.

Saxena, A. (1986). Creep crack growth under non-steady-state conditions. In: *Fracture Mechanics, Seventeenth Volume*, *ASTM STP 905*, pp. 185-201. American Society for Testing and Materials, Philadelphia, PA.

Sanena, A., Williams, R.S. & Shih, T.T. (1981). A model for representing and predicting the influence of hold times on fatigue crack growth behaviour at elevated temperatures. In: *Fracture Mechanics, Thirteenth Volume*, *ASTM STP 743*, pp. 86-99. American Society for Testing and Materials, Philadelphia, PA.

Sehitoglu, H. (1992). Thermo-mechanical fatigue life prediction methods. In: *Advances in Fatigue Lifetime Predictive Techniques*, *ASTM STP 1122*, pp. 47–76. American Society for Testing and Materials, Philadelphia, PA.

Sessions, M.L., McMahon, C.J. & Walker, J.L. (1977). Further observations on the effect of environment on the creep/rupture behaviour of a Ni-base high temperature alloys: grain size effects. *Material Sci. & Eng.*, 27, pp.17-24.

Schilke, P.W. (2004). *Advanced Gas Turbine Materials and Coatings*, GER-3569G (08/04), GE Energy, Schenectady, NY.

Smith, R.A. & Cooper, J.F. (1989). *Int. J. Pressure Vessels and Pipelines*, 36, pp. 315-326.

Speidel, M.O. (1973). Modulus of elasticity and fatigue crack growth. In: *High Temperature Materials in Gas Turbine: Proceedinds of the Symposium on High Temperature Materials*

in Gas Turbines, Brow, Boveri & Company Limited, Baden, Switzerland, pp. 212-221.

Tada, Hiroshi, Paris, P. C. & Irwin, G. R. (2000). *The Stress Analysis of Cracks Handbook (3 ed.)*. American Society of Mechanical Engineers.

Tanaka, K. & Mura, T. (1981). A dislocation model for fatigue crack initiation, *J. App. Mech.*, 48, pp. 97-103.

Telesman, J., Gabb, T.P., Garg, A., Bonacuse, P. & Gayda, J. (2008). Effect of microstructure on time dependent fatigue crack growth behaviour in a P/M turbine disc alloy. In: *Superalloys 2008*, pp. 807-816. The Metallurgical Society, Warrendale, PA.

Viswanathan, R. (1989). *Damage Mechanisms and Life Assessment of High-Temperature Components*. ASM International, Metals Park, OH.

Vitek, V. (1978). A theory of diffusion controlled intergranular creep crack growth. *Acta Metall.*, 3, pp.1345-1356.

Walker, K.P. (1981). *Research and Development Program for Nonlinear Structural Modelling with Advanced Time-Temperature Dependent Constitutive Relations*, NASA Report CR-165533, United Technologies Research Centre, East Hartford, CT.

Wang, X., Lambert, S. B. & Glinka, G. (1998). Approximate weight functions for embedded elliptical cracks. Eng. Fract. Mech. 59 (3), pp 381-392.

Wu, X.J., Koul, A.K. & Krausz, A.S. (1993). A transgranular fatigue crack growth model based on restricted slip reversibility. *Metall. Trans. A*, 24A, pp. 1373-1380.

Wu, X.J. & Krausz, A.K. (1994). A kinetics formulation for low-temperature plasticity. *J. Mater. Engng. Performance*, 3, pp. 169-177.

Wu, X.J. & Koul, A.K. (1995). Grain boundary sliding in the presence of grain boundary precipitates during transient creep," *Metall. Trans. A*, 26A, pp. 905-913.

Wu, X.J. & Koul, A.K. (1996). Modelling creep in complex engineering alloys. In: *Creep and Stress Relaxation in Miniature Structures and Components*, pp. 3-19. The Metallurgical Society, Warrendale, PA.

Wu, X.J. & Koul, A.K. (1997). Grain boundary sliding at serrated grain boundaries. *Advanced Performance Materials*, 4, pp. 409-420.

Wu, X.J., Yandt, S., Au, P. & Immarigeon, J.-P. (2001). Modelling Thermomechanical Cyclic Deformation by Evolution of Its Activation Energy, In: *Thermomechanical Fatigue Behaviour of Materials*, *4th Volume, ASTM STP 1428*, pp. 3-14. American Society for Testing and Materials, Philadelphia, PA.

Wu, X.J. (2005). A continuously distributed dislocation model of Zener-Stroh-Koehler cracks in anisotropic materials. *Int. J. Solids & Struct*. 42(7), pp. 1909-1921.

Wu, X.J. & Au, P. (2007). Deformation kinetics during dwell fatigue. *Materials Science and Technology,* 23, pp. 1446-1449.

Wu, X.J., Beres, W. & Yandt, S. (2008). Challenges in life prediction of gas turbine critical components. *Can. Aeronaut. Space J.*, 54, pp. 31-39.

Wu, X.J., Yandt, S. & Zhang, Z. (2009). A Framework of Integrated Creep-Fatigue Modelling, *Proceedings of the ASME Turbo Expo 2009*, GT2009-59087, June 8-12, 2009, Orlando, Florida, USA.

Wu, X.J. (2009a). Fatigue analysis for impact damaged Ti-6Al-4V material. *LM-SMPL-2009-0152*. Institute for Aerospace Research, National Research Council Canada.

Wu, X.J. (2009b). A model of nonlinear fatigue-creep/dwell interactions. *Trans. ASME Journal of Engineering for Gas Turbines and Power*, 131, pp. 032101/1-6.

Damage and Performance Assessment of Protective Coatings on Turbine Blades

Jaroslav Pokluda[1] and Marta Kianicová[2]
[1]Brno University of Technology, Brno,
[2]Alexander Dubcek University of Trencin, Trencin,
[1]Czech Republic
[2]Slovak Republic

1. Introduction

Many structural components operate in very severe environments characterized by a high temperature, increasing temperature gradients, thermo-mechanical stresses and a presence of oxidizing and corrosive atmosphere. In addition, an impact of hard particles can cause failure by erosion mechanisms. Turbine blades of aircraft engines stand as a perfect example of components working in such a severe environment. They are the most loaded parts of the engine owing to the high working temperature and mechanical stresses induced by forces and moments; only centrifugal forces acting on each blade can reach several tens of kN. Temperature patterns of incoming gases are inhomogeneous and, due to transient regimes, their temperature can increase in about 500 °C during a few seconds (Eskner, 2004). These components must withstand such a complex loading for a required performance and life-time. They are often made from layered material systems in which interfaces between layers play a key role for a prediction of durability. Each layer has different thermal and mechanical properties. Elastic energy of the layered material is concentrated into small volumes the fracture resistance of which is lower than that of the bulk material (Bose, 2007). Therefore, quantitative approaches based on fracture mechanics can be used to assess the damage due to crack initiation and growth. Structural materials of rotor blades and their coatings determine a maximal permissible temperature of gases incoming to the high pressure turbine.

The metallic coatings on blades serve as physical barriers between the underlying substrate and the outer environment. From the point of view of corrosive and oxidizing effects, they can be divided into two categories: diffusion and overlay coatings. Diffusion aluminide coatings (DAC) are based on the intermetallic compound β-NiAl that forms under the influence of the substrate (usually Ni superalloys). On the other hand, the composition of the overlay coatings MCrAlX remains independent of the substrate alloy. In the MCrAlX alloy system, where M means Ni, Co, Fe (or a combination of these) and X means Y, Si, Ta, Hf, etc., the properties can be controlled and balanced for a specific application.

Thermal barrier coatings (TBCs) are composed of ceramics and represent another group of so-called multilayered coatings. These surface barriers insulate the underlying substrate from the heat flux of gases, thus contributing to an improvement of the engine performance. They consist of three constituents: (i) The thermally insulating outer layer (the TBC itself),

typically of yttria-stabilized zirconia (YSZ); (ii) the aluminum containing bond coat (BC) located between the substrate and the TBC and (iii) the TGO which forms at the TBC/BC interface by reaction with the combustion gas. The efficiency of the thermal barrier systems depends on their heat conductivity and strain-tolerance. The heat conductivity should be very low and can be improved by alloying of the ceramics or, in columnar microstructures, by layering of the ceramic within each column (Tamarin, 2002). The strain-tolerance becomes excellent when the deposition of ceramics is performed using electron-beam physical vapor (EB-PVD). However, this technology raises the thermal conductivity of the barrier. For this reason the advanced technologies attempt to optimize both these crucial properties.

The coatings deposited on rotor turbine blades provide an optimal protect in the range of specified lifetime against destructive effects of high-temperature corrosion, oxidation and erosion provided the following requirements are satisfied (Nicholls, 2000):

- High oxidation and corrosion resistance.
- Interface stability.
- Good adhesion.
- Mechanical strength.

In addition to these requirements to metal coatings, the TBC must (Tamarin, 2002):

- Ensure lower average wall temperatures in cooled blades.
- To level the temperature over the blade surface and reduce thermal stresses during engine transient running.

2. Degradation mechanisms of protective coatings

Protective coatings used on turbine blades were developed to serve as physical barriers between aggressive environment and the substrate. In addition, TBCs are used as thermal barriers, retard creep degradation and reduce the severity of thermal gradients. Up to now, however, no coating that would fully survive the aggressive turbine environment has been found (Committee on coatings, 1996). The most serious degradation modes are as follows:

- High-temperature oxidation.
- Hot corrosion.
- Damage by thermal and thermo-mechanical fatigue.
- Mechanical damage by erosion.
- Creep degradation during overheating.

Inter-diffusion of elements at the interface with the substrate that results in a creation of undesirable phases is, sometimes, also mentioned as an independent degradation mode. Here, this mode will not be discussed in more details.

2.1 High-temperature oxidation

Metals and alloys exposed to oxygen or oxygen-containing gases at elevated temperatures convert some or all the metallic elements into their oxides. The oxides can create a protective phase, if they remain adherent and form thermally grown oxides (TGOs) on the top of metallic coatings by reaction with the hot gases. TGO serves as a diffusion barrier to the next oxidation and, from this point of view, the oxidation cannot be considered to be a degradation mode. The protective role of compounds such as Al_2O_3, Cr_2O_3 and SiO_2 is to be particularly mentioned. In general, Cr_2O_3 reveals to be most protective below 871 °C while

Al_2O_3 protects at all temperatures up to the melting point of the blade alloy (Donachie & Donachie, 2002). In order to form adequate thicknesses of Al_2O_3 in a reasonable time, sufficiently high temperatures are required. Without the protective oxides, however, both the coating and the substrate are environmentally exposed to a rapid deterioration of their microstructure. When the oxide layer is eroded by hot gases or rubbed accidentally by removing the oxide layer, the catastrophic oxidation of the substrate can appear if the operation is continued at lower temperatures that do not allow a rapid recovery of the protective layer. A protective scale can be maintained when the aluminum, chromium or silicon do not fall below their critical levels, e.g., 4-5 of weight % for Al (Committee on coatings, 1996). A rapid spallation of TGO can be also caused by internal oxidation, i.e., diffusion of oxygen into the coating. Disruption and spallation of the protective scale are exacerbated by a presence of impurities (mainly sulfur) on the metal/TGO interface. Elements as yttrium or hafnium are added to coatings to improve an adherence of aluminum or chromium scales to the substrate.

The adherent oxide scale also protects the metal surface from erosion. A general indicator of the protectiveness of the oxide scale is given by the Pilling-Bedworth Ratio (PBR), which is defined by the volume ratio oxide formed/metal consumed. The scale becomes fully protective when PBR ~ 1. PBR << 1 means that the oxide is porous and, consequently, looses any protective properties. PBR > 1 means that the oxide scale is highly compressed thus resulting in buckling and spallation (Bose, 2007).

Additional necessary condition to form the protective scale is a close match of coefficients of thermal expansion (CTE). Oxide scales have lower CTE than those of the underlying metals and this difference generates large stresses. Residual compressions in the TGO reach up to 3-6 GPa as the system cools to ambient. Stresses also arise during the growth of TGO, but they are much smaller, generally less than 1 GPa (Evans et al., 2001b, Tolpygo & Clarke, 1998).

In the temperature range (900 – 1000) °C, only a modest oxidation of metals has been observed due to high protective properties of oxides forming on their surfaces. However, at temperatures above ~ 1000 °C, the rate of coating oxidation raises. At the same time, the diffusion processes between the coating and the substrate speed up thus resulting in a reduction of aluminum and chromium contents.

Coatings of turbine blades are oxidized during high-temperature cycles of engine running. The oxide scale growth in isothermal oxidation follows one of the following relationships (Bose, 2007):

   i. Parabolic growth: $$x = k\sqrt{t} \qquad\qquad (1)$$

   ii. Linear growth: $$x = x_0 + kt \qquad\qquad (2)$$

   iii. Logarithmic growth: $$x = k_0 + \log(kt + 1) \,. \qquad\qquad (3)$$

Here x is the oxide scale thickness after the time exposure t, k is the temperature-dependent constant and x_0 and k_0 are constants. Generally, the mechanism of oxidation can be explained by a consumption of certain elements to form protective scales, while the rate of this consumption is temperature dependent. The metal coating serves as a reservoir of Al and Cr and amounts of these elements enter into life-time criteria. The aluminum reserve in a defined zone of the coating can be found from the following function (Tamarin, 2002):

$$m_{Al} = K\sum_{i=1}^{n} X_i \rho_i h_i \ ,$$ (4)

where m_{Al} is the aluminum mass fraction, ρ_i is the density of the zone, h_i is the zone thickness and k is the alloying factor.

2.2 Hot corrosion

At high temperatures, the structures of engine turbines are exposed not only to oxygen but also to other constituents in the form of gas such as CO_2, SO_2, molten salts like alkali and alkaline earth sulfates, chlorides and solid particles in the form of sand and fly ashes. Solid particles can be molten by their transit through the flux of heat gases. These constituents usually originate from engine fuel impurities, contaminants of incoming air or products of imperfect combustion. Their interactions with materials cause corrosion and erosion.

Hot corrosion is a chemical reaction between the metal and molten salts in the hot oxidizing flow. The term "hot corrosion" distinguishes it from the traditional low-temperature corrosion. Salts in the form of gas have not a heavy corrosion effect but both the working process and the gas turbine environment lead to a formation of molten and solid compounds. Corrosive deposits can also seriously erode moving engine parts, including the compressor and turbine blades, thus reducing the engine efficiency. Molten salts can solidify inside cooling passages, clogging the passages and reducing or eliminating the cooling airflow, increasing blade and vane operating temperatures and shortening the engine life (NASA, 2003).

Generally, two modes of hot corrosion have been recognized (Fig. 1) (Rapp, 2001):

i.   Uniform corrosion, marked as the type I or the high temperature hot corrosion (HTHC).

ii.   Pit corrosion, marked as the type II or the low temperature hot corrosion (LTHC).
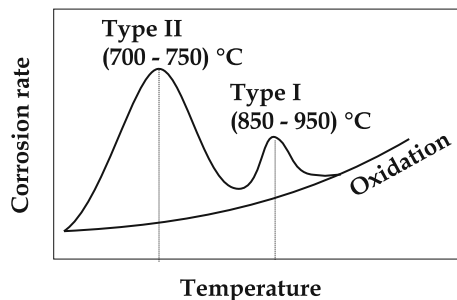

Fig. 1. Types of the hot corrosion in terms of the metal loss as a function of temperature (Bose, 2007). Copyright 2007 by Elsevier B.V., High temperature Coatings, reproduced with permission.

These forms may be affected by various conditions including the alloy composition, the thermomechanical loading, the composition of contaminants and the flux rate, the temperature cycles, the velocity and the composition of gas and erosion objects (Eliaz et al, 2002). HTHC starts with condensation of fused alkali metal salts on the surface and its microstructure consists of an outer porous oxide layer and an inner zone, depleted of γ´ phase, that contains discrete sulphide precipitates. An intermediate zone mixed from both the oxides and the matrix can be also found between these basic layers. A very small

amount of vanadium might be detected in these corrosion products. Elevated temperatures along with high compression and flow rates in the turbine are the main reasons for the formation of a uniform HTHC region. The high temperature has a major effect since it changes the chemical composition, fluidity and thermodynamic properties of corrosion products. High temperature gradients between the gas flux and the surface of cooled blades help the condensation of aggressive corrosion products which penetrate deeply into the coating and its substrate.

LTHC means a selective surface attack in the form of corrosion pits that form under long-term operation cycles at lower temperatures (around 700 – 750 °C). The research of engine operating conditions has proved that the higher the gas-flux velocity the slower the pit corrosion damage. The analysis of the chemical composition of individual corrosion products revealed the presence of vanadium of 5 - 10 weight % and a small amount of sulphur (up to 1 weight %) (Tamarin, 2002).

Both the type I and the type II of hot corrosion retard the formation of protective oxides, thus promoting the internal oxidation and sulphidation of the substrate and its coating.

2.3 Damage by thermal and thermo-mechanical fatigue

Thermo-mechanical fatigue is a degradation mode which involves simultaneous occurrence of both the thermal and the mechanical strain. During repeated startups, load changes and shutdown operations, the high-temperature components of the aircraft engine experience the thermal-induced strains and stresses that cause the thermo-mechanical fatigue (TMF) damage (Huang, 2006). The coatings of blades are exposed to thermo-mechanical fatigue under cyclic changes near their ductile/brittle transition temperature (DBTT) that depends of their composition. During the thermo-mechanical fatigue, different failure mechanisms operate below and above the DBTT. It was found that fine-grained MCrAlX coatings undergo a typical transition in their mechanical behavior as a function of temperature. They exhibit a ductile behavior and low strength at high temperatures while a brittle behavior and high strength is observed below the DBTT (Bose, 2007).

2.3.1 The stresses in the TGO

The stresses in the TGO exert a central effect on a failure of the TBC multilayered thermal protection system. There are two main sources of these stresses: one from the thermal expansion misfit upon cooling and the other one from the TGO growth (Evans, 2001b). Both stresses can be alleviated by the TGO creep and redistributed in the vicinity of imperfections; they can be also modified by thermal cycling that causes a cyclic plasticity of BC. Because of a low thermal expansion coefficient of TGO, a large in-plane compressive stresses can develop upon cooling. At ambient, when the TGO remains planar without rumpling, the compressive stresses are in the range $\sigma_{TGO} \in (-3,5;-6)GPa$, depending on the thermal expansion misfit (Evans, 2008).

In the case when rumpling of TGO occurs, the compressive stresses are reduced. During the growth under influence of lateral compressive stresses, the thin TGO layer (3 - 10 μm) seeks mechanisms to relieve the compression by means of out-of-plane displacements. Both the magnitude and the sign of these displacements are governed by mechanical properties of BC and TBC. The BC at high temperatures is relatively soft and, consequently, the displacements proceed predominately into the BC, as evident in Fig. 2. (Tolpygo et al., 2004). This process is marked as "roughening" or "ratcheting" and may lead to local separations at

the interface TBC/TGO. Imperfections of the TGO and redistribution of stresses at the interface are evident in the schematic picture, where the tensile stresses σ_{zz} develop at the concave site of TGO while the compressive stresses σ_{zz} appear at the convex site. Shear stresses $\sigma_{x'z'}$ are induced at inclined sections (see Fig. 3.). The magnitude and the sign of stresses depend on both the elastic modulus mismatch and the ratio of the amplitude A to the wavelength L.
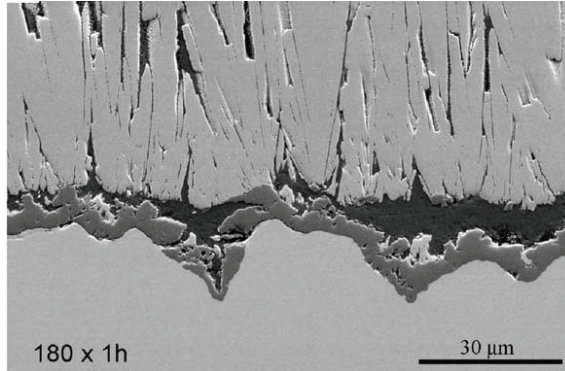

Fig. 2. The microstructure of TBC/TGO interface separation after thermal cycling at 1150 °C (Tolpygo, Clarke & Murphy, 2004). Copyright 2004 by Elsevier B.V., Surface and Coating Technology. Vol. 188-189, reproduced with permission.
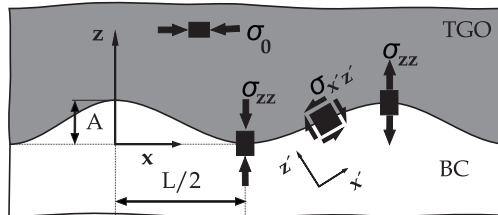
Fig. 3. The scheme of the stress redistribution on the interface.

When the TGO is thin relative to both the amplitude A and the wavelength L, i.e. h/L<<1, the stresses can be expressed as

$$\frac{\sigma_{ij}}{\sigma_0} = H_{ij}\left(\alpha_D, \frac{h}{L}\right)\frac{A}{L},$$ (5)

where σ_{ij} are the stress-tensor components ($i, j = 1, 2, 3$), σ_0 is the compressive stress in the oxide

$$\sigma_0 = \frac{E_1 \Delta\alpha\Delta T}{1 - \upsilon_1},$$ (6)

Δa is the difference in thermal expansion coefficient between the TGO and BC and ΔT is the amplitude of the temperature change (He et al., 1998). The function $H_{i,j}$ depends on the Dundurs´ parameter

$$\alpha_D = \frac{\overline{E}_1 - \overline{E}_2}{\overline{E}_1 + \overline{E}_2}, \tag{7}$$

where $\overline{E}_i \equiv \dfrac{E_i}{1-\nu_i^2}$ is the plane-strain Young´s modulus of elasticity ($\overline{E}_i \equiv E_i$ in plane stress)

and subscripts 1 and 2 refer to the materials creating interface. The thicker is the TGO (the larger the ratio h/L), the higher the values of stress components (Hutchinson & Suo, 1992). The redistribution of the normal (shear) stresses σ_{zz} ($\sigma_{x'z'}$) for particular ratios $h/L = 1$ and A/h = 0.1, 0.2, 0.3 and 0.5 is plotted in the Fig. 4. (Evans, 2001a).
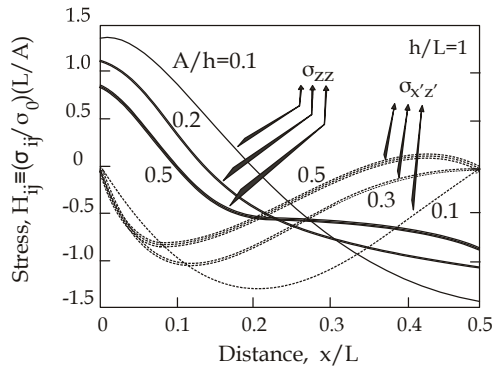
Fig. 4. Distribution of stresses on the BC/TGO interface (Evans,2001a). Copyright 2001 by Elsevier B.V., Progress in Materials Science. Vol. 46, reproduced with permission

2.3.2 Main design approaches to failure of thin layers

Nowadays, two different design approaches to bulk structures are basically applied. The stress approach is based on the measurement of strength characteristic S of the bulk material and calculation of the stress field in a real structure. If the maximum stress is lower than the material strength, i.e. $\sigma_{max} < S$, the structure is considered to be safe. The energy approach is based on the Griffith stability condition which means that the fracture toughness Γ of a cracked solid must be higher than the energy release rate G, i.e., $G < \Gamma$ (Suo, 1993). Thus, for a pre-existing crack of a length $2a$ in infinite elastic solid subjected to a tensile stress σ, the following condition of crack stability must be fulfilled:

$$\frac{\pi \sigma^2 a}{E} < \Gamma \; . \tag{8}$$

In the case of real structures with finite dimensions, the energy approach demands information about a pre-existing crack configuration, i.e., its location, geometry, size and orientation in the structure. However, such information is practically impossible to be obtained for real structures as integrated circuits or structures protected by various types of thin coatings. Therefore, the main effort was devoted to numerical solutions for typical crack configurations in the substrate-coating systems.

Components of the turbine engines are protected from the aggressive environment by thin coatings. In these layered materials, the interfaces are the most critical parts because of their
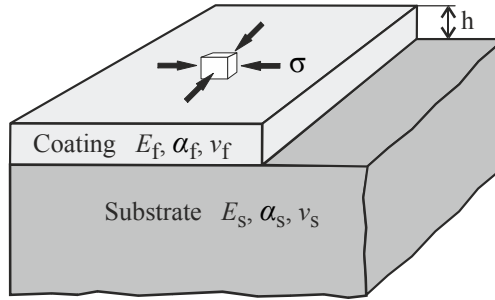
Fig. 5. Scheme of the system substrate/coating

heterogeneity, different thermal and elastic characteristics and presence of residual stresses. Failure of these systems can be, in principle, predicted using elastic fracture mechanics. The relatively simplest analysis can be done in the case of a very thick substrate and thin coatings in which an extent of plastic processes can be neglected. Let us consider a thin film h on a thick substrate according to the scheme in Fig. 5. Both the substrate and the film are assumed to be isotropic and linearly elastic, with elastic moduli, thermal expansion coefficients and fracture toughness (E_s, ν_s, a_s, Γ_s) and (E_f, ν_f, a_f, Γ_f), respectively. In general, the material constant Γ represents energy necessary for creating a crack of a unit area in the layer, substrate or at their interface. The difference in elastic moduli is characterized by Dundur´s parameters a_D and β_D. The parameter a_D, as defined by eq. (7), is a measure of incompatibility between the Young´s moduli whereas the parameter β_D measures the difference in bulk moduli. The layer is stiffer (softer) than the substrate when $\alpha_D > 0$ ($\alpha_D < 0$). While the opening mode I is usually assumed to be a proper loading mode for the crack growing in the substrate or the layer, the mixed mode I+II must be considered for the crack propagating along (or towards) an interface. The latter case is rather complicated and, therefore, we will start with the stability assessment for a crack configuration within a thin layer. Here the energy released rate reads

$$G = \frac{\Omega h \sigma_0^2}{E_f}\left(1 - \nu_f\right), \tag{8a}$$

where $\Omega \in (0.3, 4.0)$ is the dimensionless factor depending on both elastic moduli and geometrical parameters of the crack configuration and E_f is the Young modulus of the layer (Hutchinson & Suo, 1992). The strain induced by cooling from a high temperature T_0 to the ambient temperature T_T due to a contraction difference can be expressed as

$$\sigma_0 = \frac{E_f}{1 - \nu_f}\varepsilon_T = \frac{E_f}{1 - \nu_f}\left(\alpha_f - \alpha_s\right)\left(T_0 - T_T\right). \tag{9}$$

When combining eqs. (8a) and (9) along with the condition $G < \Gamma$ one obtains

$$\Gamma_f > \Omega h \varepsilon_T^2 \overline{E}_f. \tag{10}$$

The general relation (10) shows that the crack stability can be improved by reducing strain or residual stresses in the coating, lowering the coating thickness, raising the fracture

toughness Γ_f and utilizing more compliant materials. Consequently, the critical coating thickness still ensuring the crack stability is determined as follows:

$$h_c = \frac{\Gamma_f}{\Omega \varepsilon_T^2 \bar{E}_f} \ . \tag{11}$$

2.3.3 Failure modes of TGO

Cracking initiates predominantly within the TGO/substrate interface and proceeds by a small-scale buckling of the TGO layer (Wang & Evans, 1999).

This process consists of the following stages:

i.   Partial separation of TGO from the substrate that initiates at interface inhomogeneities;
ii. Buckling of the separated TGO segment and further growing of the related interface crack;
iii. Spalling of the TGO segment.

Partial separation of the TGO segment from the substrate

This failure mode can be caused by the following processes:

• Void coalescence on the interface as a result of non-equilibrium diffusion fluxes of metallic ions during the through-boundary oxidation. Unbalanced diffusion fluxes create a high concentration of vacancies that produce microvoids.

• Creep and grain-boundary sliding in the substrate leading to decohesion of the oxide film from the substrate.

• Rippling of the TGO/substrate interface induces tensile stresses that, assisted by voids and inclusions, separate the oxide layer from the substrate.

• Thickness variations during an imperfect growth of TGO, e.g., due to formation of volume-inconsistent Y_2O_3 phases.

A minimal thickness of the TGO layer $h_{f,min}$ below which no separation occurs is defined by eq. (11), where $\Omega \approx 1$ and $\Gamma_f \to \Gamma_i^O$, Γ_i^O is the fracture toughness of the interface for the opening loading mode. On the other hand, the critical thickness for TGO failure $h_{f,c}$ can be, in most cases, expressed as

$$h_{f,c} = \xi h_{f,min} \ , \tag{12}$$

where $\xi > 1$. Lower values of Γ_i^O (≈ 5 J.m-2) are usually associated with a segregation of impurities (mostly sulphur) on the TGO/substrate interface. A very tough TGO/substrate interface of $\Gamma_i^O \approx 20$ J.m-2 manifests itself by internal cracking of TGO. When using typical values $E_f = (350 - 400) MPa$, $\sigma_0 = (3 - 4) GPa$ and $\Gamma_i^O = 5 J.m^{-2}$, one obtains $h_{f,min} \in (0.1; 0.4)$ μm. Thickness values of this range are an order of magnitude smaller than those of real TGO separates (Hutchinson & Suo, 1992).

Buckling of the TGO layer

When a symmetric circular separate, subjected to a particular stress, reaches a critical radius b_b it expands to create a buckle. According to (Wang & Evans, 1999), the critical value of the biaxial compressive stress $\sigma_{b,c}$ for buckling of the circular TGO separate can be expressed as

$$\sigma_{b,c} = \Pi_c \frac{E_f}{1-\nu_f^2}\left(\frac{h_f}{b_b}\right)^2,$$ (13)

where h_f is the TGO thickness and $\Pi_c = 1{,}22$ is the so-called critical index of buckling. When assuming only dilatation-induced compressive stress on the TGO/substrate interface $\sigma_0 \approx 3{,}5\ GPa$ ($h_f = 5\ \mu m$), the critical buckling radius $b_{b,c} \approx 50\mu m$. This value is much higher than the real one, which is caused by tensile stresses that are induced on the real rippled interfaces. The buckled separate starts to extend when the energy release rate G exceeds the interface fracture toughness Γ_i, i.e., $G \geq \Gamma_i$.

Since the buckle can extend under general mixed mode I+II, the value of Γ_i depends on a particular crack-tip loading mode:

$$\Gamma_i(\psi) = \Gamma_i^O f(\psi),$$ (14)

$$f(\psi) = 1 + tg^2\left[(1-\lambda)\psi\right],$$ (15)

$$\psi = tg^{-1}\frac{K_{II}}{K_I},$$ (16)

where ψ is the loading phase angle, K_I and K_{II} are the stress intensity factors in modes I and II and λ is the coefficient depending of the interface roughness ($\lambda = 1$ corresponds to a smooth surface, $\lambda = 0$ to a rough surface). The plot of the function $f(\psi)$ can be found in (Hutchinson & Suo, 1992).

Spallation of the TGO layer

Deflection (kinking) of the crack from the interface towards the TGO interior appears in consistence with a criterion taking both the loading mode and the ratio Γ_i^O/Γ_f into account (Hutchinson & Suo, 1992). If the fracture toughness of the interface is sufficiently high, i.e. $\Gamma_i^O/\Gamma_f > 0.6$, the kinking appears before the onset of crack extension (Wang & Evans, 1998), which means that $b_{s,c} = b_{b,c}$, where $b_{s,c}$ is the critical radius of spallation (Fig. 6a.). The critical stress for the spallation of the buckled TGO segment is given by the relation

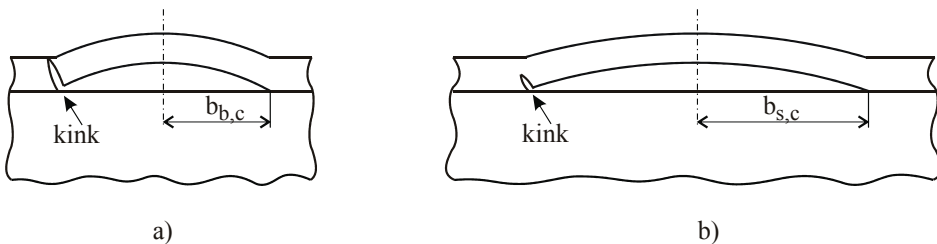$$\sigma_{s,c} = \varphi^* \sqrt{\frac{E_f \Gamma_i^O}{(1-\nu_f)h_f}},$$ (17)

Fig. 6. Kinked cracks at the radii: a) $b_{b,c}$ and b) $b_{s,c}$.

where $\varphi^* \approx 1{,}7$ (He et al., 1998). In the case of lower values Γ_i^O / Γ_f, the buckle is extended along the interface before its spallation by reaching the critical radius $b_{s,c}$ (Fig. 6b.).
According to (Hutchinson & Suo, 1992), the ratio of the critical length $b_{s,c}$ and the thickness h_f can be expressed as

$$\frac{b_{s,c}}{h_f} = \chi \sqrt{\frac{E_f}{\sigma_o}}, \tag{18}$$

where

$$\chi \approx 1{,}1 \exp\left[0{,}7 \frac{\Gamma_f}{\Gamma_i^O} - 1{,}25 \right]. \tag{19}$$

Thus, the critical parameters that control both the extension and the spallation of the TGO separate are σ_o, h_f, Γ_i^O and Γ_f. Initiation and extension of this degradation mode operating on the BC/TGO interface can be assessed by using so-called spallation maps that identify regions of individual damage stages (Wang & Evans, 1999).

2.3.4 Failure modes of TBC

Mechanism of TBC degradation assisted by heterogeneities

The presence of the thermal barrier suppresses the small buckles. Therefore, the damage proceeds by creating a large scale buckling (LSB) that develops on the interface after reaching a critical size. During the thermal exposure, the TGO/BC interface embrittles due to segregation of impurities (mainly S) that reduce its adhesion strength and fracture toughness Γ_i^O (Evans et al., 1999). This stimulates extension of separates in the vicinity of coarsed and/or rippled TGO segments. The TGO imperfections are crucial for the life span of TBC systems also because of tensile hoop stresses σ_{zz}, perpendicular to the YSZ/TGO interface that are induced in their proximity and initiate radial cracks within the TBC layer. At high temperatures, these cracks do not penetrate the TGO since the ductility of this layer causes a redistribution of stresses at their inner front. Moreover, the TGO/bond-coat interface is in compression, thus prohibiting its separation. Consequently, the cracks remain confined to the TBC during exposure. When cooling to ambient, however, the thermal expansion misfit induces tensile stresses normal to the TGO/BC interface thus inducing its separation. A mutual coalescence of interface and radial cracks is a key event of the TBC degradation (Fig. 7b.) which is surmised to happen upon cycling in the range of intermediate temperatures. In this range, the TGO layer remains brittle and the hoop tensions are not replaced by compression related to the thermal expansion misfit. Since the cracks emanating from individual imperfections are too small to satisfy large-scale buckling conditions, many such cracks must coalesce (Rabiei & Evans, 2000).
Creation of continuous cracking demands a development of a critical TGO thickness as

$$h_c = \frac{2\sqrt{\pi}\left(1 - \nu^2\right) m d^{\frac{3}{2}} K_{Tc}^{YSZ}}{(m-1) R E_{YSZ}}, \tag{20}$$

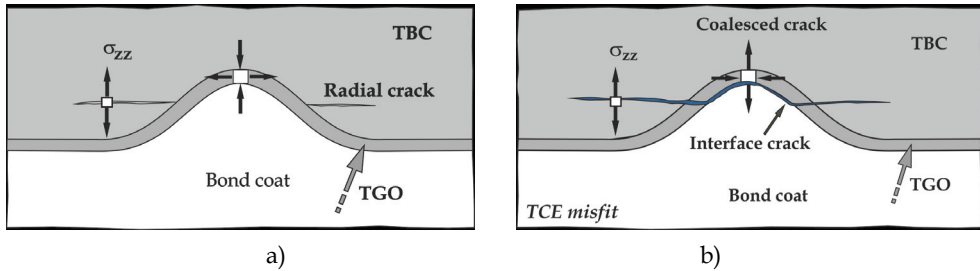a)   b)

Fig. 7. a) Radial cracks induced in the TBC; b) Coalescence of radial cracks with the interface separation caused by TGO growth and followed by cooling to ambient (Evans et al., 1999). Copyright 2000 by Elsevier B.V., Acta Materialia. Vol. 48, reproduced with permission

where m is the volume ratio of newly created TGO to exhausted BC ($m = 1$ for no volume changes), d is the half-spacing of two adjacent heterogeneities, K_{Tc}^{YSZ} is the fracture toughness of YSZ for short cracks ($a \leq 100$ µm) under mode I and R is the radius of a circular heterogeneity (Evans et al., 2001b).

Thus, both the high R and the small d of ripples at the TGO/bond-coat interface increase the probability of continuous cracking inside the thermal-barrier coatings. These ripples are formed by the ratcheting process under thermal cycling that relaxes compressive residual stresses within coatings (He et al., 2000). When the TGO becomes rippled, the shear stresses in the substrate can exceed yield stress and, consequently, the amplitude of the rippling raises by plastic deformations of the substrate. The related tensile strains ε_{zz} and stresses σ_{zz} in the YSZ layer nucleate cracks parallel to the interface according to the scheme in Fig. 7., as documented in Fig. 8. This cracking leads to the spallation (as already mentioned for LSB) or to the edge cracking. In the case of planar TGO, on the other hand, the absence of shear stresses in the substrate (except for free edges) means that there are no out-of-plane displacements as reactions on the thermal cycling (Evans et al., 2003).
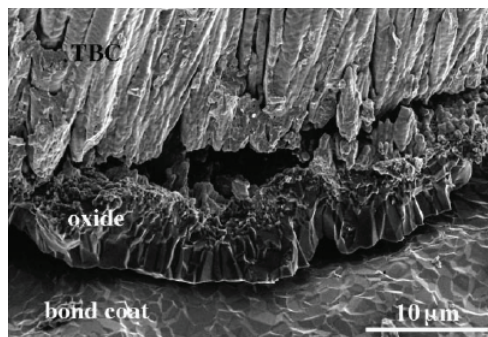

Fig. 8. Cracking of TBC due to cyclic plastic deformation and decohesion of the TBC/TGO interface (Tolpygo & Clarke, 2000). Copyright 2000 by Elsevier B.V., Acta Materialia. Vol. 48, reproduced with permission

Degradation of TBC by penetration of sulphide sediments and air sands

YSZ layers utilized for burning parts of aircraft engines are subjected to temperature gradients developing in the course of service. Recent investigations and monitoring of real

components from the burning parts of turbines reveal that the YSZ coatings are susceptible to damage in sites of a dense microstructure (Borom et al, 1996). With regard to the environment in the turbines, such dense layers can be formed not only by penetration of calcium-magnesium-alumino-silicate (CMAS) particles (CaO, MgO, SiO_2, Al_2O_3) and/or sulfides but also by sintering of the layer fringe.

The sand CMAS particles damage the turbine blades particularly in aircrafts flying at lower altitudes over arenaceous regions. The damage by sulfides is typical for components exposed to a seaside atmosphere. These very small particles (smaller than 10 µm) do not posses a sufficient kinetic energy to cause the impact damage (Strangman et al., 2007). When the temperature of the TBC surface exceeds the melting temperature $T_{mCMAS} \approx 1240\,°C$ of CMAS compounds, the CMAS layer starts to melt, bedraggle the YSZ and, by action of capillary forces, it draws in the spaces of columnar oxides to a depth where $T_{TBC} = T_{mCMAS}$.

After cooling, the CMAS layer hardens and forms a fully dense phase which thermo-mechanical properties increase its tendency to spalling (Mercer et al., 2005). The YSZ volume containing the penetrated coat has a higher elasticity modulus and, at the same time, a release of yttrium from the YSZ can cause its transformation from the tetragonal to the monoclinic structure (Borom et al., 1996). Regions penetrated by CMAS phase are also detrimental due to a reduction of thermal conductivity of the TBC barrier.

Damage of the coating can be particularly identified inside three zones (Krämer et al., 2008):

- **Zone I** – superficial penetration of CMAS; the densified region contains a number of dense vertically cracked (DVC) system, the spacing of which is about 0.2 mm. Because of a very thin CMAS layer on the surface, however, the total volume remains identical with the original one.
- **Zone II** – intermediate penetration of CMAS: damage is similar to that in the zone I but the surface is smoother.
- **Zone III** – depth penetration of CMAS: an extended infiltration of CMAS results in a network of long vertical cracks close to the bond coat (see Fig. 9.).
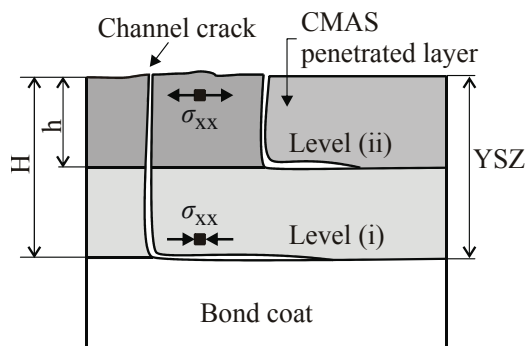

Fig. 9. Scheme of cracks at levels (i) and (ii) inside the zone III.

When the ratio of the penetration depth h to the total thickness H of the YSZ layer reaches $h/H \approx 0.5$, the cooling from high temperatures induces surface tensile stresses that drive the cracked channels to grow throughout the TBC layer. Further cooling results in accumulation of elastic energy at the level (ii) that is high enough to form and propagate mode I cracks in the direction parallel to the surface. Later on, the elastic energy accumulated in the zone III,

level (i), becomes sufficient to drive the cracks from deep channels in mixed mode over the bond coat. This means that there must be a critical penetration depth H^{*}_{pen} below which no cracking of TBC coating appears (Krämer et al., 2008). This critical depth can be expressed as

$$H^{*}_{pen} = \frac{3,6k}{\kappa \Lambda^{\frac{2}{3}}},$$ (21)

where k is the coefficient of thermal conductivity of the penetrated layer, κ is the coefficient of heat transfer on the TBC surface and $\Lambda \approx 800$ is the material constant (Mercer et al., 2005).

2.4 Mechanical damage by erosion

Mechanical damage of coatings may also be initiated by intrusion of foreign particles into the gas-air space of turbines at high operating temperatures that facilitate plastic deformations of thermal barriers. Working conditions and the turbine environment can speed the oxide particles, sized 10 - 1000 μm, to velocities as high as 200 m.s-1 (Crowel et al., 2008). In gas turbines, such a high velocity can also be reached with a help of the rotation motion of the runner. Thus, these particles cause additional mechanical damage by impact and erosion. Spallation of the coating due to both the TGO growth on the BC/TBC interface and the thermal mismatch stresses was, for a long time, the main damage process of thermal barrier coatings. Starting with the application of EB-PVD depositions, erosion and impact of hard particles became the most important damage processes in the case of TBC with a columnar structure.

2.4.1 Impact of small particle with low kinetic energy

Impact of small particles on the surface of TBCs with columnar structure initiates short cracks that do not further propagate through the coating since the column boundaries act as growth inhibitors (Wellman et al., 2005). Particularly in the case of a low kinetic energy and temperature, the formation of dense plastic surface layer is impossible and the columns remain separated. Such an elastic impact induces zones of local tensile stresses in the surface region close to the impact site. These stresses cause local bending of columns and initiate knocking off the column edges. Because such impact processes are of a very short-term character (~ 10 ns), the stresses are controlled by elastic waves. A schematic picture of this mechanism is shown in Fig. 10. (Chen et al., 2004).

2.4.2 Impact of medium-sized particle with mediate kinetic energy

Such impacts usually create the so-called densified zone (DZ) which, however, is too thin to cause damage high enough to delaminate the TBC/TGO interface. Subsequent impacts of particles form a thin DZ until tensile-stress concentrations induce a partial decohesion at the DZ/column interface. These stresses are, again, induced by elastic waves. Further impacts rebuild the DZ during the time span of 1 ms. Mechanism of such a damage is schematically depicted in Fig. 11. (Chen et al., 2004).

2.4.3 Impact of large particle with high kinetic energy

When a large particle impacts on the surface at a high temperature, the major part of its kinetic energy is absorbed by plastic deformation and creation of DZ in a close proximity of
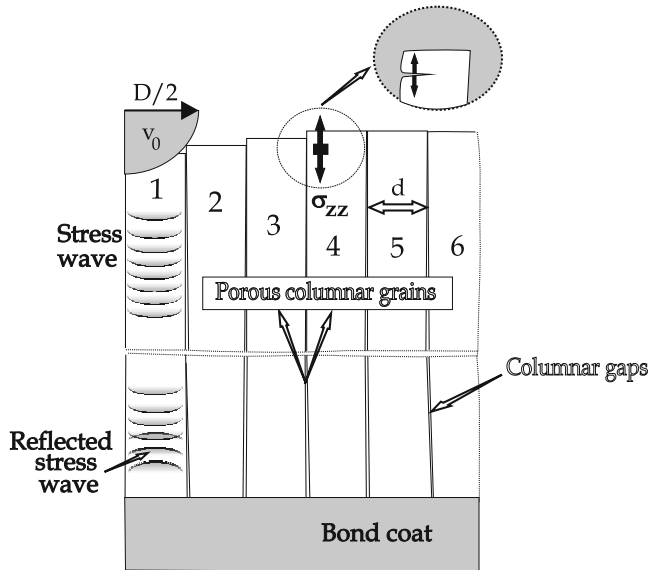
Fig. 10. Scheme of damage processes associated with an impact of a small particle (Chen at al., 2004). Copyright 2004 by Elsevier B.V., Wear. Vol. 256, reproduced with permission
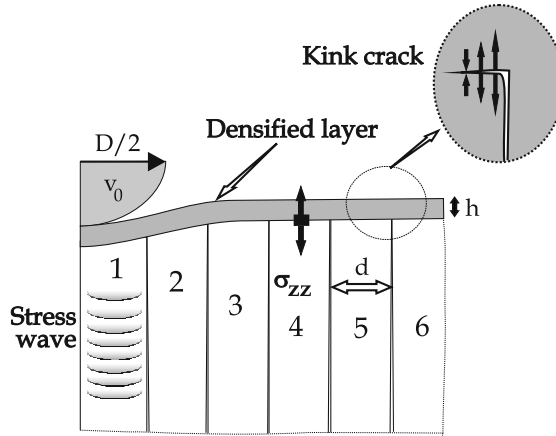

Fig. 11. Scheme of damage processes associated with an impact of a medium-sized particle (Chen et al., 2004). Copyright 2004 by Elsevier B.V., Wear. Vol. 256, reproduced with permission

the impact site. The particular damage mechanism depends on the size and velocity of particles, temperature and material (Nicholls et al., 1998). Plastic deformation within DZ might be accompanied by bands of columns that are inclined at nearly 45° from the surface and contain cracks. The width of these bands is several times higher than that of the individual column (Crowell et al., 2008). When the band reaches the TBC/TGO interface, the cracks grow along this boundary, i.e., parallel to the surface. A scheme of related damage mechanisms is shown in Fig. 12. (Chen et al., 2003).
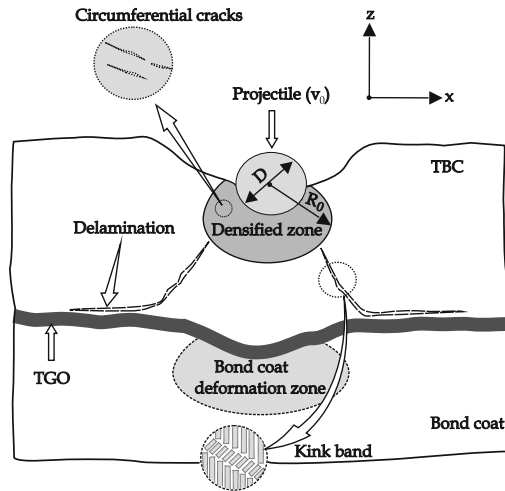
Fig. 12. Scheme of damage processes associated with an impact of a large particle (Chen et al., 2003). Copyright 2002 by Elsevier B.V., Materials Science and Engineering. Vol. 352, reproduced with permission

2.5 Creep degradation after overheating

Overheating means an exposure of a material to an excessive temperature during a short time. The excessive temperature is, however, a relative term since, for some unloaded components, it need not necessarily cause serious problems. Indeed, this could only lead to a partial reduction of materials strength and/or ductility.

In general, any temperature should be considered as the overheating one when it has the following consequences (Donachie & Donachie, 2002):

i.   melting down particularly the grain-boundary phases;
ii.   dissolving of strengthening phases in the matrix;
iii. extraordinary oxidation and corrosion.

These effects are dependent of both the temperature level and the time span. The melting of selected phases cannot be recovered by any heat treatment. Relevant melting temperatures are displayed in tab. 1 for several Ni-based cast alloys (Donachie & Donachie, 2002).

Alloy	Melting temperature (°C)	Solidus γ´ (°C)
Rene 80	1225 - 1230	1150
IN 100	1175 - 1200	1180
MAR-M-200	1260	1180 - 1200
B-1900	1260	1150
PWA 1480	1315 - 1330	-
CMSX-3	1315	-

Table 1. Melting temperatures of cast Ni-alloys and strengthening γ´ phase

Example of dissolving of grain-boundary phases after overheating associated by a reduction of creep strength is given in Fig. 13. (Donachie & Donachie, 2002).
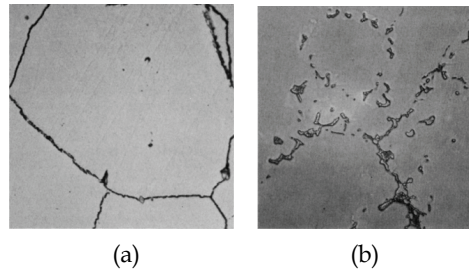

(a)   (b)

Fig. 13. Microstructure of a nickel-alloy: (a) before overheating; (b) after overheating (Donachie & Donachie, 2002, 2004). Copyright 2002 by ASM International, Superalloys: a Technical Guide, reproduced with permission

In practice, the high-temperature components as stator and rotor blades of aircraft turbines are damaged by overheating due to the following events:

i.   Escalation of the working temperature by surging, wrong composition of the combustion fuel, burning outside the combustion chamber and human factors (Pokluda et al., 2008).

ii.   Damage of air-cooled blade channels by creep deformation (Tawancy & Al-Hadrami, 2009).

iii.   Intrusion of foreign particles into the engine.

iv.   Insufficient filtration of the inlet a blocking of cooling channels by various contaminants (volcanic ash, sands) that subsequently melt in the channels (Report NASA, 2003).

If the critical temperature of gases becomes higher than nominal, damage of hot section components starts to be very extensive during a very short time and it is accompanied by plastic deformation and cracking particularly on the surface. A lot of papers deal with an effect of creep mechanisms on the degradation of superalloys with protective coatings (Tawancy & Al-Hadrami, 2009, Ciesla & Swadzba, 2006). The latter paper, for example, reports on the evaluation of damage of aluminium layers on the nickel base superalloy after short time creep tests. Analyses of specimens revealed numerous voids and microcracks at the grain boundaries of the substrate. During overheating and further thermal cycling in service, such defects can develop to cracking along and through the thickness of coatings (Tawancy & Al-Hadrami, 2008, Evans et al., 2003, Rangaraj & Kokini, 2003). Because the thermal expansion coefficient of the coating a_c is lower than that of the substrate a_s, the coating experiences compressive stresses after cooling down from the deposition temperature (Wang et al., 2005). When the service temperature is reached, the compressive stresses become substantially reduced also by the substrate/coating relaxation. During the first part of the overheating stage, however, the compressive stress again appears as a consequence of the coating/substrate temperature gradient (Rangaraj & Kokini, 2003). This is schematically shown in Fig. 14. (Pokluda & Kianicova, 2010). However, both the high heat conductivity and the low thickness of the diffusion layer eliminate the temperature gradient very quickly and, when the peak overheating temperature is nearly reached, the stress changes to a tensile one. In general, the delay between the onset of the overheating and that of the tensile stress (the range $t_1 - t_0$) depends on the layer thickness and the heat conductivity of both the diffusion layer and the substrate. The tensile stress induced in the

coating steeply increases during the first stage of the cooling period and, for a certain period of time $t_3 - t_2$, retains its sign also after the termination of the overheating period (Fig. 14.). During a further service, both the sign and the level of relatively low stresses in the coating are determined by thermal cycling around the service temperature (flight manoeuvres) and depend on the stress-strain response of both the coating and the substrate, i.e., on their mechanical hysteresis and tendency to ratcheting (Wang et al., 2005).
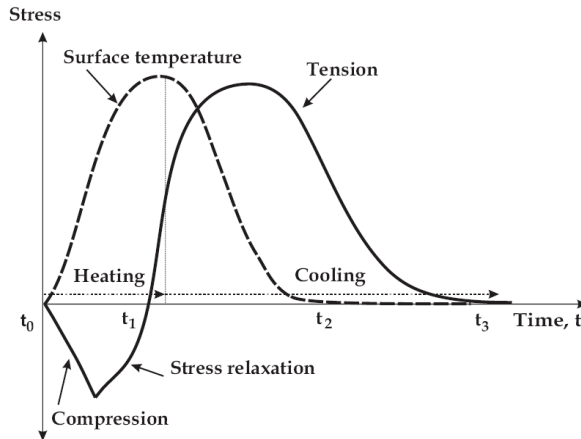
Fig. 14. Scheme of the development of thermal stresses in the coating layer during the overheating process (Pokluda & Kianicova, 2010). The heating curve and the related time-dependence of the thermal stresses are respectively plotted by the dashed and the full line. Copyright 2010 by Elsevier B.V., Engineering Failure Analysis (in print), reproduced with permission

3. Case study: assessment of performance capability of Al-Si coatings after overheating

Motivation for this study came from a demand for a substantial extension of our knowledge about microstructural degradation of diffusion Al-Si coatings (AS layers) protecting rotor blades of the aircraft engine DV2 produced by HTC-AED a.s., Považská Bystrica, Slovakia. The engine is appointed for light training combat aircrafts, where sudden changes of the engine output are in progress during flight maneuvers. Rotor blades of the high-pressure turbine are the most heavily loaded components of the runner wheel. They experience a variety of loading during starts-up and shuts-down and undergo sudden changes of loading during flight manoeuvres. Owing to surging, an overheating shock can appear so that the working temperature T of blowing gases exceeds its critical value T_c = *760 °C* (Kianicová, 2006). The producer has to decide about their further performance till the next general repair on the basis of an extract of preceding overheating data. For that purpose, an empirical degradation parameter is used as

$$D = (t_2 - t_0)(T_{max} - T_c)^3 \int_{t_0}^{t_2} [T(t) - T_c] dt, \qquad (22)$$

where $t \in\ <t_0,\ t_2>$ is the overheating duration, $T > T_c$ and T_{max} is the maximal overheating temperature (HTC-AED, 1998). By means of that procedure and Tab. 2, the producer meets a statement concerning the performance capability.

D [°C^4.s^2]	Engine status	Performance capability
$10^5 < D \leq 1.5 \times 10^9$	Full performance capability (FPC)	Operation
$1.5 \times 10^9 < D \leq 10^{10}$	Degraded layer on rotor blades of the high-pressure turbine (DHB)	Repair
$10^{10} < D \leq 10^{12}$	Degraded basic material of rotor blades of the high-pressure turbine (DBM)	Repair
$10^{12} < D \leq 10^{14}$	Degraded blades of the low-pressure turbine (DLB)	Repair
$10^{14} < D \leq 2.2 \times 10^{14}$	Degraded basic material of disks (DD)	Repair
$D > 2.2 \times 10^{14}$	Melted blades (MB)	Out of operation

Table 2. Assessment of performance capability of the aircraft engine in terms of the parameter D. Copyright 2010 by Elsevier B.V., Engineering Failure Analysis (in print), reproduced with permission

Polycrystalline rotor blades are made of nickel-based superalloy by a precise casting. They are designated for work temperatures in the range of 800 – 1050 °C. In the engine DV2 the blades of the high-pressure turbine are protected from high-temperature waste gases by using the heat-resistant AS layer. The procedure consists in the spraying of an equally balanced suspension of aluminum and silicon powders together with the coloxylin as a binder. Diffusive tempering is applied at 1000 °C in an inert argon atmosphere with the dwell time of 3 hours and subsequent slow cooling in the retort. The final microstructure of the layer consists of two sublayers. The outer one is composed of mostly alloyed aluminides and a small amount of carbides, the inner one contains aluminides of a lower Al-content and finely dispersed carbides and silicides, see also Fig. 15.
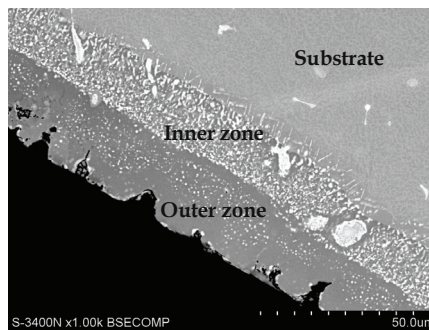

Fig. 15. The protective coatings just after deposition.

The degradation of the AS layer was analyzed for blades that were subjected to different overheating conditions during service (Pokluda et al., 2008, Kianicová et al., 2009). It was found that the relative thickness of the degraded surface layer was a monotonically decreasing function of the parameter D (Kianicová & Pokluda, 2007). This is demonstrated in Fig. 16. (Pokluda & Kianicova, 2010), where the relative thickness $h_r = h/h_0$ of the diffusive

protective layer on the back (convex side) and the trough (concave side) of the blade is plotted as a function of log D. The points indicate the results of measurements performed on blades coming from four engines that experienced overheating of various intensities (see Pokluda et al., 2008 for more detail).
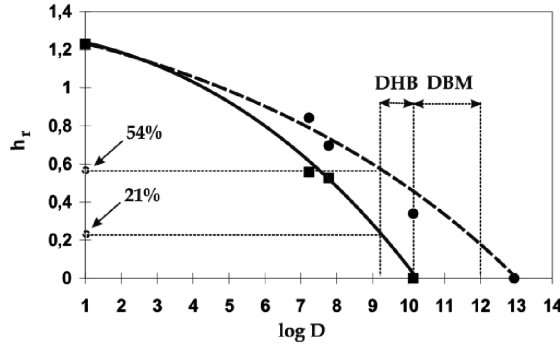

Fig. 16. Dependence of the relative thickness h_r of the coating on the level of degradation in terms of the parameter D for n = 3; p = 1/4 and q = 3/4 (Pokluda & Kianicova, 2010). The solid curve stands for through whereas the dashed one for the back of the blade. Copyright 2010 by Elsevier B.V., Engineering Failure Analysis (in print), reproduced with permission

The value $h_0 \approx 28$ μm corresponds to the average initial thickness of the virgin layer. Both curves start at $h_r = h_{max}/h_0 = 1.23$ (log D = 1) which is related to the maximum average thickness $h_{max} \approx 34$ μm of the diffusive coating. Such a thickness is achieved after several hours of service under a standard working temperature (Kianicová, 2006).
One can see that the following quadratic relationships

$$h_{rb} = 1.2734 - 0.0295 \log D - 0.0055 (\log D)^2 \qquad (23a)$$

$$h_{rt} = 1.2540 - 0.0141 \log D - 0.0108 (\log D)^2 \qquad (23b)$$

well approximate the reduction of the relative thickness on both the back (h_{rb}) and the through (h_{rt}) after the overheating events of various intensities. The damage curve for the back lies above that for the through. This means that the latter curve is crucial for the assessment of the damage level of the blade according to the benchmarks DHB and DBM given in Table 1. The value $h_{rt} = 0.21$ related to the benchmark $D_{DHB} = 1.5 \cdot 10^9$ °C^{4}s^2 that indicates an onset of the range of the necessary repair seems to be very reasonable: 79% of the original through layer and 46% of the original back layer is already removed. Moreover, the trough layer is totally removed when reaching the value $h_{rt} = 0$ which exactly corresponds to the benchmark $D_{DBM} = 10^{10}$ °C^{4}s^2 indicating a start of the degradation of the basic material. Thus, the description of blade damage using the parameter D according to eq. (22) seems to be very plausible.
The parameter D possesses an interesting physical meaning. When assuming a creep work done by tensile misfit stresses during the overheating event (Fig. 14), one can show that this parameter is directly proportional to the specific Hamiltonian´s action S_E that contains a basic information about the evolution of damage in the system (Pokluda & Kianicova, 2010).

Consequently, the damage function can be expressed in more general form as

$$S_E \propto D = (t_2 - t_0)^{1+q-np} \left[T_{max} - T_c \right]^{q(n+1)} \left\{ \int_{t_0}^{t_2} \left[T(t) - T_c \right] dt \right\}^{p(n+1)} , \qquad (24)$$

where $p + q = 1$ and $n \in (1,6)$. The parameter D defined by eq. (22) represents a special case of eq. (24) for $p = 1/4$, $q = 3/4$ and $n = 3$. Note that the value $n = 3$ indicates a plausible mixture of diffusion and dislocation damage mechanisms during the creep exposure.

On the other hand, one cannot exclude the possibilty of other suitable forms of the damage parameter since various sets of parameters n, p and q (different from $n = 3$, $p = 1/4$ and $q = 3/4$) can basically be considered as well. When retaining the physical meaning of D in terms of the unit ($^oC^{n+1}s^2$) and avoiding both fractions and negative values of powers in eq. (24), one can find 28 various possible combinations of these parameters. However, the related numerical analysis revealed that the parameter D as defined by eq. (22) can, indeed, be considered to be the best of all these alternative damage indicators (Pokluda & Kianicova, 2010). Nevertheless, a much simpler damage parameter

$$D_n = (t_2 - t_0)^2 \left[T_{max} - T_c \right]^4 , \qquad (24)$$

as a nearly equivalent to D could be found in this way. To justify a reliability of the parameter D_n would, however, need a further verification.

The assessment procedure based on the parameter D does not provide correct data in the following special cases (Kianicová et al., 2009):

i.   The overheating is caused by a gas burning outside the combustion chamber which results in a sudden decrease of turbine revolutions;

ii.   Repeated overheating of the engine.

However, these cases can be easily identified when analyzing records of the turbine revolutions and the overheating events during service (Pokluda et al., 2008).

4. Conclusion

Protective coatings on blades serve as physical barriers between the underlying substrate and the outer environment. This article presents an overview of damage mechanisms leading to failure of all basic types of coatings (diffusion, overlay and thermal barrier) on turbine blades of aircraft engines during service. Although a special emphasize is devoted to destructive effects of thermo-mechanical fatigue and overheating, the severe effects of hot corrosion, oxidation and erosion effects are also described. Most important material and design parameters of coatings are highlighted with respect to an optimum protection from damage caused by aggressive environment and thermo-mechanical loading. For this purpose, many recent results of advanced numerical models based on fracture mechanics are taken into account. A simple method for an assessment of performance capability of diffusive coatings is presented as a case study performed on rotor blades of high-pressure turbines in aircraft engines. Thus, this article provides scientists, researchers and designers with not only a deep insight into basic degradation micromechanisms of protective coatings, but also a practical example of engineering application.

5. Acknowledgement

6. References

Borom, M.P., Johnson, C.A., Peluso, L.A. (1996) Role of environment deposits and operating surface temperature in spallation of air plasma sprayed thermal barrier coatings. *Surface and Rating Technology.* Vol. 86-87, No 1, (December 1996) pp. 116-126, ISSN 0257-8972.

Bose, S. (2007) *High temperature Coatings*. Elsevier Science & Technology Books, ISBN 0750682523.

Ciesla, M., Swadzba, L. (2006). Cracking processes during creep test of JS6U superalloy with aluminum coatings. *Journal of Achievements in Materials and Manufacturing Engineering.* Vol. 17, No. 1-2, (2006) pp. 177-180. ISSN 17348412.

Committee on Coatings for High-temperature Structural Materials (1996). *Coatings for High-temperature Structural Materials; Trends and Opportunities.* National Academy Press, ISBN 978-0-309-08683-7. Washington.

Crowell, M.W., Wang, J., McMeeking, R.M., Evans, A.G. (2008) Dynamics of kink band formation in columnar thermal barrier oxides. *Acta Materialia*. Vol. 56, No. 16, (September 2008) pp. 4150-4159. ISSN 1359-6454.

Donachie, M.J., Donachie, S.J. (2002) *Superalloys: A technical guide*, Second Edition. ASM International, ISBN 0-87170-749-7. Materials Park, OH.

Eliaz, N., Shemes, G., Latanision, R.M. (2002. Hot corrosio in gas turbine components. *Engineering Failure Analysis,* Vol.9, No.1 (February 2002), pp. 31-43, ISSN 1350-6307.

Eskner, M. (2004) *Mechanical Behaviour of Gas Turbine Coatings*. Doctoral Thesis. Stockholm: Department of Materials Science and Engineering Royal Institute of Technology, 61 pp. ISBN 91-7283-786-1.

Evans, A.G., Hutchinson, J.W., Wei, Y. (1999) Interface adhesion: Effects of plasticity and segregation. *Acta Materialia.*Vol. 47, No. 15-16, (November 1999), pp. 4903-4113. ISSN 1359-6454.

Evans, A.G., Mumm, D.R., Hutchinson, J.W., Meier, G.H., Pettit, F.S. (2001a) Mechanism controlling the durability of thermal barrier coatings. *Progress in Materials Science.* Vol. 46, No. 5, (2001) pp. 505-553. ISSN 0079-6425.

Evans, A.G., Hy, M.Y., Hutchinson, J.W. (2001b) Mechanics-based scaling laws for the durability of thermal barrier coatings. *Progress in Materials Science.* Vol. 46, No. 3-4, (2001) pp. 249-271. ISSN 0079-6425.

Evans, A.G., He, M.Y., Hutchinson, J.W. (2003). Effects of interface undulation on the thermal fatigue of thin films and scales on metal substrates. *Acta Materialia*. Vol. 51, No. 7, (September 1997) pp. 2017-2030. ISSN 1359-6454.

Evans, G.E., Clarke, D.R., Levi, C.G. (2008). The influence of oxides on the performance of advanced gas turbines. *Journal of the European Ceramic Society*. Vol. 28, No. 7, (2008), pp. 1405-1419. ISSN 0955-2219.

He, M.Y., Evans, A.G., Hutchinson, J.W.(1998). Effects of morfology on the decohesion of compressed thin films. *Materials Science and Engineering A*. Vol. 245, No 2, (May 1998), pp. 168-181. ISSN 0921-5093.

He, M.Y., Evans, A.G., Hutchinson, J.W. (2000). The ratcheting of compressesd thermally grown thin films on ductile substrate. *Acta Materialia. V*ol. 48, No. 10, (June 2000), pp. 2593-2601. ISSN 1359-6454.

HTC-AED a.s. Povazska Bystrica, (1998). The manual of the turbine-design department, (1998), Slovakia.

Huang, Z.W., Wang, Z.G., Zhu, S.J., Juan, F.H., Wang, F.G. (2006). Thermomechanical fatigue behavior and life prediction of a cast nickel-based superalloy. *Materials Science and Engineering A*. Vol. 432, No. 1-2, (September 2006) pp. 308–316. ISSN 0921-5093.

Hutchinson, J.W., Suo, Z. (1992). Mixed mode cracking in layered materials. *Advances in Applied Machanics.* (1992). Vol. 29, pp. 63-191. ISBN 0-12-002029-7.

Chen, X., Wang, R., Yao, N., Evans, A.G., Hutchinson, J.W., Bruce, R.W. (2003). Foreign object damage in a thermal barrier system: mechanisms and simulations. *Materials Science and Engineering A*. Vol. 352, No 1-2, (July 2003), pp. 221-231. ISSN 0921-5093.

Chen, X., He, M.Y., Spitsberg, I., Fleck, N.A., Hutchinson, J.W., Evans, A.G. (2004). Mechanisms governing the high temperature erosion of thermal barrier coatings. *Wear*. Vol. 256, No. 7-8, (April 2004) pp. 735-746. ISSN 0043-1648.

Kianicová, M., Pokluda, J. (2007) Degradation of protective Al-Si coatings during exploitation of gas turbine blades. *Materials Science Forum,* Vol. 567-568 (December 2007) pp. 309–312. ISSN: 1662-9752.

Kianicová, M., Pospíšilová, S., Zahoran, M. (2009). Damage of protective Coating due to unstable Engine Running, *Proceedings of 12th International Conference on Fracture*. Ottawa, July 2009, National Research Council Canada.

Kianicová M., (2006). Fireproof diffusive coating degradation in consequence of short-time operating temperature exceeding, PhD Thesis, AD University in Trencin, 2006.

Krämer, S., Fauhaber, S., Chambers, M., Clarke, D.R., Levi, C.G., Hutchinson, J.W., Evans, A.G. (2008). Mechanisms of cracking and delamination within thick thermal barrier systems in aero-engines subject to calcium-magnesium-alumino-silicate (CMAS) penetration. *Materials Science and Engineering A*. Vol. 490, No 1-2, 25 (August 2008) pp. 26-35. ISSN 0921-5093.

Mercer, C., Faulhaber, S., Evans, A.G., Darolia, R. (2005). A delamination mechanism for thermal barrier coatings subject to calcium-magnesium-alumino-silicate (CMAS) infiltration. *Acta Materialia.* Vol. 53, No. 4, (February 2005), pp. 1029-1039. ISSN 1359-6454.

NASA, (2003), Report: NASA/TM-2003-212030.

Nicholls, J.R., Jaslier, Y., RIickerby, D.S. (1998). Erosion of EB-PVD thermal barrier coatings. *Materials at High Temperatures*. Vol. 15, No. 1, (February 1998) pp. 15-22. ISSN 0960-3409.

Nicholls, J.R. (2000). Designing Oxidation-Resistant Coatings. *JOM.* Vol. 52, No. 1. (January 2000) pp. 28-35. ISSN 1543-1851.

Pokluda, J., Kianicová, M., Švejcar, J. (2008). Degradation of protective coatings of turbine blades during exploitation. *Proceedings of Failures 2008*, pp. 139-159, South Africa, March 2008, Strand.

Pokluda, J., Kianicová, M. (2010). Assessment of performance capability of turbine blades with protective coatings after overheating events. *Engineering Failure Analysis.* doi:10.1016/j.engfailanal.2010.04.004.

Rabiei, A. Evans, A.G. (2000). Failure mechanisms associated with the thermally grown oxide in plasma-sprayed thermal barrier coatings. *Acta Materialia.*, Vol. 48, No. 15, (September 2000), pp. 3963-3976. ISSN 1359-6454.

Rangaraj, S., Kokini, K. (2003), Fracture in single-layer zirconia (YSZ)-bond coat alloy (NiCoCrAlY) composite coatings under thermal shock. *Acta Materialia.* Vol. 52, No. 1, (January 2003), pp. 455-465. ISSN 1359-6454.

Rapp, R.A. (2001). *Encyclopedia of Materials – Science and Technology.* Surface Coating for High-temperature Alloys. Elsevier, ISBN 978-0-08-052358-3. Amsterdam.

Strangman, T., Raybould, D., Jameel, A., Baker, W. (2007). Damage mechanisms, life prediction, development of EB-PVD thermal barrier coatings for turbine airfoils. *Surface and Coating Technology.* Vol. 202, No. 4-7, (December 2007), pp. 658-664. ISSN 0257-8972.

Suo, Z. (1993). Cracking and debonding of microlaminates. *Journal of Vacuum Science and Technology A.* Vol. 11, no. 4, pp. 1367-1372. ISSN 0734-2101.

Tamarin, Y. (2002). *Protective Coatings for Turbine Blades*. ASM International, ISBN 0-87170-759-4, Ohio.

Tawancy, H.M., Al-Hadrami, L. (2008). Applications of microstructural characterization and computational modeling in damage analysis of a turbine blade exposed to service conditions in a power plant. *Engineering Failure Analysis.* Vol. 15, No. 8, (December 2008), pp. 1027-1034. ISSN 1350-6307.

Tawancy, H.M., Al-Hadrami, L. (2009). Degradation of turbine blades and vanes by overheating in a power station. *Engineering Failure Analysis.* Vol. 16, No. 1, (January 2009), pp. 273-280. ISSN 1350-6307.

Tolpygo, V.K., Clarke, D.R. (1998). Wrinkling of α-alumina films grown by oxidation – II. Oxide separation and failure. *Acta Materialia.* Vol. 46, No. 14, (September 1998), pp. 5167-5174. ISSN 1359-6454.

Tolpygo, V.K., Clarke, D.R. (2000). Surface rumpling of a (Ni, Pt) Al bond coat induced by a cyclic oxidation. *Acta Materialia.* Vol. 48, No. 13, (August, 2000), pp. 3283-3293. ISSN 1359-6454.

Tolpygo, V.K., Clarke, D.R., Murphy, K.S. (2004). Evaluation of interface degradation during cyclic oxidation of EB-PVD thermal barrier coatings and correlation with TGO luminiscence. *Surface and Coating Technology.* Vol. 188-189, (November – December 2004) pp. 62-70. ISSN 0257-8972.

Wang, J.S., Evans, A.G. (1998). Measurement and analysis of buckling and buckle propagation in compressed oxide layers on superalloy substrates. *Acta Materialia*. Vol. 46, No. 14, (september 1998), pp. 4993-5005. ISSN 1359-6454.

Wang, J.S., Evans, A.G. (1999). Effects of strain cycling on buckling, cracking and spalling of a thermally grown alumina on a nickel-based bond coat. *Acta Materialia.* Vol. 47, No. 2, (January 1999), pp. 699-710. ISSN 1359-6454.

Wang, Q.M., Tang, J., Guo, M.H., Ke, P.L., Gong, J., Sun, C., Wen, L.S. (2005) Thermal shock cycling behavior of NiCoCrAlYSiB coatings on Ni-base superalloys II. Microstructure evolution. *Materials Science and Engineering A.* Vol. 406, No. 1-2, (October 2005), pp. 350-357.

Wellman, R.G., Deakin, M.J, Nicholls, J.R. (2005). The effect of TBC morphology and aging on the erosion rate of EB-PVD TBCs. *Tribology International*. Vol. 38, No. 9, (September 2005), pp. 798-804. ISSN 0301-679X.

Application of Structural Analysis to Improve Fault Diagnosis in a Gas Turbine

Cristina Verde and Marino Sánchez-Parra
Instituto de Ingeniería, Universidad Nacional Autónoma de Mexico
Instituto de Investigaciones Eléctricas
México

1. Introduction

This chapter deals with the fault diagnosis issues for a Gas Turbine, *GT*, of a Combined Cycle Power Plant, *CCPP*, considering diverse fault scenarios. The essential and more critical component in the plant self is the gas turbine, because it comprises complex dynamical subsystems which can fail due to faults in sensors, actuators and components and relies heavily on the control system affecting the reliability, availability and maintainability of the power plant. This issue motivated this research work oriented to design a diagnosis system by software for gas turbines of electric power plants. The key for a faults diagnosis system is the discrepancy between expected and actual behavior and this can be identified, on real time only if redundant information between the process variables is available (Frank, 1990). Artificial Intelligence and Control communities have developed methods to generate symptoms or signals by software, called residuals, which reflect the discrepancies in faults conditions Venkatasubramanian et al. (2003a), Venkatasubramanian et al. (2003c), Venkatasubramanian et al. (2003d). However previous to the residual generators design it is necessary and essential to determine which data requirements are required to solve a specific fault diagnosis issue.

To analyze under which conditions faults in sensors and actuators of a *GT* can be detected and isolated, the structural properties of the model are used here. The redundancy of the structure is studied using graph tools for the subsystems of the *GT* considering the available measurements. A non-linear complex dynamic model of the *GT* given by 37 algebraic and differential equations is considered to identify the required redundancy degrees for diverse fault scenarios of the units without numerical values. As result of the generic analysis, 10 relations are obtained which allow to detect faults in all components of the gas turbine unit. The rotors mechanical coupling to gas turbine unit for one side and the electric generator unit for the other side, is identified as a subsystem in which faults are undetectable and then, a diagnosis system for this subsystem is not feasible. This means, the standard instrumentation of the *GT* restricts its performance from safety and integrity point of view. On the base of this result and using the redundant graph concept (Verde & Mina, 2008), it is suggested here to add a sensor to increase the redundance and consequently to improve the fault detectability of the turbogenerator in the presence of mechanical and sensors faults. This is the main contribution of the work. The implementation of redundant graphs with specific simulated data of a *GT* validates this statement.

The work is organized as follows. The first part of Section 2 presents the philosophy behind an active supervision system by software. The second one introduces the structural framework to detect and isolate faults in a complex dynamic plant where the concept of redundancy graph is introduced. Section 3 describes shortly the model structure of the *GT* and the interconnection between units used in the study. Section 4 discusses in detail the analysis of the *GT* by graph tools considering the feasible fault scenarios in sensor and actuators. These scenarios determine the generic redundancy equations which have to be implemented in the supervision system of the *GT*. Following this analysis, the main contribution is given in first part of Section 5. Based on the Redundant Graph $\mathcal{RG}$, the subsystem without redundancy is here described and how to look for a new available variable in the graph to improve the detection capabilities and isolability properties of the turbogenerator unit. The second part of Section 5 includes some numerical results of the implementation of the detection system, and the discussions of the results and conclusions are given in Section 6.

2. Process supervision with fault diagnosis

The automatic supervision of power plants was mainly realized in the past by limit checking of important process variables. Usually alarms are raised if the limit values are exceeded and protection systems act manually or automatic. This simple procedure generates delayed alarms without detailed diagnosis. Modern methods based of system theory made possible to develop advanced fault detection and active diagnosis systems by software (Venkatasubramanian et al., 2003b). In this framework a fault for the study case is defined as deviations of the *GT* from its normal characteristics affecting the automatic system (Isermann, 2006). To develop modern automatic supervision and diagnosis system a combination of diverse methods have been developed by the safe process community of IFAC. The principle to solve a fault diagnosis problem is the **redundancy** and consistency of data in a system (Frank et al., 1999) together with model behavior in normal and fault condition. As example, for the model

$$y = 3u + 6u^2 - 4uy \tag{1}$$

assuming that both variables (u,y) are known, one can estimate by software y, called $\hat{y}$, based on u and Eq. (1). Then, the data of y gives a redundant information and one can check the system behavior looking for the dissimilarity between $\hat{y}$ and y.

For large scale systems, a model is not so simple as the above case. Therefore, the control theory, signals processing and artificial intelligence communities have proposed diverse methodologies to supervise the system behavior. The general frameworks are described in the books (Korbicz et al., 2004), (Ding, 2008). The analytical formulation of a discrepancy assumes the existence of two or more ways, to determine variables of a process, where one way uses a mathematical model in analytical form (Blanke et al., 2003). This means, given a vector k_i integrated by a subset of known signals $\mathcal{K}_i$ of a process, any expression of the form

$$ARR(\mathcal{K}_i) = RR(k_i, \dot{k}_i, \ddot{k}_i...) = 0 \tag{2}$$

obtained from an analytical model is called an **Analytical Redundancy Relation** *ARR* for a set of detectable faults $\mathcal{F}$, if for all $\mathcal{K}_i$ consistent with the process free of faults, *ARR* is zero; and if a fault $f_i \in \mathcal{F}$ occurs, *ARR* is inconsistent or different from zero at least in a time

interval. The relations of class (2) can be obtained by different methodologies: analytical expressions, historical data, signal processing, etc. (Korbicz et al., 2004). The number of feasible *ARR*s depends strongly on the measurements signals available and the sensors location and the structure of the plant under supervision. Thus, the more variables are measured, the better performance could have the active diagnosis system.

For the GT of a combined cycle power plant, the next issues are formulated here:

- Which are the technical conditions to get a complete fault detection? and
- How could one guarantee full scope faults isolability?

The study and considerations to solve the first task are the main contributions of this work, while the second task is focused on the selection of ARRs for specific fault sets. In particular, one should select a method which captures all possible solutions of a diagnosis issue taking in account the available measurements. Since, to deal with large scale complex dynamic systems, the generic structural approaches are more appropriated than the numerical methods; one may select analysis tools based on structure properties, which have been proposed to achieve this goal, as Structural Analysis (Cassal et al., 1994), Geometric Approach (De-Persis & Isidori, 2001), Linear Structured Systems (Dion et al., 2003), or Bond Graph (Mukherjee et al., 2006). In particular, Structural Analysis (SA) framework, which is based on graph theory, allow to study the system capabilities to detect and isolate faults. This framework has two relevant characteristics: allows dealing with complex and large scale systems and does not require numeric parameters information. So, with this approach, to know if there are redundant variables in a system, only its structure without explicit numerical values plays an important role. This is the main reason to select SA for the GT fault issues in this work.

2.1 System description by a graph

The Structural Analysis is based on relationships between variables given in the form of a bipartite graph or equivalently as an boolean incidence matrix, and it can be used in the early design phase of a supervisory system. Here one describes briefly the main tools of the *SA*, including the redundancy graph concept as an extension of the analytical redundancy relation used in the model-based fault diagnosis methods (Verde & Mina, 2008).

A system can be described by a bipartite graph $\mathcal{G}$ with its variables $\mathcal{V}$ and its equations $\mathcal{C}$ as node sets where there are edges connecting constraint with variables (Gross & Yellen, 2006). There are two form to shows the connection between nodes in a graph, by a diagram or a binary incidence matrix. The following description formalizes this concept.

Definition 1: Let a dynamic system be given by

$$\dot{x} = f_m(x, \tilde{x}, u, \theta, f, \overline{f}), \quad x \epsilon \mathfrak{R}^n, u \epsilon \mathfrak{R}^{n_u}, f \epsilon \mathfrak{R}^f, \overline{f} \epsilon \mathfrak{R}^d \tag{3}$$

$$y = h(x, \tilde{x}, u, \theta, f, \overline{f}), \quad y \epsilon \mathfrak{R}^{n_y} \tag{4}$$

$$0_p = m(x, \tilde{x}, u, \theta, f, \overline{f}), \quad \tilde{x} \epsilon \mathfrak{R}^s, 0_p \epsilon \mathfrak{R}^p \tag{5}$$

with u and y known variables, θ the parameter vector, f and $\overline{f}$ faults to be detected and neglected respectively. The bipartite graph associated to Equations (3, 4, 5) is defined by the graph $\mathcal{G} = (\mathcal{C} \cup \mathcal{V}, \mathcal{E})$ where the edges connecting set $\mathcal{E}$ is given by

$$e_{ij} = \begin{cases} (c_i, v_j) & \text{if and only if } v_j \text{ appers in } c_i \\ 0 & \text{on the contrary} \end{cases}$$

Using the matrix description an edge e_{ij} is given by • in row i, column j.

According to Eqs. (3,4,5), in the graph description, the constraints nodes set $\mathcal{C}$ has cardinality $|\mathcal{C}| = 2n + n_y + p$ and the variables nodes set $\mathcal{V} = \mathcal{X}_g \cup \mathcal{K} \cup \mathcal{F} \cup \bar{\mathcal{F}}$ is defined by

- the unknown variables set $\mathcal{X}_g = \mathcal{X} \cup \dot{\mathcal{X}} \cup \tilde{\mathcal{X}}$ with cardinality $2n + s$;
- the known variables set $\mathcal{K} = \mathcal{U} \cup \mathcal{Y}$; where the exogenous set $\mathcal{U}$ and the measurements set $\mathcal{Y}$ have cardinality n_u and n_y respectively and then $n_k = |\mathcal{K}| = n_u + n_y$;
- the fault and disturbance (neglected faults) sets $\mathcal{F}$ and $\bar{\mathcal{F}}$ have cardinality f and d respectively;
- Each state variable x_i involves a constraint

$$\dot{x}_i = \frac{dx_i}{dt} \tag{d}$$

Since a fault f which changes the normal behavior of constraint c_i means that the edges e_{ij} for any j are sensitive to f, the graph description $\mathcal{G}(\mathcal{C} \cup \mathcal{V}, \mathcal{E})$ allows to consider faults indifferently, as changes in the subset $\mathcal{C}$ or as an input node subset $\mathcal{F}$ without numerical values. This is an advantage to study the system diagnosis capability.

Example.

To show the simplicity to get a bipartite graph and the matching assignment, consider the following simple differential algebraic system

$$\dot{x}_1 = g_1(x_1, u) \tag{c1}$$

$$x_2 = g_2(x_1) \tag{c2}$$

$$y = g_3(x_2) \tag{c3}$$

In this simple case,

- the variables nodes set is given $\mathcal{V} = \{x_1, x_2, u, y, \dot{x}_1\}$,
- the constraints nodes set $\mathcal{C} = \{c1, c2, c3, d\}$ where d corresponds to the constraint $\dot{x}_1 = \frac{dx_1}{dt}$

The bipartite graph is given in Fig. 1 where a shadowed circle denotes a constraint. The respective description incidence matrix, *IM*, is shown in Table 1.

To establish relations between the variables of $\mathcal{V}$ and the constraints of $\mathcal{C}$, the edges of $\mathcal{E}$ has to be oriented. This is equivalent to define paths joining nodes of $\mathcal{V}$ with nodes of $\mathcal{C}$. This process in which each node c_i is used to express only a node of $\mathcal{V}$ is called **matching process**. In the incidence matrix framework, the matching process means rows and columns permutations, in which the symbol $\oplus$ in the row i and column j denotes that the constraint node i is used to get the variable node j. The symbols (• $\rightarrow$) denotes initial node. There are diverse matching algorithms (Krysander et al., 2008), however not all can be used for fault detection analysis, since the redundant relation between variables and the causality of a process have to be considered. From fault detection point of view, only matchings with redundant information are relevant. The Structural Analysis, *SA* deals with the systematic procedures to get the redundant relations from a bipartite graph without numerical value (Blanke et al., 2003).
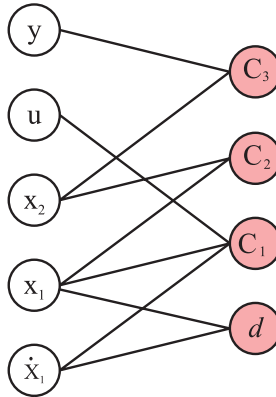
Fig. 1. Bipartite graph of system (c1,c2,c3,d)

\	x_1	x_2	$\dot{x}_1$	u	y
c1	•		•	•	
c2	•	•			
c3		•			•
d	•		•		

Table 1. Incidence Matrix of the Bipartite Graph

From matrix of Table 1, the matching with initial node y shown in Table 2 is generated and the path is read as follow: using the constraints $c3$ together with the variable y, one matches x_2, as second step, using x_2 with $c2$, one reaches x_1 and later one, by d the unknown variable $\dot{x}_1$ is determined and finally the goal node u can be evaluated by $c1$, since the rest of variables has been before calculated. Therefore if the variables pair (u,y) are known, one can estimate $\hat{u}$ by data of y and the path of evaluation, i.e.

$$\hat{u} = g_1^{-1}(d(g_2^{-1}(g_3^{-1}(y)))) \tag{6}$$

Thus, a real time comparison of $\hat{u}$ with the data of u detects any abnormal conditions involved in any of the constraints set ($c1$, $c2$, $c3$) and the difference

$$r(t) = \hat{u} - u = g_1 \circ d \circ g_2 \circ g_3(y) - u \tag{7}$$

is a symptom signal, where $\circ$ denotes concatenation. The evaluation of (7), called residual signal $r(t)$, is zero in normal ideal condition and different from zero in abnormal conditions; since $r(t)$t only depends of the data pair (u,y), then it is a analytical redundant relation, *ARR*.

\	y	x_2	x_1	$\dot{x}_1$	u
c3	• →	⊕			
c2		•	⊕		
d			•	⊕	
c1			•	•	→ ⊕

Table 2. Path to evaluate u by y
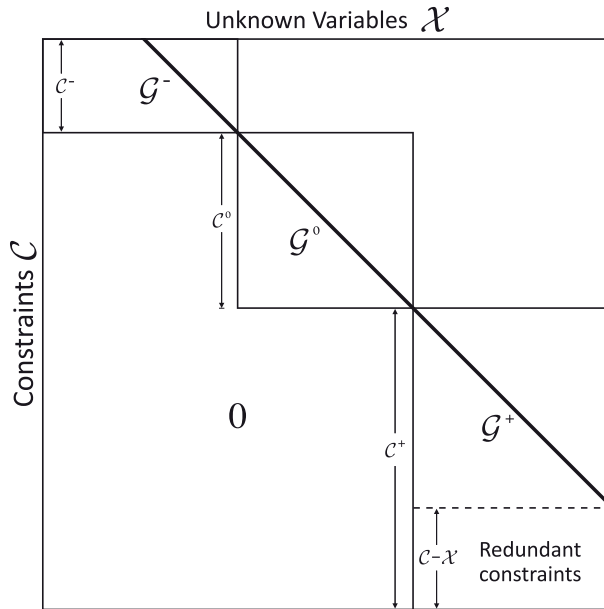
Fig. 2. Canonic Decomposition of a generic Incidence Matrix

2.2 Redundancy in a graph

In the framework of Structural Analysis, the existence of *ARR*s or relations of class (2), implies that the graph has more constraints than unknown variables and the maximum number of redundancy relations is bounded by $|\mathcal{C}| - |\mathcal{X}_g|$ (Krysander et al., 2008). Thus, the starting point of the faults structural analysis is the canonical Dulmage-Mendelsohn decomposition of the graph in three sub-graphs: the over-constrained $\mathcal{G}^+$ with more constraints than unknown variables $\mathcal{X}_g{}^+$, the just-constrained $\mathcal{G}^0$ with the same number of constraints and unknown variables, and the under-constrained $\mathcal{G}^-$ with less constraints than unknown variables. Fig. 2 shows the generic structure of a decomposed graph in three subgraphs. Furthermore, faults which affect constraints involved in $\mathcal{G}^0$ and $\mathcal{G}^-$ are not detectable (Blanke et al., 2003).

The relations between variables set $\mathcal{K}^+$ with constraints $\mathcal{C}^+$ in which the set $\mathcal{X}_g{}^+$ has been substituted, determine the *ARR*'s. This is equivalent to give an orientation to each edge, eliminating the set $\mathcal{X}_g{}^+$ using some members of $\mathcal{C}^+$. Once a matching is obtained in $\mathcal{G}^+$, the involved constraints can be interpreted as operators from a set of known variables to others where the path is determined by a concatenation process following an oriented graph. The concatenation algorithm for linear constraints is reduced to the Mason's method (Mason, 1956) and there are diverse ways to select the *ARR*s from the paths of a graph.

For the particular graph $\mathcal{G}$ given in Fig. 1, the Dulmage-Medelsohn decomposition identifies the condition $\mathcal{G}^+ = \mathcal{G}$ with 4 constraints, 3 unknown variables and the pair (u,y) as known nodes. Since the paths from y to u o viceversa pass by all constraints ($c3$, $c2$, d, $c1$), all faults associated to sensors, actuator and constraints are generic detectable. Thus, the path of Table

2 is a base to generate the *ARR*s for the model (c1,c2,c3), Eq. 7 is a particular analytical redundant relation.

2.3 Redundant graph definition
Let

$$\mathcal{K}_i = \mathcal{U}_{si} \cup y_i \tag{8}$$

be a subset of known variables matched with the subset of constraints $\mathcal{C}_i$, initial vertex of $\mathcal{U}_{si}$ and target vertex y_i, then

$$\mathcal{RG}_i(\mathcal{C}_i; \mathcal{U}_{si}; y_i) \tag{9}$$

is a **Redundant Graph** if

- Paths between the vertices of $\mathcal{U}_{si}$ and the target y_i are consistent and they can be obtained concatenating $\mathcal{C}_i$ without faults, and

- At fault condition, there is a lack of consistency in some paths between $\mathcal{U}_{si}$ and Y_i for any elements of the constraints set.

In the matrix framework, symbols $\bullet \rightarrow$ and $\rightarrow \bullet$ are used for initial and target vertices respectively. Note that for an specific $\mathcal{RG}$, members of $\mathcal{U}_{si}$ are independent variables which are correlated with y_i by paths of the redundant graph. In this framework, faults which are unknown a priori are considered inconsistent vertices in the graph.

From Table 2, one identifies the path from y to u as a $\mathcal{RG}(\{c3, c2,d, c1\};y;u)$; with y as initial node and u as target node. Other graph can be built if u is the inicial node and y the target node. Since both paths pass by the same nodes, then both are equivalent sets from redundant point of view.

General advantages of the $\mathcal{RG}_i$ are:

- One can generated distributed subgraphs where cause and effect can be indistinctly handled;

- One can build the faults symptoms (faults signature) from the $\mathcal{RG}_i$, without numeric values of a system model. This is useful to search new sensors which improve the faults signature.

- For large scale systems, the redundant subgraph allows the determination of correlated variables without numerical values. This has been used to isolate faults Mina et al. (2008).

2.3.1 $\mathcal{RG}$ algorithm

The following algorithm summarize the steps to get redundant graphs $\mathcal{RG}$s assuming known the bipartite graph of the system (3, 4, 5)

Step 1. Calculate the canonical decomposition of $\mathcal{G}$ using only the unknown variables set $\mathcal{X}$ (Pothen & Fan, 1990).

Step 2. Identify the subgraph $\mathcal{G}^+$.

Step 3. Eliminate the constraints set $\mathcal{C}_e$ which involves not invertible functions and build $\mathcal{C}_{inv}^+ = \mathcal{C}^+ \setminus \mathcal{C}_e$.

Step 4. Calculate the possible maximal number of redundant graphs given by

$$Max_{rr} = \left| \mathcal{C}_{inv}^+ \right| - \left| \mathcal{X}^+ \right|$$

Step 5. Initialize the number of initial node $n_i = 1$ in the search and the number of assigned redundant graph $n_{\mathcal{GR}} = 0$.

Step 6. Calculate the possible distinct combinations of the initial nodes for each target, selecting n_i nodes out of $n_k - 1$, with n_k the cardinality of set $\mathcal{K}$; this means

$$I = {}^{n_k - 1}\mathbf{C}_{n_i} = \binom{n_k - 1}{n_i} = \frac{(n_k - 1)!}{(n_k - 1 - n_i)!(n_i)!} \quad \text{for each target node}$$

Step 7. Assign the orientations of the I graphs using the set $\mathcal{C}_{inv}^+$ for each target node including the cycle graphs (no diagonal submatrix) and constraints of the class d.

Step 8. Bring up the number $n_{\mathcal{GR}}$ according the assigned redundant graphs; if $n_{\mathcal{GR}} = Max_{rr}$, end the algorithm, otherwise continue.

Step 9. If $n_i = n_k - 1$, end the algorithm, on the contrary $n_i = n_i + 1$ an return to step 6.

3. Gas turbine description

The *GT* behavior model used at this work simulates electrical power generation in a combined cycle power plant configuration with two *GT*, two heat recovery-steam generators and a steam turbine. At ISO conditions, the ideal power delivered for each *GT* generates 80*MW* and the steam turbine 100*MW*. This model may go from cold startup to base load generation. The main components of the *GT* shown in Fig. 3 are: compressor *C*, combustion chamber *CC*, gas turbine section *T*, electric generator *EG*, and heat recovery *HRSG*.
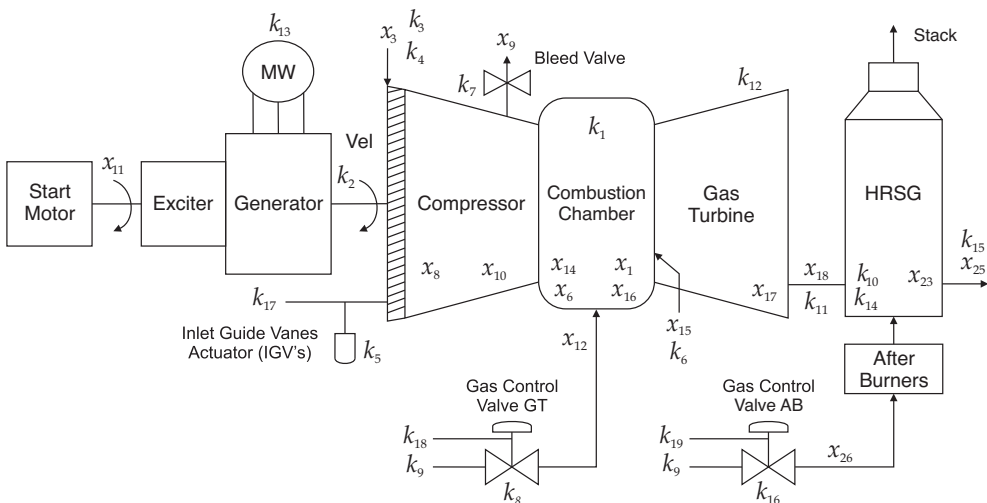
Fig. 3. Components of the Gas Turbine
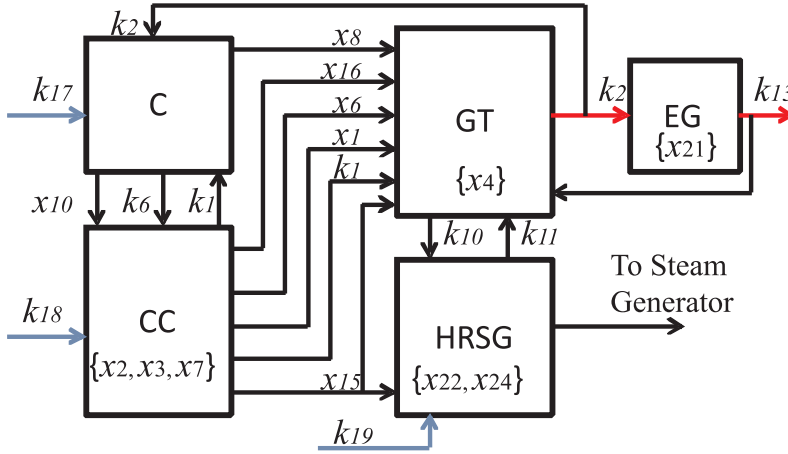
Fig. 4. Gas Turbine Variables Interconnection

The *GT* unit has two gas fuel control valves; the first supplies gas fuel to CC, and the second one supplies gas fuel to heat-recovery afterburners (starting a second- additional combustion at heat recovery for increasing the exhaust gases temperature). A generic compressor bleed valve extracts air from compressor during *GT* acceleration, avoiding an stall or surge phenomena. Also the *GT* unit has an actuator for the compressor inlet guide vanes, *IGVs*, to get the required air flow to the combustion chamber. The dynamic nonlinear model is developed in (Delgadillo & Fuentes, 1996) and it is integrated by n_c = 28 constraints, n_s = 19 static algebraic constraints, and n = 9 dynamic-differential constraints. Concerning the variables one can identify 27 unknown variables x_i and 19 known variables k_i. The generic architecture and interconnection of the GT's components are described by the block scheme given in Fig. 4. The variables and parameters for each block of the scheme are related by the constraints described in table 3. The variables are given in Appendix 8 and the description of the functions and parameters can be consulted in (Sánchez-Parra et al., 2010).

4. Analysis of the structure for the gas turbine

Considering constraints and variables of the model described in Table (3) the following sets for the graph description are identified:

- The set of known variables is given by

$$\mathcal{K} = \mathcal{Y}_s \cup \mathcal{Y}_a \cup \mathcal{U}_p \cup \mathcal{U}_c \qquad (10)$$

with cardinality 19. The process sensors is determined by the set

$$\mathcal{Y}_s = \left\{ k_1, k_2, k_6, k_{10}, k_{11}, k_{12}, k_{13}, k_{14}, k_{15} \right\} \qquad (11)$$

with $|\mathcal{Y}_s|$ =9; the position transducers from actuators define the set $\mathcal{Y}_a$ ={k_5, k_7, k_8, k_{16}}; the external physical variables determine the set $\mathcal{U}_p$ = {k_3, k_4, k_9}; and the control signals defines the set $\mathcal{U}_c$ = {k_{17}, k_{18}, k_{19}}.

- There are 28 physical parameters θ_i which are assumed constant in normal conditions Sánchez-Parra & Verde (2006).

Compressor Unit, C	Combustion Chamber Unit, CC
c1: $\quad 0 = f(x_1, x_6, k_1, \theta_0)$ c2: $\quad 0 = f(x_3, k_1, k_2, k_3, k_5, \theta_1, \theta_2, \theta_3)$ c3: $\quad 0 = f(x_3, x_8, k_1, k_3, \theta_4, \theta_5)$ c4: $\quad 0 = f(k_1, k_3, k_4, k_6, \theta_5)$ c5: $\quad 0 = f(x_9, k_1, k_3, k_6, k_7, \theta_6)$ c6: $\quad 0 = f(x_3, x_9, x_{10})$ c7: $\quad 0 = f(x_5, k_5, k_{17}, \theta_{25})$ d1: $\quad 0 = x_5 - \frac{dk_5}{dt}$	c8: $\quad 0 = f(x_6, x_{12}, k_1, k_8, k_9, \theta_7)$ c9: $\quad 0 = f(x_{10}, x_{12}, x_{14})$ c10: $\quad 0 = f(x_6, x_{15}, k_1, \theta_{21})$ c11: $\quad 0 = f(x_1, x_2, x_{14}, x_{15}, \theta_{17})$ d2: $\quad 0 = x_2 - \frac{dx_1}{dt}$ c12: $\quad 0 = f(x_1, x_6, x_7, x_{10}, x_{12}, x_{14}, k_6, \theta_8,$ $\qquad \theta_9, \theta_{17}, \theta_{18}, \theta_{19})$ d3: $\quad 0 = x_7 - \frac{dx_6}{dt}$ c13: $\quad 0 = f(x_{13}, k_8, k_{18}, \theta_{26})$ d4: $\quad 0 = x_{13} - \frac{dk_8}{dt}$
Gas Turbine Unit, GT	**Heat Recovery Unit, HR**
c14: $\quad 0 = f(x_{10}, x_{12}, x_{16}, k_6, \theta_8, \theta_9, \theta_{18})$ c15: $\quad 0 = f(x_1, x_{17}, k_1, k_{10}, \theta_{10})$ c16: $\quad 0 = f(x_1, x_{16}, x_{17}, x_{18}, k_1, \theta_{10})$ c17: $\quad 0 = f(x_6, k_{11}, k_{12})$ c18: $\quad 0 = f(x_6, k_1, k_{10}, k_{11}, \theta_{10})$ c19: $\quad 0 = f(x_{19}, k_2, \theta_{11})$ d5: $\quad 0 = x_4 - \frac{dk_2}{dt}$ c20: $\quad 0 = f(x_4, x_8, x_{11}, x_{15}, x_{16}, x_{18},$ $\qquad x_{19}, k_2, k_{13}, \theta_{20})$	c23: $\quad 0 = f(x_{23}, k_{10}, k_{14}, \theta_0)$ c24: $\quad 0 = f(x_{25}, k_3, k_{10}, k_{15}, \theta_{23})$ c25: $\quad 0 = f(x_{26}, k_9, k_{10}, k_{14}, k_{16}, \theta_{24})$ c26: $\quad 0 = f(x_{15}, x_{23}, x_{24}, x_{25}, x_{26}, \theta_{16})$ d7: $\quad 0 = x_{24} - \frac{dx_{23}}{dt}$ c27: $\quad 0 = f(x_{15}, x_{22}, x_{23}, x_{26}, k_{11}, k_{14}, \theta_9,$ $\qquad \theta_{16}, \theta_{18}, \theta_{19})$ c28: $\quad 0 = f(x_{27}, k_{16}, k_{19}, \theta_{27})$ d8: $\quad 0 = x_{22} - \frac{dk_{14}}{dt}$ d9: $\quad 0 = x_{27} - \frac{dk_{16}}{dt}$
Electric Generator Unit EG	
c21: $\quad 0 = f(x_{20}, x_{21}, k_{13}, \theta_{12}, \theta_{13}, \theta_{14}, \theta_{15})$ c22: $\quad 0 = f(x_{20}, x_{21}, k_2, \theta_{22})$ d6: $\quad 0 = x_{21} - \frac{dx_{20}}{dt}$	

Table 3. *GT* Model Equations with the variables meaning given in the appendix

- The constraints set is given by 19 static constraints and 9 state constraints which require their additional constraints (di) and known variables. Then the constraints set has cardinality 37 and is given by

$$\mathcal{C} = \{c1, c2, \ldots, c28\} \cup \{d1, d2, \ldots, d9\} \tag{12}$$

- The unknown variables are 27 and define the set

$$\mathcal{X} = \tilde{\mathcal{X}} \cup \mathcal{X} \cup \dot{\mathcal{X}} \tag{13}$$

where the dynamic unknown variables set has cardinality 4 and is given by

$$\mathcal{X} = \{x_1, x_6, x_{20}, x_{23}\}, \tag{14}$$

the unknown variables set which are related by static relations of cardinality $|\tilde{\mathcal{X}}| = 14$ are

$$\tilde{\mathcal{X}} = \left\{ x_3, x_8, x_9, x_{10}, x_{11}, x_{12}, x_{14}, x_{15}, x_{16}, x_{17}, x_{18}, x_{19}, x_{25}, x_{26} \right\} \qquad (15)$$

and the differential of the state variables are

$$\dot{\mathcal{X}} = \left\{ x_5, x_2, x_7, x_{13}, x_4, x_{21}, x_{24}, x_{22}, x_{27} \right\} \qquad (16)$$

with $| \dot{\mathcal{X}} | = 9$.

Considering the above described sets of variables and constraints, the Incidence Matrix, IM, of dimension (37 × 27) is first obtained and this is the start point of the structural analysis. Using Matlab (MATLAB R2008, 2008) the decomposed incidence matrix given in Fig. 5 is obtained. The bottom sub-matrix $IM^+ \in \mathbb{I}^{30\times20}$ is associated to $\mathcal{G}^+$ and $IM^0 \in \mathbb{I}^{7\times7}$ for $\mathcal{G}^0$ with $\mathcal{G}^- = \varnothing$. The diagnosticability analysis of the first part of the analysis takes into account only the over-constrained $\mathcal{G}^+$. The issue of the undetectability of the subgraph $\mathcal{G}^0$ will be addressed in Section 5.

4.1 Redundancy of the GT structure

Based on the subgraph $\mathcal{G}^+$, the maximum number of $\mathcal{RG}$ is given by $|\mathcal{C}^+| - |\mathcal{X}^+| = 10$. Considering the matching sequences described in the first 20 rows of Fig. 6 and concatenating these with other 10 constraints, Table 4 is obtained and the failured components which can be detected in the GT are identified. The third column indicates the variables used to detect faults involved in the respective set of constraints for each $\mathcal{RG}$. One can see that some faults can be supervised using two $\mathcal{RG}$s. As example faults in the component of constraint c_9 can be supervised by the graph $\mathcal{RG}_7$ or $\mathcal{RG}_8$ with different subsets of $\mathcal{K}$.

Table 4 is obtained and the failured components which can be detected in the GT are identified.

5. Diagnosticability improvement in the GT

The subsystem $\mathcal{G}^0$ given at the top of the matrix in Fig. 5 describes the process without redundant data and and the unique matched graph is shown in Fig. 7. It involves some of turbogenerator variables given in Table 3. Without redundant relations, it is impossible to detect a fault at the turbogenerator section with the assumed instrumentation. Giampaolo (2003) calls this subsystem, GT Thermodynamic Gas and includes the non-measured variables: compressor energy and rotor-friction energy (x_8, x_{19}); exhaust gases enthalpy and combustion chamber gases enthalpy (x_{18}, x_{16}); exhaust gases density x_{17}, rotor acceleration x_4 and the start motor power x_{11}. Thus, the main concern of this section is the identification of the unknown variables, which can be measured and converted to new known variables. So, with this the graph decomposition $\mathcal{G}^0$ will be empty and the getting of the respective ARR yields by the new measurement.

5.1 Graph structure modification

The oriented graph of $\mathcal{G}^0$ assuming the known variables subset $\mathcal{K}$ is shown in Fig. 7. The absence of paths which link a subset of known variables is recognized. The unknown variables $\mathcal{X}^0$ cannot be bypassed in any path and as consequence does not exist a $\mathcal{RG}$.

Fig. 5. Decomposed Incidence Matrix for the *GT*, where G^0 and G^+ are identified by blocks

$\mathcal{RG}$'s	Used Constraints $\mathcal{C}^+$	Known variables $\mathcal{K}$
$\mathcal{RG}_1$	c_4	k_1, k_3, k_4, k_6
$\mathcal{RG}_2$	c_{17}, c_{18}	$k_1, k_{10}, k_{11}, k_{12}$
$\mathcal{RG}_3$	d_1, c_7	k_5, k_7
$\mathcal{RG}_4$	d_4, c_{13}	k_8, k_{18}
$\mathcal{RG}_5$	d_9, c_{28}	k_{16}, k_{19}
$\mathcal{RG}_6$	$d_8, c_{10}, c_{17}, c_{23}, c_{25}, c_{27}$	$k_1, k_9, k_{10}, k_{11}, k_{12}, k_{14}, k_{16}, k_{19}$
$\mathcal{RG}_7$	$d_2, c_1, c_2, c_5, c_6, c_8, c_9, c_{10}, c_{11}, c_{17}$	$k_1, k_2, k_3, k_5, k_6, k_7, k_8, k_9, k_{11}, k_{12}$
$\mathcal{RG}_8$	$d_3, c_1, c_2, c_5, c_6, c_8, c_9, c_{12}, c_{17}$	$k_1, k_2, k_3, k_5, k_6, k_7, k_8, k_9, k_{11}, k_{12}$
$\mathcal{RG}_9$	d_6, c_{21}, c_{22}	k_2, k_{13}
$\mathcal{RG}_{10}$	$d_7, c_{10}, c_{17}, c_{23}, c_{24}, c_{25}, c_{26}$	$k_1, k_3, k_9, k_{10}, k_{11}, k_{12}, k_{14}, k_{15}, k_{16}$

Table 4. Redundant Graphs obtained from $\mathcal{G}^+$
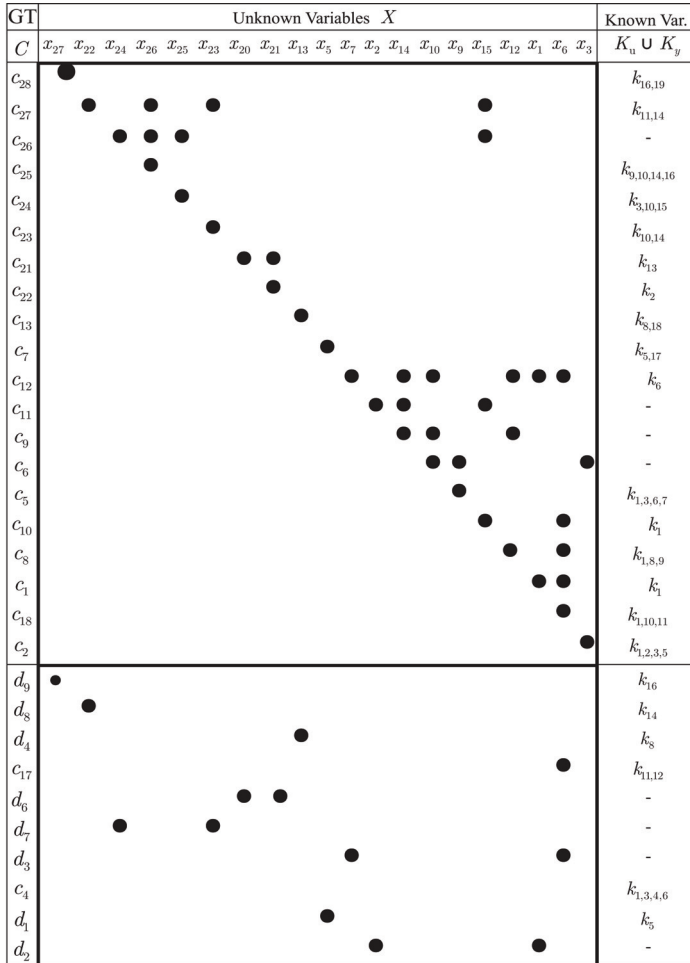
Fig. 6. Matching for the GT to get $10\mathcal{GR}$
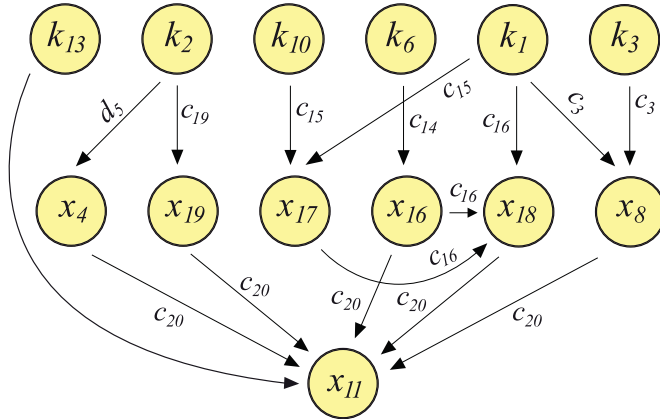
Fig. 7. Subgraph $\mathcal{G}^0$ without redundant information

To determine which variables of $\mathcal{G}^0$ could modify this lack of detectability, paths which satisfy the $\mathcal{RG}$ conditions assuming new sensors has to be builded. Then, one has to search for paths between known variables which pass by the constraint c_{20}. On the other hand, from the incidence matrix of the Table 5 one can identify that variable x_{11} appears only in the constraint c_{20}. Thus, there are not two different paths to evaluate it. To pass by c_{20} the only possibility is to asume that x_{11} is measurable.

Taking into account physical meaning of the set $\mathcal{X}^0$, it is feasible to assume that the start motor power x_{11} is known. This proposition changes the GT structure, transforming the whole structure to an over-constrained graph. In other words adding a dynamo-meter to the GT instrumentation, x_{11} became a new known variable, $k_{20} = x_{11}$, and allows the construction of the redundant graph described in Table 5. One verify that estimating first the set $\{x_1, x_3, x_{10}, x_{12}, x_{15}\}$ by subsets of $\mathcal{K}$ and $\mathcal{C}^+$, one can estimate $\hat{x}_{11}$ following the path. Thus, the relation

$$r(t) = \hat{k}_{20} - k_{20} \tag{17}$$

can be used as to generate a residual and the respective ARR_{11} depends on the variables set

$$\mathcal{K}^* = \left\{ k_1, k_2, k_3, k_5, k_6, k_7, k_8, k_9, k_{10}, k_{11}, k_{12}, k_{13}, k_{20} \right\} \tag{18}$$

and the set of constraints of the turbogenerator

$$\mathcal{C}^* = \left\{ c_1, c_2, c_3, c_5, c_6, c_8, c_{10}, c_{14}, c_{15}, c_{16}, c_{17}, c_{19}, d_5, c_{20} \right\} \tag{19}$$

Thus, any changes in the parameters and the functions involved in this set of constraints generates an inconsistent in the evaluation of the target node $\hat{k}_{20}$.

5.2 Simulation results

To validate the obtained redundant relation, a change in the friction parameter $\Delta\theta_{11} = 2$ in $c19$ of the turbogenerator non linear model has been simulated. The time evolution of the

$\mathcal{C}^0$	$\mathcal{X}^+$	$\mathcal{K}$	x_4	x_{19}	x_{17}	x_{16}	x_{18}	x_8	$k_{20}=x_{11}$
d5		$k_2\rightarrow$	⊕						
c19		$k_2\rightarrow$		⊕					
c15	x_1	$k_1,k_{10}\rightarrow$			⊕				
c14	x_{10},x_{12}	$k_6\rightarrow$				⊕			
c16	x_1	$k_1\rightarrow$				•	•	⊕	
c3	x_3	$k_1,k_3\rightarrow$					⊕		
c20	x_{15}	$k_2,k_{13}\rightarrow$	•	•		•	•	•	$\rightarrow$⊕

Table 5. Matching Sequence of $\mathcal{G}^0$ to get Fault Detectability

Base load fault detection by friction f1 (teta11x2)

Residual r11 (c20) — Time (sec)

Fault time
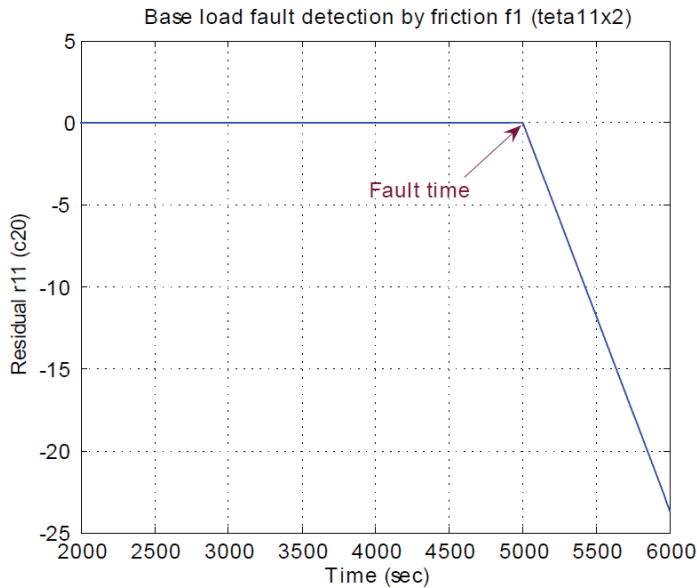
Fig. 8. Residual generated by the new ARR_{11} detecting friction fault at $5000s$

residual (17) for a fault appearing at $5000s$ is shown in Fig. 8. The fast response validates the detection system. Note that during the analysis of the detection issue, any numerical value of the turbine model can be used, giving generality to this result. The values set is used for the implementation of the residual or ARR, but not in the analysis.

6. Conclusions

A fault detection analysis is presented focused on redundant information of a gas turbine in a *CCCP* model. The study using the structural analysis allows to determine the *GT*'s monitoring and detection capacities with conventional sensors. From this analysis it is concluded the existence of a non-detectable fault subsystem. To eliminate such subsystem, a

reasonable proposition is the measure of the *GT*'s start motor power. Considering the new set of known variables and using the structural analysis, eleven *GT*'s redundant relations or symptoms generation are obtained. From these relations one identified that a diagnosis system can be designed for faults in sensors, actuators and turbo-generator. Since all constraints are involved at least one time in the 10 $\mathcal{RG}$s of Table 4 or in Eq. (17). This means, a diagnosis system could be designed integrating the residuals generator with a fault isolation logic which has to classify the faults. Due to space limitation it is reported here results only for a mechanical fault in the friction parameter. Using the eleven $\mathcal{RG}$ obtained here, one can achieve a whole fault diagnosis for any set of parameters.

7. Acknowledgement

8. References

Blanke, M., Kinnaert, M., Lunze, J. & Staroswiecki, M. (2003). *Diagnosis and Fault Tolerant Control*, Springer, Berlin.

Cassal, J. P., Staroswiecki, M. & Declerck, P. (1994). Structural decomposition of large scale systems for the design of failure detection and identification procedure, *Systems Science* 20: 31–42.

De-Persis, C. & Isidori, A. (2001). A geometric approach to nonlinear fault detection and isolation, *IEEE Trans Aut. Control* 46-6: 853–866.

Delgadillo, M. A. & Fuentes, J. E. (1996). Dynamic modeling of a gas turbine in a combined cycle power plant, *Document 5117, in spanish*, Instituto de Investigaciones Eléctricas, México.

Ding, S. X. (2008). *Model-based fault diagnosis techniques*, Springer.

Dion, J., Commault, C. & van der Woude, J. (2003). Generic propertie and control of linear structured systems: a survey, *Automatica* 39: 1125–1144.

Frank, P. (1990). Fault diagnosis in dynamic systems using analytical and knowledge-based redundancy, *Automatica* 26(2): 459–474.

Frank, P., Schreier, G. & Alcorta-Garcia, E. (1999). *Nonlinear Observers for Fault Detection and Isolation*, Vol. Lecture Notes in Control and Information Science 244, Springer, Berlin, pp. 399–466.

Giampaolo, T. (2003). *The gas turbine handbook: principles and practice*, The Fairmont Press.

Gross, J. & Yellen, J. (2006). *Graph Theory and its applications*, Vol. 1, Taylor and Francis Group.

Isermann, R. (2006). *Fault Diagnosis System*, Springer.

Korbicz, J., Koscielny, J. M., Kowalczuk, Z. & Cholewa, W. (2004). *Fault Diagnosis*, Springer, Germany.

Krysander, M., Åslund, J. & Nyberg, M. (2008). An efficient algorithm for finding minimal over-constrained sub-systems for model based diagnosis, *IEEE Trans. on Systems, Man and Cybernetics-Part A: Systems and Humans* 38(1): 197–206.

Mason, S. J. (1956). Feedback theory- further properties of signal flow graphs, *Proceedings of the I. R. E.*, pp. 960–966.

MATLAB R2008 (2008). *Toolbox Control Systems*, Math-Works, Inc., Natick, Massachuesetts.

Mina, J., Verde, C., Sánchez-Parra, M. & Ortega, F. (2008). Fault isolation with principal components structural models for a gas turbine, *ACC-08*, Seattle.

Mukherjee, A., Karmakar, R. & Kumar-Samantaray, A. (2006). *Bond Graph in Modeling, Simulation and Fault Identification*, Taylor and Francis.

Pothen, A. & Fan, C. (1990). Computing the block triangular form of a sparse matrix, *Artificial Intelligence* 16: 303–324.

Sánchez-Parra, M. & Verde, C. (2006). Analytical redundancy for a gas turbine of a combined cycle power plant, *American Control Conference-06*, USA.

Sánchez-Parra, M., Verde, C. & Suarez, D. (2010). Pid based fault tolerant control for a gas turbine, *Journal of Engineering for Gas Turbines and Power, ASME* 132(1-1): –.

Venkatasubramanian, V., Rengaswamyd, R., Yin, R. & Kavuri, S. (2003a). A review of process fault detection and diagnosis: Part i: Quantitative model based methods, *Computers and Chemical Engineering* 27: 293–311.

Venkatasubramanian, V., Rengaswamyd, R., Yin, R. & Kavuri, S. (2003b). A review of process fault detection and diagnosis; part i: Quantitative model based methods; part ii: Qualitative model and search strategies; part iii: Process history based methods, *Computers and Chemical Engineering* 27: 293–346.

Venkatasubramanian, V., Rengaswamyd, R., Yin, R. & Kavuri, S. (2003c). A review of process fault detection and diagnosis: Part ii: Qualitative model and search strategies, *Computers and Chemical Engineering* 27: 313–326.

Venkatasubramanian, V., Rengaswamyd, R., Yin, R. & Kavuri, S. (2003d). A review of process fault detection and diagnosis: Part iii: Process history based methods, *Computers and Chemical Engineering* 27: 326–346.

Verde, C. & Mina, J. (2008). Principal components structured models for faults isolation, *IFAC- 08, Seoul, Korea*.

9. Appendix

k_1	Compressor discharge pressure	x_5	Compressor IGV position rate
k_2	Turbogenerador rotor speed	x_6	CC gas temperature
k_3	Atmospheric pressure	x_7	CC gas rate temperature
k_4	Outlet temperature	x_8	Compressor energy
k_5	Compressor IGV position	x_9	Compressor bleed air flow
k_6	Compressor air discharge temperature	x_{10}	Compressor outlet air flow
k_7	Compressor air bleed valve position	x_{11}	Starting motor power
k_8	Gas turbine fuel gas valve position	x_{12}	CC gas fuel flow
k_9	Inlet fuel gas valves pressure	x_{13}	GT fuel gas valve position rate

k_{10}	Heat recovery pressure	x_{14}	CC inlet gas flow
k_{11}	Exhaust gas temperature	x_{15}	CC outlet gas flow
k_{12}	Blade path temperature (BPT)	x_{16}	CC gas enthalpy
k_{13}	Electrical generator power output	x_{17}	GT exhaust gas density
k_{14}	Heat recovery gas temperature	x_{18}	GT exhaust gas enthalpy
k_{15}	Heat recovery gas outlet temperature	x_{19}	GT energy friction losses
k_{16}	Afterburner fuel gas valve position	x_{20}	Electrical generator power angle
k_{17}	IGV control signal	x_{21}	Electrical generator power rate angle
k_{18}	GT fuel gas valve control signal	x_{22}	Heat recovery gas rate temperature
k_{19}	AB fuel gas valve control signal	x_{23}	Heat recovery gas density
k_{20}	Starting motor power	x_{24}	Heat recovery gas rate density
x_1	CC gas density	x_{25}	Heat recovery outlet gas flow
x_2	CC gas rate density	x_{26}	AB gas fuel flow
x_3	Compressor inlet air flow	x_{27}	AB fuel gas valve position rate
x_4	Turbogenerator rotor speed rate	θ_4	Compressor air density
θ_{11}	GT rotor friction parameter	θ_{20}	GT rotor inertia

Table 6. Variables and Parameter Definition of the Gas Turbine Model

Life Time Analysis of MCrAlY Coatings for Industrial Gas Turbine Blades (calculational and experimental approach)

Pavel Krukovsky[1], Konstantin Tadlya[1], Alexander Rybnikov[2],
Natalya Mozhajskaya[2], Iosif Krukov[2] and Vladislav Kolarik[3]
[1]Institute of Engineering Thermophysics, 2a, Zhelyabov Str., 03057 Kiev
*[2]Polzunov Central Boiler and Turbine Institute, 24, Politechnicheskaya Str.
194021 St. Petersburg*
*[3]Fraunhofer-Institut für Chemische Technologie, 7, Joseph-von-Fraunhofer Str.,
76327 Pfinztal*
[1]Ukraine
[2]Russia
[3]Germany

1. Introduction

Modern power gas turbine blades are subject to high-temperature oxidation and are protected by metal coatings of MCrALY type. The major element retarding oxidation of a coating is aluminium (Al) whose percentage in a coating amounts to 6-12%.

A blade coatings lifetime of 25000 h is required in stationary gas turbines at operating temperatures from 900 to 1000 °C making experimental lifetime assessment a very expensive and often a not practicable procedure. A feasible and low-cost method of coating lifetime assessment is the calculation analysis (modeling) of mass transfer processes of basic oxide-forming elements (in our case Al) over a long period of time. Oxidation **(Al_2O_3 oxide film** forming on the external coating surface) and Al diffusion both towards the oxide film border and into the basic alloy of a blade are the mass transfer processes which determine coating lifetime at the usual operating temperatures.

The existing models describing high-temperature oxidation and diffusion processes in MCrALY coatings use simple approximated empirical dependences (of power-or other type) [1-4] for oxide film mass or thickness variation with time, and differential equations describing the oxide-forming element diffusion in the «oxide-coating-basic alloy» system [5, 6].

However the practical application of these models for long-time prediction is often difficult or impossible because of the lack of reliable model input parameter values, such as diffusion factors of an oxide-forming element. Some data on element diffusion factors can be found in literature only for simple alloy compositions (two- or three-component alloys), while the alloys used in practice are more complex. In the present case a coating alloy containing 5 elements-nickel, cobalt, chromium, aluminium, yttrium – is to be investigated. Data on Al diffusion factor can be found in literature studying similar element composition, but only for three-component NiCrAl alloy [7].

It should be noted that the models, which have been described in [5, 6] disregard the importance of a number of alloys peculiarities of Al transport from the coating to the base alloy, which is, the formation of a so-called interdiffusion zone between the coating and the base alloy. In that case mass transfer from the coating to the base alloy occurs through the interdiffusion zone and the Al accumulation here begins to play an important role. The factors of its mathematical description become all the more uncertain.

This work offers to define model factors (effective Al diffusion factor, the intensity factor of aluminum segregation in the interdiffusion and other zones) using the solution of inverse problems of diffusion based on the experimental data on Al concentration distributions at different coated sample exposure times and temperatures in furnaces. The approach based on the use of short-term experimental data for model factor determination followed by the application of this model for long-term predictive calculations is called here as a calculation-experimental approach.

This approach was used for the analysis of chromium mass transfer in a coating with the formation of chromium oxide and chromium diffusion into a basic alloy [8] except for the coating life analysis.

The purpose of this work is to improve the existing model of mass transfer processes in MCrAlY-type metal coatings as well as the development and application of the calculation-experimental approach to coating life assessment based on the proposed models and the solution of inverse problems of diffusion.

2. Calculational and experimental approach

The essence of the present approach is the choice of such a mass transfer model and a set of data which, when combined, enable one to obtain a more equivalent model based on the solution of inverse problems of diffusion (IPD). The use of the model will allow for a more accurate long-term prediction of mass transfer processes and metal coating life at given lifetime criterion.

The diagram of the approach (Fig.1) to mass transfer prediction is as follows:

1. The construction (selection) of a mathematical model which gives the adequate description of major physical processes occurring in the system under consideration and determining coating life. This model makes it possible to find the calculated C_m concentration (profiles) for Al in the coating-basic alloy system.

2. The performance of short-term experimental studies in order to find regular trends of the oxide film and interdiffusion zone formation and determine Al concentration distributions in a coating and a basic metal (CE) at different times and temperatures (coated sample exposures in furnaces).

3. The identification of the unknown $P_n(T)$ model parameters from experiments based on the IPD solution, which gives the proximity of C_M and C_E profiles by minimizing the F value.

4. Long-term prediction of mass transfer processes and coating life with the use of the proposed model in p.1 together with the unknown model parameters determined in p.3.

A simpler diagram of prediction is usually used (Fig.1): model + literature $P_0(T)$ model parameters = prediction.

Generally the diagram can be applied for simple alloy compositions, for instance, for a three-component alloy [5, 6]. As for more complex compositions, it may lead to insufficiently accurate predictions due to the uncertain $P_0(T)$ model parameters. So the use of a full calculation-experimental approach diagram based on the identified $P_n(T)$ model parameters provides more accurate predictions.
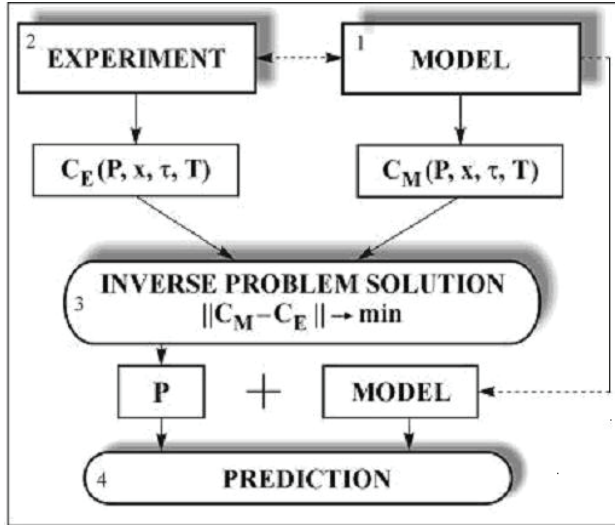
1 Experiment, 2 Model, 3 Inverse Problem Solution, 4 Prediction

Fig. 1. Diagram of the calculation and experimental approach to mass transfer and life predictive of gas turbine blade coatings.

The calculation-experimental approach under consideration suggests a search (identification) for model parameters (p.3) by means of IPD solution based on the available short-term experimental data. The IPD solution amounts to searching for such Pu (T) parameter values for which the quantity

$$ F \;=\; \left\{ \sum_{j=1}^{m} \Big[C_{j,M}\big(P(T)\big) \;-\; C_{j,E} \Big]^2 \Big/ m \right\}^{0.5} \to \min \tag{1} $$

This method of IPD solution is given in more detail in [8, 9]. Thus the calculation-experimental approach manifests itself as a way of improving the accuracy of the results of calculations and prediction of the processes at hand by identifying the mathematical model parameters based on the experimental data on the process being studied. The construction of the mathematical model required the performance of special works concerned with the study of the regularities of high-temperature material and coating behaviour during long-term exposures at high temperatures and the development of a physically valid model for coating life prediction.

3. Experiment

In this connection the purpose of short-term researches was a study of kinetics of the oxide film formation on a coating surface, structural changes in surfaces layers of coated heat-resistant alloys, and the modeling of structural-phase changes in coatings and at isothermal ageing the duration of which was sufficient for model parameter identification. Then the experiment was continued till coating life expiration in order to confirm the validity of the proposed method.

The work investigated the degradation of two coatings with different aluminum content. The coatings were applied on IN 738LC alloy samples by LPPS (Low Pressure Plasma Spray) method. The isothermal exposure times and temperatures are given in Table 1.

Coating	Coating thickness, µm	Base material	Exposure temperature, °C	Exposure time, hr
Ni30Co28Cr8AlY	100	IN 738 LC	900, 950, 1000	100, 300, 700, 1000, 5000, 10000, 15000, 20000
	200			
Ni30Co28Cr10AlY	100 200	IN 738 LC	900, 950, 1000	100, 300, 700, 1000, 5000, 10000, 15000, 20000

Table 1. The program of coated sample tests.

The samples of the same thickness and composition were obtained by cutting cylindrical bar (10 mm in diameter and 100 mm long) into pieces. The isothermal oxidation in air was carried out in laboratory muffle furnaces (LINN HIGH TERM LK 312-type) equipped with parameter control system (PID-controls) allowing to put the furnace into a specified mode and maintain the required temperature. Initial samples and those after isothermal exposure were subjected to metallographic examination by optical microscopy, X-ray spectrum microanalysis and X-ray diffraction analysis for studying the changes which had occurred in coatings. The samples were electropolated with Cu before preparation (cutting, mechanical grinding and polishing) in order to preserve the oxide film which had formed on a coating surface after exposure in the furnace.

3.1 Metallographic examination
The inverted microscope «Neophot 32» (Karl Zeiss Jena) with the «Baumer Coptronic» video camera was used for the micrographic examination. The obtained images were processed by means of «VideoTest Structure» software («Video Test», St. Petersburg, Russia). The following parameters were measured on each sample with the use of digital metallography:
- thickness of an oxide film and all layers formed in a coating and adjacent basic metal layer as a result of isothermal exposure in air;
- the volume fraction of phases existing in an initial coating and formed during isothermal exposure.

3.2 X-ray spectrum microanalysis
The X-ray spectrum microanalysis was carried out using MS46 «Camera» X-ray spectroscope analyzer. Samples before etching and poorly etched were used for study. The standards of both pure metals and compounds and known-composition alloys have been used for quantitative concentration evaluations of elements under consideration. The corrections for absorption, atomic number and characteristic radiant fluorescence effects were introduced by using special computer program. The curve for aluminium concentration variation across the depth of a coating and basic metal layer was built after each exposure. To this end, the X-ray spectrum microanalysis of coating and basic metal layers was carried out every 2 to 10 µm and up to 250 µm deep. The window size for the element analysis was 100 µm parallel and 3 µm perpendicular to the coating surface (100× 3 µm).

3.3 X-ray diffraction analysis

The oxide film formation in the first 100 hours was studied in situ by high-temperature X-ray diffraction by Fraunhofer Institute for Chemical Technology, Germany.

The experimental set-up consists of an X-ray diffractometer and a high-temperature device with a programmable thermal controler. A set of X-ray diffraction patterns with a defined time interval or temperature step was recorded in situ allowing for the identification of structural changes in the sample as a function of time or temperature. This method makes it possible

- to identify in-situ the following oxide phases,
- To follow the formation of each phase in time or as a function of temperature;
- To evaluate kinetic data on each of the reactions involved;
- To detect the thermal expansion of all phases simultaneously;
- To determine residual stresses in the oxide film or basic metal.

In order to identify the oxide phase structures ex situ after long term exposures, the X-ray diffraction analysis was performed using a DRON-3M diffract meter in Cu Kα radiation with corresponding filters. Methods of polycrystalline sample structure examination were standard.

3.4 Experimental results

3.4.1 Protective oxide film formation mechanism

The mechanism of oxide film formation and growth on coating surfaces after long exposures at high temperatures in air or pure fuel combustion products was studied (Fig.2).

Oxidation measurements were carried out on coating under isothermal conditions (900°C, 950°C and 1000°C) up to 20000 hours.

300 h	1000 h	5000 h	15000 h
3,4 μm	4,4 μm	7,1μm	12,3 μm
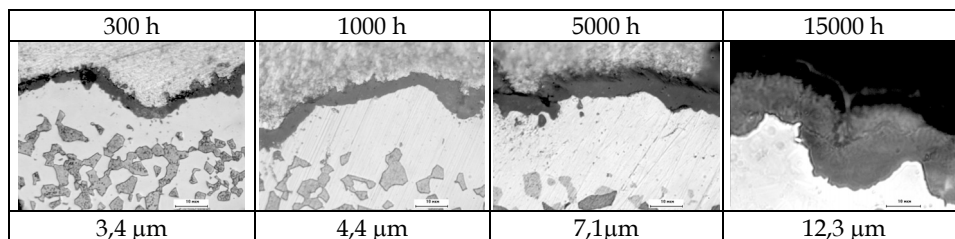
Fig. 2. Oxide film thickness on a coating surface depending on time of isothermal oxidation

The measurement of oxide film thickness after different exposure times show that the change in oxide film thickness at the initial stage of formation does not fit to the power-type dependence at longer exposures.

The studies of oxide film phase composition were performed by high-temperature X-ray diffraction method in order to find out the causes of the accelerated oxide film thickness growth at short exposures. The in-situ observation of the oxide film formation during the first 100 hours at 900 and 950 °C showed the formation of α-Al_2O_3 and θ-Al_2O_3 oxides on the surface (see Table 2).

The growth of α-Al_2O_3 and θ-Al_2O_3 at 950 °C as a function of time is given in Fig.3 as intensity curves iz(t). Both alumina phases on polished samples grow simultaneously in the first 50 hours and then the rate of θ-Al_2O_3 growth decreases and α-Al_2O_3 increases. The amount of θ-Al_2O_3 reaches maximum after 100 hours and with further exposure the oxide starts to disappear as a result of its transformation into α-Al_2O_3.

Temperature, °C	Time, hr				
	100	700	5000	10000	20000
900	θ- + α-Al$_2$O$_3$	α-Al$_2$O$_3$	α-Al$_2$O$_3$	α-Al$_2$O$_3$	α-Al$_2$O$_3$ (Me$_3$O$_4$)
950	θ- + α-Al$_2$O$_3$	α-Al$_2$O$_3$	α-Al$_2$O$_3$	α-Al2O$_3$ (Me$_3$O$_4$)	α-Al$_2$O$_3$, Me$_3$O$_4$
1000	α-Al$_2$O$_3$	α-Al$_2$O$_3$	α-Al$_2$O$_3$	α-Al$_2$O$_3$ (Me$_3$O$_4$)	α-Al$_2$O$_3$, Me$_3$O$_4$

Table 2. Oxide film phase composition on Ni30Co28Cr10AlY and Ni30Co28Cr8AlY 200 μm thick protective coatings (the phase indications in brackets mean, that their amount did not exceed 5 %).
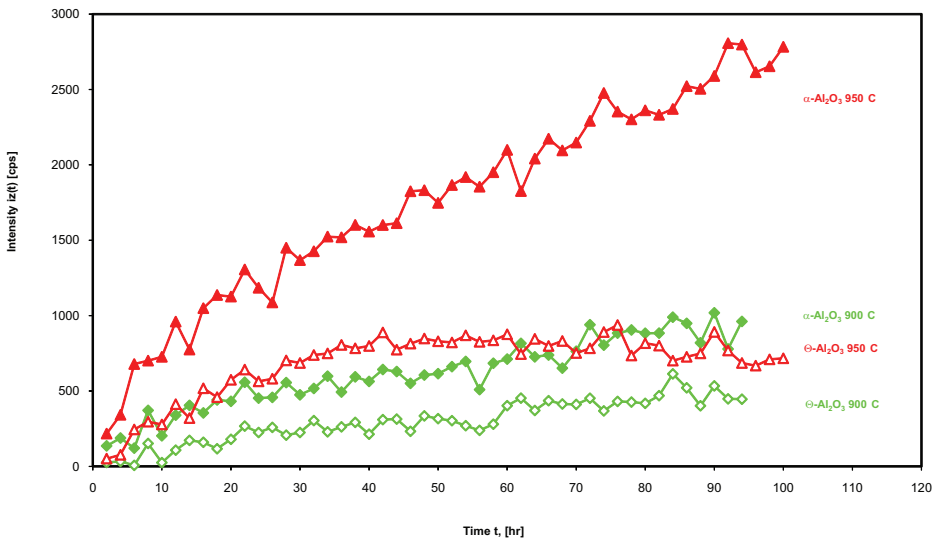
Fig. 3. Diffraction peak intensities of α-Al$_2$O$_3$ and θ-Al$_2$O$_3$ on polished coatings with 8% Al at 900°C and 900°C.

Hereinafter, these data were corrected in the developed model by splitting the oxide film growth curve into two parts (the first one refers to the period of simultaneous existence of θ-Al$_2$O$_3$ and α- Al$_2$O$_3$ oxides and the second — to period of only α- Al$_2$O$_3$).

Investigations using standard X-ray diffraction methods were performed in order to find out the oxide film growth mechanism in the range of $3 \cdot 10^2 - 2 \cdot 10^4$ hours. It has been established that the oxide film phase composition in this range depends on aluminum content.

As is seen from Table2, the oxide phase composition on coating with aluminum content over 8% (NiCoCr8alY (for instance) after exposures in this time interval presents mainly α- Al$_2$O$_3$. At long exposures ($\geq 2 \cdot 10^4$ hours), an oxide of complex composition of a spinel type (Co,Ni)(Cr,Al)$_2$O$_3$ forms on the coating surface simultaneously with α- Al$_2$O$_3$. The results of the investigations performed enabled to plot the variation of the oxide film phase composition with time and temperature (Fig.4).
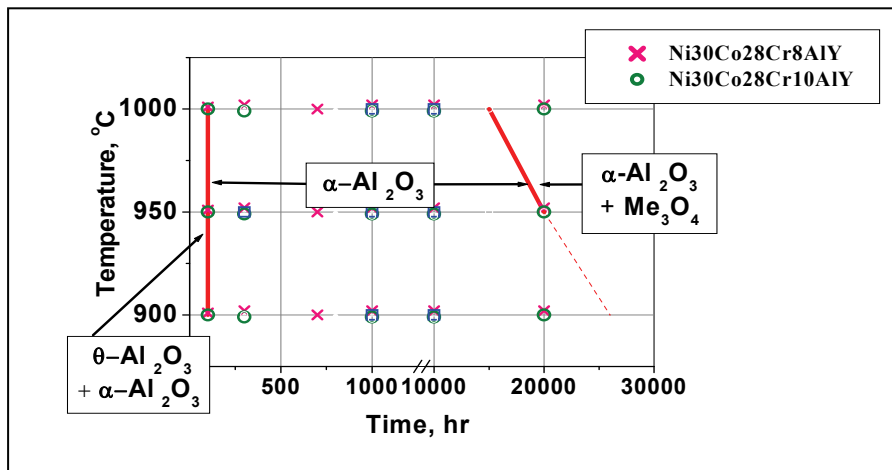
Fig. 4. Diagram of phase transformations in protective oxide film on Ni30Co28Cr8AlY and Ni30Co28Cr10AlY coating

Three areas can be seen on the diagram:

- θ- Al_2O_3 + α- Al_2O_3 corresponding to exposure time to 200 hours at all temperatures;
- α- Al_2O_3 corresponding to exposure time to $2\cdot10^4$ hours at all temperatures;
- α- Al_2O_3 + complex-composition oxide of a spinel type $(Co,Ni)(Cr,Al)_2O_3$ corresponding to exposure time over $2\cdot10^4$ at temperatures 950°C and above.

The basis for the development of methods of corrosion life modeling for these coatings was the existence of constant phase composition oxide (α- Al_2O_3) in a wide time range of exposures of Ni30Co28Cr8AlY and Ni30Co28 Cr10AlY coatings for the temperature interval from 900 to 1000°C.

3.4.2 Kinetics of changes in coating structures

The coating structural changes and the redistribution of elements between a coating and a basic metal can be observed during long isothermal exposures of the coated basic metal. These changes depend on both boundary conditions including environment composition and the thickness and composition of an oxide film forming during long exposures and the thickness of a coating layer. Both the coating and basic metal compositions and the exposure times and temperatures will naturally determine the structural changes.

The work investigated the coating depth-variation of the chemical composition and structure and the changes in the surface layer of a basic metal during long exposures in air simulating service conditions in the medium of pure fuel combustion products. The structural changes in coating and surface layers of a basic metal and the thickness of the depleted layer were studied by optical metallography and the distribution of elements in the coating and basic metal layers — by X-ray spectrum analysis. The investigations have shown that all the coatings in their initial phase composition represent a matrix with a face-centered cubic lattice — γ-solid solution (Ni,Co)-Cr-based and a β-phase (Ni,Co)Al which is uniformly distributed across the coating layer. As is known, the β-phase presents a compensation reservoir for aluminum which is spent on the protective oxide film formation on a coating surface (Brady et al., 2001).

After applying a coating and performing heat-treatments a diffusion zone is formed in the alloy. The zone width, phase composition and structure depend on coating and basic metal compositions, coating application technique and subsequent heat-treatment conditions.

The diffusion zone for all the coatings had about the same width (a. 15 µm) and the phase composition a significantly different from that for basic metal $\gamma + \gamma'$ +carbides.

The characteristic structure of this coating after high temperature exposures is given in Fig.5.
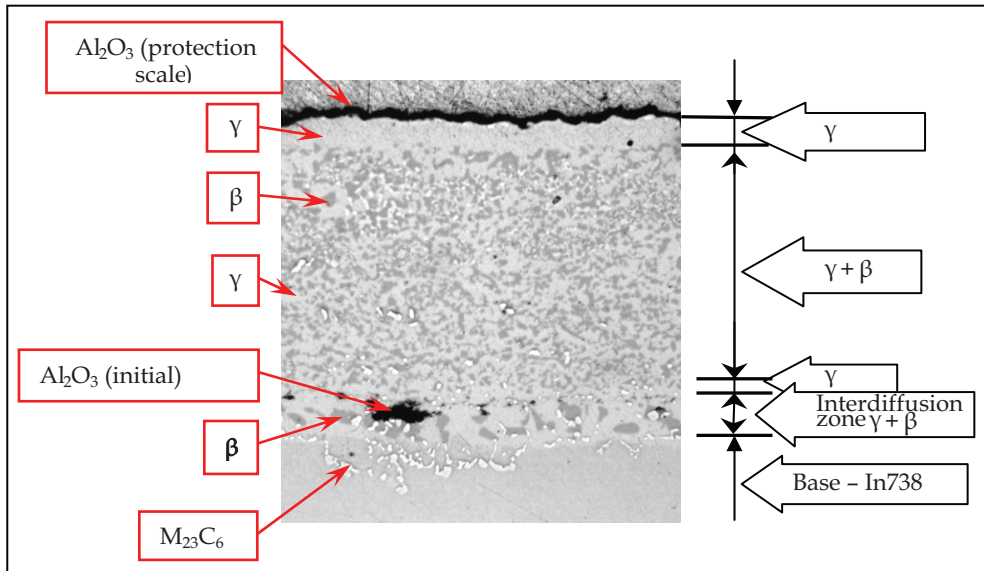
Fig. 5. Microstructure of Ni30Co28Cr8AlY coating on IN738LC alloy after exposure for 1000 hours at 950°C (×300)

During long-term exposures to high temperatures the coating structure changes due to the phase composition variation in its different zones followed by the formation of the characteristic layers.

It has been established that each of the coatings investigated after long-term exposures shows a specific character of structural changes.

The phase composition of the layers is mainly retained and their thickness changes with exposure time and temperature variation.

The changes in coating structure and phase composition depending on exposure time and temperature can be traced from the structures given in Fig.6.

It should be noted that the β-phase stabilization is observed in coatings of this composition. In relation to this, the phase transformation in a coating during its degradation at high-temperature exposure occurs in the direction $(\gamma+\beta)\rightarrow\gamma$.

The kinetics of a change in the volume fraction of the β-phase and aluminium concentration depending on exposure time and temperature can be seen from the curves in Fig.7 and 8.

The X-ray spectroscopy microanalysis of aluminium distribution in the surface layers of coatings in the initial state and after long exposure at 900 to 1000°C was performed. This microanalysis allowed to identify phases which had been found during metallographic study. The sizes of dealloyed and diffusion zones and special features of element
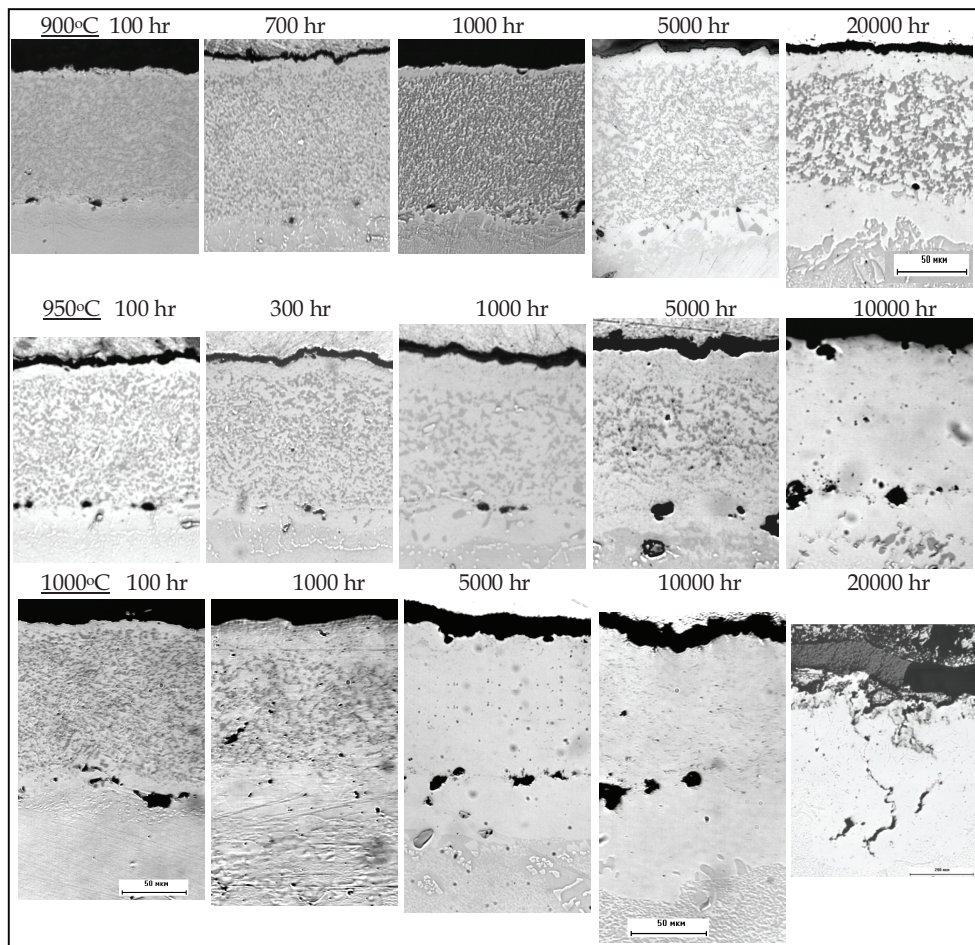
Fig. 6. The change in Ni30Co28Cr8AlY coating on IN738LC alloy after different exposures at 900°C, 950°C and 1000°C

distribution in these zones can be seen from the curves built in Fig.7. Thus, for the external dealloyed zone characteristic for all types of coatings, a sharp decrease in aluminium content is observed under the oxide film Al_2O_3 (51.78%) up to 2.5 to 3.2%, which corresponds to its content in the γ-phase. In coatings of this composition, the volume fraction of the initial β-phase amount to 45% for the Ni30Co28 Cr8AlY coating and 62% for NiCo28Cr10AlY. During the exposures this phase amount decreases according to the curves shown in Fig.8, the decrease being less intensive for the coating with greater aluminium content (and |or larger thickness) determining the coating aluminum life.

The diagrams of phase transformation proposed by Tamarin Jr. (Tamarin, 2002) are very convenient for presentation of data on the coating phase composition variation with exposure time and temperature. The external coating surface is taken as the onset of counting and considered to be constant in these phase transformation diagrams.
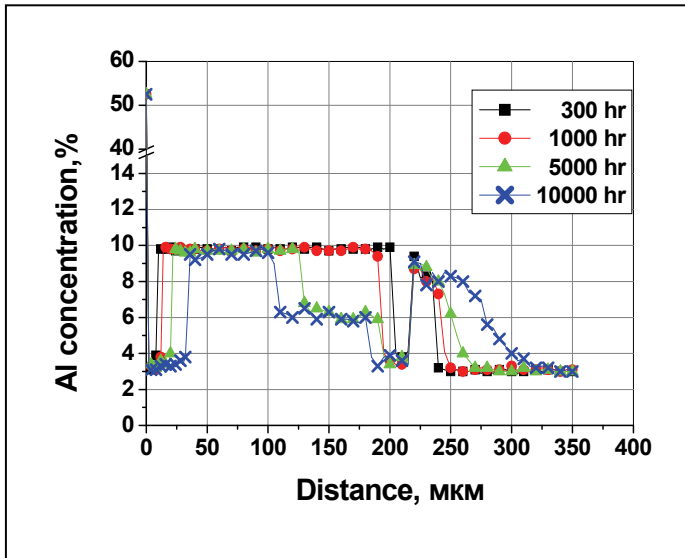
Fig. 7. The Al concentration profile across a coating after isothermal oxidation at high temperatures for up to 10 000 hour
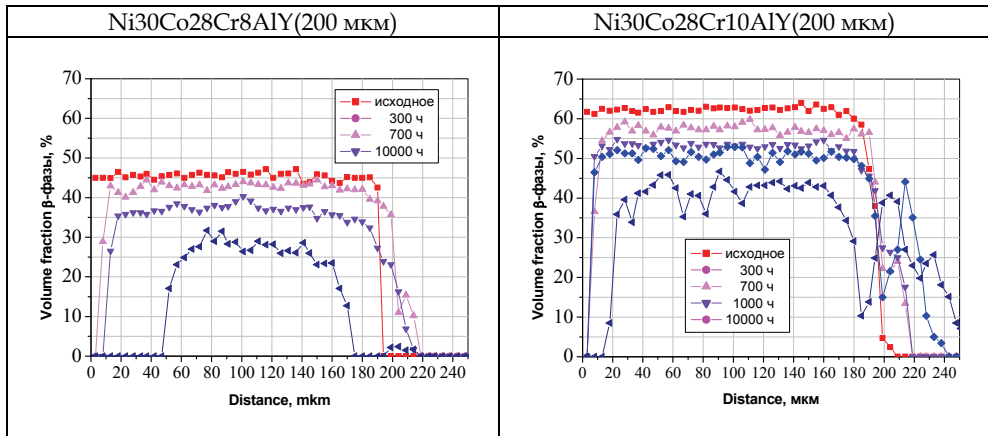
Fig. 8. The β-NiAl volume fraction in the γ+β region after different duration of exposure at 950 °C

As is seen from Fig.9 and 10 the phase changes in external layers at high-temperature exposures are observed only due to the formation of an external depleted zone the width of which increases with increasing exposure time and temperature.

This zone is formed as a result of β-phase solution and aluminium consumption for the protective oxide film Al_2O_3 formation. At the same time, significant temperature-dependent structural changes of a diffusion zone are observed at the interface «coating - basic metal». The studies performed have found out particular features of the diffusion zone formation
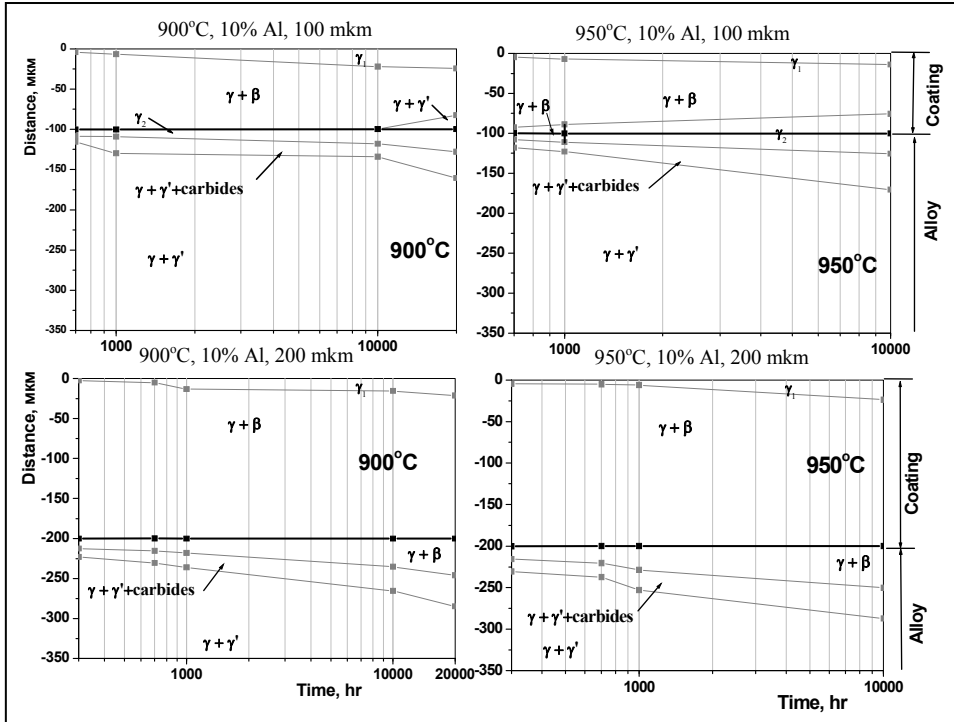
Fig. 9. Diagram of phase transformations in Ni30Co28Cr10AlY coating on IN738LC
superalloy after exposure at 900 °C and 950 °C

between a metal and a coating depending on the aluminum content in the zone: with the
aluminum content 10% the diffusion processes develop at the interface on a basic metal side
(in this case a β+γ structure is formed), while with the aluminum content 8% in a coating the
diffusion processes develop on both sides of the interface (the β+γ structure is first formed
and then it transforms to a single -phase γ-zone).

It is self-evident that the common model of the diffusion element redistribution in an oxide
film, a coating and a basic metal requires accounting for the diffusion processes of all
coating and alloy components. The practical handling the problem is however labour
intensive, ambiguous, and requires a great number of experimental data.

That is why there is a good reason to make a choice of the best concept of diffusion which
could be used as the basis of a coating corrosion life prediction according to one or another
dominant process depending on the temperature interval.

In the temperature range 900 to 1000ºC it is advisable to use aluminum redistribution
processes whose characteristics have been studied as dominant diffusion processes for
building a model.
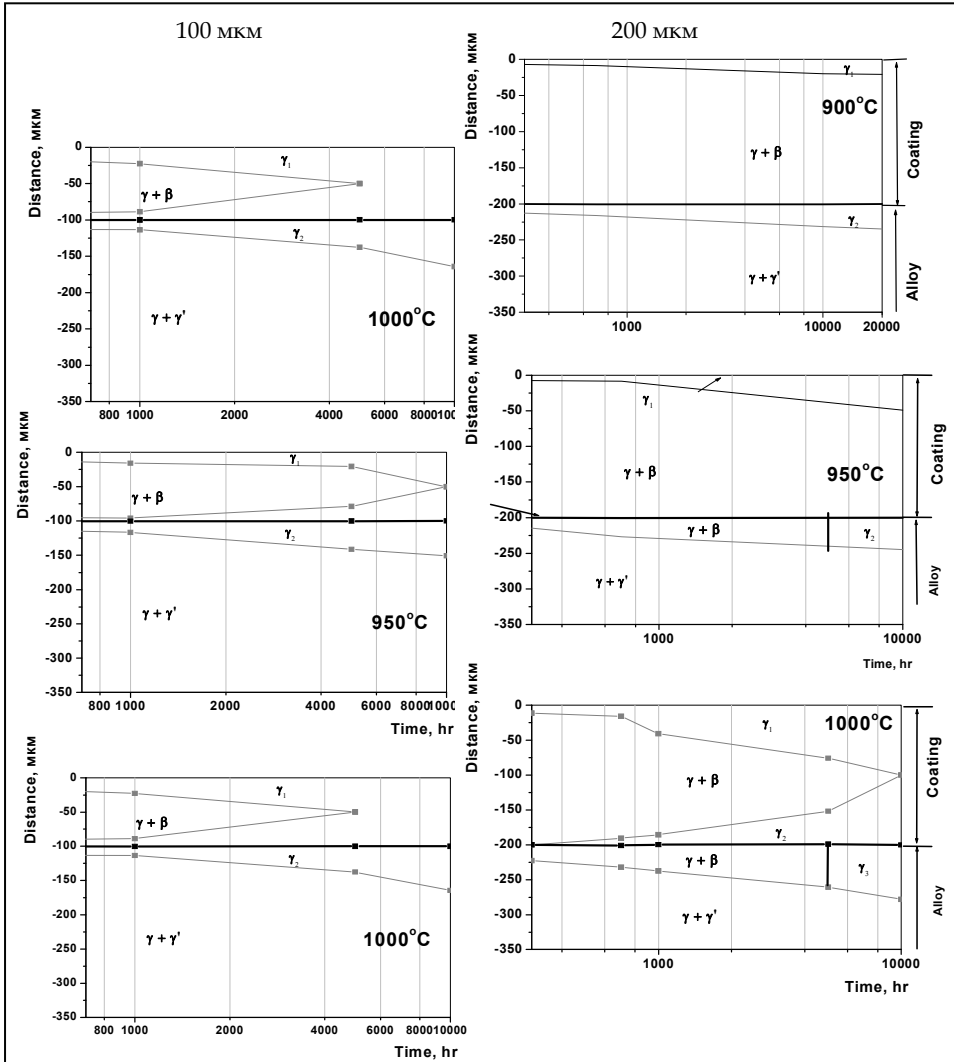
Fig. 10. The phase composition transformations in Ni30Co28Cr8AlY coating (100μm and 200 μm on IN738LC superalloy after exposures at different temperatures (900 °C, 950 °C and 1000 °C).

4. Physical and mathematical models

The physical model for aluminium diffusion redistribution in the «oxide-coating-basic metal»system obtained from the analysis of experimental studies of oxidation and diffusion processes in coatings of NiCoCrAlY-type is described as follows (Fig.11).

An oxide is formed by combining aluminuim and oxygen which is absorbed from the gaseous medium and by means of diffusion through the oxide layer $x_1 - x_0$ it reaches the interface
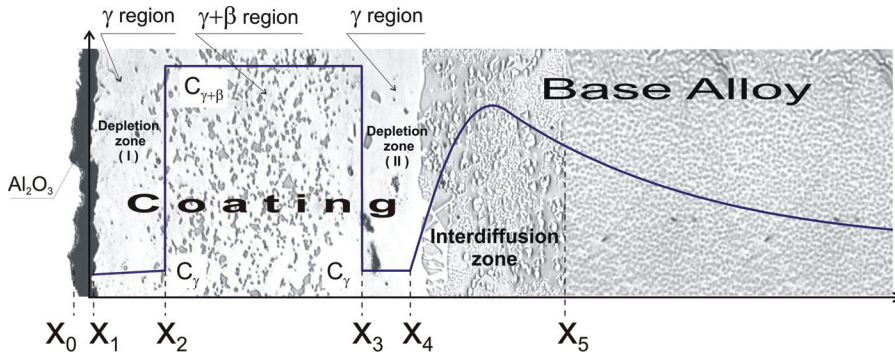
1. coating, 2. basic alloy, 3. γ -region, γ+ β region, 4. depletion zone, 5. interdiffusion zone

Fig. 11. Typical aluminium concentration distribution in an oxide, coating, and basic alloy.

x_1 **oxide - coating**. The aluminuim diffusion from the coating proceeds in two directions:
- to the interface x_1 **oxide - coating** where it enters into reaction with the arrived oxygen.
- to the interface x_4 **coating - basic alloy** where it is accumulated in the interdiffusion zone and then diffuses to the basic alloy.

The formation of aluminium-depleted single-phase zones with a decreased Al (γ-phase) content on both the oxide and basic metal side (depletion zones I and II, Fig.11) occurs at the cost of the aluminium departure from the coating (γ+β two phase zone. All aluminium leaving the coating departs from the coating (γ+β two phase zone owing to the β**-**phase disappearance. The aluminium concentration profile has the form of a stepwise curve in the region of NiCoCrAlY coating and a curve with maximum in the interdiffusion zone within the basic alloy.

Six major zones can be distinguished:
- $x_0 < x < x_1$ oxide;
- aluminium-depleted $x_1 < x < x_2$ zone where only one   γ -phase is present;
- two-phase $x_2 < x < x_3$ zone where γ - and β -phases exist simultaneously;
- $x_3 < x < x_4$ zone in the coating, also aluminium-depleted with γ -phase:
- interdiffusion aluminium-rich zone $x_4 < x < x_5$ in the basic alloy.
- $x_5 < x$ Zone in the basic metal where aluminium diffuses from the interdiffusion zone.

The aluminium accumulation in the interdiffusion zone with time occurs at the cost of the formation of different phases (γ+β and γ′+β -phases, for instance) due to the different quantitative compositions and the corresponding thermodynamical equilibrium of elements in a coating and a basic alloy. The accumulated in the interdiffusion zone aluminium diffuses partly to the basic alloy and back to the coating. In the model under consideration, all the borders apart from the border x_4 (the interface between a coating and a basic alloy) are movable. The borders x_2 and x_3 move toward each other because of the β -phase content decrease in the γ+β - two-phase coating zone $x_2 < x < x_3$ from which the aluminium diffusion occurs. The concentrations of total aluminium amount of **C** and β-phase $C_β$ in the γ+β two-phase $x_2 < x < x_3$ decrease with time.

A mathematical model presented in [6] was taken as the basis of the above-described model. The model from [6] was improved by adding the capabilities of accounting for special features of border x_2 and x_3 moving as well as the formation and growth of the interdiffusion zone which has a great effect on the aluminium mass transfer processes in the coating-basic alloy system.

Below is given this improved model according to which aluminium mass transfer processes in the region of solution $x_1 < x < x_\infty$ can be described by the main diffusion equation

$$\frac{\partial C}{\partial \tau} = \frac{\partial}{\partial x}\left[D_{ef}\frac{\partial C}{\partial x}\right] + W \tag{2}$$

$\tau > 0,$, $x_1 < x < x_\infty,$ $C = C(x,\tau),$ $W = W(x,\tau),$ $D_{ef} = D_{ef}(x),$ $x_1 = x_1(\tau),$ $x_2 = x_2(\tau),$
$x_3 = x_3(\tau),$ $x_5 = x_5(\tau),$
at the initial condition

$$C(x,\ 0) = C(x) = \begin{cases} C_n^0 & 0 < x < x_4 \\ C_{oc}^0 & x \geq x_4 \end{cases} \tag{3}$$

at the boundary condition on border x_∞

$$\frac{\partial C(x_\infty,\ \tau)}{\partial x} = 0 \tag{4}$$

and boundary condition on the movable border x_1 describing the aluminium diffusion flow from the coating to the left to form the oxide (Fig.11) at the cost of Al concentration gradient

$$J_{ox}(x_{1+},\tau) = -D_{ef}\frac{\partial C(x_1,\tau)}{\partial x} \tag{5}$$

Flow (5) together with the mass (flow) $C(x_1,\tau)\dfrac{dx_1}{d\tau}$ that was formed owing to the border movement to the right make up a total oxide film mass of Δx thickness which can be described by two parabolic equation [5,6].

$$\Delta x(\tau) = x_1(\tau) - x_0(\tau) = \begin{cases} k_{ox}^* \cdot \tau^{0.5}, & 0 < \tau < \tau^* \\ k_{ox}^{**} \cdot \sqrt{\tau - \tau^0}, & \tau^* < \tau < \infty \end{cases} \tag{6), (7}$$

where $k_{ox}^*,$ k_{ox}^{**}- intensity factors of oxide film thickness growth, in literature often called oxidation constants, τ^*- time prior to which the oxidation law (6) is valid and after which the oxidation law(6) is valid τ^0 -time prior to which the oxidation law (7) is in force.
At the moment of time τ^* the curves from equations (6) and (7) cross; τ^0 -the time (negative value) of crossing law (7) and the time axis τ. The necessity of describing the law of Al oxide growth by the two parabolic equations (6) and (7) is due to a more rapid growth of oxide θ-phase prior to the moment of time τ^* and a slower growth of α- phase of the oxide film Al_2O_3 at $\tau > \tau^*$. The factors $k_{ox}^*,$ $k_{ox}^{**},$ τ^0 and the τ^* value in (6) and (7) are determined from the experimental data on the oxide film thickness growth with time.
The border x_1 movement is described by the equation

$$\frac{dx_1}{d\tau} = 0.5\frac{k_{Al_2O_3}}{\left(1+\dfrac{1}{s}\right)}\frac{\rho_{Al_2O_3}}{\rho_n}\frac{1}{\sqrt{\tau}}$$

derived with regard to the stoichiometric relationship between Al and oxygen masses consumed to form an aluminium oxide. The relationship is used in the model of parabolic law of oxide film thickness growth (6.7).

According to the accepted model prototype [6] the following concentration values are set on movable borders x_2 and x_3:

$$C(x_{2-},\tau) = C(x_{3+},\tau) = C_\gamma, \quad C(x_{2+},\tau) = C(x_{3-},\tau) = C_{\gamma+\beta}. \tag{8}$$

Then by analogy with the boundary condition (5) for a movable border x_4 we can write the aluminium diffusion flow from a coating to the right to form the interdiffusion zone $\Delta y = x_5 - x_4$ and aluminium diffusion to a basic metal as

$$J_b(x_{4-}, \tau) = -D_{ef} \frac{\partial C(x_{4-},\tau)}{\partial x} \tag{9}$$

In compliance with the physical model (Fig.2) the aluminium flow (9) arrived from the coating takes part in the formation of new phases in the interdiffusion zone $\Delta y = x_5 - x_4$ thick and uniformly segregates in this zone, that is

$$J_b(x_{4-},\tau) = W(x,\tau) \cdot \Delta y(\tau) \tag{10}$$

where the interdiffusion zone width $\Delta y = x_5 - x_4$ increase with time due to the border x_5 movement to the right and the parabolic law of its growth, as for the oxide film, is taken in the form of

$$\Delta y(\tau) = x_5(\tau) - x_4 = k_{iz} \cdot \sqrt{\tau - \tau_{iz}^0} \tag{11}$$

k_{iz} factors and τ_{iz}^0 value in (11) are determined from the experimental data on the interdiffusion zone growth with time. The expression for Al W mass arrived from the coating and uniformly segregated in the interdiffusion zone $x_4 < x < x_5$ is taken as dependent on $C_{\gamma+\beta} - C_\gamma$. (in power m) and has the form

$$W = W(x,\tau) = \begin{cases} k_w \cdot (C_{\gamma+\beta} - C_\gamma)^m, & x_4 < x < x_5 \\ 0, & x_1 < x < x_4, \quad x > x_5 \end{cases} \tag{12}$$

where k_w -intensity factor of aluminium segregation in the interdiffusion zone. Since the balance of masses must be met in the coating-oxide film-basic alloy system the expression for the total aluminium flow departed from the coating two-phase zone, in accord with (5) and (9), will take the form

$$J_\Sigma(\tau) = J_{ox}(x_{1+},\tau) + J_b(x_{4-},\tau) \tag{13}$$

In accord with the accepted physical model all aluminium flowing from the coating departs the coating $\gamma+\beta$ two-phase zone at the cost of β-phase consumption. Then the movement of borders x_2 and x_3 as well as the aluminium concentration decrease in the $\gamma+\beta$ two-phase zone can be described by the equation of mass balance between aluminium mass flows on these borders and the flows resulted from the aluminium concentration difference in $\gamma+\beta$ - and γ - phases $\Delta C = C_{\gamma+\beta} - C_\gamma$

$$J_\Sigma = J_\gamma(x_{2-},\ \tau) + J_\gamma(x_{3+},\ \tau) = \Delta C \cdot \frac{dx_2}{d\tau} + \Delta C \cdot \frac{dx_3}{d\tau} + (x_3 - x_2)\frac{dC_{\gamma+\beta}}{d\tau} \qquad (14)$$

where

$$J_\gamma(x_{2-},\ \tau) = -D_{ef}\frac{dC(x_{2-},\ \tau)}{dx} \text{ and } J_\gamma(x_{3+},\ \tau) = -D_{ef}\frac{dC(x_{3+},\ \tau)}{dx}$$

are diffusion flows to the oxide and basic alloy due to the aluminium concentration gradients to the left and to the right of borders x_2 and x_3 respectively.

After division of all the terms by J_Σ the expression (14) has form

$$1 = \Delta C \cdot \frac{dx_2}{d\tau}\Big/ J_\Sigma + \Delta C \cdot \frac{dx_3}{d\tau}\Big/ J_\Sigma + (x_3 - x_2)\frac{dC_{\gamma+\beta}}{d\tau}\Big/ J_\Sigma = g_2 + g_3 + g_{2,3} \qquad (15)$$

where

g_2 and g_3 — total aluminium mass fractions gone from the coating due to the movement of borders x_2 and x_3 respectively, $g_{2,3} = (1 - g_2 - g_3)$ — a fraction of aluminium mass gone from the coating due to the Al β-phase amount decrease in the $x_2 < x < x_3$ zone.

The g_2 and g_3 quantities having a direct effect on the rate of borders x_2 and x_3. movement are also taken as dependent on the concentration difference $\Delta C = C_{\gamma+\beta} - C_\gamma$

$$g_2 = k_2 \cdot \frac{\Delta C}{C_n^0}, \ g_3 = k_3 \cdot \frac{\Delta C}{C_n^0} \qquad (16)$$

The laws of borders x_2 and x_3 movement and Al $C_{\gamma+\beta}$ amount decrease in a two-phase zone can be derived from expressions (15) and (16)

$$\frac{dx_2}{d\tau} = J_\Sigma \frac{k_2}{C_n^0}, \ \frac{dx_3}{d\tau} = J_\Sigma \frac{k_3}{C_n^0}, \ \frac{dC_{\gamma+\beta}}{d\tau} = J_\Sigma (x_3 - x_2)\ (1 - g_2 - g_3) \qquad (17)$$

The k_2 and k_3 coefficients of proportionality in (16) are determined from expressions (16) and (17) based on the experimental data on the dynamics of borders x_2 and x_3 movement and the value of platform $C_{\gamma+\beta}$ in the region $x_2 < x < x_3$ for different sample exposure times.

The association of total Al $C_{\gamma+\beta}$ content with the β-phase $C_\beta(\tau)$ amount in the coating is described by the expression

$$C_{\gamma+\beta}(\tau) = C_\beta(\tau) \cdot C_\beta^{Al} + \left[\ 1 - C_\beta(\tau)\right]\ \cdot C_\gamma \qquad (18)$$

where

$C_\beta^{Al} = const$ is Al amount in β-phase.

The diffusion factor D_{ef}, k_w factor and the index of power **m** in the mathematical model (2) - (18) are determined from the experimental data by solving the inverse problem of diffusion.

The diffusion factor D_{ef} in (2) is valid for all the region of solution except for the subregion $x_2 < x < x_3$ where it was taken to be equal to a large value because of the lack of a space aluminium concentration gradient. The accumulated in the interdiffusion zone aluminium

diffuses partly back to the coating as a result of the aluminium concentration gradient to the right of the borders x_4

The appearing here diffusion flow

$$J_{iz}(x_{4+},\ \tau) = -D_{ef}\frac{\partial\ C\left(x_{4+},\tau\right)}{\partial\ x}$$

returns to the interdiffusion zone by adding to the main flow (9).

The distinction of the above model from that in [6] is not only in the account for the interdiffusion zone but also in the introduction of total aluminium mass fractions g_2 and g_3 in (15) which departed the coating due to the movement of borders x_2 and x_3

This allow for a wider application of the model (2) -(18) to different coating compositions for which the rate of movement in not defined on the whole by concentration gradients on borders x_2, x_3 and x_4. In term of the thermodynamic theory of diffusion, these borders can be determined by complex processes of the β and γ phase formation dissolution in a solid solution, but the practical application of this theory for complex systems under consideration is rather conjectural. Following assumptions are accepted in this model:

- the character of main physical-chemical processes occurring in the «coating-substrate» system does not change with time;
- only one element (Al) takes part in the formation of an oxide. This assumption for the coating type at hand is conformed by experimental investigations for up to 20000 hours
- the oxide forms on the border x_1 only;
- aluminium comes to the interdiffusion zone only from a coating ;
- the diffusion factor D_{ef} derived by the IPD solution is an effective characteristic independent of time;
- the formation of new phases at the interface coating-basic alloy is not accounted for;
- no oxide film spallation takes place.

The above formulated mathematical model of diffusion and oxidation processes is integrated by means of the numerical method of finite differences using the inexplicit diagram and iterative method of nonlinearity accounting.

5. Calculation results

The application of calculation and experimental approach to the analysis of aluminium, oxidation and diffusion processes in a coating 100 **μm** thick is considered. The coating contains Ni35%, Co30%, Cr24% and Al8.4% (here and below the concentration is given in weight percents unless otherwise specified).

The mathematical model (2) -(18) was used in calculations. The above described calculation-experimental approach was used for experimental conditions at 950ºC and exposures for 700, 10000 and 20000 hours. The model parameter identification was performed with the use of exposure for 700 and 10000 hours (Fig.12a, 12b). The results of Al and **β**-phase concentration distribution prediction were compared to the results of experimental exposure for 20000 hours (Fig.12b).

The main input parameters in the model (2) -(18) were diffusion factors D_{ef}, intensity factor of aluminium segregation in the interdiffusion zone k_w, the index of power **m,** weight coefficients k$_2$, k$_3$ and coefficients k_{ox}^*, k_{ox}^{**}, and τ^0 . The coefficients k_{ox}^*, k_{ox}^{**}, and τ^0 in the parabolic equations(6,7) were found by the approximation of experimental data $\Delta x_{ex} = f(\tau)$
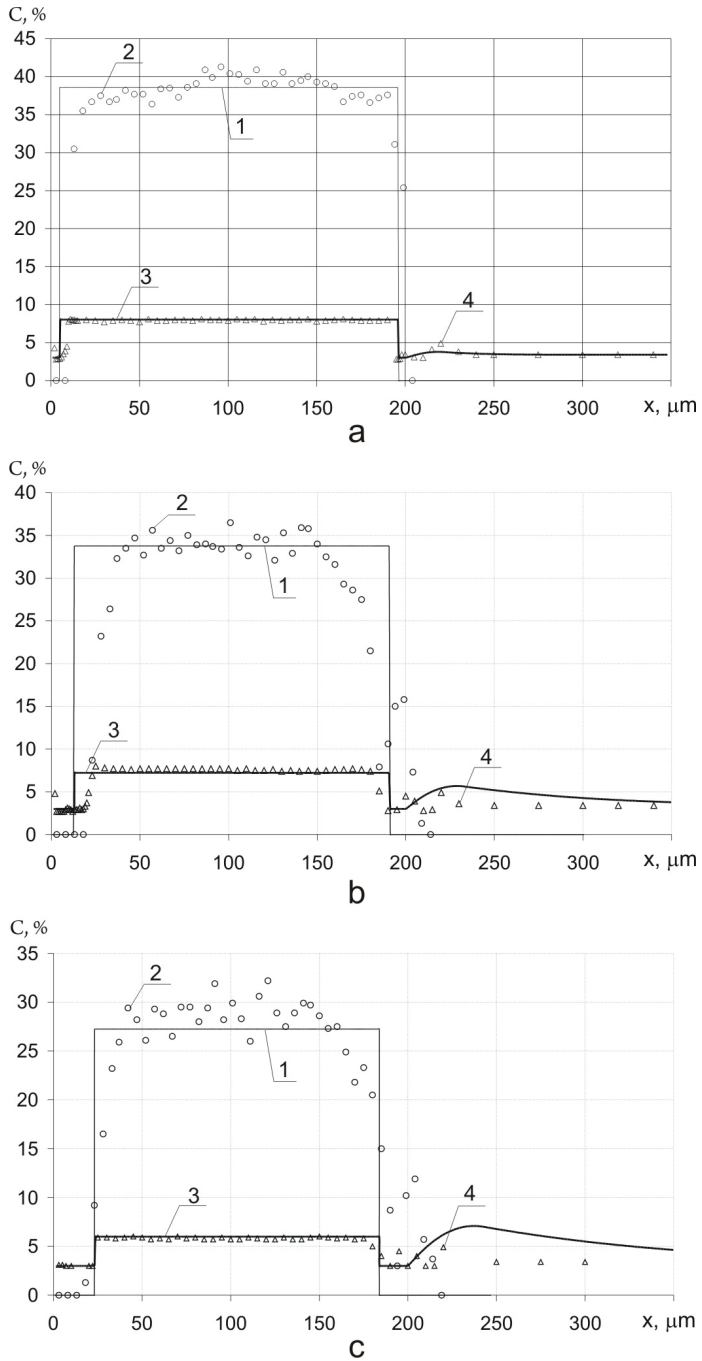
Fig. 12. Comparison of calculated and measured concentration profiles

for exposures 7000 and 10000 hours. In our case for the temperature 950°C k_{ox}^{*} = 2.88·10⁻⁹ m/s⁰·⁵, k_{ox}^{**} = 7.44·10⁻¹⁰ m/s⁰·⁵, τ^0 =-3.3·10⁷ s.

The weight coefficients were preestimated from the analysis of experimental data k_2=0.24, k_3=0.16.

The diffusion factor D_{ef}, the intensity factor of aluminium segregation in the interdiffusion zone k_w and the index of power **m** were found by IPD solution. The initial values of these factors were taken as follows: D_{ef} =1.0·10⁻¹⁵ m²/s, k_w =1.0·10⁻⁸ s⁻¹ , **m** = 0.5.

The IPD solution was performed by the method described in more detail in [10]. The parameter values found by using the IPD solution were D_{ef} =7·10⁻¹⁶ m²/s, k_w =1.37·10⁻⁷ s⁻¹ , **m** = 0.65.

The index of power appeared to be constant **m** = 0.65 for all three temperatures in the experiments. The C_γ value was taken from the experiment as equaling 3.0%.

It is commonly assumed that the time of a complete **β**- phase dissolution is a NiCoCrAlY-type coating life. This criterion is determined by the fact that after the **β**- phase disappearance the aluminium concentration in a coating is not sufficient for maintaining the protective oxide film formation. Further operation of the coating with the dissolved **β**- phase brings to the rapid oxidation of blade coating and basic alloy layers, which is impermissible.

The calculation results of the time of **β**- phase disappearance in the coating for three temperatures 900, 950 and 1000°C are given in Fig.13.

Thus with the above criterion of coating lifetime in mind a lifetime of NiCoCrAlY-type coating with the initial Al amount 8.4% and 20**μm** thick is considered to be 50 thousand hours at 900°C, 22 thousand hours at 950°C and 12.5 thousand hours at 1000°C.

By using defined model parameters the corrosion lifetime of different coatings was assessed in comparison with the obtained experimental data (Fig.14, Table3).
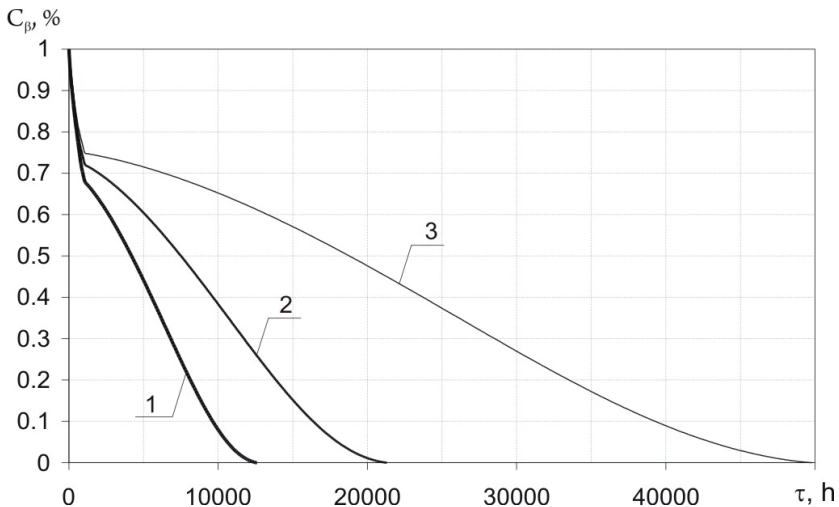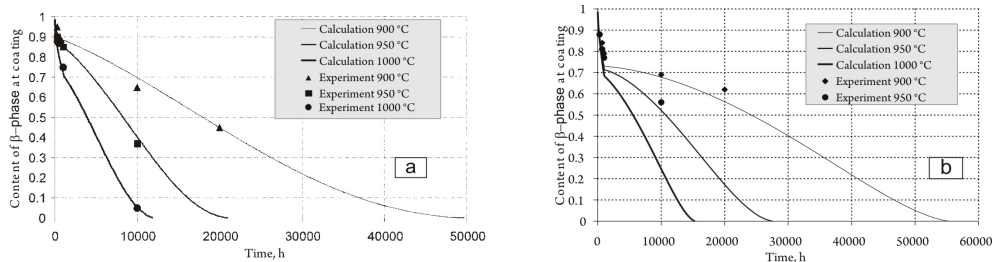

Fig. 13. B-phase C… (volume %) concentrations in a coating depending on time ….. 1- at T=1000°C, 2- at T=950°C, 3 - at T=900°C

a-   Ni30Co28Cr8AlY   200µm thickness on In738LC alloy,
b-   Ni30Co28Cr10AlY   200µm thickness on IN738LC alloy.

Fig. 14. The life of different coatings determined from the β-phase amount (volume %) versus time curves for coatings

Coating (base alloy)	Calculated coating life time (h) at temperature, ^0C			
	900	950	980	1000
Co29Cr6AlY (GS6K)	11400	5000	-	1000
Ni30Co28Cr8AlY (100 µm) (IN738 LC)	-	12500	-	-
Ni30Co28Cr8AlY (200 µm) (IN738 LC)	49000	21000	-	12000
Ni30Co28Cr10AlY (100 µm)	-	-	-	-
Ni30Co28Cr10AlY (200 µm) (IN738 LC)	55000	28000	-	-
Ni25Cr5Al2SiTaY (CM 247 LC)	46000	26000	-	8000
Ni25Co17Cr10AlYRe (Rene80)	58000	34000	-	11500
Ni25Co17Cr10AlYRe (LPPS) (PWA1483 SX)	-	51400	-	22800
Ni25Co17Cr10AlYRe (VPS) (PWA1483 SX)	52700	-	20000	-

1 -coating (on alloy), 2 - Calculated coating life (hour at temperature., 3 -on

Table 3. The results of different coating life calculations

6. Conclusions

The proposed calculation and experimental approach has shown its efficiency in lifetime assessments of gas turbine blade coatings. The model taken from [6] was significantly improved.

The existence of the interdiffusion zone was modeled and calculated and a more flexible approach to the calculation for two-phase border movement was introduced in the mathematic model as a result of model improvement.

There is a good agreement between experimental and calculated aluminium concentration profiles and β- phase amount in a coating.

The application of the approach made it possible to evaluate model input parameters, in particular, to determine aluminium diffusion factor and perform rotating blade life predictions.

7. References

P. Kolomyteev, Gaseous corrosion and strength of nickel alloys|| M.: Metallurgy, 1984, — p.216.

N. Nikitin, Metal heat-resistance calculation. M.: Metallurgy, 1989, — p.207.

Superalloys II, edited by Ch. Sims, N. Stoloff, W. Hagel. Book 2. M.: Metallurgy, 1995, — p.384.

Meirer S. M., Nissleu D. M. , Sheffer K. D. , Cruse T. A., Thermal Barrier Coating Life Prediction Model Developed|| Trans. of ASME. J. of Eng. For Gas Turbines and Power, 1992, v116, №4.p. p. 250-257.

J. Nesbitt, Numerical Modelling of High-Temperature Corrosion Processes/|| Oxidation of metals, 1996, 44, p. p. 309-338.

E.Y. Lee, D. M. Chartier, R. R. Biederman and K. D. Sisson, Modelling the microstructural evolution of M-Cr-Al-Y coatings during high-temperature oxidation.|| Surface and coatings technology, 1987, 32. p.p. 19-39.

J. Nesbitt, R. Heckel, Interdiffusion in Ni-rich, Ni-Cr-Al Alloys at 1100 and 1200ºC: Part II. Diffusion coefficients and Predicted Concentration Profiles|| Met.Trans., 1987, 18A,December, p.p. 2087-2094.

E. Kartavova, P. Krukovsky, Modelling of Heat Transfer Processes in protective coatings of GT blades:|| Industrial Heat Engineering,1996.№6, p.p. 23-30.

 P. Krukovsky, V. Kolarik, K. Tadlya, A. Rybnikov, I. Kryukov, M. Jues-Lorento, Lifetime Modelling of High Temperature Corrosion Processes.|| Proceedings of an EFC Workshop, 201, p.p. 231-245.

P. Krukovsky, Inverse Problems of Heat Transfer (general engineering approach) — Kiev, Institute of Engineering Thermal Physics NaN Ukraine, 1998. —p.218.

K. Borggreen, P. Auerkari, Assesment of the thermal damage in the superalloy GTD — Baltika V. , Condition and Life Management for Power Plants, vol. 1, 2001, p.p. 125-137.

Brady M. P. , Pint B. A., Tortorelli P. F., Whright, Hanrahan R. J. High-temperature oxidation and corrosion of intermetallic || Corrosion and environmental degradation, edited by M. Schutze|| v. II, Ch. 6, 2001 — p.p. 229-311.

Tamarin Y. Protective coating for turbine blades|| ASM International, Materials Park, ON, 2002, p.247.

Failure Investigation of Gas Turbine Generator Cooling Fan Blades by Experimental and Numerical Analysis

Ali Jahangiri
Power & Water University of Technology (PWUT)
Iran

1. Introduction

In gas turbine power plants, a fan is used as a cooling system to dissipate generated heat in coils (copper conductors) and generator electric circuits at the end sides of its rotor. the general map of generator has been shown in figure 1. The entrance and exit path of air for cooling has seen in this map. The cooler air rotates in one close cycle, in this manner, the air after passing from inside of rotor, exits from the top of generator, and with passing from one cooler, cools with water flow. The air after cooling, conducts to rotor from two sides and by the fans that are set up on the Retaining Ring, is blown in two sides of rotor.
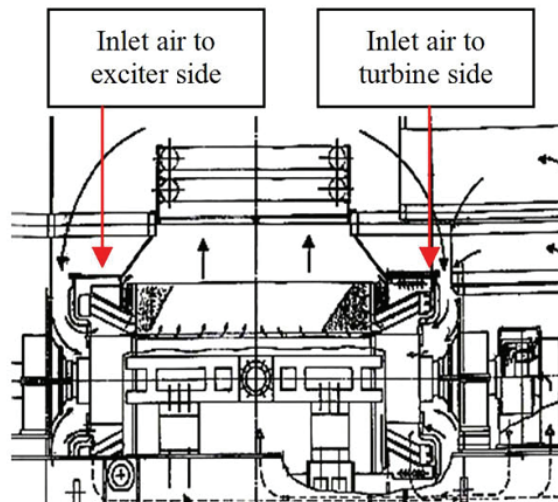
Fig. 1. Generator diagram

At each of two sides of generator sets up 11 blades as an axial fan that separates with 11 spacer pieces. Position and arrangement of blades and spacer pieces on Retaining Ring is shown in figure 2.
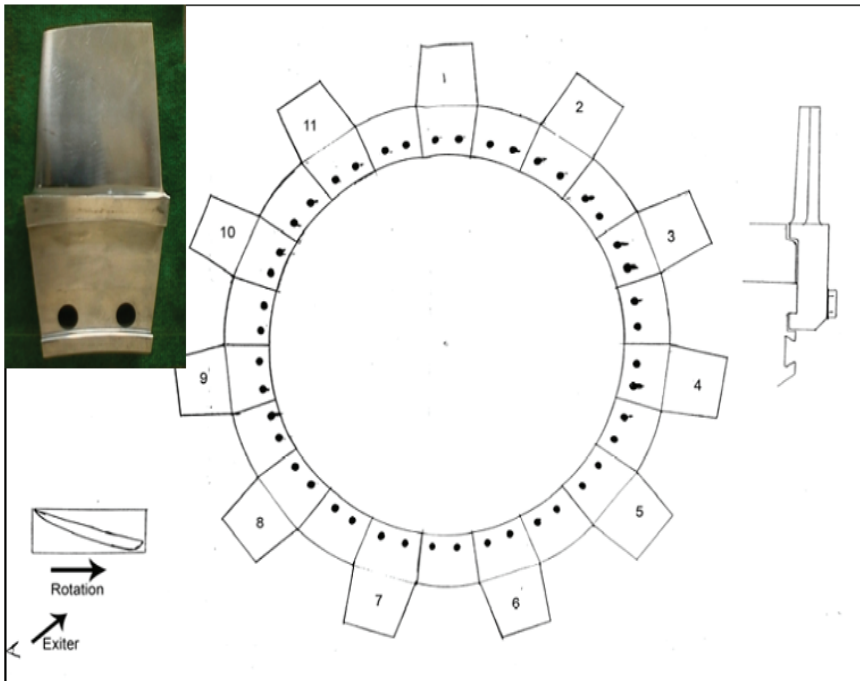
Fig. 2. Arrangement of blades around Retaining Ring

It is obvious that the fan blade has effective factors on the generator performance. In some cases, fracture of blades can cause short circuit between rotor and stator and consequently generator explosion and lots of financial loss. Cooling system equipments were supplied by GEC-ALSTHOM Belford under the following conditions; Turbine rotation=3000 rpm; output power=118 MW; The fracture of cooling fan blades has been occurred five times at the turbine side of the generator in our case study, just 10 hr after resuming operation following the last overhaul.

It must be noticed that all the failed blades had the 19° angle of attack and after failure; GEC-ALSTHOM replaced them by 14° angle of attack (without change in alloy type) in order to decrease the forces made to blades. A width of 14° blades is lower than 19°, but the height of them is same. The face of two blade types is compared in figure 3.

Figure 3 defined the deference between angle and blades dimensions.

The review of pervious blade fracture analysis notes shows that it has been a serious problem in different types of blade.

Failure investigation of blade and disk in first stage compressor in an aero engine is done and Metallurgical examination and stress analysis revealed that the design shortcoming resulted in over-compensation of centrifugal bend moment and bad contact condition (Xi et al., 2000).

A series of mechanical analysis and examination on a failed blade in gas turbine engine has been performed and nonlinear finite element to determine the stress of the blade, in order to identify the case of blade failure has been utilized (Hou et al., 2002; Beisheim & Sinclair, 2002).

Fig. 3. Deference between 2 types of blade in angle and their dimensions

The efficacy of a fracture mechanics methodology to model the crack growth behaviour of fatigue nucleated cracks obtained under test conditions similar to those found in turbine engine blade attachments has been verified and Crack propagation lives has been calculated using stress results of FEM analysis (Hutson et al., 2005) the three dimensional fatigue crack in a typical military aircraft engine fan blade attachment by Franc3D has been simulated (Barlow & Chandra, 2005; Paris et al., 1961-3). Crack propagation trajectories under mixed-mode conditions have obtained using the planner and maximum tangential stress crack extension criteria.

In the following of these papers in this note we have performed two series of analyses and their results evaluated to identify the possible causes of failure:

Mechanical and experimental Investigation as follows:

1. Review of the history of the blades repairs and/or modifications (change in blade angle of attack from 19º to 14º).[fig 3]
2. Review of the history of the unit operation.
3. Material and microstructure (quantometry).
4. Metallurgical examination of the fractures to identify the metallurgical mode of failure (SEM).

Numerical analysis on14º and 19º blades:

1. CFD analysis in order to study the imposed stresses of the fan blades due to operation.
2. Application of the finite element method for modal and harmonic analysis to calculation of the natural frequencies, stresses and Vibration.

2. Mechanical and experimental Investigation

2.1 Visual inspection

The statistical data revealed that all of these failures have happened in the first hour of operation after the first operation or repair of gas turbine, meaning that no fracture has happened after 100 hr of operation. On opening the turbine casing, three kinds of blades (for using 19º attack angle) were found. Broken blades, cracked blades and uncracked blades.

The failure was at the turbine side of the generator and there was no crack at exciter side. The failure site was in the transition radius between the blade airfoil and the blade base. Crack initiation point was at the centrally part of the airfoil on its concave surface. Some portion of the surface appeared black and pitted due to electric spark. But by changing attack angle of blades to 14° have not seen any failure. However temperature rise in generator case was been higher and it was result of decreasing in sucked air flow rate for generator cooling (Poursaeidi & Salavatian, 2009; Moussavi Torshizi et al., 2009).

2.2 Material and microstructure

Results obtained from the quantometry technique test that performed over blades show that the blade material is aluminum 2024 (table1). Also result of metallurgical examination over blades shows that blades are not produced by die casting, but rather molding, milling, shaping and finally polishing of the blades surfaces. Crystals directed in the direction of the blade length are a proof of this production method. Heat treatment performed in this blade is of the T351 heating operations (Moussavi Torshizi et al., 2009). Mechanical behaviors of aluminium 2024 are presented in table 2.

Elements	Al	Zn	Si	Fe	Mn	Mg	Cu
quantometry test	Base	0.07	0.07	0.11	0.67	1.36	3.97
Al 2024	Base	_	_	_	0.6	1.5	4.4

Table 1. Chemical composition of blade and its comparison with aluminium 2024 alloy (Joseph, 1993).

Alloy	Ultimate tensile stress σ_{ut}	Yield tensile stress σ_{yp}	Fatigue endurance limit σ_e
Al 2024	470 MPa	325 MP	140 MPa

Table 2. Mechanical strength of aluminium 2024 (ASM, 1990).

At 3000 rpm, (50Hz frequency of powerplant generators) dynamic stresses have been measured for any 14° and 19° blades, (table 3). Comparison of these stresses with the limit stresses (presented in table 2) shows that the stresses imposed to the blade are much lower from this limit and therefore there is not possibility of blade failure in normal operation conditions.

Blade number	Max.Stress in 3000 rpm
1FE	MPa 9
2FE	7.6MPa
3FE	18MPa
4FE	10.4 MPa

Table 3. Dynamic stresses in the blade (Moussavi Torshizi et al., 2009)

2.3 Study of fracture surfaces with SEM

Its obvious that one of the most important ways to investigation of the failure pieces, is being failure surfaces study. This subsection engaged to inspection the failure surfaces and defining it's result. While there is two possibility, gradual failure in the effect of endurance (fatigue) and / or failure in result of external material impact (Dimple Rupture).

In order to study of failure surface and compare quality of these 2 possible failure mechanism with standard failure handbook of this alloy (AL2024) to recognise failure main cause, has employed Scaning Electron Microscope (SEM).

Because of microstructure change in failure surface, SEM could have been able to prepare best high quality picture of surface with highest accuracy (scaled to X1000).

In this section, theory of fatigue failure and dimple rupture is considered and for which one of the mechanisms, one surface with area 1cm×1cm is prepared so that for first mechanism is used of same damaged blades at powerplant generator, breaking incident and also for preparing surface by another mechanism a piece with this alloy is broken with only one knock of external object impact.

2.4 Survey of failure (scaled by SEM) surfaces

With comparison between fig 4(a) and fig 4(b) that first is surface of broken blade at powerplant incident and second is broken in type of dimple rupture (breaking potholes) has been obviously seen, there is no any resemblance between these 2 mechanism of failure and quality of surfaces is quietly differvaried.

Therefore, existing lines in fig 4(a) doubtlessly has been fatigue lines. The faigue lines show that crack is initiated at one side and propagated in significant time.

This studies show that:

1. the wing is not interrupted in one moment in the effect of contact the external object.
2. crack is started from one or more point in the middle part of cave surface of wing (unsuitable quality of surface can be result of the start of crack) and is leaded to interruption of it , in the effect of oscillatory loading of blade, and made progress in the time of turning.
3. however cannot declare exactly the reason of the starting of the crack.

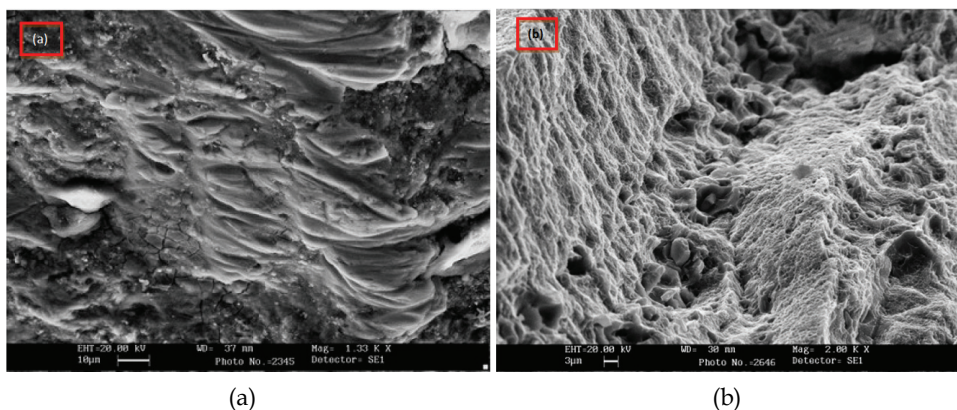(a)   (b)

Fig. 4. (a) fatigue surface failure (scaled ×1330) (b) Dimple rupture result of instant impact (scaled ×2000)

But the contact of hard particles to wing, entrance them in the surface, creation weave centralization and the starting of crack of them is very probable.

Figure 5 has shown the final failure of surface and the ration of that to fatigue failure of surface as seen, the most of surface is created with progress crack in the effect of periodically and fatigue loads.
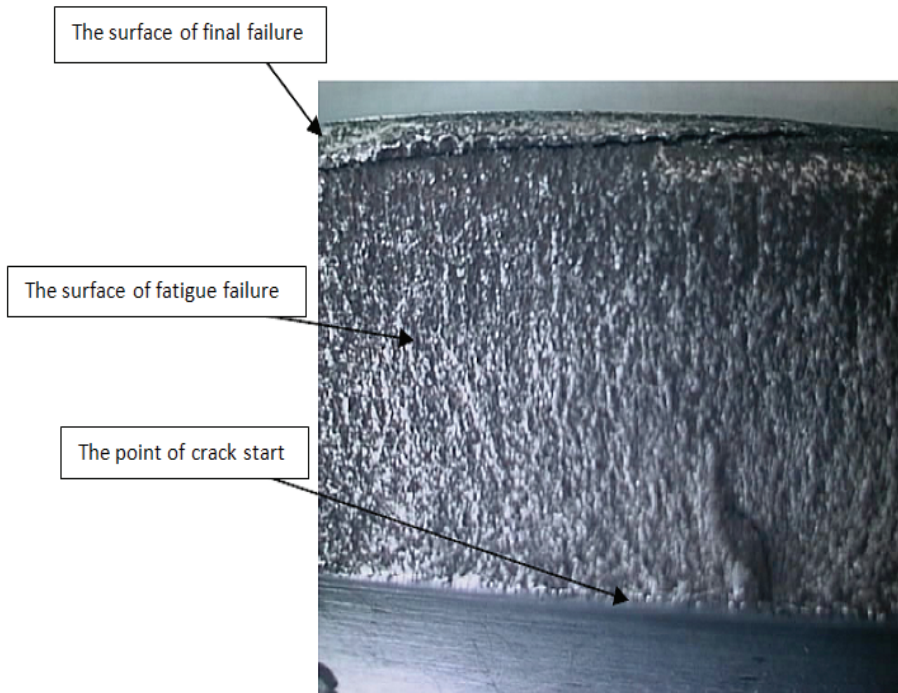

Fig. 5. Comparison between final and fatigue failure surface

3. Numerical analysis on14^o and 19° blades

In order to study the imposed stresses of the fan blades due to operation, fan should be simulated. To do this, Computational Fluid Dynamic (CFD) code and Finite Element Method (FEM) were deployed to analysis stresses and vibration. Separation phenomena and turbulent flow (vortex formation) might be cause of vibration in fan's blades.

Vibration due to oscillatory change of pressure distribution in two sides of blade may cause blade fatigue. Therefore our purpose from CFD analysis is to achieve air velocity distribution around blades and also study of air flow lines (in order to observe probable vortex and related problems) and also determination of force resulted from air pressure over blades. In this order after determination of blade profile (by using scanning digitiser camera ATOS[1] (fig 6)) modelling air passage channel is necessary, which was performed by CAD

---

[1] One of the new and careful methods for acquiring solid profile by digital 3d photography

software (fig 7). The 3-dimentional model thus obtained, is then imported to mesh generation software, which generates the meshing for the volume. This file as a case file could be imported to CFD code (fig 8).
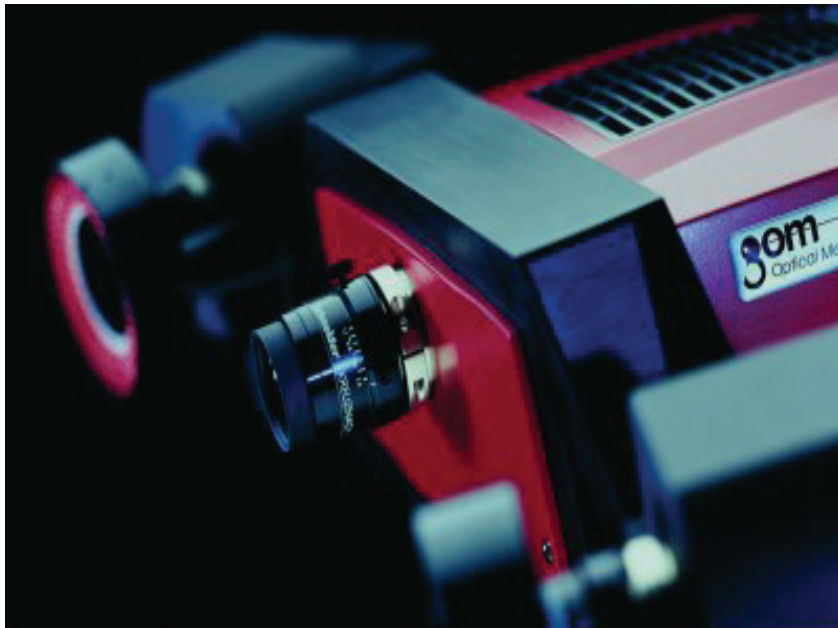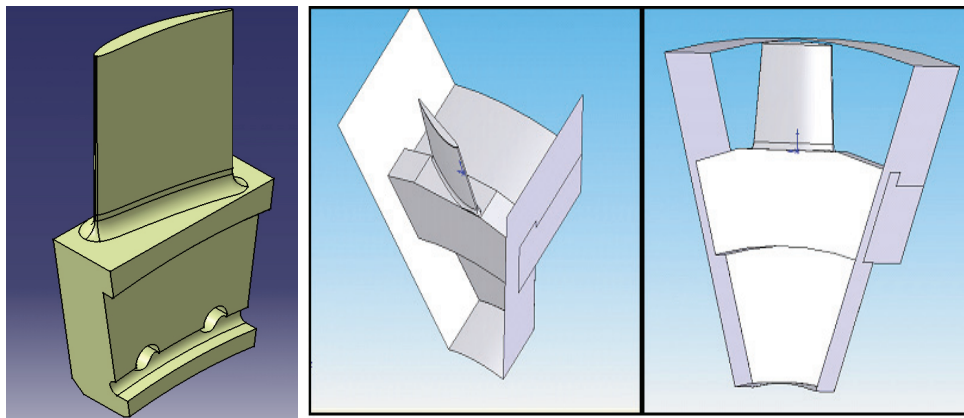

Fig. 6. Scanning digitiser camera

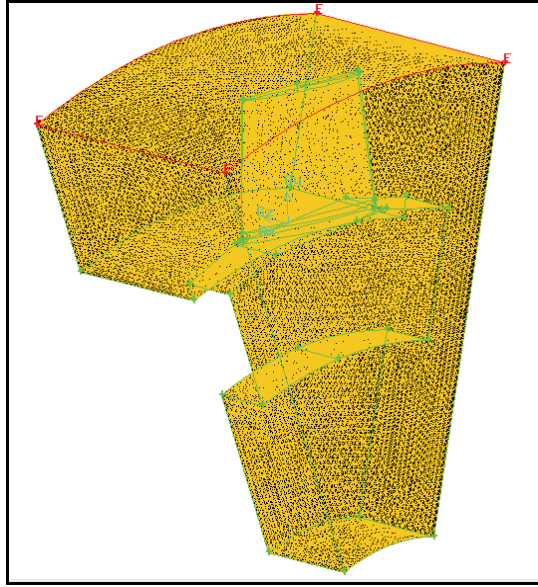Fig. 7. 3-dimentional model of blade and related passage channel

Fig. 8. Meshing domain in solution range

4. Computational Fluid Dynamics (CFD) analysis

4.1 Discretization procedure

The domain shown in Fig. 8 is divided into unstructured grids. The governing equations are solve under the boundary conditions described below by using he segregated method. Based on the finite volume method (FVM), the pressure is discretized by using the standard scheme. The momentum equations is discretized by use first order upwind scheme. The pressure–velocity coupling is treated by SIMPLE algorithm. Above discretization methods can satisfy the accuracy require under such mesh size for this problem.

"Steady state" was selected as solver and other conditions for flow and fluid are turbulent flow, compressible fluid (air) and incompressible flow (because the Mach number is less than 0.4).

4.2 Governing equations

Because of the turbulence action induced by high Reynolds swirling flow pattern, the standard k-ε two-equation turbulence model is selected and the continuity and momentum that respectively describing mass and momentum can be written as follows (White, 2003):

$$\nabla.V = 0 \tag{1}$$

$$(V.\nabla)V = -\frac{1}{\rho}\nabla P + \nabla.\left(\frac{\sigma}{\rho}\right) - \rho g + S \tag{2}$$

The turbulence equations describing turbulent kinetic energy (k) and turbulent dissipation rate (ε) are as follows:

$$(V.\nabla)k = \nabla.[(v + v_t/\sigma_k)\nabla k] + P - \varepsilon \tag{3}$$

$$(V.\nabla)\varepsilon = \nabla.[(v + v_t/\sigma_\varepsilon)\nabla\varepsilon] + c_{1\varepsilon}\frac{\varepsilon}{k}P - c_{2\varepsilon}\frac{\varepsilon^2}{k} \tag{4}$$

Here P is the generated kinetic energy of turbulence.

In these kinds of problems that a moving object is the cause of fluid flow, it is possible to take a rotational component to axial velocity of air to count blade rotation (equivalent to 314.1592 rad/s as calculated below).

$$f_r = \frac{3000 \text{r.p.m.}}{60} = 50 \text{Hz} \tag{5}$$

$$\omega = 2\pi \times f_r = 2\pi \times 50 = 314.1592 \ \text{rad/s} \tag{6}$$

4.3 Boundary conditions

"Velocity inlet" is assumed as air entrance condition. The total volumetric flow of the cooling air is 45.6 m³/s for using 19º blade, and half of that is directed towards fan of turbine end and the other half is directed towards fan of exciter end. In inlet duct cross section, which is a circle with a radius of approximately 70 cm, velocity of air is calculated as follows (Also it should be in mind that area of air passage, is the difference between channel and generator shaft cross section):

$$Q=V.A \tag{7}$$

r_1= 0.225 m (Radius of shaft) r_2= 0.696 (Radius of air channel)

Q= 45.6 m³/s

Then: $V = \dfrac{Q/2}{A} = 16.71 \, \text{m/s}$

Because air pressure is uniform for all of the outlet area and along its duct, (which will be approximately equal to ambient pressure) therefore "pressure outlet" is used. For reduction of solution domain to reach to the least logical possible domain, the periodic analysis would be used.

Solution convergence accuracy have been satisfied by iterating until residuals have decreased to minimum then result could have achieved and investigated.

4.4 Analysis of flow field & pressure

As see in fig. 9 (a) & (b), in both blade type air flow pattern has been completely usual. It is observed the path lines completely tangent over the blades and the separation phenomenon has not incurred.

Air pressure distribution over blades have also seen at these two figures. Maximum absolute value of pressure that imposed to 19º angle of attack blade have reached to 56kPa on bottom of blade surface and then resultant force over the blade is approximately equal to 346N. Tension result of this force is less than amount that solely causes to break the blade.

Also in 14º blade maximum pressure at the bottom of blade is reached to 39kPa that even is less than of 19º blade.
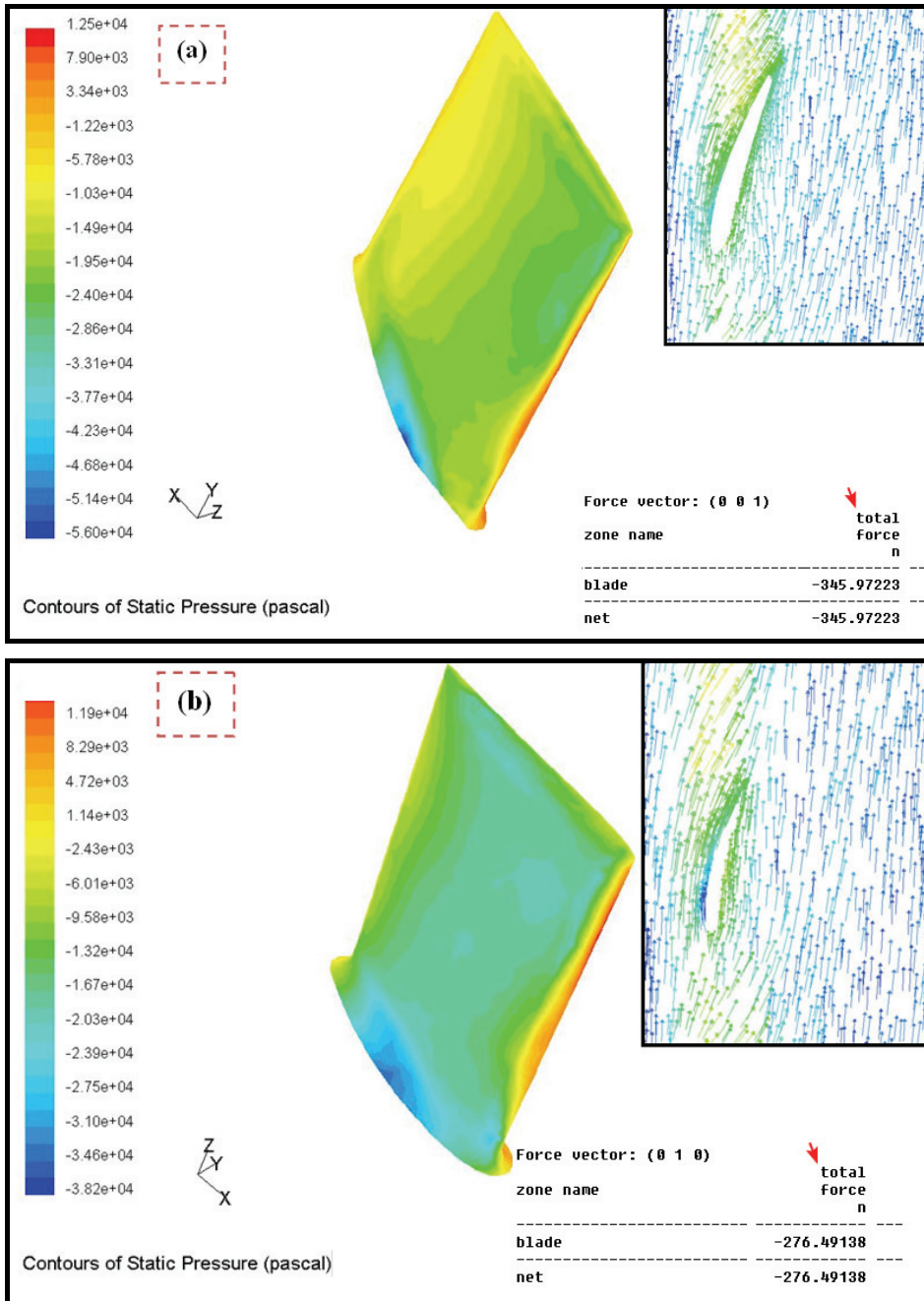
Fig. 9. (a) pressure Contour & velocity vectors passed over 19o angle of attack blade
(b) pressure Contour & velocity vectors passed over 14o angle of attack blade

While 19o angle of attack blade has been changed with 14o blade amount of force imposed to blade would decreased about 20% and is reached from 346 to 276N then, these forces caused by air flow are not enough to cause the blade rupture.

5. Finite Element Method Analysis (FEM)

In order to determine the stresses acted on the blade and survey of the possibility of its failure caused by resonance, the finite element method, was used to blade modelling and two analysis have been performed by finite element method:
1.   Modal analysis
2.   Harmonic analysis
The modal analysis on natural frequency and the harmonic analysis based on different excitation frequencies were done.

5.1 Modal analysis
First, the amount of bolts tightening was modeled and its influence on blade natural frequency was studied. To evaluate these conditions, four different states were investigated for both of 19o and 14o blade:
1.   All the points around the bolts are fixed.
2.   All the points of the same height with bolts are fixed.
3.   In addition to all the points of the same height with bolts which are fixed, the elements, which are in contact with the retaining ring, will not also move.
4.   The whole blade root is fixed in all directions.
The natural frequency in the 5 modes for these four states were calculated. In table.4 these natural frequencies for fourth state in 2 blade types has been displayed.
In figure 10 and video No 1 displacement of both of blade tip at the first modal shape has shown. With respect to the fact that the first natural frequency of the 19o angle of attack blade in the fourth state (538 Hz) was very close (almost with 2% relative difference) to the frequency of the exciting force caused by shaft rotation (11 blades × 50 rad/s = 550 Hz) and therefore the incurrence of resonance in above conditions is very probable, This state has been selected for finite element harmonic numerical simulation. Wheras 19o blades is replaced with 14o blades the first natural frequency in fourth state (413.49 Hz) will not be close (with 33% relative difference) to exciting frequency and therefore resonance condition will not occurred.

Mode Shape Number	Natural Frequency (Hz) 19o blade	Natural Frequency (Hz) 14o blade
Mode No 1	537.88	413.49
Mode No 2	1339.8	1232.6
Mode No 3	2693.8	2365.9
Mode No 4	2637.1	2794.5
Mode No 5	3879.5	3837.1

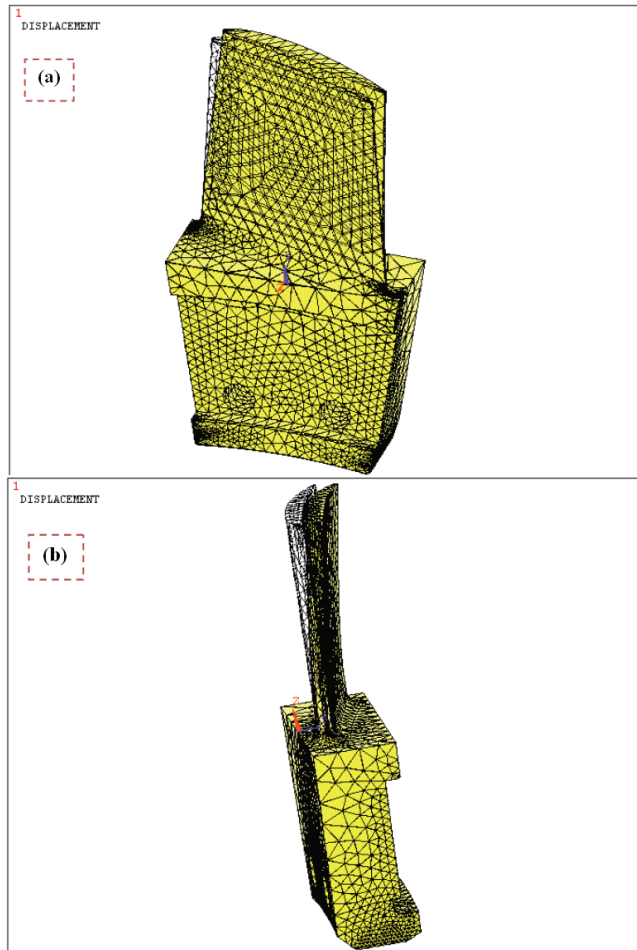Table 4. Calculated natural frequency in the 5 modes for 19o and 14o blade

Fig. 10. (a) blade tip displacement at the first modal shape for 19o angle of attack blade
(b) blade tip displacement at the first modal shape for 14o angle of attack blade

5.2 Harmonic analysis

In harmonic analysis, the frequency of external forces (air flow and shaft rotating force) acted to blades, increases step by step, (from zero to 1000Hz) then, domain, difference shapes of vibrations and tension result of these acting external forces with, changing in blade type, account for various frequences.

5.2.1 Harmonic analysis for 19° blade

From CFD analysis force acted by air flow on 19o blade was calculated about 346N. By acting these external forces to blade in the various frequencies (between 0 to 1000 Hz), blade tip oscillation domain (blade tip displacement), is accounted. Blade tip displacement for these conditions is shown in figure 11.
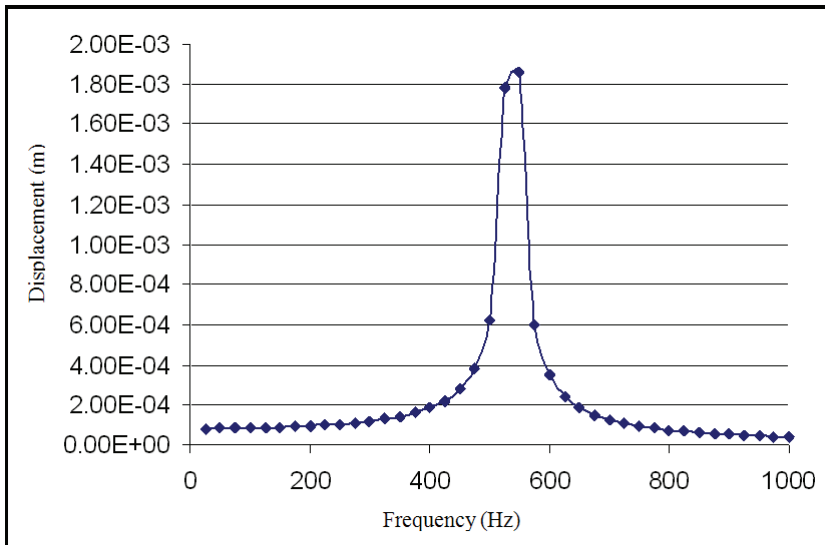
Fig. 11. 19oBlade tip displacement at various frequencies in first mode of vibration
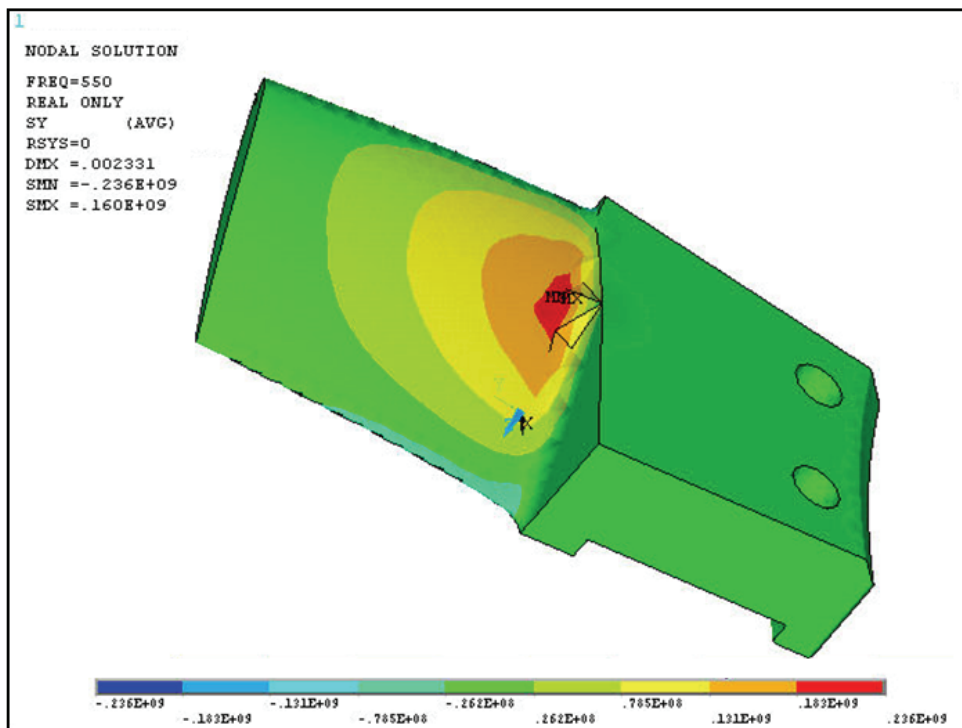

Fig. 12. Contour of computed Von Mises tension exerted on 19oBlade at 550Hz frequency

As seen, in 50Hz frequency blade tip displacement is reached to about 82μm this value grows with increasing frequency to the extent of 425 to 450 Hz reached to 220 to 280 μm.

In first Natural frequency vicinity, displacement is increased intensely and is reached to about 1.8mm and hereafter by frequency increasing, the blade tip displacement again decreases intensely.

With notice to figure 11 resonance condition happening will be imminent, when the blade has been excited with 550Hz frequency, that is near to first natural frequency. The blade will been vibrated intensely in this condition and as seen in fig 12, Von Mises tension at sensitive spaces of blade (bade root) is reached to 236MPa.

By referral to table 2 is been obvious that tension with amount of 236Mpa is far less than any mechanical strength of alloy except fatigue endurance limit, namely, blade material could be able to endure any forced statistical loads even at resonance state.

But thence that maximum amount of von mises tension is larger (68%) than fatigue endurance limit (236MPa > 140MPa) therefore, when blade is been encountered to fatigue condition at resonance condition, 19º blade couldn't be able to endure fatigue condition infinitely and blade fracture will be unavoidable.

5.2.2 Harmonic analysis for 14º blade

From CFD analysis force acted by air flow on 14º blade was calculated about 276.5N. By acting these external forces to blade in the various frequencies (between 0 to 800 Hz), blade tip displacement, is accounted. Blade tip displacement for these conditions is shown in figure 13.

As seen, in 420Hz frequency blade tip displacement is reached to about maximum quantity (4mm) because of this reality that 420Hz frequency is nearest value to first natural frequency of 14º blade (413.49Hz). This amount of displacement (4mm) has been even more than of 19º blade at vicinity of its first natural frequency (1.8mm).

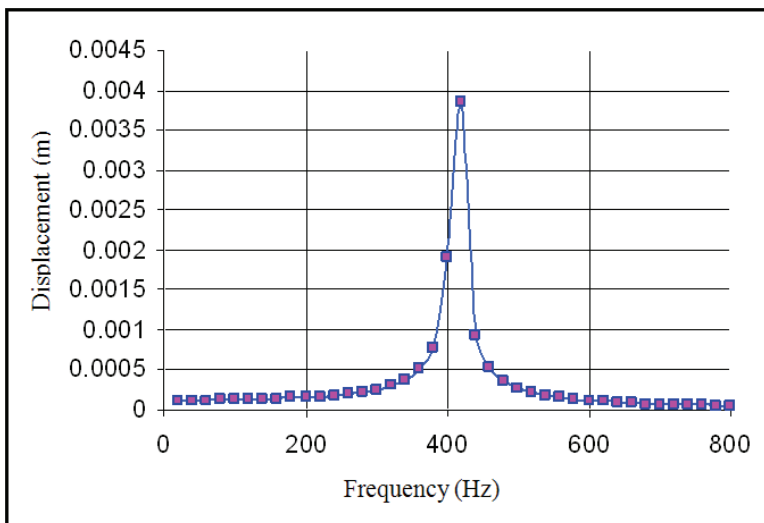Fig. 13. 14ºBlade tip displacement at various frequencies in first mode of vibration

With notice to figure 13 in 420Hz frequency resonance condition happening will be imminent, The blade will been vibrated intensely in this condition and as seen in fig 14, Von Mises tension at sensitive spaces of blade (bade root) is reached to 388MPa. So again when 14° blade is been encountered to fatigue condition at resonance condition, couldn't be able to endure fatigue condition infinitely and blade fracture will be unavoidable.
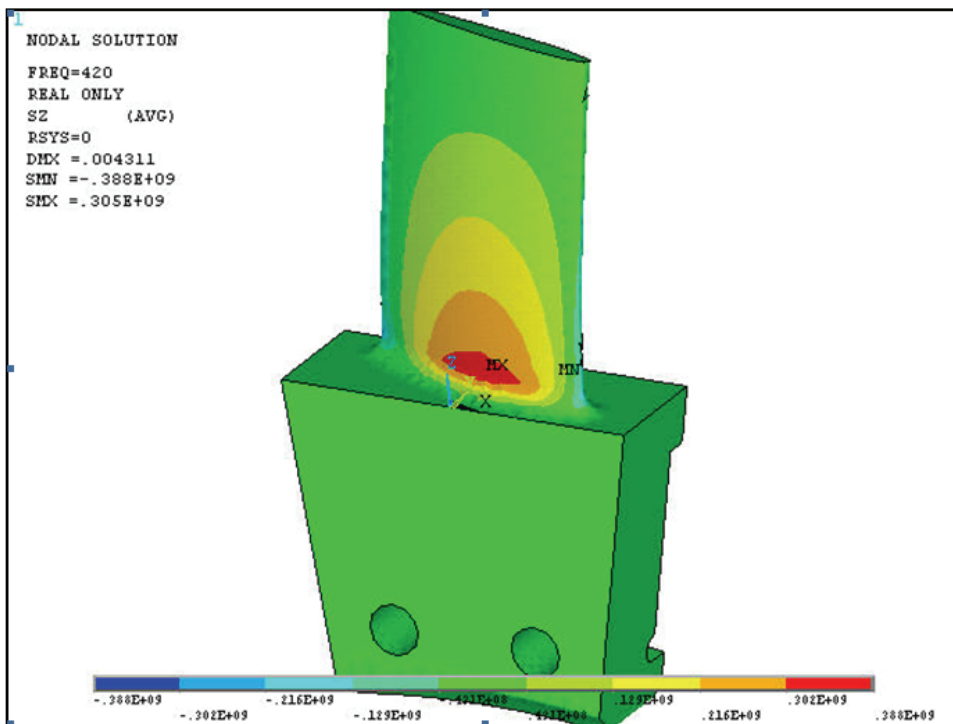

Fig. 14. Contour of computed Von Mises tension exerted on 19°Blade at 550Hz frequency

But as seen in fig 13, when the blade has been excited with 550Hz frequency, that is frequency of the exciting force caused by shaft rotation, 14° blade tip displacement will be less than 160µm. Therefore in this condition resonance state will not been happened and Von Mises tension encountered to 14° blade root will be less than 10MPa that is so small to comprised. Blade failure will never been occurred for 14° blade in this condition.

6. Conclusion

1. Experimental study of ruptured surfaces shows that the probability of a collision of a large external object and its instantaneous rupture is impossible.
2. CFD analysis shows that the forces caused by air flow are not enough to cause the blade rupture.
3. With respect to the obtained results, this analysis shows that the value of normal stress in most of conditions for 19 & 14° blades is about 10 MPa except in resonance state.

4. In the case of applying a force with a frequency of nearby 550 Hz, 19º blade will be exposed to a resonance frequency (As a result, with unsuitable blade fastening of the blade, resonance condition is probable) and because of applying stress at range of 160–236 MPa cyclically and exceeds the endurance limit of the material, it will reduce working life of the blade and lead to failure after a number of cycle.

5. In the case of applying a force with a frequency of nearby 550 Hz, 14º blade will not be exposed to a resonance condition and because of applying stress at limit of 10MPa, Blade failure will never been occurred.

6. Concerning the large number of turbines and regarding to this point that fracture happened in five case, early after operation (less than 100 h) and after the first operation or repair, and the point that if the element has not broken early after operation and has continued its usual work obtained results from CFD and vibration analysis, the most probable reason for breakage phenomenon is the way blades have been fastened (how fixed are bolts).

7. Acknowledgements

8. References

Anderson, T.L. (1995). *Fracture mechanics fundamental and applications,* CRC Press, 9780849316562, Colorado, USA

Alsthom Company report in conjunction with someone Gas Power Plant (1997)

ASM.; (1990). *Asm Handbook, Properties and Selection, Nonferrous Alloys and Special-Purpose Materials, VOL 2,* ASM International, 0-87170-378-5, USA

Barlow, K.W. & Chandra, R. (2005). Fatigue crack propagation simulation in an aircraft engine fan blade attachment. *Int J Fatigue*, 27., (1661-1668)

Beisheim, J.R. & Sinclair, G.B. (2002). On the three-dimensional finite element analysis of dovetail attachment. *Proceedings of ASME Turbo Expo,* ASME, Amsterdam

Biner, S.B. (2001). Fatigue crack growth studies under mixed-mode loading. *Int J Fatigue*, 23., (259–263)

Erdogan, F. Sih, G.C. (1963). On the crack extension in plates under plane loading and transverse shear. *J Basic Engng – Trans ASME*, 85., (519–527)

Failure analysis report of Iran-Montazer-Ghaem unit6. Iran Power Plant Repair Co; (2004)

Failure analysis report of Iran-Montazer-Ghaem unit4. Iran Power Plant Repair Co; (2004)

Failure analysis report of Iran-Neyshabour unit2B. Iran Power Plant Repair Co; (2003)

Forman, R.G.; Shivakumar, V. & Newman, J.r.J.c. (1994). Fatigue crack growth computer program. *NASA/FLAGRO,* Johnson Space Center, Houston, Texas.

FRANC3D Menu & Dialog Reference V2.2, (2002). *The Cornell Fracture Group,* Cornell University

Harter, J.A. (2004). *AFGROW users and guide technical manual*, Air Force Research Laboratory, AFRL-VA-WP-TR-2004, USA

Harter, J.A. (2008). *AFGROW USERS GUIDE AND TECHNICAL MANUAL,* AFGROW Directorate, Air Force Research Laboratory, Wright-Patterson AFB, OH, AFRL-VA-WP-TR-2008, USA

Hou, j.; Bryon, J.; Wicks and Ross A. (2002). An investigation of fatigue failures of turbine blades in a gas turbine engine by mechanical analysis. *Engineering Failure Analysis,* 9., (201-211)

http://www.cfg.cornell.edu/software/software.htm.

Hutson, A. Nicholas, T. & Johnc R. (2005). Fretting fatigue crack analysis in Ti–6Al–4V, *Int J Fatigue*, 27., (1582–1589), 10-1210-12

Jahed Motlagh, H.; Noman, M. & Eshraghi, M. (2003). *Limied section ANSYS,* Tehran university publication, Iran,.

Joseph, R. (1993). *ASM Specialty Handbook, Aluminum and aluminum Alloys,* ASM International, 087170496X, USA (448–449)

Mills, K.; (1993). *Metals Handbook, Volume 12, Fractography*, ASM International, 978-0-87170-018-6, USA

Moussavi Torshizi, S.E.; Yadavar Nikravesh, S.M. & Jahangiri, A. (2009). Failure analysis of gas turbine generator cooling fan blades. *Engineering Failure Analysis,* 16., (1686–1695)

Newman, J.r.J.C. (1984). A crack opening stress equation for fatigue crack growth. *Int J Fract*, 24(4)., (131–135)

Newman, J.r.J.C, & Raju, I.S. (1984). Prediction of fatigue crack-growth patterns and lives in three-dimensional cracked bodies. *Advances in fracture research (Fracture 84), sixth international conference on fracture*, 3., (1597–1608)

OSM. Menu and Dialog Reference, (2002). *Developed by the Cornell Fracture Group,* Cornell University, V2.2

Poursaeidi, E. & Salavatian, M. (2007). Failure analysis of generator rotor fan blades. *Engineering Failure Analysis,* 14., (851–860)

Poursaeidi, E. & Salavatian, M. (2009). Fatigue crack growth simulation in a generator fan blade. *Engineering Failure Analysis*, 16., (888–898)

Rahimi ASL, R. & Soltani, M. (2003). *Calculating Fluid Dynamic (CFD) by the aid of FLUENT,* Nashre Tarrah publications

Paris, P.C.; Gomez, M.P. & Anderson, W.E. (1961). A rational analytical theory of fatigue. *Trend Eng*, 13(1)., (9–14)

Paris , P.C. & Erdogan, F. (1963). A critical analysis of crack propagation laws. *J Basic Eng*, 85., (528–534)

Popov, E.P. (1968). Introduction to mechanics of solids. *Prentice-Hall*, United States of America

Soh, A.K. & Bian, L.C. (2001). Mixed mode fatigue crack growth criteria. *Int J Fatigue,* 23., (427–439)

Steven, R.; (1993). *ASM Handbook, Volume 19, Fatigue and Fracture,* ASM International, 978-0-87170-385-9, USA

Tada, H.; Paris, P.C. & Irwin, G.R. (1985). The stress analysis of cracks handbook. 2nd ed. St Louis, MO: *Paris Productions Inc*, 2.2.

Vroman, G.A. (1983). Material thickness effect on critical stress intensity. *Monograph #106, TRW Space & Technology Group*

White, F.M. (2003). Fluid mechanics. *McGrow-Hill*, United States of America

Xi, N.S.; Zhong, P.D.; Huang, H.Q.; Yan, H. & Tao, C.H. (2000). Failure investigation of blade and disk in first stage compressor. *Eng Fail Anal*, 7., (385–392)